Catalytic Proton-Coupled Reductions of Dinitrogen and Cyanide

Thesis by

Christian Marinelli Johansen

In Partial Fulfillment of the Requirements for the

Degree of

PhD of Chemistry

CALIFORNIA INSTITUTE OF TECHNOLOGY

Pasadena, California

2025

(Defended March 18th, 2025)

Christian Marinelli Johansen

ORCID: 0000-0003-0066-4424

ACKNOWLEDGEMENTS

Bergvæg, brist med drøn og brag
for mit tunge hammerslag!
Nedad må jeg vejen bryde,
til jeg hører malmen lyde.

Henrik Ibsen, «Bergmannen»**,** 1861

A PhD, especially one as long as mine, requires many people's personal and scientific support. First, I must thank Professor Jonas Peters for his guidance and partnership throughout. A PhD is a maturation process both as a scientist and a person, but I came to Caltech probably lacking more in both areas than is ideal. Thankfully, I ended up in Jonas' group, where his patience and belief in me have allowed me to develop substantially, and he has had a tremendous influence on how I think about chemistry, problem-solving, and narrative. He has impeccable instincts, and for many of the projects discussed in this thesis, I can point to direct comments from Jonas in making these projects work. I will miss our discussions and jabs back and forth during group meetings. The Peters group is a wonderful place, consistently producing fascinating and novel science, and it all works because of Jonas' excitement for science, humor, and love for his students.

Throughout my time at Caltech, the Peters group has always been a great source of feedback, discussion, and camaraderie. Every past and present member has provided interesting ideas and feedback throughout. I have been fortunate to collaborate with several group members throughout my PhD. Emily and I worked on two projects (Chapters 4 & 6); both times, she was a fantastic collaborator, and while they were intense times, they are certainly some of the most memorable of my PhD. Beyond these projects, her opinion is one I have relied on heavily. Emily is also a great karaoke partner; I hope we have not done our final rendition of "Under the Bridge".

I have also had the pleasure of working with Drew and Seungju on projects relating to Samarium photochemistry and iron cyanide reductions, respectively. I recommend having younger students with better hands and more creative experimentation follow up on your leads; seeing where they are taking this chemistry is exciting. Elisabetta worked with me on the mechanism of Hantzsch ester photoreductions, providing key transient absorbance data

and was a useful sounding board as the mechanism was put together. In addition, Yueshen and Nick provided key support on gas quantification and Sayan on computations, all critical to the works discussed herein.

In addition to my direct collaborators for this thesis work, there are many other group members to thank. As noted, I arrived at Caltech quite undercooked. Encouragement and inspiration from older students, particularly Matt, Meaghan, Nina, and Kareem, were critical in getting me up to speed. Neither of these projects are in this thesis, but I learned much from working with Matt on nitrite reduction and Nina on Cobalt hydride chemistry. Meaghan's critical eye is something I still try to apply when thinking about mechanisms, and I learned a lot from sitting next to her for the first year and a half in the Peters group.

I joined the Peters group with Pat and Teddy in my cohort; while both left the group within two years, they were still important in my settling in. Dirk and Mike, in the years above and below me, respectively, were also valuable people to chat with through the years, and I learned a lot from Mike's drive. Many postdocs, Alonso, Cooper, Heejun, Pablo, Joe, Lucie, Stefan, John, and Hoimin have been a combination of sounding board and friends to grab a beer with after work. Looking back, I think the encouragement from Lucie and Heejun was vital in gaining confidence and, ultimately, some success in my chemistry. John and Stefan have been good friends in the later years, and I have had many memorable outings with both.

I am also thankful to my bay-mates, Meaghan, Sasha, Enric, Joe, and Teja for many fun chats, science and otherwise, over the years, I have drawn upon their knowledge and opinions a lot. Similarly, I must thank my box-mates, Marcus, Nina, Ammar, Sasha, Seungju, and Sungchan, for putting up with me all these years. Marcus and Nina were also invaluable in helping me in the glovebox work in the early years. Somehow falling outside all these categories, Madeline, Mengdi, Catherine, and Alex have also been fun people to chat with in lab, at group retreats, and around campus. I have also had the pleasure of mentoring two undergrads, Sanjana and Luke. Their excitement for science has been inspiring, and I look forward to seeing what they continue to do.

While I have probably underutilized my committee, I am thankful for their support and insight during our meetings and beyond. In addition to Professor Theo Agapie's role as

my chair, I have learned a lot from his class and TAing for him (and Jonas) in 2020. Professor Greg Fu has always been a friendly face around Schlinger; he is always very good about sending thanks every time you help out one of his students, something I have always appreciated. I have also gotten a lot from Theo and Professor Karthish Manthiram's input during the RSI impact grant meetings in the last two years. In addition, Karthish allowed me to attend his group meetings in the summer of 2024; this experience helped me define what I want to do going forward.

One of the things that makes Caltech such a wonderful place to learn and do chemistry is the engaged and knowledgeable staff of scientists and the top facilities they maintain. Although I have never taken full advantage of his skills and instrumentation, Paul Oyala has always been fantastic for any EPR questions that might arise. He is also a great guy to grab a beer with at a chemistry social, or go to a bar with for a game, trivia, or otherwise. His humor and levelheadedness have been important in getting me through my PhD.

Dave Vande Velde runs an excellent NMR facility and provides great help and pulse-sequencing as required. Nathan Dalleska's Minnesotan charm and GC insights were key to the methane detection for the cyanide reduction project. I might have a record for the fewest crystal structures for a Peters' group PhD, but at the times I needed them, Mike Takase and Larry Henling provided great help. Nate has always been a friendly face, and his glassblowing skills have enabled many experiments I have wanted to try. In addition to the scientific staff, the administration and facilities at CCE are all wonderful. Julianne's role as the group admin has been particularly critical to my time here, both for scheduling and stopping by for a friendly chat.

Other research groups have provided good friends and discussions over the years. The Agapie lab has been home to many, like Arnaud, Linh, Angela, and Mike. The importance of such friends was felt recently as Mike, Adjeoda, and I sheltered at Angela's parent's house in Irvine during the recent fires in Pasadena/Altadena. Angela is also one of the few people I can text with about professional cycling, and I have had much fun live-commenting on the bike races with her. Jaron has also always been a kind and supportive friend. I am also thankful to countless grad students and postdocs in the Fu, Reisman, Stoltz,

Hadt, Gray, Arnold, and Manthiram groups for their help with experiments, instrumentation, discussion, and lending of chemicals over the years.

Many have already been thanked, but the reborn “Inspector Gadget” trivia team, with regulars Paul, John, Emily, Nate, Katie, and irregulars Erica and Fernando, has been a great source of fun in the last year. My roommates in my first year, Stephen, Richard, and Nicki, as well as Tom, were important in settling into Pasadena, and we have had many fun nights over the years.

Beyond Caltech, I am very thankful to my early chemistry teachers, Kristian Vestli in high school, Professor Jonathan Goodman at Cambridge, and Professor Ullrich Steiner, Antonio Abate, and Bart Roose, during my research stay in Switzerland in the summer of 2016. All of them were important to my current path.

My friends in Norway and the UK have remained an important support network throughout, and I have had a lot of good times with them during my PhD. Notable events include going to Yannis and Ellie (F.) visiting LA, meeting up with Rex halfway in New York, meeting up with Aaron and Ben nowhere near halfway in Barcelona, seeing the whole UK gang at Freddie’s house in the Forest of Dean, my friends in Norway visiting me the summer I worked in Bergen, as well as dinners, parties, concerts, and trips to the mountains, with some combination of Eivind, Johannes, Eirik, Helle, and Vilde when I am home in Oslo. I also have a tremendously supportive collection of grandparents, aunts, uncles, and cousins on the East Coast and in Norway. Particularly memorable are various visits to California from Celia, Roger, Zach, Laura, Ashley, and Mike, lunches/dinners with my grandparents in Oslo and Rockville, and going out with my cousins. My siblings, Emma and Thomas, have also given a lot of support, and I have been able to show both of them the Pacific during my time here.

Finally, I need to thank my parents for their unconditional love and support. I have inherited my love of science from my father, and he has given me a lot of good advice over the years. As an added bonus, my mother has experience dealing with the ups and downs of watching a Norwegian try to get their PhD in the US and has known how to support me when needed. I could not have done it without them.

ABSTRACT

This thesis, directly and indirectly, focuses on mechanisms and strategies for the $6H^+/6e^-$ reduction of N_2 to NH_3 (nitrogen reduction; N_2R) using well-defined molecular catalysts. In nature, nitrogenases reduce N_2 to NH_3, but nitrogenases can also reduce cyanide to CH_4 and NH_3, making CN^- and N_2 reduction interesting to compare. We describe the highly selective catalytic reduction of CN^- to NH_3 and CH_4 by a mononuclear Fe-catalyst related to Fe-based N_2R systems. Mechanistic studies suggest several intermediates, including iron isocyanides (FeCNH), aminocarbynes ($FeCNH_2$), and aminocarbenes ($FeC(H)NH_2^+$), allowing a comparison to N_2R. We then show the $2H^+/2e^-$ equilibration of iron cyanide to the iron aminocarbyne complexes of these early intermediates of catalysis. Such reversible triple bond activations are rare. We show that key to this transformation is the H-bond facilitated multisite proton-coupled electron transfer (MS-PCET).

Next, seeking alternative ways to drive N_2R, a photodriven approach is explored. The Hantzsch ester (HEH_2), a dihydropyridine, is utilized as a $2H^+/2e^-$ photoreductant, and when partnered with a suitable catalyst (Mo) and an organic buffer (collidine/collidinium; Col/$ColH^+$) under blue light irradiation allows for photodriven N_2R. Catalysis is enhanced by addition of a photoredox catalyst (Ir). This photodriven N_2R is thermodynamically comparable to the industrial hydrogenation of N_2, but light is used to drive the reaction. Mechanistic studies of the Ir-free conditions show that Col-buffer is essential for transferring H^+/e^- from HEH_2 to N_2. An H-bonded pre-association can form between $[ColH]^+$ and HEH_2, allowing for rapid oxidative quenching of the excited HEH_2. Subsequently, the base deprotonates $HEH_2^{\bullet+}$, circumventing back electron transfer. In net $ColH^\bullet$ and $HEH^\bullet$, two potent H-atom donors are generated. This reagent combination is competent for the photoreduction of organic substrates as well. Lessons from this mechanistic study drove the development of photodriven methods for Sm^{III}-to-Sm^{II} reduction, an appealing prospect given SmI_2 being a potent and selective reductant, including for N_2R. HEH_2 can serve either as a direct photoreductant or as the reductive quencher for an Ir photoredox catalyst. Both methods for SmI_2 generation translate to proof-of-concept photodriven, Sm-catalyzed reductive cross-coupling reactions.

PUBLISHED CONTENT AND CONTRIBUTIONS

1. Johansen, C. M.; Peters, J. C. *J. Am. Chem. Soc.* **2024**. 146, 5343–5354. https://doi.org/10.1021/jacs.3c12395.

In this manuscript, I performed all of the experiments and wrote the manuscript with J.C.P.

2. Johansen, C. M.; Boyd, E. A.; Peters, J. C. *Sci. Adv.* **2022**. 8, eade3510. https://doi.org/10.1126/sciadv.ade3510.

In this manuscript, I contributed to the conception of the project, designed and conducted catalytic and mechanistic experiments, and wrote the manuscript with the other authors.

3. Johansen, C. M.; Boyd, E. A.; Tarnopol, D. E.; Peters, J. C. *J. Am. Chem. Soc.* **2024**. 146, 25456–25461. https://doi.org/10.1021/jacs.4c10053.

In this manuscript, I contributed to the conception of the project, designed and conducted catalytic and mechanistic experiments, and wrote the manuscript with the other authors.

TABLE OF CONTENTS

LIST OF ILLUSTRATIONS AND TABLES

Chapter 3

Chapter 4

Chapter 5

Chapter 6

NOMENCLATURE

AO. Ammonia oxidation.

ATP. Adenosine Triphosphate.

Atm. Atmosphere.

[BAr$^{F}_{4}$]$^{-}$. Tetrakis[3,5-bis(trifluoromethyl)phenyl]borate.

BET. Back electron transfer.

BDFE. Bond dissociation free energy.

Col. 2,4,6-trimethylpyridine.

CO_2R. CO_2 reduction.

Cp. Cyclopentadienyl.

Cp*. Pentamethylcyclopentadienyl.

CPET. Concerted proton-electron transfer.

cw-EPR. Continuous wave-EPR.

DBU. 1,8-Diazabicyclo(5.4.0)undec-7-ene.

depe. 1,2-Bis(ethylphosphino)ethane.

DFT. Density functional theory.

DMSO. Dimethylsulfoxide.

dppe. 1,2-Bis(phenylphosphino)ethane.

dtbbpy. 4,4′-Di-tert-butyl-2,2′-dipyridyl.

DTPA. Diethylenetriaminepentaacete.

EDA. Electron donor-acceptor.

EIE. Equilibrium isotope effect.

EPR. Electron paramagnetic resonance.

equiv. Equivalents.

ET. Electron transfer.

^{Et}Cp. Ethyl cyclopentadienyl

Et_2O. Diethyl ether.

Fc. Ferrocene.

FWHM. Full-width half max.

HAT. Hydrogen atom transfer.

H-bonding. Hydrogen bonding.

HER. Hydrogen evolution reaction.

HMPA. Hexamethylphosphoramide.

IR. Infrared.

KIE. Kinetic isotope effect.

LED. Light-emitting diode.

Ln. Lanthanide.

Lut. 2,6-dimethylpyridine.

^{Me4}Cp. Tetramethylcyclopentadienyl.

MeCN. Acetonitrile.

MS-PCET. Multisite proton-coupled electron transfer.

NADH. Nicotinamide-adenine dinucleotide.

NMR. Nuclear magnetic resonance.

N_2R. N_2 reduction.

N_2RR. N_2 reduction reaction.

[OTf]$^-$. Trifluromethanesulfonate.

[OTs]$^-$. Toluenesulfonate.

PCET. Proton-coupled electron transfer.

PCP. 1,3-bis((di-*tert*-butylphosphino)methyl)benzimidazol-2-ylidene.

PNP. 2,6-bis(di-tert-butylphosphinomethyl)pyridine.

PT. Proton transfer.

P_3^B. tris-(o-diisopropylphophinophenyl)borane**.**

P_3^{Si}. tris-(o-diisopropylphophinophenyl)silyl.

PhBP$^{iPr}_3$. tris-(diisopropylphophinomethyl)phenylborate.

ppy. 2-phenyl pyridine.

Pyr. Pyridine.

ROH. Protic donor (water or alcohol).

RT. Room temperature.

sub. substrate.

TA. Transient absorbance.

TBA. Tetrabutylammonium.

TBD. 1,5,7-Triazabicyclo[4.4.0]dec-5-ene.

TD-DFT. Time-dependent density-functional theory.

[TFSI]$^-$. bis(trifluoromethane)sulfonimide.

THF. Tetrahydrofuran.

tol. tolyl

$t_{1/2}$. Half-life.

12-c-4. 1,4,7,10-tetraoxacyclododecane.

UV-vis. Ultraviolet-visible.

Chapter 1

Introduction

1.1 Motivation

This thesis explores the reductive protonation of triply bonded small molecules, such as dinitrogen (N_2) and the cyanide anion (CN^-). Particularly critical is the reduction of N_2. All nitrogen in biomolecules is sourced from N_2, primarily through its industrial and biological reduction to ammonia (NH_3).[1] NH_3 also holds potential as a solar fuel due to its energy density and the availability of N_2.[2]

The industrial Haber-Bosch reaction, critical to synthetic fertilizer production, hydrogenates N_2 to NH_3.[1] This is a mildly exothermic reaction, but requires high temperatures and pressures, as well as a catalyst to activate kinetically inert N_2 (Figure 1.1). These reaction conditions are associated with high energy requirements and favor large, centralized NH_3 production. In addition, the H_2 for the Haber-Bosch process is sourced from steam reformation of methane, resulting in considerable CO_2 emissions.[1]

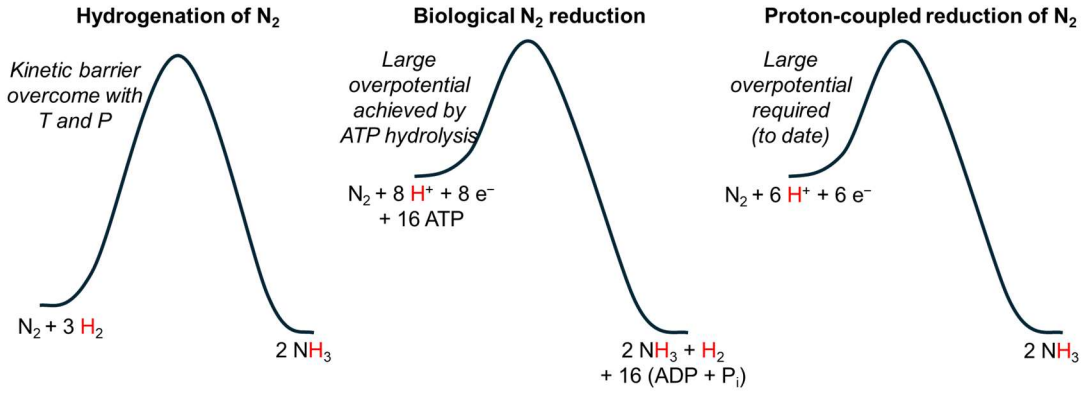

Figure 1.1. The energy input for industrial, biological, and chemically/electrochemically driven N_2R.

As an alternative, N_2 can be reductively protonated by $6H^+/6e^-$ at ambient conditions to yield NH_3 (nitrogen reduction, N_2R), with heterogeneous,[3] homogeneous,[4] and enzymatic[5] examples. However, to overcome the barriers associated with N_2 activation, examples of N_2R utilize a chemical overpotential − ATP hydrolysis in biological N_2R[6] or a highly cathodic overpotential or strong reductants in heterogeneously/homogeneously catalyzed N_2R (Figure 1.1).[4,7] The works discussed herein are directly or indirectly concerned with this overpotential. Two major topics are covered: the Fe-catalyzed chemical reduction of CN^-, a

reaction with interesting parallels to N_2R, and the development of photodriven N_2R and resulting photochemical insights. This introduction will provide context for these two topics and present some overarching themes.

1.2 Definitions relating to proton-coupled electron transfers

This thesis concerns proton-coupled reductions, a field that suffers from a variety of similar and ever-developing terms. It is therefore useful to define some phrases as I use and understand them.[8,9] A *proton-coupled reduction* (used interchangeably with *reductive protonation*) involves the addition of H^+/e^- to a substrate, forming X–H bonds during substrate reduction. Relevant to this thesis is the $6H^+/6e^-$ reduction of N_2 to 2 equivalents of NH_3 and the $7H^+/6e^-$ reduction of CN^- to yield CH_4 (methane) and NH_3. Both these transformations require a catalyst to activate the substrate, but the reagent(s) supplying H^+ and e^- are also critical.

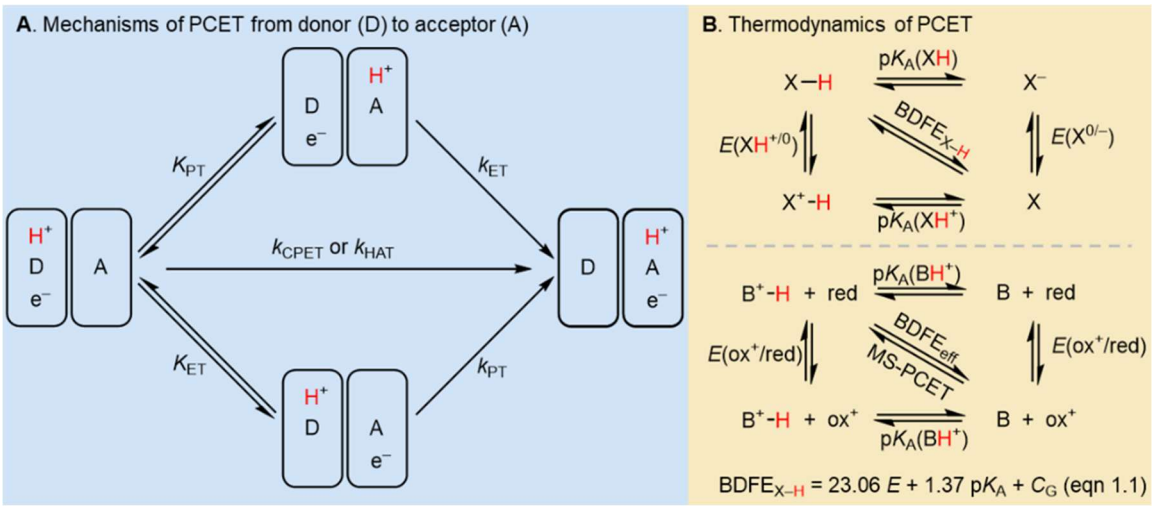

Figure 1.2. Mechanisms and thermodynamics of proton-coupled electron transfer.

Proton-coupled reductions might involve one or more *proton-coupled electron transfer* (PCET) steps. PCET implies that the transfer of a proton and an electron from a donor to an acceptor is kinetically or thermodynamically coupled. A PCET mechanism may still occur via sequential proton transfer (PT) and electron transfer (ET), e.g., via a pre-equilibrium (Figure 1.2A). If the PT and ET are kinetically coupled, we might designate the step as a concerted proton-electron transfer (CPET) or a hydrogen atom transfer (HAT). The

distinction lies in whether the H^+ and e^- are transferred to different orbitals (CPET) or the same orbital (HAT).[10]

An important mode of PCET reactivity is multisite-PCET (MS-PCET).[11,12] In the reductive direction, such reactions involve transferring the H^+ and e^- from different molecules to form one X−H bond. The entropic barrier associated with these termolecular steps often requires pre-coordination of one of the reagents, e.g., via H-bonding.

The thermodynamics of net $H^\bullet$ transfer between PCET reagents can be readily compared using the Bordwell equation (Figure 1.2B, eqn 1.1).[13,14] The inputs of reduction potential, acidity, and a solvent-dependent constant (C_G) allow us to calculate the bond dissociation free energy (BDFE) for a (net) HAT donor or a combination of reagents that perform MS-PCET (designated as effective BDFE; $BDFE_{eff}$). The $BDFE_{eff}$ values determined can be related to the thermodynamics of a proton-coupled reduction. For example, $BDFE_{eff}$ can be compared to $BDFE(H_2)_{H–H}$ or $BDFE(NH_3)_{N–H,\ ave}$ to assess the thermodynamics of hydrogen evolution reaction (HER) or N_2R, respectively.[7,15] Similarly, the $BDFE_{eff}$ can inform the kinetics of a reductive protonation. Simply stated, the weakest X−H bond formed during reductive protonation of a substrate is rarely much weaker than the $BDFE_{eff}$ supplied by reagent(s).[7,16] This basic principle can be used to rationalize and predict much of the reactivity discussed herein.

1.3 Biological Reductions of Dinitrogen and Cyanide

With this framework in place, we can introduce the proton-coupled reductions discussed in this thesis. Given our interest in modeling enzymatic reactivity to test and constrain mechanistic hypotheses, we first introduce the biological context for N_2 and CN^- reduction. Nitrogenase enzymes are the only class of enzymes known to reduce N_2 to NH_3.[5,6] This occurs at a metal-sulfur cluster active site, $[MFe_7S_9C]$ (M = V, Fe or Mo, abbreviated as [FeM]-cofactor; Figure 1.3 depicts the [FeMo]-cofactor, also know as FeMoco).[17] Two equivalents of NH_3 are generated, alongside one equivalent of H_2, with two ATP hydrolyzed per ET (i.e., 16 ATP are hydrolyzed per N_2 reduced, Figure 1.3). Nitrogenase enzymes are selective for NH_3 among N-fixed products, although the [VFe]-protein produces some hydrazine (N_2H_4; 4 e^- product).[18] Many parts of the mechanism of biological N_2R remain

poorly understood, such as the site(s) of N_2 binding, the six N−H bond formations, and the N−N bond cleavage step. However, the existence of [FeFe]-nitrogenases[19] and spectroscopic evidence from the heterometallic cofactors[20,21] suggest one or more Fe-sites play a key role in substrate binding and reduction.

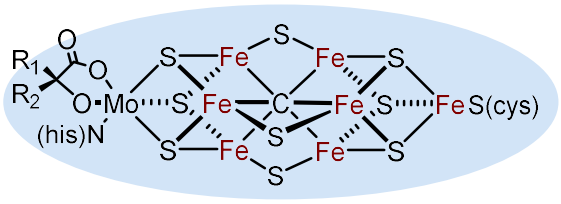

FeMo-cofactor - Active site of MoFe-protein

$N_2 + 8\,H^+ + 8\,e^- + 16\,ATP \xrightarrow[20\text{-}40\ ^\circ C]{\text{Nitrogenase}} 2\,NH_3 + H_2 + 16\,ADP$ (1 atm)

Ratio:N_2H_4/NH_3
MoFe protein: 0.0
VFe protein: 0.001-0.01

$HCN + 6\,H^+ + 6\,e^- + 12\,ATP \xrightarrow[25\ ^\circ C,\ 1\ atm\ Ar]{\text{Nitrogenase}} NH_3 + CH_4 + 12\,ADP$

Ratio: CH_3NH_2/CH_4
MoFe protein: 0.4
VFe protein: 0.6-1.1
Trace C_2H_4, C_2H_6 and CH_2NH

Figure 1.3. Comparison of N_2 reduction and HCN reduction at nitrogenase enzymes.

Interestingly, nitrogenases can reductively protonate several other substrates, including triply bonded small molecules like acetylene (HCCH),[22] carbon monoxide (CO),[23] methyl isocyanide (CNMe),[24,] and hydrogen cyanide (HCN).[25] Similar to N_2R, these reactions occur at the [FeM]-cofactor and require ATP to drive ET. HCN is reduced to primarily CH_4+NH_3 (6 e^- product) and methyl amine (CH_3NH_2; 4 e^- product), with methyl imine (CH_2NH; 2 e^- product) and trace C_2 products (ethane and ethylene) also detected (Figure 1.3).[16,26,27,28] Unlike the reduction of N_2, the coevolution of H_2 is not required. The isolobal analogy between substrate and products in cyanide and nitrogen reduction has motivated the mechanistic comparison of these two proton-coupled reductions.[29,30]

1.4 Catalytic N_2 reduction with well-defined molecular complexes

Well-defined molecular complexes, more amenable to spectroscopic studies and systematic variation, can also reduce N_2 to NH_3.[4,31] These systems can guide hypotheses

relating to substrate reduction at the nitrogenase active site and provide strategies for more efficient N_2R.

Building on studies of the protonation of terminal dinitrogen complexes ($M{-}N_2$; M = Mo or W) to yield NH_3,[32,33] Yandulov and Schrock demonstrated the first example of the catalytic reduction of N_2 to NH_3 with a well-defined molecular catalyst.[31,34] This first catalytic system used a (trisamidato)amine molybdenum ($(N_3N'Mo)$) precatalyst and decamethylchromocene (Cp^*_2Cr; $E_{1/2}(Cr^{III/II}) = -1.47$ V vs. $Fc^{+/0}$ in THF; all redox potentials are vs. $Fc^{+/0}$ in THF)[35] and 2,6-dimethylpyridinium ([LutH]BAr^F_4, pK_a 9.5 in THF, all pK_a in THF)[36] as the e^- and H^+ sources.

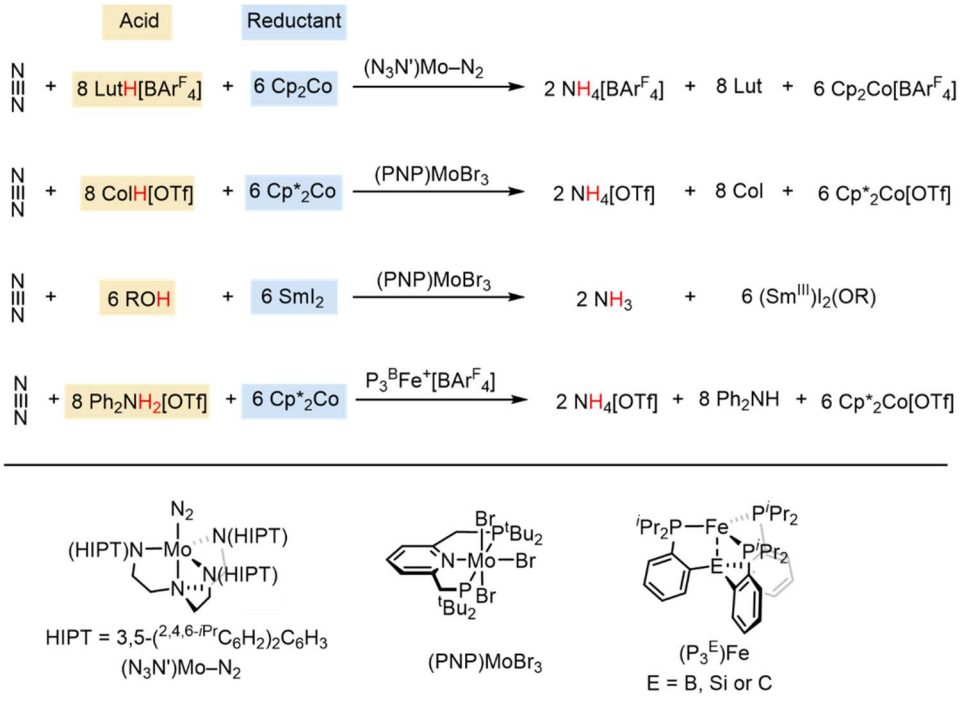

Figure 1.4. Conditions and catalysts for molecular catalytic N_2R critical to the work discussed in this thesis.

In 2011, Nishibayashi and coworkers introduced the bis(phosphino)pyridine pincer-molybdenum complex, $[((Mo)(N_2)_2)_2(\mu\text{-}N_2)]$ as a precatalyst for N_2R.[37] This first report used cobaltocene (Cp_2Co; $E_{1/2}(Co^{III/II}) = -1.33$ V) and LutH[OTf] as the e^-/H^+ source. Later it was shown that using trihalide precatalysts, $(PNP)Mo^{III}X_3$ (X = I or Br), and a more potent

reductant, decamethylcobaltocene (Cp^*_2Co; $E_{1/2}(Co^{III/II})$ = −1.97 V), and 2,4,6-trimethylpyridinium triflate ($[ColH]^+$; pK_a 10.4) acid, yields and rates improved.[38] Further improvements were achieved using SmI_2 ($E_{1/2}(Sm^{III/II})$ = −1.55 V) as a reductant and alcohol as the proton source (ROH, e.g., ethylene glycol).[39] These Sm-based reactions yield $Sm^{III}(OR)$ as the spent acid/reductant. Since this report, remarkable progress has been made in recovering such reagents[40] including a photochemical method presented in Chapter 6.

The proposed role of Fe in biological N_2R has motivated the study of Fe-catalyzed N_2R. The Peters group reported the first example of catalytic N_2R using an iron tris(phosphino)borane precatalyst (P_3^BFe) and initially with $[H(OEt_2)_2]BAr^F_4$ (pK_a < 0) and reductant KC_8 ($E(K^{0/+})$ <−3 V) as the H^+/e^- source.[41] Subsequent studies have shown that softer reagents, Cp^*_2Co and chlorinated anilinium triflates ($ArNH_3[OTf]$; pK_a 1.2 to 8.0, best yields with pK_a 4.3), showed improved yields.[42,43] Interestingly, the N-fixed products of Fe-catalyzed N_2R can be shifted from NH_3 to N_2H_4 by shifting the precatalyst,[44] acid/reductant choice,[45] or irradiation.[46]

Mechanistic experiments and the characterization of intermediates have allowed detailed mechanistic pictures to be built up for these described molecular systems. The Chatt cycles, initially used to describe stoichiometric N_2 protonations, have found significant utility in describing the Schrock group's Mo-catalyzed N_2R and the Fe-catalyzed systems described by the Peters group.[4,47] The Chatt cycles are monometallic pathways starting from terminal dinitrogen complexes (M−N≡N; Figure 1.5). In the Distal Chatt cycle, $3H^+/3e^-$ are first added to N_β, with N−N bond cleavage giving an equivalent of NH_3 and a metal nitride (M≡N). The nitride is then reductively protonated to yield a 2nd equivalent of NH_3. The Alternating Chatt cycle sequentially forms N_β−H and N_α−H bonds and can yield N_2H_4 from hydrazyl intermediates ($MN(H)NH_2$). However, evidence from both W and Fe complexes has shown that stoichiometric reactivity of the respective terminal hydrazido complexes ($M{=}N{-}NH_2$) can also yield N_2H_4.[32,48] It is proposed that N_α−H bond formation from the hydrazido yields the hydrazyl intermediate, allowing for N_2H_4 formation (this is designated as the Hybrid Distal-to-Alternating cycle). Therefore, hydrazidos are often the selectivity-determining intermediate in N_2R (at least for N-fixed products).

While hydrazidos are selectivity-determining intermediates, the overpotential of molecular N_2R via a Chatt cycle is proposed to be determined by the 1st N–H bond formation, i.e., to form the metal diazenido (M–N=N–H). In fact, there is often a close correlation between $BDFE_{N–H}$(M(NN–H)) and the $BDFE_{eff}$ of acid/reductant combinations used in the described catalytic reactions.[7]

Another pathway relevant to catalytic N_2R is the nitride splitting pathway. Access to a bimetallic dinitrogen complex allows splitting into two metal nitrides[49] that can be reductively protonated to yield NH_3 (Figure 1.5).[4] N_2R with (PNP)$MoBr_3$ precatalysts (Cp^*_2Co/ColH[OTf] or SmI_2/ROH as reactants) are thought to proceed through this mechanism via a [Mo^I–N≡N–Mo^I] intermediate.[50]

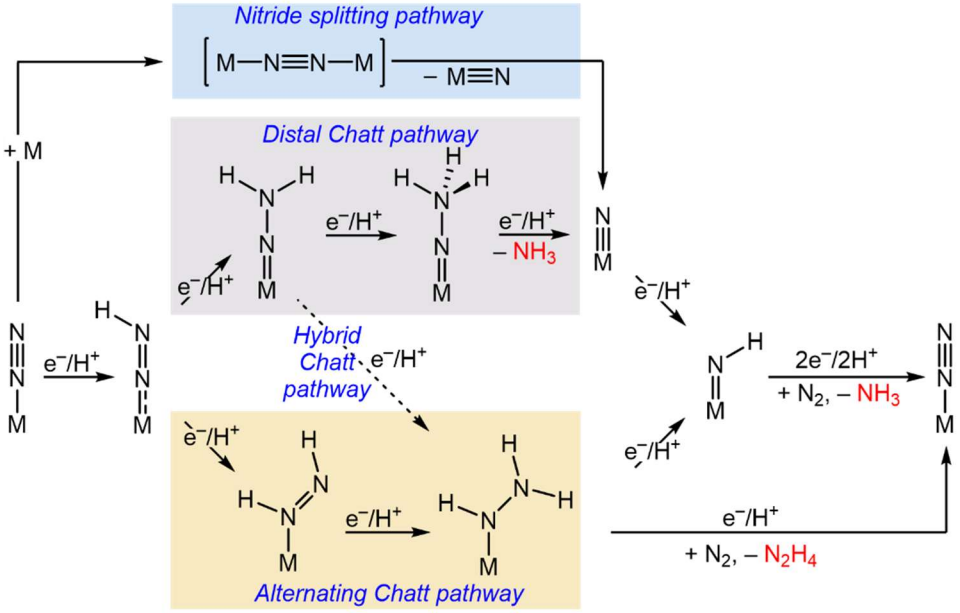

Figure 1.5. Mechanisms of catalytic N_2R at well-defined molecular complexes.

1.5 Cyanide Reduction

The role of HCN as a non-native substrate of nitrogenase has motivated the study of cyanide reduction. ATP-independent reductions of CN^- with extracted or synthetic Fe–S clusters have been reported using Eu^{II}(DTPA)/pH 8 buffer or SmI_2/[LutH]OTf as a reductant/acid.[51,52,53,54] These Fe–S cluster-catalyzed reactions yield substantial C_{2+} products

(~20%) regardless of the choice of precatalyst or conditions. While the observed C_{2+} products are undoubtedly interesting, this does suggest a mechanism that diverges from that observed by nitrogenase under ATP-dependent conditions. In addition, a lack of spectroscopic or mechanistic data has limited comparisons to N_2R. Electrochemical reduction and hydrogenation of HCN using heterogeneous catalysts have also been demonstrated.[55,56]

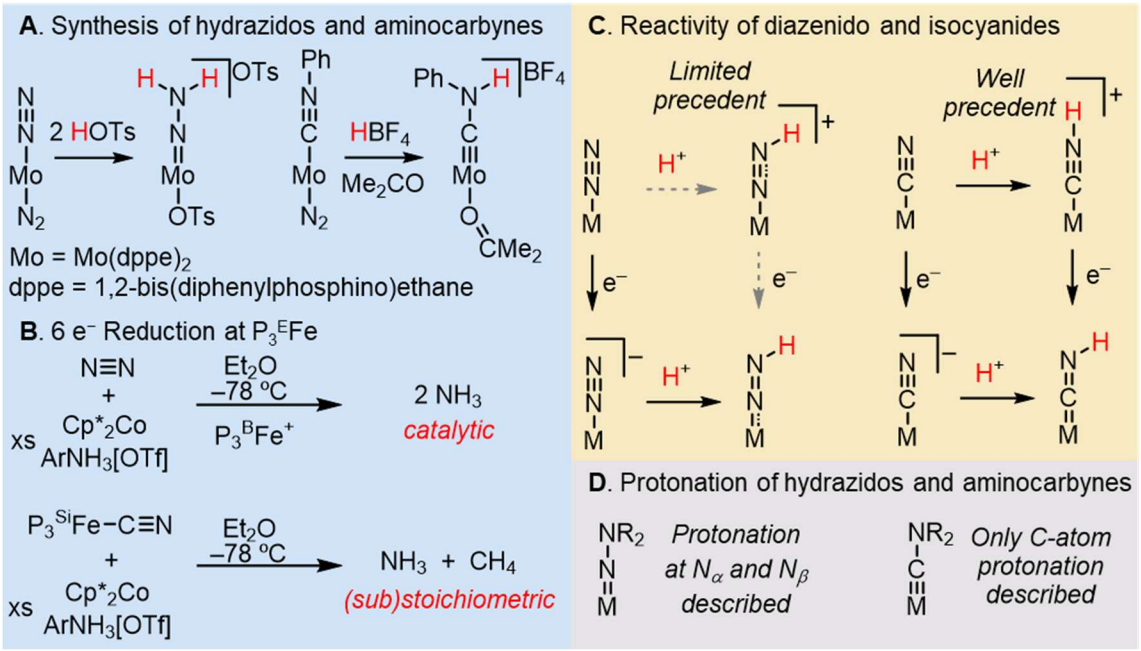

Figure 1.6. Comparison of molecular CN^- reduction and N_2R. $ArNH_3$ = $^{2,5\text{-Cl}}PhNH_2$.

Stoichiometric reductions of cyanide and isocyanide with well-defined molecular complexes have also been explored, often using the framework provided by the Chatt cycles.[57,58] The monoprotonation of d^6 alkyl and aryl isocyanide complexes yields aminocarbynes,[59,60,61,62] analogs of the hydrazidos invoked in N_2R (Figure 1.6A).[63] Further protonation of these complexes can yield primary amines, consistent with 6 e^- reduction of the isocyanide ligand. However, low amounts of CH_4 suggest hydrolysis is a considerable side reaction.[60,64,64] Our laboratory has previously shown stoichiometric CN^- reduction to CH_4 and NH_3 at a mononuclear Fe-complex with a tris(phosphino)sylil ligand (P_3^{Si}).[65] This reaction resembles the Fe-catalyzed N_2R with similar catalysts and reagent combinations (Figure 1.6B). Iron aminocarbynes were characterized and invoked as intermediates of this cyanide reduction.

With the molecular reduction of N_2 and CN^- introduced, we can highlight some key contrasts explored in Chapters 2 and 3. The CN^- ligand is more basic than N_2, with linear ($\angle$C−N−H ~ 180°) isocyanide geometries that maintain the C−N triple bond readily available (Figure 1.6C).[66] By contrast, the N_2 ligand requires greater activation before it can be protonated, with diazenido species typically featuring bent geometries and decreased N−N bonding. These differences might allow for different mechanisms of early N−H bond formation.

Following early N−H bond formation, the differing reactivity of hydrazidos and aminocarbynes might provide interesting contrasts. As noted, transition metal hydrazidos often determine selectivity for NH_3 or N_2H_4 via N_β or N_α−H bond formation, with catalytic and stoichiometric evidence for both reactivity patterns.[33,48**Error! Bookmark not defined.**,67,68,69] By contrast, examples of aminocarbyne protonation exclusively show C−H bonds to yield aminocarbenes,[70,71,72] an interesting observation in light of the selectivity for CH_4 and NH_3 observed in many CN^- reduction reactions (Figure 1.6D). However, discussions of the frequently observed selectivity for CH_4 and NH_3 were lacking in the literature.

1.6 Photodriven N_2R: Motivation and approach

As noted, N_2R requires an energy input, which, under ambient conditions with molecular catalysts, is supplied by a chemical overpotential from strong reductants and/or acids (Figure 1.1). How to lower this overpotential is a fascinating question that has motivated a lot of beautiful chemistry, and I would direct readers to some of the chemistry developed in parallel with my own thesis work.[73,74] However, zooming out, it is striking that despite considerable improvements in turnover number, utility, rate, and selectivity, the overpotential for chemical N_2R has not improved in 20 years. This motivated the exploration of alternate methods to generate high overpotentials.

An alternate approach to achieve large chemical overpotentials with otherwise mild reagents is to use light as the additional energy input. While small molecule activations such as hydrogen evolution,[75] CO_2 reduction (CO_2R),[76] and water oxidation[77] have received considerable attention, such an approach had not previously been disclosed in the molecular N_2R literature. Proposed examples of photodriven N_2R with semiconductors, including in

concert with nitrogenase, have been reported, but low yields and/or high amounts of non-N_2 derived NH_3 remain issues.[78,79,80,81]

Upon excitation by a photon, the reducing power of a photoreductant or photocatalyst increases, allowing it to be the strong reductant required for N_2R. Based on this principle, we envisioned a chemical system for which a dark reaction has an overpotential for N_2R close to 0, but upon irradiation, sufficient driving force is generated by photogenerated reductants (Figure 1.7C, left panel). Such a system might provide a thermodynamic analog of the Haber-Bosch reaction, but instead of temperature and pressure, the reaction would be driven by light.

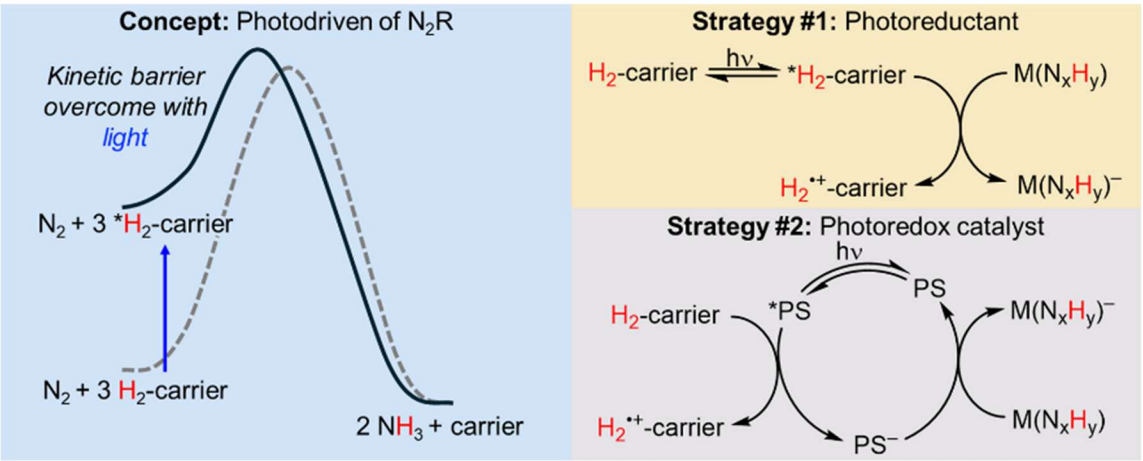

Figure 1.7. Concept for photodriven N_2R with molecular complexes. The overpotential required for N_2R with molecular catalysts is supplied by excitation; two strategies are shown.

Ideally, H_2 could be used directly, but while there are examples of photoactivation of H_2 or N_2, integration into catalytic N_2R cycles remains challenging.[82,83,84] As an alternative, H_2-carriers, reagents with labile H-atoms with a comparable overpotential for hydrogenation to H_2 can be used.[85,86] Such reagents can be directly photoexcited[87,88] or used in conjugation with a photoredox catalyst.[89,90] Unlike alkyl amines, common reductive quenchers in photodriven CO_2R or HER, H_2-carriers allow a large pK_a window for added buffers or acids, desirable attributes for N_2R, where a low pK_a is often required. In addition, clean oxidation of the carrier would allow for careful thermodynamic analysis.

The challenge then becomes how to, upon irradiation, convert the H^+/e^- stored in the H_2-carrier into reagents competent for the proton-coupled reduction of N_2. Using conditions for thermal N_2R as a guide, we envisioned two strategies in which the H_2-carrier might be activated to reduce N_2R intermediates (generalized as $M(N_xH_y)$). A photoactive H_2-carrier could directly reduce $M(N_xH_y)$ from the excited state (Figure 1.7, Strategy 1). Examples of such systems being employed in photodriven small molecule reductions are limited, but photooxidants, particularly quinones, have found use in water oxidation.[91,92,93] Alternatively, an explicit photosensitizer could be used (Strategy 2). Following excitation, the photosensitizer can then be reduced by the H_2-carrier to generate a persistent reduced photosensitizer. ET from the reduced photosensitizer to $M(N_xH_y)$, in net transfers e^- from the H_2-carrier. In both strategies, the oxidized H_2-carrier is a potent donor for $2H^+/e^-$ allowing for further ET and PT steps in N_2R.[94,95] The inclusion of a buffer was posited to help facilitate these PT steps.

1.7 Hantzsch ester photoreductions

In short, both strategies worked, although the photoreductant strategy operates by a mechanism quite different from what we first envisioned. Attempting to understand this mechanism motivated investigations into the photochemistry of a specific H_2-carrier, the Hantzsch ester (HEH_2; Figure 1.8A), and given its importance in the latter half of this thesis, a short introduction is warranted.

HEH_2 is a dihydropyridine, similar to biological energy carriers like NADH. It was first synthesized in 1881[96] and has been known as a photoreductant for over 60 years.[87,97,98] The capabilities and limitations of the excited state of HEH_2 ($*HEH_2$) can be summarized in two key photophysical properties (Figure 1.8B): the excited state reduction potential, $E(HEH_2^{\bullet+}/*HEH_2) = -2.5$ V and excited state lifetime, $\tau_{1/2} = 200$ ps.[99] $*HEH_2$ will reduce many substrates, but the short, excited state lifetime limits diffusional reactivity. Therefore, $*HEH_2$ will reduce substrates that can pre-associate HEH_2 in the ground state (Figure 1.8C). π-stacked electron donor-acceptor (EDA) complexes are the most common mode by which such interactions have been described, utilized both in the reduction of simple organic

compounds and to activate R•-donors such as Katritzky salts ([$^{2,4,6\text{-Ph}}$PyrR]BF_4)[100] and *N*-hydroxyphthalimide esters.[101,102]

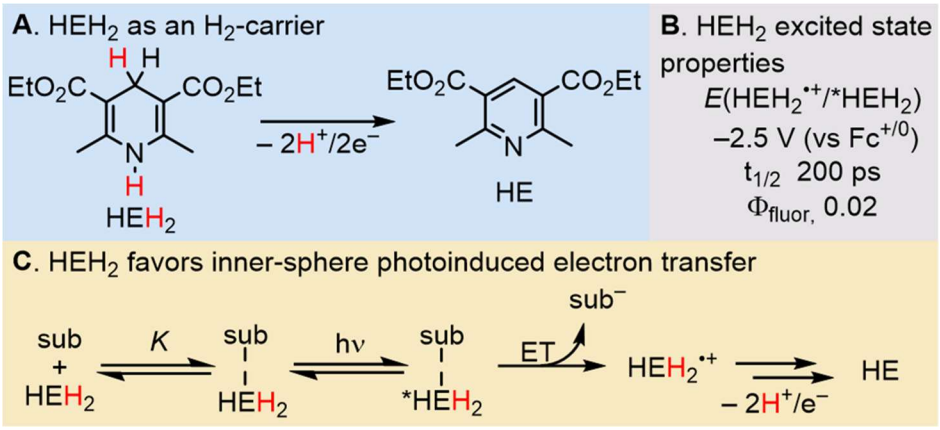

Figure 1.8. Key parameters of Hantzsch ester photoreactivity and potential utilization in selective reduction of substrates.

A question that arises when exploring HEH_2 photochemistry is the potential utility.[88] Are these photocatalyst-free reactions mere curiosities, or might they offer advantages beyond saving a few mol% precious metal photocatalysts? The short lifetime of *HEH_2 might provide a potential avenue by which one can achieve selectivity in photoreductions. Unlike long-lived or persistent photocatalysts, HEH_2 photoreductions require pre-association of the oxidant. This could allow for selective reductions in a pool of potential redox partners if one of them more strongly pre-associates to HEH_2. This motivates the further exploration of HEH_2 photochemistry beyond its application in N_2R, particularly understanding modes of pre-interaction and subsequent photoinduced electron-transfer steps.

1.8 Overview of the individual chapters

In **Chapter 2,** we developed conditions for the catalytic reduction of CN^- to CH_4 and NH_3 with high selectivity at a mononuclear Fe-site, $P_3^{Si}Fe$ using excess reductant ($(C_6H_6)_2Cr$; $E(Cr^{+/0}) = -1.22$ V) and acid (Ph_2NH_2[OTf]) to supply the required $7H^+/6e^-$. Following this discovery, we explored the mechanism of this reduction reaction, finding that terminal iron aminocarbynes ($P_3^{Si}FeCNH_2$) and iron aminocarbenes ($P_3^{Si}FeC(H)(NH_2)]^+$) as likely

intermediates. This mechanism is then compared to CN^- reduction at Fe−S clusters and N_2R at tris(phosphino)iron complexes, emphasizing the high selectivity for CH_4 and NH_3.

In **Chapter 3,** the initial steps of catalytic CN^- reduction, the $2H^+/2e^-$ conversion of $P_3^{Si}FeCN$ to $P_3^{Si}FeCNH_2$, are examined in detail. We demonstrate that these species can interconvert reversibly, an unusual observation in small-molecule triple bond reductions. The reductive reaction is studied over a wider range of conditions, with the previously measured thermochemistry of early N−H bonds of the iron cyanide platform found to be powerful predictors of reactivity. In addition, we analyze the kinetics of iron cyanide reduction to the iron aminocarbyne, finding that H-bonding to iron cyanide is key to a low barrier transformation. Finally, we evaluate factors enabling reversibility and discuss implications for lowering the driving force in Fe-catalyzed N_2R.

In **Chapter 4,** we develop conditions for the blue-light-driven reduction of N_2 to NH_3 using (PNP)$MoBr_3$ as a catalyst, HEH_2 as the H_2-donor, and Col-buffer. Unusually for a photodriven reduction reaction, an explicit photocatalyst was not required to observe N_2R. Still, the inclusion of an Ir-photocatalyst ($[Ir(ppy)_2(dtbbpy)]BAr^F_4$) boosted yields and rates. Under either set of conditions, the conversion of HEH_2 to the $2H^+/2e^-$ oxidized form, HE, allows for careful assessment of the thermodynamic effects of irradiation and suggests the possibility of photoreductant recovery/recycling. These conditions were also found to be competent for the reduction of nitrate to ammonia and acetylene to ethylene (with trace ethane).

Given the unusual efficiency of photodriven N_2R in the absence of a photocatalyst, in **Chapter 5**, we investigate the mechanism of this reaction further, focusing on the interaction of HEH_2 and Col-buffer. Through spectroscopic study, a detailed mechanism for the activation of HEH_2 by Col-buffer is proposed. In short, we observe H-bonding between HEH_2 and $[ColH]^+$ in the ground state. $[ColH]^+$ readily quenches $*HEH_2$, via a static quenching pathway, proposed as ET between the pre-associated species. Transient absorbance and EPR data suggest the base plays a critical role, rapidly deprotonating $HEH_2^{\bullet+}$. This results in the (net) formation of two potent H-atom donors, $ColH^\bullet$ and $HEH^\bullet$, with the

reduction of organic substrates used to benchmark their reactivity. Finally, some lessons for the photoreactivity of HEH_2 are discussed.

Finally, in **Chapter 6**, given the importance of SmI_2 as a selective one-electron reducing reagent for organic and inorganic reactions motivates the development of methods for Sm^{III} regeneration. However, photochemical methods illustrated to date were limited. Using lessons from Chapters 4 and 5, we developed conditions for the reduction of Sm^{III} precursors to SmI_2 via both a photoreductant approach with HEH_2 and a photoredox approach using HEH_2 as a reductive quencher with a photocatalyst, $[Ir(ppy)_2(dtbbpy)]PF_6$. Subsequently, we developed a proof-of-concept catalytic Sm-mediated ketone-acrylate coupling reaction.

1.9 Cited References

1. Smil, V. Enriching the Earth: Fritz Haber, Carl Bosch, and the Transformation of World Food Production; MIT Press: Cambridge, MA, USA, 2000.
2. Valera-Medina, A.; Xiao, H.; Owen-Jones, M.; David, W. I. F.; Bowen, P. J. *Prog. Energy Combust. Sci.* **2018**. 69, 63–102. .
3. Suryanto, B. H. R.; Matuszek, K.; Choi, J.; Hodgetts, R. Y.; Du, H.-L.; Bakker, J. M.; Kang, C. S. M.; Cherepanov, P. V.; Simonov, A. N.; MacFarlane, D. R. *Science* **2021**. 372, 1187. .
4. Chalkley, M. J.; Drover, M. W.; Peters, J. C. *Chem. Rev.* **2020**. 120, 5582–5636.
5. Seefeldt, L. C.; Yang, Z.-Y.; Lukoyanov, D. A.; Harris, D. F.; Dean, D. R.; Raugei, S.; Hoffman, B. M. *Chem. Rev*. **2020**. 120, 5082–5106.
6. Seefeldt, L. C.; Hoffman, B. M.; Peters, J. W.; Raugei, S.; Beratan, D. N.; Antony, E.; Dean, D. R. *Acc. Chem. Res.* **2018**. 51, 2179–2186.
7. Chalkley, M. J.; Peters, J. C. *Eur. J. Inorg. Chem*. **2020**. 2020, 1353–1357.
8. These terminologies largely align with those used in the following review, although this review uses *Concerted electron-proton transfer* (CEPT) instead of CPET.

Concerted-PCET is also used to describe the same phenomena. Ugh! Tyburski, R.; Liu, T.; Glover, S. D.; Hammarström, L. *J. Am. Chem. Soc.* **2021**. 143, 560–576.

9. While the discussions here focus on reductive PCET steps the same considerations can be applied to oxidative PCET steps.
10. Mayer, J. M.; Hrovat, D. A.; Thomas, J. L.; Borden, W. T. *J. Am. Chem. Soc.* **2002**. 124, 11142–11147.
11. Waidmann, C. R.; Miller, A. J. M.; Ng, C.-W. A.; Scheuermann, M. L.; Porter, T. R.; Tronic, T. A.; Mayer, J. M. *Energy Environ. Sci.* **2012**, 5, 7771–7780.
12. Morris, W. D.; Mayer, J. M. *J. Am. Chem. Soc.* **2017**. 139, 10312–10319.
13. Bordwell, F. G.; Cheng, J. Pei.; Harrelson, J. A. *J. Am. Chem. Soc.* **1988**. 110, 1229–1231.
14. Agarwal, R. G.; Coste, S. C.; Groff, B. D.; Heuer, A. M.; Noh, H.; Parada, G. A.; Wise, C. F.; Nichols, E. M.; Warren, J. J.; Mayer, J. M. *Chem. Rev.* **2022**. 122, 1–49.
15. Lindley, B. M.; Appel, A. M.; Krogh-Jespersen, K.; Mayer, J. M.; Miller, A. J. M. *ACS Energy Lett.* **2016**. 1, 698–704.
16. Gentry, E. C.; Knowles, R. R. *Acc. Chem. Res.* **2016**. 49, 1546–1556.
17. Einsle, O.; Rees, D. C. *Chem. Rev.* **2020**. 120, 4969–5004.
18. Dilworth, M. J.; Eady, R. R. *Biochem. J.* **1991**. 277, 465–468.
19. Chisnell, J. R.; Premakumar, R.; Bishop, P. E. *J. Bacteriol.* **1988**. 170, 27–33.
20. Spatzal, T.; Perez, K. A.; Einsle, O.; Howard, J. B.; Rees, D. C. *Science* **2014**. 345, 1620–1623.
21. Harris, D. F.; Lukoyanov, D. A.; Kallas, H.; Trncik, C.; Yang, Z.-Y.; Compton, P.; Kelleher, N.; Einsle, O.; Dean, D. R.; Hoffman, B. M.; Seefeldt, L. C. *Biochemistry* **2019**. 58, 3293–3301.
22. Lee, C. C.; Hu, Y.; Ribbe, M. W. *Science* **2010**. 329, 642–642.
23. Dilworth, M.J. *Biochim. Biophys. Acta BBA - Gen. Subj.* **1966**. 127, 285–294.
24. Rubinson, J. F.; Corbin, J. L.; Burgess, B. K. *Biochemistry* **1983**. 22, 6260–6268.

25. Kelly, M.; Postgate, J. R.; Richards, R. L. *Biochem. J.* **1967**. 102, 1-3C.
26. Li, J.; Burgess, B. K.; Corbin, J. L. *Biochemistry* **1982**. 21, 4393–4402.
27. Lowe, D. J.; Fisher, K.; Thorneley, R. N. F.; Vaughn, S. A.; Burgess, B. K. *Biochemistry* **1989**. 28, 8460–8466.
28. Fisher, K.; Dilworth, M. J.; Newton, W. E. *Biochemistry* **2006**. 45, 4190–4198.
29. Burgess, B. K.; Lowe, D. J. *Chem. Rev.* **1996**. 96, 2983–3012.
30. Pombeiro, A. J. L.; Richards, R. L. *Coord. Chem. Rev.* **1990**. 104 , 13–38.
31. Yandulov, D. V.; Schrock, R. R. *Science* **2003**. 301, 76–78.
32. Chatt, J.; Pearman, A. J.; Richards, R. L. *J. Chem. Soc.-Dalton Trans.* **1977**. 19, 1852–1860.
33. Anderson, S. N.; Fakley, M. E.; Richards, R. L.; Chatt, J. *J. Chem. Soc. Dalton Trans.* **1981**. 9, 1973–1980.
34. Schrock, R. R. *Acc. Chem. Res.* **2005**. 38, 955–962.
35. Connelly, N. G.; Geiger, W. E. *Chem. Rev.* **1996**. 96, 877–910.
36. Garrido, G.; Rosés, M.; Ràfols, C.; Bosch, E. *J. Solut. Chem.* **2008**. 37, 689–700. .
37. Arashiba, K.; Miyake, Y.; Nishibayashi, Y. *Nat. Chem.* **2011**. 3, 120–125.
38. Arashiba, K.; Eizawa, A.; Tanaka, H.; Nakajima, K.; Yoshizawa, K.; Nishibayashi, Y. *Bull. Chem. Soc. Jpn.* **2017**. 90, 1111–1118.
39. Ashida, Y.; Arashiba, K.; Nakajima, K.; Nishibayashi, Y. *Nature* **2019**. 568, 536–540.
40. The chemical and electrochemical recovery of $Sm^{III}I_2(OR)$ is an interesting topic that colleagues have made exceptional progress in the last few years, see: Boyd, E. A.; Shin, C.; Charboneau, D. J.; Peters, J. C.; Reisman, S. E. *Science* **2024**. 385, 847–853.
41. Anderson, J. S.; Rittle, J.; Peters, J. C. *Nature* **2013**. 501, 84–87.
42. Chalkley, M. J.; Del Castillo, T. J.; Matson, B. D.; Roddy, J. P.; Peters, J. C. *ACS Cent. Sci.* **2017**. 3, 217–223. .

43. Chalkley, M. J.; Del Castillo, T. J.; Matson, B. D.; Peters, J. C. *J. Am. Chem. Soc.* **2018**. 140, 6122–6129.
44. Hill, P. J.; Doyle, L. R.; Crawford, A. D.; Myers, W. K.; Ashley, A. E. *J. Am. Chem. Soc.* **2016**. 138, 13521–13524.
45. Boyd, E. A.; Peters, J. C. *J. Am. Chem. Soc.* **2023**. 145, 14784–14792.
46. Garrido-Barros, P.; Chalkley, M. J.; Peters, J. C. *Angew. Chem. Int. Ed.* **2023**. 62, e202216693.
47. Pickett, C. J. *J. Biol. Inorg. Chem.* **1996**. 1, 601–606.
48. Rittle, J.; Peters, J. C. *J. Am. Chem. Soc.* **2016**. 138, 4243–4248.
49. Laplaza, C. E.; Cummins, C. C. *Science* **1995**. 268, 861–863.
50. Bruch, Q. J.; Malakar, S.; Goldman, A. S.; Miller, A. J. M. *Inorg. Chem.* **2022**. 61, 2307–2318.
51. Lee, C. C.; Hu, Y.; Ribbe, M. W. *Angew. Chem. Int. Ed Engl.* **2012**. 51, 1947–1949.
52. Lee, C. C.; Hu, Y.; Ribbe, M. W. *Proc. Natl. Acad. Sci.* **2012**. 109, 6922–6926.
53. Tanifuji, K.; Lee, C. C.; Ohki, Y.; Tatsumi, K.; Hu, Y. L.; Ribbe, M. W. *Angew. Chem.-Int. Ed.* **2015**. 54, 14022–14025.
54. Tanifuji, K.; Sickerman, N.; Lee, C. C.; Nagasawa, T.; Miyazaki, K.; Ohki, Y.; Tatsumi, K.; Hu, Y.; Ribbe, M. W. *Angew. Chem. Int. Ed.* **2016**. 55, 15633–15636.
55. Debus, H. *J. Chem. Soc.* **1863**. 16, 249–260.
56. Fedurco, M.; Sartoretti, C. J.; Augustynski, J. *J. Am. Chem. Soc.* **1999**. 121, 888–889.
57. Pombeiro, A. J. L.; Guedes da Silva, M. F. C.; Michelin, R. A. *Coord. Chem. Rev.* **2001**. 218, 43–74.
58. By contrast examples of bimetallic CN^- cleavage (in analogy to the nitride splitting mechanism) have yet to be reported, see the following reference for a valiant effort: Peters, J. C.; Baraldo, L. M.; Baker, T. A.; Johnson, A. R.; Cummins, C. C. *J. Organomet. Chem.* **1999**, 591, 24–35.
59. Pombeiro, A. J. L.; Richards, R. L. *Transit. Met. Chem.* **1980**. 5, 281–284.

60. Chatt, J.; L. Pombeiro, A. J.; L. Richards, R. *J. Chem. Soc. Dalton Trans.* **1980**. 3, 492–498.
61. Seino, H.; Nonokawa, D.; Nakamura, G.; Mizobe, Y.; Hidai, M. *Organometallics* **2000**. 19, 2002–2011.
62. Hughes, D. L. ; Mohammed, M. Y.; Pickett, C. J. *J. Chem. Soc. Chem. Commun.* **1989**. 18, 1399–1400.
63. Chatt, J.; Leigh, G. J. *Chem. Soc. Rev.* **1972**, 1, 121–144.
64. Carvalho, M. F. N. N.; Pombeiro, A. J. L.; Schubert, U.; Orama, O.; Pickett, C. J.; Richards, R. L. *J. Chem. Soc. Dalton Trans*. **1985**. 10, 2079–2084.
65. Rittle, J.; Peters, J. C. *Angew. Chem. Int. Ed.* **2016**. 55, 12262–12265.
66. Pombeiro, A. J. L. *Inorg. Chem. Commun.* **2001**. 4, 585–597.
67. Galindo, A.; Hills, A.; Hughes, D. L.; Richards, R. L. *J. Chem. Soc. Chem. Commun.* **1987**. 24, 1815–1816. .
68. Glassman, T. E.; Vale, M. G.; Schrock, R. R. *J. Am. Chem. Soc.* **1992**, 114, 8098–8109.
69. Thompson, N. B.; Green, M. T.; Peters, J. C. *J. Am. Chem. Soc.* **2017**. 139, 15312–15315.
70. Filippou, A. C.; Wössner, D.; Lungwitz, B.; Kociok-Köhn, G. *Angew. Chem. Int. Ed. Engl.* **1996**, 35, 876–878.
71. Filippou, A. C.; Lungwitz, B.; Kociok-Köhn, G. *Eur. J. Inorg. Chem.* **1999**. 1999, 1905–1910. .
72. Cook, D. J.; Hill, A. F. *Organometallics* **1997**, 16, 5616–5617.
73. Garrido-Barros, P.; Derosa, J.; Chalkley, M. J.; Peters, J. C. *Nature* **2022**. 609, 71–76.
74. Boyd, E. A.; Jung, H.; Peters, J. C. *J. Am. Chem. Soc.* **2025**. 147, 4695–4700.
75. Esswein, A. J.; Nocera, D. G. *Chem. Rev.* **2007**, 107, 4022–4047.

76. Yamazaki, Y.; Takeda, H.; Ishitani, O. *J. Photochem. Photobiol. C Photochem. Rev.* **2015**. 25, 106–137.
77. Bofill, R.; García-Antón, J.; Escriche, L.; Sala, X. *J. Photochem. Photobiol. B* **2015**. 152, 71–81.
78. Brown, K. A.; Harris, D. F.; Wilker, M. B.; Rasmussen, A.; Khadka, N.; Hamby, H.; Keable, S.; Dukovic, G.; Peters, J. W.; Seefeldt, L. C.; King, P. W. *Science* **2016**. 352, 448–450.
79. Brown, K. A.; Ruzicka, J.; Kallas, H.; Chica, B.; Mulder, D. W.; Peters, J. W.; Seefeldt, L. C.; Dukovic, G.; King, P. W. *ACS Catal.* **2020**. 10, 11147–11152.
80. Schrauzer, G. N.; Guth, T. D. *J. Am. Chem. Soc.* **1977**, 99, 7189–7193.
81. Edwards, J. G.; Davies, J. A.; Boucher, D. L.; Mennad, A. *Angew. Chem. Int. Ed. Engl.* **1992**, 31, 480–482. .
82. Park, Y.; Kim, S.; Tian, L.; Zhong, H.; Scholes, G. D.; Chirik, P. J. *Nat. Chem.* **2021**. 13, 969–976.
83. Kim, S.; Park, Y.; Kim, J.; Pabst, T. P.; Chirik, P. J. *Nat. Synth.* **2022**. 1, 297–303.
84. Forrest, S. J. K.; Schluschaß, B.; Yuzik-Klimova, E. Y.; Schneider, S. *Chem. Rev.* **2021**. 121, 6522–6587.
85. Chen, M.-W.; Wu, B.; Liu, Z.; Zhou, Y.-G. *Acc. Chem. Res.* **2023**. 56, 2096–2109 .
86. Wang, D.; Astruc, D. *Chem. Rev.* **2015**. 115, 6621–6686.
87. Kurz, J. L.; Hutton, R.; Westheimer, F. H. *J. Am. Chem. Soc.* **1961**. 83, 584–588.
88. Crisenza, G. E. M.; Mazzarella, D.; Melchiorre, P. *J. Am. Chem. Soc.* **2020**. 142, 5461–5476.
89. Wang, P.-Z.; Chen, J.-R.; Xiao, W.-J. *Org. Biomol. Chem.* **2019**. 17, 6936–6951.
90. Prier, C. K.; Rankic, D. A.; MacMillan, D. W. C. *Chem. Rev.* **2013**, 113, 5322–5363.
91. Awad, M. K.; Anderson, A. B. *J. Am. Chem. Soc.* **1989**. 111, 802–806.
92. Hong, Y. H.; Jung, J.; Nakagawa, T.; Sharma, N.; Lee, Y.-M.; Nam, W.; Fukuzumi, S. *J. Am. Chem. Soc.* **2019**, 141, 6748–6754.

93. Hong, Y. H.; Lee, Y.-M.; Nam, W.; Fukuzumi, S. *J. Am. Chem. Soc.* **2022**, 144, 695–700. .
94. Shen, G.-B.; Fu, Y.-H.; Zhu, X.-Q. *J. Org. Chem.* **2020**. 85, 12535–12543.
95. Schmittel, M.; Burghart, A. *Angew. Chem. Int. Ed.* **1997**. 36, 2550–2589.
96. Hantzsch, A. *Berichte Dtsch. Chem. Ges.* **1881**, 14, 1637–1638.
97. Ohnishi, Y.; Kagami, M.; Ohno, A. *Chem. Lett.* **1975**, 4, 125–128.
98. Suresh Yedase, G.; Venugopal, S.; P., A.; Reddy Yatham, V. *Asian Journal of Organic Chemistry* **2022**. 11, e202200478.
99. Jung, J.; Kim, J.; Park, G.; You, Y.; Cho, E. J. *Adv. Synth. Catal.* **2016**. 358, 74–80.
100. Wu, J.; Grant, P. S.; Li, X.; Noble, A.; Aggarwal, V. K. *Angew. Chem. Int. Ed.* **2019**. 58, 5697–5701.
101. Kammer, L. M.; Badir, S. O.; Hu, R.-M.; Molander, G. A. *Chem. Sci.* **2021**. 12, 5450–5457.
102. Li, J.; Siang Tan, S.; Kyne, S. H.; Wai Hong Chan, P. *Adv. Synth. Catal.* **2022**. 364, 802–810.

C h a p t e r 2

Catalytic Cyanide Reduction to Methane and Ammonia at a Mononuclear Fe-site

Adapted from:

Johansen, C. M.; Peters, J. C. *J. Am. Chem. Soc.* **2024**. 146, 5343–5354.

DOI: 10.1021/jacs.3c12395.

2.1 Introduction

Nitrogenases catalyze nitrogen reduction to ammonia (N_2R) as well as the reductive protonation of non-native substrates,[1,2,3,4] including cyanide (CN^-).[5,6,7,8,9,10,11,12,13] These are mechanistically fascinating bio-organometallic transformations which, for the case of CN^- (and CO/CO_2 as well), may involve metal-to-carbon intermediates such as alkyls, carbenes, and carbynes/carbides that are conceptually related to posited intermediates of N_2R (e.g., NNH, NNH_2, NH).

Whereas substantial attention from the synthetic community has been directed towards functional N_2R models with associated mechanistic studies,[14,15,16] there has been only limited attention paid to catalytic cyanide reduction by comparison.[17,18,19,20,21,22] Given potential mechanistic parallels between catalytic N_2 and CN^- reduction, including an isolobal relationship between aminocarbynes (e.g., $M{\equiv}CNR_2$)[23,24,25,26] and their hydrazido ($M{\equiv}NNR_2$) counterparts,[27,28,29] mechanistically well-defined CN^- reduction catalysts present an attractive target for further study. In contrast to terminal hydrazido systems, the reductive protonation of terminal carbynes to liberate products (e.g. CH_4/NH_3) has rarely been observed.[25,30,31,32,33] Indeed, catalytic transformations involving *bona fide* carbyne intermediates, outside of the scope of metathesis reactions,[34,35] are essentially without precedent.

Towards these objectives, our lab reported in 2016 a single-site iron model system capable of mediating the (sub) stoichiometric reductive protonation of CN^- to CH_4 and NH_3.[25] We also characterized a number of species as plausible intermediates of the overall transformation, most notably the carbyne complex $(P_3^{Si})Fe(CNH_2)^+$ (P_3^{Si} represents a tris(phosphino)silyl ligand; Figure 2.1, top).[25] The product distribution observed mimics that of ATP-dependent cyanide reduction by nitrogenases (Figure 2.1, middle), where the major observed products under most conditions studied are methane and ammonia (6 e^- reduction); methylamine (H_3CNH_2; 4 e^- reduction) and methyleneimine ($H_2C{=}NH$; 2 e^- reduction) can also be observed as minor products, along with trace ethane and ethylene.[25,26,27,28]

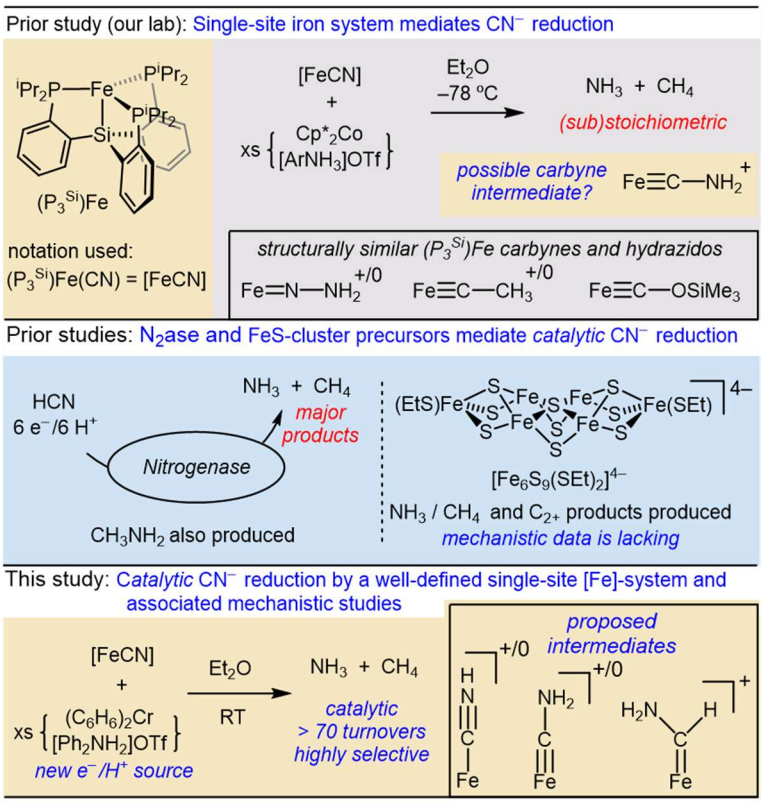

Figure 2.1. Summary of prior studies on stoichiometric and catalytic cyanide reductions mediated by iron complexes as context for this study.[8,22,25,26,44]

Several synthetic Fe–S clusters have also been shown to catalyze cyanide reduction and exhibit substantially higher selectivities for C–C coupled products than has been observed with nitrogenase enzymes as the catalysts (Figure 2.1, middle).[10,11,12,20,21,22] Catalytically relevant species in trans20formations employing such clusters as precatalysts are ill-defined and to date associated mechanistic information has not been forthcoming.

Against this backdrop we have sought conditions for *catalytic* cyanide reduction via our well-defined (P_3^{Si})Fe-system, ideally manifesting product distributions akin to nitrogenases (chiefly favoring the C_1 products CH_4 and CH_3NH_2) and amenable to mechanistic scrutiny. This study presents our findings (Figure 2.1, bottom).

Guided by measured and estimated thermochemical parameters (Figure 2.2A),[36] we show herein that the iron complex (P_3^{Si})Fe(CN) (abbreviated as [FeCN]) efficiently catalyzes cyanide reduction in the presence of acids and reductants. By employing a combination of synthetic, ^{57}Fe Mössbauer, optical, and theoretical studies, we outline a

mechanistic scheme for the catalytic cycle, which can be juxtaposed with that of catalytic nitrogen fixation mediated by analogous iron complexes.

2.2 Results

2.2.1 Canvassing conditions for more efficient [FeCN] reduction

To target the catalytic reduction of CN^- we sought conditions for the proton-coupled reduction of [FeCN] to produce NH_3/CH_4 (or CH_3NH_2) and an [Fe] byproduct that might re-enter a catalytic cycle. In our original report,[25] we described the proton-coupled reduction of [FeCN] using excess [$^{2,5\text{-Cl}}$PhNH$_3$]OTf and Cp*$_2$Co (pK_a 4.5 for [$^{2,5\text{-Cl}}$PhNH$_3$]OTf in THF; all pK_a's reported in THF;[36] $E°$ = −1.9 V for Cp*$_2$Co; all redox potentials are reported in THF and referenced to $Fc^{+/0}$).[37] Such reaction mixtures invariably afforded low yields of NH_3/CH_4 (Figure 2.1A) despite being effective for catalytic N_2R.[38]

Curiously, in our original study we had observed that the cationic aminocarbyne, [FeCNH$_2$]OTf, prepared via double protonation of [FeCN][Na(12-c-4)$_2$],[25] decays upon warming to liberate 0.09 equiv NH_3/Fe and 0.07 CH_4/Fe (Figure 2.2), with [FeCNH]OTf and [FeOTf] as the major Fe-products. This NH_3 yield represents ~50% of that theoretically possible for a disproportionation reaction assuming a stoichiometry of five equivalents of [FeCNH$_2$]OTf providing five H-atom equivalents ([FeCNH$_2$]$^+$→ [FeCNH]$^+$ + H$^+$/e$^-$) to reduce one equivalent [FeCNH$_2$]OTf to NH_3 and CH_4 (Eqn 2.1).

$$6\,[\mathrm{FeCNH_2}] \rightarrow 5[\mathrm{FeCNH}]\mathrm{OTf} + [\mathrm{FeOTf}] + \mathrm{NH_3} + \mathrm{CH_4} \quad \text{(Eqn 2.1)}$$

Based on thermochemical data (Figure 2.2A),[36] removal of a H$^+$/e$^-$ pair from [FeCNH$_2$]$^+$ is equivalent to removal of 1H$^+$/1e$^-$ from an acid/reductant pair with pK_a ~ 7 and $E°$ ~ −1.3 V. Reagents suiting these values would be significantly milder than [$^{2,5\text{-Cl}}$PhNH$_3$]OTf and Cp*$_2$Co. Hence, once [FeCNH$_2$]$^+$ is formed *in situ* via reductive protonation of [FeCN] (pK_a 5.6), comparatively mild reagents should drive net CN^- reduction. Because [FeCN] can be converted to [FeCNH$_2$]OTf with a reductant strength of $E°$ ≈ −1.3 V, we deduced that the 7H$^+$/6e$^-$ reduction of [FeCN] should be accessible with reductants at $E°$ ≈ −1.3 V.

Gratifyingly, stirring [FeCN] with $(C_6H_6)_2Cr$ ($E°$ = −1.2 V, Figure A.23)[39] and $[Ph_2NH_2]OTf$ (pK_a 3.2)[40] in Et_2O at −78 °C and then allowing the reaction mixture to warm to RT overnight yielded 0.75 equiv NH_3/Fe (75% yield per reductant) with [FeOTf] as the major Fe product (Figure 2.2B, and Figure A.9). Moreover, it was established that [FeOTf] reacts cleanly with excess [TBA][CN] to reform [FeCN], setting the stage for catalysis (Figure A.10).

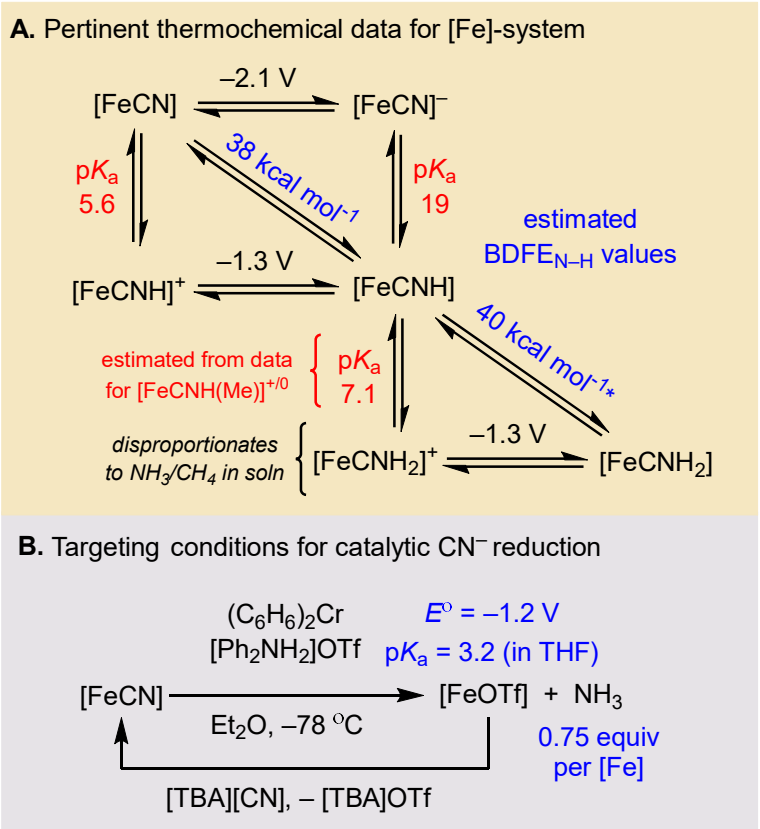

Figure 2.2. Thermochemistry and reagents for stoichiometric [FeCN] reduction. (A) Relevant, previously measured, thermochemical data (values in THF at 25 °C; $E°$ in referenced to $Fc^{+/0}$).[28] (B) Exploring new conditions for reductive protonation of [FeCN].

2.2.2 Catalytic CN^- Reduction

Thus, using [FeCN] (0.72 mM) as a precatalyst, in a reaction mixture containing 140 equiv [TBA][CN] (100 mM), 480 equiv $[Ph_2NH_2]OTf$, and 360 equiv $(C_6H_6)_2Cr$ in Et_2O at 25 °C, yielded 28±5 equiv NH_3/Fe after 80 minutes (Table 2.1, entry 1).

Using these same catalytic conditions, we also analyzed the gaseous products. CH_4 was observed as the major reduced carbon product, with a yield of 25±4 equiv of CH_4/Fe, consistent with a net $7H^+/6e^-$ reduction of CN^- (Eqn 2.2; yield based on consumed $(C_6H_6)_2Cr$ is 47±8%).

$$CN^- + 7\,H^+ + 6\,e^- \rightarrow CH_4 + NH_3 \quad \text{(Eqn 2.2)}$$

Under these conditions trace C_2 products ethylene and ethane were also identified (0.4 equiv C_2H_4 and 0.3 equiv C_2H_6 per Fe). These products correspond to $10H^+/8e^-$ and $12H^+/10e^-$ reductions of CN^-. Combined, these C_2 evolving reactions accounted for less than 2% of the consumed reductant. Hence, the [FeCN] catalyst is nearly quantitatively selective for C_1 products, as is observed via the nitrogenase enzyme.[25,26] H_2 accounts for most of the remaining reducing equivalents (yield based on $(C_6H_6)_2Cr$: 29±11 %). Neither CH_3NH_2 ($4e^-$ product) or CH_2NH ($2e^-$) was detected, regardless of initial temperature, using [FeCN] as a catalyst.

Curiously, whereas synthetic iron catalysts for N_2R have shown highest efficiency at low temperatures due to mitigated HER (Hydrogen evolution reaction) and entropically favored N_2 binding,[41] no such advantage is observed for catalytic cyanide reduction by [FeCN] (entries 2-4). Instead, background HER via combination of this reductant and acid is comparatively slow (*vide infra*). Also, CN^- binds favorably to [Fe(II)] at RT. For reactions started at −78 °C catalytic turnover is slow, reflecting a slow OTf^- for CN^- metathesis step needed to turn the system over (*vide infra*); most of the observed catalysis occurs as the reaction is warmed. For a catalytic reaction run at −20 °C and quenched after 20 minutes, 1.7 equiv NH_3 was detected, demonstrating that catalytic turnover occurs at this temperature, but is relatively slow.

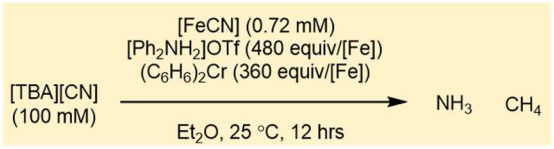

Entry	Change from standard conditions	NH_3 (equiv/Fe)	CH_4 (equiv/Fe)	Yield per reductant (%)[a]
1	None	28±5	25±4	47±8
2	−78 °C → 25 °C	33±6	33±3	55±10
3	−20 °C → 25 °C	35±8	–	58±13
4	0 °C → 25 °C	26±2	–	43±3
5	2.9 mM [FeCN][b]	9.7±0.2	–	65±1
6	0.15 mM [FeCN][b]	73±4	–	24±1
7	No [FeCN][b]	<0.4	<0.3	<1
8	No [TBA][CN][b]	0.7	–	1.2
9	8.0 mM $FeCl_2$ as cat.[b]	0.3	–	5.5
10	8.0 mM $CrCl_2$ as cat.[b]	<0.05	–	<1
11	2.9 mM $(PhBP^{iPr}_3)FeBr$ as cat.[b]	1.4±0.7	1.0±0.1	12±3[c]
12	2.9 mM $(P_3^B)Fe[BAr^F_4]$ as cat.[b]	2.3±0.3	1.6	15.6±0.6
13	Cp_2Co instead of $(C_6H_6)_2Cr$	2.8±0.8	–	12±4
14	Cp^*_2Cr instead of $(C_6H_6)_2Cr$	13.5±3	–	32±6
15	[FeOTf] as cat.	32	–	53
16	Reloaded catalysis[d]	4.1±1.0	–	6.8±1.7

Table 2.1. Results for the catalytic reduction of CN^- to ammonia. (a) Yields assume net 6 e^- reduction to generate NH_3. (b) Catalysis initiated at −78 °C and then allowed to warm gradually to 25 °C (total reaction time of 12 hours). (c) This yield includes 0.6±0.2 equiv CH_3NH_2. (d) After 80 min catalysis under standard conditions (entry 1), soluble Fe species were extracted into Et_2O and then re-exposed to the standard catalytic conditions.

Increasing the catalyst loading to 2.9 mM (entry 5) modestly increased the NH_3 yield relative to reductant present (65±1%). Lowering the catalyst loading (0.15 mM; entry 6) improved the TON for produced NH_3 (73±4 equiv) but led to a corresponding drop in yield per $(C_6H_6)_2Cr$ (24±1%).

A catalyst-free reaction yielded no detectable NH_3, CH_4, or other gaseous carbon products (entry 7). This conclusion is further supported by experiments with [TBA][^{13}CN] as the cyanide source. ^{13}C NMR spectroscopy of catalytic runs using [TBA][^{13}CN] confirmed the formation of $^{13}CH_4$ and consumption of $^{13}CN^-$ (Figures A.5 and A.6). By contrast, a corresponding catalyst-free reaction (under otherwise identical conditions) showed negligible consumption of $^{13}CN^-$ and no observable $^{13}CH_4$. These observations

collectively establish the Fe-catalyst is required for consumption of substrate and responsible for the NH_3 and CH_4 products.

Catalysis run in the absence of [TBA][CN] produced 0.7 equiv NH_3, with [FeC^{15}N] used to demonstrate that this NH_3 arose solely precatalyst reduction and not N_2R (entry 8, Figure A.4).

The nature of the phosphine-ligated iron catalyst appears to be critical. $FeCl_2$ instead of [FeCN] produced only 0.3 equiv NH_3 under the standard conditions (entry 9), and $CrCl_2$ instead of [FeCN] produced no detectable NH_3 (entry 10). The tris(phosphino)iron complexes $(P_3^B)Fe[BAr^F_4]$[16] and $(PhBP^{iPr}_3)FeBr$[42] (P_3^B represents a trisphosphine borane ligand; $PhBP^{iPr}_3$ represents a trisphosphine borate ligand) showed very moderate activity as (pre)catalysts compared to [FeCN] (entries 11-12). Curiously, for $(PhBP^{iPr}_3)FeBr$, a small amount of methylamine, CH_3NH_2 (0.6±0.2), was detected as a product. These iron phosphine precatalysts produce CH_4 as the major hydrocarbon product, but with a lower selectivity. The ratio of C_2/C_1 products produced is 0.16 and 0.11 for $(P_3^B)Fe[BAr^F_4]$ and $(PhBP^{iPr}_3)FeBr$, respectively (Table A.3), compared to 0.02 for [FeCN].

While $(C_6H_6)_2Cr$ is the favored reductant for CN^- reduction, other reductants including Cp_2Co ($E°$ = −1.33 V, Figure A.25; entry 13) and Cp^*_2Cr ($E°$ = −1.47 V, Figure A.27; entry 14) were modestly competent. The low yields for these reductants do not appear to correlate with the reduction potential of the chemical reductant. Instead, we attribute the strong attenuation in yield to enhanced background HER. Accordingly, we find that the rate of reaction of each reductant independently with $[Ph_2NH_2]OTf$ (to produce H_2), as measured by cyclic voltammetry, inversely correlates with the NH_3 TON observed in a catalytic run when CN^- is present under the standard conditions (see appendix, section A.8.2 for details).

To summarize, we have established a highly selective catalytic system for NH_3 and CH_4 production via reductive protonation of CN^-; the choice of catalyst ([FeCN]) and reductant ($(C_6H_6)_2Cr$) are crucial for observing high turnover and significant yields.

2.2.3 Mechanistic studies

Scheme 2.1 provides a working outline for the catalytic CN^- reduction cycle starting from [FeCN], emphasizing early intermediates of the cycle. To guide the following discussion, summary remarks concerning a plausible pathway are as follows: [FeCN] is first protonated (step a) to form independently characterized $[FeCNH]^+$,[25] which is then reduced (to [FeCNH]; step b) and protonated (step c) to afford the independently characterized aminocarbyne, $[FeCNH_2]^+$.[25] $[FeCNH_2]^+$ is in redox equilibrium with $[FeCNH_2]$ in the presence of $(C_6H_6)_2Cr$ (step d). These carbyne intermediates are suggested to be rate contributing to overall CN^- reduction (see below). Along the ET-PT pathway, $[FeCNH_2]$ can be protonated to form a posited carbene intermediate (step e), $[FeC(H)(NH_2)]^+$. This carbene is modeled via independent generation of its methylated analogue, $[FeC(H)(NMe_2)]^+$ via protonation of $[FeCNMe_2]$ (see below). This observation, and computational evidence, each lend support to C–H bond formation to produce $[FeC(H)(NH_2)]^+$ during catalysis. A direct PCET (proton-coupled electron transfer) pathway from $[FeCNH_2]^+$ to $[FeC(H)(NH_2)]^+$ is also plausible (step f). Finally, a series of downstream (as yet undefined), facile reductive protonation steps of $[FeC(H)(NH_2)]^+$ are proposed to release NH_3 and CH_4 along with [FeOTf] (step g); the latter is returned to [FeCN] via metathesis with [TBA][CN], a step (h) that is turnover limiting.

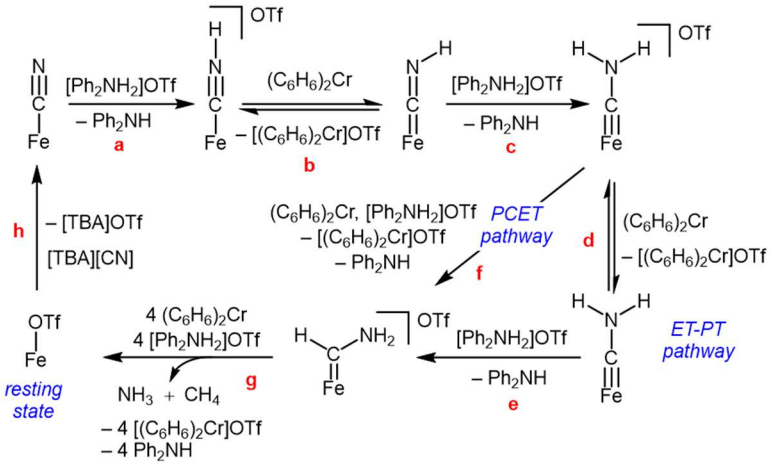

Scheme 2.1. Proposed mechanism for CN^- reduction to NH_3 and CH_4 as catalyzed by [FeCN].

2.2.4 Probing catalyst resting state and deactivation

To probe speciation during catalysis, we prepared [^{57}FeCN] to facilitate monitoring the catalysis by ^{57}Fe Mössbauer spectroscopy via low temperature quenching of catalytic runs initiated at 25 °C. Related studies proved insightful for N_2R catalysis by related Fe systems.[40,43]

Freeze-quenching (77 K) the catalysis after one minute at 25 °C, we found [^{57}FeOTf] as the sole iron-species present (see section S6.2).[44] This result points to [FeOTf] as the catalyst resting state, with metathesis step (h) being turnover limiting. Consistent with this observation, [FeOTf] performs analogous to [FeCN] as a catalyst (Table 1, entry 15). Freeze-quenched snapshots at later reaction times show attenuation in the signal for [^{57}FeOTf] and the growth of unknown iron species. After 80 min, all of the [^{57}FeOTf] has been consumed; the remaining iron species showed poor activity following extraction and (re)subjection to catalytic conditions at 25 °C with fresh acid, reductant and [TBA][CN], yielding only an additional 4.1±1 equiv NH_3 (entry 16). NMR analysis of the post-catalysis mixture revealed evidence of a diamagnetic iron hydride (possibly [Fe(H)($NHPh_2$)]) with the (P_3^{Si})Fe platform intact, as well as free Si(H)P_3 (Figure A.13). Relatedly, iron hydrides (e.g., [Fe(H)(N_2)]) have been shown to be off cycle sinks during catalytic N_2R.[43,45,46]

While our mechanistic studies have focused on the most efficient catalyst, [FeCN], initial studies of the reactivity of (P_3^B)Fe[BAr^F_4] and ($PhBP^{iPr}_3$)FeBr suggest that these less efficient precatalysts are also less stable to excess CN^-. When reacted with 20 equiv [TBA][CN] in Et_2O (in the absence of acid or reductant), free phosphine is observed, indicating partial demetallation as a pathway for deactivation, offering a plausible reason for the lower turnover numbers (Figure A.14 and A.15).

2.2.5 Early N–H Bond Forming Steps

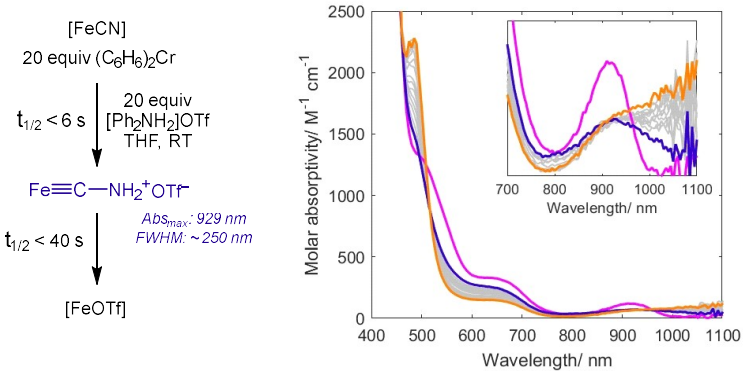

Figure 2.3. UV-vis data showing *in situ* formation of [FeCNH$_2$]OTf (pink trace, 6 s after acid addition) in the reduction of [FeCN] (blue trace) to [FeOTf] (orange trace, 240 s after acid addition).

Since metathesis to produce [FeCN] from [FeOTf] appeared to be turnover limiting we turned to stoichiometric experiments to probe the role/s of early intermediates of reductive protonation in this catalysis.

Exposing a solution containing a mixture of [FeCN] and a large excess (20 equiv) of $(C_6H_6)_2Cr$ (unreactive in the absence of acid) to $[Ph_2NH_2]OTf$ (20 equiv, added via syringe) caused distinct color changes that could be monitored by UV-vis spectroscopy (Figure 2.3). While higher energy absorptions (λ < 600 nm) are complicated by the absorption spectrum of $(C_6H_6)_2Cr^{+/0}$, the lower energy transitions provide a useful handle for the iron speciation. Upon addition of the acid (all 20 equiv) at RT, the characteristic near IR absorption of [FeCN] (λ_{max} = 905 nm, FWHM ≈ 100 nm; blue trace) decayed rapidly ($\tau_{1/2}$ < 6 s) and a new, broader absorbance characteristic of $[FeCNH_2]^+$ (λ_{max} = 929 nm, FWHM ≈ 250 nm; pink trace) was observed.[25] This feature decayed more slowly ($\tau_{1/2}$ ~ 40 s under the conditions studied) with simultaneous growth of a shoulder that extends further into the near-IR, and a strong absorption centered at 485 nm (orange trace). These latter features are consistent with formation of [FeOTf], as was also confirmed by ^{1}H NMR spectroscopy (Figure A.12). Products were also analyzed (1.0 equiv NH_3/Fe and 0.9 equiv CH_4/Fe). These data demonstrate the aminocarbyne $[FeCNH_2]^+$ as an observable on-path intermediate in the conversion of [FeCN] to [FeOTf]. Isosbestic points at 520 nm and 900

nm establish that no further downstream intermediates build-up as $[FeCNH_2]^+$ is converted to [FeOTf] during liberation of NH_3 and CH_4.

To interrogate shorter-lived intermediates, we next studied the consumption of [FeCN] at lower temperature, using fewer equivalents of reductant and acid. Mixing $[^{57}FeCN]$ with $[Ph_2NH_2]BAr^F_4$ and $(C_6H_6)_2Cr$ (2.5 equiv each) in Et_2O at −78 °C for 1 minute, followed by freeze-quench (77 K) and analysis by Mössbauer spectroscopy, showed primarily $[^{57}FeCNH_2]BAr^F_4$ (Figure 2.4A; $\delta = 0.13$ mm s^{-1} and $\Delta E_Q = 1.47$ mm s^{-1}), again supporting the proposed intermediacy of $[FeCNH_2]^+$ during catalysis.[25] These low temperature conditions also allowed identification of the first intermediate of protonation, $[^{57}FeCNH]BAr^F_4$ ($\delta = 0.407$ mm s^{-1} and $\Delta E_Q = 3.20$ mm s^{-1}),[25] as a minor component, consistent with step (a) (Scheme 1).

We also obtained evidence for a facile redox equilibrium between $[FeCNH_2]^{+/0}$ and $(C_6H_6)_2Cr^{+/0}$, as can be expected based on the estimated difference in their reduction potentials ($E°(Fe^{+/0}) \sim -1.2$ V, $E°(Cr^{+/0}) = -1.2$ V; see section S8.3 for data). Relatedly, the available data imply that single electron reduction of $[FeCNH_2]^+$ to $[FeCNH_2]$ (step d) is feasible under conditions relevant to the catalysis. Accordingly, addition of 2.5 equiv $[Ph_2NH_2]BAr^F_4$ to a THF solution of [FeCN] at −80 °C resulted in the immediate formation of $[FeCNH]BAr^F_4$ (Figure 2.4B, blue trace).[25,47] Following this, the solution was titrated with 0-6 equiv $(C_6H_6)_2Cr$ to study its response (Figure 2.4B). During the addition of the 1st equivalent of $(C_6H_6)_2Cr$, UV-vis maxima for $[FeCNH]^+$ (800 nm and 610 nm) decreased in intensity and new maxima appeared reflecting the growth of $[FeCNH_2]^+$ (929 nm and 570 nm; pink trace). Isosbestic points at 570 nm and 860 nm establish no other intermediates build up. Upon addition of further equivalents of $(C_6H_6)_2Cr$, the signals for $[FeCNH_2]^+$ attenuate with corresponding growth of a strong absorbance with a shoulder around 560 nm (orange trace). These changes are consistent with the reduction of $[FeCNH_2]^+$ to $[FeCNH_2]$. Still, even after addition of 6 equiv $(C_6H_6)_2Cr$ a large fraction of $[FeCNH_2]^+$ remained.[48] These results confirm a redox equilibrium between $[FeCNH_2]^{+/0}$ and $(C_6H_6)_2Cr^{+/0}$ (step (d)).

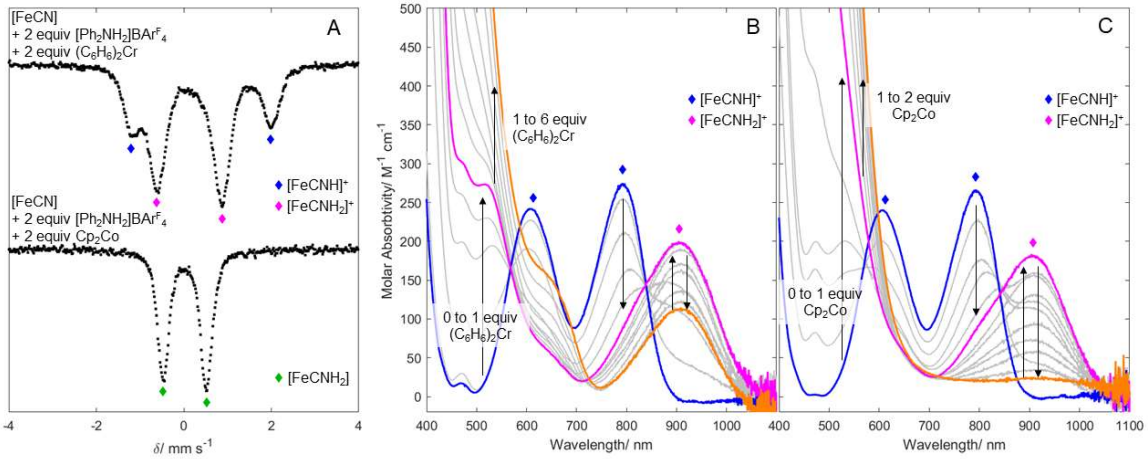

Figure 2.4. Formation of aminocarbynes. (A) ^{57}Fe Mössbauer spectra of reaction of [FeCN] with $[Ph_2NH_2]BAr^F{}_4$ and $(C_6H_6)_2Cr$ or Cp_2Co. (B and C) UV-vis data for reaction of [FeCN] with $[Ph_2NH_2]BAr^F{}_4$ and $(C_6H_6)_2Cr$ (B) or Cp_2Co (C) to form early intermediates $[FeCNH]BAr^F{}_4$ (blue trace), $[FeCNH_2]BAr^F{}_4$ (pink trace) and $[FeCNH_2]^0$ (orange trace).

As expected for such a redox-equilibrium, cobaltocene, a stronger reductant than $(C_6H_6)_2Cr$ ($E°(Cp_2Co^{3+/2+})$ = −1.3 V), completely reduces $[FeCNH_2]^+$ to $[FeCNH_2]$. Accordingly, ^{57}Fe Mössbauer spectra of the reaction between [^{57}FeCN] with $[Ph_2NH_2]BAr^F{}_4$ and Cp_2Co (2.5 equiv each) at −78 °C in Et_2O reveals the formation of a single new species ($\delta = 0.02$ mm s^{-1} and $\Delta E_Q = 0.99$ mm s^{-1}; Figure 2.4A). These parameters closely resemble those of $[FeCNMe_2]$ ($\delta = 0.06$ mm s^{-1} and $\Delta E_Q = 1.12$ mm s^{-1}),[25] consistent with formation of $[FeCNH_2]$. Complete formation of $[FeCNH_2]$ with only 2.5 equivalents of reductant differs markedly from conditions using $(C_6H_6)_2Cr$. Titrations monitored by UV-vis spectroscopy using Cp_2Co still showed $[FeCNH_2]^+$ as an intermediate upon addition of just 1 equiv of Cp_2Co to a mixture of [FeCN] and $[Ph_2NH_2]BAr^F{}_4$ (Figure 2.4C, pink trace). Upon addition of a 2nd equiv of Cp_2Co, $[FeCNH_2]^+$ is fully consumed with concomitant formation of $[FeCNH_2]$ (orange trace).

2.2.6 Evidence for C−H Bond Formation via $Fe=C(H)NH_2^+$

The intermediacy of iron carbynes $[FeCNH_2]^{+/0}$ in catalytic CN^- reduction corresponds to the intermediacy of isolobal hydrazidos $[FeNNH_2]^{+/0/-}$, during Fe-catalyzed

N_2R.[27,28,29,49,50] With this analogy in mind, we wondered whether iron carbynes might be selectivity determining in CN^- reduction, with final N−H bond formation releasing NH_3 (analogous to N_β−H bond formation in N_2R via hydrazido intermediates), resulting in the observed 6 e^- products (CH_4 and NH_3), possibly via a transient carbide [Fe(C)] intermediate. Computational evidence and a study of the reactivity of the methylated carbyne [$FeCNMe_2$] complex instead support C−H bond formation via a carbene intermediate, $[Fe{=}C(H)(NH_2)]^+$, as the next step of the cycle. This path implies that the aminocarbyne is not selectivity determining in the present system; C−N bond cleavage occurs later in the catalytic cycle.

As intermediates downstream of [$FeCNH_2$] cannot be identified during the CN^- reduction process, we studied the reactivity of the more tractable, methylated [$FeCNMe_2$] analogue (Scheme 2). Thus, a reaction between [$FeCNMe_2$] and [Ph_2NH_2]OTf in the absence of added reductant affords a new paramagnetic species, observed via UV-vis and ^{1}H NMR spectroscopy (see SI, section S9); some competing oxidation to $[FeCNMe_2]^+$ (with loss of H_2) is also observed in the reaction mixture, frustrating isolation and purification of the new species. Nonetheless, on the basis of reactivity and ^{57}Fe Mössbauer (*vide infra*), we assign the product of protonation as the aminocarbene $[FeC(H)(NMe_2)]^+$. Its formation is reversible; [$FeCNMe_2$] is cleanly regenerated upon addition of triazabicyclodecene (TBD) base (Scheme 2.2 and Figure A.32).

Scheme 2.2. Protonation and proton-coupled reduction of [FeCNMe$_2$] as a model of [FeCNH$_2$] reactivity.

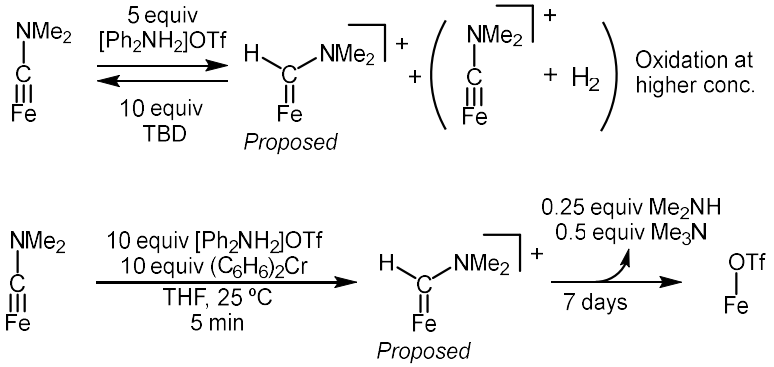

[FeCNMe$_2$] also reacts with 10 equiv [Ph$_2$NH$_2$]OTf in the presence of 10 equiv (C$_6$H$_6$)$_2$Cr in THF at room temperature, and is gradually converted to [FeOTf] over a period 7 days, with Me$_2$NH (0.25 equiv) and (curiously) Me$_3$N (0.5 equiv) detected as the N–containing products.[51] Notably, we had previously observed that [FeCNMe$_2$] is not reduced in combination with Cp*$_2$Co and [$^{2,5\text{-Cl}}$PhNH$_3$]OTf.[25]

While formation of [FeOTf] from [FeCNMe$_2$] is slow in the presence of [Ph$_2$NH$_2$]OTf and (C$_6$H$_6$)$_2$Cr (at 10 equiv each), the [FeCNMe$_2$] is consumed rapidly ($\tau_{1/2}$ ≈ 1 minute at 25 °C) and the same paramagnetic (presumed) carbene species is now also observed as an intermediate. Hence, reacting [FeCNMe$_2$] with excess (C$_6$H$_6$)$_2$Cr and [Ph$_2$NH$_2$]OTf and freeze-quenching the reaction after 5 minutes, revealed a new major species with the parameters δ = 0.40 mm s^{-1} and ΔE_Q =2.25 mm s^{-1} (Figure A.37), consistent with an S = 1 [FeC(H)(NMe$_2$)]$^+$ species with parameters similar to previously characterized S = 1 (P_3^{Si})Fe^{II}–L$^+$ species (L = CO, CNR or N$_2$).[36,52] Taken together these data are highly consistent with [FeC(H)(NMe$_2$)]$^+$ as an intermediate during the reductive protonation of [FeCNMe$_2$] to liberate [FeOTf] and the amine products and suggest [FeC(H)(NH$_2$)]$^+$ would form readily via protonation of [FeCNH$_2$] during CN$^-$ reduction catalysis.

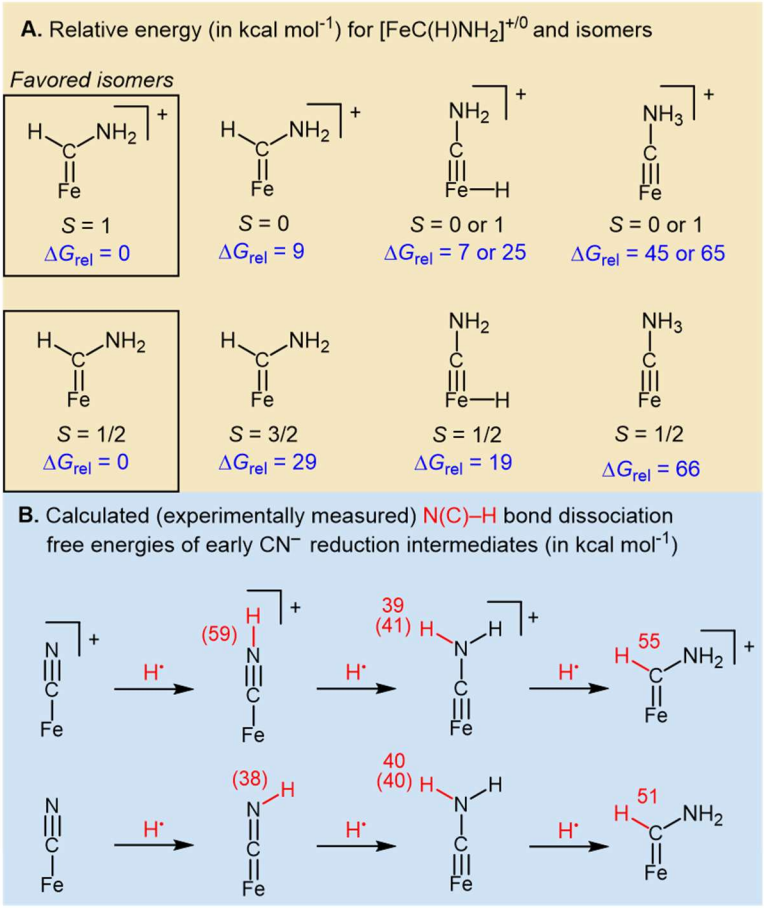

Figure 2.5. Computational study of bond strengths of early N−H bonds (A) Comparing energies of isomers in specified spin states for $[FeC(H)(NH_2)]^{+/0}$. (B) Calculated N−H bond and C–H bond dissociation free energies (BDFE's). Experimentally determined values are provided in parenthesis, for carbynes these are estimated from $[FeCN(H)(Me)]^{+/0}$.[36]

To gain further support for this proposed $[Fe{=}C(H)(NH_2)]^{+}$ intermediate we turned to computational methods to explore the energy of aminocarbene species versus other plausible isomers. The TPSS functional[53] and a def2-TZVP basis set on Fe, with a def2-SVP basis set on all other atoms,[54] reliably replicates experimentally estimated BDFEs for complexes similar to those discussed here.[55] We thus used this approach to compare plausible isomers, with specified spin states, under the addition of H• to the $[FeCNH_2]^{+/0}$ carbynes (Figure 2.5A). We find that iron carbenes $[Fe{=}C(H)(NH_2)]^{+/0}$ in their corresponding $S = 1$ and $S = 1/2$ spin states, respectively, are the lowest energy isomers ($\Delta G_{rel} = 0$ kcal mol^{-1}) when compared to their corresponding ammonium carbyne isomers

($[Fe{\equiv}C{-}NH_3]^{+/0}$; ΔG_{rel} = 45-66 kcal mol^{-1}) and iron carbyne hydrides ($[(H)Fe{\equiv}C{-}NH_2]^{+/0}$; ΔG_{rel} = 7-25 kcal mol^{-1}). Alternative spin states of the iron carbenes (S = 0 or 3/2) are also higher in energy (ΔG_{rel} = 9 and 29 kcal mol^{-1}, respectively). The small ΔG_{rel} of $[(H)Fe{\equiv}C{-}NH_2]^+$ is interesting given that iron hydrides can be catalytic sinks for this system;[46] isomerization between the on-path iron carbene and this iron carbyne hydride might be a relevant deactivation pathway.

The thermodynamic favorability of C−H bond formation (over N−H bond formation) can be rationalized by considering the basicity of the N and C atoms of the iron aminocarbyne. $[FeCNH_2]$ features a planar sp^2-hybridized N atom, suggesting substantial π donation from N, which can be expected to make the N atom less basic than the carbyne C atom. Such a scenario would favor C atom protonation, as observed.

Computationally the carbene $[FeC(H)(NH_2)]^{+/0}$ C−H bonds (51 – 55 kcal mol^{-1}) are much stronger than the carbyne $[FeCNH_2]^{+/0}$ N−H bonds (39-40 kcal mol^{-1}; Figure 2.5B), consistent with the conversion of carbyne to carbene being a thermodynamically favorable step in [FeCN] reduction (Figure 2.6). However, the build-up of $[FeCNH_2]^+$ as an observable intermediate when [FeCN] is reduced to NH_3 and CH_4 (Figure 3), and the slow protonation observed for $[FeCNMe_2]^0$ (Scheme 2.2), suggest a significant kinetic barrier in converting $[FeCNH_2]^{+/0}$ to $[FeC(H)(NH_2)]^{+/0}$ (Figure 2.6). This can be rationalized by a rehybridization at carbon with a corresponding change in spin state upon protonation, which would correlate with a significant kinetic barrier.

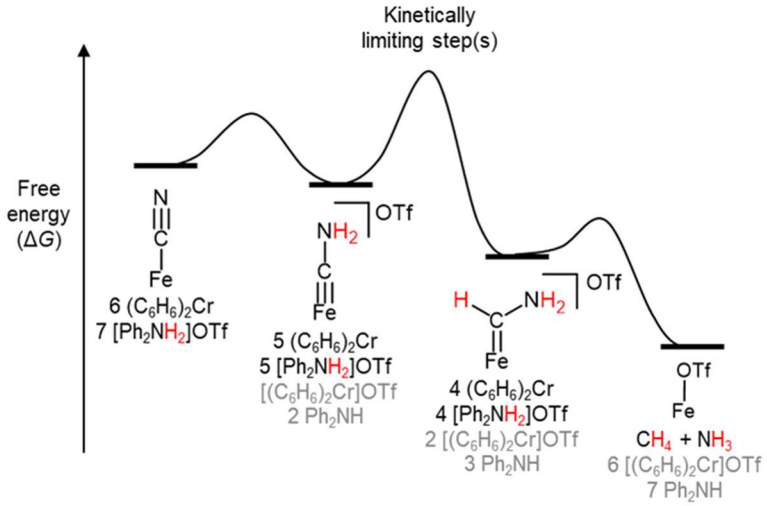

Figure 2.6. Proposed qualitative energy barriers for transformation of [FeCN] to [FeOTf] with key intermediates, $[FeCNH_2]^+$ and $[FeC(H)(NH_2)]^+$ indicated.

2.3 Discussion

2.3.1 Comparison to other Fe-based Catalysts

As introduced above, reported Fe-catalysts for cyanide (or HCN) reduction have exclusively been Fe–S clusters, either as the protein active sites of nitrogenase enzymes,[5,25,26,27,28,13] the extracted cofactors (e.g., FeMoco),[10,11,12] or synthetic clusters.[20,21,22] The extracted cofactors and synthetic clusters studied have been shown to reduce CN^- using weak acids (lutidinium or pH 8 buffered solutions) and lanthanide (II) reductants (SmI_2 or Eu^{II}(DTPA)) as a source of H^+/e^- equivalents. Invariably these systems have produced substantial amounts of C_{2+} products, accounting for 20-40% of the total reduced carbon products, in addition to C_1 products, including CH_4 (and NH_3) or CH_3NH_2.[10,11,12,20,21,22]

By contrast, the [FeCN] catalyst studied herein shows <2% C_{2+} products. Curiously, its reactivity profile more closely resembles that of HCN reduction by MoFe nitrogenase, where C_{2+} products account for <0.1% of the total reduced carbon.[25,26] Still, [FeCN] shows much higher selectivity for the 6 e^- reduction products ($CH_4 + NH_3$) than has been observed for the nitrogenases studied (MoFe and VFe variants), which also show significant CH_3NH_2 production (MoFe, $CH_3NH_2 : CH_4 = 0.39$; VFe, $CH_3NH_2 : CH_4 = 0.66$-1.1).[28] The complex $(PhBP^{iPr}_3)FeBr$, while a less active catalyst system for CN^- reduction (Table 1,

entry 10), more faithfully captures the selectivity of nitrogenases, producing substantial CH_3NH_2 as well as (CH_4 + NH_3). As functional models, the (P_3^B)Fe– and (P_3^{Si})Fe–systems we have studied are distinct in that both have been shown to display catalytic activity for N_2R and CN^- reduction, akin to ATP-dependent nitrogenase enzymes.[1,5,16,43]

2.3.2 Mechanistic findings

The data presented above allow us to posit several important intermediates we believe to be on path for catalytic CN^- reduction by [FeCN] (Scheme 1), and to further consider the observed selectivity. A key observation from low temperature UV-vis titrations includes the finding that [FeCN] is readily protonated by $[Ph_2NH_2]OTf$. The resulting isocyanide $[FeCNH]^+$ can be reduced by $(C_6H_6)_2Cr$, and the resulting $[FeCNH]^0$ product is rapidly protonated to afford the observable aminocarbyne $[FeCNH_2]^+$. With $(C_6H_6)_2Cr$ present as the reductant, $[FeCNH_2]^+$ and $[FeCNH_2]$ have been shown to be in redox equilibrium.

While we observe downstream conversion of $[FeCNH_2]^+$ to [FeOTf] at room temperature (associated with liberation of NH_3 and CH_4), we have been unable to characterize intermediates of this transformation, even at low temperature. However, by reconciling computational data with the observed reactivity of a methylated analogue, $[FeCNMe_2]$, we favor a C–H bond forming step to produce $[FeC(H)(NH_2)]^+$ as the next intermediate from $[FeCNH_2]^+$ along the catalytic pathway (possibly via ET-PT (steps d and e in Scheme 1) or PCET (step f)). This Fischer-type aminocarbene would plausibly be on path for either CH_4 + NH_3 (6 e^-), or CH_3NH_2 (4 e^-), products. The selectivity determining C–N bond cleaving step that produces the 6 e^- products in this system must therefore occur at a later stage of the catalytic cycle, with additional (and facile) $4H^+/4e^-$ transfers (Scheme 1, step g).

From the Fischer carbene (or its one electron reduced congener) several pathways can account for CH_4 and NH_3 products (depicted in Figure 2.7A). Guided by theoretical studies, we can, qualitatively at least, compare them. Ultimately, each specific H^+ and e^- step likely needs to be examined to fully account for CH_4 and NH_3/CH_3NH_2 selectivity, as has been the case for NH_3/N_2H_4 selectivity during N_2R (Figure 2.7B).[28,29,50] However,

acknowledging increased error in theoretical calculations when studying changes in charge state,[56] we have opted to limit our present considerations to the thermodynamics of the addition of a net H-atom to $[FeC(H)_x(NH_2)]^{+/0}$ (x = 1, 2) species, and the associated C−N bond strengths of the ammonium intermediates, $[FeC(H)_x(NH_3)]^{+/0}$, that form. The combined H^+/e^- transfers (Figure 2.7A) are referenced to the combination of $(C_6H_6)_2Cr$ (e^-) and $[Ph_2NH_2]OTf$ (H^+; see appendix A for details).

We consider three pathways in Figure 2.7A (*i-iii*) as an expansion on step g introduced in Scheme 1. Pathways *i-iii* proceed either via cationic or neutral intermediates and we use +/0 to differentiate between these charge states in the figure.

Starting from the aminocarbene +/0 intermediates, addition of the next H^+/e^- equivalent at N would yield an ammonium carbene, $[FeC(H)(NH_3)]^{+/0}$, which could liberate NH_3 and an iron methylidyne, $[Fe{\equiv}C{-}H]^{+/0}$. The methylidyne is envisioned to be reductively protonated to form CH_4 and [FeOTf] (Figure 2.7A, pathway *i*). The plausibility of iron methylidyne intermediacy in this $P_3^{Si}Fe$ catalyst system is supported by our recent report of the isolation and structural characterization of the methylated analogues $[P_3^{Si}Fe{\equiv}C{-}CH_3]^{+/0}$.[44]

Alternatively, C−H instead of N–H bond formation from $[FeC(H)(NH_2)]^{+/0}$ would yield an iron alkylamine product. We consider computationally such a species as two spin-isomers, a low spin (S = 0, 1/2) η^2-iminium adduct ($[Fe(\eta^2{-}CH_2NH_2)]^{+/0}$) and an intermediate spin (S = 1, 3/2) η^1–alkylamine ($[Fe(\eta^1\text{-}CH_2NH_2)]^{+/0}$). In $[Fe(\eta^1\text{-}CH_2NH_2)]^{+/0}$ intermediates, N−H bond formation is likely kinetically favorable (see below), but from the η^2-iminium adduct we anticipate similar barriers for C−H and N−H bond formation. From either alkylamine isomer, N−H bond formation would yield an alkylammonium product $[FeC(H)_2(NH_3)]^{+/0}$ (pathway *ii*). C−N bond cleavage releases NH_3 and an iron methylidene ($[Fe{=}CH_2]^{+/0}$). While we have not previously characterized a terminal $P_3^{Si}Fe{=}CR_2$ carbene (for R = H or alkyl), cationic, diamagnetic iron methylidenes, $[CpFe(L_2){=}CH_2]^+$ (L = phosphine or CO), have been synthesized by O-atom protonation of a corresponding methoxymethyl iron complex, followed by C−O bond cleavage.[57,58,59]

Such a scenario is akin to the C−N bond cleavage suggested here. Addition of a further $2H^+/2e^-$, releases CH_4 from $[FeCH_2]^{+/0}$.

A CH_3NH_2 selective pathway, $(iii)^{+/0}$ has also been considered, where the addition of H^+/e^- to the C–atom of $[Fe(\eta^2\text{-}CH_2NH_2)]^{+/0}$ results in a methylamine adduct, $[FeNH_2CH_3]^{+/0}$. The latter should readily liberate CH_3NH_2 upon reduction, as has been demonstrated for the ammonia-complex, $[P_3^{Si}FeNH_3]^+$.[60]

Computational analysis of the intermediates along these three pathways shows that C−H bond formation is always thermodynamically favored. Consequently, if the strongest bond is always formed, CN^- reduction would produce CH_3NH_2 instead of CH_4 and NH_3 (Figure 2.7A; pathway *iii*). Hence, to account for the observed CH_4 and NH_3 products, we propose the bulky ^{i}Pr-groups on the P_3^{Si} ligand limit access to the carbyne C-atom and thereby kinetically favor N−H bond formation. This leads to ammonium intermediates $[FeC(H)_x(NH_3)]^{+/0}$ (x = 1,2) that ultimately liberate NH_3 (and then CH_4; Figure 2.7A, pathway *i* and *ii*). This rationalization accommodates the observed mixture of CH_3NH_2 and NH_3 observed when using $(PhBP^{iPr}_3)FeBr$ as a catalyst instead of [Fe] (Table 1, entry 10); the 4-coordinate Fe center in $(PhBP^{iPr}_3)FeBr$ affords a more accessible carbyne intermediate C-atom.[61] Accordingly, the rate of C−H bond formation can compete with N−H bond formation and CH_3NH_2 is an observable product. Relatedly, we suspect that the increased steric bulk at N in $[FeCNMe_2]$ slows the rate of N−H bond formation, leading to the observed product distribution (2:1 Me_3N:Me_2NH).

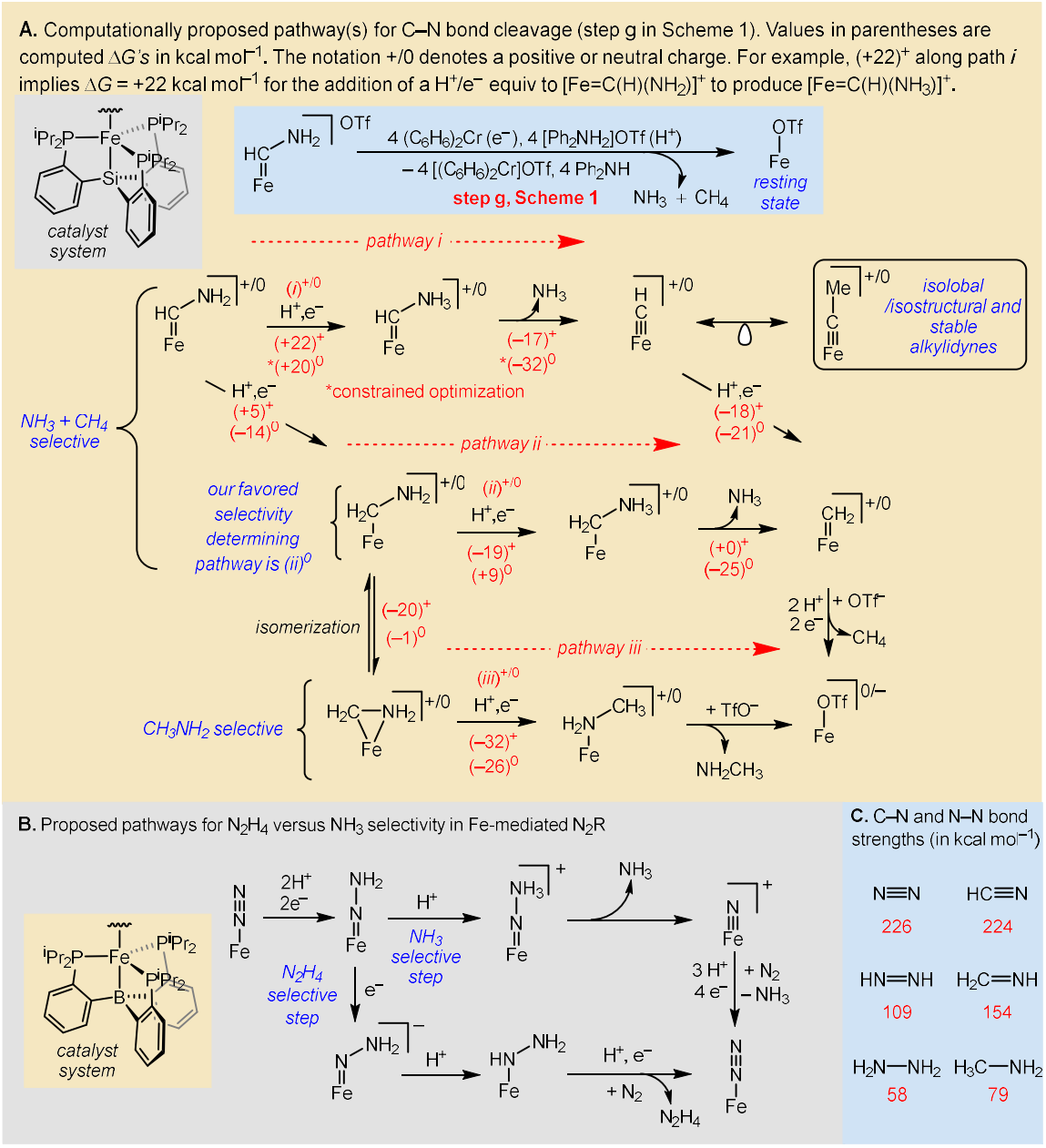

Figure 2.7. Mechanism of C−N bond cleavage and comparison to N−N bond cleavage. (A) Plausible pathways *i* – *iii* for C−N bond cleavage via step g in Scheme 1 for CN^- reduction by the P_3^{Si}Fe-system, attempting to rationalize selectivity, with associated thermodynamic data for stepwise e^-/H^+ transfers en route to product, with values for both cationic (+) and neutral (0) species. Pathway ii^0 is our favored pathway. (B) Comparison with N−N bond cleavage in Fe-mediated N_2R by the P_3^BFe-system, accounting for NH_3 versus N_2H_4 selectivity.[29,50] (C) Comparison of N−N and C−N bond strengths in N_2 and HCN and their further reduced derivatives.[62]

With these considerations, we next compare the NH_3/CH_4 selective pathways (*i* and *ii*). We favor pathway $(ii)^0$ as a pathway involving exothermic and mildly endergonic steps, with C−N bond cleavage occurring from $[FeCH_2NH_3]^0$. Considering pathways $(i)^{+/0}$, they feature highly endergonic N−H bond formation steps (+22 and + 20 kcal mol^{-1}, respectively). As this step is followed by exothermic C−N bond cleavage and reductive protonation of the resulting methylidyne, pathways $(i)^{+/0}$ may nevertheless be kinetically competent.[63] Path $(ii)^+$ features downhill or mildly endergonic steps. We nevertheless disfavor this pathway (compared to $(ii)^0$) due to the high favorability of the diamagnetic $[Fe(\eta^2\text{-}CH_2NH_2)]^+$ (−20 kcal mol^{-1} compared to $[Fe(\eta^1\text{-}CH_2NH_2)]^+$), with subsequent $H^\bullet$ addition at C rather than N being very exothermic from $[Fe(\eta^2\text{-}CH_2NH_2)]^+$.

Our favored path $(ii)^0$ points to a selectivity determining step at the addition of a (net) $H^\bullet$ to $[Fe(\eta^1\text{-}CH_2NH_2)]^0$; the latter constitutes a $4H^+/4e^-$ intermediate of [FeCN] reduction. By contrast, the proposed selectivity determining intermediate during N_2R is $[FeNNH_2]$, a $2H^+/2e^-$ intermediate (Figure 2.7B). Compared to isolobal N≡N, $C{\equiv}N^-$ requires a greater degree of reduction before C−N bond cleavage can occur. This is consistent with the respective C−N and N−N sigma bond strengths: while their triple bond strengths are similar, the bond weakening upon decrease in bond order is much greater for N_2 (Figure 2.7C).[62]

In addition to the high selectivity for CH_4 and NH_3, CN^- reduction of [FeCN] has high C_1 selectivity compared to other Fe-catalysts. When considering the origin of this selectivity, it is worth noting that the addition of multiple cyanide ligands bound to Fe has not been observed during catalysis or chemical experiments. This might be critical for the high selectivity for C_1 products. The precedent for C–C coupling of CO or CNR ligands at mononuclear metal sites requires two of these ligands bound to the metal prior to coupling.[64,65,66,67] The sterically encumbered, four-coordinate $P_3{}^{Si}$-ligand hinders the facile addition of multiple equivalents of CN^-, maintaining the trigonal bipyramidal geometry during catalysis.[68] We propose that this results in the high yields for C_1 products. Accordingly, the more flexible $(P_3{}^B)$Fe-platform[14,55] and the less encumbered $(PhBP^{iPr}_3)$Fe-platform[61] both have high C_2/C_1 ratios (0.16 and 0.11, respectively) compared to [FeCN] (0.02). Relatedly,

a previously synthesized and stable compound, $(PhBP^{iPr}_3)Fe(CNR)_2$, demonstrates that $(PhBP^{iPr}_3)Fe$ could accommodate two CN^- ligands (or further protonated derivatives) in a 5-coordinate structure, likely needed for C_2 product formation.[69]

Finally, it is interesting to compare the strength of the reductant used herein for the CN^- reduction ($(C_6H_6)_2Cr$; E °= −1.2 V), with a common reductant used for N_2R via related iron catalysts Cp^*_2Co (E° = −1.9 V). Proposed pathways for catalysis require a turnover limiting potential (E° ≈ −2.0 V) that generates an FeN_2^- species before protonation (to generate FeN_2H) can occur, necessitating reductants as strong as Cp^*_2Co.[38,40,70]

By contrast, the basicity of the CN^- ligand enables protonation of [FeCN] prior to an ET step.[25,36] Consequently, the turnover limiting potential is that of $[FeCNH]^{+/0}$ ($E(Fe^{II/I})$ = –1.3 V), not $[FeCN]^{0/-}$ ($E(Fe^{II/I})$ = –2.1 V), allowing the use of a comparatively mild reductant like $(C_6H_6)_2Cr$. If initial protonation, or PCET, occurs before any independent ET steps, the turnover limiting potential for catalysis can be significantly less reducing. Indeed, Schrock's original triamidoamine Mo-N_2 catalyst system is thought to proceed via an initial PT step, and it is compatible with correspondingly milder reductants (e.g., Cp^*_2Cr) for turnover.[15,71,72]

2.4 Conclusions

In conclusion, we have described the catalytic reductive protonation of CN^- to primarily NH_3 and CH_4, by a mononuclear Fe-complex, with selectivities comparable to those observed for CN^- reduction by nitrogenase. We also report mechanistic studies that show terminal iron aminocarbynes ($FeCNH_2$) intermediates, which are structurally similar to iron hydrazido intermediates ($FeNNH_2$) of Fe-mediated N_2R, as on-path in the CN^- reduction cycle. Experimental and computational studies suggest that these aminocarbynes undergo further C−H bond formation(s) prior to C−N bond cleavage, resulting in the selectivity observed, in contrast to iron hydrazidos during N_2R. Via this study, a terminal transition metal carbyne is hence invoked as a critical intermediate in the catalytic reductive protonation of a robust small molecule (CN^-).

2.5 Cited References

1. Seefeldt, L. C.; Yang, Z.-Y.; Lukoyanov, D. A.; Harris, D. F.; Dean, D. R.; Raugei, S.; Hoffman, B. M. *Chem. Rev.* **2020**. 120, 5082–5106.
2. Seefeldt, L. C.; Rasche, M. E.; Ensign, S. A. *Biochemistry* **1995**. 34, 5382–5389.
3. Lee, C. C.; Hu, Y.; Ribbe, M. W. *Science* **2010**. 329, 642–642.
4. Spatzal, T.; Perez, K. A.; Einsle, O.; Howard, J. B.; Rees, D. C. *Science* **2014**. 345, 1620–1623.
5. Hardy, R. W. F.; Knight, E. *Biochim. Biophys. Acta BBA - Enzymol.* **1967**. 139, 69–90.
6. Kelly, M.; Postgate, J. R.; Richards, R. L. *Biochem. J.* **1967**. 102, 1-3C.
7. Li, J.; Burgess, B. K.; Corbin, J. L. *Biochemistry* **1982**. 21, 4393–4402.
8. Lowe, D. J.; Fisher, K.; Thorneley, R. N. F.; Vaughn, S. A.; Burgess, B. K. *Biochemistry* **1989**. 28, 8460–8466.
9. Fisher, K.; Dilworth, M. J.; Newton, W. E. *Biochemistry* **2006**. 45, 4190–4198.
10. Lee, C. C.; Hu, Y.; Ribbe, M. W. *Angew. Chem. Int. Ed Engl.* **2012**. 51, 1947–1949.
11. Lee, C. C.; Hu, Y.; Ribbe, M. W. *Angew. Chem. Int. Ed Engl.* **2015**. 54, 1219–1222.
12. Lee, C. C.; Hu, Y.; Ribbe, M. W. *Proc. Natl. Acad. Sci.* **2012**. 109, 6922–6926.
13. Roth, L. E.; Tezcan, F. A. *J. Am. Chem. Soc.* **2012**. 134, 8416–8419.
14. Chalkley, M. J.; Drover, M. W.; Peters, J. C. *Chem. Rev.* **2020**. 120, 5582–5636.
15. Yandulov, D. V.; Schrock, R. R. *Science* **2003**. 301, 76–78.
16. Anderson, J. S.; Rittle, J.; Peters, J. C. *Nature* **2013**. 501, 84–87.
17. L. Hughes, D.; Y. Mohammed, M.; J. Pickett, C. *J. Chem. Soc. Chem. Commun.* **1989**. 18, 1399–1400.
18. Pombeiro, A. J. L.; Richards, R. L. *Coord. Chem. Rev.* **1990**. 104, 13–38.
19. Pombeiro, A. J. L.; Guedes da Silva, M. F. C.; Michelin, R. A. *Coord. Chem. Rev.* **2001**. 218, 43–74.

20. Tanifuji, K.; Sickerman, N.; Lee, C. C.; Nagasawa, T.; Miyazaki, K.; Ohki, Y.; Tatsumi, K.; Hu, Y.; Ribbe, M. W. *Angew. Chem. Int. Ed.* **2016**. 55, 15633–15636.
21. Sickerman, N. S.; Tanifuji, K.; Lee, C. C.; Ohki, Y.; Tatsumi, K.; Ribbe, M. W.; Hu, Y. *J. Am. Chem. Soc.* **2017**. 139, 603–606.
22. Tanifuji, K.; Lee, C. C.; Ohki, Y.; Tatsumi, K.; Hu, Y. L.; Ribbe, M. W. *Angew. Chem.-Int. Ed.* **2015**. 54, 14022–14025.
23. Fischer, E. O.; Schneider, J.; Neugebauer, D. *Angew. Chem. Int. Ed. Engl.* **1984**. 23, 820–821.
24. Mokhtarzadeh, C. C.; Moore, C. E.; Rheingold, A. L.; Figueroa, J. S. *Angew. Chem. Int. Ed.* **2017**. 56, 10894–10899.
25. Rittle, J.; Peters, J. C. *Angew. Chem.-Int. Ed.* **2016**. 55, 12262–12265.
26. Lee, Y.; Peters, J. C. *J. Am. Chem. Soc.* **2011**, 133, 4438–4446.
27. Anderson, J. S.; Cutsail, G. E.; Rittle, J.; Connor, B. A.; Gunderson, W. A.; Zhang, L.; Hoffman, B. M.; Peters, J. C. *J. Am. Chem. Soc.* **2015**. 137, 7803–7809.
28. Rittle, J.; Peters, J. C. *J. Am. Chem. Soc.* **2016**. 138, 4243–4248.
29. Thompson, N. B.; Green, M. T.; Peters, J. C. *J. Am. Chem. Soc.* **2017**. 139, 15312–15315.
30. Pombeiro, A. J. L.; Richards, R. L. *Transit. Met. Chem*. **1980**. 5, 281–284.
31. Carvalho, M. F. N. N.; Pombeiro, A. J. L.; Schubert, U.; Orama, O.; Pickett, C. J.; Richards, R. L. *J. Chem. Soc. Dalton Trans.* **1985**. 10, 2079–2084.
32. For an example of protonation and substrate release from a bridging carbyne see: Whitmire, K.; Shriver, D. F. *J. Am. Chem. Soc.* **1980**. 102, 1456–1457.
33. Holt, E. M.; Whitmire, K. H.; Shriver, D. F. *J. Organomet. Chem.* **1981**. 213, 125–137.
34. Wengrovius, J. H.; Sancho, J.; Schrock, R. R. *J. Am. Chem. Soc.* **1981**. 103, 3932–3934.
35. Fürstner, A. *J. Am. Chem. Soc.* **2021**. 143, 15538–15555.

36. Rittle, J.; Peters, J. C. *J. Am. Chem. Soc.* **2017**. 139, 3161–3170.
37. Chalkley, M. J.; Oyala, P. H.; Peters, J. C. *J. Am. Chem. Soc.* **2019**. 141, 4721–4729.
38. Chalkley, M. J.; Del Castillo, T. J.; Matson, B. D.; Peters, J. C. *J. Am. Chem. Soc.* **2018**. 140, 6122–6129.
39. Connelly, N. G.; Geiger, W. E. *Chem. Rev.* **1996**. 96, 877–910.
40. Chalkley, M. J.; Del Castillo, T. J.; Matson, B. D.; Roddy, J. P.; Peters, J. C. *ACS Cent. Sci.* **2017**. 3, 217–223.
41. Ung, G.; Peters, J. C. *Angew. Chem. Int. Ed.* **2015**. 54, 532–535.
42. Betley, T. A.; Peters, J. C. *J. Am. Chem. Soc.* **2003**. 125, 10782–10783.
43. Del Castillo, T. J.; Thompson, N. B.; Peters, J. C. *J. Am. Chem. Soc.* **2016**. 138, 5341–5350.
44. Citek, C.; Oyala, P. H.; Peters, J. C. *J. Am. Chem. Soc.* **2019**. 141, 15211–15221.
45. Buscagan, T. M.; Oyala, P. H.; Peters, J. C. *Angew. Chem. Int. Ed.* **2017**. 56, 6921–6926.
46. Creutz, S. E.; Peters, J. C. *Chem. Sci.* **2017**. 8, 2321–2328.
47. The protonation of [FeCN] to [FeCNH][BAr^F_4] was monitored by observing the shift in the UV-visible spectra maxima at 910 and 540 nm to 790 and 610 nm upon addition of the acid, see Appendix A.
48. Addition of more equivalents $(C_6H_6)_2Cr$ was not possible due to solubility limitations interfering with the UV-vis measurements.
49. Garrido-Barros, P.; Chalkley, M. J.; Peters, J. C. *Angew. Chem. Int. Ed.* **2023**. 62, e202216693..
50. Boyd, E.A.; Peters, J.C. *J. Am. Chem. Soc.* **2023**. 145, 14784–14792.
51. The observation of substantial amounts of Me_3N is perhaps unexpected given the selectivity for NH_3 + CH_4 in the catalytic cyanide reduction reaction. We note that while [$FeCNMe_2$] and [$FeCNH_2$]$^{+/0}$ react with a combination of $(C_6H_6)_2Cr/Ph_2NH_2$]OTf at similar rates, the proposed intermediate [$FeC(H)NMe_2$]$^+$

is consumed much more slowly. This could suggest an alternative reaction pathway, such as bimolecular Me• transfer.

52. L represents a 2 e^- ligand (e.g., carbene, CO, CNMe, N_2). Relevant Mössbauer data for other S = 1 species, where $(P_3^{Si})Fe^{II}–L^+$ represents the cationic species $(P_3^{Si})Fe(CO)^+$, $(P_3^{Si})Fe(CNMe)^+$, and $(P_3^{Si})Fe(N_2)^+$, are: δ = 0.31 mm s^{-1}, ΔE_Q = 4.12 mm s^{-1} ; δ = 0.41 mm s^{-1}, ΔE_Q = 3.14 mm s^{-1}; δ = 0.53 mm s^{-1}, ΔE_Q = 2.39 mm s^{-1} respectively.
53. Tao, J.; Perdew, J. P.; Staroverov, V. N.; Scuseria, G. E. *Phys. Rev. Lett.* **2003**. 91, 146401–146404.
54. Weigend, F. *Phys. Chem. Chem. Phys.* **2006**. 8, 1057–1065.
55. Matson, B. D.; Peters, J. C. *ACS Catal.* **2018**. 8, 1448–1455.
56. As an example, explicit solvent interactions are often required to accurately predict reduction potentials, as recently observed for persulfate oxidation: Hosseini, S.; Janusz, J. N.; Tanwar, M.; Pendergast, A. D.; Neurock, M.; White, H. S. *J. Am. Chem. Soc.* **2022**. 144, 21103–21115.
57. Jolly, P. W.; Pettit, R. *J. Am. Chem. Soc.* **1966**. 88, 5044–5045.
58. Brookhart, M.; Tucker, J. R.; Flood, T. C.; Jensen, J. *J. Am. Chem. Soc.* **1980**. 102, 1203–1205.
59. Aghazada, S.; Munz, D.; Heinemann, F. W.; Scheurer, A.; Meyer, K. *J. Am. Chem. Soc.* **2021**. 143, 17219–17225.
60. Lee, Y.; Mankad, N. P.; Peters, J. C. *Nat. Chem.* **2010**. 2, 558–565.
61. Mankad, N. P.; Whited, M. T.; Peters, J. C. *Angew. Chem. Int. Ed.* **2007**. 46, 5768–5771.
62. Benson, S. W. *J. Chem. Educ.* **1965**. 42, 502.
63. Attempts to optimize $[Fe{=}C(H)NH_3]^0$ showed *in silico* C−N bond cleavage; the energy of this intermediate was hence estimated by constrained geometry optimization with the C−N bond set to 1.6 Å.

64. Suess, D. L. M.; Peters, J. C. *J. Am. Chem. Soc.* **2013**. 135, 12580–12583.

65. Wang, Y.; Silva, J. J. R. F. D.; L. Pombeiro, A. J.; Angela Pellinghelli, M.; Tiripicchio, A.; A. Henderson, R.; L. Richards, R. *J. Chem. Soc. Dalton Trans.* **1995**. 7, 1183–1191.

66. Filippou, A. C.; Grünleitner, W.; Völkl, C.; Kiprof, P. *Angew. Chem. Int. Ed. Engl.* **1991**. 30, 1167–1169.

67. Filippou, A. C.; Völkl, C.; Grünleitner, W.; Kiprof, P. *J. Organomet. Chem.* **1992**. 434, 201–223.

68. The overaddition of CN^- ligand was not observed in the reaction of (P_3^{Si})FeOTf and [TBA][CN]. Similarly, (P_3^{Si})FeCN is synthesized with excess NaCN in refluxing 1:1 THF:MeOH, but addition of multiple equivalents of CN^- has not been observed.

69. Turculet, L.; Feldman, J. D.; Tilley, T. D. *Organometallics* **2003**. 22, 4627–4629.

70. Hill, P. J.; Doyle, L. R.; Crawford, A. D.; Myers, W. K.; Ashley, A. E. *J. Am. Chem. Soc.* **2016**. 138, 13521–13524.

71. Yandulov, D. V.; Schrock, R. R. *Inorg. Chem.* **2005**. 44, 1103–1117.

72. Thimm, W.; Gradert, C.; Broda, H.; Wennmohs, F.; Neese, F.; Tuczek, F. *Inorg. Chem.* **2015**. 54, 9248–9255.

Chapter 3

Reversible, equilibrium interconversion of an iron cyanide and an iron aminocarbyne via an H-bond mediated proton-coupled electron transfer

3.1 Introduction

The storage of chemical energy as solar fuels has motivated the development of proton-coupled reductions of small molecules at ambient conditions and low applied overpotential.[1,2] This effort requires catalysts that lower the kinetic barriers and level the energy between intermediates , as well as strategies to deliver multiple H^+/e^-.[3] Considerable progress has been made towards the reversible interconversion of $2H^+/2e^-$ energy carriers (e.g., H^+/H_2, CO_2/HCO_2H, CO_2/CO, O_2/H_2O_2) with molecular,[4,5,6,7,8,9] heterogeneous[10,11] and enzymatic examples.[12,13,14,15] By contrast, examples of the deep (> 2 e^-) reductions of small molecule triple bonds, N_2 or CO,[16,17,18,19,20,21,22,23] which would yield desirable energy carriers, like NH_3 or CH_3OH, require a considerable thermodynamic driving force at ambient conditions. Likewise, the corresponding oxidation reactions, ammonia and methanol oxidation requires a large driving force.[24,25,2627,28,29,30] The lowest driving force conditions reported for N_2 reduction to NH_3 (Nitrogen reduction, N_2R) and oxidation of NH_3 to N_2 (ammonia oxidation, AO) occur at an overpotential of ~80 kcal mol^{-1} per equiv N_2 (Scheme 3.1).[18,26]

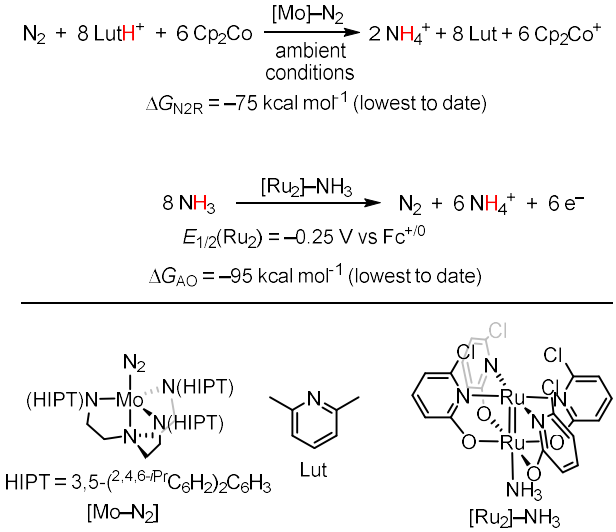

Scheme 3.1. Lowest overpotential catalytic N_2R and AO with molecular complexes reported to date.[18,26]

As a complementary approach to the study of these catalytic reactions, the development and characterization of systems that can undergo multiple reversible H^+/e^-

transfers during triple bond activation might aid the development of new strategies for efficient small molecule reduction. Pioneering studies by Meyer and coworkers have demonstrated multiproton-and-electron reversible interconversions of transition metal oxos with the corresponding aquo complexes.[31,32] However, examples of reversible reduction of transition metal activated small molecule triple bonds are limited to the $2H^+/2e^-$ reduction of Os-bound MeC≡N to the corresponding imine (Figure 3.1).[33] The bidirectional $2H^+/2e^-$ interconversion of a tungsten cyanide complex (W(CN)) and the corresponding aminocarbyne ($W(CNH_2)$) (Figure 3.1), provides another notable example of triple bond activation.[34] However, this reaction does not occur at equilibrium, requiring a $\Delta E > 1$ V between the oxidative and reductive reactions.

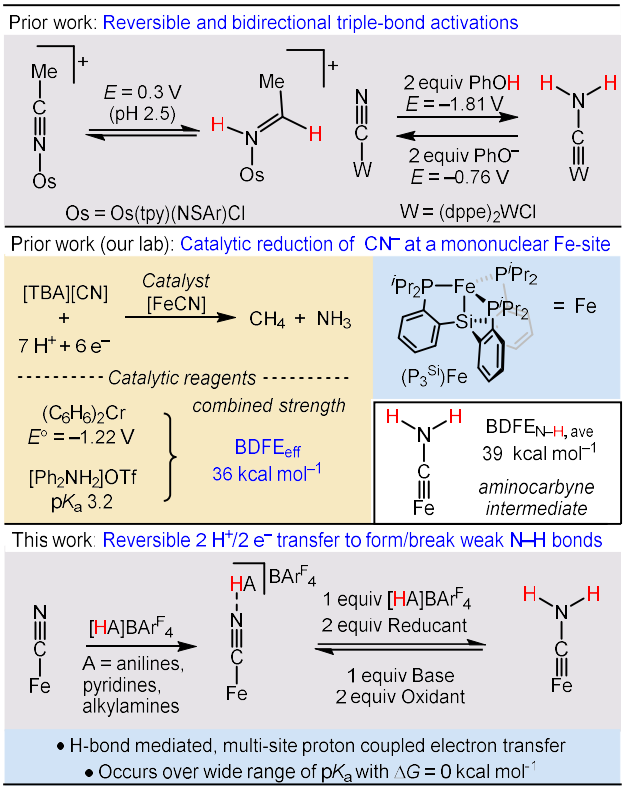

Figure 3.1. Background on reversible small molecule activation and CN^- reduction as context for this study.[23,33,34,36]

Our laboratory recently reported conditions for the catalytic, 7 H^+/6 e^- reduction of [TBA][CN] to CH_4 and NH_3 at a mononuclear iron tris(phosphino)sylil platform, $P_3^{Si}Fe$ (abbreviated as [Fe] throughout this report), using $(C_6H_6)_2Cr$ and $[Ph_2NH_2]OTf$ as e^- and H^+

source, respectively (Figure 3.1, middle).[23] In this study, the $2H^+/2e^-$ reduction product of the [Fe−C≡N] precatalyst,[35] a terminal iron aminocarbyne [Fe≡C−NH_2], was observed as a catalytic intermediate (Figure 3.1, middle). Aminocarbyne formation occurred at a mild thermodynamic overpotential[36] and despite weak N−H bonds (Figure 3.1) the aminocarbyne was stable at low temperature (−80 °C). The close BDFE matches of the species (Figure 3.2) indicate an energy match between [FeCN], [FeCNH] and [$FeCNH_2$]. These attributes suggested the $2H^+/2e^-$ equilibration of [FeCN]↔[$FeCNH_2$] might be observable and could provide an interesting point of comparison for early N−H bond formation in N_2R (nitrogen reduction).[36,37]

Reversible interconversion of [FeCN]↔[$FeCNH_2$], would require reagents that can approach both the reductive ([FeCN]→[$FeCNH_2$]) and oxidative ([$FeCNH_2$]→[FeCN]) proton-coupled redox reactions at minimal driving force. In the catalytic conditions, reduction of [FeCN] (pK_a 5.6, all pK_a's in THF, Figure 3.2) occurred via initial proton transfer (PT) to [FeCN] by the strong acid [Ph_2NH_2]OTf (pK_a 3.2).[23,36] However, as proton-coupled oxidation of [$FeCNH_2$] would require a base capable of deprotonating $[FeCNH_2]^+$ (the related methylated analogue $[FeCN(H)Me]^+$ has pK_a 7.1), we initially sought alternative strategies to reduce [FeCN] utilizing weaker acids.

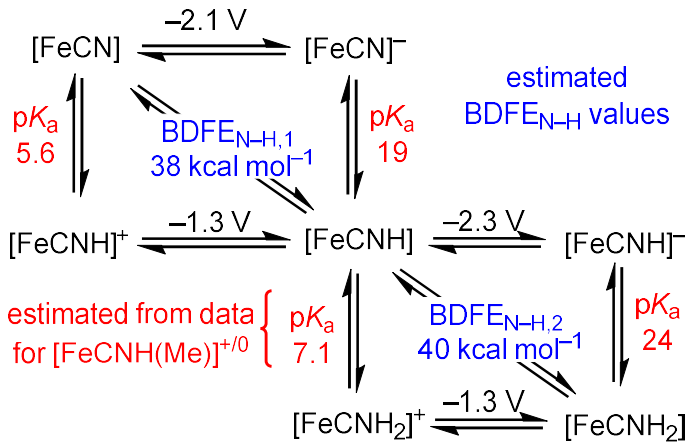

Figure 3.2. Pertinent thermochemical measurements for [FeCN], [FeCNH(Me)] (as a model for [$FeCNH_2$]), and relevant intermediates. Values are measured in THF at 25 °C.[36]

Noting that H-bonding to terminal cyanide ligands is well-established,[38] and H-bonds, in turn, can facilitate multisite-proton coupled electron transfers (MS-PCET),[39] pathways with lower enthalpic barriers than stepwise alternatives,[40,41,42] we targeted such a strategy for [FeCN] reduction.

$$\mathrm{BDFE_{eff}} = 23.06\,E^{\circ} + 1.37\ \mathrm{p}K_a + C_{\mathrm{G}} \quad \text{(eqn 3.1)}$$

$$\Delta G = 2\ \mathrm{BDFE_{eff}} - (\mathrm{BDFE_{N-H,1}} + \mathrm{BDFE_{N-H,2}}) \quad \text{(eqn 3.2)}$$

MS-PCET strategies also allow ready tuning of the thermodynamic driving force by decoupling acid/base and reductant/oxidant pairs.[39,40] The combined reagent strength can be estimated using the effective bond dissociation free energy ($BDFE_{eff}$; eqn 3.1), a measure of the net thermodynamic H-atom donor ability of a reagent pair, with inputs E(reductant/oxidant), pK_a(acid/base), and a solvent and temperature dependent constant C_G, which is 59.9 kcal mol^{-1} in THF at 25 °C.[43,44] Comparing the $BDFE_{eff}$ to the $BDFE_{N-H}$ of [FeCN−H] (38 kcal mol^{-1}) and [FeCN(Me)−H] (40 kcal mol^{-1}; an analogue of [$FeCNH_2$]) allows for an estimate of driving force (ΔG; eqn 3.2) for [$FeCNH_2$] formation, and a helpful metric for choosing reagents that might allow an equilibrium reaction. Using these principles, we develop the rapid equilibrium $2H^+/2e^-$ interconversion between [FeCN] and [$FeCNH_2$] (Figure 3.1, bottom).

3.2 Results

3.2.1 Characterization and reduction of H-bonded adduct to [FeCN]

To target H-bond formation between [FeCN] and acid, we wanted to remove competitive Brönsted basic sites in solution (e.g., solvent, counteranion), thereby favoring acid coordination to N_{CN}.[45]

The addition of [$PhNH_3$]BAr^F_4 (pK_a 8.0)[46] to [FeCN] in Et_2O at −80 °C resulted in a color change from red to purple. This color change can be monitored by UV-vis with the diagnostic d-d transition of [FeCN] (absorption maxima: 530 nm, 909 nm, Figure B.1) shifting slightly (new maxima: 550 nm and 895 nm), but less than upon the full protonation

to [FeCNH]BAr^F_4 (absorption maxima: 600 nm and 790 nm). ^{57}Fe Mössbauer of the frozen mixture of [^{57}FeCN] + 2.5 equiv [$PhNH_3$]BAr^F_4 showed a single new species with Mössbauer parameters $\delta = 0.44$ mm s^{-1} and $\Delta E_Q = 2.06$ mm s^{-1} (Figure 3.3), similar, but distinctly shifted from starting material, [^{57}FeCN] ($\delta = 0.44$ mm s^{-1} and $\Delta E_Q = 1.77$ mm s^{-1}). IR data shows a slight shift in $\nu_{C\equiv N}$ upon adding acid (2075 cm^{-1}, compared to 2082 cm^{-1} in the absence of acid), consistent with slight activation of the CN^- ligand. These data together support the formation of an H-bonded adduct, [$FeCN\cdots HNH_2Ph$]BAr^F_4.

With this H-bonded complex in hand, we explored its reductive chemistry. The addition of 2.5 equiv Cp^*_2Cr ($E(Cr^{III/II})$=−1.47 V)[47] to a solution of [FeCN] and 2.5 equiv [$PhNH_3$]BAr^F_4 at −80 °C in Et_2O was monitored by UV-vis and rapid consumption ($\tau_{1/2}$ <10 s) of [$FeCN\cdots HNH_2Ph$]$^+$ was observed, with a new shoulder growing in at 590 nm, consistent with the formation of [$FeCNH_2$] (Figure B.13). As we have previously observed, the aminocarbyne is stable at −80 °C, but under these conditions, upon warming to 0 °C, it decays to reform [FeCN]. Monitoring this reaction by ^{57}Fe Mössbauer spectroscopy confirmed the formation of [$FeCNH_2$] with the parameters δ = 0.04 mm s^{-1} and ΔE_Q = 0.98 mm s^{-1}, diagnostic for the aminocarbyne (Figure 3.3).[23]

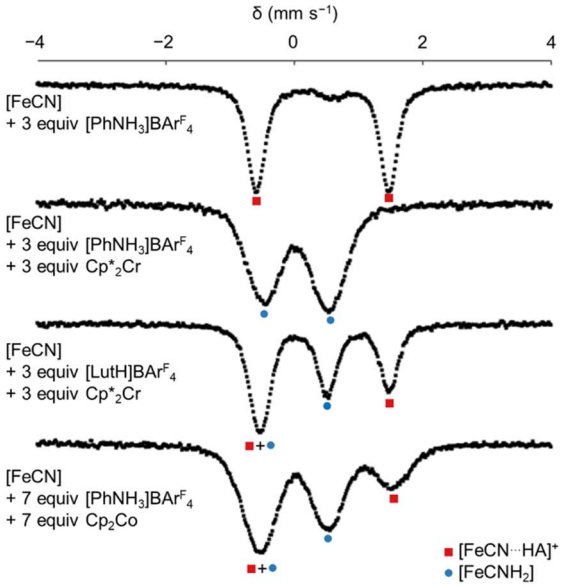

Figure 3.3. ^{57}Fe Mössbauer spectra of selected reactions of [FeCN] with acid and reductant.[48]

Interestingly, the first N−H bond formation, converting [FeCN] to [FeCN−H], cannot be (readily) accounted for via stepwise proton and electron transfers, as $[PhNH_3]^+$ is not acidic enough to protonate [FeCN] and Cp^*_2Cr does not reduce [FeCN] (Figure 3.2). Along with the observed H-bonded complex, these observations align with our initially posited MS-PCET reaction, although kinetic studies (*vide infra*) provided more reliable evidence of this mechanism.

This reagent combination is competent for reducing [FeCN] to release NH_3: reacting [FeC^{15}N] with 20 equiv Cp^*_2Cr and 20 equiv $[PhNH_3]OTf$ yields $^{15}NH_3$ (0.2 equiv NH_3/Fe). However, these yields are much lower than for the reduction of [FeCN] by the catalytic reagents $[Ph_2NH_2]OTf$ and $(C_6H_6)_2Cr$ (0.75 equiv NH_3/Fe). [23]

Table 3.1. Comparison of reagent strengths and the observation of aminocarbyne formation.

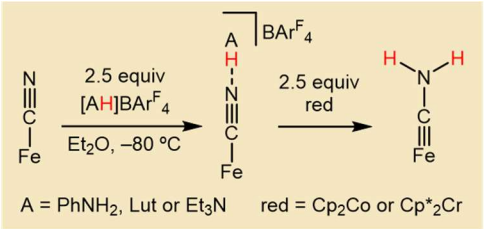

Reagent strength:		$BDFE_{eff}$ (kcal mol^{-1})	ΔG (kcal mol^{-1})	
Cp^*_2Cr (−1.47 V)	$[PhNH_3]BAr^F_4$ (pK_a 8.0)	37	−5	Complete formation of $[FeCNH_2]$
Cp^*_2Cr (−1.47 V)	$[LutH]BAr^F_4$ (pK_a 9.5)	39	−1	Partial formation of $[FeCNH_2]$
Cp_2Co (−1.33 V)	$[PhNH_3]BAr^F_4$ (pK_a 8.0)	40	+2	Partial formation of $[FeCNH_2]$
Cp_2Co (−1.33 V)	$[LutH]BAr^F_4$ (pK_a 9.5)	42	+6	No reaction
Cp^*_2Cr (−1.47 V)	$[Et_3NH]BAr^F_4$ (pK_a 13.7)	45	+11	No reaction

3.2.3 Thermodynamics of aminocarbyne formation

With the rapid reduction of [FeCN] to $[FeCNH_2]$ established, we used eqn 3.1 and 3.2 to assess reaction thermodynamics. For the combination Cp^*_2Cr ($E(Cr^{III/II}) = –1.47$ V)[23] and $[PhNH_3]^+$ (pK_a 8.0)[46] the $BDFE_{eff}$ = 37 kcal mol^{-1}, giving ΔG = –5 kcal mol^{-1} (Table 3.1). Reductions with either slightly weaker acid or reductant would shift ΔG towards 0.

Accordingly, reacting [^{57}FeCN] with 3 equiv [LutH]BAr^F_4 (Lut = 2,6-dimethylpyridine; pK_a 9.5)[46] followed by 3 equiv Cp^*_2Cr in Et_2O at −80 °C, freeze-quenching and analyzing by ^{57}Fe Mössbauer spectroscopy revealed two major species formed in about a 1:1 ratio, assigned as [$FeCNH_2$], and [$FeCN^{\cdots}HLut]^+$ (Figure 3.3 and Table 3.1). The observation of unconsumed starting material is consistent with this reaction's small, estimated driving force (ΔG = −1 kcal mol^{-1}; Table 3.1).[49] Alternatively, the reaction of [^{57}FeCN] with 7 equiv Cp_2Co (cobaltocene; $E(Co^{III/II})$=–1.33 V)[23] and 7 equiv [$PhNH_3$]BAr^F_4 at −80°C similarly analyzed by ^{57}Fe Mössbauer also shows a mixture of [$FeCNH_2$] and [$FeCN^{\cdots}HNH_2Ph]^+$ (Figure 3.3 and Table 3.1; ΔG = +2 kcal mol^{-1}).[50]

As expected, when the $BDFE_{eff}$ is increased further using either Cp^*_2Cr/[Et_3-NH]BAr^F_4 (ΔG = +11 kcal mol^{-1}, Table 3.1 and Figure B.18) or Cp_2Co/[LutH]BAr^F_4 (ΔG = +6 kcal mol^{-1}, Table 3.1 and B.14) no reduction of [FeCN] was observed by UV-vis.

3.2.3 Establishing reversibility

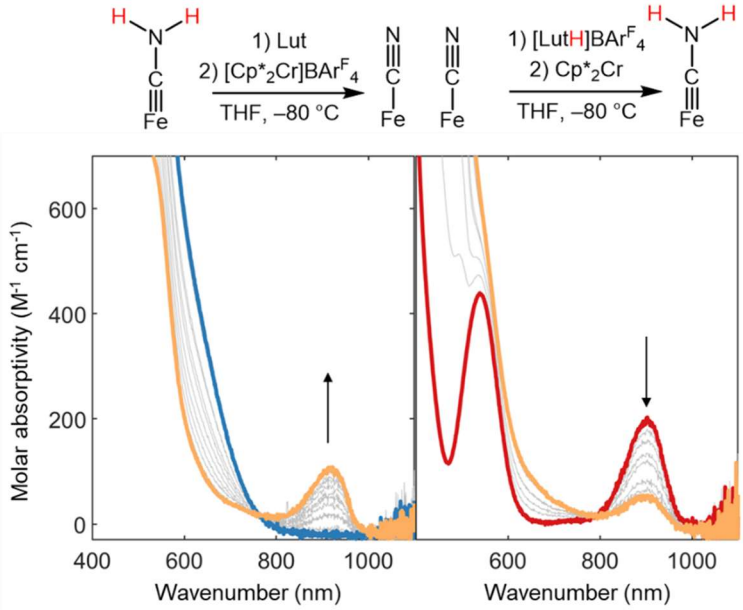

Figure 3.4. Reversible interconversion of iron cyanide and iron aminocarbyne. (Top) UV-vis titration of [Cp^*_2Cr]BAr^F_4 (4.5 mM) into 1.5 mM [$FeCNH_2$] with Lut (4.5 mM), at −80°C in THF. (Bottom) UV-vis titration of Cp^*_2Cr (4.5 mM) into 1.5 mM [FeCN] with [LutH]BAr^F_4 (4.5 mM) at −80°C in THF.

Having demonstrated that the $2H^+/2e^-$ reduction of [FeCN] to [$FeCNH_2$] can occur at $\Delta G \approx 0$, we attempted the reverse, proton-coupled aminocarbyne oxidation to confirm a bidirectional reaction. We have previously developed the *in situ* synthesis of [$FeCNH_2$] with [K]BAr^F_4 via the low temperature (−80°C) double protonation of generated [FeCN]K_2 (see appendix section B.2.2 for details).[23] Generation of [$FeCNH_2$] in this fashion in THF,[51] followed by addition of Lut (3 equiv), and finally the titration of [Cp^*_2Cr]BAr^F_4 (0 to 3 equiv), we observed the growth of a feature around 900 nm associated with formation of [FeCN···H−Lut]BAr^F_4, demonstrating the oxidation of [$FeCNH_2$] →[FeCN] (Figure 3.4, left panel). However, only partial oxidation is observed, consistent with a reaction close to equilibrium. The isosbestic point at about 790 nm indicates a clean transformation. To confirm that this reaction was occurring at equilibrium, we also assessed the reductive reaction under identical conditions. Cp^*_2Cr was titrated into a mixture of [FeCN] and 3 equiv [LutH]BAr^F_4 in THF at – 80 °C, observing now a partial bleaching of the diagnostic feature at 900 nm and an isosbestic point at 790 nm (Figure 3.4, right panel).

Both the oxidative and reductive titrations establish mixtures of [FeCN] and [$FeCNH_2$], consistent with the ΔG ~0 for the [LutH]BAr^F_4/Cp^*_2Cr reagent pair. This confirms this reaction as a $2H^+/2e^-$ reversible equilibrium.

3.2.4 Exploring a wider range of reagent strengths

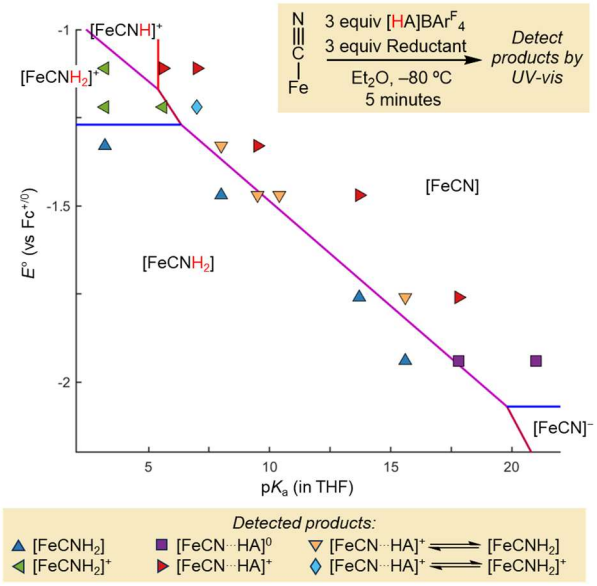

Figure 3.5. Pourbaix diagram for reaction of 2 equiv reductant and acid with [FeCN]. Markers show observed products, while lines indicate predicted products based on the previously measured thermochemistry.

With equilibrium reversibility between [FeCN] and [FeCNH$_2$] established, we next explored the reduction of [FeCN] over a wider range of acid and reductant strengths by UV-vis spectroscopy. To solutions of [FeCN] at −80°C in Et$_2$O, acids (pK_a 3.2 – 21) and reductants ($E°_{red}$ = −1.22 V to −1.96 V) of varying strength were added. Over this range, we observed a variety of [FeCN] reduction products, which can be plotted against the reagent strengths as a Pourbaix diagram (Figure 3.5). In short, our previously measured thermochemistry accurately predicts the observed products, albeit with some interesting deviations (*vide infra*).

Using strong acids and relatively weak reductants, such as [Ph$_2$NH$_2$]BAr$^F_4$/(C$_6$H$_6$)$_2$Cr or Cp$_2$Cr (E(Cr$^{III/II}$)=−1.11 V), the cationic aminocarbyne, [FeCNH$_2$]BAr$^F_4$, is the major product. This is in line with our previous report, where only upon addition of a larger excess of (C$_6$H$_6$)$_2$Cr is the [FeCNH$_2$]$^{+/0}$ reduction accessed.[23] Neither of these reductants are of sufficient strength to reduce [FeCNH]$^+$ (E(Fe$^{II/III}$) =−1.27 V, Figure 3.2), however, the

presence of excess $[Ph_2NH_2]BAr^F_4$ should give rapid protonation of *in situ* formed $[FeCNH]^0$, driving product formation towards $[FeCNH_2]^+$, the favored product.

As stronger reductants and weaker acids are used, $[FeCNH_2]$ becomes the favored product and varying the acid pK_a from 8.0-15.4, if paired with a reductant of sufficient strength such that $BDFE_{eff} \approx 39$ kcal mol^{-1} an equilibrium of $[FeCN] \leftrightarrow [FeCNH_2]$ is established. The relationship between reagent strength and products is consistent, with 59.4 mV/ΔpK_a expected for a $2H^+/2e^-$ transfer. Notably, despite these thermochemical measurements being made in THF at 25 °C, the values reasonably accurately predict reactivity in Et_2O at –80 °C. Considering that reagent strengths are often measured at 25 °C, while many reactions, such as Fe-based N_2R, are performed at lower temperatures[17,52] these results demonstrate that room temperature thermochemical values can still accurately predict reaction products.

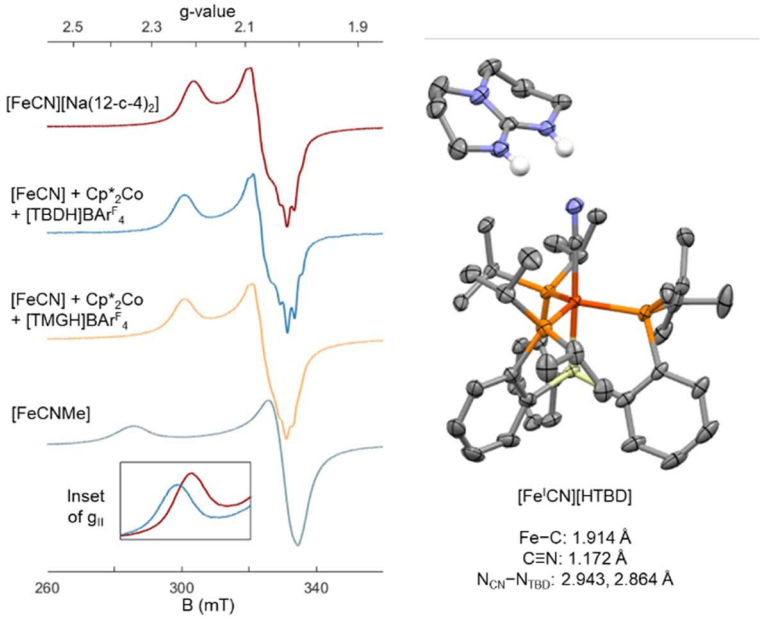

Figure 3.6. Formation of $[Fe^ICN][HTBD]$. (Left) EPR spectra of $[Fe^ICN][HTBD]$ and $[Fe^ICN][HTMG]$ with reference complexes $[Fe^ICN][Na(12\text{-c-}4)_2]$ and $[Fe^ICNMe]^0$. (Right) Solid-state structure of [FeCN][HTBD] with thermal ellipsoids displayed at 50% probability, H-atoms except H-bonding protons omitted for clarity.

Our previous thermochemical measurements do not predict the reactivity of [FeCN] with weak acids (pK_a >18) and strong reductants ($E(red^{+/0}) \sim -2.0$ V). Reacting [FeCN] with

Cp^*_2Co (decamethylcobaltocene; $E(Co^{III/II})$ = −1.96 V)[52] and $[TBDH]BAr^F_4$ (TBD = Triazabicyclodecene, pK_a 21)[46] results in partial consumption of starting material (Figure B.24), despite the thermochemical measurements suggesting no reaction should occur (ΔG = +9 kcal mol^{-1}). Analysis by continuous wave-EPR (cw-EPR) demonstrates that the product is not $[FeCNH_2]$ but a new S = ½ species. The freeze-quenched reaction of [FeCN] with Cp^*_2Co and $[TBDH]BAr^F_4$ generates a spectrum similar to $[FeCN][Na(12\text{-c-}4)_2]$.[35] However, a slight shift in $g_\parallel$ ($g_\parallel$ = 2.23 compared to $g_\parallel$ = 2.21 for $[FeCN][Na(12\text{-c-}4)_2]$, Figure 3.6A) is observed, suggesting mild activation of the CN^- ligand. This degree of activation is much less than for the previously characterized *bona fide* iron isocyanide [FeCNMe].[36]

We posited that these observations could be attributed to the formation of H-bonded adduct to $[FeCN]^-$ ($[Fe^ICN\cdots HTBD]^0$), resulting in a slightly activated CN^- ligand, which also shifts the $E°(Fe^{I/II})$, such that more Fe^I is observed. This assignment was confirmed by independent synthesis of the adduct $[Fe^ICN\cdots HTBD]^0$ via the low-temperature addition of [TBDH]OTf to $[FeCN][Na(12\text{-c-}4)_2]$, which allowed crystallization and analysis by XRD (Figure 3.6B). Particularly diagnostic was the C−N bond length of this new adduct (1.172 Å), which is much closer to $[FeCN][Na(12\text{-c-}4)_2]$ (1.170 Å)[35] than [FeCNMe] (1.186 Å).[36] The short distance between N_{CN} and N_{TBD} (2.94 and 2.86 Å) is consistent with an H-bond interaction between the acid and $[FeCN]^-$.[53] This complex also displays an activated $\nu_{C\equiv N}$ (1978 cm^{-1} compared to 2014 cm^{-1} for $[FeCN][Na(12\text{-c-}4)_2]$).

$[TMGH]BAr^F_4$, which should establish an equilibrium mixture of $[FeCN]\leftrightarrow[FeCNH_2]$ (ΔG = +0.6 kcal mol^{-1}), instead also generates a similar cw-EPR spectrum (Figure 3.6A), with a slightly shifted $g_\parallel$, suggesting that this reduced H-bonded adduct can also be favored over full N−H bond formation.

3.2.5 Probing electrochemical reversibility

Given the precedent for electrochemically reversible multiproton-and-electron activations we were motivated to explore electrochemical reductions of [FeCN] as well. The cyclic voltammogram (CV, Figure 3.7, blue trace) of [FeCN] (1 mM) in 0.2 M $[TBA]PF_6$ in

THF displays to two reversible redox couples, an oxidative $E(Fe^{II/III})$ = −0.38 V and a reductive feature $E(Fe^{I/II})$ = −2.07 V.[35] Upon the addition of [$PhNH_3$]OTf (pK_a 8.0; 5 to 20 equiv, Figure 3.7 red trace and Figure B.64), the reductive peak shifts to E = −1.31 V. The charge passed in this new couple is about ~ 2x that of $[FeCN]^{+/0}$ or $[FeCN]^{0/-}$ couples, consistent with a $2e^-$ redox reaction. This transformation occurs at $BDFE_{eff}$ = 40 kcal mol^{-1}, similar to $BDFE_{N-H,\ ave}$. As expected for an electrochemical H^+/e^- transfer the redox couple is sensitive to the addition of base, shifting cathodically when increasing the amount of [$PhNH_2$] (Appendix B). These observations are all consistent with the 2 e^- reduction expected for the interconversion of [FeCN]/[$FeCNH_2$].

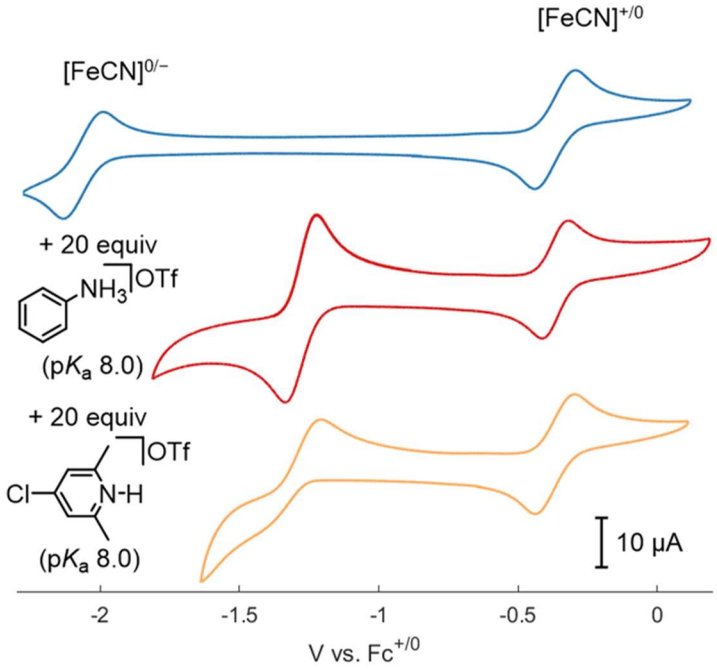

Figure 3.7. Cyclic voltammogram of [FeCN] 1 mM (blue trace) with 20 equiv [$PhNH_3$]OTf (red trace) or [$^{4\text{-Cl-2,6-Me}}$pyrH]OTf (yellow trace) added. All voltammograms collected in in 0.2 M [TBA][PF_6] in THF at 100 mV s^{-1} scan rate.

Unlike the chemical reductions which can be described by simple thermodynamic equations (eqn 3.1 and 3.2) over a large pK_a/E_{red} range, the electrochemical reduction of [FeCN] is highly sensitive to acid choice (Figure B.63). As an example, addition of 20 equiv [$^{4\text{-Cl-2,6-Me}}$pyrH]OTf (pK_a 8.0, Figure 3.7, yellow trace) to [FeCN] , despite having the same pK_a as $[PhNH_3]^+$, does not yield a fully reversible 2 e^- couple by CV. We note that these

electrochemical measurements are conducted at 25 °C in a more coordinating solvent in the presence of electrolyte, all factors that should disfavor H-bond formation. Hypothesizing that this might contribute to the lack of reversibility with [$^{4\text{-Cl-2,6-Me}}$pyrH]OTf we measured the $K_{\text{H-bond}}$ (eqn 3.3) with [$PhNH_3$]OTf and [$^{4\text{-Cl-2,6-Me}}$pyrH]OTf in THF at 25 °C with 0.2 M [TBA][PF_6] to reveal a stronger $K_{\text{H-bond}}$ with [$PhNH_3$]$^+$ ($K_{\text{H-bond}}(PhNH_3^+)$ = 60 ± 10 M^{-1}; $K_{\text{H-bond}}(^{4\text{-Cl-2,6-Me}}pyrH^+)$ = 20 ± 5 M^{-1}).

$$K_{\text{H-bon}}\ (\text{HA}) = \frac{[\text{FeCN}\cdots\text{HA(OTf)}]}{[\text{FeCN}][\text{HA(OTf)}]} \quad \text{(eqn 3.3)}$$

Consistent with this weaker H-bonding pre-equilibrium, the cyclic voltammogram of [FeCN] in the presence of [$^{4\text{-Cl-2,6-Me}}$pyrH]OTf approaches reversibility as the acid loading is increased further (Figure B.67).

3.2.6 Kinetics of [FeCN] reduction

Finally, we wanted to study the mechanism of reduction of [FeCN] to [$FeCNH_2$] with intermediate strength acid/reductant, such as the initially described Cp^*_2Cr/[$PhNH_3$]BAr^F_4 combination.[54] As previously noted, [FeCN] reduction with these reagents is rapid at −80 °C. To slow the reaction rate, we switched the solvent to a eutectic mixture of 4:1 2-MeTHF:THF, which has a freezing point of −160 °C and sufficient viscosity at −145 °C to study this transformation.[55] Under these conditions, we found that Cp^*_2Cr is insufficiently soluble for kinetic studies; we therefore turned to a more soluble reductant of comparable strength, $^{Et}Cp_2Co$ (1,1-diethylcobaltocene; $E(Co^{III/II})$ = −1.45 V; Figure B.69). The addition of $^{Et}Cp_2Co$ in pseudo-first order excess via syringe to a solution of [FeCN] (1.2 mM) and [$PhNH_3$]BAr^F_4 (3.6 mM) showed complete consumption of the diagnostic [FeCN] peak at 895 nm within 120 s (Figure 3.8A). Plotting of ln(abs_{895}) vs time demonstrated this reaction to be first order in [FeCN] (Figure 3.8B), and use of [$PhND_3$]BAr^F_4 showed a small, normal kinetic isotope effect (KIE) of 1.4±0.1.

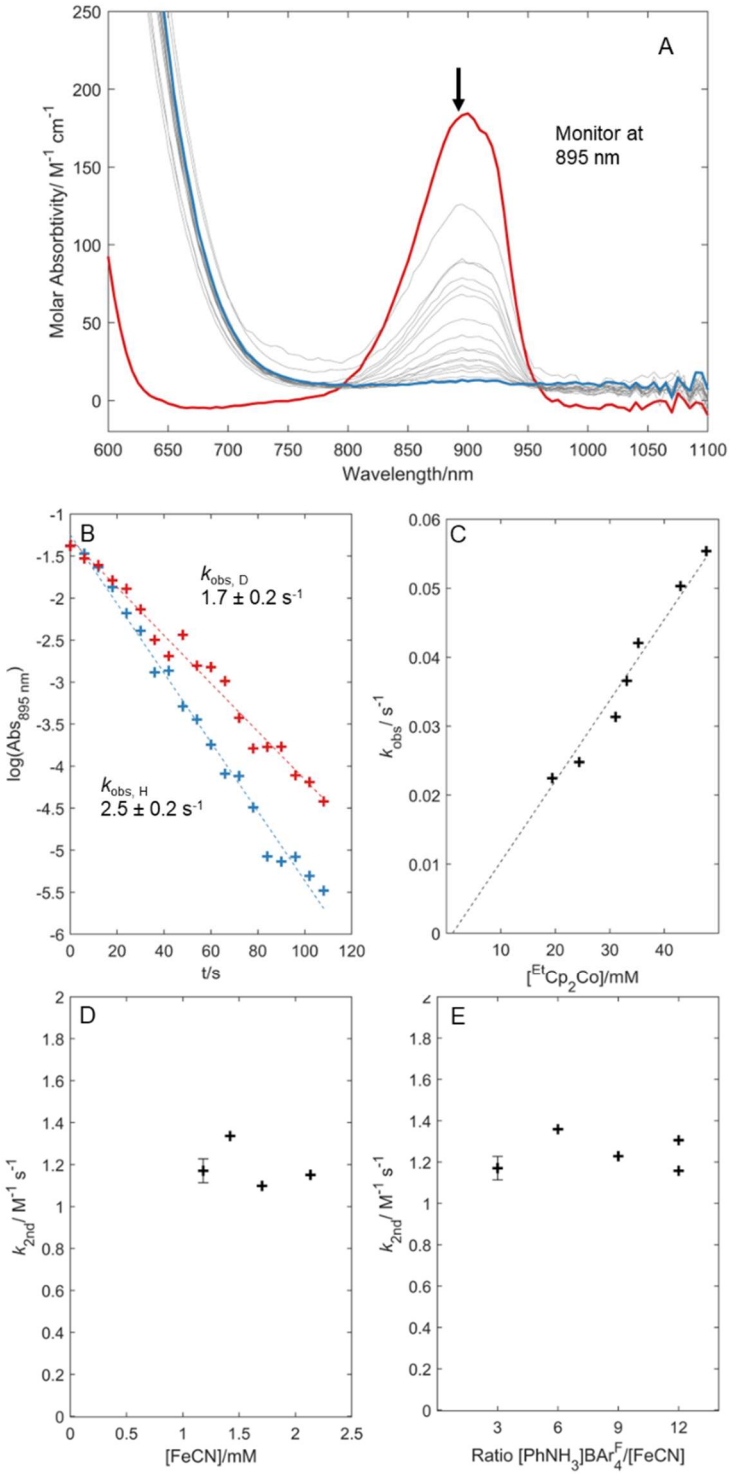

Figure 3.8. Kinetic data for reaction of [FeCN] with $[PhNH_3]BAr^F{}_4$ and $^{Et}Cp_2Co$. All data presented collected at -145 °C in 4:1 2-MeTHF:THF (A) $[FeCN\cdots HNH_2Ph]BAr^F{}_4$ (red trace) is reduced upon addition of $^{Et}Cp_2Co$ (Grey traces every 2 seconds, blue trace after

120 s). (B) Plot of log(Abs$_{[FeCN]}$) against time using either [PhNH$_3$]BAr$^F_4$ (Blue trace) or [PhND$_3$]BAr$^F_4$ (Red trace) with 1.2 mM [FeCN] and 25 equiv ^{Et}Cp$_2$Co. (C) k_{obs} for 1st order decay of [FeCN$\cdots$HNH$_2$Ph]BAr$^F_4$ upon addition of [^{Et}Cp$_2$Co] plotted against [^{Et}Cp$_2$Co]. (D) k_{2nd} plotted against starting [FeCN] concentration. The ratio of [PhNH$_3$]BAr$^F_4$:[FeCN] was kept constant (at 3). (E) k_{2nd} plotted against [FeCN] to [PhNH$_3$]BAr$^F_4$ ratio. Error bars for the 1st data point in plots (E) and (F) represent errors for the 2nd order rate constant determined from the slope in (C).

The pseudo-first order rate constant showed dependence on the reductant concentration, but not [FeCN] or the [PhNH$_3$]BAr$^F_4$:[FeCN] ratio (Figure 3.8C-E and Figure 3.9A) consistent with a rate law = k_2[^{Et}Cp$_2$Co][FeCN], where k_2 =1.17±0.07 M^{-1} s^{-1}. A mechanistic model consistent with these observations is the 1st reduction event being rate limiting with partial proton transfer also occurring in this rate-limiting step (Figure 3.9B). However, since the reaction is independent [PhNH$_3$]BAr$^F_4$:[FeCN] ratio, this would require a pre-association of the acid and [FeCN], e.g., through H-bond formation. This supports an H-bond mediated MS-PCET to form the 1st N−H bond as the rate-limiting step of aminocarbyne formation (Figure 3.9B).

As the 1st N−H bond formation is the rate-limiting step, it is difficult to study the mechanism of the 2nd N−H bond formation. Nonetheless, two mechanisms seem plausible, likely depending on the specific reagent combinations (Figure 3.9C). For combinations of strong acids and weak reductants (e.g., [PhNH$_3$]BAr$^F_4$/^{Et}Cp$_2$Co), we would expect a PT-ET mechanism to form the 2nd N−H bond, with [FeCNH] being rapidly protonated to give [FeCNH$_2$]$^+$, which can be reduced to [FeCNH$_2$]. The acidity of [FeCN(H)Me]$^+$ (pK_a 7.1) provides a useful guide as to what acids might access this protonation. However, reagent combinations utilizing weak acids and strong reductants to form [FeCNH$_2$] (e.g., [pyrrH]BAr$^F_4$/(^{Me4}Cp)$_2$Co; pyrr = pyrrolidine, ^{Me4}Cp = tetramethylcyclopentadienyl), this 2nd protonation should not be accessible, nor should reduction of the intermediate [FeCNH] to [FeCNH]$^-$ (Figure 3.2).[56] Instead, we propose the disproportionation of *in situ* formed [FeCNH] to yield 0.5 equiv [FeCN] and 0.5 equiv [FeCNH$_2$], similar to what we have previously observed for [FeNN−H].[36] Accordingly, attempts to generate [FeCNH]^0 in solution via reduction of [FeCNH]$^+$, protonation of [FeCN]$^-$ or deprotonation of [FeCNH$_2$]$^+$ rapidly converge to 1:1 mixtures of [FeCN]:[FeCNH$_2$] (see appendix section B.2.3).

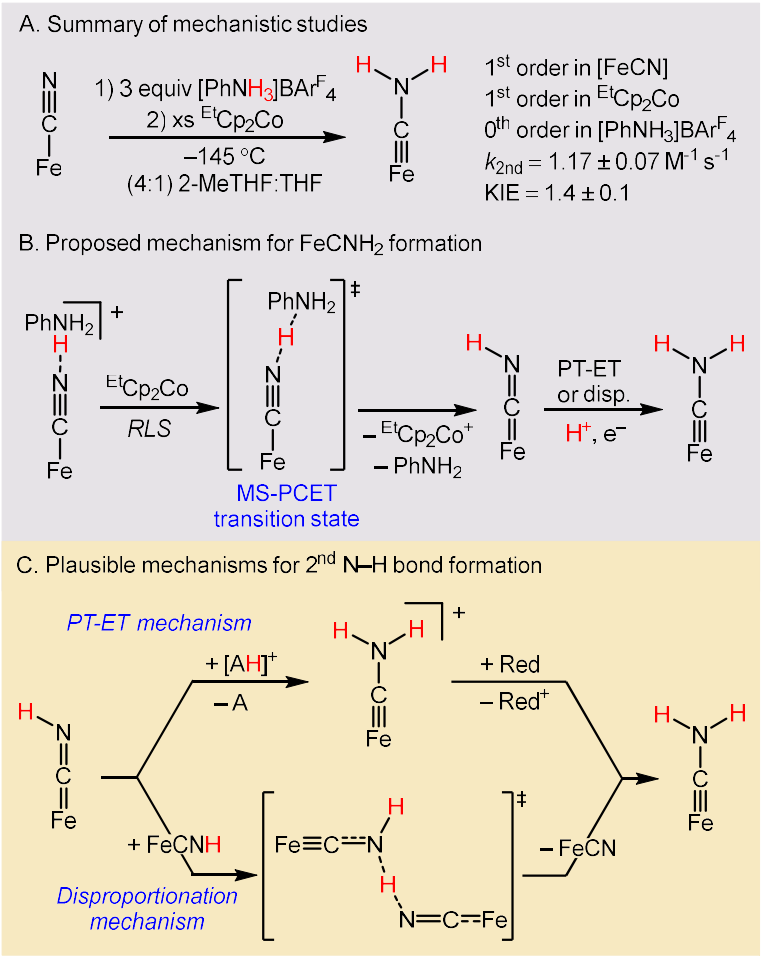

Figure 3.9. Summary of kinetic studies and proposed mechanism of 1st and 2nd N–H bond formations.

3.3 Discussion

Reversibility can be observed in the chemical and electrochemical reduction of [FeCN] to [$FeCNH_2$] (Figure 3.10). This contrast the reduction of transition metal dinitrogen complexes (M–N≡N) to the corresponding hydrazidos (M=N–NH_2), where the overpotential is limited by formation of the diazenido complex (M=N=NH). Equilibrating over multiple early intermediates would allow for lower overpotential for N_2R (and perhaps other small molecule reductions), motivating an analysis of the factors allowing for reversibility interconversion between [FeCN] and [$FeCNH_2$].

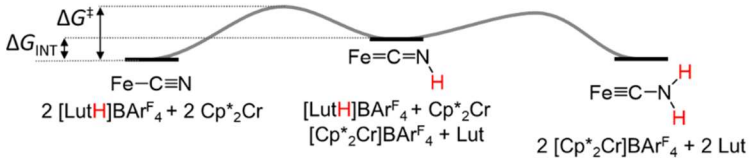

Figure 3.10. Energy diagram for reduction of [FeCN] to [$FeCNH_2$].

Two attributes of the [$FeCNH_x$] platform appear critical: small kinetic barriers for the N−H bond formation (Figure 3.10, $\Delta G^{\ddagger}$) and energy leveling (ΔG_{INT}) of the intermediate [FeCNH] and the starting material ([FeCN]) and product ([$FeCNH_2$]). The small kinetic barriers, which we attribute, at least for the 1st (and limiting) N−H bond formation, to the MS-PCET mechanism facilitated by the initial H-bond formation.[42] As noted for many MS-PCET reactions, the H-bond removes the entropic barrier of associated with the termolecular rate-limiting step.[39,40] The importance of this H-bond is readily apparent in our electrochemical studies, where formation of the H-bond pre-complex appears to be a requirement for achieving reversible transformations under electrochemical conditions.

While the design of reagents for efficient transfer of H^+/e^- to substrates is by no means trivial, strategies, particularly the tethering of H^+ and e^- donors,[42,43,57,58,59,60,61] have been detailed and demonstrated in many applications including N_2R.[62,63] By contrast, strategies for energy leveling (lowering ΔG_{INT}) between early intermediates of deep proton-coupled reductions are less well-defined, meriting further discussion. Early N−H bond formation during N_2R catalyzed by P_3^BFe (P_3^B = trisphosphinoborane ligand) specifically the conversion of the neutral dinitrogen complex ($P_3^BFe-N{\equiv}N$) to the neutral hydrazido ($P_3^BFe{=}N-NH_2$) provides a useful case study. The products and intermediates of this reaction should have the same spin states as the conversion of [FeCN] to [$FeCNH_2$]. However, the 1 H^+/ 1 e^- intermediate, the iron diazenido (P_3^BFeNNH), has a notably weaker N−H bond ($BDFE_{N-H}$ = 27 kcal mol^{-1}) than the $2H^+/2e^-$ product $P_3^BFeNNH_2$ ($BDFE_{N-H}$ = 38 kcal mol^{-1}), resulting in a large ΔG_{INT}.[64] Equilibration would require stabilizing the iron diazenido with respect to the terminal dinitrogen adduct and neutral hydrazido.

Several reports demonstrate that transition metal diazenidos can be stabilized by the addition of Lewis acids.[65,66,67,68] However, these interactions are too strong and have yielded persistent Lewis acid-stabilized diazenido species, not lower overpotentials for

N_2R (Figure 3.11A and B). To achieve lower overpotential N_2R we emphasize that the effect of a Lewis acid on the whole sequence P_3^BFeNN, P_3^BFeNNH and $P_3^BFeNNH_2$ must be considered.

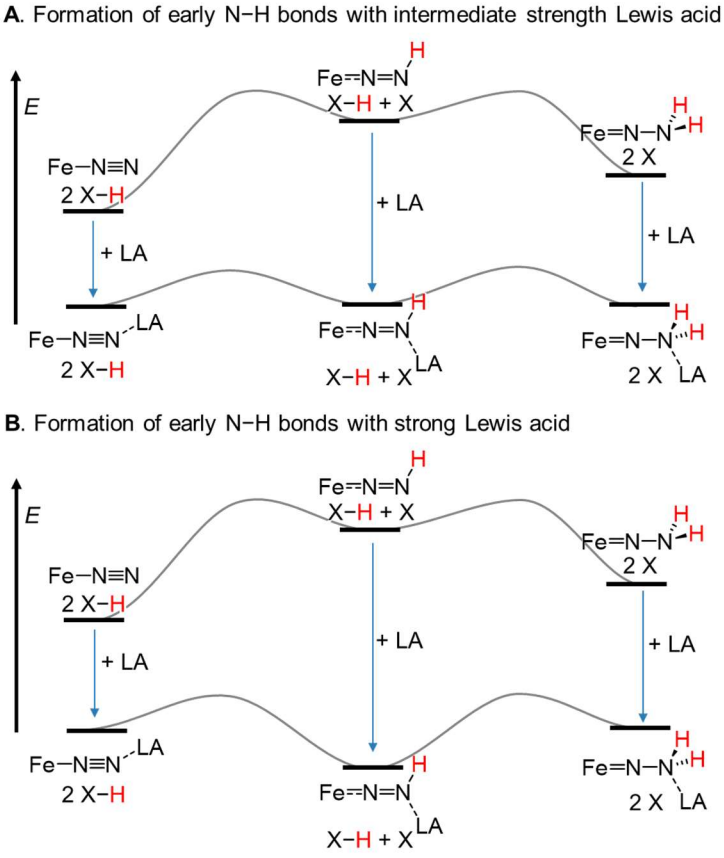

C. ECW model applied to early N−H bond in N_2R

$$-\Delta H = E_A E_B + C_A C_B + W \quad \text{(eqn 3.4)}$$

Lewis Base (L_B)	E_B	C_B	$BDFE_{N-H}$ (kcal mol^{-1})	$BDFE_{N-H}$ (L_B-Zn($NTMS_2$)$_2$) (kcal mol^{-1})	$BDFE_{N-H}$ (L_B-BMe_3) (kcal mol^{-1})
P_3^BFeNN	0.8	0	-		
P_3^BFeNNH	2.8	0.4	27	31	34
$P_3^BFeNNH_2$	2.1	0	38	35	35

Figure 3.11. Proposed energy diagrams for early steps of N_2R with intermediate (A) and strong (B) Lewis acids. For simplicity the transfer of H^+/e^- from an X−H donor is depicted.

To guide this analysis we employed the empirical ECW model of Lewis acid-base pair interactions (eqn 3.4), which estimates Lewis adduct enthalpies from $E_{A/B}$ (electrostatic) and $C_{A/B}$ (covalent) parameters, providing a useful way to classify Lewis bases both in strength and hardness/softness.[69,70] This also allows us to estimate the bond strengths of intermediates across a range of Lewis acids (see Table B.8). The computationally estimated E_B and C_B parameters for $P_3^BFe(N_2)$, $P_3^BFe(NNH)$ and $P_3^BFe(NNH_2)$, show C_B values close to 0, but larger E_B values of 0.8, 2.7 and 2.1, respectively. These E_B suggest that the iron diazenido is the strongest Lewis base, allowing for it to be stabilized relative to $P_3^BFe(NN)$ and $P_3^BFe(NNH_2)$. It also provides a guide for what Lewis acids are of an appropriate strength, with $Zn(NTMS_2)_2$ and BMe_3 being two possible candidates (Figure 3.11C).

Interestingly, comparing these computationally derived ECW parameters to other Lewis bases we find that both the diazenido and hydrazido resemble carbonyls (see Figure B.71). Lanthanide reductants, like SmI_2, have long been known to provide excellent selectivity for carbonyl-cross couplings via inner-sphere reduction.[71,72] It is therefore perhaps not surprising that lanthanide reductants have found significant utility in molecular N_2R in recent years as well.[63,73,74] Further tailoring these reagents might allow targeted energy-leveling and ultimately allow more efficient N_2R. Experiments to validate these hypotheses are underway.

3.4 Cited References

1. Bolton, J. R. *Science* **1978**. 202 (4369), 705–711.
2. Savéant, J.-M. *ACS Catal*. **2018**., 8, 7608–7611.
3. Fourmond, V.; Plumeré, N.; Léger, C. *Nat. Rev. Chem.* **2021**. 5, 348–360.
4. Hu, X.; Brunschwig, B. S.; Peters, J. C. *J. Am. Chem. Soc.* **2007**. 129, 8988–8998.
5. Smith, S. E.; Yang, J. Y.; DuBois, D. L.; Bullock, R. M. *Angew. Chem. Int. Ed.* **2012**. 51, 3152–3155.

6. Cunningham, D. W.; Barlow, J. M.; Velazquez, R. S.; Yang, J. Y. *Angew. Chem. Int. Ed.* **2020**. 59, 4443–4447.
7. Guria, S.; Dolui, D.; Das, C.; Ghorai, S.; Vishal, V.; Maiti, D.; Lahiri, G. K.; Dutta, A. *Nat. Commun.* **2023**. 14, 6859.
8. Suzuki, W.; Kotani, H.; Ishizuka, T.; Kojima, T. *J. Am. Chem. Soc.* **2019**. 141, 5987–5994.
9. Rodriguez, G. M.; Trotta, C.; Tensi, L.; Macchioni, A. *J. Am. Chem. Soc.* **2024**. 146, 34298–34303
10. Eftekhari, A. *Int. J. Hydrog. Energy* **2017**. 42, 11053–11077.
11. Kortlever, R.; Peters, I.; Koper, S.; Koper, M. T. M. *ACS Catal*. **2015**. 5, 3916–3923.
12. Hexter, S. V.; Grey, F.; Happe, T.; Climent, V.; Armstrong, F. A. *Proc. Natl. Acad. Sci.* **2012**. 109, 11516–11521.
13. Can, M.; Armstrong, F. A.; Ragsdale, S. W. *Chem. Rev.* **2014**. 114, 4149–4174.
14. Bassegoda, A.; Madden, C.; Wakerley, D. W.; Reisner, E.; Hirst, J. *J. Am. Chem. Soc.* **2014**. 136, 15473–15476.
15. Reda, T.; Plugge, C. M.; Abram, N. J.; Hirst, J. *Proc. Natl. Acad. Sci.* **2008**. 105, 10654–10658.
16. Yandulov, D. V.; Schrock, R. R. *Science* **2003**. 301, 76–78.
17. Chalkley, M. J.; Drover, M. W.; Peters, J. C. *Chem. Rev.* **2020**. 120, 5582–5636.
18. Ritleng, V.; Yandulov, D. V.; Weare, W. W.; Schrock, R. R.; Hock, A. S.; Davis, W. M. *J. Am. Chem. Soc.* **2004**. 126, 6150–6163.
19. Wu, Y.; Jiang, Z.; Lu, X.; Liang, Y.; Wang, H. *Nature* **2019**. 575, 639–642.
20. Boutin, E.; Wang, M.; Lin, J. C.; Mesnage, M.; Mendoza, D.; Lassalle-Kaiser, B.; Hahn, C.; Jaramillo, T. F.; Robert, M. *Angew. Chem. Int. Ed.* **2019**. 58, 16172–16176.
21. Tanifuji, K.; Lee, C. C.; Ohki, Y.; Tatsumi, K.; Hu, Y.; Ribbe, M. W. *Angew. Chem. Int. Ed.* **2015**. 54, 14022–14025.

22. Sickerman, N. S.; Tanifuji, K.; Lee, C. C.; Ohki, Y.; Tatsumi, K.; Ribbe, M. W.; Hu, Y. *J. Am. Chem. Soc.* **2017**. 139, 603–606.
23. Johansen, C. M.; Peters, J. C. *J. Am. Chem. Soc.* **2024**. 146, 5343–5354.
24. Habibzadeh, F.; Miller, S. L.; Hamann, T. W.; Smith, M. R. *Proc. Natl. Acad. Sci.* **2019**. 116, 2849–2853.
25. Zott, M. D.; Garrido-Barros, P.; Peters, J. C. *ACS Catal.* **2019**. 9, 10101–10108.
26. Trenerry, M. J.; Wallen, C. M.; Brown, T. R.; Park, S. V.; Berry, J. F. *Nat. Chem.* **2021**. 13, 1221–1227.
27. Brownell, K. R.; McCrory, C. C. L.; Chidsey, C. E. D.; Perry, R. H.; Zare, R. N.; Waymouth, R. M. *J. Am. Chem. Soc.* **2013**. 135, 14299–14305.
28. Liu, Y.; Zhao, S.-F.; Guo, S.-X.; Bond, A. M.; Zhang, J.; Zhu, G.; Hill, C. L.; Geletii, Y. V. *J. Am. Chem. Soc.* **2016**. 138, 2617–2628.
29. Chen, C.-P.; Alharbi, W.; Cundari, T. R.; Hamann, T. W.; Smith, M. R. I. *J. Am. Chem. Soc.* **2023**. 145, 26339–26349.
30. Wang, Z.; Johnson, S. I.; Wu, G.; Ménard, G. *Inorg. Chem.* **2021**. 60, 8242–8251.
31. Huynh, M. H. V.; Meyer, T. J. *Chem. Rev.* **2007**. 107, 5004–5064.
32. Pipes, D. W.; Meyer, T. J. *J. Am. Chem. Soc.* **1984**. 106, 7653–7654.
33. Huynh, M. H. V.; Baker, R. T.; Morris, D. E.; White, P. S.; Meyer, T. J. *Angew. Chem. Int. Ed.* **2002**. 41, 3870–3873.
34. L. Hughes, D.; K. Ibrahim, S.; Moh'd Ali, H.; J. Pickett, C. *J. Chem. Soc. Chem. Commun.* **1994**. 4, 425–427.
35. Rittle, J.; Peters, J. C. *Angew. Chem. Int. Ed.* **2016**, 55, 12262–12265.
36. Rittle, J.; Peters, J. C. *J. Am. Chem. Soc.* **2017**. 139, 3161–3170.
37. Chalkley, M. J.; Peters, J. C. *Eur. J. Inorg. Chem.* **2020**. 2020, 1353–1357.
38. Pombeiro, A. J. L. *Inorg. Chem. Commun.* **2001**. 4, 585–597.
39. Morris, W. D.; Mayer, J. M. *J. Am. Chem. Soc.* **2017**. 139, 10312–10319.
40. Gentry, E. C.; Knowles, R. R. *Acc. Chem. Res.* **2016**, 49, 1546–1556.

41. Waidmann, C. R.; Miller, A. J. M.; Ng, C.-W. A.; Scheuermann, M. L.; Porter, T. R.; Tronic, T. A.; Mayer, J. M. *Energy Environ. Sci.* **2012**, 5, 7771–7780.
42. Tyburski, R.; Liu, T.; Glover, S. D.; Hammarström, L. *J. Am. Chem. Soc.* **2021**, 143, 560–576.
43. Agarwal, R. G.; Coste, S. C.; Groff, B. D.; Heuer, A. M.; Noh, H.; Parada, G. A.; Wise, C. F.; Nichols, E. M.; Warren, J. J.; Mayer, J. M. *Chem. Rev.* **2022**. 122, 1–49.
44. Bordwell, F. G.; Cheng, J. Pei.; Harrelson, J. A. *J. Am. Chem. Soc.* **1988**. 110, 1229–1231.
45. Previously measured pK_a of [FeCN] measured in THF with TfO^- counteranion at 25°C did not result in observable H-bonding interactions with $[Et_3NH]OTf$ or [LutH]OTf , see ref 36.
46. Garrido, G.; Rosés, M.; Ràfols, C.; Bosch, E. *J. Solut. Chem.* **2008**. 37, 689–700.
47. Connelly, N. G.; Geiger, W. E. *Chem. Rev.* **1996**. 96, 877–910.
48. Interestingly, the linewidth for the Mössbauer spectra generated with $[PhNH_3]BAr^F{}_4$ are much broader than those generated with $[LutH]BAr^F{}_4$. We attribute this to H-bonding between the conjugate base and $[FeCNH_2]$, the bulkier lutidine base allows fewer modes of H-bonding and accordingly more narrow speciation and sharper linewidths.
49. It is worth commenting on the discrepancy in the 1:1 ratio of starting material:product observed compared to the 3:97 ratio expected at 195 K for an energy difference of −1 kcal mol^{-1}, which is attributable to a variety of effects. As these driving force equations do not directly relate to $[FeCNH_2]$ as the BDFE of the neutral carbyne is measured for [FeCN(Me)H]. In addition, there are hydrogen bonding effects in both starting material and product, which are not accounted for in these simple driving force calculations.

50. Since ΔG = +2 kcal mol^{-1}, a larger excess acid and reductant was required to form appreciable [FeCNH$_2$], allowing product detection by ^{57}Fe Mössbauer.
51. Efforts to synthesize this complex in Et$_2$O failed, likely due to insolubility of [FeCN]K$_2$, with invariably substantial oxidation to [FeCN]K or [FeCNH$_2$]$^+$ observed, prompting the switch to THF solvent for the oxidative reaction.
52. Chalkley, M. J.; Del Castillo, T. J.; Matson, B. D.; Roddy, J. P.; Peters, J. C. *ACS Cent. Sci.* **2017**. 3, 217–223.
53. Steiner, T. *Angew. Chem. Int. Ed.* **2002**. 41, 48–76.
54. When using strong acid (e.g., [Ph$_2$NH$_2$]BAr$^F_4$ or [$^{2\text{-Cl}}$PhNH$_3$]BAr$^F_4$) or strong reductant (Cp$^*_2$Co) [FeCN] reduction occurs via either PT or ET first mechanisms evidenced by full or partial formation of [FeCNH]$^+$ or [FeCN]$^-$ with these reagents.
55. Chiang, L.; Keown, W.; Citek, C.; Wasinger, E. C.; Stack, T. D. P. *Angew. Chem. Int. Ed.* **2016**. 55, 10453–10457.
56. As [FeCNH] is unstable we have not been able to determine its reduction potential electrochemically, but use the methylated analogue gives a reasonable estimate of the [FeCNH]$^{0/-}$ reduction potential.
57. Chalkley, M. J.; Garrido-Barros, P.; Peters, J. C. *Science* **2020**. 369, 850–854.
58. Anson, C. W.; Stahl, S. S. *J. Am. Chem. Soc.* **2017**. 139, 18472–18475.
59. Boyd, E. A.; Peters, J. C. *J. Am. Chem. Soc.* **2022**. 144, 21337–21346.
60. Dey, S.; Masero, F.; Brack, E.; Fontecave, M.; Mougel, V. *Nature* **2022**. 607, 499–506.
61. Adillon, E. H.; Peters, J. C. *J. Am. Chem. Soc.* **2024**. 146, 30204–30211.
62. Garrido-Barros, P.; Derosa, J.; Chalkley, M. J.; Peters, J. C. *Nature* **2022**. 609, 71–76.
63. Boyd, E. A.; Peters, J. C. *J. Am. Chem. Soc.* **2023**. 145 (27), 14784–14792.
64. Matson, B. D.; Peters, J. C. *ACS Catal.* **2018**, 8, 1448–1455.

65. Geri, J. B.; Shanahan, J. P.; Szymczak, N. K. *J. Am. Chem. Soc.* **2017**. 139, 5952–5956.

66. Ouellette, E. T.; Magdalenski, J. S.; Bergman, R. G.; Arnold, J. *Inorg. Chem.* **2022**. 61, 16064–16071.

67. Rempel, A.; Mellerup, S. K.; Fantuzzi, F.; Herzog, A.; Deißenberger, A.; Bertermann, R.; Engels, B.; Braunschweig, H. *Chem. – Eur. J.* **2020**. 26, 16019–16027.

68. Yin, Z.-B.; Wang, G.-X.; Yan, X.; Wei, J.; Xi, Z. *Nat. Commun.* **2025**, 16, 674.

69. Drago, R. S.; Wayland, B. B. *J. Am. Chem. Soc.* **1965**. 87, 3571–3577.

70. Vogel, G. C.; Drago, R. S. *J. Chem. Educ.* **1996**. 73, 701.

71. Girard, P.; Namy, J. L.; Kagan, H. B. *J. Am. Chem. Soc.* **1980**. 102, 2693–2698.

72. Szostak, M.; Fazakerley, N. J.; Parmar, D.; Procter, D. J. *Chem. Rev.* **2014**. 114, 5959–6039.

73. Ashida, Y.; Arashiba, K.; Nakajima, K.; Nishibayashi, Y. *Nature* **2019**. 568, 536–540.

74. Boyd, E. A.; Jung, H.; Peters, J. C. *J. Am. Chem. Soc.* **2025**. 147, 4695–4700.

C h a p t e r 4

Catalytic transfer hydrogenation of N_2 to NH_3 via a photoredox catalysis strategy

Adapted from:

Johansen, C. M.†; Boyd, E. A.†; Peters, J. C. *Sci. Adv.* **2022**. 8, eade3510. DOI: 10.1126/sciadv.ade3510.

† These authors contributed equally to this work.

4.1 Introduction

Multi-electron reductive transformations of small molecule substrates (e.g., N_2, CO_2, NO_3^-) are challenging to mediate in homogeneous catalysis and most typically require considerable energy input via harsh chemical reagents and/or conditions to be driven forward. The nitrogen reduction reaction (N_2RR) offers a case in point; substantial progress has now been made in molecular catalyst design but significant overpotentials are generally needed to observe NH_3 product.[1,2,3] For nitrogen reduction (N_2R), kinetic challenges also prevail for enzymatic and heterogeneous catalysis that require substantial energy inputs, via ATP hydrolysis for the former and high temperature and pressure or electrochemical overpotential for the latter,[4,5,6] despite a thermally favorable Gibbs free energy of formation, $\Delta G_f(NH_3)$ (Figure 4.1A).

The organometallic catalysis field has pursued photochemical strategies as a means of driving small molecule reductions, with considerable success being achieved for CO_2 reduction (CO_2R, typically by 2 e^-/2 H^+) as the target transformation.[7,8] Such strategies are still challenged by the widespread use of sacrificial donors whose oxidation products are not readily recycled. While design schemes are envisaged to someday couple photodriven CO_2R catalysis with water oxidation, photodriven transfer hydrogenation using a suitable precatalyst offers an approach to reductive small molecule catalysis, especially if the net H_2-donor (H_2-carrier; Figure 4.1B) derives from a structure than can be efficiently recycled, for example via hydrogenation or electrochemically.

Reduced Hantzsch esters (HEH_2, Figure 4.1B) and chemically related structures (e.g., reduced acridine, phenanthridine) have been explored for thermally and photochemically driven reductive hydride (H^-; NADH-like) and H-atom transfers in organic synthesis.[9] Moreover, they are highlighted for their chemical (and electrochemical) recyclability via net hydrogenation of the spent pyridine-type oxidation product.[10,11] Whereas the types of transformations they participate in are most typically two-electron processes, they are also tempting to explore for deeper multi-electron reductions of the type pursued in small molecule reductive catalysis. Focusing on N_2R,[12] we noted that despite long known and still debated studies of photocatalytic nitrogen fixation using

semiconductors,[13,14,15] and photodriven N_2R mediated by nitrogenase coupled with CdS,[16,17] as yet there were no examples of photochemically driven catalytic N_2R using well-defined molecular systems. Hence, photoinduced N_2R via transfer hydrogenation from a Hantzsch ester or related donor, which requires the donors to engage in successive transfers to mediate a deep 6 e^-/6 H^+ reduction process, provides an excellent test case of this strategy for small molecule substrates.

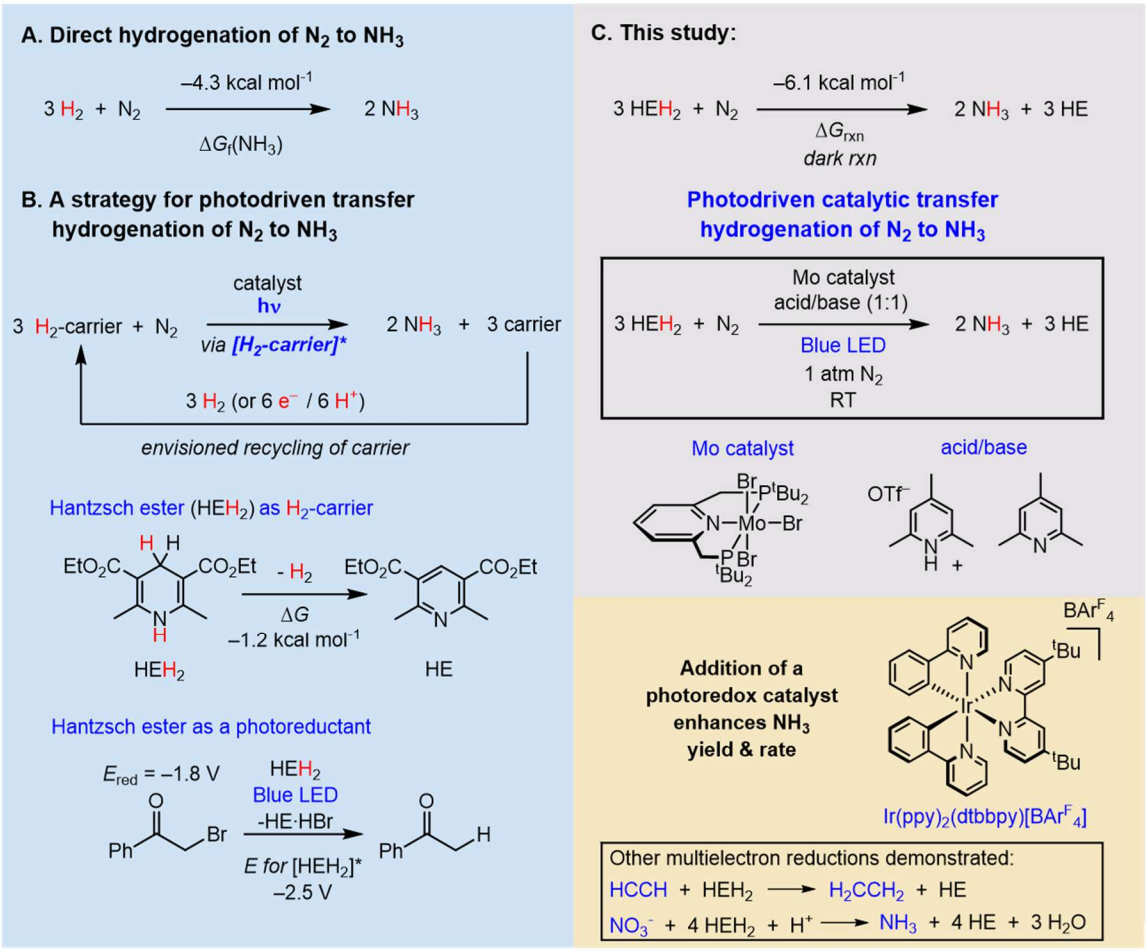

Figure 4.1. Thermodynamics and strategies for hydrogenation of N_2. (A) Thermodynamics of hydrogenation of N_2 to NH_3;[1] (B) Schematic of an overall design for light-driven transfer hydrogenation of N_2; chemical structure of the Hantzsch ester used in this study (HEH_2);[19] representative reduction of α-bromo acetophenone;[18] (C) Net stoichiometry and estimated driving force of transfer hydrogenation from HEH_2 to N_2 forming NH_3; photodriven (blue LED) process described in this study, in the absence and presence of a photoredox catalyst.

All thermochemical values are given in MeCN at 25 °C with ferrocenium/ferrocene ($Fc^{+/0}$) as reference potential.

Considering thermodynamic parameters relevant to the aforementioned goals, in its ground state the first C–H bond dissociation free energy ($BDFE_{C–H}$) of HEH_2 is 62.3 kcal $mol^{–1}$ in MeCN at 25 °C (all following thermochemical values are defined at these conditions), which is not weak enough to bimolecularly liberate H_2.[18] Photoexcitation of HEH_2, however, renders an excited state that is highly reducing (E_{ox} for $[HEH_2]^*$ is ~ –2.6 V vs $Fc^{+/0}$; Fc = ferrocene).[19,20] Photodriven (blue LED) reduction of α-bromo acetophenone to acetophenone by HEH_2 illustrates its capacity to deliver an H_2 equivalent (Figure 4.1B).[19] For a dark N_2R reaction, we estimate the overpotential for reduction of N_2 by HEH_2 to generate NH_3 as 1.8 kcal $mol^{–1}$ (($\Delta\Delta G_f(NH_3)$, Figure 4.1C). Using light (blue LED), we show herein that it is indeed possible to catalyze photoinduced transfer hydrogenation from HEH_2 to N_2 using Nishibayashi's molybdenum pre-catalyst (Figure 4.1C)[21] at atmospheric pressure and 23 °C. The inclusion of an Ir-photoredox catalyst (Figure 4.1C) within this system, while not necessary for turnover, enhances the yields and rates of NH_3 generation.

For our present catalysis system, we noted that a photoreduction step from the excited state of HEH_2, $[HEH_2]^*$, liberates the ground state radical cation $HEH_2^{\bullet+}$, which is a sufficiently strong oxidant (E_{red} = 0.48 V vs $Fc^{+/0}$) to be deleterious to N_2R.[18] We therefore reasoned that inclusion of a base to deprotonate $HEH_2^{\bullet+}$ (pK_a ~ −1) would be prudent.[18] However, the presence of a moderate Brønsted acid is typically required for chemically driven N_2R, suggesting a buffered system might be needed. A collidine/collidinium (abbreviated Col/$[ColH]^+$; Col = 2,4,6-trimethylpyridine) mixture was chosen as Col will readily deprotonate $HEH_2^{\bullet+}$ while $[ColH]^+$, with a pK_a of 15 in MeCN,[22] has been previously shown to be compatible with chemically driven N_2R using $(PNP)MoBr_3$ as a pre-catalyst (PNP = 2,6-bis(di-tert-butylphosphinomethyl)pyridine) with $(Cp^*)_2Co$ ($E_{1/2}(Co^{III/II})$ = −1.91 V; Cp* = pentamethylcyclopentadienyl) as the reductant.[21,23]

4.2 Results

Entry	Change from "standard conditions"	NH_3 (equiv/ Mo)	NH_3 yield/ HEH_2 (%)
1	none	9.5 ± 1	26.5 ± 3
2	0.57 mM Mo	21.8 ± 0.8	15.1 ± 0.6
3	no Mo	<0.1	<0.3
4	no light	<0.1	<0.3
5	no buffer	0.9 ± 0.2	2.6 ± 0.5
6	5 equiv Col/[ColH]OTf	2.9 ± 0.2	8.0 ± 0.6
7	benzene instead of THF	4.7 ± 0.1	13 ± 0.3
8	216 equiv Col/[ColH]OTf	20.3 ± 1.1	56 ± 3
9	10 equiv [TBA]Br	8.8 ± 0.3	23.6 ± 0.8
10	with $[Ir]BAr^F_4$	24 ± 4	67 ± 10
11	with $[Ir]BAr^F_4$, 5 equiv Col/[ColH]OTf	15.8 ± 0.8	44 ± 2
12	with $[Ir]BAr^F_4$, t = 1/2 h instead of 12 h	18.6 ± 0.9	52 ± 3
13	t = 2 h instead of 12 h	7.6 ± 2	21 ± 6
14	with $[Ir]BAr^F_4$, 5 equiv Col/[ColH]OTf, 0.57 mM Mo	26 ± 0.4	18.4 ± 0.4
15	with $[Ir]BAr^F_4$, 5 equiv Col/[ColH]OTf, no light	<0.1	<0.3
16	with $[Ir]BAr^F_4$, 5 equiv Col/[ColH]OTf, no Mo	<0.1	<0.3
17	with $[Ir]BAr^F_4$, 5 equiv Col/[ColH]OTf, no HEH_2	<0.1	<0.3
18	with $[Ir]BAr^F_4$, H_2-carrier = 9,10-dihydroacridine	6.4 ± 0.3	17.7 ± 0.8
19	with $[Ir]BAr^F_4$, H_2-carrier = 5,6-dihydrophenanthridine	4.6 ± 0.8	13 ± 2
20	with $[Ir]BAr^F_4$, H_2-carrier = 1-benzyl-1,4-dihydronicotinamide	1.2 ± 0.1	3.3 ± 0.3
21	with $[Ir]BAr^F_4$, 0.5 atm H_2, 0.5 atm N_2	14 ± 4	36 ± 9
22	with $[Ir(dF(CF_3)ppy)_2(dtbbpy)]PF_6$, t = 2 h instead of 12 h	2.2 ± 0.6	6 ± 1
23	with $[Ir]PF_6$, t = 2 h instead of 12 h	21 ± 4	58 ± 10
24	with $[Ir(p\text{-}F(Me)ppy)_2(dtbbpy)]PF_6$, t = 2 h instead of 12 h	22 ± 1	62 ± 3
25	with $Ir(ppy)_3$, t = 2 h instead of 12 h	7 ± 1	19 ± 4
26	with $[Ir]BAr^F_4$, no Col/[ColH]OTf	7.4 ± 0.4	20.7 ± 1

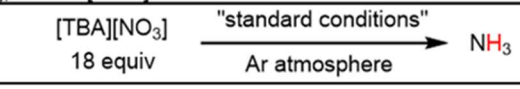

Entry	Change from "standard conditions"	NH_3 (equiv/Mo)	NH_3 yield/ HEH_2 (%)
27	none	9.8 ± 1.2	73 ± 9
28	with Mo, with $[Ir]BAr^F_4$	10.4 ± 0.5	77 ± 4
29	no Mo	1.7 ± 0.3	13 ± 2
30	no Mo, with $[Ir]BAr^F_4$	4.2 ± 1.2	31 ± 9
31	no light, with Mo, with $[Ir]BAr^F_4$	0.1 ± 0.05	0.7 ± 0.3

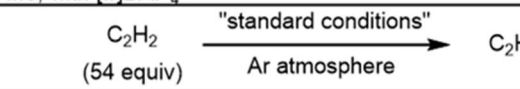

Entry	Change from "standard conditions"	C_2H_4 (equiv/Mo)	C_2H_6 (equiv/Mo)	Total yield/ HEH_2 (%)
32	none[a]	10 ± 2	1.5 ± 0.3	24 ± 5
33	with Mo,[a] with $[Ir]BAr^F_4$[b]	6 ± 1	1.1 ± 0.3	15 ± 3
34	no Mo	0.054 ± 0.008	< 0.03	< 0.3
35	no Mo, with $[Ir]BAr^F_4$[b]	2 ± 2	0.08 ± 0.08	4 ± 3
36	no light, with Mo,[a] with $[Ir]BAr^F_4$[b]	< 0.01	< 0.01	< 0.04

Table 4.1. Catalytic yields for photodriven transfer hydrogenation of N_2 to NH_3, NO_3^- to NH_3, and acetylene to ethylene and ethane . Reactions performed with 2.3 mM $[Mo]Br_3$

concentration, using a single 34 W Kessel H150 Blue lamp unless otherwise noted. All yields reported are an average of at least two runs. All runs with Ir used 2.3 mM photosensitizer loading unless otherwise noted. [a]3.6 mM [Mo]Br_3. [b]3.6 mM Ir. Ir = $[Ir(ppy)_2(dtbbpy)]BAr^F{}_4$; ppy = 2-phenylpyridinyl; dtbbpy = 4,4′-di-tert-butyl-2,2′-bipyridine; $BAr^F{}_4$ = tetrakis(3,5-bis(trifluoromethyl)phenyl)borate; dF(CF_3)ppy = 5-trifluoromethyl-2-(3,5-difluoro-phenyl)-pyridine; *p*-F(Me)ppy = 5-methyl-2-(5-fluoro-phenyl)-pyridine; PF_6^- = hexafluorophosphate).

We find that [Mo]Br_3 (1 equiv at 2.3 mM) in the presence of 54 equiv each of HEH_2, [ColH]OTf (OTf = triflate), and Col in THF, under an N_2 atmosphere and blue LED irradiation at 23 °C for 12 hours, yields 9.5 ± 1 equiv NH_3/Mo (Table 4.1, entry 1). Assuming HEH_2 is a 2 e^- donor in this process provides an NH_3 yield with respect to HEH_2 of ~25%. Use of $^{15}N_2$ confirmed N_2 as the source of the NH_3 produced (Figure C.1). To cement this interpretation, using either ^{15}N-labeled HEH_2 or ^{15}N-labeled Col/[ColH]OTf produced only $^{14}NH_3$. Analysis of the organic products following catalysis revealed complete consumption of HEH_2, with the fully oxidized Hantzsch ester pyridine (HE) as the major organic biproduct, consistent with HEH_2 acting as a 2 e^-/2 H^+ donor. We note that the yield of HE is ~90%; similarly, ~10% of the initial buffer loading is not recovered (Figure C.5). In addition to HE and recovered buffer, a complex mixture of organic species is observed following catalysis. A significant component of this mixture is generated independently via irradiation of HEH_2 and buffer in the absence of metal catalysts (Figure C.6), possibly as a result of light-induced reductive coupling as has been previously observed upon irradiation of HE in the presence of amine reductants.[24] Another factor limiting NH_3 selectivity per HEH_2 concerns background hydrogen evolution under blue light irradiation (see Figure C.8).

Higher yields of NH_3 per Mo center could be obtained by decreasing the [Mo]Br_3 loading (21.8 ± 0.8 equiv/Mo; entry 2), but with a loss in the yield of NH_3 with respect to HEH_2. The Mo-catalyst and irradiation were required to generate NH_3, and yields were substantially lower without the added buffer (entries 3-5). Attempts to use catalytic amounts of Col/[ColH]OTf (5 equiv per [Mo]Br_3) substantially lowered the NH_3 yields (entry 6). The reaction run in benzene instead of THF solvent remained catalytic but gave

attenuated yields (4.7 ± 0.1 equiv NH_3/Mo; entry 7), likely due to the lower solubility of [ColH]OTf in benzene.

While future studies are needed to probe the mechanism of this transformation, the fate of photoexcited $[HEH_2]^*$ is likely key. Two limiting scenarios to consider are the direct reduction of N_2R intermediates by $[HEH_2]^*$ (Figure C.16), or the reduction of the [ColH]OTf to $[ColH]^{\bullet}$ radical, which then reacts with $M(N_2)$ (Figure 4.2A) to form an N–H bond via $M(N_2H)$. Pyridinyl radicals have been posited as possible intermediates of N_2R in thermally driven catalysis with molecular systems.[25] Increasing the buffer concentration to 216 equiv/Mo boosted the NH_3 yield to 20.3 ± 1.1 equiv NH_3/Mo (entry 7). This observation points to a pathway whereby reduction of [ColH]OTf by $[HEH_2]^*$ dominates (Figure 4.2A), consistent with the high reactivity expected of $[HEH_2]^*$ ($E_{ox} \sim -2.6$ V; pK_a ~ –20; $BDFE_{C–H} \sim -8.5$ kcal mol^{-1}), as well as its short solution lifetime (0.419 ns in DMSO solvent at 25 °C).[18,20] Accordingly, steady state-fluorimetry studies show efficient quenching of $[HEH_2]^*$ upon titrating in [ColH]OTf (Figure C.9). Similar titrations of Col revealed less efficient quenching (Figure C.10). However, as some NH_3 can be detected under irradiation even in the absence of buffer (entry 4), other photoinduced pathways for N–H bond formation via HEH_2 are clearly accessible. The addition of 10 equiv of tetrabutylammonium bromide (TBABr) had no effect on the NH_3 yield (entry 8), suggesting that reductive Br^- loss from the precatalyst is not a limiting factor.

Figure 4.2A provides a generalized mechanistic outline to help illustrate how a photon might facilitate delivery of H_2 from HEH_2 to $M(N_2)$, to first generate an $M(NNH_2)$ intermediate, and ultimately NH_3 via successive H_2-transfers. For simplicity we show only this one scenario in Figure 4.2A but emphasize that other scenarios, including the early generation and then reduction of a terminal nitride intermediate ($Mo{\equiv}N + HEH_2 \rightarrow Mo(NH_2) + HE$) (Figure C.17), are also very plausible.[26] A recent study showed that a $Mn^V{\equiv}N$ can be photoreduced by 9,10-dihydroacridine to liberate NH_3.[27]

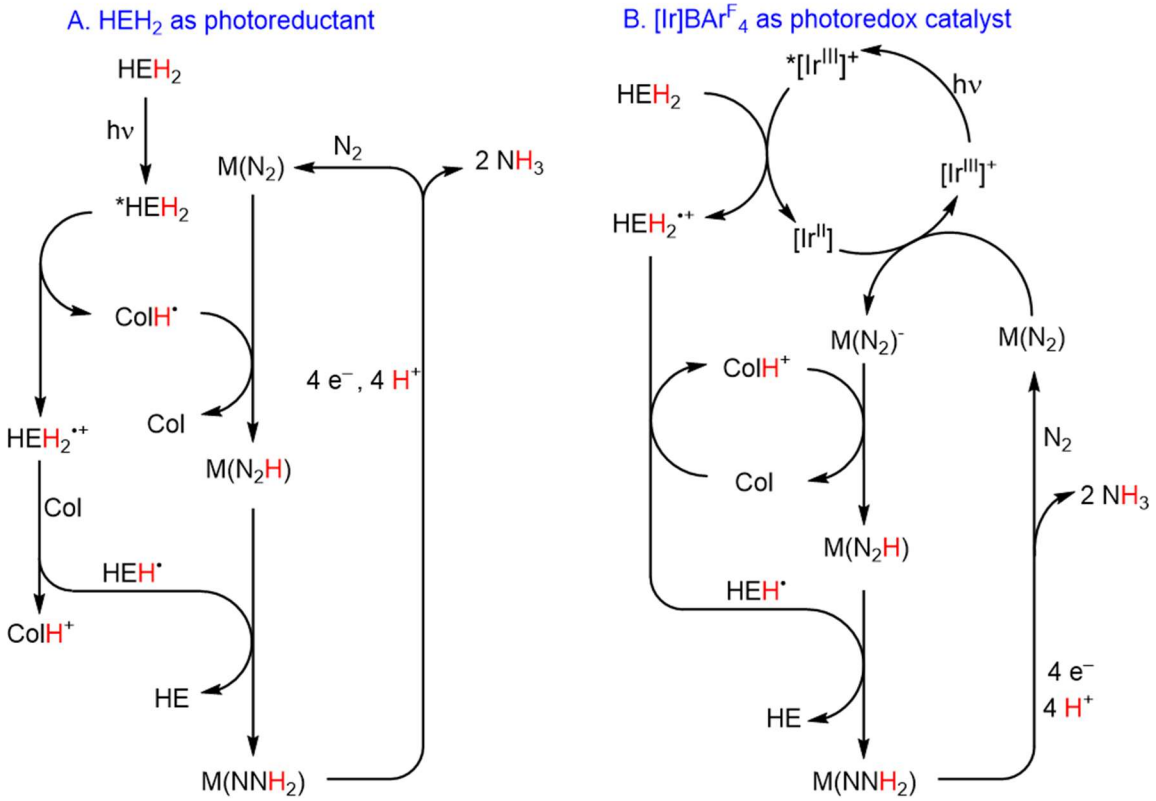

Figure 4.2. Possible scenarios for photodriven transfer hydrogenation from HEH_2 to N_2 mediated by a metal catalyst and buffer system (Col/$[ColH]^+$). (A) Scenario in absence of photoredox catalyst, in which $[HEH_2]$* is oxidatively quenched by $[ColH]^+$ to generate $[ColH]^\bullet$. (B) Scenario with photoredox catalyst, in which $[Ir^{III}]^+$* is reductively quenched by HEH_2. Pathways involving N≡N bond cleavage to yield M≡N intermediates (not shown) are also plausible (Figure C.17).

Limitations stemming from a short $[HEH_2]$* excited-state lifetime and low quantum yield (0.031)[20] for HEH_2 motivated us to explore a photosensitizer to enhance this photodriven catalysis. To test this idea, $[Ir(ppy)_2(dtbbpy)]BAr^F_4$ ($[Ir]BAr^F_4$; $E_{1/2}(Ir^{III/II})$ = −1.90 V) was chosen as its reduction potential is close to that of Cp^*_2Co and hence should be compatible with N_2R using $[Mo]Br_3$.[21,28]

Including $[Ir]BAr^F_4$ with $[Mo]Br_3$ (1 equiv, both at 2.3 mM), in addition to 54 equiv each of HEH_2 and Col/[ColH]OTf in THF, under an N_2 atmosphere and blue LED irradiation for 12 hours at room temperature, yields 24 ± 4 equiv of NH_3/Mo (entry 10). Assuming HEH_2 is a 2 e^-/2 H^+ donor, these conditions correspond to an overall NH_3 yield of 67 ± 10% with respect to HEH_2. Furthermore, in the presence of the Ir photosensitizer,

catalytic amounts of buffer can be used, producing 15.8 ± 0.8 equiv NH_3/Mo (entry 11). In addition to higher yields, the inclusion of [Ir]BAr^F_4 enhances the photocatalytic rate; the catalysis is ~80% complete after 30 minutes (entry 12). By contrast, under Ir-free conditions, 2 hour reaction times are required to achieve ~80% completion (entry 13). Comparing this photodriven Mo-catalyzed N_2R via HEH_2 with thermally driven Mo-catalyzed N_2R using $(Cp^*)_2Co$ and [ColH]OTf as reported by Nishibayashi, we find the NH_3 yields with respect to reductant to be quite similar (69% for the latter case).[21]

As in the Ir-free process, lowering the [Mo]Br_3 loading increased turnover for NH_3 with catalytic buffer (26.0 ± 0.4 equiv NH_3/Mo, entry 14), but with decreased total yield. No NH_3 is produced without irradiation (entry 16), and the presence of [Mo]Br_3 and HEH_2 are likewise essential (entries 16-17). Similar to the Ir-free reaction, HE was found to be the major organic product (>80%) and complete consumption of HEH_2 was observed. Solvent screening suggests that the reaction is most efficient when all components are soluble (see Table C.5). By contrast, other catalytic N_2R methods rely on low solubility of either the acid or reductant to attenuate competing H_2 evolution, demonstrating an advantage to using a terminal H-atom source which is not competent for H_2 release in the ground state.[1]

A range of candidate H_2-carriers should be explored in future studies to identify donors whose spent products can be recycled efficiently, perhaps *in situ*, via hydrogenation with H_2 or electrochemically (2 e^-/2 H^+). In an initial survey, the Ir-photosensitizer cocatalyst enables catalytic production of NH_3 under irradiation with 9,10-dihydroacridine or 5,6-dihydrophenanthridine as the H_2 donor (6.4 ± 0.3 equiv NH_3/Mo and 4.6 ± 0.8 equiv NH_3/Mo, respectively, entries 18-19). While non-catalytic, N_2-to-NH_3 conversion is also achieved with [Ir]BAr^F_4 and the hydride donor 1-benzyl-1,4-dihydronicotinamide (1.2 ± 0.1 equiv NH_3/Mo, entry 20). In the absence of [Ir]BAr^F_4, none of these H_2 or H^- carriers are competent for the photoinduced N_2RR (see Table C.2). The reaction with HEH_2 tolerates a 1:1 mixture of N_2 and H_2 (1 atm total pressure, 14 ± 4 equiv NH_3/Mo, entry 21), indicating that the Mo-catalyst is not (at least irreversibly) poisoned by H_2 under these conditions, important for considering downstream recycling of the spent donor.

In addition to varying the H_2-carriers we have examined the effect of varying the Ir-photosensitizer. [Ir(dF(CF_3)ppy)$_2$(dtbbpy)]PF_6 yielded substantially less NH_3 (entry 22) than [Ir]PF_6 (entry 23) or [Ir]$BAr^F{}_4$ (entries 10 and 12, Table 4.1). [Ir^{II}(dF(CF_3)ppy)$_2$(dtbbpy)] is also less reducing ($E_{1/2}(Ir^{III/II})$ = −1.75 V),[29] possibly pointing to a redox based cut-off for photodriven N_2R. Accordingly, [Ir(*p*-F(Me)ppy)$_2$(dtbbpy)]PF_6 ($E_{1/2}(Ir^{III/II})$ = −1.88 V) restores the yields observed in the parent system (entry 24).[30] However, Ir(ppy)$_3$, despite having the strongest reduction potential ($E_{1/2}(Ir^{III/II})$ = −2.57 V), gave attenuated NH_3 yields (entry 25) and therefore suggests multiple factors may be at play.

Figure 4.2B provides a working model to account for the role of [Ir]$BAr^F{}_4$. Upon excitation of $[Ir^{III}]^+$ to $[Ir^{III}]^+$*, reductive quenching by HEH_2 would generate $[Ir^{II}]$, as has been established in related reductions of organic substrates (Figure 4.2B).[9] This proposed pathway is consistent with the lack of enhancement observed with Ir(ppy)$_3$, with which reductive quenching by HEH_2 is very uphill($E_{1/2}(*Ir^{III/II})$ = −0.08 V, ($E_{1/2}(HEH_2{}^{0/+})$ = 0.48 V).[29] The resulting radical cation $HEH_2^{\bullet+}$ is then deprotonated by Col, mitigating back-electron transfer from $[Ir^{II}]$. As noted above, $[Ir^{II}]$ is assumed to be sufficiently reducing to generate an $M(N_2)^-$ species from $M(N_2)$. The former would then undergo protonation by $[ColH]^+$ to form an N−H bond via $M(N_2H)$, which itself can be reduced further by diffusing $HEH^\bullet$ to generate $M(NNH_2)$. As noted for Figure 4.2A, this series of steps is plausible but is only one of several related scenarios that may be viable (e.g., $[Ir^{II}]$ might be oxidized by $[ColH]^+$ instead of a [Mo]-species) and future mechanistic studies are needed.

In contrast to the Ir-free conditions, the system with the photosensitizer remains catalytically competent even without added buffer, albeit with an attenuation in turnover (7.4 ± 0.4 equiv NH_3/Mo, entry 22). Presumably, under a Col/$[ColH]^+$-free cycle, the liberated radical cation $HEH_2^{\bullet+}$ (formed via reductive quenching) can be consumed via proton or H-atom transfer with a $[Mo]N_xH_y$ intermediate.

Having established photodriven transfer hydrogenation as a viable strategy for N_2R, we have begun to explore the deep reduction of other substrates. While success here will ultimately be best realized by exploring a broader array of transition metal catalysts,

promising early results with the [Mo]Br_3 catalyst discussed herein include the complete reduction of nitrate to ammonia (8 e^-/9 H^+) and acetylene to ethylene (major product, 2 e^-/2 H^+) and ethane (minor product, 4 e^-/4 H^+). These transformations have been previously explored by photochemical methods, including with semiconductors as for N_2.[31,32] Also of relevance is the photoinduced hydroalkylation of alkynes using Hantzsch ester derivatives, though transfer hydrogenation from HEH_2 to acetylene has not to our knowledge been previously reported.[33]

Reduction of [TBA]NO_3 with HEH_2 in the presence of buffer and [Mo]Br_3 under blue LED irradiation and argon atmosphere yields 9.8 ± 1.2 equiv NH_3/Mo, representing a 73 ± 9% yield with respect to HEH_2 (Table 1, entry 27). The reaction carried out with [TBA]$^{15}NO_3$ yielded $^{15}NH_3$ (Figure C.13), confirming NO_3^- as the source of N-atoms. In contrast to N_2R, addition of [Ir]$BAr^F{}_4$ did not enhance catalysis (entry 28). Distinct from N_2 as the substrate where no background reactivity is observed (entry 3), there is some background reactivity for NO_3^- even in the absence of the Mo-catalyst; this reactivity is enhanced by the Ir-photocatalyst (entries 29-30; see section C.5.5 for further discussion). Only trace NH_3 was detected in the absence of light (entry 31).

The reduction of acetylene under the same conditions (HEH_2, Col/[ColH]OTf buffer, and [Mo]Br_3 under blue LED irradiation and argon atmosphere) provides a mixture of ethylene and ethane in a ~6:1 ratio and a total yield of 24 ± 5% with respect to HEH_2 (entry 32). Addition of [Ir]$BAr^F{}_4$ to this reaction marginally decreases the yield (entry 33). However, as in the NO_3^- reduction reaction, [Ir]$BAr^F{}_4$ enhances Mo-free reactivity (entries 34-35). Again, no reduced products could be detected in the absence of light (entry 36). In sum, each of these three substrates (N_2, NO_3^-, HCCH) illustrate the capacity of HEH_2 to deliver H_2 equivalents via photodriven transfer hydrogenation.

4.3 Discussion

Reagent strengths			$BDFE_{eff}$	$\Delta\Delta G_f(NH_3)$
HEH_2 BDFE 62.3 kcal mol^{-1}	+	HEH$^{\bullet}$ BDFE 40.5 kcal mol^{-1}	51.4 kcal mol^{-1}	1.8 kcal mol^{-1}
$^{*}[HEH_2]$ E_{ox} −2.5 V	+	ColH^{+} pK_a 15	15.5 kcal mol^{-1}	109 kcal mol^{-1}
$Ir^{II}(ppy)_2(dtbbpy)$ E_{ox} −1.9 V	+	ColH^{+} pK_a 15	29.3 kcal mol^{-1}	68 kcal mol^{-1}

$$BDFE_{eff} = 23.06(E_{ox}) + 1.37(pK_a) + C_G \quad \text{(eqn 4.1)}$$

$$\Delta\Delta G_f(NH_3) = 3((BDFE_{H2})/2 - BDFE_{eff}) \quad \text{(eqn 4.2)}$$

Figure 4.3. Estimated $BDFE_{eff}$ values and corresponding $\Delta\Delta G_f(NH_3)$ for the transformations of interest herein. Values estimated using eqns 4.1 and 4.2.

To close, it is instructive to consider the thermodynamics of the photodriven N_2R system described here and its hypothetical dark reaction (Figure 4.1C). To do this one can compare the $BDFE_{eff}$ (Figure 4.3, eqn 4.1), a measure of the thermodynamics of H-atom transfer from a set of reagents, to the BDFE of H_2 (103.9 kcal mol^{-1}).[34,35,36] The difference between these values provides an overpotential for N_2 hydrogenation, expressed as $\Delta\Delta G_f(NH_3)$ (eqn 4.2).[37] For the dark reaction, the $BDFE_{eff}$ is the average of the first (C−H) and second (N−H) BDFE's for HEH_2 and HEH$^{\bullet}$, respectively, correlating to a very small overpotential ($\Delta\Delta G_f(NH_3)$ = 1.8 kcal mol^{-1}).[18] NH_3 synthesis via transfer hydrogenation from HEH_2 to N_2 is therefore thermodynamically comparable to N_2 hydrogenation by the Haber-Bosch process. Where the latter uses high temperature and pressure to overcome the high kinetic barrier, the photodriven process described here obtains excess driving force directly from visible light. More specifically, under conditions that exclude the photosensitizer, using the estimated excited-state reduction potential of $[HEH_2]^*$ and the pK_a of $[ColH]^+$ to estimate $BDFE_{eff}$, blue light affords access to a large added driving force ($\Delta\Delta G_f(NH_3)$ = 123 kcal mol^{-1}; Figure 4.3) to push the transfer hydrogenation forward. In the presence of the Ir-photosensitizer, a smaller but still significant driving force ($\Delta\Delta G_f(NH_3)$ = 68 kcal mol^{-1}) is available. Regardless, the key point is that light generates an overpotential from an otherwise unreactive source of 2 e$^-$/2 H$^+$ stored within HEH_2 that

is sufficient to perform, via successive transfers, a net 6 e^-/6 H^+ reduction of N_2 in the presence of an appropriate catalyst and cocatalyst buffer, with additional benefit gained from inclusion of a photoredox cocatalyst. Important future goals for the work presented here include extensive mechanistic studies as well as studies aimed at *in situ* recycling of the spent HE back to HEH_2.

4.4 Cited References

1. Chalkley, M. J.; Drover, M. W.; Peters J. C. *Chem. Rev*. **2020**. 120, 5582–5636.
2. Nishibayashi, Y. *Dalton Trans*. **2018**. 47, 11290–11297.
3. Schrock, R. R. *Angew. Chem. Int. Ed*. **2008**. 47, 5512–5522.
4. Seefeldt, L. C.; Hoffman, B. M.; Peters, J. W.; Raugei, S.; Beratan, D. N.; Antony, E.; Dean, D. R. *Acc. Chem. Res*. **2018**. 51, 2179–2186.
5. Smil, V. *Enriching the Earth: Fritz Haber, Carl Bosch, and the Transformation of World Food Production*. **2000**. MIT Press.
6. Shima, T.; Hu, S.; Luo, G.; Kang, X.; Luo, Y.; Hou, Z.; *Science* **2013**. 340, 1549–1552.
7. Yamazaki, Y.; Takeda, H.; Ishitani, O. *J. Photochem. Photobiol. C: Photochem. Rev.* **2015**. 25, 106–137.
8. Elgrishi, N.; Chambers, M. B.; Wang, X. Fontecave, M. *Chem. Soc. Rev*. **2017**. 46, 761–796.
9. Wang, P.-Z.; Chen, J.-R.; Xiao, W.-J. *Org. Biomol. Chem*. **2019**. 17, 6936–6951.
10. Chen, Q.-A.; Chen, M.-W.; Yu, C.-B.; Shi, L.; Wang, D.-S.; Yang, Y.; Zhou, Y.-G. *J. Am. Chem. Soc*. **2011**. 133, 16432–16435.
11. Abou-Elenein, G. M.; Ismail, N. A.; Mohammed, Z. F.; Fahmy, H. M.; *Egypt. J. Pharmaceutical Sci*. **1992**. 33, 953–962.
12. Comer, B. M.; Fuentes, P.; Dimkpa, C. O.; Liu, Y.-H.; Fernandez, C. A.; Arora, P.; Realff, M.; Singh, U.; Hatzell, M. C.; Medford, A. J. *Joule* **2019**. 3, 1578–1605.

13. Schrauzer, G. N.; Guth, T. D. *J. Am. Chem. Soc*. **1977**. 99, 7189–7193.
14. Edwards, J. G.; Davies, J. A.; Boucher, D. L.; Mennad, A. *Angew. Chem. Int. Ed*. **1992**. 31, 480–482.
15. Medford, A. J.; Hatzell, M. C.; *ACS Catal.* **2017**. 7, 2624–2643.
16. Brown, K. A.; Harris, D. F.; Wilker, M. B.; Rasmussen, A.; Khadka, N.; Hamby, H.; Keable, S.; Dukovic, G.; Peters, J. W.; Seefeldt, L. C.; King, P. W. *Science* **2016**. 352, 448–450.
17. Brown, K. A.; Ruzicka, J.; Kallas, H.; Chica, B.; Mulder, D. W.; Peters, J. W.; Seefeldt, L. C.; Dukovic, G.; King, P. W. *ACS Catal*. **2020**. 10, 11147–11152.
18. Shen, G.-B.; Fu, Y.-H.; Zhu, X.-Q. *J. Org. Chem*. **2020**. 85, 12535–12543.
19. Jung, J.; Kim, J.; Park, G.; You, Y.; Cho, E. J. *Adv. Synth. Catal*. **2016**. 358, 74–80.
20. Zhu, D.-L.; Wu, Q.; Li, H.-Y.; Li, H.-X.; Lang, J.-P. *Chem. – Eur. J*. **2020**. 26, 3484–3488.
21. Arashiba, K.; Eizawa, A.; Tanaka, H.; Nakajima, K.; Yoshizawa, K.; Nishibayashi, Y. *Bull. Chem. Soc. Jpn*. **2017**. 90, 1111–1118.
22. Tshepelevitsh, S.; Kütt, A.; Lõkov, M.; Kaljurand, I.; Saame, J.; Heering, A.; Plieger, P. G.; Vianello, R.; Leito, I. *Eur. J. Org. Chem*. **2019**. 2019, 6735–6748.
23. Connelly, N. G.; Geiger, W. E. *Chem. Rev*. **1996**. 96, 877–910.
24. Kano, K.; Matsuo, T. *Bull. Chem. Soc. Jpn.* **1976**. 49, 3269–3273.
25. Munisamy, T.; Schrock, R. R. *Dalton Trans*. **2011**, 41, 130–137.
26. Tanaka, H.; Arashiba, K.; Kuriyama, S.; Sasada, A.; Nakajima, K.; Yoshizawa, K.; Nishibayashi, Y. *Nature Commun*. **2014**. 5, 3737–3787.
27. Wang, D.; Loose, F.; Chirik, P. J.; Knowles, R. R. *J. Am. Chem. Soc*. **2019**. **141**, 4795–4799.
28. Slinker, J. D.; Gorodetsky, A. A.; Lowry, M. S.; Wang, J.; Parker, S.; Rohl, R.; Bernhard, S.; Malliaras, G. G. *J. Am. Chem. Soc*. **2004**. 126, 2763–2767.

29. Koike, T.; Akita, M. *Inorg. Chem. Front*. **2014**. 1, 562–576.
30. Capacci, A. G.; Malinowski, J. T.; McAlpine, N. J.; Kuhne, J.; MacMillan, D. W. C. *Nat. Chem.* **2017**. 9, 1073–1077.
31. Hirakawa, H.; Hashimoto, M.; Shiraishi, Y.; Hirai, T. *ACS Catal*. **2017**. 7, 3713–3720).
32. Boonstra, A. H.; Mutsaers, C. A. H. A. *J. Phys. Chem.* **1975**. 79, 2025–2027.
33. Zhang, Y.; Tanabe, Y.; Kuriyama, S.; Nishibayashi, Y. *Chem. – Eur. J*. **2022**. 28, e202200727.
34. Bordwell, F. G.; Cheng, J. P.; Harrelson, J. A. *J. Am. Chem. Soc*. **1988**. 110, 1229–1231.
35. Tilset, M.; Parker, V. D. *J. Am. Chem. Soc*. **1989**. 111, 6711–6717.
36. Agarwal, R. G.; Coste, S. C.; Groff, B. D.; Heuer, A. M.; Noh, H.; Parada, G. A.; Wise, C. F.; Nichols, E. M.; Warren, J. J. ; Mayer, J. M. *Chem. Rev*. **2022**. 122, 1–49.
37. Chalkley, M. J.; Peters, J. C. *Eur. J. Inorg. Chem*. **2020**. 2020, 1353–1357.

C h a p t e r 5

On the Mechanism of Photodriven Hydrogenations of N_2 and Other Substrates by Hantzsch Ester: Buffer is Key to Generation of Reactive H-atom Donors

5.1 Introduction

The utility of proton-coupled electron transfer (PCET) in small molecule reductions (e.g., N_2) and organic transformations has motivated the development of reagents and catalysts with weak (net) X−H bonds capable of driving the reductive protonation of substrates.[1,2,3,4,5] Photoinduced weakening of X–H bonds offers a promising strategy; following excitation the X–H bond dissociation free energy ($BDFE_{X–H}$) can decrease dramatically, converting unreactive X−H bonds into potent H-atom donors (Figure 5.1A).[6,7] Model studies have for example demonstrated such reactivity via ruthenium photosensitizers with acidic ligands[8,9] and photoexcited metal hydrides.[10] Further, this strategy has recently been utilized in catalytic systems with H_2,[11,12,13] or $H^+/e^–$ equivalents derived from an acid and an electrode (Figure 5.1A).[14] While these strategies show promise, it remains a challenge to photogenerate species featuring highly reactive $H^+/e^–$ equivalents with sufficiently long lifetimes to facilitate PCET to highly unactivated substrates, such as N_2, unactivated alkenes, carbonyls, or CO.

Recently, our laboratory,[15] followed closely by a report from Nishibayashi and coworkers,[16] introduced photocatalytic N_2R using a well-defined synthetic system. In our study, catalytic blue-light-driven transfer hydrogenation of N_2 to 2 NH_3 (i.e., nitrogen reduction, N_2R) using 3 equivalents of the Hantzsch ester (HEH_2) as a source of the $H^+/e^–$ equivalents required for this transformation. An N_2R catalyst, $PNPMoBr_3$ ([$MoBr_3$]; PNP, 2,6-bis(di-tert-butylphosphinomethyl)pyridine),[17,18] was used to activate N_2, but curiously a 1:1 mixture of [ColH]OTf:Col (Col-buffer; Col = 2,4,6-trimethylpyridine; Figure 5.1B) was needed for efficient N_2R. *While this specific reagent cocktail showed substantial N_2R activity even in the absence of a photoredox catalyst* (e.g., Ir), other dihydropyridines we have canvassed required the addition of a photoredox catalyst; addition of an Ir photoredox catalyst enhanced the N_2R reactivity with HEH_2 as well. The related Nishibayashi study focused on systems using a photoredox catalyst to facilitate N_2R.[16]

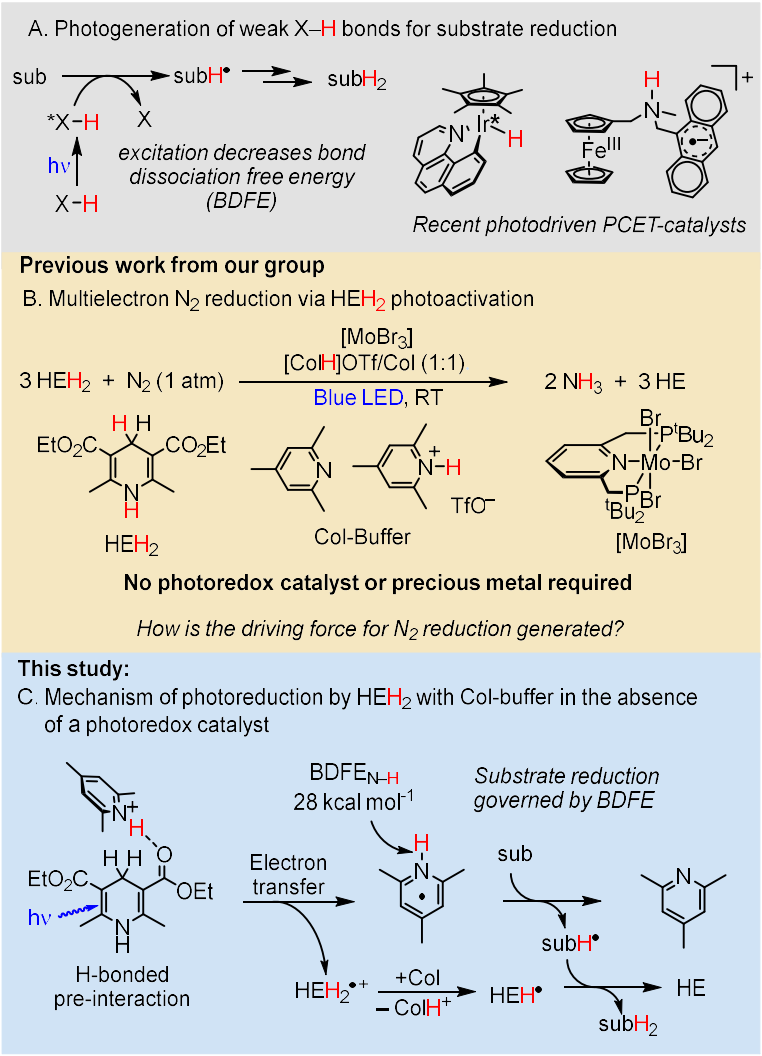

Figure 5.1. Photogenerated H-atom transfer reagents. (A) Photogeneration of PCET-donors for reductive reactions.[11,14] (B) Photodriven transfer hydrogenation for N_2R reduction with [$MoBr_3$], HEH_2, and Col-buffer.[15] (C) The mechanism proposed in this work for reduction by HEH_2 and Col-buffer.

The Mo-catalyst activates N_2 for proton-coupled reduction, but thermally driven N_2R with [$MoBr_3$] still requires a combination of highly reactive acids and reductants capable of generating (net) H-atom equivalents with effective bond dissociation free energy ($BDFE_{eff}$) of ~30 kcal mol^{-1}.[16,17,19,20] This corresponds to an overpotential of ~+65 kcal mol^{-1} per NH_3 formed. By contrast, a hypothetical dark reaction using HEH_2 has an overpotential of only +6 kcal mol^{-1}.[15]

Our prior report speculated that N_2R occurred via a mechanism similar to thermal N_2R by generating the required overpotential via irradiation of HEH_2 in the presence of Col-buffer. Specifically, we suggested that access to the reducing excited state of HEH_2 ($*HEH_2$) was critical for photodriven N_2R. Further, we suggested that $*HEH_2$ reduces [ColH]OTf to generate ColH$^{\bullet}$, a potent PCET donor. Here, we directly probe these hypotheses, providing evidence largely in support of the initially proposed scheme but also detailing how Col-buffer increases the photoreducing capacity of HEH_2 (Figure 5.1C).

Given the proposed role of HEH_2, it is useful to briefly review its photochemistry. The excited state of HEH_2 can be accessed by blue-light irradiation. Curiously, while the thermochemistry of $*HEH_2$ suggests it is a highly potent donor of e^- or H^+/e^- ($E(HEH_2^{\bullet+}/*HEH_2)$ = −2.5 V; $BDFE_{C–H}$ = −7 kcal mol^{-1}, Figure 5.2A),[21] its observed reactivity had previously been limited to activated organic substrates with extended electron-poor π-systems, e.g., nitroarenes,[22] imines,[23] α-bromoketones,[24] and electron-poor alkenes (Figure 5.2B).[25] This has been rationalized by the short lifetime and low quantum yield of $*HEH_2$ (Figure 5.2A).[24,26] The available data suggests that ground state pre-association between HEH_2 and substrate is required to observe substrate reduction; π-stacked, electron donor-acceptor (EDA) complexes between the electron-rich dihydropyridine and electron-poor aromatics are commonly invoked (Figure 5.2B). As such, substrate reduction is kinetically limited by the substrates' ability to form this pre-association complex, rather than the thermodynamics of HAT/ET from $*HEH_2$ to the substrate.

A contrast to the direct hydrogenation of substrates by HEH_2 is its use as a photoreductant in combination with R$^{\bullet}$-donors, such as Katritzky salts ($[^{2,4,6\text{-Ph}}PyrR]BF_4$)[27] or *N*-hydroxyphthalimide esters (Figure 5.2C).[28,29,30] Here, a π-stacked EDA complex forms between HEH_2 and the R$^{\bullet}$-donor. Irradiation results in electron transfer to release R$^{\bullet}$. As a pre-interaction between HEH_2 and substrate is not required in such a scenario, a wider range of substrates have been explored, e.g., Giese acceptors,[100] pyridines,[102] and Ni cross-coupling intermediates (Figure 5.2C).[101]

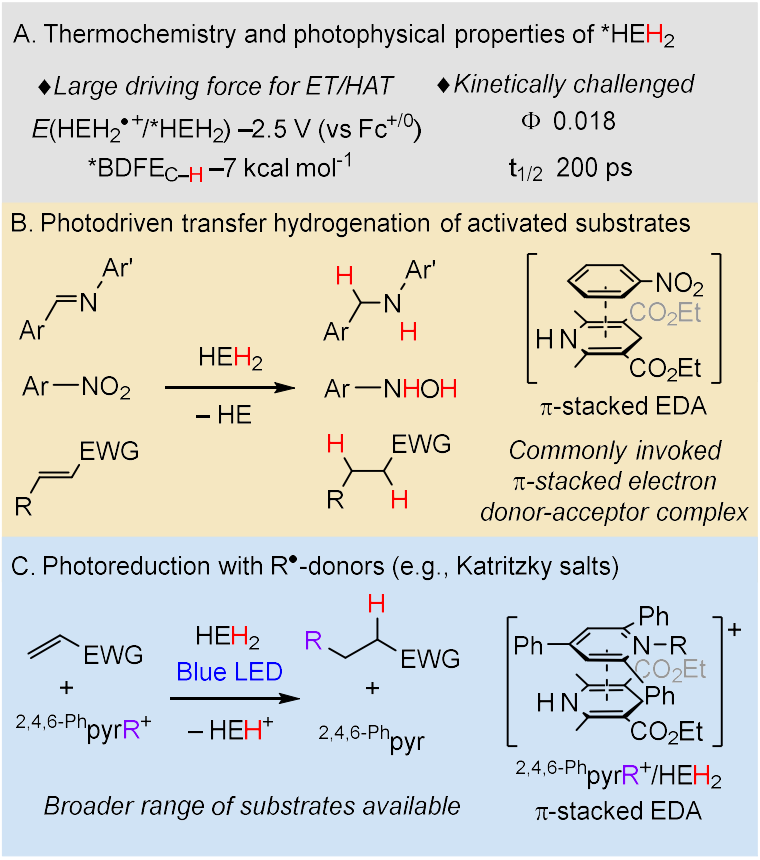

Figure 5.2. Overview of HEH_2 excited state properties and reactivity.[23,27,30]

Recent reports, including our previous study,[15] utilize HEH_2 as a photoreductant in transition metal or lanthanide-catalyzed reduction reactions where, based on the substrates, π-stacked EDA complexes are not likely operative.[31,32,33,34,35,36,37] However, despite the increasing utility of these HEH_2-driven photoreductions, limited mechanistic data hampers the development of new reactivity.[38]

Against this backdrop, we have interrogated the activation of HEH_2 by Col-buffer owing to its relevance to photodriven N_2R. A mechanism is mapped by addressing ground and excited state interactions of HEH_2 and buffer, and by monitoring the formation of organic radicals (Figure 5.1C). We find that an H-bonded adduct between $[ColH]^+$ and HEH_2 precedes the productive irradiation pathway. Following excitation of this associated pair, ET from HEH_2 to $[ColH]^+$ furnishes $ColH^•$. The latter is a potent H-atom donor ($BDFE_{N–H}$ = 28 kcal $mol^{–1}$). $[HEH_2]^{•+}$, the byproduct of this ET step, is deprotonated by

Col to generate the $HEH^{\bullet}$ radical and reforming $[ColH]^{+}$ as well. $HEH^{\bullet}$ serves as a second reactive H-atom donor. These pyridinyl radicals can reduce diverse substrates without the kinetic limitations observed by direct HEH_2 photoreductions.

5.2 Results

5.2.1 N_2R dependence on irradiation wavelength, buffer, and dihydropyridine

As noted, our previous report proposed blue light excitation of HEH_2 during photodriven N_2R. However, we had used broad (400-500 nm) LED lamps, which overlay with the UV-vis spectra of both HEH_2 and the $[MoBr_3]$ catalyst (Figure 5.3). To more reliably determine the photosensitized species during catalysis, we compared the N_2R reaction products at different irradiation wavelengths to the absorbance spectra of components of the catalytic reaction (akin to an action spectrum).[39]

Comparing the NH_3/Mo yield (Figure 5.3) at different wavelengths (Kessil™ LED H160 lamps at specific wavelengths; see Figure D.1 for emission spectra) to the UV-vis spectra of the reaction components, we find a relationship between N_2R and wavelength consistent with irradiation of HEH_2 (light blue trace, Figure 5.3) as a requisite to produce NH_3. Only when the strongly absorbing π-π* transition of HEH_2, with onset at ~435 nm (slightly red-shifted upon addition of Col-buffer, dark blue trace), is excited are the N_2R products NH_3 and oxidized Hantszch ester (HE, see Table D.2) observed. Specifically, we found that with loadings of 2.3 mM $[MoBr_3]$, 124 mM HEH_2, and 124 mM Col:[ColH]OTf in THF solvent, irradiating for 12 hours with 20 W at 427 nm and 440 nm reduced N_2 to NH_3 (6.6 ± 0.9 and 1.5 ± 0.5 equiv NH_3/Mo, respectively); no NH_3 was produced at 456 nm. While the overlap between the HEH_2 absorbance and the lamp emission spectra increases with lower wavelength across this series, $[MoBr_3]$ (yellow trace) absorbs similarly at 427, 440, and 456 nm. If $[MoBr_3]$ excitation is required for N_2R, such significant differences in NH_3 yield as a function of wavelength would not be expected. This conclusion is supported by the exploration of photodriven N_2R with a different precatalyst, $PCPMoCl_3$ (PCP = 1,3-bis((di-*tert*-butylphosphino)methyl)benzimidazol-2-

ylidene),[40] under otherwise identical conditions. The same trend is observed; N_2R occurs when irradiating at 440 or 427 nm but not at 456 nm (Table D.3).

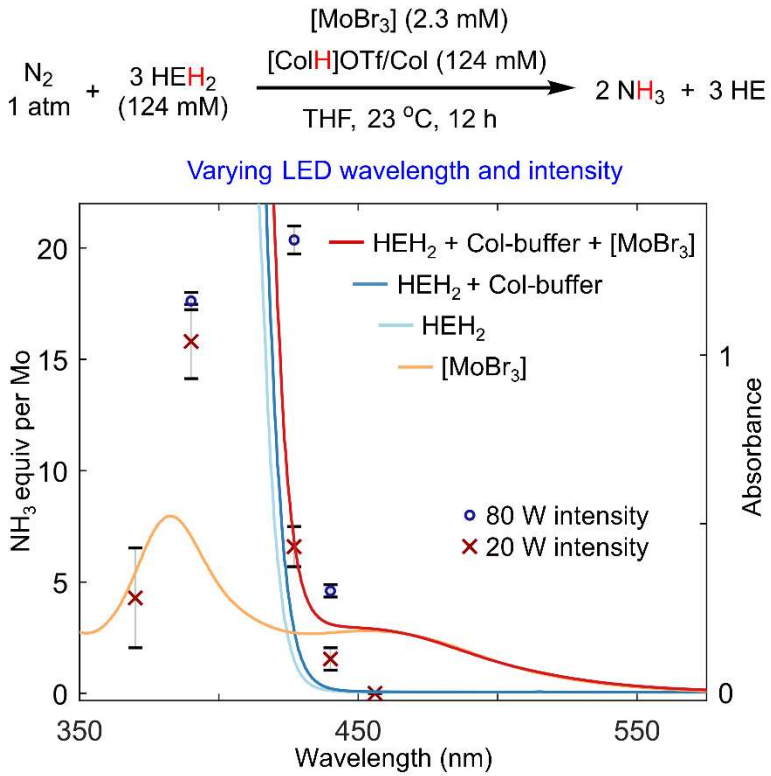

Figure 5.3. Plot of NH_3 yields per Mo at varying wavelengths (Black crosses and circles, left-hand axis) against the optical spectra of reaction components. Optical spectra were collected at catalytic concentrations in a 1 mm path length cuvette.

Oxidized Hantzsch pyridine (HE) is observed as the organic product for a balanced N_2R reaction. With [$MoBr_3$], when irradiating at 456 nm, only 12% of HEH_2 is converted to HE, consistent with the consumption of HEH_2 and N_2R being coupled. Further, irradiation at 440 nm at 20 W intensity for 12 hours results in incomplete consumption of HEH_2. Accordingly, when the light intensity and reaction time are increased (40 W, 24 hours), the NH_3 yields increase (4.6 ± 0.3 equiv NH_3/Mo). In this latter case, all of the HEH_2 was consumed, with about 85% recovered as HE. The amount of recovered HE is similar to what we previously reported using broader wavelength LEDs.[15]

Increasing the irradiation intensity at 427 nm (80 W, 12 hours) results in a substantial boost of the NH_3 yield (20.4 ± 0.6 equiv NH_3/Mo). These yields are more than

double those achieved in our previous report at the same catalyst and reagent loading, emphasizing the importance of irradiation wavelength and intensity. By lowering the catalyst loading (0.575 mM [$MoBr_3$]), the yields increase further to 28 ± 3 equiv NH_3/Mo, the highest yields achieved for molecular photodriven N_2R in the absence of precious metals (see Table D.1). Somewhat higher yields have been reported using a structurally related precatalysts, a Ir photocatalyst and a dihydroacridine organic H-atom donor.[16]

Lower wavelength light (390 nm light) shows high N_2R yields (15.8 ± 1.7 NH_3/Mo) even at low (20 W) intensity, consistent with more efficient excitation of HEH_2 (Figure D.18). However, increasing the intensity at this wavelength (80 W, 12 hours), only gives a slight boost in yield (17.6 ± 0.4 NH_3/Mo). A 390 nm irradiation, the HE yields decrease (HE recovered ~70%; Table D.2), suggesting increased side-reactivity, possibly via C−C coupling between HEH_2 and $ColH^+$. Still higher energy photons (370 nm) sharply decrease the NH_3 yield (4.3 ± 2.2 equiv/Mo). In addition to (likely) increased side-reactivity as deeper UV absorbances are excited, the excitation efficiency of HEH_2 drops at 370 nm.

We also explored a range of other buffers and dihydropyridines for photodriven N_2R, detailed in the Appendix D (see Figure D.2 and Table D.7). These studies established that any significant deviation of the structure of the Col-buffer or the dihydropyridine substantially attenuates NH_3 yields. The present study therefore focuses on the mechanism of HEH_2 activation by Col-buffer to understand how N_2R is facilitated by this particular combination of reagents.

5.2.2 Study of ground state interactions between HEH_2 and Col-buffer

Adding buffer to HEH_2 results in a red shift of the onset of the intense HEH_2 π-π* transition. The same shift is observed in the presence of just [ColH]OTf, but not Col alone, consistent with the primary interaction being between [ColH]OTf and HEH_2 (Figures 5.4A and D.15). Similar red-shifts have been observed upon the formation of π-stacked EDA complexes[22,100,101,41] or Lewis acid coordination to HEH_2 (presumably though the carbonyls).[35,42] This suggests two plausible pre-interaction scenarios between $[ColH]^+$ and HEH_2: H-bonding through the carbonyls, or π-stacking.

The HEH_2 ν(C=O) bands were probed (IR, 10 mM) as a function of added [ColH]OTf (0 to 160 mM, Figure 5.4B). A decrease in the intensity of the ν(C=O) bands at 1698 and 1685 cm^{-1} is observed as acid is added. New features grow in concomitantly; a blue-shifted feature appears at 1735 cm^{-1} and a red-shifted shoulder at ~1600 cm^{-1}. These shifts are consistent with H-bonding to one of the ester carbonyls, weakening this vibrational frequency, and in turn strengthening the other ν(C=O). A series of 4-phenyl substituted Hantzsch ester derivatives exhibits a similar splitting of vibrational modes in ethanol solvent (compared to solution state IR in aprotic solvents), albeit with a smaller magnitude.[43]

Computational methods (TPSS functional[44] def2-TZVP orbitals[45] using a CPCM to model the THF solvent[46]) provide additional insight into the pre-association of HEH_2 and $[ColH]^+$. Evaluating possible interactions, we find that while both arrangements are slightly disfavored over the free HEH_2/$[ColH]^+$, an H-bonded complex is favored over a π-stacking interaction ($\Delta G_{\text{H-bond}}$ = +1.3 kcal mol^{-1}, $\Delta G_{\pi\text{-stack}}$ = +3.5 kcal mol^{-1}; Figure 5.4C). For the H-bonded complex, time-dependent DFT (TD-DFT; a TPSSh functional[44] and def2-TZVP basis set[45]) calculations predict a red-shift in the UV-vis spectrum ($\Delta\lambda_{\text{abs, max, calc}}$ = + 4 nm; Figure D.78) as well as an increase in the vibrational frequency of one C=O mode ($\Delta\nu_{\text{calc}}$ = +7 cm^{-1}; Figure D.79) and decrease of the other mode ($\Delta\nu_{\text{calc}}$ = −40 cm^{-1}). In contrast, for the π-stacked EDA complex, the observed spectroscopic changes are not reproduced computationally: the optical spectrum predicts a low energy EDA band ($\lambda_{\text{abs, max, calc}}$ = 600 nm; Figure D.78) and a slight decrease of both vibrational modes ($\Delta\nu_{\text{calc}}$ =−2, −2 cm^{-1}; Figure D.79). Based on these experimental observations and computational predictions, we favor an H-bonded pre-association between HEH_2 and $[ColH]^+$.

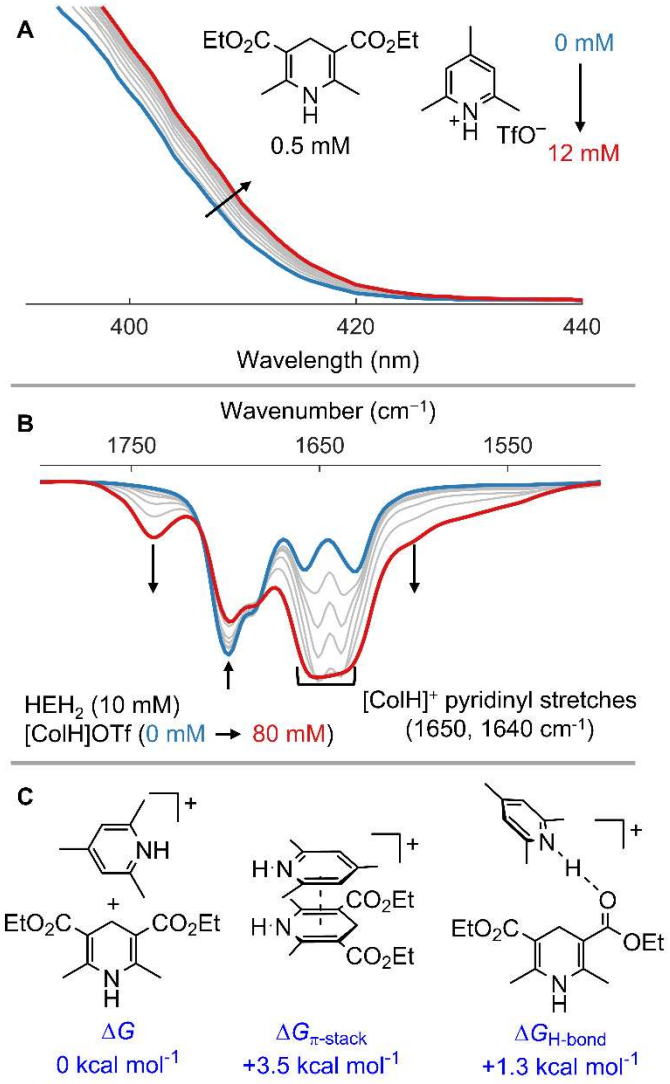

Figure 5.4. Study of ground-state interactions between HEH_2 and $[ColH]^+$. (A) UV-vis spectra of HEH_2 and [ColH]OTf. (B) Solution state infrared spectra of HEH_2 and $[ColH]^+$. (C) Computational analysis of possible pre-interaction complexes of HEH_2 and [ColH]OTf.

5.2.3 Photophysical studies

To study the interaction of Col-buffer with the excited state of HEH_2, we turned to photophysical measurements. Steady-state fluorescence spectroscopy data show that HEH_2 (in the absence of acid and base) is excited by $\lambda_{exc} < 430$ nm, with a distinct emission spectrum ($\lambda_{em\ max}$ at 455 nm, Figure 5.5A) and a low fluorescence quantum yield (0.018; Figure D.20). The excited state decay establishes a lifetime $t_{1/2} = 200$ ps (Figure D.23). The

short excited-state lifetime and low quantum yield match previous reports for HEH_2 in DMSO or MeCN.[24,26] The small Stokes shift and short lifetime are consistent with population of a singlet excited state, as has been observed in MeCN.[26]

The addition of [ColH]OTf red-shifts the excitation spectrum of HEH_2 slightly. In addition, substantial quenching is observed upon adding [ColH]OTf, yielding a Stern-Volmer[47] quenching constant of $K_{SV} = 22\ M^{-1}$ (Figure 5.5B and C). By contrast Col as base does not quench $*HEH_2$ or noticeably perturb the emission profile (Figure D.22).

$$\frac{I_0}{I_{[ColH(OTf)]}} \approx 1 + K_{SV}[ColH(OTf)] \quad \text{(eqn 5.1)}$$

$$K_{SV} = (K_{stat} + K_{dyn}) \text{ (eqn 5.2)}$$

The lifetime quenching effect of [ColH]OTf on $*HEH_2$ was measured to establish a small dynamic quenching constant $K_{dyn} = 1.4\ M^{-1}$ (Figure 5.5C, light blue line, and Figure D.25). Since this constant is an order of magnitude lower than the Stern-Volmer quenching constant (see eqn 5.1 and 5.2), the data point to $*HEH_2$ undergoing primarily static quenching by [ColH]OTf. To interrogate the initially formed product/s of $*HEH_2$ quenching by [ColH]OTf, we turned to transient absorption spectroscopy. The excitation of HEH_2 (1.2 mM) at 355 nm in the presence of [ColH]OTf (12 mM) was measured and shows the formation of a long-lived species ($\tau_{1/2}$ ~ 16 μs, Figure 5.6A, and C) with a maximum at 550 nm, and concomitant bleaching at 370 nm, consistent with HEH_2 consumption. This signal only forms in the presence of [ColH]OTf.

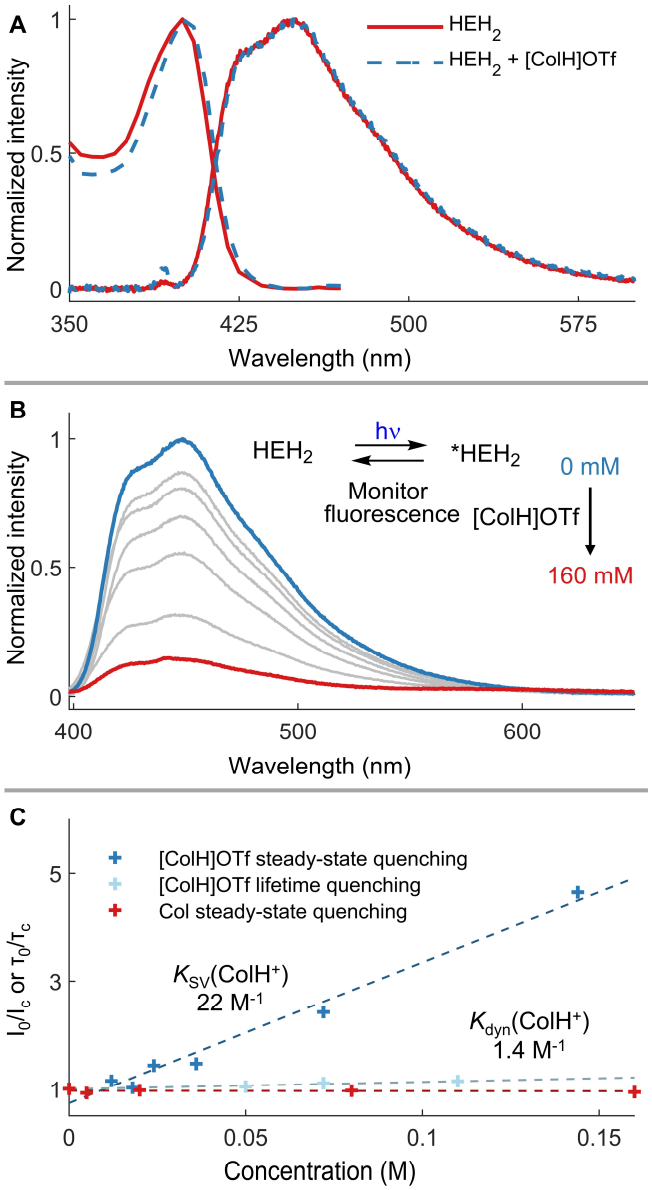

Figure 5.5. Steady-state fluorescence measurements of HEH_2 in the presence of [ColH]OTf. (A) Emission (Right) and excitation (left) spectra of HEH_2 (0.5 mM) in the absence (solid red) and presence of [ColH]OTf (20 mM, dashed blue). (B) Steady-state emission quenching of HEH_2 (0.5 mM) by [ColH]OTf (0 to 160 mM). (C) Steady-state and lifetime quenching plots of HEH_2 in the presence of [ColH]OTf and Col.

Based on time-dependent density functional theory (Figure D.82) predictions of the absorption spectra of several candidate organic species ($[HEH_2]^{\bullet+}$, $HEH^{\bullet}$, $^3HEH_2$, and $ColH^{\bullet}$), we find that the observed absorption is most consistent with assignment as

$[HEH_2]^{\bullet+}$ (red bars in Figure 5.6C). Dihydropyridine radical cations, albeit to our knowledge not $[HEH_2]^{\bullet+}$, have been generated via similar flash-photolysis experiments in the presence of electron acceptors, with transient absorption maxima ranging from 550-650 nm.[48,49,50]

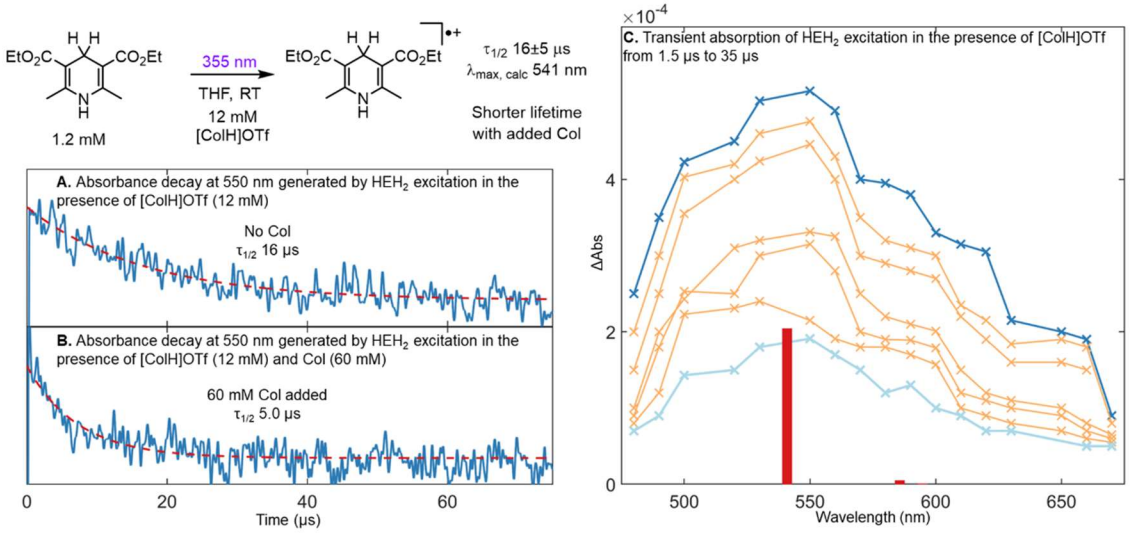

Figure 5.6. Transient absorption measurements of HEH_2 in the presence of [ColH]OTf and Col in THF. (A) Absorption decay of signal generated from HEH_2 (0.5 mM) in the presence of [ColH]OTf (12 mM) was monitored at 550 nm. (B) Same as A, but with added Col (60 mM). (C) TA spectrum of short-lived radical species. Intensity decreases from 1.5 μs (blue trace) to 35 μs. TD-DFT predicted absorbance maxima for $HEH_2^{\bullet+}$ at 541 and 586 nm, indicated by red bars.

In the presence of both [ColH]OTf and Col, we find that a similar signal decays faster (Figure 5.6B and Figure D.29). An explanation for this observation involves the deprotonation of $[HEH_2]^{\bullet+}$ by Col as a new decay pathway. Plotting the lifetimes as a function of base concentration allows determination of a deprotonation constant ($k = 2.4 \pm 0.6\ 10^6\ M^{-1}\ s^{-1}$; Figure D.40). This value matches data for previously reported deprotonations of dihydropyridine radical-cations.[50,51]

The formation of $[HEH_2]^{\bullet+}$ is readily rationalized by electron transfer from $^*HEH_2$ to [ColH]OTf, which would also furnish ColH$^{\bullet}$. Ground-state pre-association of HEH_2 with [ColH]OTf (vide supra) via a H-bond interaction sets the stage for ET. Following excitation, ET from $^*HEH_2$ ($E_{ox} = -2.5$ V) to the associated [ColH]OTf ($E_{red} = -2.0$ V)[52]

is favorable and would account for the static quenching pathway. Electron transfers through H-bonds are well precedented.[53,54,55]

In addition to observed ET from *HEH_2 we wondered if excited state proton transfer from *HEH_2 might play a role in catalysis. However, the excited state pK_a of HEH_2 was measured to 23.8 ± 0.9 in MeCN (see section A11), representing a weak acid, and in the context of this report a much weaker acid than the buffer ([ColH]OTf/Col, pK_a 15).[56]

5.2.4 Detection and characterization of photogenerated organic radicals by EPR spectroscopy

To study ground-state populations of organic species that may build up when HEH_2 and Col-buffer are irradiated, we turned to EPR spectroscopy. HEH_2 (100 mM), Col (100 mM), and [ColH]OTf (100 mM) in THF were irradiated with blue light and freeze-quenched after 1 minute and then analyzed by continuous-wave (CW) EPR. The data show formation of an $S = 1/2$ species with g = 2.002, consistent with an organic radical (Figure 5.7A). While narrow and in low yield (~10 μM), the radical is also characterized by a diagnostic apparent sextet (Figure 5.7B) in the 2nd derivate spectra. The intensity and spectral shape are unchanged upon varying the time of freeze-quenching (1 to 60 minutes; Figure D.42); both light and HEH_2 were required to observe any signal. While signals attributable to organic radicals could also be observed in the absence of Col-buffer, these had lower intensity and were distinct from those generated by HEH_2 and Col-buffer (Figure D.43). The apparent sextet can be formed in either toluene or 2-MeTHF, implying this signal is not related to the solvent (Figure D.46).

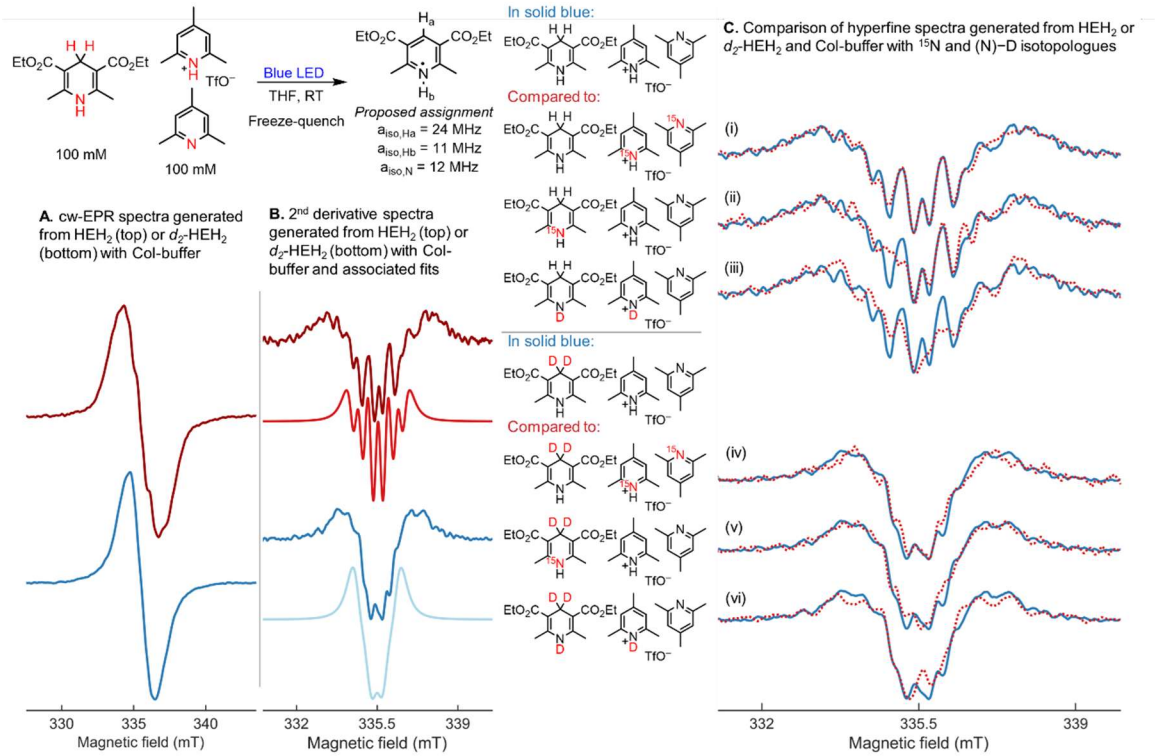

Figure 5.7. EPR detection of organic radicals. (A) CW-EPR spectra generated by irradiating HEH_2 or d_2-HEH_2 (100 mM) with Col-buffer (100 mM). Red atoms have been isotopically labeled to aid the assignment of the observed organic radical(s). (B) 2nd derivative spectra from irradiating HEH_2 or d_2-HEH_2 (100 mM) with Col-buffer (100 mM). Fits generated from proposed parameters. (C) 2nd derivative spectra comparing ^{15}N labeling in either HEH_2 or Col-buffer, N−D labeling (both [ColD]OTf and d_1-HEH_2) and comparison of same isotopologues using d_2-HEH_2 (C_4-deuteration). Acquisition parameters: temperature = 77 K; MW frequency = 9.38 GHz; MW power = 2 mW; modulation frequency = 100 kHz; modulation amplitude = 0.1 mT; conversion time = 20.5 ms.

To aid assignment we synthesized a series of isotopologues, including ^{15}N-HEH_2, ^{15}N-Col buffer, d_2-HEH_2 (double deuterated at C_4−H positions), d_1-HEH_2 (N−H deuterated), [ColD]OTf, d_3-HEH_2, and ^{15}N-d_2-HEH_2. Spectra generated with d_2-HEH_2 show a collapse of much of the hyperfine structure, suggesting significant coupling to the C_4 H-atom(s) (Figure 5.7A and B). Other changes upon labeling were subtler but could be identified by careful comparison of 2nd derivative spectra (Figure 5.7B and C). Given the significant spectral change observed using d_2-HEH_2, comparison of labeled samples (^{15}N or N−D) to samples prepared with either natural abundance HEH_2 (Figure 5.7C, traces i-

iii) or d_2-HEH_2 (traces iv-vi) were used to confirm differences that might be observed more reliably. ^{15}N-labeling of either Col-buffer (traces i and iv) or HEH_2 (traces ii and v) demonstrated changes in the spectra only upon labeling HEH_2, suggesting an HEH_2-derived radical. We also observed changes in the 2nd derivative spectra upon N−D labeling, using both H and D-labeled at the C_4–H positions to confirm this (traces iii and vi).

To account for these observations and provide reasonable simulated fits, a species with coupling to two types of H atoms, one C_4–*H* (a_{iso} = 24 MHz) and one N−*H* (a_{iso} = 11 MHz), as well as coupling to the HEH_2 *N*-atom (a_{iso} =12 MHz) is proposed. The relative magnitudes of these values closely match previous hyperfine values measured for carbonyl-substituted pyridinyl radicals.[57,58] This analysis points to $HEH^{\bullet}$ as the species in question, expected following rapid deprotonation of $[HEH_2]^{\bullet+}$ invoked in the photophysical measurements discussed above.

5.2.5 Substrate reduction studies and benchmarking the effective driving force for H-atom delivery by irradiation of HEH2 and Col-buffer

The spectroscopic data discussed above suggests that irradiation of HEH_2 in the presence of Col-buffer generates $HEH^{\bullet}$ and (by implication) $ColH^{\bullet}$. These pyridinyl radicals serve as potential donors of H-atom equivalents to Mo-bound N_2R intermediates ($Mo–N_xH_y$), and other substrates. Unsaturated organic substrates can allow for estimation of the driving force for net H-atom delivery; this motivated reactivity studies to calibrate the advantage of Col-buffer for chemical transformations beyond N_2R.

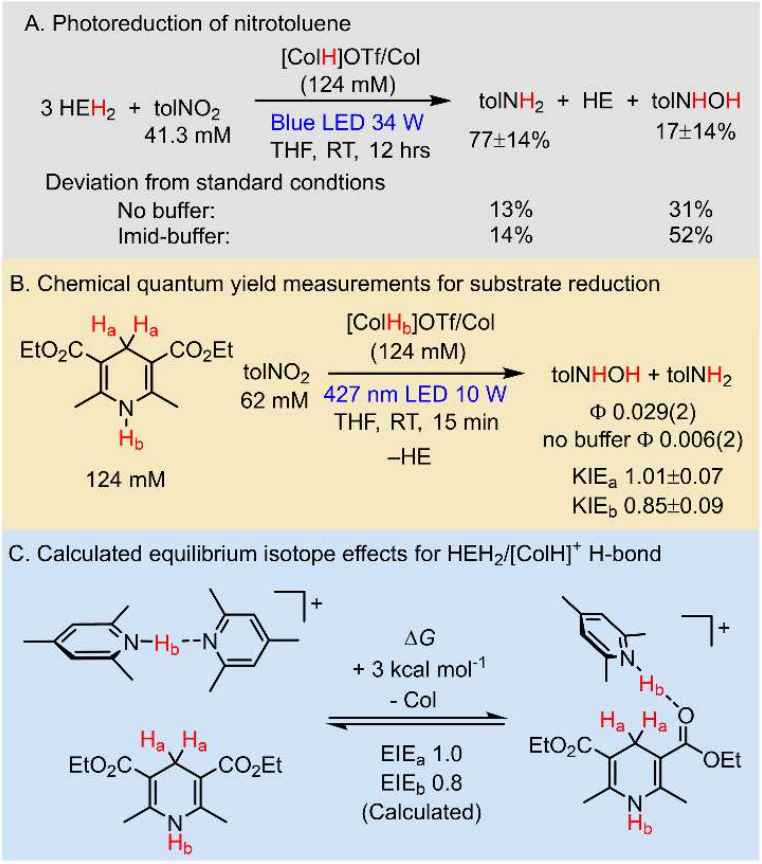

Figure 5.8. Photoreduction of $tolNO_2$ by HEH_2 and Col-buffer.

HEH_2 photoreductions are well established, though studies of these reactions in the presence of Brønsted acids or bases are rare;[25,59] the effects of Col-buffer on organic photoreductions by HEH_2 had not been explored. For the substrates examined here, HEH_2 photoreductions show improved yields and increased selectivity for more reduced products, with Col-buffer displaying distinct behavior. For example, the photoreduction of $tolNO_2$ (4-nitrotoluene) by HEH_2 in the absence of buffer occurs over 72 hours to yield primarily tolNHOH (4-tolyl hydroxylamine).[22] By contrast, irradiation of HEH_2 (124 mM) in the presence of $tolNO_2$ (41.3 mM, 0.33 equiv per HEH_2) and Col-buffer (124 mM) for just 12 hours furnished primarily aniline (2.7:1 ratio $tolNH_2$:tolNHOH, Figure 5.8A) and a high total yield of reduced products (97%). Using an imidazolium/imidazole buffer instead (Imid; pK_a 15.1 compared to pK_a 15.0 for Col in MeCN, Figure 5.8A)[56] furnished lower yields for reduced products and favored tolNHOH, pointing again to Col-buffer as special.

The chemical quantum yield for tolNO_2 reduction was determined to be 0.029(2) in the presence of Col-buffer. This value is greater than the measured fluorescence quantum yield of HEH_2 (0.018), intimating enhanced reactivity in the presence of Col-buffer (Figure 5.8B). The quantum yield for tolNO_2 reduction decreases fivefold in the absence of Col-buffer. Additionally, measurements of the quantum yield with the C_4–*H* (H_a ; Figure 5.8B) and N–*H* (H_b) deuterated isotopologues of HEH_2 and Col-buffer were performed to probe the kinetic isotope effects (KIE) for tolNO_2 reduction. Curiously, while there is no KIE using d_2-HEH_2 (deuterated C_4–H bonds, KIE_a 0.99 ± 0.06), N–D deuteration (d_1-HEH_2 and d_1-Col-buffer, KIE_b) shows a small, inverse KIE (0.84 ± 0.09).

Computational studies suggest that the proposed H-bonding pre-equilibrium between HEH_2 and Col-buffer can be used to rationalize these KIE data. By computation, the preferred conformation of HEH_2 and Col-buffer is free HEH_2 and an H-bonding homo-dimer $[ColH^{\cdots}Col]^+$.[60] However, the H-bond interaction of HEH_2 and $[ColH]^+$ is only slightly uphill (ΔG = 3.0 kcal mol^{-1}; Figure 5.8C). Shifting this equilibrium towards the H-bond interaction of HEH_2 and [ColH]OTf should favor substrate reduction. Thermodynamically, the proton (versus the deuteron) will favor the stronger H-bond of the $[ColH^{\cdots}Col]^+$ homo-dimer. Accordingly, computationally derived EIE_a and EIE_b (equilibrium isotope effects) provide values of 0.97 and 0.80, within the error of the experimentally measured KIEs for tolNO_2 reduction.

HEH_2 and Col-buffer are also competent for the reduction of other N–O bonds (Figure 5.9), including nitroalkanes ($^nPrNO_2$ to $^nPrNH_2$; 30 ± 5% yield per HEH_2), nitrate ($[NO_3]^-$ to NH_3, yield 35 ± 2% per HEH_2, confirmed by ^{15}N-labeling; Figure D.10), and amine N-oxides (Me_3N–O to Me_3N, yield 91 ± 5%). Electron-rich aromatic aldehydes $^{4\text{-}Me2N}$PhCHO and $^{4\text{-}MeO}$PhCHO can also be photoreduced by this approach, with the major product being a diol, consistent with radical addition of H• to the aldehyde to form the α-hydroxybenzyl radical, followed by bimolecular pinacol coupling. The low yields for pinacol coupling of aldehydes by HEH_2 in the absence of buffer is consistent with previous reports.[59] HEH_2 could not reduce less activated carbonyls, such as aliphatic ketones (benzylacetone), or activated aromatic esters (dimethylterphatalate), even with Col-buffer.

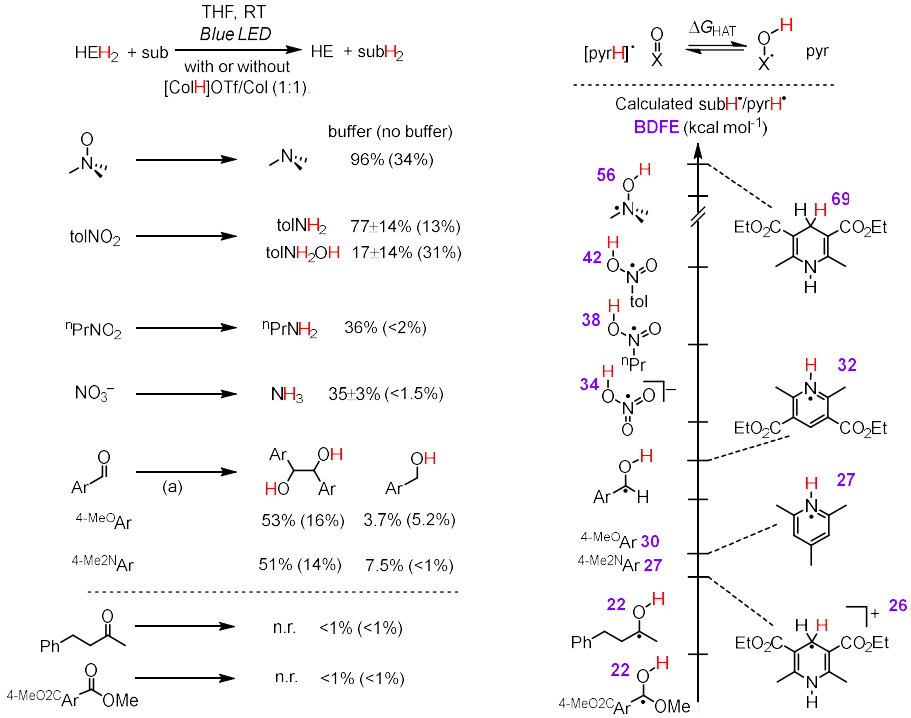

Figure 5.9. Photoreduction of organic substrates by HEH_2 (124 mM) and [ColH]OTf/Col (124 mM of each) in THF. All reactions run for 12 hours using Blue LED H150 lamps at 68 W except where noted. [a]Reaction run using H160 427 nm lamp (40 W) for 4 hours to minimize background reactivity. All yields given from the average of a minimum of two experiments.

This scope of substrates allows us to bracket the thermodynamic driving force for H^+/e^- transfer accessed by irradiation of HEH_2/Col-buffer. When analyzing the computationally derived $BDFE_{O–H}$ (TPSS def2-TZVP; Figure 5.9) following the addition of an H-atom to substrates, we find that only substrates with a sub–H$^\bullet$ $BDFE_{O–H,\ calc}$ ~ 27 kcal mol^{-1} or higher can be reduced. This suggests that irradiation of HEH_2/Col-buffer generates a driving force for H^+/e^- transfer equivalent to a BDFE ~27 kcal mol^{-1}. This bond strength is comparable to some of the weakest isolable or *in situ* formed thermally generated PCET reagents.[61] Highly reactive photogenerated PCET donors have also been detailed.[11,14,62]

We find that the reactivity observed correlates closely with the weak BDFE calculated for [ColH]$^\bullet$ ($BDFE_{N–H,\ calc}$ = 27 kcal mol^{-1}) or [HEH_2]$^{\bullet+}$ ($BDFE_{N–H,\ calc}$ = 26 kcal mol^{-1}) as the donor/s of H-atoms during photoreduction. By contrast, other C/N–H bonds

that might be invoked in solution, such as HEH$^{\bullet}$ ($BDFE_{N-H,\ calc}$ = 32 kcal mol^{-1}, $BDFE_{estimated}$ = 41 kcal mol^{-1}, see section S11)[21] or HEH_2 ($BDFE_{N-H,\ calc}$ = 70 kcal mol^{-1}) feature stronger N/C−H bonds: these species should not be competent to reduce the less activated substrates, at least at the first H^+/e^- transfer step.

The role of $[HEH_2]^{\bullet+}$ ($BDFE_{N-H,\ calc}$ = 26 kcal mol^{-1}) as a potential PCET donor during irradiation cannot be ruled out (see Figure D.72 for a representative scheme). However, as $[HEH_2]^{\bullet+}$ is rapidly deprotonated by Col, we surmise this pathway is at most a minor contributor to substrate reduction, pointing to highly reactive [ColH]$^{\bullet}$ as the probable primary donor of H^+/e^-.

5.3 Discussion

The data obtained via this study allow us to propose a mechanistic outline by which HEH_2 and Col-buffer interact to reduce substrates. This is illustrated in Figure 5.10 via the elementary steps **a** to **h**.

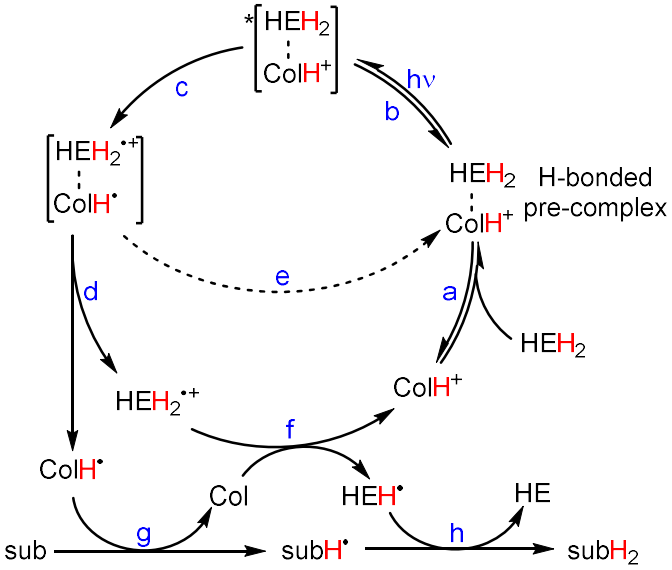

Figure 5.10. Proposed mechanism for 2 $H^+/2e^-$ reduction of substrates by HEH_2 mediated by Col-buffer with steps a-h labeled.

HEH_2 and [ColH]OTf associate via an H-bonded adduct (**a**) in a pre-equilibrium first step. Excitation (**b**) results in ET from *HEH_2 to [ColH]OTf to furnish the charge-transfer product (**c**), which then dissociates to release free ColH$^{\bullet}$ and $[HEH_2]^{\bullet+}$ (**d**). Back ET (BET, **e**) competes with this step but the reaction is driven forward by deprotonation of $[HEH_2]^{\bullet+}$

by Col to produce $HEH^{\bullet}$ and $[ColH]^{+}$ (**f**). Additionally, charge-transfer through an H-bonded complex may present a distinct advantage to the forward process. Following the ET step the H-bond strength should decrease; $ColH^{\bullet}/[HEH_2]^{\bullet+}$ is a much weaker acid/base pair than $[ColH]^{+}/HEH_2$.[63] By contrast, rapid unimolecular fragmentations are often required following ET in π-stacked EDA complexes to avoid BET.(41) Once formed, $[Col{-}H]^{\bullet}$ ($BDFE_{N-H,\ estimated}$ = 28 kcal mol^{-1}, see section S11) can transfer an H-atom to substrate (**g**), regenerating Col. Further reactivity of $[HEH]^{\bullet}$ may proceed by direct reduction of the semi-reduced substrate ($subH^{\bullet}$, **h**) or by disproportionation to yield HE and HEH_2 (see Figure D.64 for a representative scheme).

Based on this mechanistic outline, we can rationalize the improved efficiency upon adding Col-buffer. Pre-association of $[ColH]^{+}$ and HEH_2, and subsequent static quenching to produce $ColH^{\bullet}$, decouples substrate reduction from the pre-association step. Instead, forward reduction is determined by the ability to transfer $H^{\bullet}$ from $[Col{-}H]^{\bullet}$ to substrate, which, given the low $BDFE_{N-H}$ (28 kcal mol^{-1}) of $[Col{-}H]^{\bullet}$, will occur for many substrates. This scenario is comparable to the generation of $R^{\bullet}$ from R^{+}-donors and HEH_2, where R = H. Whereas $*HEH_2$ is thermodynamically potent ($BDFE_{C-H}$ = −7 kcal mol^{-1}) for PCET, it is kinetically challenged in terms of productive reactivity. Adding Col-buffer generates a kinetically accessible weak N−H bond. Additionally, the buffer-free reaction is likely also limited by rapid BET between reduced substrates and $[HEH_2]^{\bullet+}$, as $[HEH_2]^{\bullet+}$ is not effectively removed from solution by deprotonation (Figure D.75). This model suggests that while the primary mechanism of $*HEH_2$ oxidation is quenching by acid, the presence of base is also crucial for efficient substrate reduction. The special combination of Col-buffer and HEH_2 in photodriven N_2R (and other reductions discussed herein) can be traced to $[ColH]^{+}$ being a reducible acid with a low propensity for parasitic homocoupling as the reduced radical ($ColH^{\bullet}$) as well as the presence of carbonyl substituents in the 3,5-positions of HEH_2, necessary for H-bonding with $[ColH]^{+}$ in the pre-association step.

An instructive comparison can be made between the excited state reactivity of $*HEH_2$ and a recently developed 12-aryl dihydrobenzoacridine photocatalyst (Figure 5.11A, acrH).[64] Enhanced reducing power is observed for the latter upon addition of an

exogenous base (e.g., MeTBD; MeTBD = 7-Methyl-1,5,7-triazabicyclodecene). A multisite-PCET (MS-PCET) oxidation[65] of the *[acrH] N–H bond, with substrate (e.g., aryl bromides) serving as oxidant, is proposed. Analogously, one can view *HEH_2 reactivity in the presence of Col-buffer as a MS-PCET oxidation of the C–H bond, with $[ColH]^+$ serving as the oxidant and Col as the base (Figure 5.11B, right). While the base is not strictly required to drive the overall transformation (*HEH_2 should readily reduce $[ColH]^+$), it is necessary to circumvent BET.

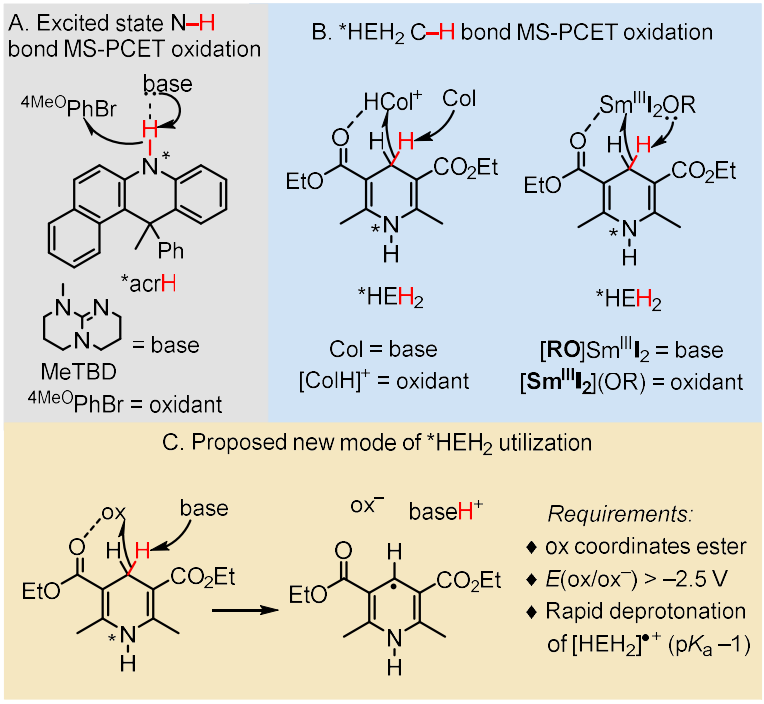

Figure 5.11. A framework for viewing the reactivity of *HEH_2 as the oxidation of the C–H bond relevant to Col-buffer interaction is described and extended to previous work exploring $Sm^{III/II}$ reductions.

In MS-PCET oxidations pre-association of the base with substrate via an acidic X–H bond is typically operative, with the substrate then being oxidized.[66] The carbonyl groups of HEH_2 allow pre-association of the oxidant instead of the base, resulting in oxidation of the less basic *HEH_2 C–H bond. Interestingly, as the C–H bond is oxidized we anticipate a large reorganization energy due to a change in hybridization (sp^3 to sp^2) and a poorer H-bonding interaction with the C-atom of the semi-oxidized species (HEH•).

This should mitigate the rate of back-PCET (in analogy to BET) compared with an O/N−H bond oxidation, resulting in more efficient reduction of $[ColH]^+$ to ColH•.

As an additional point of comparative context, it has been found that $*HEH_2$ can reduce Cr^{III} as well as Sm^{III}-alkoxides (see Chapter 6) to their corresponding divalent metal products and alcohol.[31,35] The photogenerated Sm^{II} and Cr^{II} products can be utilized in Sm-catalyzed cross-coupling and a catalytic-in-Cr Nozaki–Hiyama–Kishi reaction. Initial carbonyl coordination of the Lewis acidic metal ion may be operative in these systems, as observed with $[ColH]^+$ here (Figure 5.11B).

Taken together, these observations point to a new mode for direct reductions by $*HEH_2$ (Figure 5.11C). A Lewis acidic oxidant capable of both coordinating the ester carbonyl functionality and undergoing ET from $*HEH_2$ (E = −2.5 V) is key. Addition of a base helps to avoid BET. Utilizing these simple principles we anticipate the development of photoreductions of oxophilic, redox-active moieties by HEH_2, which in turn may catalyze desired reductive photochemistry.

5.4 Cited References

1. Warren, J. J.; Tronic, T. A.; Mayer, J. M. *Chem. Rev.* **2010**. 110, 6961–7001.
2. Weinberg, D. R.; Gagliardi, C. J.; Hull, J. F.; Murphy, C. F.; Kent, C. A.; Westlake, B. C.; Paul, A.; Ess, D. H.; McCafferty, D. G.; Meyer, T. J. *Chem. Rev.* **2012**. 112, 4016–4093.
3. Murray, P. R. D.; Cox, J. H.; Chiappini, N. D.; Roos, C. B.; McLoughlin, E. A.; Hejna, B. G.; Nguyen, S. T.; Ripberger, H. H.; Ganley, J. M.; Tsui, E.; Shin, N. Y.; Koronkiewicz, B.; Qiu, G.; Knowles, R. R. *Chem. Rev.* **2022**. 122, 2017–2291.
4. Tyburski, R.; Liu, T.; Glover, S. D.; Hammarström, L. *J. Am. Chem. Soc.* **2021**. 143, 560–576.
5. Chalkley, M. J.; Garrido-Barros, P.; Peters, J. C. *Science* **2020**. 369, 850–854.
6. Lennox, J. C.; Kurtz, D. A.; Huang, T.; Dempsey, J. L. *ACS Energy Lett.* **2017**. 2, 1246–1256.

7. Wenger, O. S. *Chem. – Eur. J.* **2011**. 17, 11692–11702.
8. Wenger, O. S. *Acc. Chem. Res.* **2013**. 46, 1517–1526.
9. Pannwitz, A.; Wenger, O. S. *Phys. Chem. Chem. Phys.* **2016**. 18, 11374–11382.
10. Barrett, S. M.; Pitman, C. L.; Walden, A. G.; Miller, A. J. M. *J. Am. Chem. Soc.* **2014**. 136, 14718–14721.
11. Park, Y.; Kim, S.; Tian, L.; Zhong, H.; Scholes, G. D.; Chirik, P. J. *Nat. Chem.* **2021**. 13, 969–976.
12. Kim, S.; Park, Y.; Kim, J.; Pabst, T. P.; Chirik, P. J. *Nat. Synth.* **2022**. **1**, 297–303.
13. Park, Y.; Tian, L.; Kim, S.; Pabst, T. P.; Kim, J.; Scholes, G. D.; Chirik, P. J. *JACS Au* **2022**. 2, 407–418.
14. Garrido-Barros, P.; Romero, C. G.; Winkler, J. R.; Peters, J. C. *J. Am. Chem. Soc.* **2024**. 146, 12750–12757.
15. Johansen, C. M.; Boyd, E. A.; Peters, J. C. *Sci. Adv.* **2022**. 8, eade3510.
16. Ashida, Y.; Onozuka, Y.; Arashiba, K.; Konomi, A.; Tanaka, H.; Kuriyama, S.; Yamazaki, Y.; Yoshizawa, K.; Nishibayashi, Y. *Nat. Commun.* **2022**. 13, 7263.
17. Arashiba, K.; Miyake, Y.; Nishibayashi, Y. *Nat. Chem.* **2011**. 3, 120–125.
18. Arashiba, K.; Eizawa, A.; Tanaka, H.; Nakajima, K.; Yoshizawa, K.; Nishibayashi, Y. *Bull. Chem. Soc. Jpn.* **2017**. 90, 1111-1118.
19. Ashida, Y.; Arashiba, K.; Nakajima, K.; Nishibayashi, Y. *Nature* **2019**. 568, 536–540.
20. Chalkley, M. J.; Drover, M. W.; Peters, J. C. *Chem. Rev.* **2020**. 120, 5582–5636.
21. Shen, G.-B.; Fu, Y.-H.; Zhu, X.-Q. *J. Org. Chem.* **2020**. 85, 12535–12543.
22. Konev, M. O.; Cardinale, L.; Jacobi von Wangelin, A. *Org. Lett.* **2020**. 22, 1316–1320.
23. Singh, S.; Sharma, V. K.; Gill, S.; Sahota, R. I. K. *J. Chem. Soc. Perkin 1,* **1985**. 0, 437–440 (1985).
24. Jung, J.; Kim, J.; Park, G.; You, Y.; Cho, E. J. *Adv. Synth. Catal.* **2016**. 358, 74–80.

25. Ohnishi, Y.; Kagami, M.; Ohno, A. *Chem. Lett.* **1975**. 4, 125–128.
26. Deng, G.; Xu, H.-J.; Chen, D.-W. *J. Chem. Soc., Perkin Trans. 2,* **1990**. 7, 1133–1137.
27. Wu, J.; Grant, P. S.; Li, X.; Noble, A.; Aggarwal, V. K. *Angew. Chem. Int. Ed.* **2019**. 58, 5697–5701.
28. Kammer, L. M.; Badir, S. O.; Hu, R.-M.; Molander, G. A. *Chem. Sci.* **2021**. 12, 5450–5457.
29. Li, J.; Siang Tan, S.; Kyne, S. H.; Wai Hong Chan, P. *Adv. Synth. Catal.* **2022**. 364, 802–810.
30. Suresh Yedase, G.; Venugopal, S.; P., A.; Reddy Yatham, V. *Asian J. Org. Chem.* **2022**. 11, e202200478.
31. Liu, Y.; Lin, S.; Zhang, D.; Song, B.; Jin, Y.; Hao, E.; Shi, L. *Org. Lett.* **2022**. 24, 3331–3336.
32. Bergamaschi, E.; Mayerhofer, V. J.; Teskey, C. J. *ACS Catal.* **2022**. 12, 14806–14811.
33. Ji, C.-L.; Han, J.; Li, T.; Zhao, C.-G.; Zhu, C.; Xie, J. *Nat. Catal.* **2022**. 5, 1098–1109.
34. Buzzetti, L.; Prieto, A.; Roy, S. R.; Melchiorre, P. *Angew. Chem. Int. Ed.* **2017**. 56, 15039–15043.
35. Johansen, C. M.; Boyd, E. A.; Tarnopol, D. E.; Peters, J. C. *J. Am. Chem. Soc.* **2024**. 146, 25456–25461.
36. Buzzetti, L.; Prieto, A.; Roy, S. R.; Melchiorre, P. *Angew. Chem. Int. Ed.* **2017**. 56, 15039–15043.
37. van Leeuwen, T.; Buzzetti, L.; Perego, L. A.; Melchiorre, P. A. *Angew. Chem. Int. Ed.* **2019**. 58, 4953–4957.
38. Wang, K.; Bao, X. *J. Am. Chem. Soc.* **2024**. 146, 7679–7689.
39. Coohill, T. P. *Photochem. Photobiol.* **1991**. 54, 859–870.

40. Eizawa, A.; Arashiba, K.; Tanaka, H.; Kuriyama, S.; Matsuo, Y.; Nakajima, K.; Yoshizawa, K.; Nishibayashi, Y. *Nat. Commun.* **2017**. 8, 14874.
41. Wortman, A. K.; Stephenson, C. R. J. . *Chem* **2023**. 9, 2390–2415.
42. Pitre, S. P.; Allred, T. K.; Overman, L. E. *Org. Lett.* **2021**. 23, 1103–1106.
43. Zega, A.; Srčič, S.; Mavri, J.; Bešter-Rogač, M. *J. Mol. Struct.* **2008**. 875, 354–363.
44. Tao, J.; Perdew, J. P.; Staroverov, V. N.; Scuseria, G. E. *Phys. Rev. Lett.* **2003**. 91, 146401–146404.
45. Weigend, F. *Phys. Chem. Chem. Phys.* **2006**. 8, 1057–1065.
46. Barone, V.; Cossi, M. *J. Phys. Chem. A* **1998**. 102, 1995–2001.
47. Lakowicz, J. R., *Principles of Fluorescence Spectroscopy*. **2006** Springer.
48. Czochralska, B.; Lindqvist, L. *Chem. Phys. Lett.* **1983**. 101, 297–299.
49. Anne, A.; Hapiot, P.; Moiroux, J.; Neta, P.; Saveant, J. M. *J. Am. Chem. Soc.* **1992**. 114, 4694–4701.
50. Zielonka, J.; Marcinek, A.; Adamus, J.; Gębicki, J. *J. Phys. Chem. A* **2003**. 107, 9860–9864.
51. Fukuzumi, S.; Koumitsu, S.; Hironaka, K.; Tanaka, T. *J. Am. Chem. Soc.* **1987**. 109**,** 305–316.
52. Munisamy, T.; Schrock, R. R. *Dalton Trans.* **2011**. 41, 130–137.
53. Cheng, T.; Shen, D. X.; Meng, M.; Mallick, S.; Cao, L.; Patmore, N. J.; Zhang, H. L.; Zou, S. F.; Chen, H. W.; Qin, Y.; Wu, Y. Y.; Liu, C. Y. *Nat. Commun.* **2019**. 10, 1531.
54. de Rege, P. J. F.; Williams, S. A.; Therien, M. J. *Science* **1995**. 269, 1409–1413.
55. Yan, T.; Yang, J.; Yan, K.; Wang, Z.; Li, B.; Wen, J. *Angew. Chem. Int. Ed.* **2024**. 63, e202405186.
56. Tshepelevitsh, S.; Kütt, A.; Lõkov, M.; Kaljurand, I.; Saame, J. ; Heering, A.; Plieger, P. G.; Vianello, R.; Leito, I. *Eur. J. Org. Chem.* **2019**. 2019, 6735–6748.
57. Zeldes, H.; Livingston, R. *J. Magn. Reson. (1969)* **1979**. 34, 543–552.

58. Dohrmann, J. K.; Becker, R. *J. Magn. Reson. (1969)* **1977**. 27, 371–384.
59. Cao, K.; Tan, S. M.; Lee, R.; Yang, S.; Jia, H.; Zhao, X.; Qiao, B.; Jiang, Z. *J. Am. Chem. Soc.* **2019**. 141, 5437–5443.
60. Golubev, N. S.; Smirnov, S. N.; Schah-Mohammedi, P.; Shenderovich, I. G.; Denisov, G. S.; Gindin, V. A.; Limbach, H. H. *Russ. J. Gen. Chem.* **1997**. 67, 1082–1087.
61. Boyd, E. A.; Peters, J. C. *J. Am. Chem. Soc.* **2022**. 144, 21337–21346.
62. Zhang, J.; Mück-Lichtenfeld, C.; Studer, A. *Nature* **2023**. 619, 506–513.
63. Zhao, G.-J.; Han, K.-L. *Acc. Chem. Res.* **2012.** 45, 404–413.
64. Bortolato, T.; Simionato, G.; Vayer, M.; Rosso, C.; Paoloni, L.; Benetti, E. M.; Sartorel, A.; Lebœuf, D.; Dell'Amico, L. *J. Am. Chem. Soc.* **2023**. 145, 1835–1846.
65. Darcy, J. W.; Koronkiewicz, B.; Parada, G. A.; Mayer, J. M. *Acc. Chem. Res.* **2018**. 51, 2391–2399.
66. Morton, C. M.; Zhu, Q.; Ripberger, H.; Troian-Gautier, L.; Toa, Z. S. D.; Knowles, R. R.; Alexanian, E. J. *J. Am. Chem. Soc.* **2019**. 141, 13253–13260.

Chapter 6

Photodriven Sm(III)-to-Sm(II) Reduction for Catalytic Applications

Adapted from:

Johansen, C. M.†; Boyd, E. A.†; Tarnopol, D. E.; Peters, J. C. *J. Am. Chem. Soc.* **2024**. 146, 25456–25461. DOI: 1010.1021/jacs.4c10053.

† These authors contributed equally to this work.

6.1 Introduction

Samarium diiodide (SmI_2) is an exceptionally versatile single-electron reductant. The large and labile coordination sphere of Sm^{II} can recruit one or multiple substrates and additives to achieve selectivity in both organic synthesis and small-molecule reductions (Figure 6.1A).[1,2,3,4] However, SmI_2 is employed stoichiometrically in all but a few select cases[5,6,7,8] because its reactions typically terminate in the formation of highly stable Sm^{III}–alkoxide species. Catalytic regeneration of the Sm^{II} state requires abstraction of OR^- by a stoichiometric oxophile (EX) to generate a Sm^{III} species that can be reduced by a relatively mild reductant (Figure 1A). The difficulty associated with this transformation has been cited as a motivation for the development of a variety of alternative photo- and electrochemically driven methods for ketyl radical generation.[9,10,11,12,13]

Early strategies for reductive Sm catalysis relied on harsh combinations of halosilane oxophiles (R_3SiX) and low valent metals (Mg^0 for X = Cl; Zn^0 for X = I) or an applied electrochemical potential as the reductant.[14,15,16,17,18,19,20,21,22] In a collaborative effort with the Reisman laboratory, we recently disclosed comparatively mild silane-free thermal and electrochemical conditions for catalytic turnover of SmI_2 in reductive coupling of ketones and acrylates through combination of cationic Brønsted acids with either Zn^0 or an applied potential of −1.55 V vs $Fc^{+/0}$ ($Fc^{+/0}$ = ferrocenium/ferrocene; all potentials referenced to $Fc^{+/0}$).[23]

Given the growing interest in (metalla)photoredox catalysis,[24] photodriven strategies for $Ln^{III/II}$ catalysis remain surprisingly underexplored.[25,26] In a strategy recently showcased by the groups of Borbas[27] and Nemoto,[28] photosensitizers are incorporated into the secondary coordination spheres of Ln^{III} complexes (Ln = Sm, Eu; Figure 6.1B). Intramolecular oxidative quenching of the excited sensitizer by the Ln^{III} center produces a potent Ln^{II} reductant which can carry out a variety of transformations.

While this and other strategies show promise,[25,26,27,28] the chelating ligand platforms used thus far in photodriven $Ln^{III/II}$ catalysis (cryptands, bidentate phosphine oxides) restrict the coordination sphere and/or shift $E°(Ln^{III/II})$ to strongly negative potentials, belying direct

translation to the rich stoichiometric chemistry of $SmI_2(L)_n$ as an inner sphere reductant (L = solvent molecule, typically THF).

Lewis acidic metal ions are commonly used to template substrates in photodriven reductive coupling reactions.[10,29,30] Recently, in contrast to the use of photocatalysts, several Lewis acid-mediated photoreductions utilize the blue-light absorbing Hantzsch ester (HEH_2) as a photoreductant ($E(HEH_2^{+\bullet}/{}^*HEH_2) = -2.5$ V).[31,32,33,34] Photoexcited HEH_2 ($^*HEH_2$) carries out Cr^{III} reduction in a catalytic-in-Cr photodriven Nozaki–Hiyama–Kishi reaction (Figure 6.1C).[35] Alternatively, HEH_2 acts as a photoreductant in a $Gd(OTf)_3$-mediated Giese addition of an *N*-hydroxyphthalimide (NHPI) ester-derived alkyl radical into α,β-unsaturated ketones or lactone (Figure 6.1C).[36] In the latter study, an interaction between Gd and HEH_2 is observed, but Gd^{III} reduction to Gd^{II} is not accessible even by $^*HEH_2$.[23]

Based on these precedents we noted that $^*HEH_2$ should be capable of reducing Sm^{III}-species such as SmI_3 ($E°(SmI_3/(SmI_2 + I^-)) = -1.58$ V; Figure E.35). Because Sm and Gd are similar in size and oxophilicity, we envisioned that photoexcitation of HEH_2 bound to Sm^{III} could also result in intramolecular oxidative quenching to produce Sm^{II} (Figure 6.1D). Crucially, however, a more dynamic Sm-chromophore interaction might allow access to coordinatively unsaturated $SmI_2(L)_n$ species which could carry out inner-sphere reduction in a photodriven Sm-catalyzed cross-coupling reaction. Importantly, both HEH_2 and its $2H^+/2e^-$ oxidized congener, HE, are weak bases and are therefore compatible with the acidic conditions necessary for recovery of inactive Sm^{III}–OR species by protonolysis.

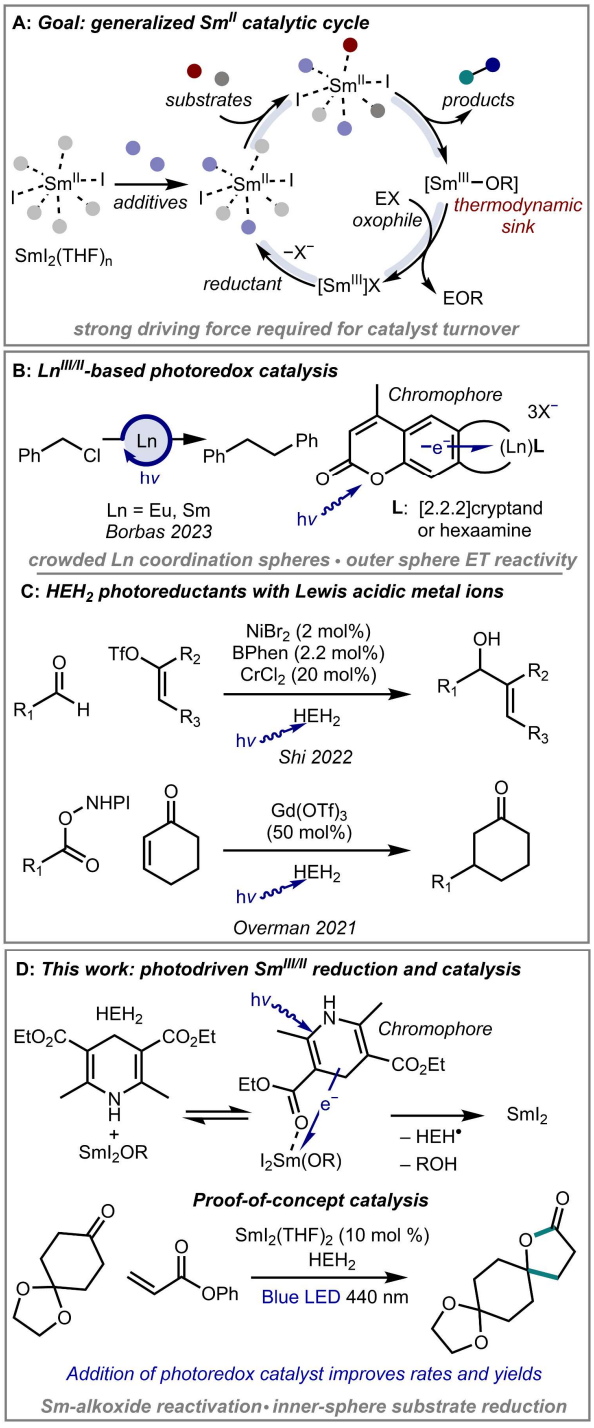

Figure 6.1. Summary of key challenges for Sm-turnover;[23] prior studies exploiting $Ln^{III/II}$ photochemistry and photoreductions with HEH_2 and Lewis acidic metals;[27,35,36] and this work describing photodriven generation of SmI_2.

6.2 Results

Gratifyingly, HEH_2 proved competent as a photoreductant for Sm^{III}-to-Sm^{II} conversion. Monitoring the UV-visible absorption spectrum of a solution of SmI_3 (2 mM), HEH_2 (60 mM) and 2,6-lutidine base (Lut, 60 mM) following irradiation at 440 nm for 5 min in THF reveals the characteristic profile of blue $SmI_2(THF)_n$ with λ_{max} at 555 and 618 nm (Figure 6.2A, left panel). Extended irradiation (120 minutes) results in increasing SmI_2 generation, with maximum yield ~25%. Interestingly, in the absence of base this reaction does not proceed (Figure E.17), likely due to rapid back-electron transfer (BET) between $HEH_2^{\bullet+}$ and SmI_2. However, $HEH_2^{\bullet+}$ can be deprotonated in the presence of base, circumventing BET.

We next evaluated conditions for photogeneration of $SmI_2(THF)_n$ from $Sm(O^iPr)_3$ as a model Sm^{III}-alkoxide. Irradiation of $Sm(O^iPr)_3$ (2 mM), tetra-*n*-heptylammonium iodide (^{n}Hep$_4$NI, 6 mM), and HEH_2 (60 mM) at 440 nm in THF shows no evidence of SmI_2 formation (Figure E.19). However, upon the addition of only 1.5 equiv of the acid *bis*-trifluoromethylsulfonylimide (HTFSI) to $Sm(O^iPr)_3$, $SmI_2(THF)_n$ is generated upon irradiation with ^{n}Hep$_4$NI and HEH_2 (Figure 6.2A, right panel). Parallel CV studies demonstrate that no SmI_3 is generated from $Sm(O^iPr)_3$ at this acid loading (Figure 6.2B, compare light and dark blue traces), and current attributable to Sm^{III} reduction (presumably of an intermediate mixture of solvated "$SmI(O^iPr)_2$" and "SmI_2O^iPr") does not onset until −2.3 V. In contrast to SmI_3, no external base is needed, suggesting that the Sm-bound alkoxide might additionally serve the role of deprotonating $HEH_2^{\bullet+}$ to avoid BET. UV-vis studies reveal that addition of the colorless Sm^{III}–O^iPr species (grey trace in Figure 6.2A) gives rise to a significantly red-shifted shoulder in the HEH_2 absorption profile (compare light and dark red traces in Figure 6.2A), consistent with pre-association.

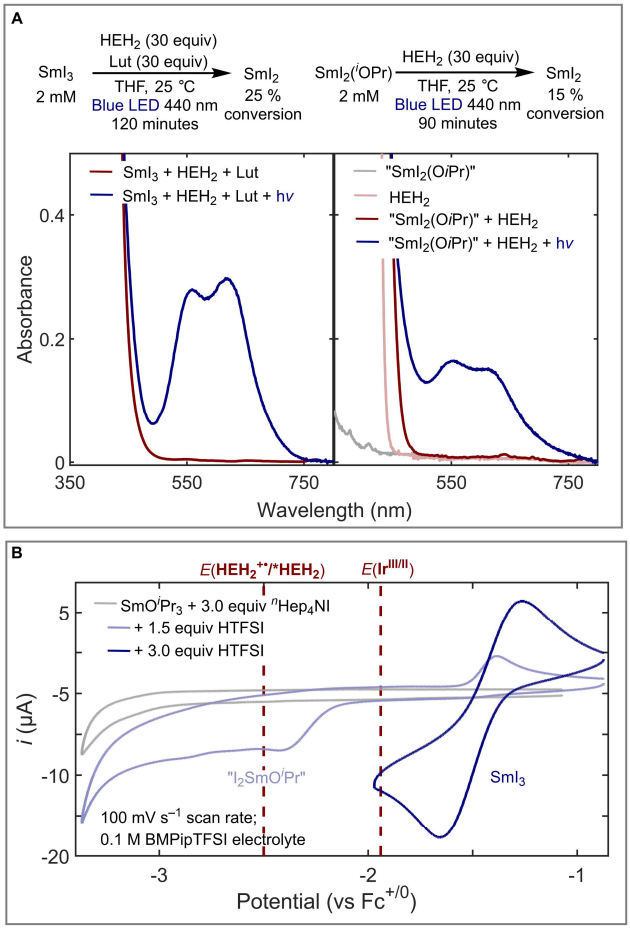

Figure 6.2. Photogeneration of SmI_2. (A) UV-vis spectra following photoreduction of SmI_3 (left) and $L_nSm(^iOPr)I_2$ to form SmI_2. CVs of $Sm(O^iPr)_3$ (2 mM) in the presence of iodide and proton sources in THF.

The modest yields and rates of these reactions motivated the study of Sm^{III} reduction with a photoredox catalyst to overcome the low quantum yield and excited state lifetime (220 ps in MeCN)[37] of HEH_2. We selected $[Ir(dtbbpy)(ppy)_2]^+$ ($[\mathbf{Ir^{III}}]^+$)[38] as a photosensitizer, which could undergo reductive quenching by a sacrificial electron donor to generate $\mathbf{Ir^{II}}$. $\mathbf{Ir^{II}}$ is thermodynamically capable of reducing SmI_3 to SmI_2 ($E°(\mathbf{Ir^{III/II}}) = -1.94$ V, Figure 6.2B and Figure E.36).

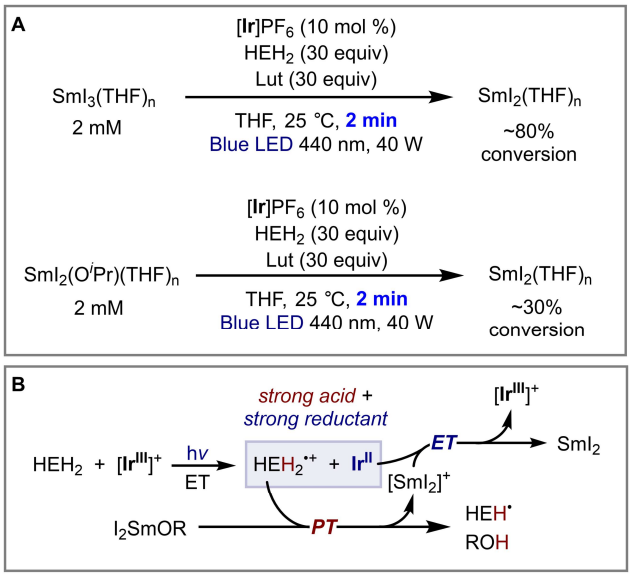

Figure 6.3. Photogeneration of SmI_2 with Ir photocatalyst. (A) Photoreductions of Sm^{III} species with $[Ir]PF_6$ photocatalyst. (B) Rationale for net photoinduced proton- and electron-transfer from HEH_2 to $[Sm^{III}–OR]$ species.

Irradiating SmI_3 or SmI_2O^iPr (2 mM) with $[\mathbf{Ir^{III}}]PF_6$ (0.2 mM), HEH_2 (60 mM) as sacrificial reductant, and Lut (60 mM) rapidly generates SmI_2 (80% or 30% conversion in 2 min, Figure 6.3A). Again, the weak base Lut enhances the process (Figures E.20-E.21).

The accelerated reduction of SmI_2O^iPr is curious, as electron transfer from $\mathbf{Ir^{II}}$ to this Sm^{III} species is uphill by 400 mV (Figure 6.2B). A rationale for these observations is provided in Figure 6.3B: reductive quenching of $*[\mathbf{Ir^{III}}]^+$ by HEH_2 generates not only the strong reductant $\mathbf{Ir^{II}}$, but also the strong acid $HEH_2^{\bullet+}$ (pK_a −1 in MeCN),[39,40] the combination of which can carry out net proton-coupled electron transfer to $Sm^{III}–O^iPr$.[41] Proton transfer from $HEH_2^{\bullet+}$ to a $Sm^{III}–O^iPr$ species, likely via proton relay mediated by Lut, liberates ^{i}PrOH and $[SmI_2]^+$.[42] The latter can then be reduced to SmI_2 by $\mathbf{Ir^{II}}$.

Development of Sm-catalysis leveraging diverse ligand coordination to modulate reactivity is an attractive goal. Exploration of Sm^{II} generation in the presence of potential coligands was carried out pursuant to these interests.

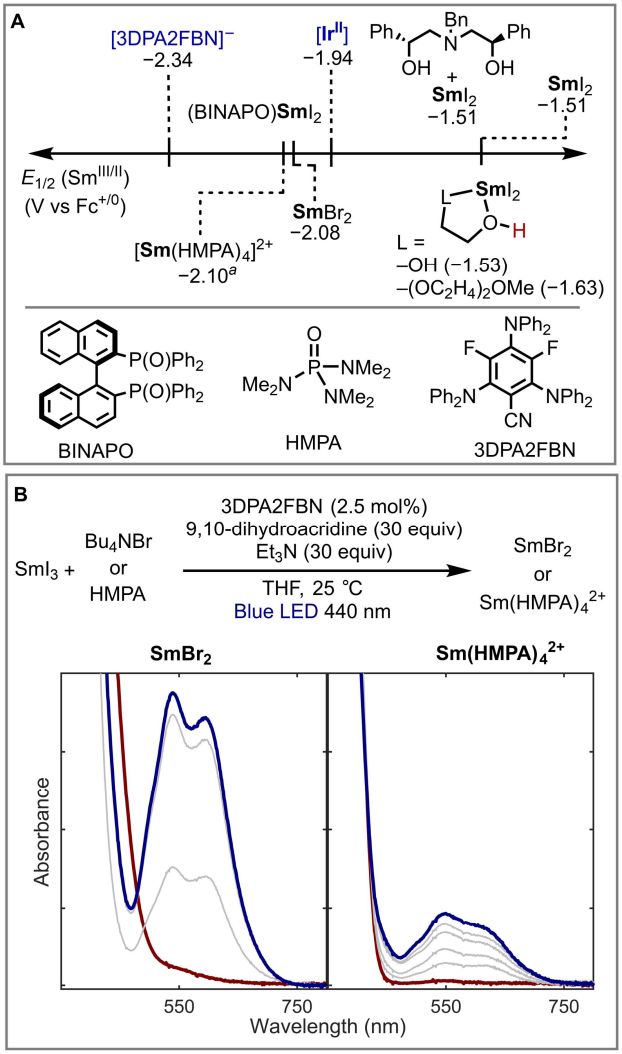

Figure 6.4. Photogeneration of Sm^{II} with alternate ligands. (A) Ligand coordinated Sm-species generated by a photoredox approach. See Appendix E for relevant electrochemical data. Choice of a sufficiently reducing photocatalyst remains crucial to observe Sm^{II}. (B) UV-vis spectra following photogeneration of $SmBr_2$ and $Sm(HMPA)_4^{2+}$.

Satisfyingly, Sm^{II} is readily photogenerated from SmI_3 by $[\mathbf{Ir^{III}}]^+$ and quencher (HEH_2 or Et_3N) in the presence of several protic additives (ethylene glycol, *N,N*-dimethylaminoethanol, Figures E.23-E.24),[3,43,44,45] including a chiral aminediol (Figure 6.4A, Figure E.25) that has been utilized in several enantioselective SmI_2 transformations.[46,47,48]

The reduction potential and reactivity of Sm^{II} is highly sensitive to coordination of Lewis-basic additives (HMPA, Br^-; Figure 6.4A).[49] While [$\mathbf{Ir^{II}}$] is insufficiently reducing to access such species, the more reducing photocatalyst 3DPA2FBN, [50] when paired with the more reducing quencher 9,10-dihydroacridine and Et_3N as base, mediates generation of both $SmBr_2$ and $Sm(HMPA)_4^{2+}$ (Figure 6.4B). 3DPA2FBN also facilitates Sm^{III} reduction and binding to the chiral BINAPO ligand (Figures 6.4A and E.34).[51,52]

Having established two different photochemical approaches to Sm^{II} generation, we targeted an intermolecular ketone-acrylate coupling as a model reaction to benchmark photodriven Sm-catalysis (Table 6.1). This reaction is representative of the qualities that set SmI_2 apart as a stoichiometric reductant. Inner sphere electron transfer to one or both of the carbonyl substrates is obligatory based on comparison of outer-sphere reduction potentials.[23] Importantly, a Sm-alkoxide is generated as the byproduct of lactonization, enabling evaluation of the ability of a set of conditions to overcome this critical barrier to generalizable Sm catalysis.

Irradiation of ketone **1** (0.04 mmol), phenyl acrylate (2 equiv), and $SmI_2(THF)_2$ (10 mol %) in the presence of HEH_2 (4.0 equiv) in 2-MeTHF (0.02 M) at 440 nm for 90 min yields lactone **2** in 76% yield (Table 6.1, entry 1, method A). Addition of a photoredox catalyst ([**Ir**]PF_6, 1 mol%) with pyridine (2 equiv) results in an increase in yield to 89% (Entry 1, method B). Light and Sm were required for catalytic formation of **2** by either method (entries 3 and 4). $Sm(OTf)_3$ is a competent precatalyst with 50 mol% MgI_2 included as an iodide source (entry 4). Substitution of $Gd(OTf)_3$ for $Sm(OTf)_3$ results in trace product formation, supporting a key role for Sm^{II} in catalysis (entry 5).

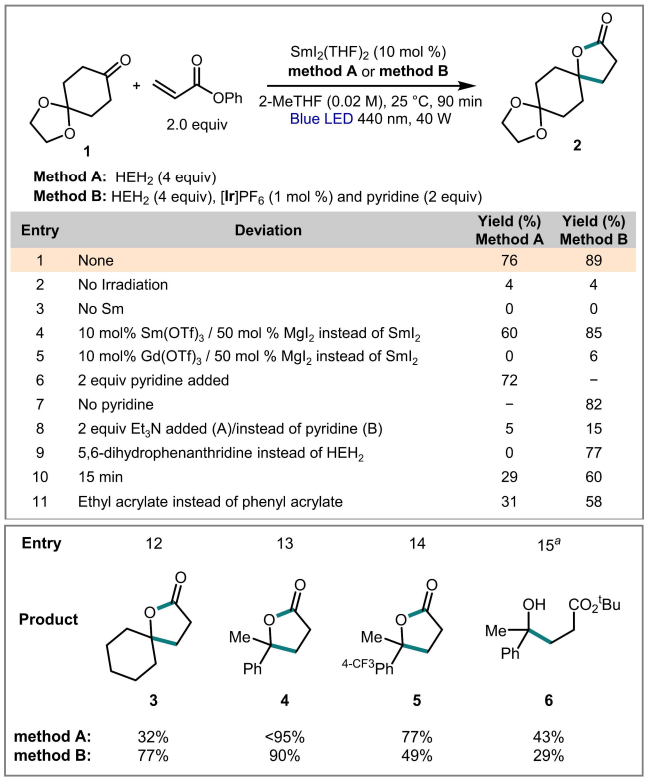

Entry	Deviation	Yield (%) Method A	Yield (%) Method B
1	None	76	89
2	No Irradiation	4	4
3	No Sm	0	0
4	10 mol% $Sm(OTf)_3$ / 50 mol % MgI_2 instead of SmI_2	60	85
5	10 mol% $Gd(OTf)_3$ / 50 mol % MgI_2 instead of SmI_2	0	6
6	2 equiv pyridine added	72	–
7	No pyridine	–	82
8	2 equiv Et_3N added (A)/instead of pyridine (B)	5	15
9	5,6-dihydrophenanthridine instead of HEH_2	0	77
10	15 min	29	60
11	Ethyl acrylate instead of phenyl acrylate	31	58

	12	13	14	15[a]
method A:	32%	<95%	77%	43%
method B:	77%	90%	49%	29%

Table 6.1. Photodriven Sm-catalyzed coupling of ketones and phenyl acrylate to form lactone products. Yields were determined by ^{1}H NMR analysis. For additional reaction data, see Table E.2. [a]*tert*-butyl acrylate used as coupling partner; lactonization observed only upon acidic workup.

Both methods are competent in the presence/absence of pyridine (entries 1, 6, and 7), but yields are greatly diminished in the presence of a stronger base (Et_3N, entry 8). This suggests that the dynamics of Sm-alkoxide protonation play an important role in turnover.[23] Interestingly, the use of a dihydropyridine without carbonyl groups, 5,6-dihydrophenanthridine, only shows product formation with [**Ir**]$^+$ (entry 9). In the absence of Ir, the specific interaction between Sm and HEH_2 appears to be required. The Ir-catalyzed reaction is also faster, achieving 60% conversion in 15 minutes, compared to 29% by method A (entry 10).

Methods A and B were tested against alternative coupling partners to assess their relative efficacies. When using less activated substrate pairs (aliphatic ketones and alkyl acrylates, entries 1, 11 and 12), method B is favored, perhaps because these slower cross-couplings require rapid Sm^{III}-to-Sm^{II} conversion. Method A is preferred when using aryl

ketones (entries 13-15), as method B gives considerable pinacol-coupled side-products (Table E.3). With method A, selective inner-sphere photogeneration of Sm^{II} by Sm^{III}–HEH_2 may favor Sm^{II}-mediated cross-coupling, while with method B background Ir-mediated substrate reduction to homocoupled products can dominate.

A proposed mechanism for this photodriven lactonization reaction (by method A) is presented in Figure 6.5. The mechanism can be divided into two parts, a photoreduction side in which Sm^{III} is reduced to Sm^{II}, and a SmI_2 cross-coupling side where the organic substrates are coupled. Starting from $SmI_2(OPh)$, coordination to HEH_2 (as demonstrated in Figure 6.2A) followed by excitation to $*HEH_2$ allows for the proton and electron transfer required to generate SmI_2, with PhOH and $HEH^{\bullet}$ as additional products. Subsequently, SmI_2 couples the acrylate and ketone to form a radical intermediate.[53,54] $HEH^{\bullet}$ is capable of reducing this intermediate as a potent H-atom donor, although alternative schemes for reduction of the radical intermediate can be envisioned (Figure E.45). Following reduction and lactonization, **2** is formed along with $SmI_2(OPh)$.

With $[\mathbf{Ir}]^+$, a similar mechanism is proposed, differing in the regeneration of Sm^{II}, which can be regenerated from Sm^{III}-alkoxide as depicted in Figure 6.3B (see Figure E.46 for full scheme).

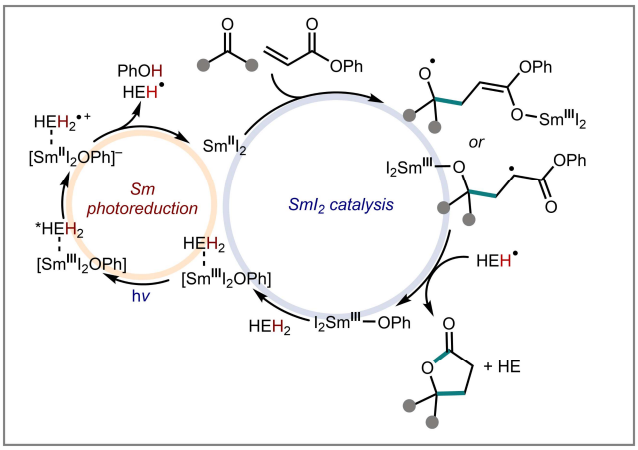

Figure 6.5. Proposed mechanism of Sm cross-coupling under Ir-free conditions (method A).

6.3 Conclusions

In summary, we have demonstrated photodriven generation of $SmI_2(THF)_2$ from Sm^{III} precursors using both a photoreductant and a photoredox catalyst. These conditions translate to proof-of-concept photodriven reductive Sm-catalyzed ketone-acrylate coupling. Distinct from reported methods, photodriven Sm-catalysis occurs in the absence of competing Lewis-acidic metal additives and byproducts (e.g., Mg^{2+} and Zn^{2+} salts),[14,15,16,17,18,19,20,21,22,23] which may be of utility in development of Sm-catalysis with ligands.[3,18,43,46,47,48,49,50,51] These findings are anticipated to facilitate applications of Sm-catalysis beyond the types of thermally driven transformations studied thus far.

6.4 Cited references

1. Girard, P.; Namy, J. L.; Kagan, H. B. *J. Am. Chem. Soc.* **1980**. 102, 2693–2698.
2. Szostak, M.; Fazakerley, N. J.; Parmar, D.; Procter, D. J. *Chem. Rev.* **2014**. 114, 5959–6039.
3. Ashida, Y.; Arashiba, K.; Nakajima, K.; Nishibayashi, Y. *Nature* **2019**. 568, 536–540.
4. Lee, C. C.; Hu, Y.; Ribbe, M. W. *Angew. Chem. Int. Ed.* **2015**. 54, 1219–1222.
5. Net redox-neutral SmI_2-catalyzed radical relay processes have been explored; see the following and refs 5-8: Huang, H.-M.; McDouall, J. J. W.; Procter, D. J. *Nat. Catal.* **2019**. 2, 211–218.
6. Agasti, S.; Beattie, N. A.; McDouall, J. J. W.; Procter, D. J. *J. Am. Chem. Soc.* **2021**. 143, 3655–3661.
7. Agasti, S.; Beltran, F.; Pye, E.; Kaltsoyannis, N.; Crisenza, G. E. M.; Procter, D. J. A *Nat. Chem.* **2023**. 15, 535–541.
8. Mansell, J. I.; Yu, S.; Li, M.; Pye, E.; Yin, C.; Beltran, F.; Rossi-Ashton, J. A.; Romano, C.; Kaltsoyannis, N.; Procter, D. J. *J. Am. Chem. Soc.* **2024**. 146, 12799–12807.

9. Edgecomb, J. M.; Alektiar, S. N.; Cowper, N. G. W.; Sowin, J. A.; Wickens, Z. K. *J. Am. Chem. Soc.* **2023**. 145, 20169–20175.
10. Lee, K. N.; Lei, Z.; Ngai, M.-Y. *J. Am. Chem. Soc.* **2017**. 139, 5003–5006.
11. Derosa, J.; Garrido-Barros, P.; Peters, J. C. *Inorg. Chem.* **2022**. 61, 6672–6678.
12. Tarantino, K. T.; Liu, P.; Knowles, R. R. *J. Am. Chem. Soc.* **2013**. 135, 10022–10025.
13. Seo, H.; Jamison, T. F. *Org. Lett.* **2019**. 21, 10159–10163.
14. Corey, E. J.; Zheng, G. Z. *Tetrahedron Lett.* **1997**. 38, 2045–2048.
15. Nomura, R.; Matsuno, T.; Endo, T. *J. Am. Chem. Soc.* **1996**. 118, 11666–11667.
16. Aspinall, H. C.; Greeves, N.; Valla, C. *Org. Lett.* **2005**. 7, 1919–1922.
17. Sun, L.; Sahloul, K.; Mellah, M. *ACS Catal.* **2013**. 3, 2568–2573.
18. Maity, S.; Flowers, R. A. *J. Am. Chem. Soc.* **2019**. 141, 3207–3216.
19. Hébri, H.; Duñach, E.; Heintz, M.; Troupel, M.; Périchon, J. *Synlett* **1991**. 1991, 901–902.
20. Hebri, H.; Duñach, E.; Périchon, J. *J. Chem. Soc., Chem. Commun.* **1993**. 6, 499–500.
21. Hebri, H.; Duñach, E.; Périchon, J. *Synth. Commun.* **1991**. 21, 2377–2382.
22. Espanet, B.; Duñach, E.; Périchon, J. *Tetrahedron Lett.* **1992**. 33, 2485–2488.
23. Boyd, E. A.; Shin, C.; Charboneau, D. J.; Peters, J. C.; Reisman, S. E. *Science* **2024**. 385, 837-843.
24. Chan, A. Y.; Perry, I. B.; Bissonnette, N. B.; Buksh, B. F.; Edwards, G. A.; Frye, L. I.; Garry, O. L.; Lavagnino, M. N.; Li, B. X.; Liang, Y.; Mao, E.; Millet, A.; Oakley, J. V.; Reed, N. L.; Sakai, H. A.; Seath, C. P.; MacMillan, D. W. C. *Chem. Rev.* **2022**. 122, 1485–1542.
25. Meyer, A. U.; Slanina, T.; Heckel, A.; König, B. *Chem. Eur. J.* **2017**. 23, 7900–7904.

26. Jenks, T. C.; Bailey, M. D.; Hovey, J. L.; Fernando, S.; Basnayake, G.; Cross, M. E.; Li, W.; Allen, M. J. *Chem. Sci.* **2018**. 9, 1273–1278.
27. Tomar, M.; Bhimpuria, R.; Kocsi, D.; Thapper, A.; Borbas, K. E. *J. Am. Chem. Soc.* **2023**. 145, 22555–22562.
28. Kuribara, T.; Kaneki, A.; Matsuda, Y.; Nemoto, T. *J. Am. Chem. Soc.* **2024**. 146, 20904-20912.
29. Yoon, T. P. *Acc. Chem. Res.* **2016**. 49, 2307–2315.
30. Huang, X.; Luo, S.; Burghaus, O.; Webster, R. D.; Harms, K.; Meggers, E. *Chem. Sci.* **2017**. 8, 7126–7131.
31. Jung, J.; Kim, J.; Park, G.; You, Y.; Cho, E. J. *Adv. Synth. Catal.* **2016**. 358, 74–80.
32. Ohnishi, Y.; Kagami, M.; Ohno, A. *Chem. Lett.* **1975**. 4, 125–128.
33. Johansen, C. M.; Boyd, E. A.; Peters, J. C. *Science Advances* **2022**. 8, eade3510.
34. Ji, C.-L.; Han, J.; Li, T.; Zhao, C.-G.; Zhu, C.; Xie, J. *Nat. Catal.* **2022**. 5, 1098–1109.
35. Liu, Y.; Lin, S.; Zhang, D.; Song, B.; Jin, Y.; Hao, E.; Shi, L. *Org. Lett.* **2022**. 24, 3331–3336.
36. Pitre, S. P.; Allred, T. K.; Overman, L. E. *Org. Lett.* **2021**. 23, 1103–1106.
37. Deng, G.; Xu, H.-J.; Chen, D.-W. *J. Chem. Soc., Perkin Trans. 2* **1990**. 7, 1133–1137.
38. Slinker, J. D.; Gorodetsky, A. A.; Lowry, M. S.; Wang, J.; Parker, S.; Rohl, R.; Bernhard, S.; Malliaras, G. G. *J. Am. Chem. Soc.* **2004**. 126, 2763–2767.
39. Shen, G.-B.; Fu, Y.-H.; Zhu, X.-Q. *J. Org. Chem.* **2020**. 85, 12535–12543.
40. Schmittel, M.; Burghart, A. *Angew. Chem. Int. Ed.* **1997**. 36, 2550–2589.
41. Boyd, E. A.; Peters, J. C. *J. Am. Chem. Soc.* **2022**. 144, 21337–21346.
42. Analogous net proton-coupled electron transfer to Ti(IV)-alkoxide species to generate Ti(III) has been proposed in photodriven Ti redox catalysis: Gualandi, A.;

Calogero, F.; Mazzarini, M.; Guazzi, S.; Fermi, A.; Bergamini, G.; Cozzi, P. G. *ACS Catal.* **2020**. 10, 3857–3863.

43. Chciuk, T. V.; Flowers, R. A. *J. Am. Chem. Soc*. **2015**. 137, 11526–11531.
44. Kolmar, S. S.; Mayer, J. M. *J. Am. Chem. Soc.* **2017**. 139, 10687–10692.
45. Boekell, N. G.; Bartulovich, C. O.; Maity, S.; Flowers, R. A. I. *Inorg. Chem.* **2023**. 62, 5040–5045.
46. Kern, N.; Plesniak, M. P.; McDouall, J. J. W.; Procter, D. J. *Nature Chem.* **2017**. 9, 1198–1204.
47. Evans, D. A.; Nelson, S. G.; Gagne, M. R.; Muci, A. R. *J. Am. Chem. Soc.* **1993**. 115, 9800–9801.
48. Wang, Y.; Zhang, W.-Y.; Yu, Z.-L.; Zheng, C.; You, S.-L. *Nat. Synth* **2022**. 1, 401–406.
49. Miller, R. S.; Sealy, J. M.; Shabangi, M.; Kuhlman, M. L.; Fuchs, J. R.; Flowers, R. A. *J. Am. Chem. Soc.* **2000**. 122, 7718–7722.
50. Speckmeier, E.; Fischer, T. G.; Zeitler, K. *J. Am. Chem. Soc.* **2018**. 140, 15353–15365.
51. Mikami, K.; Yamaoka, M. *Tetrahedron Lett.* **1998**. 39, 4501–4504.
52. CV experiments suggest that speciation of 1:1 SmI_3:BINAPO is a complex mixture with $Sm^{III/II}$ redox waves negative of −2 V (Figure E.43).
53. Substrate coupling could be initiated either by ketone or acrylate reduction, leading to either an α-ester radical or an alkoxy radical intermediate, respectively, following addition to the corresponding coupling partner. In the case of difficult-to-reduce ketone substrates such as **1**, neither pathway can be reliably ruled out. See the following and ref 54 for detailed examination of this mechanistic question: Hansen, A. M.; Lindsay, K. B.; Sudhadevi Antharjanam, P. K.; Karaffa, J.; Daasbjerg, K.; Flowers, R. A.; Skrydstrup, T. *J. Am. Chem. Soc.* **2006**. 128, 9616–9617.
54. Sono, M.; Hanamura, S.; Furumaki, M.; Murai, H.; Tori, M. *Org. Lett.* **2011**. 13, 5720–5723.

A p p e n d i x A

Supplementary Information for Chapter 2

A.1. Experimental section

A.1.1 General Considerations

All manipulations were carried out using standard Schlenk or glovebox techniques under an N_2 atmosphere. Solvents were deoxygenated and dried by thoroughly sparging with N_2, followed by passage through an activated alumina column in a solvent purification system by SG Water, USA LLC. Nonhalogenated solvents were tested with sodium benzophenone ketyl in tetrahydrofuran (THF) to confirm the absence of oxygen and water. Deuterated solvents were purchased from Cambridge Isotope Laboratories, Inc., degassed, and dried over activated 3-Å molecular sieves prior to use. [FeCN],[1] [$FeCNMe_2$],[1] [$P_3{}^{B}Fe$]$BAr^{F}{}_4$,[2] $^{Ph}B(^{iPr2}P)_3FeBr$,[3] [Ph_2NH_2]OTf,[4] KC_8,[1] [$H(OEt_2)_2$]$BAr^{F}{}_4$,[5] [TBA][^{13}CN][6] were synthesized using literature methods. $(C_6H_6)_2Cr$, Cp^*_2Cr and Cp_2Co were purchased from Strem and used without further purification.

A.1.2 Physical Methods

NMR: Nuclear Magnetic Resonance (NMR) measurements were recorded with a Varian 400 MHz spectrometer. ^1H NMR chemical shifts are reported in ppm relative to tetramethylsilane, using ^1H resonances from residual solvent as internal standards.[7]

UV-Vis: Ultraviolet-visible (UV-vis) absorption spectroscopy measurements were collected with a Cary 50 UV-vis spectrophotometer using a 1 cm path length quartz cuvette. All samples had a blank sample background subtraction applied. Temperature regulation for UV-Vis measurements was carried out with a Unisoku cryostat. Time course UV-Vis spectra were collected with the Scanning Kinetics application of the Cary WinUV software.

Mössbauer spectra: ^{57}Fe Mössbauer spectroscopy measurements were recorded on a spectrometer from SEE Co. (Edina, MN) operating in the constant acceleration mode in a transmission geometry. The sample was kept in an SVT-400 cryostat from Janis (Wilmington, MA). The quoted isomer shifts are relative to the centroid of the spectrum of a metallic foil of α-Fe at room temperature (RT). Solution samples were transferred to a sample cup, freeze-quenched with liquid nitrogen inside the glovebox,

and then immersed in liquid N_2 until mounted in the cryostat. Data analysis was performed using version 4 of the program WMOSS (wmoss.org), and quadrupole doublets fit Lorentzian lineshapes.

A.2 Ammonia production and quantification studies

A.2.1 Standard NH_3 Generation Reaction Procedure

All solvents are stirred with Na/K for ≥2 hours and filtered prior to use. In a nitrogen-filled glovebox, the precatalysts ([FeCN] or other Fe-complexes) are weighed in individual vials.* The precatalysts are then transferred quantitatively into a Schlenk tube using benzene. The benzene is then lyophilized to provide a fluffy powder of precatalyst at the bottom of the Schlenk tube. The tube is then charged with a stir bar, and the acid ($[Ph_2NH_2]OTf$), reductant (e.g., $(C_6H_6)_2Cr$)) and [TBA][CN], all added as solids. The tube is sealed and cooled to 77 K in a cold well. To the cold tube 1 mL Et_2O solvent is added to produce the desired precatalyst concentration. For reactions run above -20 °C additional Et_2O was added taking into account the headspace of the tube and the vapor pressure of Et_2O such that the reaction volume remained 1 mL. The temperature of the system is allowed to equilibrate for 5 minutes and then the tube is sealed with a Teflon screw-valve. This tube is passed out of the box into a liquid N_2 bath and transported to a fume hood. For experiments run at -78 °C, the tube is then transferred to a dry ice/isopropanol bath, where it thaws and is allowed to stir for a minimum of three hours before warming. For experiments run at -20 °C, the tube is instead transferred to a 3:1 ice:NaCl bath, where it thaws and is allowed to stir for a minimum of one hour before warming. For experiments run at 0 °C, the tube is transferred to an ice bath where it thaws and is allowed to stir for a minimum of three hours before warming. For experiments run at 25 °C, the tube is transferred to a water bath where it thaws and is allowed to stir for a minimum of 80 minutes. To ensure reproducibility, all experiments were conducted using 10 mm egg-shaped stir bars, and stirring was conducted at ~600 rpm.

* In cases where less than 2.3 μmol of precatalyst were used, stock solutions were used to avoid having to weigh very small amounts.

A.2.2 NH_3 detection by ^1H NMR

Following the completed reaction, the reaction flask was cooled to 77 K and allowed to freeze. The reaction vessel is then opened to atmosphere and to the frozen solution is slowly added an excess KO^{t}Bu as a solid (in at least two-fold excess with respect to acid) and THF (2 mL). This solution is allowed to freeze, then the headspace of the tube is evacuated, and the tube is sealed. The tube is then allowed to warm to RT and stirred at RT for at least 10 minutes. An additional Schlenk tube is charged with HCl (3 mL of a 2.0 M solution in Et_2O, 6 mmol) to serve as a collection flask. The volatiles of the reaction mixture are vacuum transferred into this collection flask. After completion of the vacuum transfer, the collection flask is sealed and warmed to RT. Solvent is removed *in vacuo*, and the remaining residue is dissolved in a known amount of (1 mL or 0.5 mL) DMSO-d_6 containing 1,3,5-trimethoxybenzene as an internal standard. Integration of the ^1H NMR peak observed for NH_4^+ (δ 7.25 t, J = 52 Hz, 4H) is then integrated against the two peaks of 1,3,5-trimethoxybenzene to quantify the ammonium present. A typical spectrum is shown in Figure A.1. $MeNH_3Cl$ (when detected) is characterized in a similar fashion with the integration of diagnostic peaks ($MeNH_3$.Cl δ 7.78, br, 3H, δ 2.35, q, J = 8 Hz, 3H) against 1,3,5-trimethoxybenzene. A typical spectrum is shown in Figure A.2.

A.2.3 Reload experiments

For the reload experiments (Table 2.1 entry 16), catalysis is set up as detailed in section A.1, except that following the sealing of the tube, it was allowed to thaw inside the glovebox and stirred for 80 minutes at 25 °C. After 80 minutes, the reaction mixture is filtered through a Celite pipette, with the flask and filter cake washed with an additional 2x(1 mL) dry Et_2O. The extracted Et_2O soluble products are added to a fresh Schlenk flask, and the solvent is removed *in vacuo*.

The (fresh) tube is then charged with a stir bar, the acid ($[Ph_2NH_2]OTf$), reductant ($(C_6H_6)_2Cr$)) and [TBA][CN]. The tube is sealed and cooled to 77 K in a cold well. To the cold tube Et_2O is added, taking into account the headspace of the tube and the vapor pressure of Et_2O such that the reaction volume remained 1 mL at 25 °C. The temperature of the system

is allowed to equilibrate for 5 minutes and then the tube is sealed with a Teflon screw-valve. This tube is passed out of the box into a liquid N_2 bath and transported to a fume hood. The reaction is warmed to room temperature and allowed to stir for 12 hours. The reloaded tube is analyzed as detailed in section A.2.2.

The first catalytic run is also analyzed for NH_3 (as detailed in section A.2.2), with the solids remaining on the Celite pipette being added back to the flask.

A.2.4 A note on error bars and the solubility of species during catalysis

Compared to similar N_2 reduction reactions, somewhat greater error between individual runs is observed.[4,5] We attribute this to the relative heterogeneity in the reaction mixture. $[Ph_2NH_2]OTf$ is insoluble in Et_2O, while [FeCN], $(C_6H_6)_2Cr$ and [TBA][CN] are all sparingly soluble. As a result, sufficient and consistent stirring was required to achieve reproducibility, but some variation was observed.

The relatively low catalyst solubility also necessitated the lyophilization of the precatalyst, particularly for low-temperature experiments. The increased surface area of lyophilized materials helps more rapidly solubilize the catalyst, which was found to be crucial to achieving efficient catalysis. Attempts to counteract these effects, e.g., by using THF for increased solubility, gave lower yields (Table A.1 runs A3 and B3), possibly due to a greater rate of background hydrogen evolution.

A.2.5 NH_3 detection results

Table A.1. Catalytic yields for reduction of [TBA][CN] to yield NH_3. [a]Assuming 6 e^- reduction. [b]CH_3NH_2 products also taken into account as a 4 e^- product.

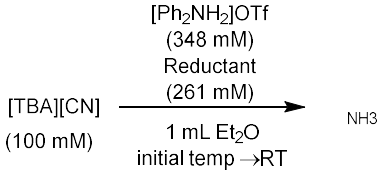

Entry	Catalyst loading (µmol) ([FeCN] is catalyst unless specified)	Conditions, ($(C_6H_6)_2Cr$ is the reductant unless specified)	NH_3 (equiv/ Fe)	Yield per reductant (%)[a]
A1	0.72 µmol	25 °C, Et_2O	20.5	34.1
B1	0.72 µmol	25 °C, Et_2O	32.8	54.6
C1	0.72 µmol	25 °C, Et_2O	24.3	40.5
D1	0.72 µmol	25 °C, Et_2O	32.5	54.2
Table 2.1, entry 1	**0.72 µmol**	**25 °C, Et_2O**	**28±5**	**47±8**
E1	0.72 µmol	–20 °C, Et_2O	27.6	46
F1	0.72 µmol	–20 °C, Et_2O	43.4	72
Table 2.1, entry 2	**0.72 µmol**	**–20 °C, Et_2O**	**35±8**	**58±13**
G1	0.72 µmol	0 °C, Et_2O	27.6	46
H1	0.72 µmol	0 °C, Et_2O	24.3	40.5
Table 2.1, entry 3	**0.72 µmol**	**0 °C, Et_2O**	**26±2**	**43±3**
I1	0.72 µmol	–78 °C, Et_2O,	16.2	23
J1	0.72 µmol	–78 °C, Et_2O	39.0	55
K1	0.72 µmol	–78 °C, Et_2O	30.7	44
L1	0.72 µmol	–78 °C, Et_2O	46.2	66
Table 2.1, entry 4	**0.72 µmol**	**–78 °C, Et_2O**	**33±6**	**55±10**
M1	2.9 µmol	–78 °C, Et_2O	9.5	63
N1	2.9 µmol	–78 °C, Et_2O	10.0	66
Table 2.1, entry 5	**2.9 µmol**	**–78 °C, Et_2O**	**9.7±0.2**	**65±1**
O1	0.15 µmol	–78 °C, Et_2O	76.5	25.5
P1	0.15 µmol	–78 °C, Et_2O	69	23
Table 2.1, entry 6	**0.15 µmol**	**–78 °C, Et_2O**	**73±4**	**24±1**

Entry	Catalyst loading (μmol) ([FeCN] is catalyst unless specified)	Conditions, ($(C_6H_6)_2Cr$ is the reductant unless specified)	NH_3 (equiv/ Fe)	Yield per reductant (%)[a]
Q1	No catalyst	–78 °C, Et_2O	<0.05	<1
R1	No catalyst	–78 °C, Et_2O	<0.05	<1
Table 2.1, entry 7	**No catalyst**	**–78 °C, Et_2O**	**<0.05**	**<1**
S1 Table 2.1, entry 8	**No [TBA][CN], [FeC^{15}N] precatalyst**	**–78 °C, Et_2O**	**0.7**	**1.1**
T1 Table 2.1, , entry 9	**$FeCl_2$ 8 μmol**	**–78 °C, Et_2O**	**0.3**	**5.5**
U1 Table 2.1, , entry 10	**$CrCl_2$ 8 μmol**	**–78 °C, Et_2O**	**<0.03**	**<0.5**
V1	$PhB(CH_2{}^iPr_2P)_3$ FeBr (2.9 μmol)	–78 °C, Et_2O	1.1 +0.4 $MeNH_2$ (equiv/Fe)	9.1
W1	$PhB(CH_2{}^iPr_2P)_3$ FeBr (2.9 μmol)	–78 °C, Et_2O	1.7 +0.85 $MeNH_2$ (equiv/Fe)	15.1
Table 2.1, entry 11	**$PhB(CH_2{}^iPr_2P)_3$ FeBr 2.9 μmol**	**–78 °C, Et_2O**	**1.4±0.7 +0.6±0.2 $MeNH_2$ (equiv/Fe)**	**12±3[b]**
X1	$[P_3{}^BFe]BAr^F{}_4$ 2.9 μmol	–78 °C, Et_2O	2.2	14.7
Y1	$[P_3{}^BFe]BAr^F{}_4$ 2.9 μmol	–78 °C, Et_2O	2.4	16.0
Table 2.1, entry 12	**$[P_3{}^BFe]BAr^F{}_4$ 2.9 μmol**	**–78 °C, Et_2O**	**2.3±0.1**	**15.3±0.6**
Z1	0.72 μmol	25 °C, Et_2O, Cp_2Co reductant	3.6	6
A2	0.72 μmol	25 °C, Et_2O, Cp_2Co reductant	2.0	3.3

Table 2.1, entry 13	**0.72 µmol**	**25 ℃, Et_2O, Cp_2Co reductant**	**2.8±0.8**	**4.6±1.3**

Entry	Catalyst loading (µmol) ([FeCN] is catalyst unless specified)	Conditions, (($C_6H_6)_2Cr$ is the reductant unless specified)	NH_3 (equiv/ Fe)	Yield per reductant (%)[a]
B2	0.72 µmol	25 ℃, Et_2O, $(Cp^*)_2Cr$ reductant	10.9	18.2
C2	0.72 µmol	25 ℃, Et_2O, $(Cp^*)_2Cr$ reductant	16.1	26.8
Table 2.1, entry 14	**0.72 µmol**	**25 ℃, Et_2O, $(Cp^*)_2Cr$ reductant**	**13.5±3**	**22±5**
D2, Table 2.1, entry 15	**0.72 µmol**	**25 ℃, Et_2O**	**32.4**	**54**
E2	0.72 µmol	25 ℃, Et_2O	3.1	5.2
F2	0.72 µmol	25 ℃, Et_2O	5.1	8.5
Table 2.1, entry 16	**0.72 µmol**	**25 ℃, Et_2O**	**4.1±1**	**7±2**

Additional catalytic runs

Entry	Catalyst loading (µmol) ([FeCN] is catalyst unless specified)	Conditions, (($C_6H_6)_2Cr$ is the reductant unless specified)	NH_3 (equiv/ Fe)	Yield per reductant (%)[a]
A3	0.72 µmol	–78 ℃, THF	12.3	
B3	0.72 µmol	–78 ℃, THF	16.7	27.8
	0.72 µmol	**–78 ℃, THF**	14.5±2.2	**24±4**
C3[c]	2.9 µmol	–78 ℃, Et_2O	2.3	46
D3[c]	2.9 µmol	–78 ℃, Et_2O	3.6	72
E3[c]	2.9 µmol	–78 ℃, Et_2O	4.1	82
	2.9 µmol	**–78 ℃, Et_2O**	3.3±0.6	66±12

[c] loadings of 30 equiv $(C_6H_6)_2Cr$ (87 mM)/ 40 equiv $[Ph_2NH_2]OTf$ (116 mM)/ 6 equiv [TBA][CN] (17.4 mM).

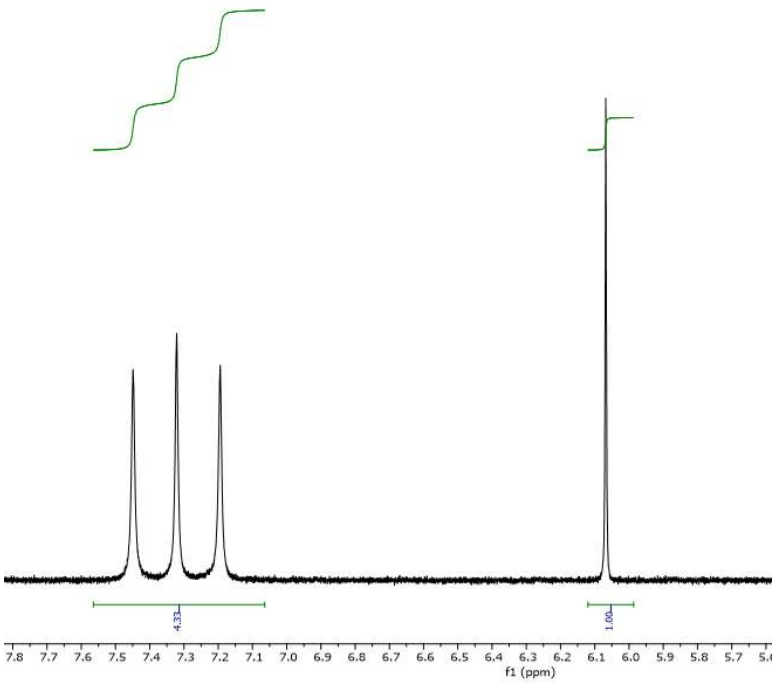

Figure A.1. Typical spectra for ^{1}H NMR detection of $[NH_4]Cl$ (triplet, J=52 Hz at 7.31 ppm), with 10 μmol 1,3,5-trimethoxbenzene (TMB) added.

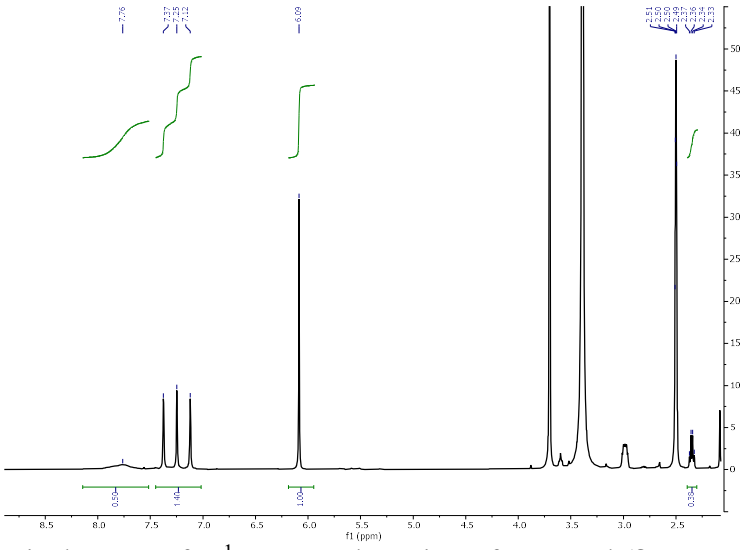

Figure A.2. Typical spectra for ^{1}H NMR detection of $[NH_4]Cl$ (δ 7.31 ppm (t), J=52 Hz) and $[CH_3NH_3]Cl$ (δ 7.78, br, 3H, δ 2.35, q, J = 8 Hz, 3H), with 5 μmol 1,3,5-trimethoxbenzene (TMB) added.

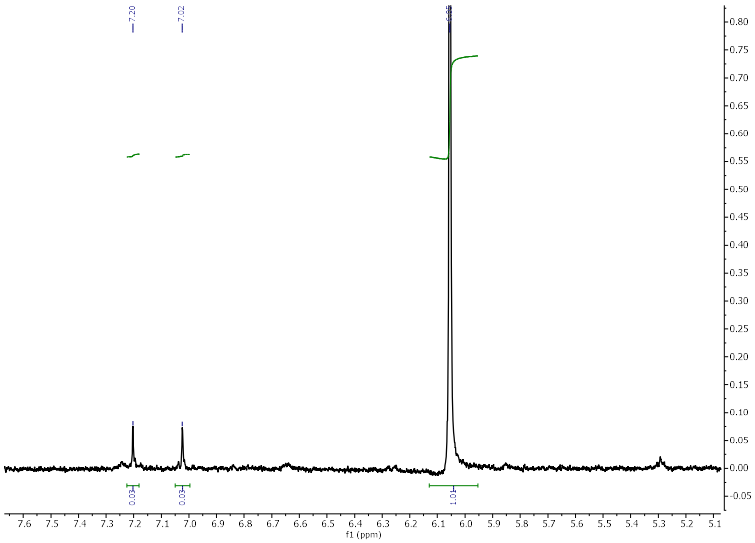

Figure A.3. ^{1}H NMR detection of [$^{15}NH_4$]Cl (δ 7.1 ppm (d), *J*=72 Hz) from reduction of [FeC^{15}N] (360 equiv $(C_6H_6)_2Cr$ and 480 equiv $[Ph_2NH_2]OTf$), in the absence of [TBA][CN], quantified with 10 μmol 1,3,5-trimethoxybenzene (TMB) added. Lack of [$^{14}NH_4$]Cl rules out possible background N_2R.

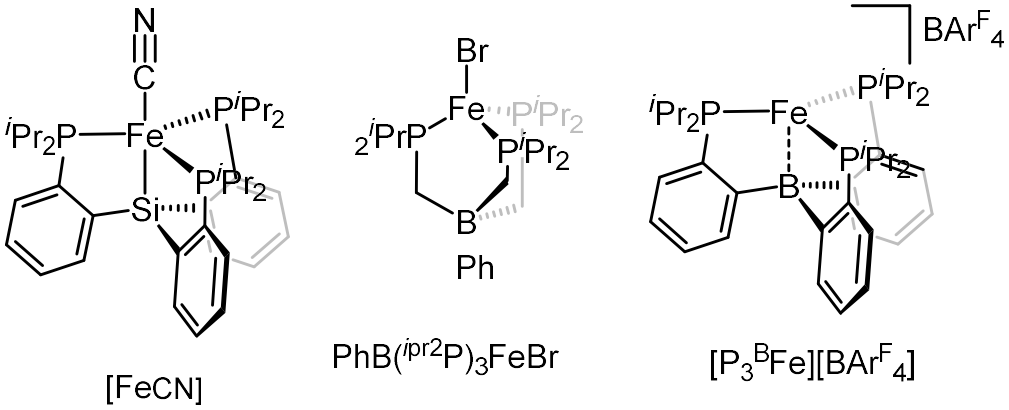

Figure A.4. Structures of molecular complexes employed as precatalysts.

A.3 Detection and quantification of gaseous products

A.3.1 General considerations

When using standard catalytic conditions, the acid, reductant and cyanide all constitute an appreciable wt% ($[Ph_2NH_2]OTf$ wt. 12 %, $(C_6H_6)_2Cr$ wt. 6 % and [TBA][CN] wt. 4 %) of the reaction mixture and have an unknown effect on the solubility of gaseous organic products. We find that these reagents result in a greater amount of CH_4 absorbed in solution than expected for Et_2O alone.

To initially quantify the amount of CH_4 produced, 4 tubes with chemical reagents ([TBA][CN], $[Ph_2NH_2]OTf$ and $(C_6H_6)_2Cr$, standard loadings table 1 entry 1) with and without [FeCN] (0.72 mM) and with and without 500 μL CH_4 added (at 25°C, 1 atm equals 20.5 μmol or 29.4 equiv per [Fe] at 0.72 mM catalyst loading) were prepared. After completion of the reaction, an aliquot from the headspace was injected on an HP 5890 GC-FID (30 M column length, 0.280 mm column diameter, He carrier gas), and the respective ratios of the CH_4 peak were compared (retention time=3.7 min). Using these measurements, the CH_4 yields were calculated (Table A.2). While we did not quantify C_2 products they were observed as possible minor components in the GC-FID, motivating the use of a gas analysis method on a different instrument that was previously calibrated for quantification of other gases C_2H_4, C_2H_6, and H_2.

With the amount of CH_4 quantified, samples were manually injected on a combined GC-FID/TCD (SRI 8610C, in Multi Gas 5 configuration equipped with HayeSep D and Molsieve 5A columns). Hydrocarbons were detected by a S4 methanizer-flame ionization detector (FID), and the hydrogen was detected by a thermal conductivity detector (TCD). H_2, C_2H_6, and C_2H_4 were calculated with respect to CH_4 (Table A.3 and Table A.4). Using this same internal calibration, gaseous products from reactions run at room temperature and with the tris(phosphine) iron precatalysts were also quantified.

Table A.2. Detection of CH_4 with control and leak test

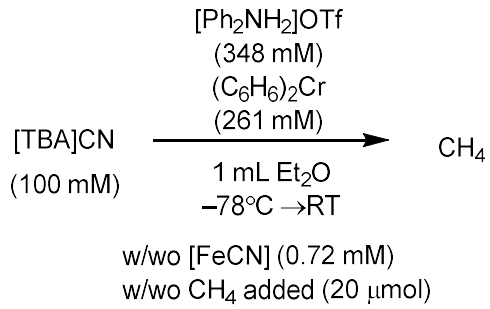

Sample	Signal Area CH_4	Amount of CH_4 added	Amount of CH_4 detected	Amount of CH_4 produced
[Fe]	1754	0 μmol	22.3 μmol	22.0 μmol
[Fe] + 0.5 mL CH_4 (27.8 equiv)	3655	20 μmol	46.4 μmol	26.1 μmol
No Fe	28	0 μmol	0.3 μmol	
No Fe + 0.5 mL CH_4 (27.8 equiv)	1575	20 μmol	20 μmol	
			Average	24±2 μmol
				33±3 CH_4 per Fe

A.3.2 Quantification of additional gases

To quantify the additional gaseous products observed, a GC-FID/TCD was used with a previously measured calibration curve. It was assumed that gas absorption (in the reaction mixture) was similar across gasses, as such the headspace gasses were used to calculate the ratios of H_2/CH_4, C_2H_4/CH_4, and C_2H_6/CH_4. This same internal calibration gaseous products at room temperature were also quantified in runs C and D, with $^{Ph}BP_3FeBr$ precatalysts in runs D and E and $P_3{}^{B}Fe[BAr^{F}{}_4]$ precatalyst in runs F.

Table A.3. Summary of quantification of additional gaseous products.

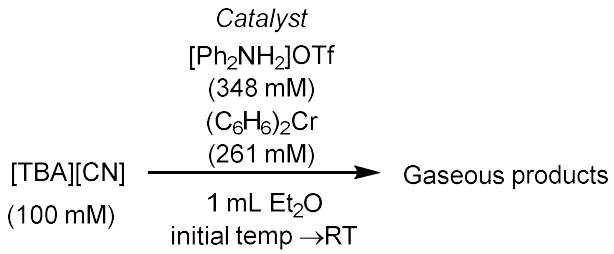

Catalyst (Loading)	Initial T	CH_4 equiv/Fe (yield%/Cr)	H_2 equiv/Fe (yield%/Cr)	C_2H_4 equiv/Fe (yield%/Cr)	C_2H_6 equiv/Fe (yield%/Cr)	C_2/C_1 ratio
[FeCN] (0.575 mM)	−78°C	33±3 (55±5%)	53±15 (29±8%)	0.28±0.02 (0.6±0.04%)	0.21±0.02 (0.6±0.04%)	0.015
[FeCN] (0.575 mM)	25°C	27±4 (45±6%)	53±20 (29±11%)	0.33 (0.7%)	0.26±0.10 (0.7±0.3%)	0.022
$^{Ph}BP_3FeBr$ (2.9 mM)	−78°C	1.0±0.1 (7.3±1%)	5.1±0.1 (11±0.2%)	0.09±0.01 (0.7±0.1%)	0.06±0.01 (0.8±0.1%)	0.11
$P_3{}^BFe[BAr^F{}_4]$ (2.9 mM)	−78°C	1.6 (11%)	16 (36%)	0.1 (0.1%)	0.1 (0.1%)	0.16

Table A.4. Quantification of additional gases and room temperature catalysis. *Headspace concentrations are relative based on GC-calibration.

Gas		CH_4	H_2	C_2H_4	C_2H_6
Run A (20 mL reaction volume)	Area	744	238	13.3	8.7
	Headspace concentration*	3250 ppm	4195 ppm	27 ppm	19.4 ppm
	Ratio to CH_4	-	129%	0.8%	0.6%
Run B (20 mL reaction volume)	Area	762	366	15	10
	Headspace concentration*	3334 ppm	6485 ppm	31 ppm	22 ppm
		-	195%	0.9%	0.7%
Average ratio to CH_4			162±46%	0.85±0.07%	0.65±0.07%
Yield per Fe		33±3	53±15	0.28±0.02	0.21±0.02
Yield per $(C_6H_6)_2Cr$		55±5	29±8%	0.6±0.04%	0.6±0.04%
Room temperature gas analysis					
Run C (150 mL reaction volume)	Area	118.9	108.7	2.4	0.6
	Headspace concentration*	406 ppm	995 ppm	4.6 ppm	2 ppm
	Ratio to CH_4 runs(A+B)	92%	220%	1%	0.5%
Run D (150 mL reaction volume)	Area	101.2	54.2	2.4	1.4
	Headspace concentration*	302 ppm	443 ppm	4.6 ppm	4.9 ppm
	Ratio to CH_4 (runs A+B)	70%	100%	1%	1.1%
Average ratio to CH_4			160±60%	1%	0.8±0.3%

Yield per Fe		27±4	53±20	0.33	0.26±0.10
Yield per $(C_6H_6)_2Cr$		45±6	29±11%	0.7%	0.7±0.3%
Gas		**CH_4**	**H_2**	**C_2H_4**	**C_2H_6**
Catalytic run with $^{Ph}BP_3FeBr$ (2.9 mM)					
Run E (20 mL reaction volume)	Area	105.3	109.7	19.4	9.2
	Headspace concentration*	360 ppm	2012 ppm	37 ppm	21 ppm
	Ratio to CH_4 runs(A+B)	11% (0.9 equiv)	61% (5 equiv)	1.1% (0.09 equiv)	0.6% (0.05 equiv)
Run F (20 mL reaction volume)	Area	127.7	114	19	10.8
	Headspace concentration*	434 ppm	2091 ppm	36 ppm	26 ppm
	Ratio to CH_4 (runs A+B)	13% (1.1 equiv)	64% (5.3 equiv)	1.1% (0.09 equiv)	0.8% (0.07 equiv)
Average ratio to CH_4		12±1%	38.5±0.5%	1.1%	0.7±0.01%
Yield per Fe		1.0±0.1	5.1±0.1	0.09±0.01	0.06±0.01
Yield per $(C_6H_6)_2Cr$		7.3±1%	11±0.2%	0.7±0.1%	0.8±0.1%
Catalytic run with $(P_3^BFe)BAr^F_4$ (2.9 mM)					
Run G (20 mL reaction volume)	Area	182	356	21.6	12.5
	Headspace concentration*	622 ppm	6530 ppm	41.2 ppm	43.9 ppm
	Ratio to CH_4 runs(A+B)	19% (1.6 equiv)	198%	1.2%	1.3%
Yield per Fe		1.6	16	0.1	0.1
Yield per $(C_6H_6)_2Cr$		10.6%	36%	0.9%	1.1%

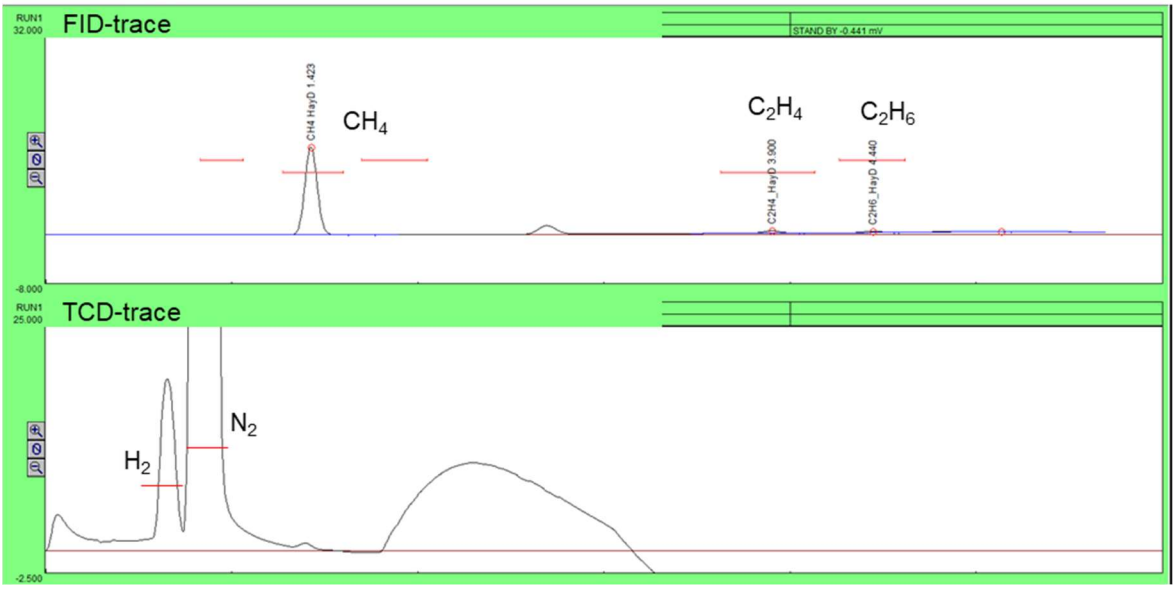

Figure A.5. Typical trace for GC-FID (top) and TCD (bottom) of gases detected, with CH_4, C_2H_4, C_2H_6 and H_2 highlighted.

A.4 Additional control experiments

A.4.1 Monitoring of [TBA]^{13}CN consumption by NMR

To monitor the consumption of $[CN]^-$ and the formation of methane derived from $[CN]^-$, [TBA][^{13}CN] was used in a ^{13}C NMR experiment. Two J. Young NMR tubes were loaded with [TBA][^{13}CN] (100 mM), $(C_6H_6)_2Cr$ (261 mM), and $[Ph_2NH_2]OTf$ (348 mM); one of these tube was also loaded with [FeCN] (2.9 mM). The tubes were cooled to -78 ˚C, d_8-THF was added, and the tubes were sealed. The tubes were allowed to warm up slowly with occasional mixing (by hand, every 10 minutes) for the first 2 hours of the reaction. Upon completion, analysis by ^{13}C NMR showed that only the tube loaded with [FeCN] had consumed $^{13}CN^-$ and produced $^{13}CH_4$.

The use of THF was required to get sufficient solubility of reaction components, given the worse mixing in the J. Young tube. It was confirmed that setting up catalysis in THF still yields NH_3 (14.5±2.2, Table A.1, runs A3 and B3).

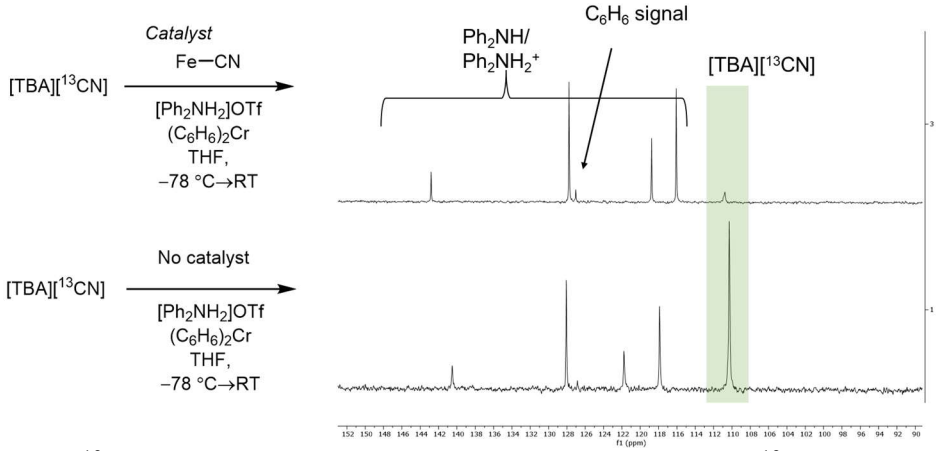

Figure A.6. ^{13}C NMR spectra showing the reaction of [TBA][^{13}CN] with $(C_6H_6)_2Cr$, $[Ph_2NH_2]OTf$ in the presence and absence of [FeCN] catalyst. As compared to the peaks corresponding to $Ph_2NH/[Ph_2NH_2]^+$ $[^{13}CN]^-$ is only appreciable consumed in the presence of [FeCN] (top spectrum).

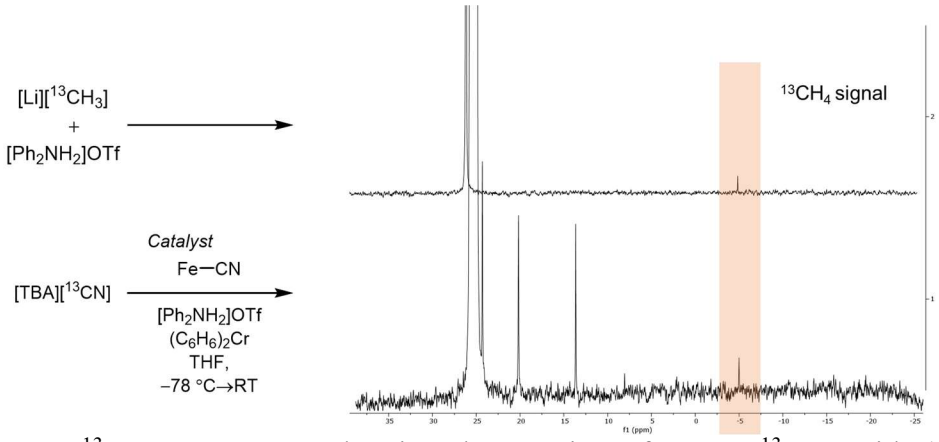

Figure A.7. ^{13}C NMR spectra showing the reaction of [TBA][^{13}CN] with $(C_6H_6)_2Cr$, $[Ph_2NH_2]OTf$ in the presence of [FeCN] catalyst, with a $^{13}CH_4$ peak (δ – 4.8 ppm, s), as compared to a sample generated upon the addition of acid to [Li][$^{13}CH_3$].

A.4.2 Using [FeC^{15}N] precatalyst.

To determine that the precatalyst CN^- ligand is consumed, we used [FeC^{15}N] labeled precatalyst but otherwise set up catalysis as usual (i.e., using natural abundance [TBA][CN]). Low reactant loading conditions were used to not swamp out the ^{15}N signal (2.9 mM FeC^{15}N, 6 equiv [TBA][CN], 30 equiv $(C_6H_6)_2Cr$/ 40 equiv $[Ph_2NH_2]OTf$). 0.8 equiv [$^{15}NH_4$]Cl is detected along with about 3 equivalents [$^{14}NH_4$]Cl by ^1H NMR, consistent with most of the

bound [FeC^{15}N] ligand being consumed. Catalysis with similar loading yielded similar amounts of NH_3 (**Table A.1** entry C3-E3).

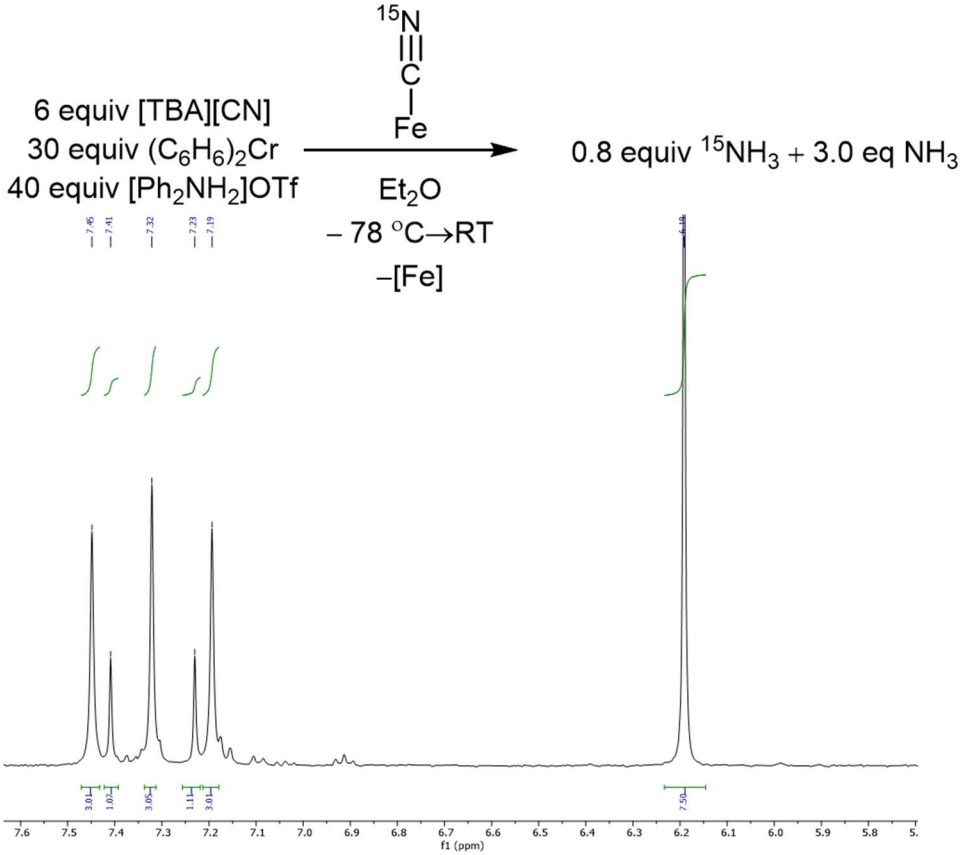

Figure A.8. ^{1}H NMR detection of [$^{15}NH_4$]Cl (triplet, J = 52 Hz at 7.32 ppm), and [$^{15}NH_4$]Cl (doublet, J = 72 Hz at 7.32 ppm) with 10 μmol 1,3,5-trimethoxbenzene (TMB) added.

A.5 Additional NMR experiments

A.5.1 Stoichiometric reactions

A.5.1.1 Reduction of [FeCN]

[FeCN] (2 mg, 2.9 μmol) was deposited in a Schlenk flask as a lyophilized powder, followed by the addition of $(C_6H_6)_2Cr$ (3.6 mg, 6 equiv, 17.4 μmol) and $[Ph_2NH_2]OTf$ (7.4 mg, 8 equiv, 23 μmol). The flask was cooled to −78 °C, and Et_2O (1 mL) was added via syringe. The flask was allowed to warm up slowly overnight and, after completion, was brought back into the glovebox. The solvent was removed *in vacuo,* and the contents were taken up in C_6D_6 and analyzed by ^{1}H NMR to find P_3^{Si}FeOTf as the only detectable Fe-

species. In a separate experiment, the contents of the flask were worked up as described in section **A.2.2**.

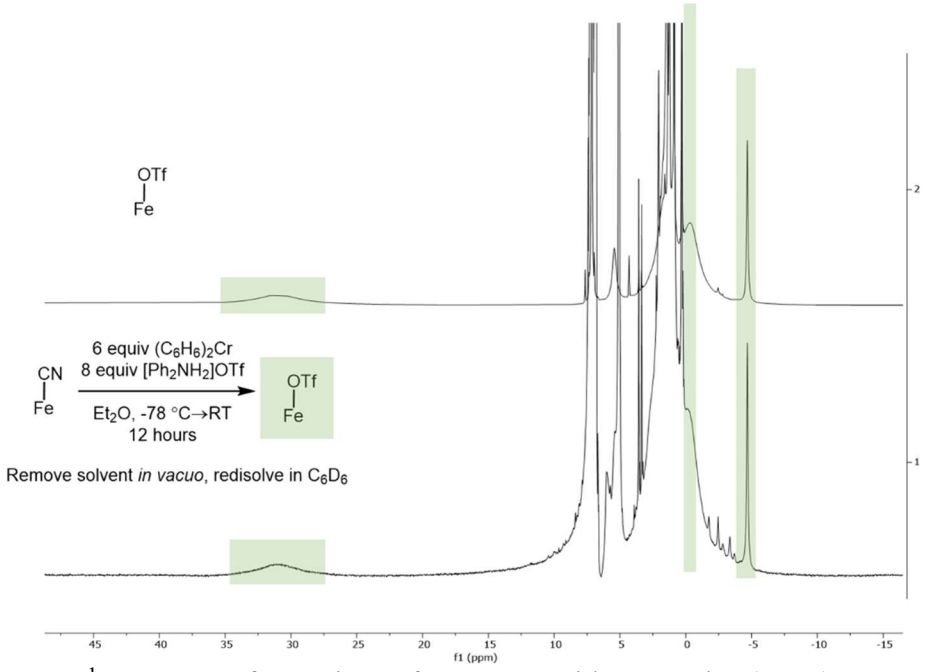

Figure A.9. ^1H NMR of reaction of [FeCN] with 6 equiv $(C_6H_6)_2Cr$ and 8 equiv $[Ph_2NH_2]OTf$ in Et_2O. After completed reaction, solvent was removed *in vacuo* and the sample was redissolved in C_6D_6. ^1H NMR showed that the [Fe] product was primarily [FeOTf], green boxes for comparison to authentic sample.

A.5.1.2 Metathesis of [FeOTf] to [FeCN]

[FeOTf][8] (5 mg, 6 μmol) and [TBA][CN] (8.8 mg, 10 equiv, 60 μmol) were stirred in Et_2O at room temperature for 5 minutes, color change (orange to red) suggested a change in Fe-speciation consistent with [FeCN] formation. The solvent was removed *in vacuo*, and the contents were redissolved in C_6D_6 to confirm [FeCN] formation by ^1H NMR. ^{19}F NMR showed mostly free TfO^- but some [FeOTf].

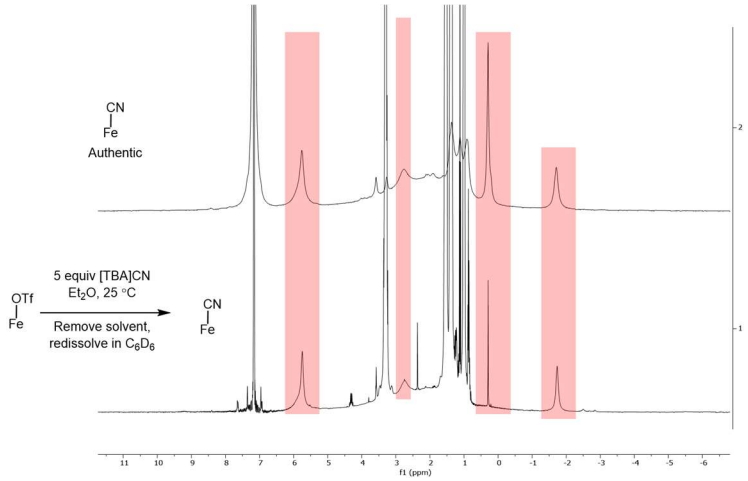

Figure A.10. ^{1}H NMR of reaction of [FeOTf] with 10 equiv [TBA][CN] in Et_2O, stirred at 25 °C for 5 minutes at room temperature. ^{1}H NMR showed that the [Fe] product was primarily [FeCN], red boxes for comparison to authentic sample.

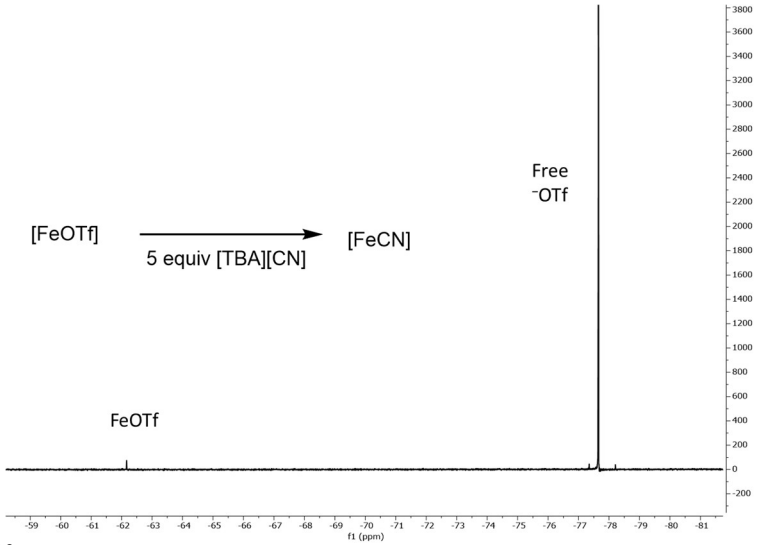

Figure A.11. ^{19}F NMR of reaction of [FeOTf] with 10 equiv [TBA][CN] in Et_2O, stirred at 25 °C for 5 minutes at room temperature. ^{19}F NMR showed that the ^{19}F-product was primarily TfO^{-}.

A.5.1.3 Reduction of [FeCN] at room temperature

To confirm the assignment of [FeOTf] in Figure 2.3 (see main text), a parallel NMR experiment was run. In the glovebox, [FeCN] (2 mg, 2.9 μmol) was deposited in a J. Young tube as a lyophilized powder, followed by the addition of $(C_6H_6)_2Cr$ (12 mg, 20 equiv, 68 μmol) and d_8-THF (0.6 mL). $[Ph_2NH_2]OTf$ (22 mg, 20 equiv, 68 μmol) was added as a solid.

Within 5 minutes of acid addition, a ^{1}H NMR of the reaction was collected, confirming the formation of [FeOTf]. CH_4 and NH_3 were confirmed in separate experiments, with the reaction being sampled or quenched after a 10-minute reaction time.

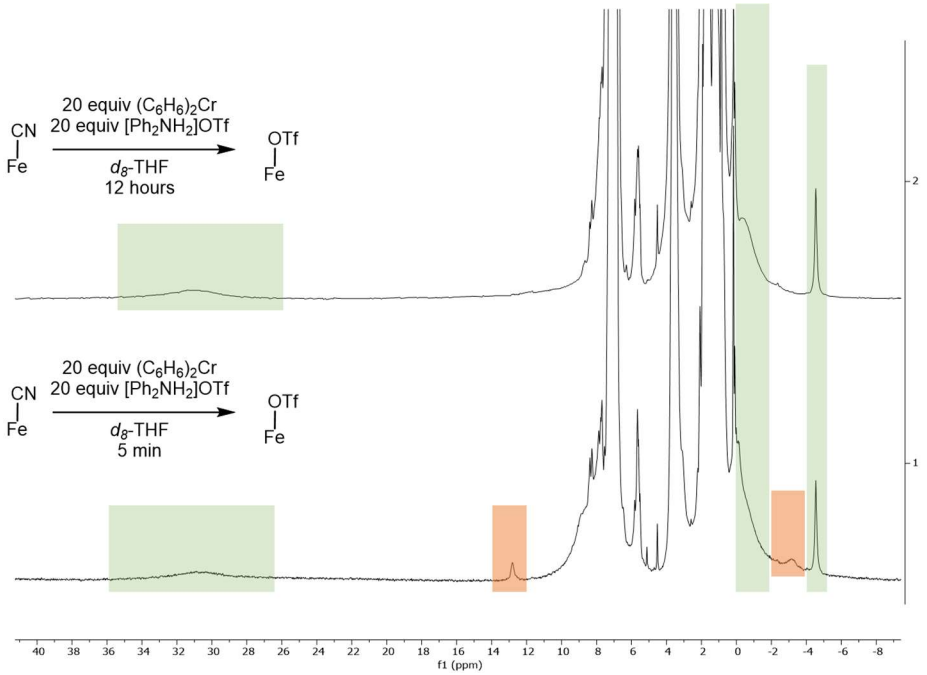

Figure A.12. ^{1}H NMR of reaction of [FeCN] with 20 equiv $(C_6H_6)_2Cr$ and 20 equiv $[Ph_2NH_2]OTf$ in THF. After 5 minutes, multiple Fe-species are formed, including [FeOTf] and an unknown species (orange boxes). Overnight, this species disappears, and [FeOTf] is the only identifiable Fe-species.

A.5.2 Analysis of post-catalysis products

Catalysis was setup as described in section 2.1. To more readily detect [Fe] products, the higher loadings (2.9 mM [FeCN]; **Table 1**, entry 5) were used. After completed catalysis (12 hours), the reaction flask was brought back into the glovebox. The flask was filtered and extracted with additional Et_2O. The solvent was removed *in vacuo*, redissolved in C_6D_6, and analyzed. Fe−H species were detected, notably a doublet of triplets at δ −15.5 ppm. In addition, no [FeOTf] was observed (characteristic peaks δ 31.5, −4.5 ppm were not observed).

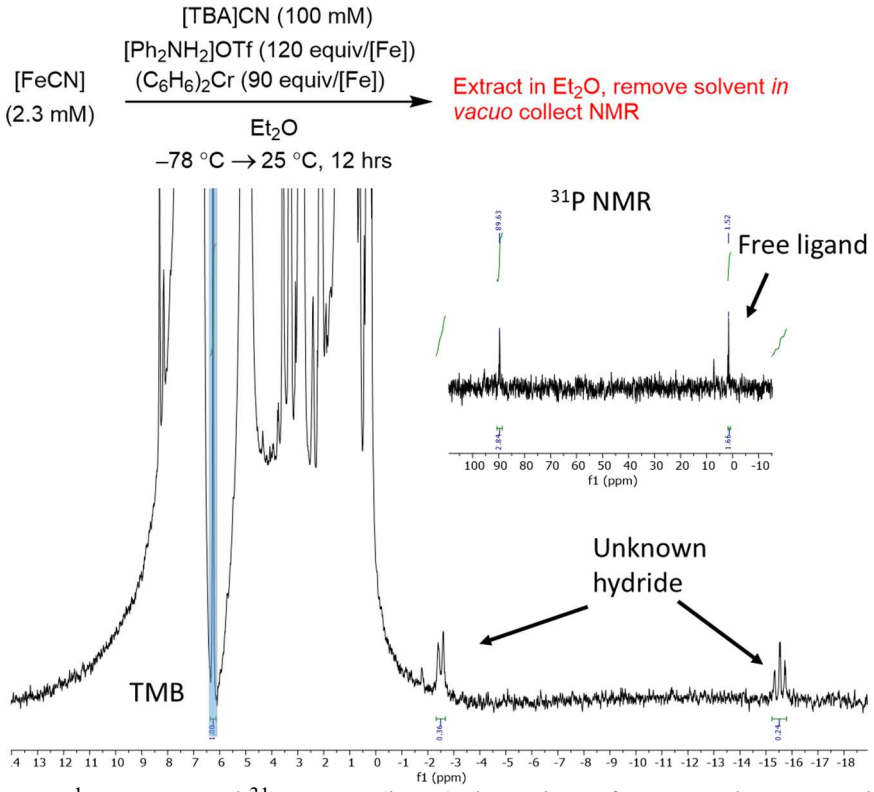

Figure A.13. ^{1}H NMR and ^{31}P NMR (inset) detection of extracted post-catalysis products, integrated against 1,3,5-trimethoxbenzene internal standard. Peak at δ -15.5 ppm, td (J = 81.2 Hz; 11.4 Hz) is consistent with a hydride bound to $P_3{}^{Si}Fe$ with $^{2}J_{P–H}$ couplings. For comparison δ(Fe-H; $P_3{}^{Si}Fe(N_2)(H)$) has previously been characterized with td (J = 83.2 Hz; 19.8 Hz).[9]

A.5.3 Stability measurements of other iron phosphine precatalysts

To assess possible reasons for poorer performance from the $(P_3{}^{B})Fe[BAr^{F}{}_4]$ and $(^{Ph}BP_3)FeBr$, these catalysts (2.3 mM) were reacted with excess (20 equiv) [TBA][CN] in Et_2O. Analysis of the reaction mixture by ^{31}P NMR after 15 minutes revealed free ligand from both precatalysts. In addition, a low spin Fe-bound product was observed upon the reaction of [TBA][CN] with $^{Ph}BP_3FeBr$, possibly arising from the formation of $[^{Ph}BP_3Fe(Br)(CN)]^{-}$.

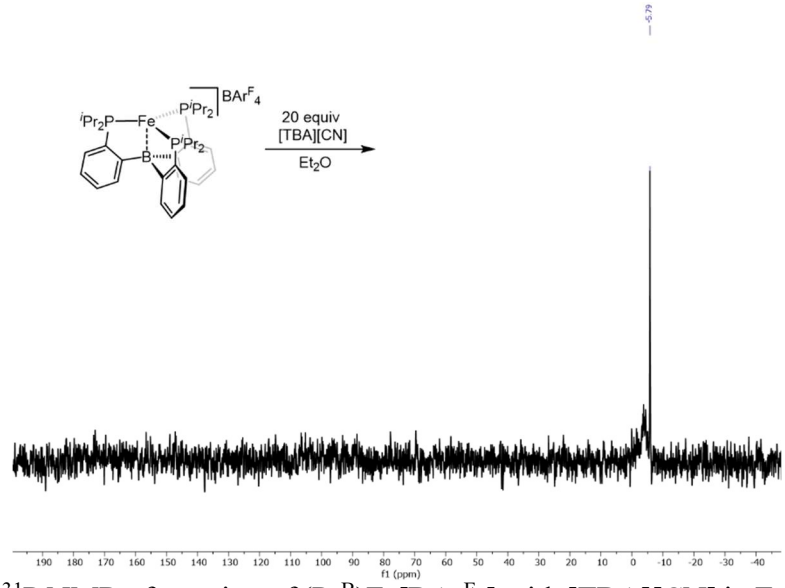

Figure A.14. ^{31}P NMR of reaction of (P_3^B)Fe[BAr^F_4] with [TBA][CN] in Et_2O. Sharp peak at –6.8 ppm is consistent with unligated phosphine, with another broad peak (–3 ppm) also observed.

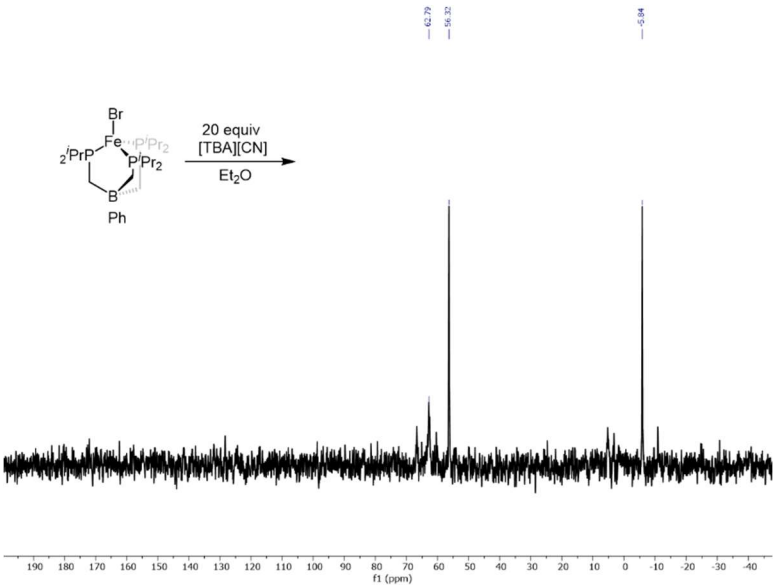

Figure A.15. ^{31}P NMR analysis of reaction of ($^{Ph}BP_3$)FeBr with [TBA][CN] in Et_2O. Sharp peak at – 5.9 ppm is consistent with unligated phosphine. Another major peak at 56.3 ppm suggests the formation of diamagnetic Fe-species, perhaps from the formation of formation of [$^{Ph}BP_3$Fe(Br)(CN)]$^-$ or [$^{Ph}BP_3$Fe(Br)$(CN)_2$]$^-$ with the CN^- ligand binding inducing a change of spin state from ($^{Ph}BP_3$)FeBr (S = 1). Additional, small peaks are also observed (65 ppm, 63 ppm, 4 ppm).

A.6 Mössbauer data

A.6.1 Note on the fitting of Mössbauer spectra

Data analysis was performed using version 4 of the program WMOSS (www.wmoss.org), and quadrupole doublets fit Lorentzian lineshapes. Simulations were constructed from the minimum number of quadrupole doublets required to attain a quality fit to the data (convergence of χ_R^2). Quadrupole doublets were constrained to be symmetric. Using the non-linear error analysis algorithm provided by WMOSS, the errors in the computed parameters are estimated to be 0.02 mm s^{-1} for δ and 2% for ΔE_Q.

A.6.2 Freeze-Quenched Mössbauer spectroscopy of catalytic reactions

A.6.2.1 General procedure for freeze-quenched catalytic reactions

All solvents are stirred with Na/K for ≥ 2 hours and filtered prior to use. In a nitrogen-filled glovebox, the desired ^{57}Fe species (0.0023 mmol) is quantitatively transferred using benzene to a Schlenk flask and then lyophilized to yield a powder. That flask is charged with a stir bar and the other catalytic reagents as solids (analogous to catalytic reduction as described in section A.2.1). The tube is then chilled to 77 K in the glovebox cold-well and allowed to equilibrate for five minutes. To the chilled tube is added 1 mL of Et_2O and this flask is allowed to equilibrate for another five minutes. The flask is then transferred to a stir plate, where it is allowed to thaw. When the stir bar is freed from the frozen solvent and begins to stir the time is started. At the time noted, the stirring is stopped, and using a pipette, the reaction mixture is transferred in one portion to a Mössbauer cup sitting in a vial. The vial is then placed into the 77 K cooled cold well, allowing the reaction mixture to freeze in approximately twenty seconds. The sample is allowed to equilibrate for 20 minutes before being removed from the glovebox, immediately submerged in liquid nitrogen, and then mounted following standard procedure.

The resulting signals had broad ^{57}Fe Mössbauer spectra, for which meaningful fits could not be readily generated. However, noting the chemistry of [FeCN] in the presence of excess $[Ph_2NH_2]OTf$ and $(C_6H_6)_2Cr$ (Figures 2.3 and A.12) and the known spectra of [FeOTf] (δ = 0.66 mm s^{-1}, ΔE_Q = <0.2 mm s^{-1}, black line in figure A.14 is centered at 0.66

mm s^{-1}) we are reasonably confident that [FeOTf] is present at early times. NMR analysis of the mixtures at 80 minutes shows no evidence of [FeOTf] (Figure A.13).

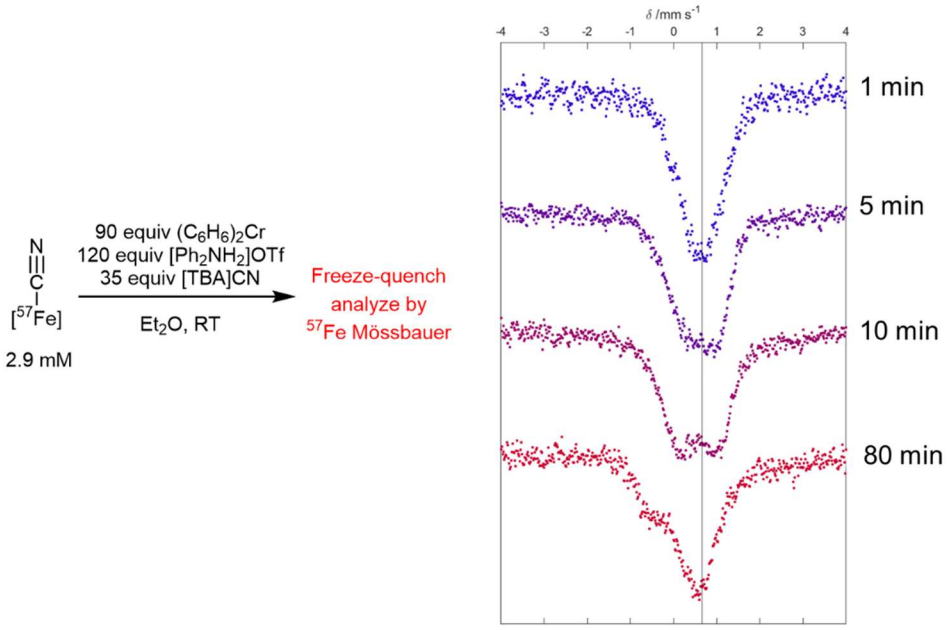

Figure A.16. ^{57}Fe Mössbauer spectra of freeze-quenched catalytic reactions reacting [^{57}FeCN] (2.9 mM) with 90 equiv $(C_6H_6)_2Cr$, 120 equiv $[Ph_2NH_2]OTf$ and 35 equiv [TBA][CN] in Et_2O for variable time. [FeOTf], reported as a species with δ = 0.66 mm s^{-1}; ΔE_Q = <0.2 mm s^{-1} is observed within 1 minute (Black line at 0.66 mm s^{-1}).[10] Over time, other species appear, but we have not been able to assign them to known Fe-species.

A.6.3 Mössbauer spectroscopy of reactions of [FeCN] with reductant and acid

A.6.3.1 General Procedure for Freeze-Quenched Reactions

All solvents are stirred with Na/K for ≥ 2 hours and filtered prior to use. In a nitrogen-filled glovebox, the desired ^{57}Fe species (0.0023 mmol) is dissolved in 0.3 mL Et_2O and cooled to −78 °C in a stirring vial in the glovebox cold well. Acid ($[Ph_2NH_2]BAr^F{}_4$, 0.00575 mmol) was added in 0.1 mL Et_2O. Reductant ($(C_6H_6)_2Cr$ or Cp_2Co, 0.00575 mmol) was added in 0.3 mL to the chilled vial. The reaction was allowed to stir for 5 minutes before it was rapidly transferred to a pre-chilled Mössbauer cup. The cold well was then changed from −78°C (195 K) to 77 K and the solution froze within 5 minutes. The Mössbauer cup was kept at 77 K for minimum 20 minutes before being rapidly taken out of the glovebox and submerged in liquid N_2 and then mounted following standard procedure.

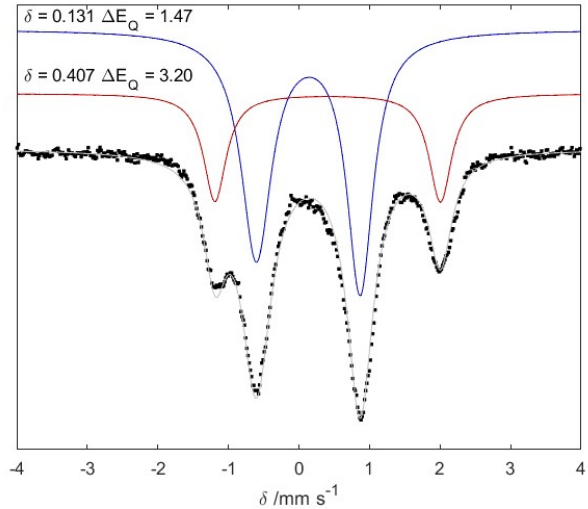

Trace	δ (mm s^{-1})	ΔE_Q (mm s^{-1})	Relative area	Assignment
Blue	0.13±0.01	1.47±0.01	71 %	$[FeCNH_2]^+$
Red	0.41±0.01	3.20±0.01	29%	$[FeCNH]^+$

Figure A.17. ^{57}Fe mössbauer spectrum of reaction of [^{57}FeCN] with 2.5 equiv each of $(C_6H_6)_2Cr$ and $[Ph_2NH_2]BAr^F{}_4$. Spectra fit as two species.

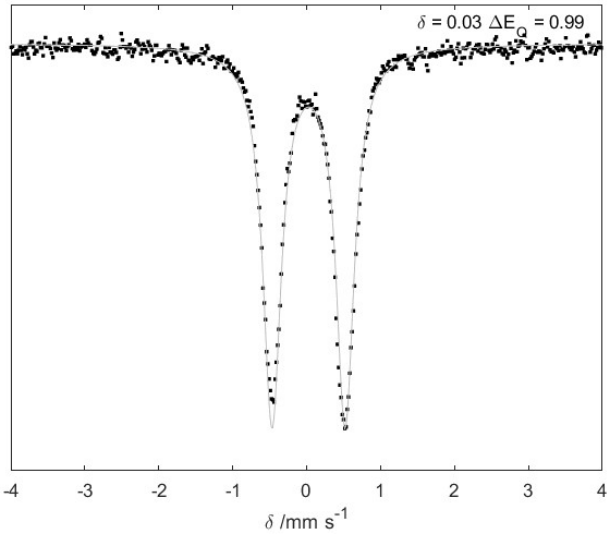

Figure A.18. ^{57}Fe Mössbauer spectrum of reaction of [^{57}FeCN] with 2.5 equiv each of Cp_2Co and $[Ph_2NH_2]BAr^F{}_4$. Spectra fit as a single species, δ = 0.03±0.01 mm s^{-1}, ΔE_Q = 0.99±0.01 mm s^{-1}.

A.6.4 Alternative synthesis of [FeCNH$_2$] Mössbauer sample

A.6.4.1 Synthetic procedure

[FeCN] (20 mg, 29 μmol) was dissolved in 0.5 mL THF in a 20 ml vial. The solution was cooled to −78 °C, and excess KC_8 was added. The reaction mixture was then filtered through a pipette loaded with a filter paper, Celite, and KC_8 3 times to form (proposed) [FeCN]K_2. The reaction mixture was filtered a final time to remove graphite and excess KC_8, giving a jet-black solution. This *in situ* formed material was used directly to form [FeCNH$_2$]. Alternatively, transferring this solution to a Mössbauer cup while maintaining the temperature, freezing the reaction mixture at 77 K, and analyzing by ^{57}Fe Mössbauer revealed a Mössbauer spectrum with parameters $\delta = 0.20$ mm s^{-1}, $\Delta E_Q = 0.18$ mm s^{-1} (Figure A.19 A), with a minor impurity.

For generation of [FeCNH$_2$], 2 equiv [H(OEt$_2$)$_2$]BAr$^F{}_4$ (59 mg, 58 μmol) dissolved in 0.3 mL THF, was added slowly to *in situ* formed [FeCN]K_2, with an orange solution formed. Transferring this solution to a Mössbauer cup while maintaining the temperature, freezing the reaction mixture at 77 K, and analyzing by ^{57}Fe Mössbauer revealed a Mössbauer spectrum with parameters $\delta = 0.02$ mm s^{-1}; $\Delta E_Q = 0.96$ mms^{-1} (Figure A.19 B), with some oxidized material also formed. The parameters of the major species fit those observed for [FeCNH$_2$] synthesized with [Ph$_2$NH$_2$]BAr$^F{}_4$ and Cp$_2$Co.

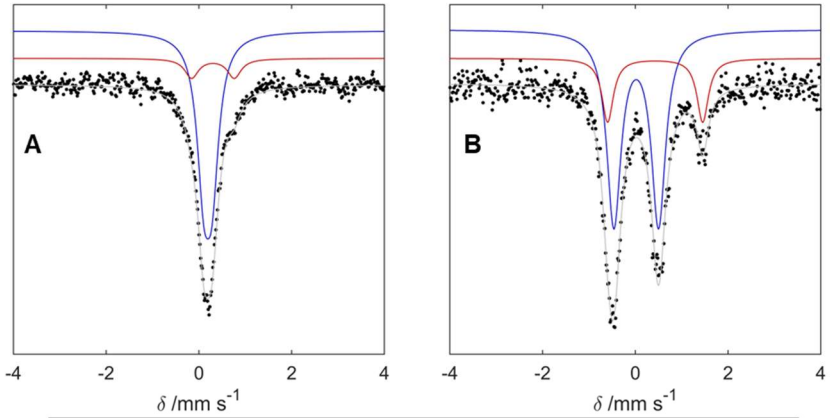

^{57}Fe spectra A			
δ(mm s^{-1})	ΔE_Q (mm s^{-1})	Γ (mm s^{-1})	Rel. area
0.20±0.01	0.18±0.05	0.35±0.05	86% (Blue)
0.30±0.01	0.92±0.05	0.36±0.03	14% (Red)

^{57}Fe spectra B			
δ(mm s^{-1})	ΔE_Q (mm s^{-1})	Γ (mm s^{-1})	Rel. area
0.02±0.01	0.96±0.01	0.37±0.01	80% (Blue)
0.43±0.01	2.09±0.01	0.30±0.01	20% (Red)

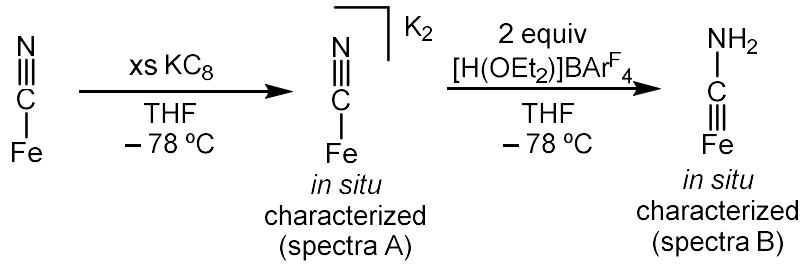

Figure A.19. ^{57}Fe mössbauer of reaction of [^{57}FeCN] with KC_8 (excess) to form proposed [^{57}FeCN]K_2 (spectra A) and reaction of proposed [^{57}FeCN]K_2 with 2 equiv $[H(OEt_2)_2]BAr^F{}_4$ to form [$FeCNH_2$] (spectra B).

A.7. UV-visible measurements

A.7.1 General procedure for room temperature reduction of [FeCN] monitored by UV-vis spectroscopy

A 1 cm path length cuvette was loaded with [FeCN] (1 mM) and $(C_6H_6)_2Cr$ (20 mM) in THF in the glovebox. The cuvette was sealed with a septum with N_2 flowed through the septum to maintain an O_2-free atmosphere. To this solution, $[Ph_2NH_2]OTf$ was rapidly added via syringe, and the reaction was monitored, collecting a spectrum every 6 seconds.

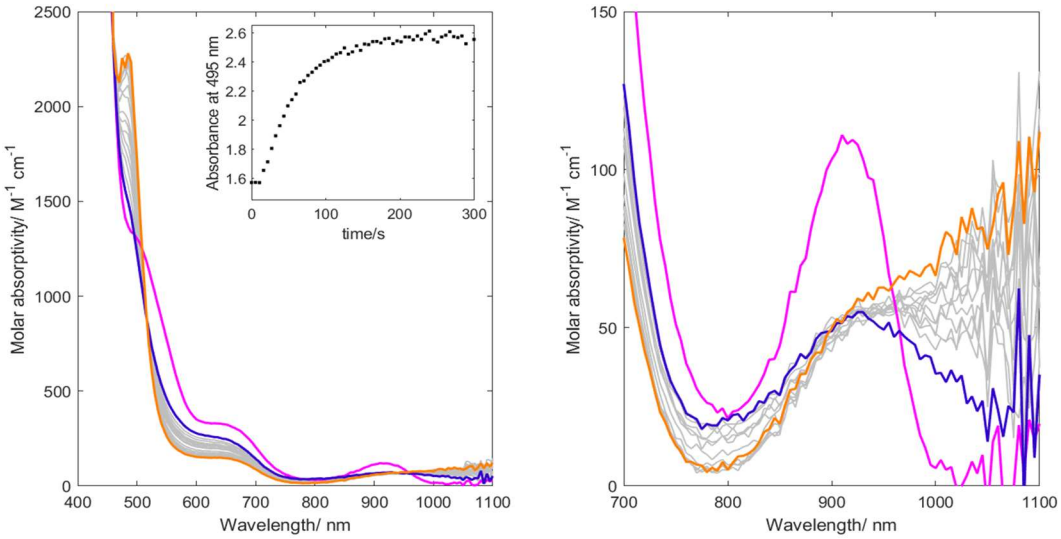

Figure A.20. Inset shows absorbance peak at 495 nm, which has previously been noted as characteristic for [FeOTf]. This peak grew in with a $\tau_{1/2}$ = 40 s. Zoomed out spectrum shows isosbestic point at 510 nm and sharp absorption at 495 nm characteristic of [FeOTf].

A.7.2 General procedure for low-temperature UV-vis spectroscopy (Figure 2.4 B and C)

A 1 cm path length cuvette was loaded with [FeCN] (1 mM) in THF in the glovebox. It was sealed with a septum. It was brought out and allowed to equilibrate at the given temperature for 20 minutes. The temperature was maintained at -80°C, with constant stirring during data collection. The acid was dissolved in 0.5 mL THF and added to the temperature-equilibrated cuvette. This resulted in the immediate formation of $[FeCNH]^+$ (Figure A.21). Then, 2 equivalents of reductant were dissolved in 1 mL THF in the glovebox, brought out of the glovebox, and titrated into the solution via syringe. A spectrum was collected 2 minutes

after each addition of reductant. In the case of $(C_6H_6)_2Cr$ an additional 4 equivalents of reductant were dissolved in an additional 1 mL of solvent to continue the titration. The spectra were plotted against molar absorptivity, adjusting for the change in concentration of [Fe] throughout the titration experiment (Figure 2.4B and C).

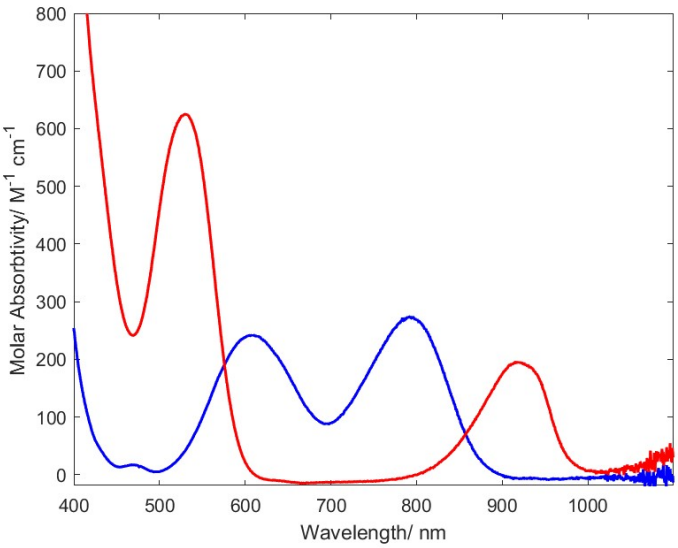

Figure A.21. UV-vis spectrum of starting [FeCN] (red) and after addition of $[Ph_2NH_2]BAr^F{}_4$ (blue) in THF at -80 °C. Features match what has been previously observed for [FeCN] and $[FeCNH]^+$.[1,10]

A.8. Electrochemical measurements

A.8.1 General procedure

Electrochemical measurements were conducted with a glassy carbon working electrode, a platinum wire counter electrode, and Ag/AgOTf (1mM AgOTf in 0.2 M [TBA][OTf]) reference electrode isolated by a CoralPor™ frit (obtained from BASi) and referenced externally to $Fc^{+/0}$. Unless otherwise specified, NaK dried THF was used as solvent, with 0.2 M [TBA]OTf electrolyte. Measurements were conducted with a CH Instruments 600B electrochemical analyzer.

A.8.2 Acid reduction current with different reductants

To test the ability of each reductant to perform the hydrogen evolution reaction, we used electrochemical methods. Beginning the oxidized form of the reductants ([red]BAr^F_4; red = $(C_6H_6)_2Cr$, Cp_2Co, Cp^*_2Cr) for each [red]BAr^F_4 the current associated with reduction is enhanced upon addition of $[Ph_2NH_2]OTf$. The increase in current is proposed to occur due to a catalytic EC mechanism (Figure A.20), with the reduction of [red]BAr^F_4 followed by protonation and hydrogen evolution. The increase in current upon the addition of acid to each reductant becomes a measure of the rate of reaction between the reductant and $[Ph_2NH_2]OTf$, proposed to reflect the rate of background hydrogen evolution during catalysis.

[red]BAr^F_4 (Red = $(C_6H_6)_2Cr$, Cp_2Co, Cp^*_2Cr) was prepared in an analogous way to $[Cp^*_2Co]BAr^F_4$[11] previously. 1 mM solutions were prepared in [TBA]OTf electrolyte (0.2 M) in THF. Acids were added as solids to avoid a change in concentration of [red]BAr^F_4.

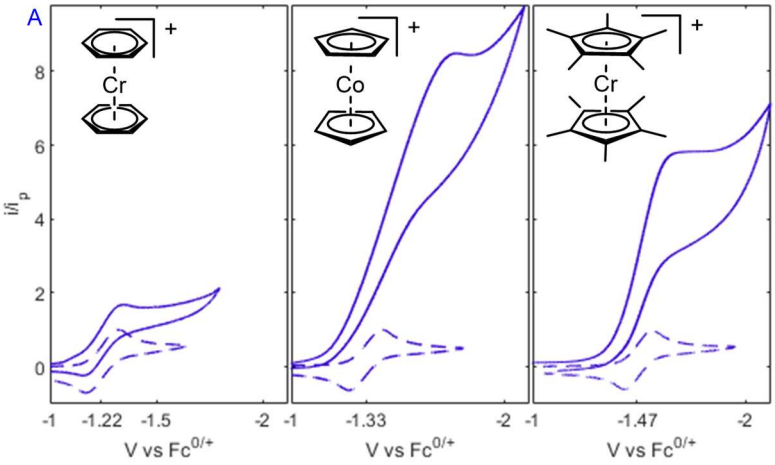

B

Reductant	E° (V vs $Fc^{+/0}$)	i_{cat}/i_p	TON (NH_3)
$(C_6H_6)_2Cr$	-1.22	1.7	27 ± 6
Cp^*_2Cr	-1.47	5.8	13.5 ± 3
Cp_2Co	-1.33	8.5	2.8 ± 0.8

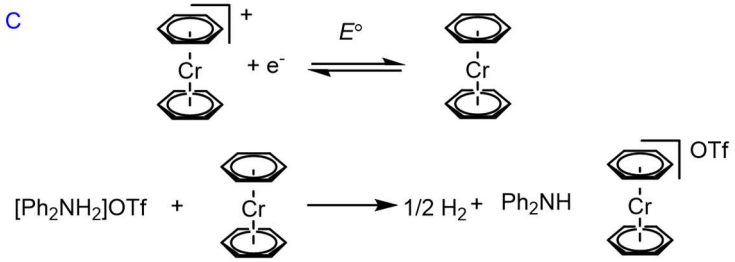

Figure A.22. Proton reduction by chemical reductants as measured by cyclic voltammetry. (A): Cyclic voltammograms of [red]BAr^F_4 (1 mM) in 0.2 M [TBA]OTf, with 0 equiv $[Ph_2NH_2]OTf$ (dashed) and 50 equiv $[Ph_2NH_2]OTf$ (solid lines) (100 mv s^{-1} scan rate). After addition of $[Ph_2NH_2]OTf$ catalytic current is observed, but to a differing extent. The catalytic current measures the rate of reaction between acid and reductants. (B): Comparing the acid free current to the catalytic proton reduction current (i_{cat}/i_p) we find that i_{cat}/i_p correlates inversely to TON (NH_3), with $(C_6H_6)_2Cr > Cp_2Co > Cp^*_2Cr$ being the order of NH_3 TON and $(C_6H_6)_2Cr < Cp_2Co < Cp^*_2Cr$ being the order of i_{cat}/i_p. Interestingly, there is no correlation between i_{cat}/i_p and the reduction potential of the different reductants. (C) Proposed mechanism for electrochemical acid reduction, mediated by [red]BAr^F_4, exemplified for red = $(C_6H_6)_2Cr$.

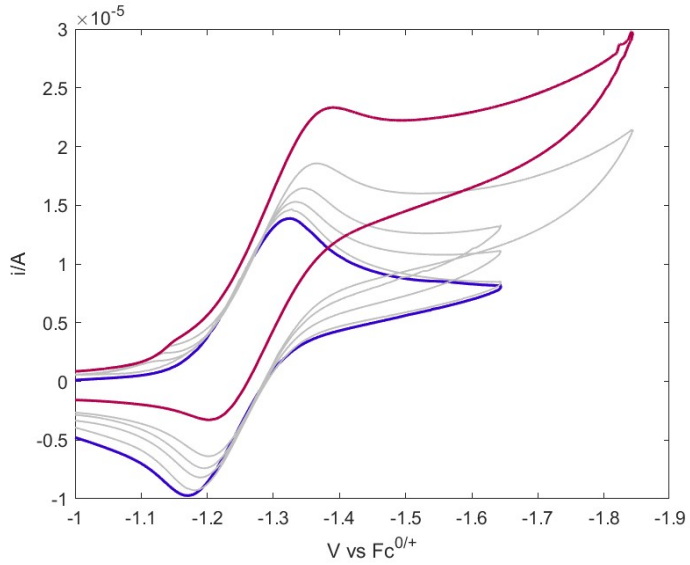

Figure A.23. Cyclic voltammograms of $[(C_6H_6)_2Cr]BAr^F{}_4$ (1 mM, dashed lines) in 0.2 M [TBA]OTf, with increasing $[Ph_2NH_2]OTf$ added from 0 (blue trace) to 50 equiv (red trace) at 100 mV s^{-1} scan rate.

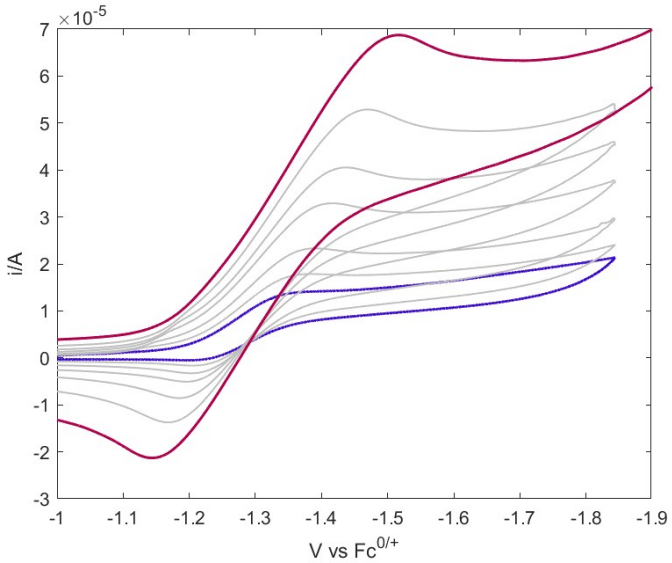

Figure A.24. Cyclic voltammograms of $[(C_6H_6)_2Cr]BAr^F{}_4$ (1 mM, dashed lines) in 0.2 M [TBA]OTf, with 50 equiv $[Ph_2NH_2]OTf$ added, with varying scan rate from 25 (blue trace) to 1600 mv s^{-1} (red trace).

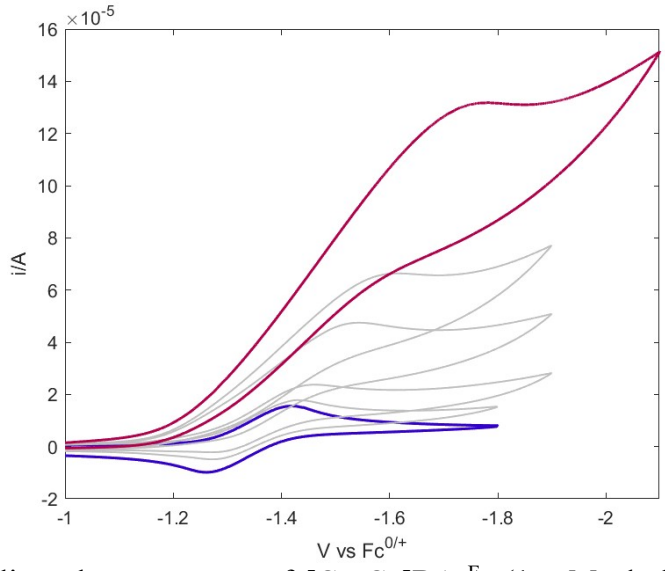

Figure A.25. Cyclic voltammograms of $[Cp_2Co]BAr^F{}_4$ (1 mM, dashed lines) in 0.2 M [TBA]OTf, with increasing $[Ph_2NH_2]$OTf added from 0 (blue trace) to 50 equiv (red trace) at 100 mV s^{-1} scan rate.

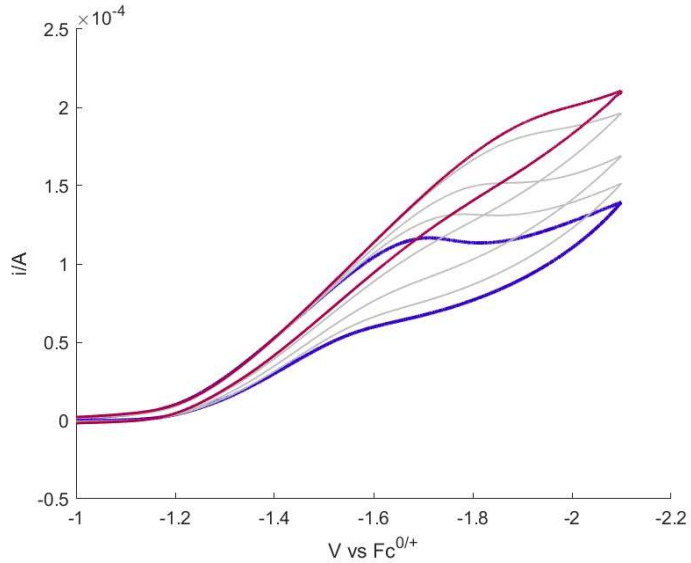

Figure A.26. Cyclic voltammograms of $[Cp_2Co]BAr^F{}_4$ (1 mM, dashed lines) in 0.2 M [TBA]OTf, with 50 equiv $[Ph_2NH_2]$OTf added, with varying scan rate from 50 (blue trace) to 800 mv s^{-1} (red trace).

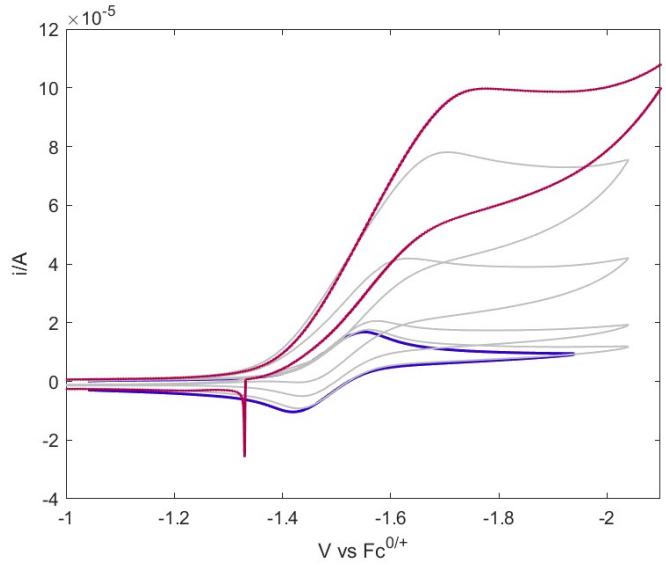

Figure A.27. Cyclic voltammograms of $[Cp^*_2Cr]BAr^F_4$ (1 mM, dashed lines) in 0.2 M [TBA]OTf, with increasing $[Ph_2NH_2]OTf$ added from 0 (blue trace) to 50 equiv (red trace) at 100 mV s^{-1} scan rate.

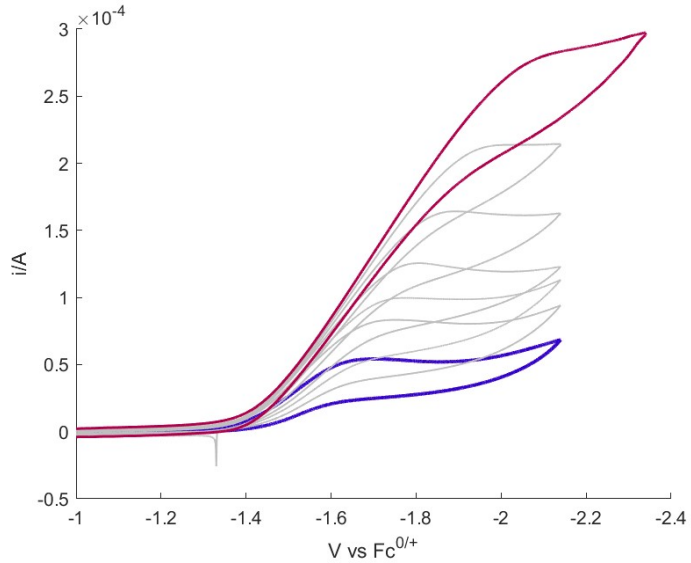

Figure A.28. Cyclic voltammograms of $[Cp^*_2Cr]BAr^F_4$ (1 mM, dashed lines) in 0.2 M [TBA]OTf, with 50 equiv $[Ph_2NH_2]OTf$ added, with varying scan rate from 25 (blue trace) to 1600 mv s^{-1} (red trace).

A.8.3 Electrochemical mechanistic studies with [FeCN]

Studies of the electrochemistry of [FeCN] support that catalysis can occur with weak reductants like $(C_6H_6)_2Cr$. We have previously measured the reduction potential of $[FeCN]^{0/-}$ at E_{red}= –2.07 V vs. $Fc^{+/0}$,[1] which is not accessible using $(C_6H_6)_2Cr$ reductant (E_{ox}= –1.22 V). Upon addition of $[Ph_2NH_2]OTf$ to a solution of $[Fe^{II}CN]$ in THF with 0.2 M $[TBA]PF_6$ electrolyte at 25 °C, we observed that this Fe^{II}/Fe^{I} couple shifts to $E° \approx$ –1.2 V (Figure A.29, inset), close to what has been previously observed for $[FeCNH]^+[BAr^F{}_4]$ (E_{red}= –1.27 V).[1]

Upon closer inspection, this new reductive couple was composed of two features that partially overlap, with current maxima at E_p = –1.15 V and E_p = –1.28 V (Figure A.29)., attributed to $E([FeCNH]^{+/0})$ and $E([FeCNH_2]^{+/0})$, respectively. The irreversibility of the first peak ($E°_{1/2}$= –1.10 V) is attributed to the rapid protonation of electrochemically generated [FeCNH]. The second peak ($E°_{1/2}$= –1.23 V) is irreversible at high acid loadings and slow scan rates (Figure A.30), which is consistent with a multielectron process occurring after the protonation of electrochemically generated $[FeCNH_2]$. Using normalized current $i_{normalized} = i/\sqrt{\nu}$ shows a decrease in current with increasing scan rate, as expected for a catalytic current.

These cyclic voltammetry experiments support our proposed early steps for catalysis. It is worth noting that the measured reduction potential of $[FeCNH_2]^{+/0}$ (−1.23 V) would suggest the formation of an equilibrium of these species when $(C_6H_6)_2Cr$ (−1.22 V) is employed as a reductant, as we observe experimentally (Figure 2.4). Based on this analysis, we cite the $E°([FeCNH_2]^{+/0})$ as ∼−1.2 V in the main text. The electrochemical and chemical reactions, as described, are summarized in **Figure A.31**.

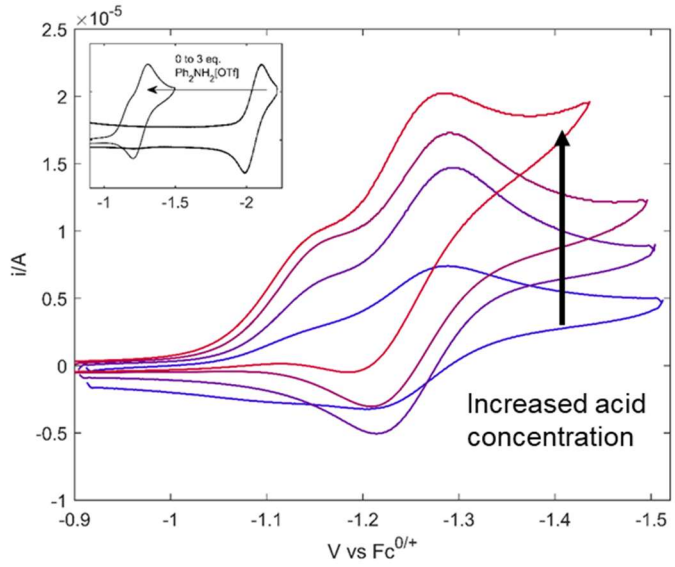

Figure A.29. Cyclic voltammograms monitoring the titration of $[Ph_2NH_2]OTf$ to [FeCN], at 100 mV s^{-1} scan rate: 0 to 3 equiv shown in inset, 3 equiv to 20 equiv shown in main figure.

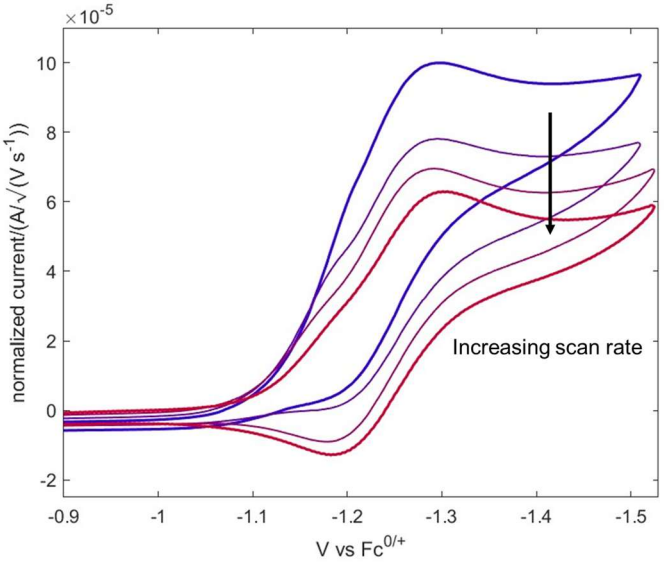

Figure A.30. Cyclic voltammograms monitoring scan rate dependence for [FeCN] reduction in the presence of 20 equiv $[Ph_2NH_2]OTf$ from 10 mV s^{-1} to 75 mV s^{-1}. Normalized current decreases with scan rate as expected for a multielectron process.

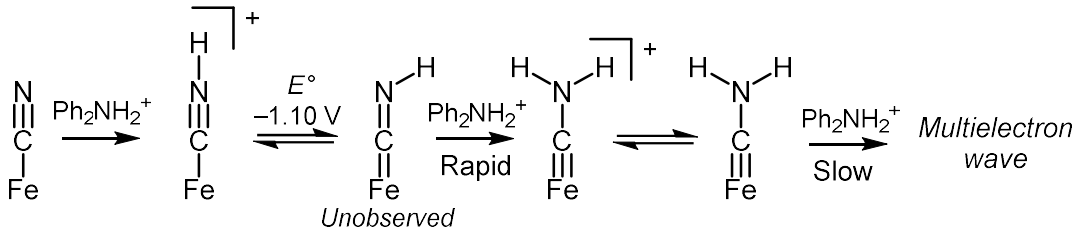

Figure A.31. Proposed scheme for cyclic voltammetry measurements.

A.9. Generation of proposed $[FeC(H)(NMe_2)]^+$

For ease of the reader, ^{1}H-NMR, UV-vis, and ^{57}Fe Mössbauer data associated with the synthesis of the proposed carbene species $[FeC(H)(NMe_2)]^+$ are all collated in section A.9, instead of having the individual spectra in the appropriate spectroscopic sections.

A.9.1 Generation of UV-vis spectrum of $[FeC(H)(NMe_2)]^+$ in the absence of reductant

A cuvette of dilute $[FeCNMe_2]$[1] (1 mM) in THF was prepared in the glovebox and sealed with a septum. It was brought out of the glovebox and cooled to 0 °C, with a positive flow of N_2 supplied with a needle. After equilibration, 5 equiv $[Ph_2NH_2]OTf$ in 0.25 mL THF were added by syringe, and the reaction was monitored. Within 20 minutes, the initial peak at 420 nm had been consumed with new maxima appearing at 585 nm and 790 nm, as well as a feature that grows beyond the detection limit of the spectrometer (1100 nm). The addition of 10 equiv strong base (TBD) resulted in a loss of these new features and restoration of the initial absorbance at 420 nm, diagnostic for $[FeCNMe_2]$.

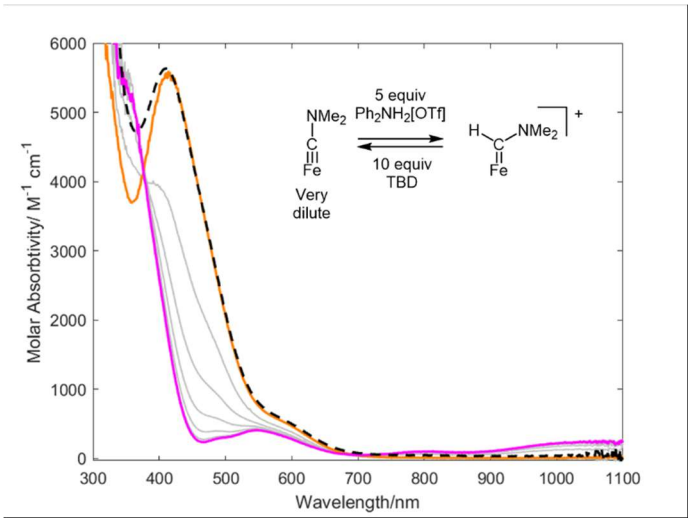

Figure A.32. UV-vis monitoring of reaction of [FeCNMe$_2$] (orange trace) and 5 equiv [Ph$_2$NH$_2$]OTf to form [FeC(H)NMe$_2$] (pink trace). 5 minutes between scans, reaction run at 0 °C. The product was monitored to ensure no further reactivity occurred. Excess TBD was added, and the spectrum rapidly regenerated the initially observed spectra of [FeCNMe$_2$] (Black, dashed trace).

A.9.2 Generation of UV-vis spectrum of [FeC(H)(NMe$_2$)]$^+$ with reductant.

A cuvette of [FeCNMe$_2$][1] (1.5 mM) in THF was prepared in the glovebox and sealed with a septum. It was brought out of the glovebox with a positive flow of N_2 supplied with a needle during UV-vis monitoring. The cuvette was cooled to −20°C, and after equilibration (10 min), 10 equiv [Ph$_2$NH$_2$]OTf in 0.25 mLTHF was added via syringe, followed by 10 equiv (C$_6$H$_6$)$_2$Cr in 0.5 mL THF (also added by syringe). The reaction was monitored, with the absorption maxima at 420 nm associated with [FeCNMe$_2$] consumed with and new maxima growing in at 790 nm, as well as a feature that grows beyond the detection limit of the spectrometer (1100 nm). These new maxima matched the spectra for the proposed [FeC(H)(NMe$_2$)]$^+$ formed from the reaction of [FeCNMe$_2$] with [Ph$_2$NH$_2$]OTf (Figure A.32). High energy transitions were obscured by (C$_6$H$_6$)$_2$Cr$^{0/+}$.

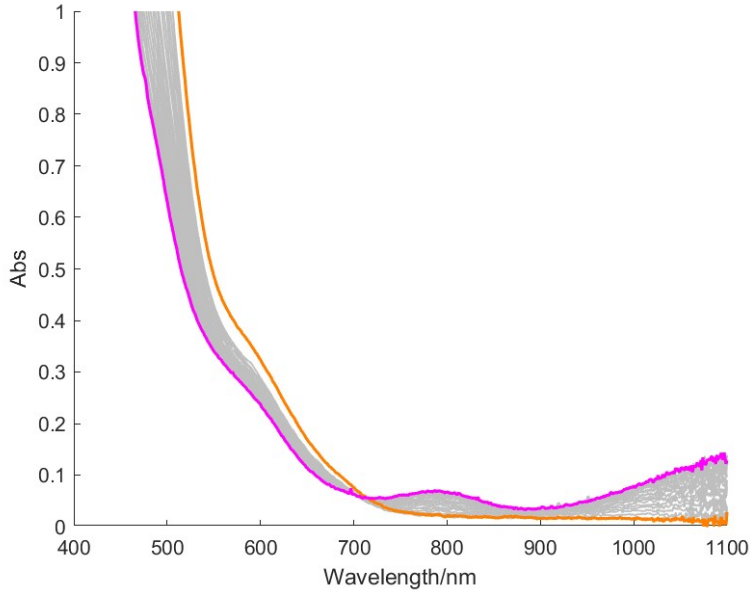

Figure A.33. UV-vis monitoring of reaction of [FeCNMe$_2$] (pink trace) and with 10 equiv [Ph$_2$NH$_2$]OTf and 10 equiv (C$_6$H$_6$)$_2$Cr to form [FeC(H)NMe$_2$]$^+$ (pink trace) at room temperature. 30 seconds between scans.

A.9.3 [FeC(H)(NMe$_2$)]$^+$ generation for NMR experiments

A J. Young NMR tube was loaded with [FeCNMe$_2$] (5 mM) in d_8-THF (0.5 mL) in the glovebox. [Ph$_2$NH$_2$]OTf (25 μmol, 10 equiv) was added as a solid, and ^{1}H NMR was collected. The formation of [FeCNMe$_2$]$^+$, H$_2$ and a new species were observed. Characteristic peaks (that do not overlap with acid or [FeCNMe$_2$]$^+$), for this new species were at 23.4 ppm, 5.08 ppm, -2.00 ppm. Addition of (C$_6$H$_6$)$_2$Cr (25 μmol, 10 equiv) resulted in complete consumption of [FeCNMe$_2$]$^+$ and an increase concentration of the new species. Over time, this species decays to form [FeOTf]. After one week, [FeOTf] was the only major paramagnetic Fe-species left. The contents of the tube were cooled to -78°C and transferred to a Schlenk flask, which was subsequently frozen to 77 K. Once frozen, the flask was opened to air, and KO^{t}Bu was added as a solid. The volatiles were vacuum transferred onto a receiving flask of 3 ml 1 M HCl in Et$_2$O. The receiving flask was thawed, and solvent was removed *in vacuo* to leave a solid precipitate. This was taken up in d_6-DMSO with a known amount of 1,3,5-trimethoxybenzene added, with [Me$_2$NH$_2$]Cl and [Me$_3$NH]Cl both detectable as volatile basic products (Figure A.36).

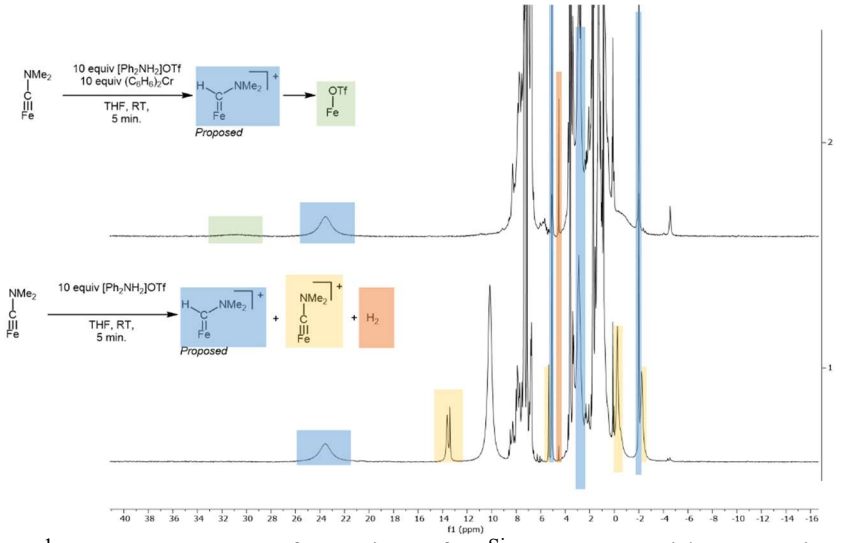

Figure A.34. ^{1}H NMR spectra of reaction of $P_3^{Si}FeCNMe_2$ with 10 equiv $[Ph_2NH_2]OTf$ (top) and reaction of $P_3^{Si}FeCNMe_2$ with 10 equiv $[Ph_2NH_2]OTf$ and 10 equiv $(C_6H_6)_2Cr$ (bottom). Peaks diagnostic for $[FeCNMe_2]^+$,[1] [FeOTf],[8] H_2,[7] and the proposed $[FeC(H)(NMe_2)]^+$ are highlighted.

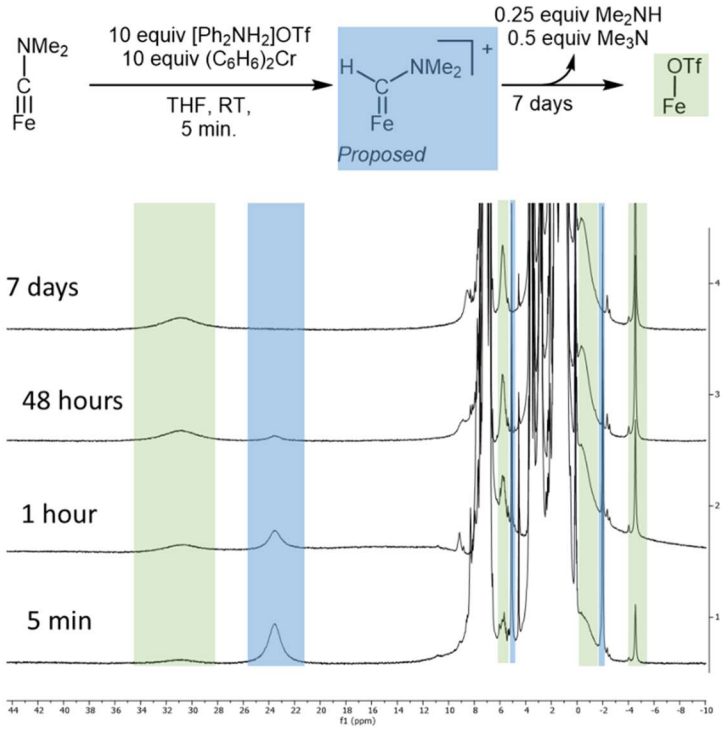

Figure A.35. Reaction of $P_3^{Si}FeCNMe_2$ with 10 equiv $[Ph_2NH_2]OTf$ and 10 equiv $(C_6H_6)_2Cr$ (bottom), monitored overtime. Peaks diagnostic for [FeOTf] and the proposed $[FeCHNMe_2]$ are highlighted.

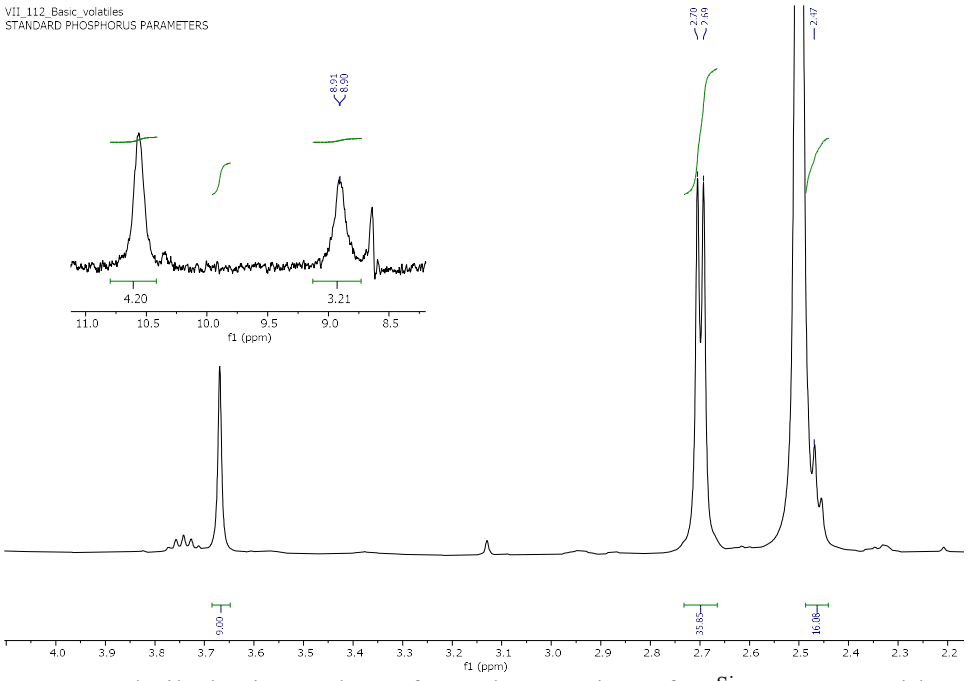

Figure A.36. Volatile basic products from the reaction of $P_3{}^{Si}FeCNMe_2$ with 10 equiv $[Ph_2NH_2]OTf$ and 10 equiv $(C_6H_6)_2Cr$, with $[Me_2NH_2]Cl$ (δ 8.8, br, 2H, δ 2.48, t, J = 6 Hz, 6H) and $[Me_3NH]Cl$ (δ 10.6, br, 2H, δ 2.69, d, J = 5.2 Hz, 9H) products.

A.9.4 Mössbauer experiment

The Mössbauer spectrum of this proposed carbene species ($[FeC(H)(NMe_2)]^+$) was generated by reacting $[FeCNMe_2]$ (25 mg, 35 μmol) with 10 equiv $(C_6H_6)_2Cr$ (72 mg, 350 μmol) and 10 equiv $[Ph_2NH_2]OTf$ (95 mg, 350 μmol) in 0.8 mL THF at room temperature for 5 minutes. The reaction was transferred to a Mössbauer cup and frozen at 77 K.

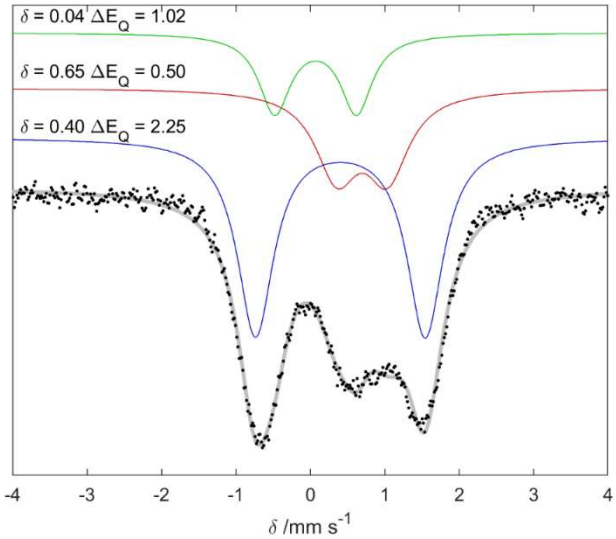

Trace	δ (mm s^{-1})	ΔE_Q (mm s^{-1})	Relative area	Assignment
Blue	0.40±0.01	2.25±0.01	54 %	$[FeC(H)(NMe_2)]^+$
Red	0.65±0.05	0.5±0.1	26%	[FeOTf]
Green	0.04±0.05	1.02±0.1	19 %	$[FeCNMe_2]$

Figure A.37. Mössbauer spectrum of reaction of $P_3{}^{Si}FeCNMe_2$ with 10 equiv each of $(C_6H_6)_2Cr$ and $[Ph_2NH_2]OTf$. The major species (blue) is proposed to be $[FeC(H)(NMe_2)]^+$, with the other species matching previously characterized [FeOTf][10] and $[FeCNMe_2]$.[1]

A.10 Derivation of estimated BDFE for early N−H bonds

To derive the early N−H bond Bond Dissociation Free Energies (BDFE), we have used previously measured values,[10] but with updated C_G constants, which have, since our initial publication, been measured in THF (C_G = 59.9 kcal mol^{-1}),[12] allowing us to derive BDFEs and not only BDEs. For clarity, the thermochemical parameters previously measured are presented again in Table A.5. The BDFEs are derived using these values.

In addition, we derive the $BDFE_{eff}$ for the combination of $(C_6H_6)_2Cr/[Ph_2NH_2]OTf$ used as a reference for the ΔG derived for H^+/e^- addition in Figure 2.7 in the main text.

Table A.5. E_{ox} and pK_a for [FeCNH$_x$] species and $(C_6H_6)_2Cr$ and $[Ph_2NH_2]OTf$ used to derive $BDFE_{N\text{-}H}$ and $BDFE_{eff}$.

Compound	E_{ox} (vs. $Fc^{+/0}$ in THF)	pK_a (in THF)
[FeCN]	−0.38 V	
$[FeCNH]^+$	−0.17 V	5.6
[FeCNH]	−1.27 V	
$[FeCN(Me)H]^+$		7.1
[FeCN(Me)H]	−1.27 V	
[FeCNMe]	−1.31 V	
$(C_6H_6)_2Cr$	−1.22 V	
$[Ph_2NH_2]OTf$		3.2

Estimation of the N–H BDFE of $[FeCNH]^+$:
$[FeCNH]^+ \rightleftharpoons [FeCN] + H^+$ $1.37(pK_a([FeCNH]^+)) = 7.7$ kcal mol^{-1}
$[FeCN] \rightleftharpoons [FeCN]^+ + e^-$ $23.06(E_{ox}([FeCN])) = -8.8$ kcal mol^{-1}
$H^+ + e^- \rightleftharpoons H^\bullet$ $C_G = 59.9$ kcal mol^{-1}
$[FeCNH]^+ \rightleftharpoons [FeCN]^+ + H^\bullet$ $BDFE_{N-H}([FeCNH]^+) = 58.8$ kcal mol^{-1}

Estimation of the N–H BDFE of [FeCNH]:
$[FeCNH] \rightleftharpoons [FeCNH]^+ + e^-$ $23.06(E_{ox}([FeCN])) = -29.3$ kcal mol^{-1}
$[FeCNH]^+ \rightleftharpoons [FeCN] + H^+$ $1.37(pK_a([FeCNH]^+)) = 7.7$ kcal mol^{-1}
$H^+ + e^- \rightleftharpoons H^\bullet$ $C_G = 59.9$ kcal mol^{-1}
$[FeCNH] \rightleftharpoons [FeCN] + H^\bullet$ $BDFE_{N-H}([FeCNH]) = 38.3$ kcal mol^{-1}

Estimation of the N–H BDFE of $[FeCN(Me)H]^+$:
$[FeCN(Me)H]^+ \rightleftharpoons [FeCNMe] + H^+$ $1.37(pK_a([FeCN(Me)H]^+)) = 9.7$ kcal mol^{-1}
$[FeCNMe] \rightleftharpoons [FeCNMe]^+ + e^-$ $23.06(E_{ox}([FeCNMe])) = -30.2$ kcal mol^{-1}
$H^+ + e^- \rightleftharpoons H^\bullet$ $C_G = 59.9$ kcal mol^{-1}
$[FeCN(Me)H]^+ \rightleftharpoons [FeCNMe]^+ + H^\bullet$ $BDFE_{N-H}([FeCN(Me)H]^+) = 39.4$ kcal mol^{-1}
Estimation of the N–H BDFE of [FeCN(Me)H]:
$[FeCN(Me)H] \rightleftharpoons [FeCN(Me)H]^+ + e^-$ $23.06(E_{ox}([FeCN(Me)H])) = -29.3$ kcal mol^{-1}
$[FeCN(Me)H]^+ \rightleftharpoons [FeCNMe] + H^+$ $1.37(pK_a([FeCN(Me)H]^+)) = 9.7$ kcal mol^{-1}
$H^+ + e^- \rightleftharpoons H^\bullet$ $C_G = 59.9$ kcal mol^{-1}
$[FeCN(Me)H] \rightleftharpoons [FeCNMe] + H^\bullet$ $BDFE_{N-H}([FeCN(Me)H]) = 40.3$ kcal mol^{-1}

Estimation of the $BDFE_{eff}$ of $(C_6H_6)_2Cr/[Ph_2NH_2]OTf$:
$(C_6H_6)_2Cr \rightleftharpoons (C_6H_6)_2Cr^+ + e^-$ $23.06(E_{ox}((C_6H_6)_2Cr)) = -28.1$ kcal mol^{-1}
$[Ph_2NH_2]^+ \rightleftharpoons [Ph_2NH] + H^+$ $1.37(pK_a([Ph_2NH_2]^+)) = 4.4$ kcal mol^{-1}
$H^+ + e^- \rightleftharpoons H^\bullet$ $C_G = 59.9$ kcal mol^{-1}
$(C_6H_6)_2Cr/[Ph_2NH_2]OTf \rightleftharpoons [(C_6H_6)_2Cr]OTf/Ph_2NH + H^\bullet$ $BDFE_{eff} = 36.2$ kcal mol^{-1}

A.11 Computational Methods

A.11.1 General overview of computational details

As stated in the main text for our computational studies, we employed the TPSS functional[13] and a def2-TZVP basis set on transition metals and a def2-SVP basis set on all other atoms,[14] which we have previously demonstrated accurately replicate BDFEs on similar platforms.[15] The ORCA open-source software package was used.[16]

The numerical frequencies of the minimized structures were calculated to ensure that these structures represented local minima and not saddle points. Entropic and internal energy contributions were calculated at 195 K, 253 K, 273 K, and 293 K to compute the ΔG_f at these temperatures.

For the analysis in Figure 2.6, a comparison of the lowest energy isomers is presented in Tables A.6, A.7, and A.8. Key bond lengths and their comparison to relevant crystallographic data are presented in Table A.9. For the analysis in Figure 2.7, the energy of each pathway is presented in Figures A.38 and A.39. The final step(s) to convert the final intermediate in pathways *i-iii* (as defined in Figure 2.7) to an on-path species $[FeCNH]^{+/0}$ is presented in Figure A.39. The calculations to derive the ΔG in Figure 2.7 and Figure A.38, A.39 are summarized in Tables A.10-A.14.

A.11.2 Treatment of H•

The treatment of $S(H^{\bullet})$ in calculations can be a source of systematic error in DFT calculations, therefore it is useful to detail how this value has been derived. We have taken an *ab initio* approach to $S(H^{\bullet})$ using the !PRINTTHERMOCHEM function in ORCA 5.0[17] to calculate the translational entropy and internal energy of H• at temperatures 195 K, 253 K, 273 K, and 293 K. These values are used directly to derive the $\Delta G_f(H^{\bullet})$ values as presented in Table A.9.

A.11.3 Calculating Δ*G* for bond formations in Figure 2.7

In the analysis of step g in Figure 2.7, we use the computations presented in Figures A.38-A.39 and Tables A.10-A.14 to guide the discussion. However, for clarity for bond formation steps, we reference these H-atom transfers from the addition of H^+ from

$[Ph_2NH_2]OTf$ and e^- from $(C_6H_6)_2Cr$ to the $BDFE_{eff}$ of this reagent combination, derived in section A.10 to be 36.2 kcal mol^{-1}.

For example, for the addition of an H-atom to $[FeC(H)(NH_2)]^+$ to $[FeC(H)(NH_3)]^+$, the $BDFE_{N\text{-}H}$ of this bond is 14 kcal mol^{-1} (Table A.11). The ΔG, as reported in Figure 2.7 and Figures A.38-A.39, is then given as $\Delta G = BDFE_{eff} - BDFE_{N-H} = 36\text{-}14 = +22$ kcal mol^{-1}.

Table A1.6. Table of experimental[10] and computationally derived bond dissociation free energies and comparison to relevant experimental values.

	$BDFE_{195K}$ (kcal mol^{-1})	$BDFE_{253K}$ (kcal mol^{-1})	$BDFE_{273K}$ (kcal mol^{-1})	$BDFE_{298K}$ (kcal mol^{-1})	$BDFE_{298\ K,\ exp}$ (kcal mol^{-1})
$P_3^{Si}FeCNH_2^+ \rightarrow P_3^{Si}FeCNH^+ + H^\bullet$	42	40	39	38	
$P_3^{Si}FeCHNH_2^+ \rightarrow P_3^{Si}FeCNH^+_2 + H^\bullet$	55	53	53	52	
$P_3^{Si}FeCHNH_2 \rightarrow P_3^{Si}FeCNH_2 + H^\bullet$	49	48	47	47	
$P_3^{Si}FeCNH_2 \rightarrow P_3^{Si}FeCNH + H^\bullet$	38	36	35	35	
$P_3^{Si}FeCN(Me)H^+ \rightarrow P_3^{Si}FeCNMe^+ + H^\bullet$					41
$P_3^{Si}FeCN(Me)H \rightarrow P_3^{Si}FeCNMe + H^\bullet$					40

Table A.7. Computationally derived free energies of intermediates of ($P_3^{Si}FeCNH_2 + H^\bullet$).

Compound	Spin state	$\Delta G_{f,195}$ (Eh)	$\Delta G_{f,253}$ (Eh)	$\Delta G_{f,273}$ (Eh)	$\Delta G_{f,298}$ (Eh)	$\Delta G_{rel,195}$ (kcal mol^{-1})	$\Delta G_{rel,253}$ (kcal mol^{-1})	$\Delta G_{rel,273}$ (kcal mol^{-1})	$\Delta G_{rel,298}$ (kcal mol^{-1})
$P_3^{Si}Fe(CNH_3)^+$ species									
$P_3^{Si}FeC(H)(NH_2)^+$	triplet	-4076.57	-4076.59	-4076.59	-4076.60	0.0	0.0	0.0	0.0
$P_3^{Si}FeC(H)(NH_2)^+$	singlet	-4076.55	-4076.57	-4076.58	-4076.59	9.3	9.5	9.6	9.7
$P_3^{Si}FeC(H)(NH_2)^+$	quintet	-4076.51	-4076.53	-4076.53	-4076.54	39.1	38.7	38.6	38.4
$P_3^{Si}FeCNH_3^+$	singlet	-4076.50	-4076.51	-4076.52	-4076.53	45.1	45.6	45.7	46.0
$P_3^{Si}FeCNH_3^+$	triplet	-4076.46	-4076.48	-4076.49	-4076.50	65.5	65.7	65.8	65.9
$P_3^{Si}Fe(H)CNH_2^+$	singlet	-4076.56	-4076.57	-4076.58	-4076.59	6.9	7.7	7.8	8.0
$P_3^{Si}FeC^+$	singlet	-4019.92	-4019.94	-4019.94	-4019.95	-	-	-	-
$P_3^{Si}FeC^+ + NH_3$	singlet	-4076.48	-4076.51	-4076.51	-4076.52	53.3	51.2	50.5	49.6
$P_3^{Si}Fe(CNH_3)$ species									
$P_3^{Si}FeC(H)(NH_2)$	doublet	-4076.73	-4076.75	-4076.75	-4076.76	0.0	0.0	0.0	0.0
$P_3^{Si}FeC(H)(NH_2)$	quartet	-4076.68	-4076.70	-4076.71	-4076.72	28.6	28.4	28.4	28.3
$P_3^{Si}FeCNH_3$	doublet	-4076.62	-4076.64	-4076.65	-4076.66	66.1	66.0	66.0	65.9
$P_3^{Si}Fe(H)CNH_2$	doublet	-4076.70	-4076.72	-4076.72	-4076.73	18.5	19.1	19.1	19.0
$P_3^{Si}FeC$	doublet	-4020.10	-4020.12	-4020.13	-4020.14	-	-	-	-
$P_3^{Si}FeC + NH_3$	doublet	-4076.67	-4076.69	-4076.70	-4076.71	39.2	36.9	36.0	35.0

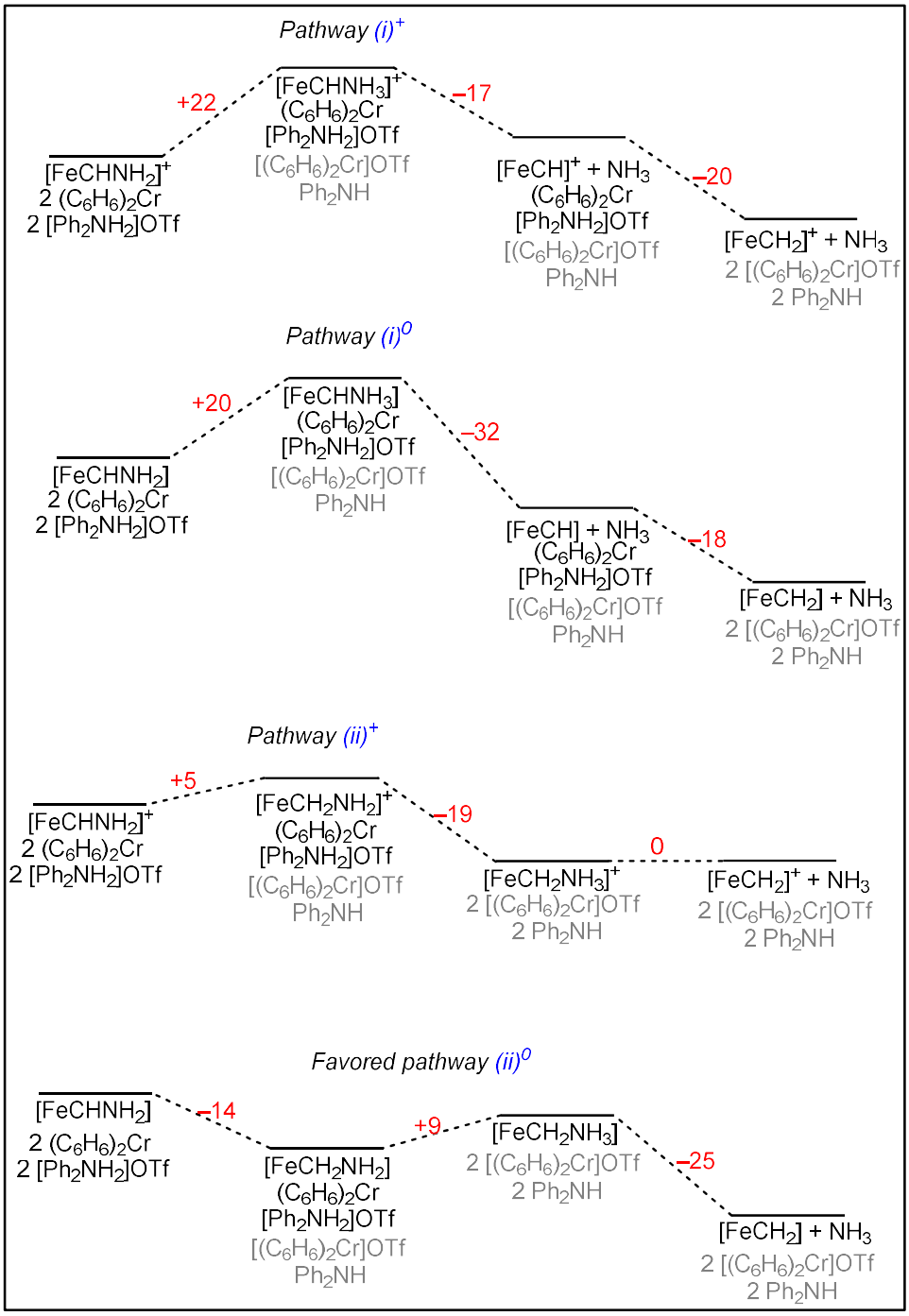

Figure A.38. Thermodynamic barriers for CH_4 and NH_3 selective pathways *i-ii*.

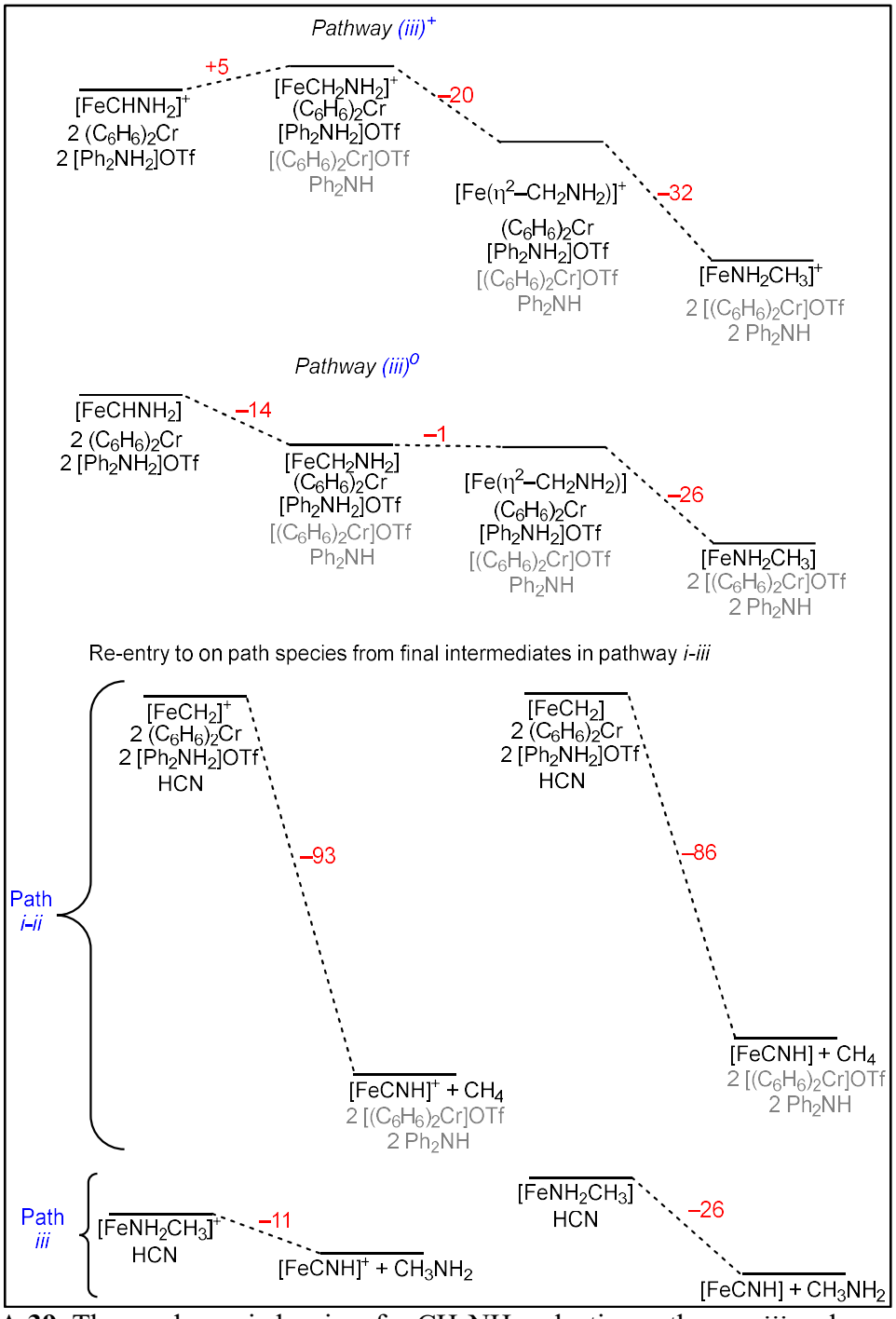

Figure A.39. Thermodynamic barriers for CH_3NH_2 selective pathways *iii* and thermodynamic barriers for release of substrate, and rebinding of CN^-.

Table A.18. Computationally derived free energies of early intermediates of $P_3^{Si}FeCN$ reduction.

Compound	Spin state	$\Delta G_{f,195}$ (Eh)	$\Delta G_{f,253}$ (Eh)	$\Delta G_{f,273}$ (Eh)	$\Delta G_{f,298}$ (Eh)
$P_3^{Si}FeCNH^+$	triplet	-4075.40	-4075.42	-4075.43	-4075.44
$P_3^{Si}FeCNH$	doublet	-4075.58	-4075.60	-4075.60	-4075.61
$P_3^{Si}FeCNH_2^+$	doublet	-4075.98	-4075.99	-4076.00	-4076.01
$P_3^{Si}FeCNH_2$	singlet	-4076.14	-4076.16	-4076.17	-4076.18

Table A.9. Experimentally[1,8,10] and computationally derived key bond lengths and comparison with known crystallographic data.

In general, the Fe−P and Fe−Si bonds are very reliably reproduced computationally. Increased error is observed in the C−N bond. This is likely partially attributable to the use of methylated analogs (due to the instability of the compounds) and the hydrogen bonds formed to N−H in $P_3^{Si}FeCNH^+$ and $P_3^{Si}FeCNH_2^+$. The Fe−C bond length is consistently overestimated by about 0.05 Å by DFT.

Compound		C−N (Å)	Fe−C (Å)	Fe−P_{ave} (Å)	Fe−Si (Å)	<Fe−C−N
$P_3^{Si}FeCNH^+$	Computed	1.186	1.857	2.368	2.331	177.1
$P_3^{Si}FeCNH^+$	Crystal.	1.144	1.913	2.384	2.305	178.4
$P_3^{Si}FeCNH$	Computed	1.228	1.774	2.266	2.289	175.6
$P_3^{Si}FeCNMe$	Crystal	1.186	1.821	2.273	2.273	177.6
$P_3^{Si}FeCNH_2^+$	Computed	1.317	1.684	2.316	2.358	176.5
$P_3^{Si}FeCNH_2^+$	Crystal	1.223	1.799	2.314	2.311	174.2
$P_3^{Si}FeCNMe_2^+$	Crystal	1.310	1.736	2.364	2.358	173.8
$P_3^{Si}FeCNH_2$	Computed	1.337	1.675	2.214	2.310	179.1
$P_3^{Si}FeCNMe_2$	Crystal	1.328	1.710	2.230	2.305	177.8
$P_3^{Si}FeCH^+$	Computed		1.65	2.30	2.38	
$P_3^{Si}FeCMe^+$	Crystal	-	1.70	2.34	2.39	-
$P_3^{Si}FeCH$	Computed		1.65	2.21	2.32	
$P_3^{Si}FeCMe$	Crystal	-	1.67	2.25	2.33	-

Table A.10. Computationally derived energies of small molecules relevant to calculations.

Compound	Spin state	$\Delta G_{f,195}$ (Eh)	$\Delta G_{f,253}$ (Eh)	$\Delta G_{f,273}$ (Eh)	$\Delta G_{f,298}$ (Eh)
HCN	singlet	-93.47	-93.48	-93.48	-93.48
$MeNH_2$	singlet	-95.86	-95.87	-95.87	-95.87
CH_4	singlet	-40.51	-40.51	-40.51	-40.51
NH_3	singlet	-56.57	-56.57	-56.57	-56.57
H•	doublet	-0.5062	-0.5086	-0.5094	-0.5105

Table A.11. Table of computationally derived energies of isomers and spin states of $P_3{}^{Si}Fe(CNH_4)$. Values derived here are used in Figures 2.7, A.37, and A.38.

Compound	Spin state	$\Delta G_{f,195}$ (Eh)	$\Delta G_{f,253}$ (Eh)	$\Delta G_{f,273}$ (Eh)	$\Delta G_{f,298}$ (Eh)	$\Delta G_{rel,195}$ (kcal mol^{-1})	$\Delta G_{rel,253}$ (kcal mol^{-1})	$\Delta G_{rel,273}$ (kcal mol^{-1})	$\Delta G_{rel,298}$ (kcal mol^{-1})
$P_3{}^{Si}FeCHNH_2{}^+ + H\cdot$	-	-4077.07	-4077.10	-4077.10	-4077.11	0	0	0	0
$P_3{}^{Si}FeCHNH_3{}^+$	doublet	-4077.10	-4077.12	-4077.13	-4077.14	-17	-15	-14	-14
$P_3{}^{Si}FeCH^+$	doublet	-4020.55	-4020.57	-4020.58	-4020.59	-	-	-	-
$P_3{}^{Si}FeCH^+ + NH_3$	doublet	-4077.12	-4077.14	-4077.15	-4077.16	-29	-30	-30	-30
$P_3{}^{Si}FeCH_2NH_2{}^+$	quartet	-4077.13	-4077.15	-4077.15	-4077.16	-34	-32	-32	-31
$P_3{}^{Si}Fe(\eta^2\text{-}CH_2NH_2)^+$	doublet	-4077.16	-4077.18	-4077.19	-4077.20	-54	-52	-52	-51

Table A.12. Table of computationally derived energies of isomers and spin states of $P_3{}^{Si}Fe(CNH_4)$. Values derived here are used in Figures 2.7, A.37, and A.38.

Compound	Spin state	$\Delta G_{f,195}$ (Eh)	$\Delta G_{f,253}$ (Eh)	$\Delta G_{f,273}$ (Eh)	$\Delta G_{f,298}$ (Eh)	$\Delta G_{rel,195}$ (kcal mol^{-1})	$\Delta G_{rel,253}$ (kcal mol^{-1})	$\Delta G_{rel,273}$ (kcal mol^{-1})	$\Delta G_{rel,298}$ (kcal mol^{-1})
$P_3{}^{Si}FeCHNH_2 + H\cdot$		-4077.24	-4077.26	-4077.26	-4077.27	0	0	0	0
$P_3{}^{Si}FeCHNH_3$ constrained	singlet	-4077.26	-4077.28	-4077.29	-4077.30	-17	-17	-16	-16
$P_3{}^{Si}FeCH$	singlet	-4020.74	-4020.76	-4020.77	-4020.78	-	-	-	-
$P_3{}^{Si}FeCH + NH_3$	singlet	-4077.31	-4077.33	-4077.34	-4077.35	-47	-48	-48	-48
$P_3{}^{Si}FeCH_2NH_2$	triplet	-4077.32	-4077.34	-4077.34	-4077.35	-52	-51	-50	-50
$P_3{}^{Si}Fe(\eta^2\text{-}CH_2NH_2)$	singlet	-4077.32	-4077.34	-4077.35	-4077.36	-54	-52	-52	-51

Table A.13. Table of computationally derived energies of isomers and spin states of $P_3^{Si}Fe(CNH_5)^+$. Values derived here are used in Figures 2.7, A.37, and A.38.

Compound	Spin state	$\Delta G_{f,195}$ (Eh)	$\Delta G_{f,253}$ (Eh)	$\Delta G_{f,273}$ (Eh)	$\Delta G_{f,298}$ (Eh)	$\Delta G_{rel,195}$ (kcal mol^{-1})	$\Delta G_{rel,253}$ (kcal mol^{-1})	$\Delta G_{rel,273}$ (kcal mol^{-1})	$\Delta G_{rel,298}$ (kcal mol^{-1})
$P_3^{Si}Fe(\eta^2\text{-}CH_2NH_2)^+ + H.$		-4077.67	-4077.69	-4077.70	-4077.71	0	0	0	0
$P_3^{Si}FeCH_2NH_3^+$	triplet	-4077.73	-4077.75	-4077.75	-4077.76	-37	-36	-36	-35
$P_3^{Si}FeCH_2^+$	triplet	-4021.16	-4021.17	-4021.18	-4021.19	-	-	-	
$P_3^{Si}FeCH_2^+$	singlet	-4021.15	-4021.17	-4021.18	-4021.19	-	-	-	
$P_3^{Si}FeCH_2^+ + NH_3$	triplet	-4077.72	-4077.74	-4077.75	-4077.76	-34	-35	-35	-36
$P_3^{Si}FeNH_2CH_3^+$	triplet	-4077.78	-4077.80	-4077.80	-4077.81	-70	-69	-68	-68

Table A.14. Table of computationally derived energies of isomers and spin states of $P_3^{Si}Fe(CNH_5)$. Values derived here are used in Figures 2.7, A.37, and A.38.

Compound	Spin state	$\Delta G_{f,195}$ (Eh)	$\Delta G_{f,253}$ (Eh)	$\Delta G_{f,273}$ (Eh)	$\Delta G_{f,298}$ (Eh)	$\Delta G_{rel,195}$ (kcal mol^{-1})	$\Delta G_{rel,253}$ (kcal mol^{-1})	$\Delta G_{rel,273}$ (kcal mol^{-1})	$\Delta G_{rel,298}$ (kcal mol^{-1})
$P_3^{Si}Fe(\eta^2\text{-}CH_2NH_2) + H.$		-4077.83	-4077.85	-4077.86	-4077.87	0	0	0	0
$P_3^{Si}FeCH_2NH_3$	doublet	-4077.87	-4077.89	-4077.90	-4077.91	-28	-27	-27	-26
$P_3^{Si}FeCH_2$	doublet	-4021.34	-4021.36	-4021.37	-4021.38	-	-	-	
$P_3^{Si}FeCH_2 + NH_3$	doublet	-4077.91	-4077.93	-4077.94	-4077.95	-50	-51	-51	-52
$P_3^{Si}FeNH_2CH_3$	doublet	-4077.93	-4077.95	-4077.96	-4077.97	-64	-63	-63	-62

A.12 References for Appendix A

1. Rittle, J.; Peters, J. C. *Angew. Chem. Int. Ed.* **2016**. 55, 12262–12265.
2. Anderson, J. S.; Moret, M.-E.; Peters, J. C. *J. Am. Chem. Soc.* **2013**. 135, 534–537.
3. Betley, T. A.; Peters, J. C. *J. Am. Chem. Soc.* **2004**, 126, 6252–6254.
4. Chalkley, M. J.; Del Castillo, T. J.; Matson, B. D.; Roddy, J. P.; Peters, J. C. *ACS Cent. Sci.* **2017**, 3, 217–223. .
5. Del Castillo, T. J.; Thompson, N. B.; Peters, J. C. *J. Am. Chem. Soc.* **2016**, 138, 5341–5350.
6. Erhardt, S.; Grushin, V. V.; Kilpatrick, A. H.; Macgregor, S. A.; Marshall, W. J.; Roe, D. C. *J. Am. Chem. Soc.* **2008**, 130, 4828–4845.
7. Fulmer, G. R.; Miller, A. J. M.; Sherden, N. H.; Gottlieb, H. E.; Nudelman, A.; Stoltz, B. M.; Bercaw, J. E.; Goldberg, K. I. *Organometallics* **2010**, 29, 2176–2179.

8. Citek, C.; Oyala, P. H.; Peters, J. C. *J. Am. Chem. Soc.* **2019**, 141, 15211–15221.
9. Lee, Y.; Kinney, R. A.; Hoffman, B. M.; Peters, J. C. *J. Am. Chem. Soc.* **2011**, 133, 16366–16369.
10. Rittle, J.; Peters, J. C. *J. Am. Chem. Soc.* **2017**, 139, 3161–3170.
11. Chalkley, M. J.; Del Castillo, T. J.; Matson, B. D.; Peters, J. C. *J. Am. Chem. Soc.* **2018**, 140, 6122–6129. .
12. Agarwal, R. G.; Coste, S. C.; Groff, B. D.; Heuer, A. M.; Noh, H.; Parada, G. A.; Wise, C. F.; Nichols, E. M.; Warren, J. J.; Mayer, J. M. *Chem. Rev.* **2022**, 122, 1–49.
13. Tao, J.; Perdew, J. P.; Staroverov, V. N.; Scuseria, G. E. *Phys. Rev. Lett.* **2003**, 91, 146401–146404.
14. Weigend, F. *Phys. Chem. Chem. Phys.* **2006**, 8, 1057–1065.
15. Matson, B. D.; Peters, J. C. *ACS Catal.* **2018**, 8, 1448–1455.
16. Neese, F.; Wennmohs, F.; Becker, U.; Riplinger, C. *J. Chem. Phys.* **2020**, 152, 224108.
17. *Thermodynamics — ORCA tutorials 5.0 documentation*. orcasoftware.de/tutorials_orca/prop/thermo.html (accessed 2023-10-22).

Appendix B

Supplementary Information for Chapter 3

B.1 Materials and Methods

B.1.1 General Considerations

All manipulations were carried out using standard Schlenk or glovebox techniques under an N_2 atmosphere. Solvents were deoxygenated and dried by thoroughly sparging with N_2, followed by passage through an activated alumina column in a solvent purification system by SG Water, USA LLC. Nonhalogenated solvents were tested with sodium benzophenone ketyl in tetrahydrofuran (THF) to confirm the absence of oxygen and water. Deuterated solvents were purchased from Cambridge Isotope Laboratories, Inc., degassed, and dried over activated 3-Å molecular sieves prior to use. [FeCN],[1] [$FeCNH_2$]$BAr^F{}_4$,[1] [FeCN][Na(12-c-4)$_2$],[1] [FeCNH]$BAr^F{}_4$,[1] [FeCNMe],[2] [$H(OEt_2)_2$]$BAr^F{}_4$,[3] $^{Me4}Cp_2Co$,[4] and triflate acids ([AH]OTf)[5] and [$BAr^F{}_4$] acids ([AH]$BAr^F{}_4$)[6] were synthesized using literature methods. $(C_6H_6)_2Cr$, Cp^*_2Cr and Cp_2Co, Cp_2Cr, Cp^*_2Co, $^{Et}Cp_2Co$ were purchased from Strem and used without further purification. All bases were purchased from Sigma and purified before use, liquid bases (aniline, lutidine, collidine, pyrrolidine, triethylamine, tetramethylguanidine) were distilled, solid anilines (2-chloroaniline, 4-chloroaniline and diphenylamine) were sublimed and triazabicyclodecene was recrystallized from by cooling a saturated Et_2O solution to -35°C and decanting.

B.1.2 Physical Methods

NMR: Nuclear Magnetic Resonance (NMR) measurements were recorded with a Varian 400 MHz spectrometer. ^{1}H NMR chemical shifts are reported in ppm relative to tetramethylsilane, using ^{1}H resonances from residual solvent as internal standards.[7]

UV-Vis: Ultraviolet-visible (UV-vis) absorption spectroscopy measurements were collected with a Cary 50 UV-vis spectrophotometer using a 1 cm path length quartz cuvette. All samples had a blank sample background subtraction applied. Temperature regulation for UV-Vis measurements was carried out with a Unisoku cryostat. Time course UV-Vis spectra were collected with the Scanning Kinetics application of the Cary WinUV software.

Mössbauer spectra: Mössbauer spectra were recorded on a spectrometer from SEE Co. (Edina, MN) operating in the constant acceleration mode in a transmission

geometry. The sample was kept in an SVT-400 cryostat form Janis (Wilmington, MA). The quoted isomer shifts are relative to the centroid of the spectrum of a metallic foil of α-Fe at room temperature (RT). Solution samples were transferred to a sample cup, freeze-quenched with liquid nitrogen inside the glovebox, and then immersed in liquid N_2 until mounted in the cryostat. Data analysis was performed using version 4 of the program WMOSS (www.wmoss.org) and quadrupole doublets were fit to Lorentzian lineshapes.

EPR Spectroscopy: X-band EPR spectra were obtained on a Bruker EMX spectrometer. Samples were collected at powers of 2 mW with modulation amplitudes of 4.00 G, modulation frequencies of 100.00 kHz, over a range of 1800 to 4500 Gauss. Spectra were baseline corrected. EPR spectra were modeled using the easyspin program.[8]

IR Spectroscopy: Infrared measurements were obtained on a Bruker Alpha spectrometer equipped with a diamond ATR probe (solid state) or in the liquid state in a cell with KBr windows.

X-Ray Crystallography: XRD studies were carried out at the Beckman Institute Crystallography Facility on a Brüker Kappa Apex II diffractometer (Mo Kα radiation). Structures were solved using SHELXS or SHELXT and refined against F2 on all data by full-matrix least squares with SHELXL. The crystals were mounted on a glass fiber under Paratone N oil.

B.2 Experimental procedures

B.2.1 Direct generation of $[FeCN\cdots HTBD]^0$

To confirm the assignment of the reaction of [FeCN] + Cp^*_2Co + $[TBDH]BAr^F_4$ as an H-bonded adduct, $[FeCN\cdots HTBD]^0$ we developed the direct synthesis of this species.

A solution of $[FeCN][Na(12\text{-}c\text{-}4)_2]$ (20 mg, 19 μmol) in 1 mL THF was cooled to −78°C and [TBDH]OTf (5.5 mg, 19 μmol) in 0.5 mL was added dropwise. The solution was allowed to stir for 30 minutes, after which it was filtered into and layered with pentane. All operations were done in the cold-well using pre-cooled glassware and solvent. Upon storage at −35°C overnight, dark orange crystals formed. However, substantial amounts of a red

complex (assumed [FeCN]) were also observed. Still, crystals sufficient for XRD could be selected, allowing crystallographic analysis.

B.2.2 Stepwise generation of [FeCNH$_2$]

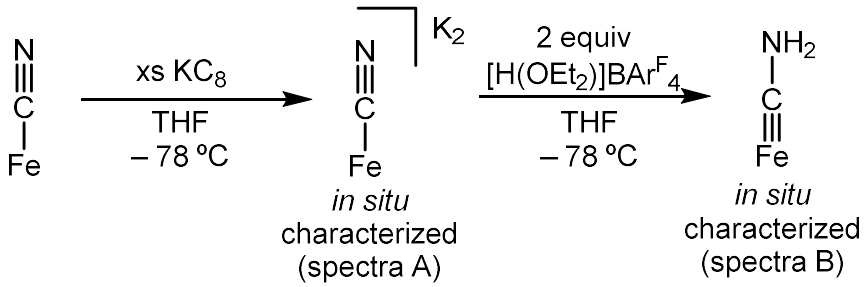

B.2.2.1 Generation of Mössbauer sample

[FeCN] (20 mg, 29 μmol) was dissolved in 0.5 mL THF in a 20 ml vial. The solution was cooled to −78 °C, and excess KC_8 was added. The reaction mixture was then filtered through a pipette loaded with filter paper, cellite, and KC_8 3xtimes to form. The reaction mixture was filtered to remove graphite and excess KC_8 to give a jet-black solution. This *in situ* formed material was used directly to form [FeCNH$_2$]. Alternatively, transferring this solution to a Mössbauer cup while maintaining the temperature, freezing the reaction mixture at 77 K, and analyzing by ^{57}Fe Mössbauer revealed a Mössbauer spectrum with parameters $\delta = 0.20$ mm s^{-1}, $\Delta E_Q = 0.18$ mm s^{-1} (Figure B.54A), with a minor impurity.

For generation of [FeCNH$_2$], 2 equiv [H(OEt$_2$)$_2$]BAr$^F_4$ (59 mg, 58 μmol) dissolved in 0.3 mL THF, was added slowly to *in situ* formed [FeCN]K$_2$, with an orange solution formed. Transferring this solution to a Mössbauer cup while maintaining the temperature, freezing the reaction mixture at 77 K, and analyzing by ^{57}Fe Mössbauer revealed a Mössbauer spectrum with parameters $\delta = 0.02$ mm s^{-1}; $\Delta E_Q = 0.96$ mms^{-1} (Figure B.54B), with some oxidized material also formed. The parameters of the major species fit those observed for [FeCNH$_2$] synthesized with [Ph$_2$NH$_2$]BAr$^F_4$ and Cp$_2$Co.

B.2.2.2 Generating UV-vis sample of [FeCNH$_2$]

[FeCN] (1 mg, 1.4 μmol) was dissolved in 2 mL THF in a 20 ml vial. The solution was cooled to −78 °C, and excess KC_8 was added. The reaction mixture was then filtered through a pipette loaded with filter paper, cellite, and KC_8 3xtimes to form. The reaction mixture was filtered to remove graphite and excess KC_8 to give a jet-black solution. This *in*

situ formed material was transferred to a cuvette, which was sealed with a septum. The cuvette was transferred out of the glovebox into a pre-cooled UNISOKO apparatus at −80°C and kept air-free by continuous purging by an N_2 needle.

For generation of [FeCNH$_2$], 2 equiv [H(OEt$_2$)$_2$]BAr$^F_4$ (2.9 mg, 2.8 μmol) dissolved in 0.5 mL THF, was added slowly to *in situ* formed [FeCN]K$_2$, with an orange solution formed (see Figure B.24). Addition of a third equivalent [H(OEt$_2$)$_2$]BAr$^F_4$ resulted in clean oxidation to [FeCNH$_2$]$^+$, with characteristic peaks at 900 nm and 520 nm.

B.2.3 Attempts to generate [FeCNH]

B.2.3.1 Reduction of [FeCNH]$^+$

A solution of [^{57}FeCNH]BAr$^F_4$ (3 mg, 2.1 μmol) was dissolved in 0.5 mL 2-MeTHF and cooled to −115°C. Cp*$_2$Cr (0.6 mg, 2.1 μmol) in 0.2 mL 2-MeTHF was added, and the solution was allowed to stir for 1 minute, rapidly transferred to a pre-cooled Mössbauer cup, and frozen to 77 K. The resulting Mössbauer sample was loaded and analyzed, showing a 1:1 mixture of [FeCN] and [FeCNH$_2$] (see Figure B.56).

B.2.3.2 Protonation of [FeCN][Na(12-c-4)$_2$]

A solution of [^{57}FeCN][Na(12-c-4)$_2$] (2 mg, 1.9 μmol) was dissolved in 0.5 mL 2-MeTHF and cooled to −115°C. [H(OEt$_2$)$_2$]BAr$^F_4$ (1.9 mg, 1.9 μmol) in 0.2 mL 2-MeTHF was added, the solution was allowed to stir for 1 minute, rapidly transferred to a pre-cooled Mössbauer cup and frozen to 77 K. The resulting Mössbauer sample was loaded and analyzed, showing a 1:1 mixture of [FeCN] and [FeCNH$_2$], as well as some unreacted starting material (see Figure B.55).

B.2.3.3 Deprotonation of [FeCNH$_2$][BAr$^F_4$]

A solution of [FeCNH$_2$][BAr$^F_4$] (2 mg, 1.9 μmol) was dissolved in 2.5 mL 2-MeTHF, added to a cuvette that was sealed with a septum, brought out of the glovebox, into a pre-cooled UNISOKO apparatus and cooled to −130°C. NEt$_3$ (1 mg, 1.5 μl, 9.5 μmol) in 0.5 mL 2-MeTHF was added. Analysis by UV-vis showed peaks consistent with the formation of [FeCN] and [FeCNH$_2$] (see Figure B.25).

B.3 UV-vis spectroscopy

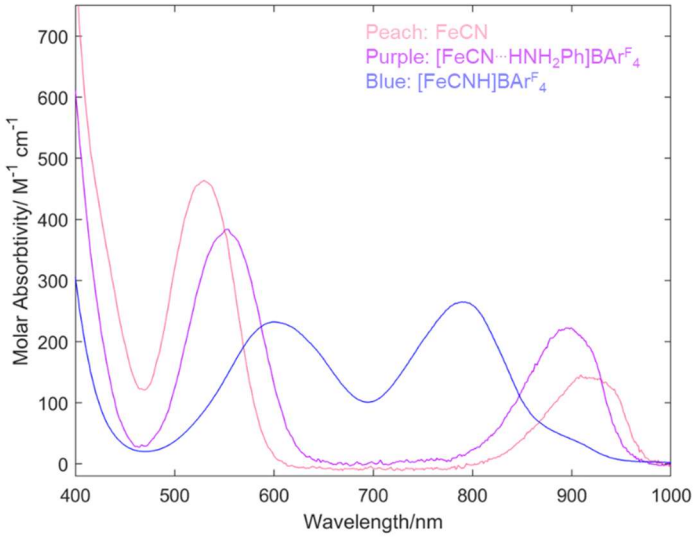

Figure B.1. UV-vis spectra of [FeCN···HNH_2Ph]BAr^F_4 compared to [FeCN], [FeCNH]BAr^F_4.

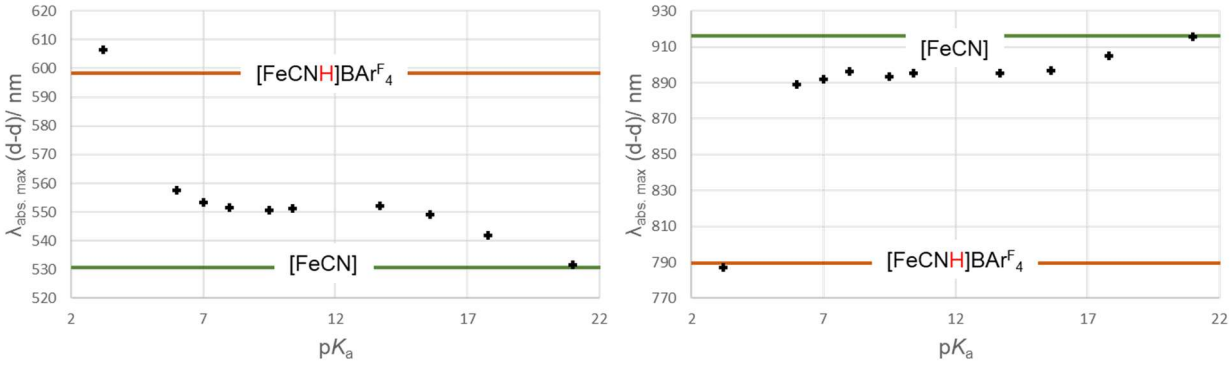

Figure B.2. Shift in position of d-d transition of UV-vis maxim upon varying acid strength, solid lines represent [FeCN] (green) and [FeCNH]BAr^F_4 (orange).

B.3.1 Titrations demonstrating reversible interconversion of [FeCN] and [$FeCNH_2$]

B.3.1.1 Oxidation of [$FeCNH_2$]

A cuvette with [$FeCNH_2$] (2 mg, 2.9 μmol) was generated at −80 °C (see section S2.3.2), sealed with a septum, with a N_2 needle constantly purging to ensure an air-free system. Lut (3 equiv, 0.9 mg, 8.7 μmol) in 0.5 mL THF was added via syringe. Then [Cp^*_2Cr][BAr^F_4] (3 equiv, 10.3 mg, 8.7 μmol) in 0.5 mL was titrated via syringe with

spectrum collected between every addition of oxidant, with peaks consistent with [FeCNH$_2$] disappearing and [FeCN] forming. THF had to be used to generate [FeCNH$_2$]; attempts using Et$_2$O were unsuccessful due to the low solubility of [FeCN]K$_2$ under these conditions.

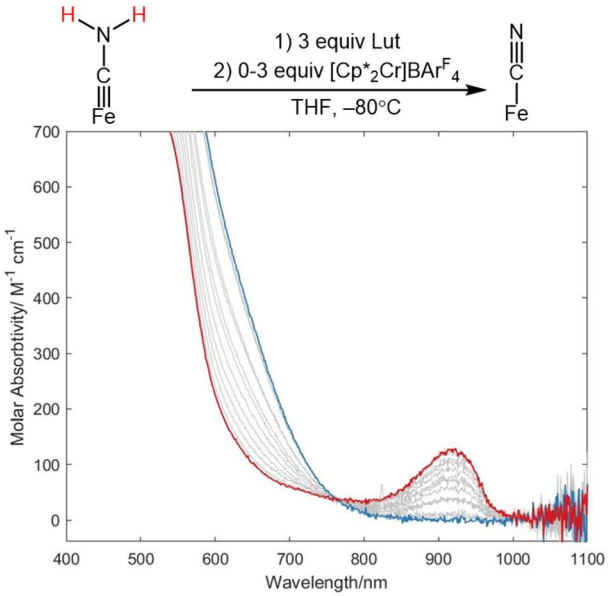

Figure B.3. UV-vis titration of [Cp*$_2$Cr]BAr$^F_4$ (3 equiv per Fe) into mixture of [FeCNH$_2$] (1.2 mM) and Lut (3 equiv per Fe) (Blue) in THF at −80°C. The final trace (Red) shows consumption of [FeCNH$_2$] and formation of [FeCN].

B.3.1.2 Reduction of [FeCN]

A cuvette was loaded [FeCN] (2.5 mg, 3.6 µmol) in 3 mL THF with [PhNH$_3$]BAr$^F_4$ (3 equiv, 10.6 mg, 10.8 µmol) at −80 °C sealed with a septum, with a N$_2$ needle constantly purging to assure an air-free system. To this, Cp*$_2$Cr (3 equiv, 3.5 mg, 10.8 µmol) in 0.5 mL was titrated via syringe with a spectrum collected between every addition of reductant, with peaks consistent with [FeCN] disappearing and [FeCNH$_2$] forming. THF had to be used to generate [FeCNH$_2$].

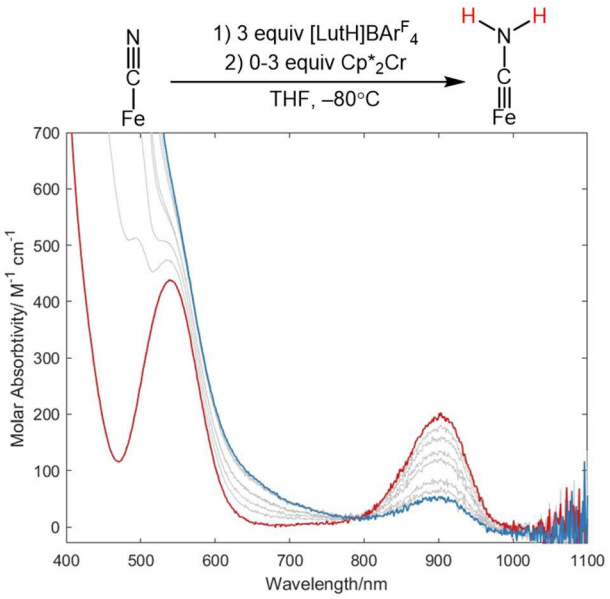

Figure B.4. UV-vis titration of [Cp*$_2$Cr] (3 equiv per Fe) into mixture of [FeCN] (1.2 mM) and [LutH]BAr$^F_4$ (3 equiv per Fe) (Red) in THF at −80°C. The final trace (Blue) shows consumption of [FeCN] and formation of [FeCNH$_2$].

B.3.2 Generation of Pourbaix diagram

B.3.2.1 General procedure

A cuvette was loaded with [FeCN] (1.25 mM) in Et$_2$O and sealed with a septum inside the glovebox. The cuvette was then taken out of the glovebox and loaded into a UNISOKO cooling apparatus connected to the UV-vis. The cuvette was cooled to −80°C and allowed to equilibrate for at least 10 minutes. Spectra were typically collected every minute while equilibrating to ensure no ice formation on the cuvette. The system was kept air-free by an N$_2$ needle through the septa. Acid [HA]BAr$^F_4$ (2.5 equiv) in 0.5 mL Et$_2$O was added via syringe, and the reaction was allowed to equilibrate for an additional 5 minutes. Reductant (2.5 equiv) was then added via syringe, and the reaction was monitored by UV-vis.

Products were assigned by comparing the spectra to known spectra of [FeCNH$_2$]$^+$, [FeCN], [FeCNH]$^+$ and [FeCNH$_2$]. In addition, when uncertain, ^{57}Fe Mössbauer, cw-EPR, and reductant titrations were used to aid the assignment. The reagent strengths are presented in Table B.2, along with the observed products formed. The driving force for [Fe]-products

based on previous thermochemistry,[2] is presented in Table B.2. The individual UV-vis spectra are presented in Figures B.5-B.23 and Table B.1.

B.3.3.2 Thermodynamic considerations for Pourbaix diagram

For the generation of the Pourbaix diagram (Figure 3.5), the general procedure and summary of resulting products are provided in section 3.3. In Figure 3.5, the lines provide the predicted products. To supplement this analysis, we provide a Table B.2 which shows the ΔG (kcal mol-1) for the formation of the 4 products formed, $[FeCNH_2]$, $[FeCNH]^+$, $[FeCN]^-$ and $[FeCNH_2]^+$ given by equations B.1-B.4. If all products are disfavored, [FeCN] (or $[FeCN]^{\cdots}HA^+$) is the predicted product.

For a given reductant $E(red^{+/0})$ and acid (pK_a), $BDFE_{eff}$ is given by:

$$BDFE_{eff} = 23.06\ E(red^{+/0}) + 1.37\ pK_a(acid) + C_G \quad \text{(eqn B.1)}$$

where $C_G = 59.9$ kcal mol^{-1} in THF

Based on the thermochemistry of $[FeCNH_x]$ (main text Figure 3.5)[2] the ΔG (kcal mol^{-1}) for various products is as follows:

$$\Delta G(FeCNH_2) = 2*(BDFE_{eff} - 39) \text{ (eqn B.2)}$$

$$\Delta G(FeCNH^+) = 1.37(pK_a(acid) - 5.6) \text{ (eqn B.3)}$$

$$\Delta G(FeCN^-) = 23.06(E(red^{+/0}) - 2.1\ V) \text{ (eqn B.4)}$$

$$\Delta G(FeCNH_2^+) = 1.37(pK_a(acid) - 7.1) + (BDFE_{eff} - 38) \text{ (eqn B.5)}$$

Table B.1. Summary of product formation studies varying acid and reductant for [FeCN] reduction, reduction potential, and acid used to calculate $BDFE_{eff}$ and ΔG using eqn B.1-B.4.

Reductant (V vs $Fc^{+/0}$)	Acid (pK_a in THF)	$BDFE_{eff}$ (kcal mol^{-1})	ΔG (kcal mol^{-1})	Products
Cp_2Cr (−1.11)	$[^{2\text{-Cl}}PhNH_3]BAr^F{}_4$ (5.6)	42.0	5.4	$[FeCN\cdots HA]^+$
Cp_2Cr (−1.11)	$[^{4\text{-Cl}}PhNH_3]BAr^F{}_4$ (5.6)	43.9	9.2	$[FeCN\cdots HA]^+$
$(C_6H_6)_2Cr$ (−1.22)	$[Ph_2NH_2]BAr^F{}_4$ (3.2)	36.2	-6.3	$[FeCNH_2]^+$
$(C_6H_6)_2Cr$ (−1.22)	$[^{2\text{-Cl}}PhNH_3]BAr^F{}_4$ (5.6)	39.4	0.3	$[FeCNH_2]^+$
$(C_6H_6)_2Cr$ (−1.22)	$[^{4\text{-Cl}}PhNH_3]BAr^F{}_4$ (7.0)	41.4	2.2	$[FeCN]\leftrightarrow[FeCNH_2]^+$
Cp_2Co (−1.33)	$[Ph_2NH_2]BAr^F{}_4$ (3.2)	33.6	-11.4	$[FeCNH_2]$
Cp_2Co (−1.33)	$[^{4\text{-Cl}}PhNH_3]BAr^F{}_4$ (7.0)	38.8	-1.0	$[FeCN]\leftrightarrow[FeCNH_2]$
Cp_2Co (−1.33)	$[PhNH_3]BAr^F{}_4$ (8.0)	40.2	1.8	$[FeCN]\leftrightarrow[FeCNH_2]$
Cp_2Co (−1.33)	$[LutH]BAr^F{}_4$ (9.5)	42.2	5.9	$[FeCN\cdots HA]^+$
$Cp^*{}_2Cr$ (−1.47)	$[PhNH_3]BAr^F{}_4$ (8.0)	37.0	-4.7	$[FeCNH_2]$
$Cp^*{}_2Cr$ (−1.47)	$[LutH]BAr^F{}_4$ (9.5)	39.0	-0.6	$[FeCN]\leftrightarrow[FeCNH_2]$
$Cp^*{}_2Cr$ (−1.47)	$[ColH]BAr^F{}_4$ (10.4)	40.2	1.9	$[FeCN]\leftrightarrow[FeCNH_2]$
$Cp^*{}_2Cr$ (−1.47)	$[Et_3NH]BAr^F{}_4$ (13.7)	44.8	10.9	$[FeCN\cdots HA]^+$
$^{Me4}Cp_2Co$ (−1.76)	$[Et_3NH]BAr^F{}_4$ (13.7)	38.1	-2.4	$[FeCNH_2]$
$^{Me4}Cp_2Co$ (−1.76)	$[pyrrH]BAr^F{}_4$ (15.6)	40.7	2.8	$[FeCN]\leftrightarrow[FeCNH_2]$
$^{Me4}Cp_2Co$ (−1.76)	$[TMGH]BAr^F{}_4$ (17.8)	43.7	8.8	$[FeCN\cdots HA]^+$
$Cp^*{}_2Co$ (−1.94)	$[pyrrH]BAr^F{}_4$ (15.6)	36.5	-5.5	$[FeCNH_2]$
$Cp^*{}_2Co$ (−1.94)	$[TMGH]BAr^F{}_4$ (17.8)	39.5	0.5	$[FeCN\cdots HTMG]^0$
$Cp^*{}_2Co$ (−1.94)	$[TBDH]BAr^F{}_4$ (21.0)	43.9	9.3	$[FeCN\cdots HTBD]^0$

Table B.2. Thermodynamics of [Fe]-product formations for [FeCN] reduction, using different acids and reductants and eqn B.2-B.5

Reductant (V vs $Fc^{+/0}$)	Acid (pK_a in THF)	ΔG (kcal mol^{-1}) for products			
		$[FeCNH_2]$	$[FeCNH]^+$	$[FeCN]^-$	$[FeCNH_2]^+$
Cp_2Cr (−1.11)	$[^{2\text{-Cl}}PhNH_3]BAr^F_4$ (5.6)	5.4	0.0	22.1	2.6
Cp_2Cr (−1.11)	$[^{4\text{-Cl}}PhNH_3]BAr^F_4$ (5.6)	9.2	1.9	22.1	6.4
$(C_6H_6)_2Cr$ (−1.22)	$[Ph_2NH_2]BAr^F_4$ (3.2)	-6.3	-3.3	19.6	-6.5
$(C_6H_6)_2Cr$ (−1.22)	$[^{2\text{-Cl}}PhNH_3]BAr^F_4$ (5.6)	0.3	0.0	19.6	0.0
$(C_6H_6)_2Cr$ (−1.22)	$[^{4\text{-Cl}}PhNH_3]BAr^F_4$ (7.0)	4.1	1.9	19.6	3.9
Cp_2Co (−1.33)	$[Ph_2NH_2]BAr^F_4$ (3.2)	-11.4	-3.3	17.1	-9.1
Cp_2Co (−1.33)	$[^{4\text{-Cl}}PhNH_3]BAr^F_4$ (7.0)	-1.0	1.9	17.1	1.3
Cp_2Co (−1.33)	$[PhNH_3]BAr^F_4$ (8.0)	1.8	3.3	17.1	4.1
Cp_2Co (−1.33)	[LutH]BAr^F_4 (9.5)	5.9	5.3	17.1	8.2
Cp^*_2Cr (−1.47)	$[PhNH_3]BAr^F_4$ (8.0)	-4.7	3.3	13.8	0.8
Cp^*_2Cr (−1.47)	[LutH]BAr^F_4 (9.5)	-0.6	5.3	13.8	5.0
Cp^*_2Cr (−1.47)	[ColH]BAr^F_4 (10.4)	1.9	6.6	13.8	7.4
Cp^*_2Cr (−1.47)	$[Et_3NH]BAr^F_4$ (13.7)	10.9	11.1	13.8	16.5
$^{Me4}Cp_2Co$ (−1.76)	$[Et_3NH]BAr^F_4$ (13.7)	-2.4	11.1	7.1	9.8
$^{Me4}Cp_2Co$ (−1.76)	[pyrrH]BAr^F_4 (15.6)	2.8	13.7	7.1	15.0
$^{Me4}Cp_2Co$ (−1.76)	[TMGH]BAr^F_4 (17.8)	8.8	16.7	7.1	21.0
Cp^*_2Co (−1.94)	[pyrrH]BAr^F_4 (15.6)	-5.5	13.7	3.0	10.8
Cp^*_2Co (−1.94)	[TMGH]BAr^F_4 (17.8)	0.5	16.7	3.0	16.9
Cp^*_2Co (−1.94)	[TBDH]BAr^F_4 (21.0)	9.3	21.1	3.0	25.6

S3.3.3 UV-vis spectra of reactions of [FeCN] with acid and reductant

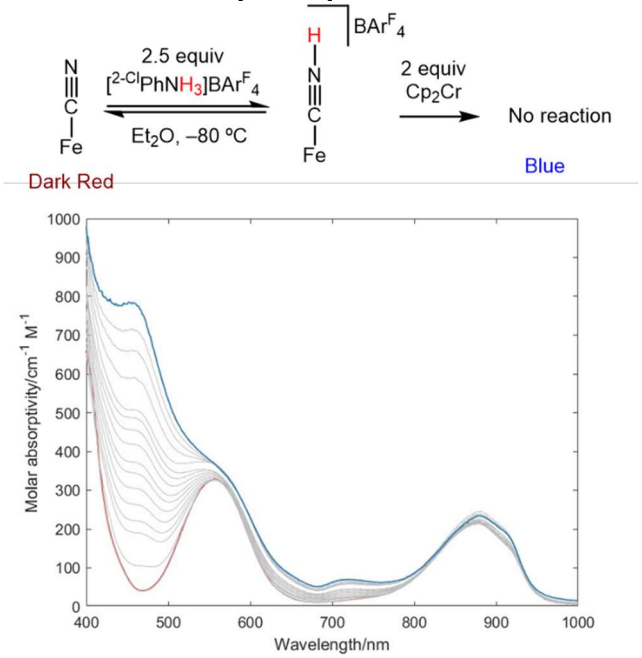

Figure B.5. UV-vis titration of Cp_2Cr (2.5 equiv per Fe) into mixture of [FeCN] (1.2 mM) and $[^{2\text{-Cl}}PhNH_3]BAr^F{}_4$ (2.5 equiv per Fe) (Red) in Et_2O at −80°C. The final trace (Blue) shows no consumption of [FeCN] starting material.

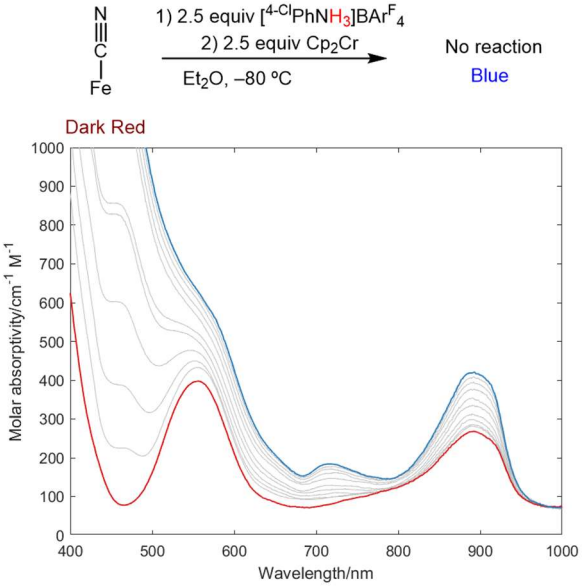

Figure B.6. UV-vis titration of Cp_2Cr (2.5 equiv per Fe) into mixture of [FeCN] (1.2 mM) and $[^{4\text{-Cl}}PhNH_3]BAr^F{}_4$ (2.5 equiv per Fe) (Red) in Et_2O at −80°C. The final trace (Blue) shows no consumption of [FeCN] starting material.

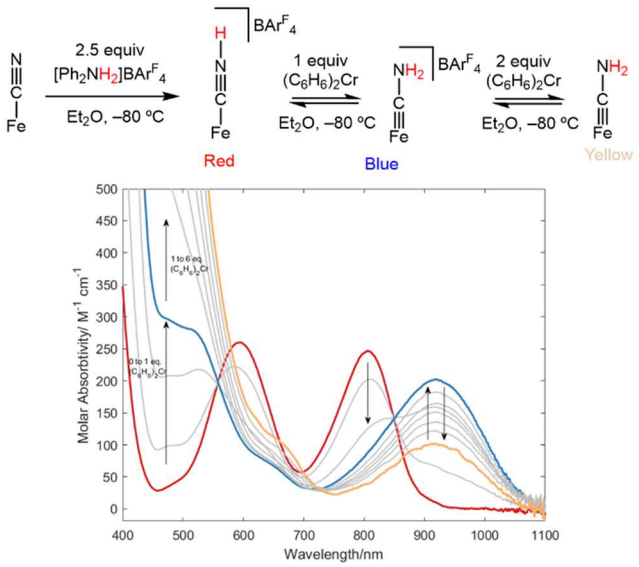

Figure B.7. UV-vis titration of $(C_6H_6)_2Cr$ (0-6 equiv per Fe) into mixture of [FeCN] (1.2 mM) and $[Ph_2NH_2]BAr^F{}_4$ (2.5 equiv per Fe) (Red) in Et_2O at −80°C. Initially, $[FeCNH_2]^+$ is formed. Upon addition of more equivalents of reductant, some $[FeCNH_2]$ begins to form.

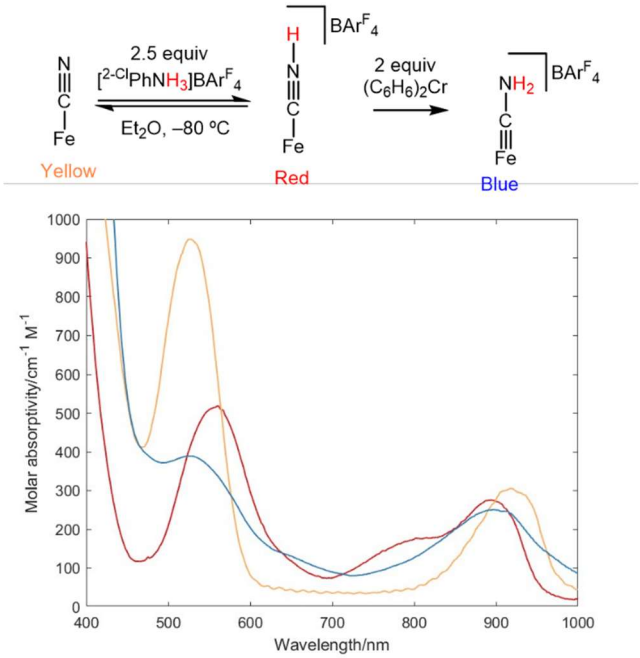

Figure B.8. UV-vis monitored addition of $(C_6H_6)_2Cr$ (2.5 equiv per Fe) into mixture of [FeCN] (1.2 mM) and $[^{2\text{-Cl}}PhNH_3]BAr^F{}_4$ (2.5 equiv per Fe) (Red) in Et_2O at −80°C. The final trace (Blue) shows consumption of [FeCN] and formation of $[FeCNH_2]^+$. Upon addition of acid to [FeCN] (yellow trace is without acid), a mixture of [FeCN]↔$[FeCNH]^+$ is established.

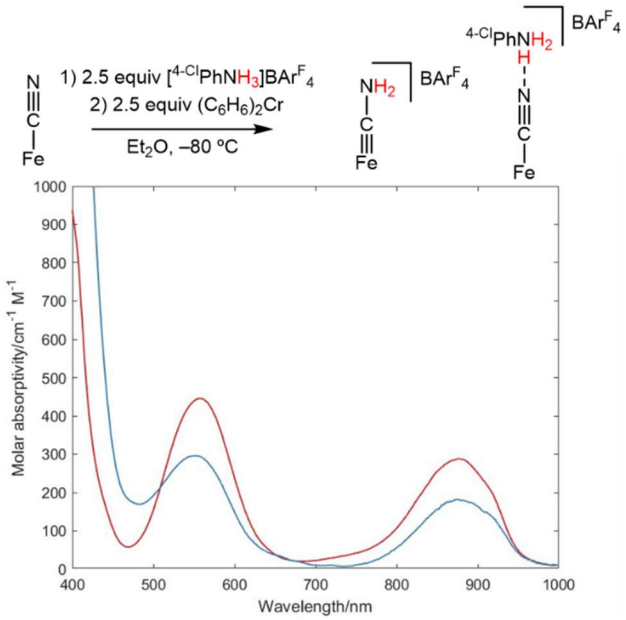

Figure B.9. UV-vis monitored addition of $(C_6H_6)_2Cr$ (2.5 equiv per Fe) into mixture of [FeCN] (1.2 mM) and $[^{4\text{-Cl}}PhNH_3]BAr^F{}_4$ (2.5 equiv per Fe) (Red) in Et_2O at −80°C. The final trace (Blue) shows partial consumption of [FeCN] and a mixture of $[FeCN]\leftrightarrow[FeCNH_2]^+$.

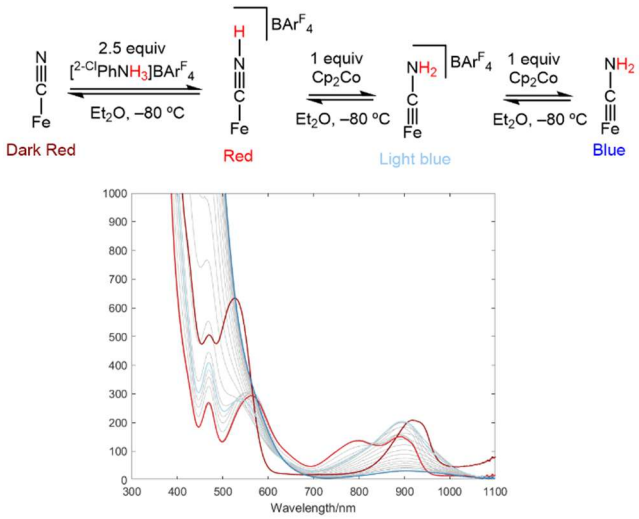

Figure B.10. UV-vis monitored titration of Cp_2Co (2.5 equiv per Fe) into mixture of [FeCN] (1.2 mM) and $[^{2\text{-Cl}}PhNH_3]BAr^F{}_4$ (2.5 equiv per Fe) (Red) in Et_2O at −80°C. The final trace (Blue) shows consumption of [FeCN] and formation of $[FeCNH_2]$. Upon addition of one equivalent of Cp_2Co (light blue trace), $[FeCNH_2]^+$ is formed. Upon addition of acid to [FeCN] (dark red trace is without acid), a mixture of $[FeCN]\leftrightarrow[FeCNH]^+$ is established.

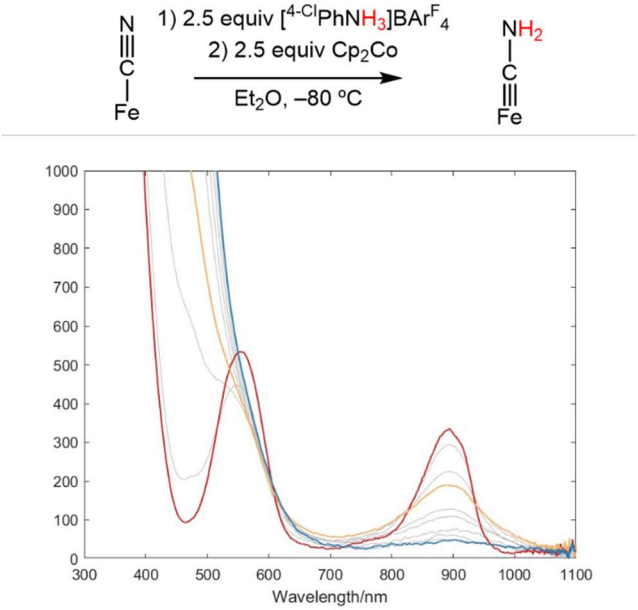

Figure B.11. UV-vis monitored titration of Cp_2Co (2.5 equiv per Fe) into mixture of [FeCN] (1.2 mM) and $[^{4\text{-Cl}}PhNH_3]BAr^F{}_4$ (2.5 equiv per Fe) (Red) in Et_2O at −80°C. The final trace (Blue) shows consumption of [FeCN] and formation of $[FeCNH_2]$. Upon addition of one equivalent of Cp_2Co (yellow trace), $[FeCNH_2]^+$ is formed.

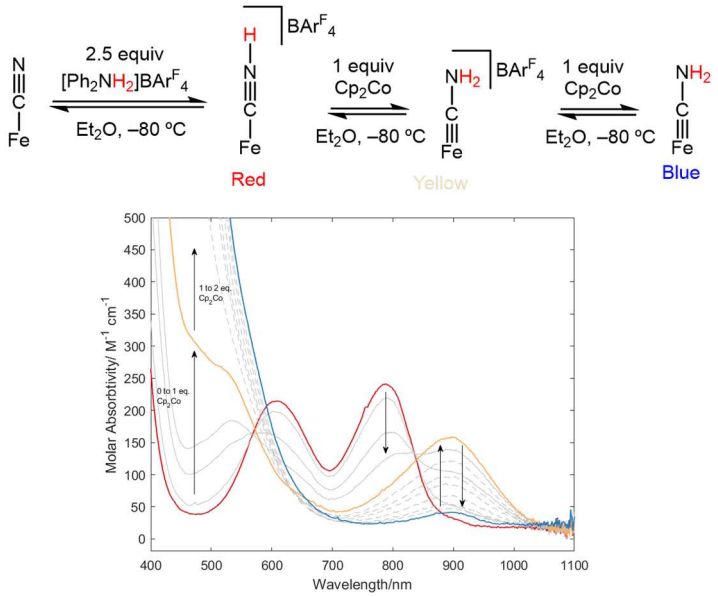

Figure B.12. UV-vis monitored titration of Cp_2Co (2.5 equiv per Fe) into mixture of [FeCN] (1.2 mM) and $[Ph_2NH_2]BAr^F{}_4$ (2.5 equiv per Fe) (Red) in Et_2O at −80°C. The final

trace (Blue) shows consumption of [FeCN] and formation of [$FeCNH_2$]. Upon addition of one equivalent of Cp_2Co (yellow trace), $[FeCNH_2]^+$ is formed.

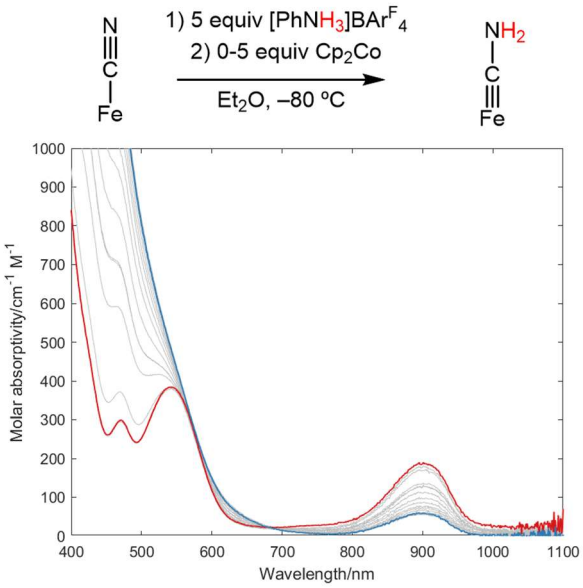

Figure B.13. UV-vis monitored titration of Cp_2Co (5 equiv per Fe) into mixture of [FeCN] (1.2 mM) and $[PhNH_3]BAr^F_4$ (5 equiv per Fe) (Red) in Et_2O at −80°C. The final trace (Blue) shows consumption of [FeCN] and partial formation of [$FeCNH_2$].

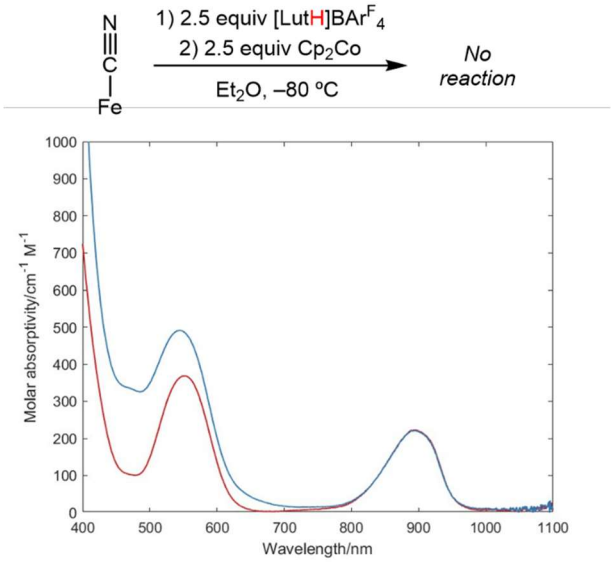

Figure B.14. UV-vis monitored addition of Cp_2Co (2.5 equiv per Fe) into mixture of [FeCN] (1.2 mM) and [LutH]BAr$^F_4$ (2.5 equiv per Fe) (Red) in Et_2O at −80°C. The final trace (Blue) shows no consumption of [FeCN].

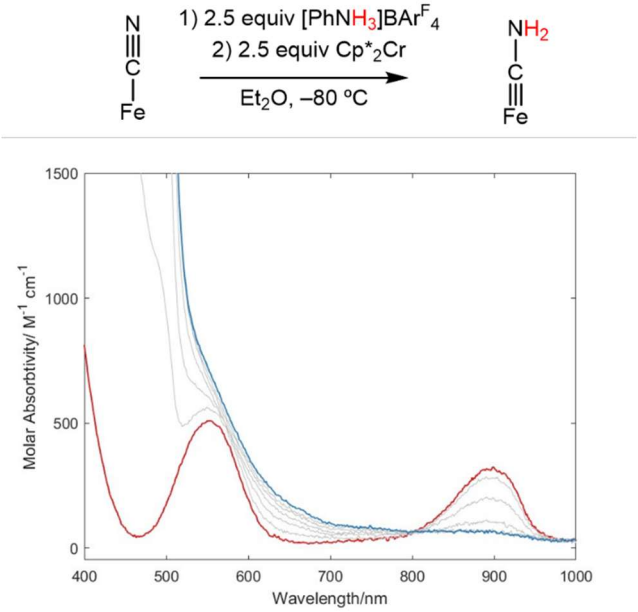

Figure B.15. UV-vis monitored titration of Cp*$_2$Cr (2.5 equiv per Fe) into mixture of [FeCN] (1.2 mM) and [PhNH$_3$]BAr$^F_4$ (2.5 equiv per Fe) (Red) in Et_2O at −80°C. The final trace (Blue) shows consumption of [FeCN] and formation of [FeCNH$_2$].

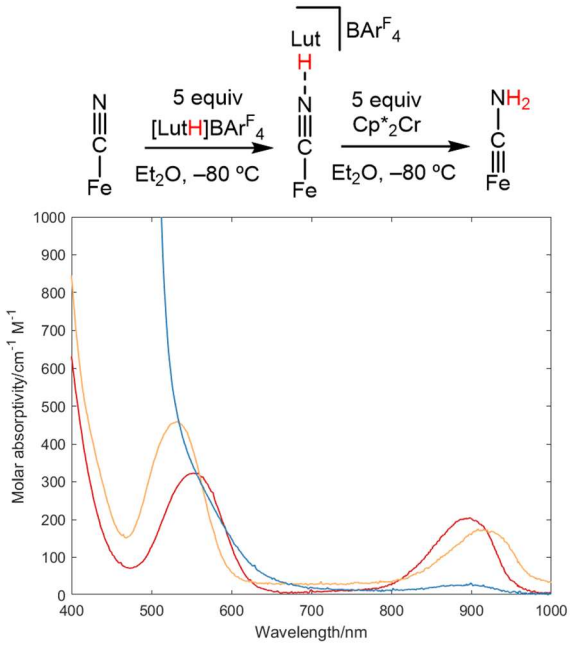

Figure B.16. UV-vis monitored addition of Cp*$_2$Cr (5 equiv per Fe) into mixture of [FeCN] (1.2 mM) and [LutH]BAr$^F_4$ (5 equiv per Fe) (Red) in Et$_2$O at −80°C. The final trace (Blue) shows formation of consumption of [FeCN] and formation [FeCNH$_2$]. Comparing [FeCN] before (yellow trace) and after addition of [LutH]BAr$^F_4$ shows changes similar to those observed upon addition of [PhNH$_3$]BAr$^F_4$, suggesting formation of an H-bond.

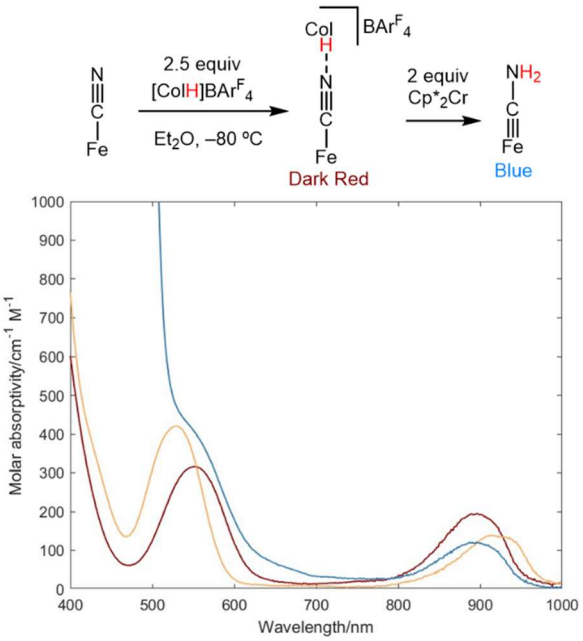

Figure B.17. UV-vis monitored addition of Cp*$_2$Cr (2.5 equiv per Fe) into mixture of [FeCN] (1.2 mM) and [ColH]BAr$^F_4$ (2.5 equiv per Fe) (Red) in Et$_2$O at −80°C. The final

trace (Blue) shows formation of partial consumption of [FeCN] and concomitant formation [$FeCNH_2$]. Comparing [FeCN] before (yellow trace) and after addition of [ColH]$BAr^F{}_4$ (dark red) shows changes similar to those observed upon addition of [$PhNH_3$]$BAr^F{}_4$, suggesting formation of an H-bond.

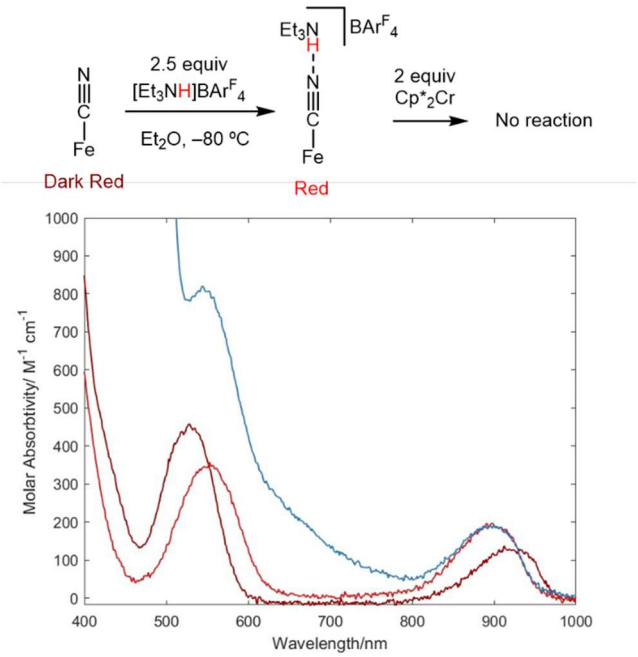

Figure B.18. UV-vis monitored addition of $Cp^*{}_2Cr$ (2.5 equiv per Fe) into mixture of [FeCN] (1.2 mM) and [Et_3NH]$BAr^F{}_4$ (2.5 equiv per Fe) (Red) in Et_2O at −80°C. The final trace (Blue) shows no consumption of [FeCN]. Comparing [FeCN] before (dark red trace) and after addition of [Et_3NH]$BAr^F{}_4$ shows changes similar to those observed upon addition of [$PhNH_3$]$BAr^F{}_4$, suggesting formation of an H-bond.

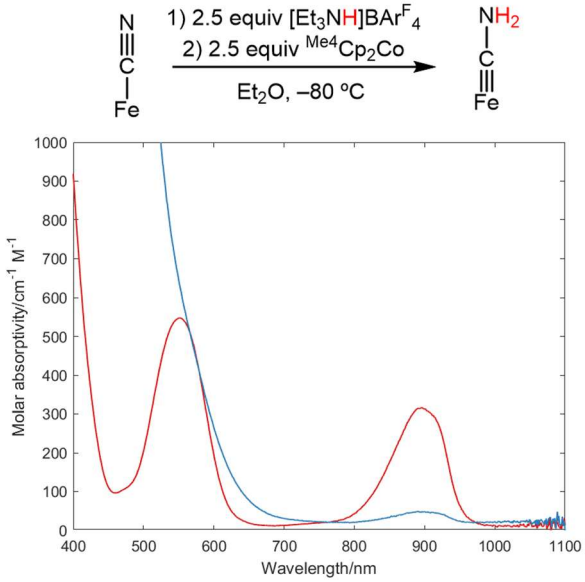

Figure B.19. UV-vis monitored addition of $^{Me4}Cp_2Co$ (2.5 equiv per Fe) into mixture of [FeCN] (1.2 mM) and $[Et_3NH]BAr^F{}_4$ (2.5 equiv per Fe) (Red) in Et_2O at −80°C. The final trace (Blue) shows consumption of [FeCN] and formation of $[FeCNH_2]$.

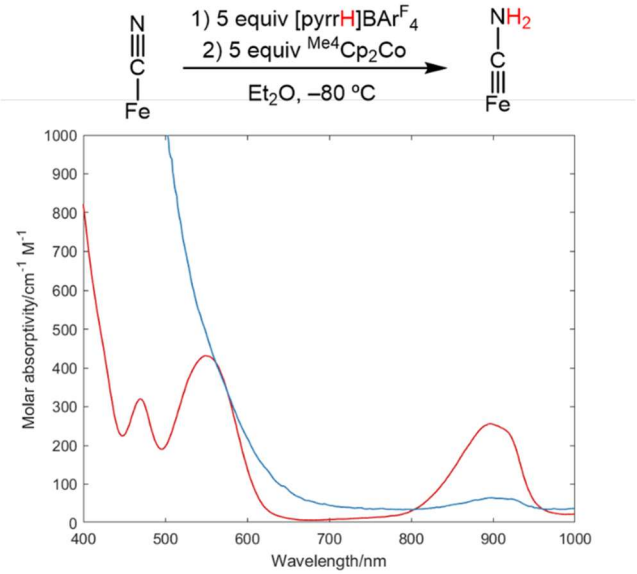

Figure B.20. UV-vis monitored addition of $^{Me4}Cp_2Co$ (2.5 equiv per Fe) into mixture of [FeCN] (1.2 mM) and $[pyrrH]BAr^F{}_4$ (2.5 equiv per Fe) (Red) in Et_2O at −80°C. The final trace (Blue) shows partial consumption of [FeCN] and concomitant formation $[FeCNH_2]$.

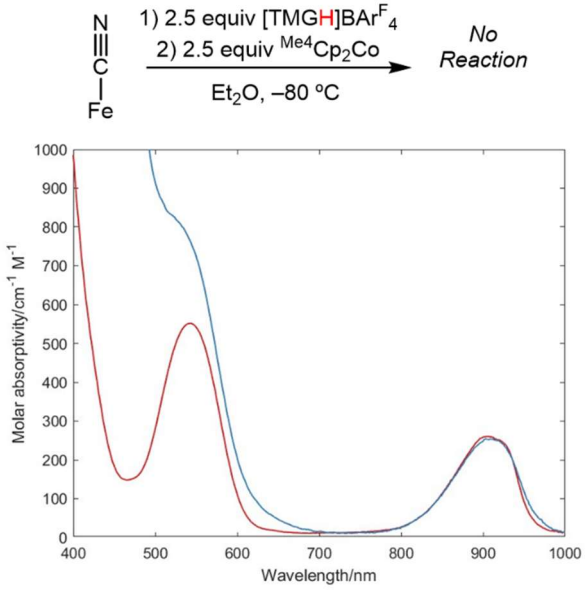

Figure B.21. UV-vis monitored addition of $^{Me4}Cp_2Cr$ (2.5 equiv per Fe) into mixture of [FeCN] (1.2 mM) and [TMGH]BAr$^F_4$ (2.5 equiv per Fe) (Red) in Et_2O at −80°C. The final trace (Blue) shows no consumption of [FeCN].

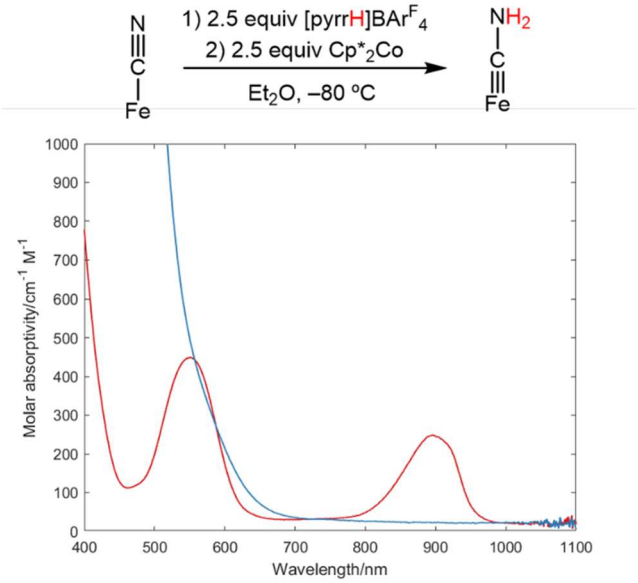

Figure B.22. UV-vis monitored addition of Cp^*_2Co (2.5 equiv per Fe) into mixture of [FeCN] (1.2 mM) and [pyrrH]BAr$^F_4$ (2.5 equiv per Fe) (Red) in Et_2O at −80°C. The final trace (Blue) shows formation of [FeCNH$_2$] and consumption of [FeCN].

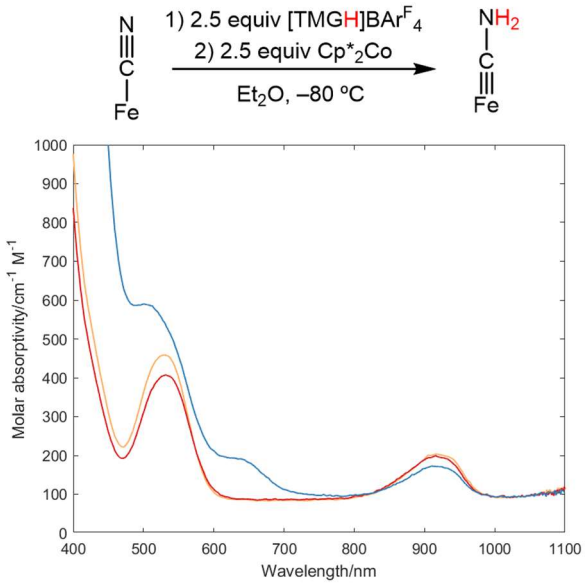

Figure B.23. UV-vis monitored addition of Cp*$_2$Co (2.5 equiv per Fe) into mixture of [FeCN] (1.2 mM) and [TMGH]BAr$^F_4$ (2.5 equiv per Fe) (Red) in Et_2O at −80°C. The final trace (Blue) shows formation of $[FeCN]^-$ and partial consumption of [FeCN]. Comparing [FeCN] before (red trace) and after addition of [TBDH]BAr$^F_4$ shows modest changes compared to those observed upon addition of [PhNH$_3$]BAr$^F_4$, suggesting only a weak interaction between [FeCN] and [TMGH]BAr$^F_4$.

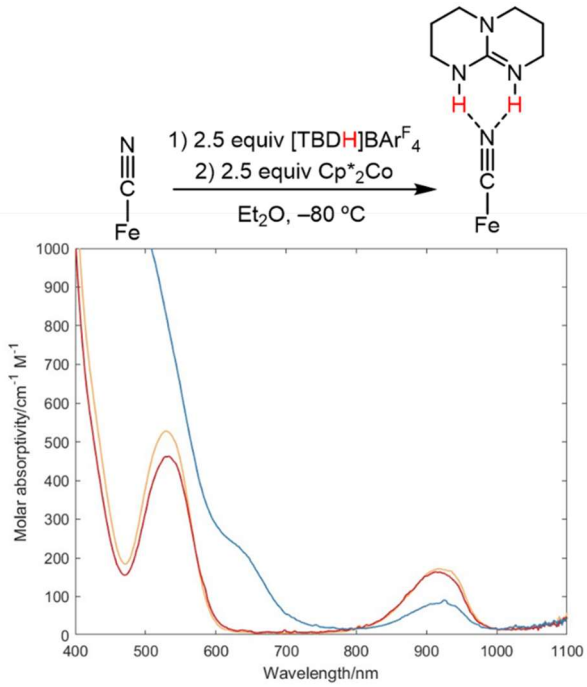

Figure B.24. UV-vis monitored addition of Cp*$_2$Co (2.5 equiv per Fe) into mixture of [FeCN] (1.2 mM) and [TBDH]BAr$^F_4$ (2.5 equiv per Fe) (Red) in Et_2O at −80°C. The final trace (Blue) shows formation of $[FeCN]^-$ and consumption of [FeCN]. Comparing [FeCN] before (red trace) and after addition of [TBDH]BAr$^F_4$ shows small changes compared to those observed upon addition of [PhNH$_3$]BAr$^F_4$, suggesting only a weak interaction between [FeCN] and [TBDH]BAr$^F_4$.

B.3.4 Additional UV-vis experiments

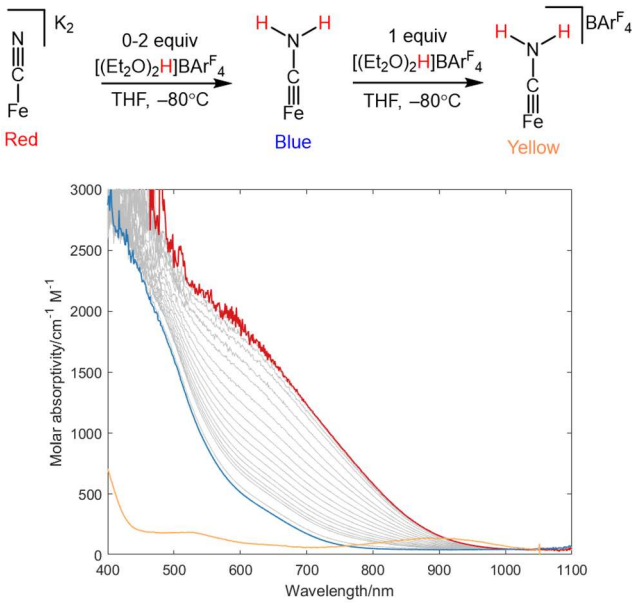

Figure B.25. UV-vis monitored addition double protonation of $[FeCN]K_2$ (red) to yield $[FeCNH_2]$ (Blue), which is similar to $[FeCNMe_2]$ with a shoulder at 620 nm and a maxima growing towards 490 nm. Addition of a third equivalent $[H(OEt_2)_2]BAr^F{}_4$ results in clean oxidation to $[FeCNH_2]BAr^F{}_4$ (yellow).

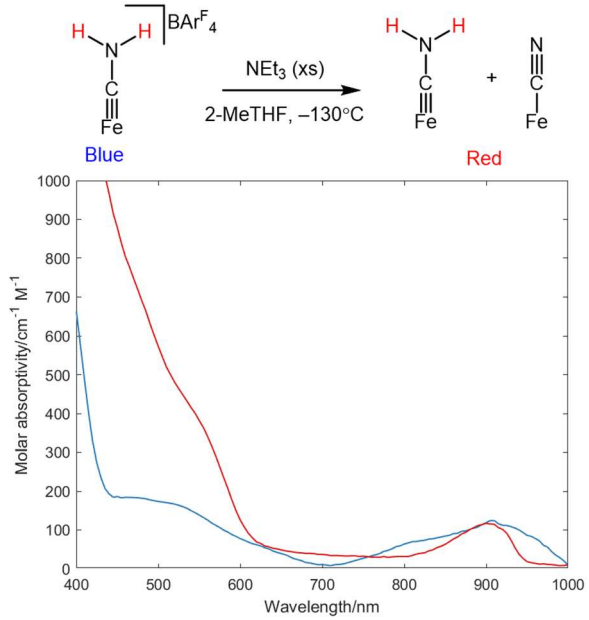

Figure B.26. UV-vis monitored deprotonation of $[FeCNH_2]BAr^F{}_4$ (Blue) by NEt_3 to yield a mixture of [FeCN] (characteristic peak at 900 nm) and $[FeCNH_2]$ (Mixture in red).

B.3.5 Measurement of equilibrium constants for H-bond formation in THF with [TBA][PF_6]

B.3.5.1 General procedure

A cuvette was loaded with [FeCN] (1 mM) in THF in 0.2 M [TBA][PF_6], sealed with a septum inside the glovebox, and then taken out of the glovebox. The system was kept air-free by an N_2 needle through the septa. Acid [HA]OTf (0 to 100 equiv) was titrated into the cuvette, with spectra recorded between titrations. The analyzed spectra were normalized to account for the decreasing concentration of [FeCN].

B.3.5.2 Data analysis

The differences between the UV-vis spectra of the H-bonded and non-H-bonded species are subtle, limiting the possibility of measuring the equilibrium constant at a single wavelength. Accordingly, we used a multivariate approach to analyzing the data and extracting equilibrium constants.[9] The following methodology was implemented in Matlab™.

For a set of collected data of titrations at varying acid concentration, the data can be presented as a matrix **Y** (dimensions: (wavelengths) x (acid concentrations)). Defining a matrix **A** as the absorbance spectra of j number of species in solution (dimensions: (wavelengths) x (j concentrations) and a matrix **C** as the concentration of j species with varying acid concentration (dimensions: (j) x (acid concentrations)) we define an equation:

$$\mathbf{Y} = \mathbf{AC} + \mathbf{R} \quad \text{(eqn B.6)}$$

where **R** is the residual.

Building a model around the equilibrium:

$$[\text{FeCN}][\text{HA(OTf)}] = K[\text{FeCN}\cdots\text{HA(OTf)}] \quad \text{(eqn B.7)}$$

We can readily calculate the matrix $\mathbf{C}(K)$ for a given equilibrium constant. Seeking to minimize $\mathbf{R^2}$ for a given K we can calculate the absorbance spectra $\mathbf{A'}(K)$ using equation eqn B.8.

$$\mathbf{A'}(K) = \mathbf{Y}(\mathbf{C}(K)^{+}) \quad \text{(eqn B.8)}$$

Where $\mathbf{C}^{+}(K)$ is the pseudo-inverse of $\mathbf{C}(K)$.

This allows us to define **R** as a function of K

$$\mathbf{R}(K) = \mathbf{A'}(K)\mathbf{C}(K) \quad \text{(eqn B.9)}$$

which the square $\mathbf{R^2}$ can be minimized against K.

To analyze the model's predicted absorbances of [FeCN] and [FeCN···HA(OTf)] are printed along with the residuals. In addition, the absorbance at 563 nm and 880 nm, areas with larger divergence, were used to estimate the concentration of [FeCN] and [FeCN···HA(OTf)] and compared to the calculated concentration. The error bars were determined by testing varying sizes of K to see when the predicted absorbances±error bar could capture ~70% of the measured absorbances.

B.3.5.3 Titration experiments

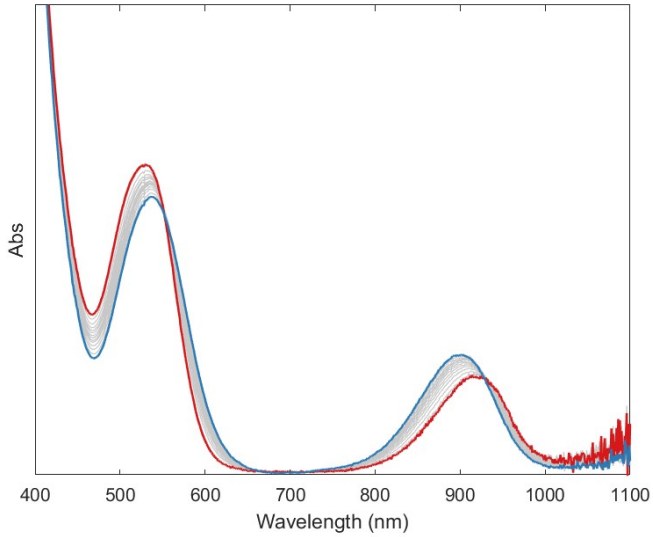

Figure B.27. UV-vis monitored titration of [$PhNH_3$]OTf (0 to 100 mM) into [FeCN] 1 mM in THF with 0.2 M [TBA][PF_6] at 25 °C.

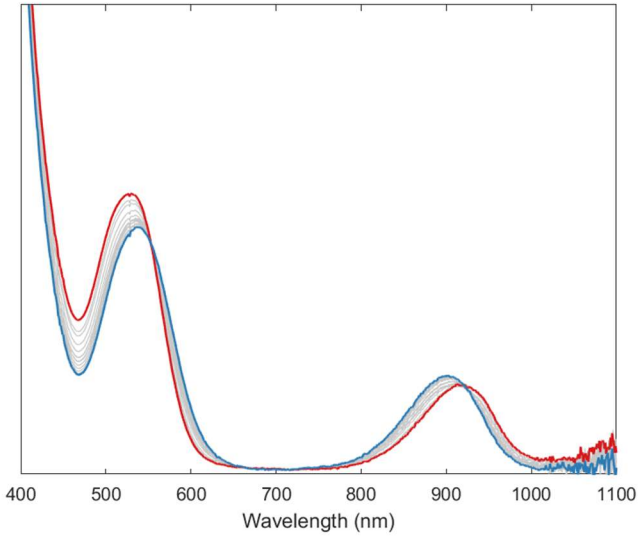

Figure B.28. UV-vis monitored titration of [$^{4\text{-Cl-2,6-Me}}$pyH]OTf (0 to 100 mM) into [FeCN] 1 mM in THF with 0.2 M [TBA][PF_6] at 25 °C.

B.3.5.4 Outputs from Multivariate Fitting Model

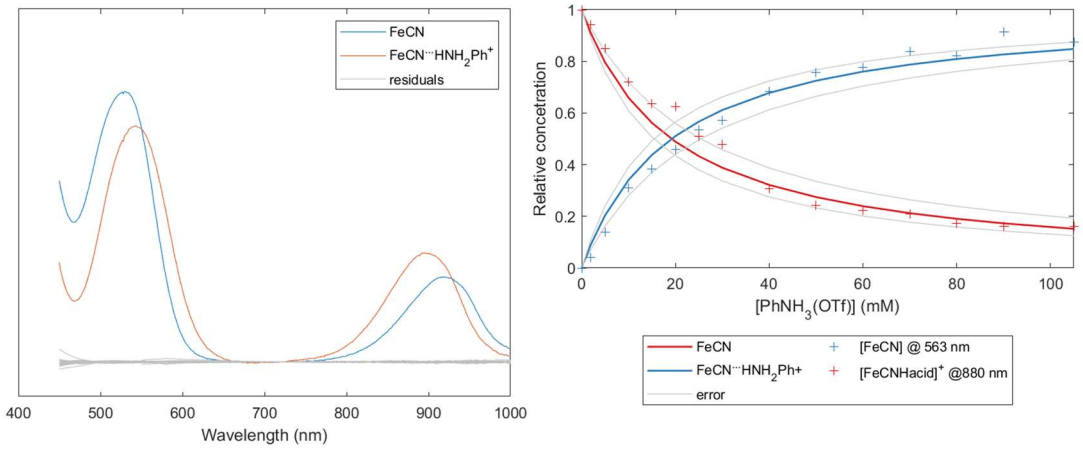

Figure B.29. Predicted spectra (left) of [FeCN] and [FeCN···HNH_2Ph(OTf)] with residual spectra shown in grey. Calculated solid lines (red) were compared to those implied by absorbances (right), with error bars indicated. An equilibrium constant of K = 62 ±15 M^{-1} was determined.

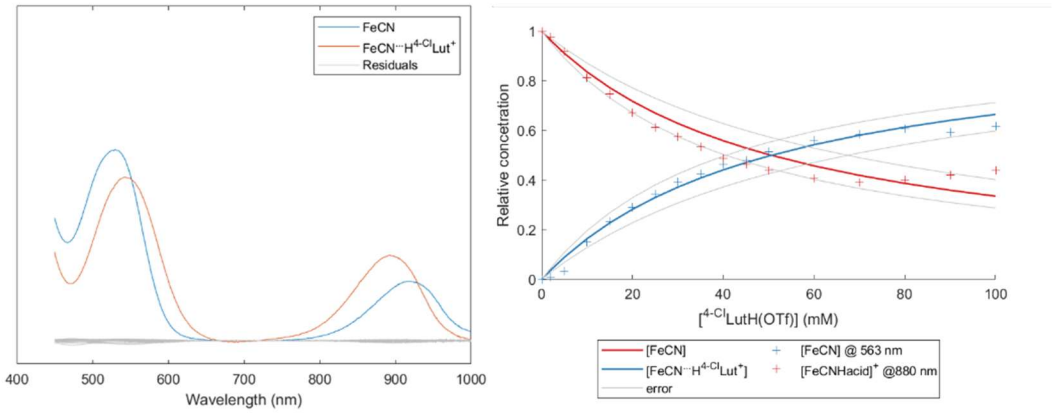

Figure B.30. Predicted spectra (left) of [FeCN] and [FeCN···H(4-Cl-2,6-mepyr)(OTf)] with residual spectra shown in grey. Calculated solid lines (red) were compared to those implied by absorbances (right), with error bars indicated. An equilibrium constant of $K = 20 \pm 5$ M^{-1} was determined.

B.4 Kinetic studies

B.4.1 General procedure

Kinetic analysis was performed by UV-vis, using the Cary *ScanningKinetics* program to record UV-vis traces (every 6 seconds). A cuvette was loaded with [FeCN] and $[PhNH_3]BAr^F{}_4$ in 4:1 2MeTHF:THF, sealed with a septa in the glovebox. It was then taken out and loaded into a UNISOKO cooling apparatus connected to the UV-vis. The cuvette was then cooled to −145°C and allowed to equilibrate for at least 20 minutes. Spectra were typically collected every minute while equilibrating to ensure no icing on the cuvette and sufficient stirring. The system was kept air-free by an N_2 needle through the septa.

After equilibration, the reductant was added via syringe. A thick syringe (18 gauge) was found to be most suitable, as the greater force of addition allowed for faster mixing of the solution. Similarly, the needle had to be long enough to be submerged in the ethereal solution, such that the reductant was added directly into the solution, not on top of the liquid. With these precautions, mixing was fast enough (<10 s) that kinetic analysis was possible, monitoring the decay of [FeCN] by loss of the characteristic peak at 895 nm. The kinetic values are summarized in **Table B.3**. Plots of Abs_{895} vs. t and log(A895) vs. t are supplied in Figure **B.32-B.47**. It was found that the data generally fit a 1st order plot, not a 2nd order plot (**Figure B.31**).

The error was analyzed for the kobs and k2nd derived for each individual kinetic run (**Table B.3**). The mean error for each run (±0.06 M^{-1} s^{-1} for k_{2nd}) closely resembles the spread in values for the straight-line plot used to derive k_{2nd} (±0.07 M^{-1} s^{-1}).

Table B.3. Summary of kinetics data with slope and associated rate constants derived from slope.

	Concentrations (mM)			Ratio to [FeCN]					
Run	**FeCN**	**$[PhNH_3]BAr^F_4$**	**$^{Et}Cp_2Co$**	**$[PhNH_3]BAr^F_4$**	**$^{Et}Cp_2Co$**	**Slope**	**k_{obs} (s^{-1})**	**k_{2nd} (M^{-1} s^{-1})**	**Notes**
A	1.2	3.7	19.4	3	16	-1.35±0.09	2.25±0.15 ·10^{-2}	1.16±0.08	Varying reductant
B	1.2	3.5	43.0	3	37	-3.0±0.2	5.0±0.4·10^{-2}	1.17±0.09	"
C	1.2	3.5	33.1	3	28	-2.19±0.08	3.66±0.13·10^{-2}	1.11±0.04	"
D	1.1	3.4	47.7	3	42	-3.3±0.2	5.5±0.3·10^{-2}	1.16±0.07	"
E	1.2	3.6	24.4	3	20	-1.5±0.25	2.5±0.4·10^{-2}	1.02±0.17	"
F	1.2	3.5	35.2	3	30	-2.52±0.09	4.21±0.15·10^{-2}	1.19±0.04	"
G	1.2	3.6	31.1	3	26	-1.88±0.06	3.13±0.10·10^{-2}	1.01±0.03	"
								1.17±0.07	k_{2nd} averaged
H	2.1	6.4	29.9	3	14	-2.06±0.06	3.44±0.10·10^{-2}	1.15±0.03	Varying [FeCN]
I	1.7	5.1	26.5	3	16	-1.75±0.09	2.91±0.15·10^{-2}	1.10±0.06	"
J	1.4	4.3	37.1	3	26	-3.0±0.4	5.0±0.7·10^{-2}	1.34±0.19	"
K	1.2	7.0	38.1	6	33	-3.1±0.14	5.2±0.2·10^{-2}	1.36±0.06	Varying acid
L	1.1	10.1	20.9	9	19	-1.54±0.07	2.57±0.12·10^{-2}	1.23±0.06	"
M	1.1	13.3	25.8	12	23	-1.8±0.10	3.0±0.2·10^{-2}	1.16±0.07	"
N	1.1	13.5	20.9	12	19	-1.64±0.07	2.73±0.11·10^{-2}	1.31±0.05	"
O(D)	1.2	3.5	33.1	3	28	-1.72±0.06	2.86±0.09·10^{-2}	0.86±0.03	Deuterated acid
P(D)	1.2	3.5	33.1	3	28	-1.66±0.04	2.76±0.06·10^{-2}	0.83±0.02	Deuterated acid
								0.85±0.02	k_{2nd} averaged, deuterated
							KIE	1.37±0.06	

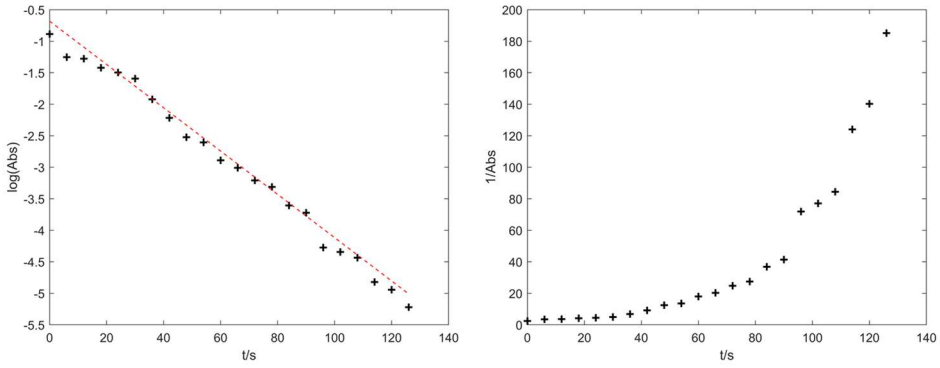

Figure B.31. Plots of log(abs) vs. t (1st order) and 1/Abs vs. t (2nd order) of [FeCN] decay after the addition of reductant. Straight-line is only observed for 1st order plot, suggesting a reaction first order in [FeCN]. This was confirmed (Figure 3.8D, runs H-J), where no difference was found in the k_{2nd} when varying [FeCN].

B.4.2 First-order plots for individual runs

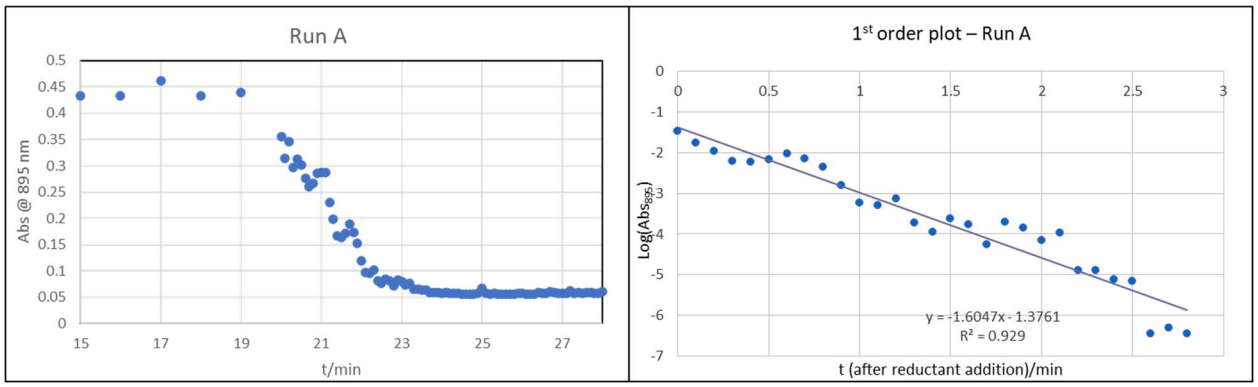

Figure B.32. Trace of Abs_{895} vs. t (left) and log(Abs895) vs. t plot (right) for run A.

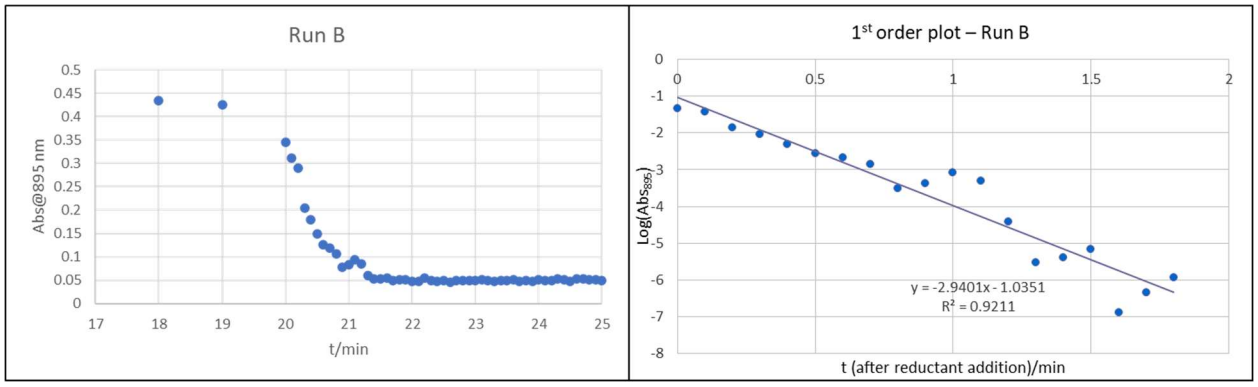

Figure B.33. Trace of Abs_{895} vs. t (left) and log(Abs895) vs. t plot (right) for run B.

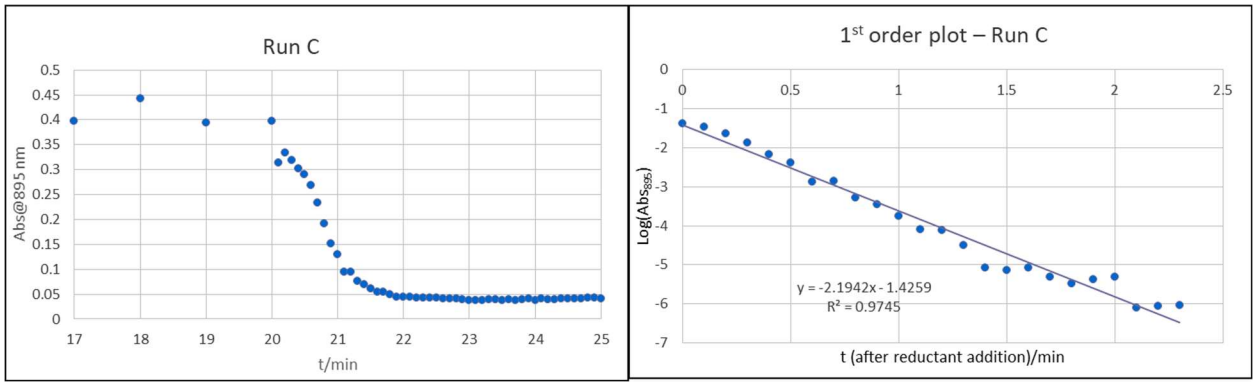

Figure B.34. Trace of Abs_{895} vs. t (left) and log(Abs895) vs. t plot (right) for run C.

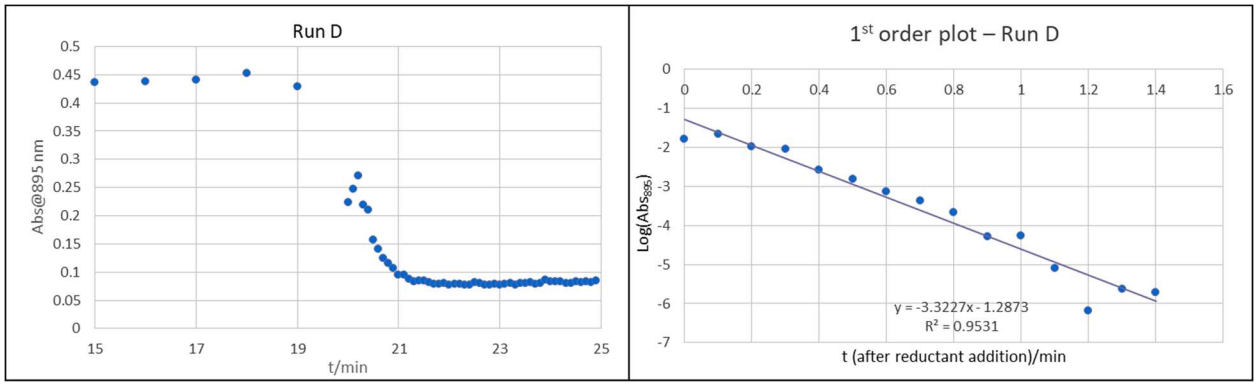

Figure B.35. Trace of Abs_{895} vs. t (left) and log(Abs895) vs. t plot (right) for run D.

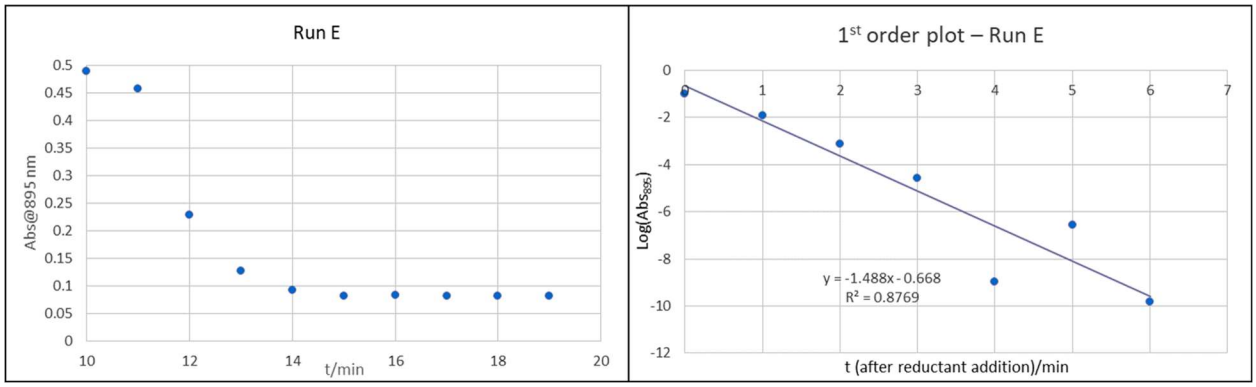

Figure B.36. Trace of Abs_{895} vs. t (left) and log(Abs895) vs. t plot (right) for run E.

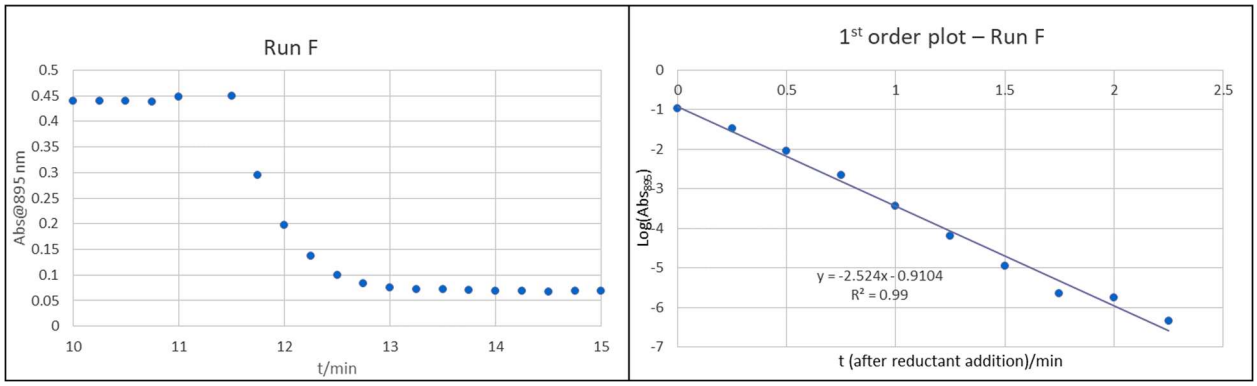

Figure B.37. Trace of Abs_{895} vs. t (left) and log(Abs895) vs. t plot (right) for run F.

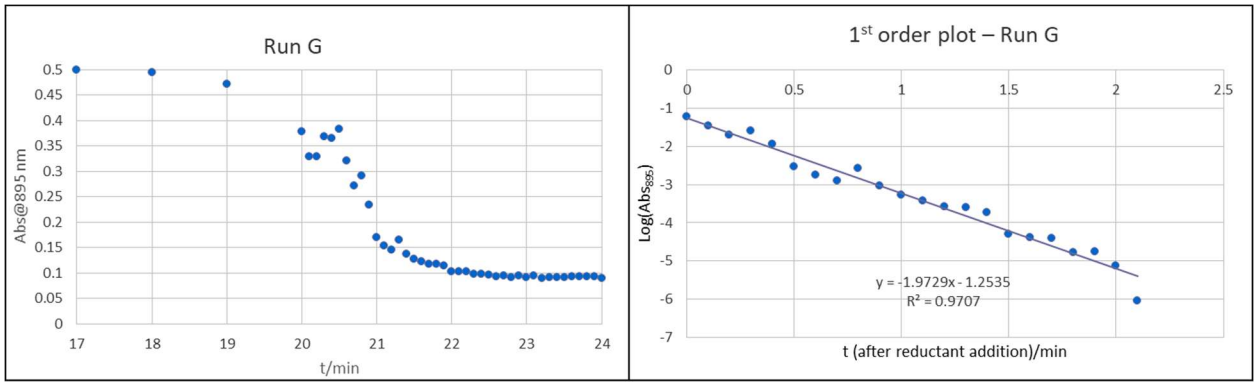

Figure B.38. Trace of Abs_{895} vs. t (left) and log(Abs895) vs. t plot (right) for run G.

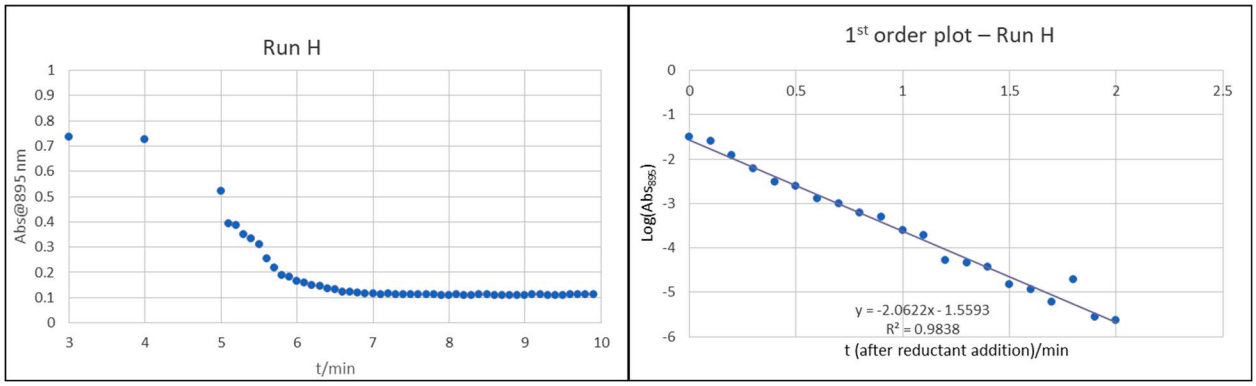

Figure B.39. Trace of Abs_{895} vs. t (left) and log(Abs895) vs. t plot (right) for run H.

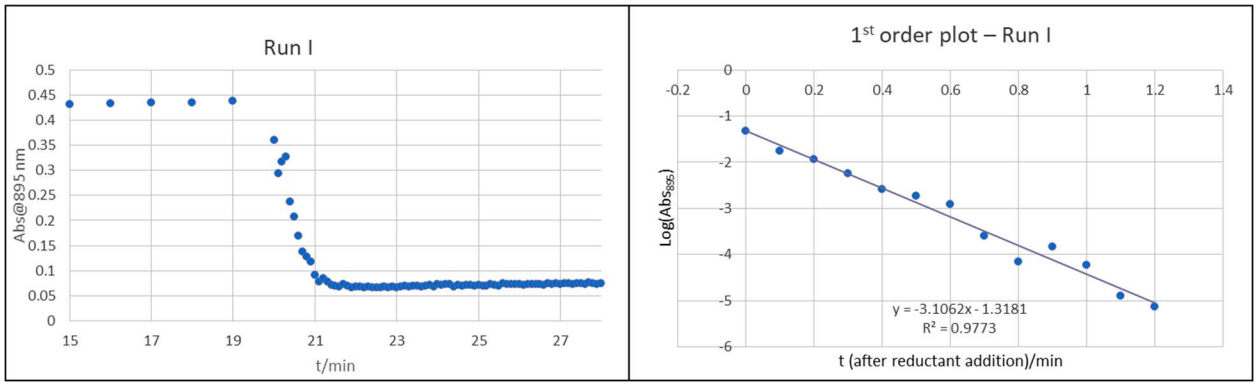

Figure B.40. Trace of Abs_{895} vs. t (left) and log(Abs895) vs. t plot (right) for run I.

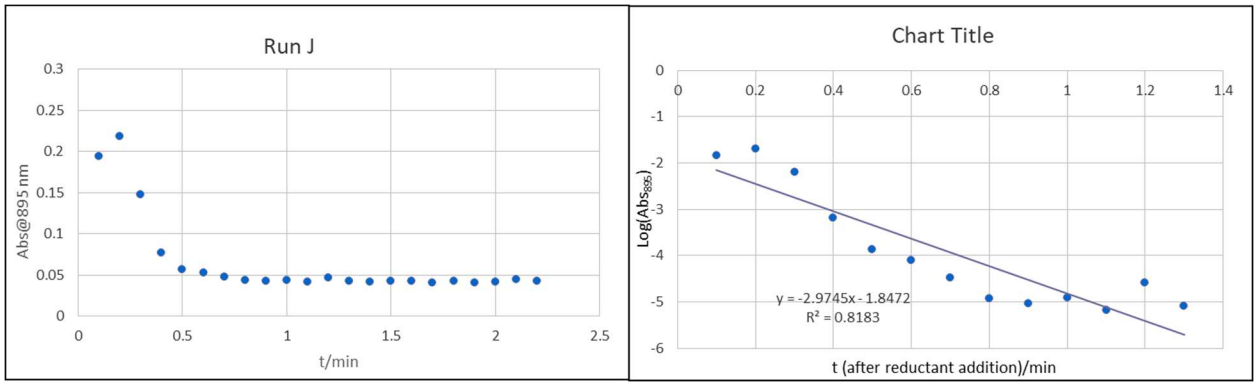

Figure B.41. Trace of Abs_{895} vs. t (left) and log(Abs895) vs. t plot (right) for run J.

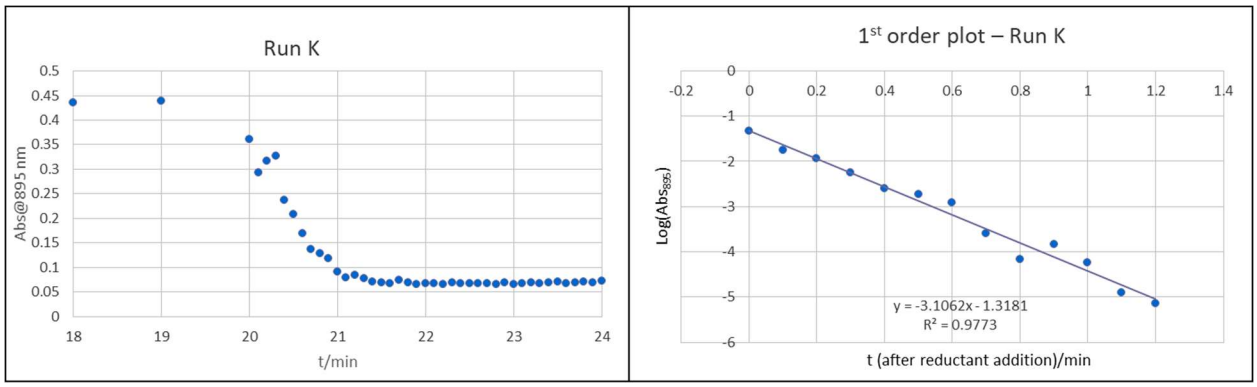

Figure B.42. Trace of Abs_{895} vs. t (left) and log(Abs895) vs. t plot (right) for run K.

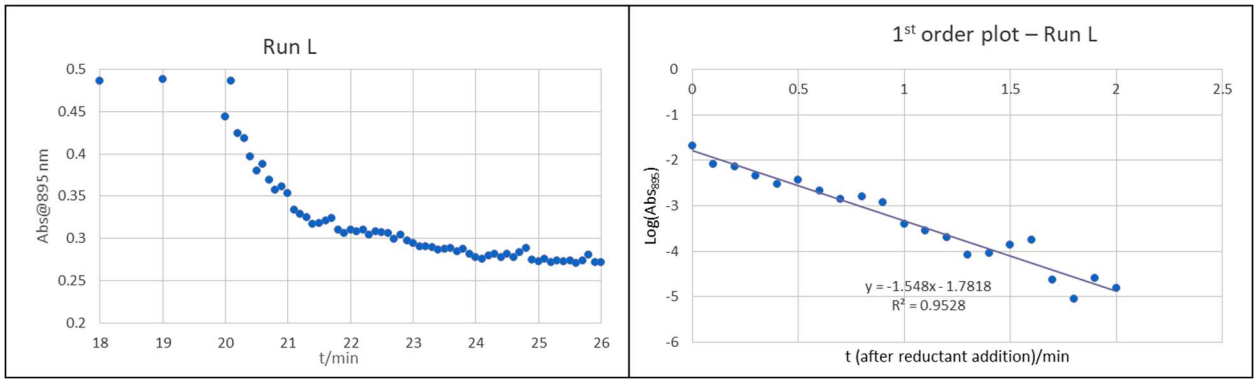

Figure B.43. Trace of Abs_{895} vs. t (left) and log(Abs895) vs. t plot (right) for run L.

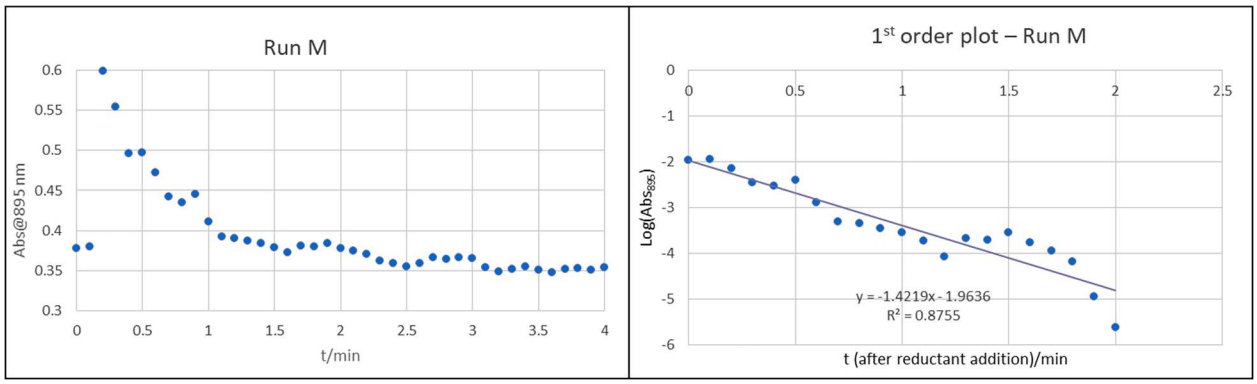

Figure B.44. Trace of Abs_{895} vs. t (left) and log(Abs895) vs. t plot (right) for run M.

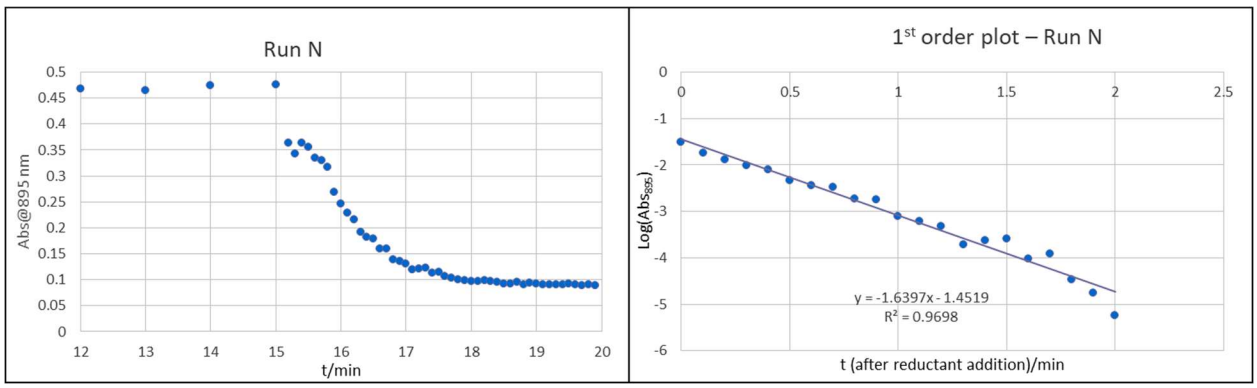

Figure B.45. Trace of Abs_{895} vs. t (left) and log(Abs895) vs. t plot (right) for run N.

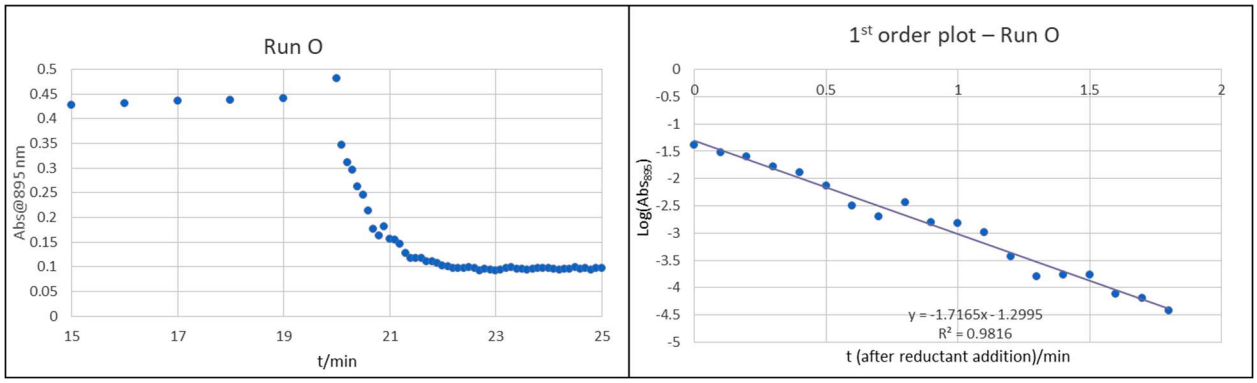

Figure B.46. Trace of Abs_{895} vs. t (left) and log(Abs895) vs. t plot (right) for run O.

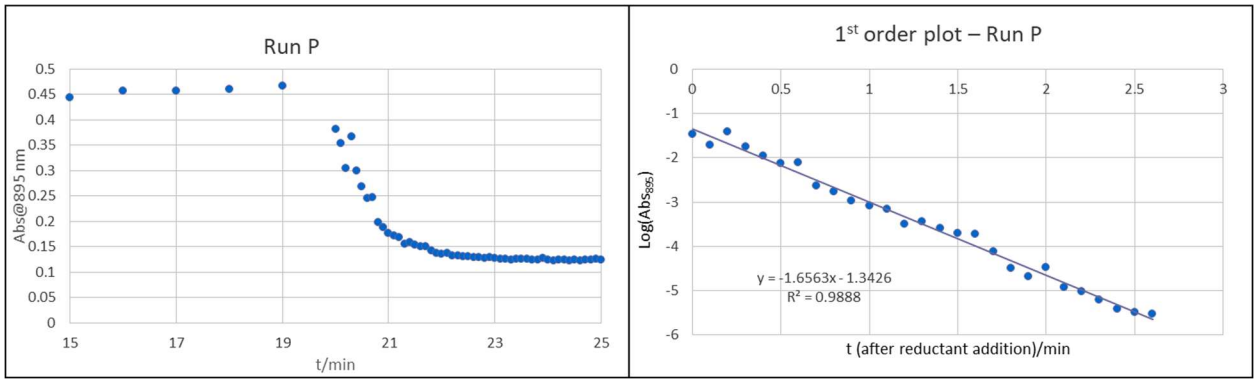

Figure B.47. Trace of Abs_{895} vs. t (left) and log(Abs895) vs. t plot (right) for run P.

B.5 ^{57}Fe Mössbauer spectroscopy

B.5.1 Note on the fitting of Mössbauer spectra

Data analysis was performed using version 4 of the program WMOSS (www.wmoss.org) and quadrupole doublets were fit to Lorentzian lineshapes. Simulations were constructed from the minimum number of quadrupole doublets required to attain a quality fit to the data (convergence of χ_R^2). Quadrupole doublets were constrained to be symmetric. Using the non-linear error analysis algorithm provided by WMOSS, the errors in the computed parameters are estimated to be 0.02 mm s^{-1} for δ and 2% for ΔE_Q.

B.5.2 Freeze-Quenched Mössbauer spectroscopy of reduction reactions

General Procedure for Freeze-Quench Mössbauer Spectroscopy of reactions. All solvents are stirred with Na/K for ≥ 2 hours and filtered prior to use. In a nitrogen filled

glovebox, the desired ^{57}Fe species (0.0023 mmol) is dissolved in 0.3 mL Et_2O and cooled to -78 °C in a stirring vial in the glovebox cold well. Acid was added in 0.1 mL Et_2O. Reductant was added in 0.3 mL to the chilled vial. The reaction was allowed to stir for 5 minutes before it was rapidly transferred to a pre-chilled Mössbauer cup. The cold well was then changed from -78°C (195 K) to 77 K and the solution froze within 5 minutes. The Mössbauer cup was kept at 77 K for minimum 20 minutes before being rapidly taken out of the glovebox and submerged in liquid N_2 before being mounted on the Mössbauer spectrometer.

B.5.3 Freeze-Quenched ^{57}Fe Mössbauer spectra of individual reactions

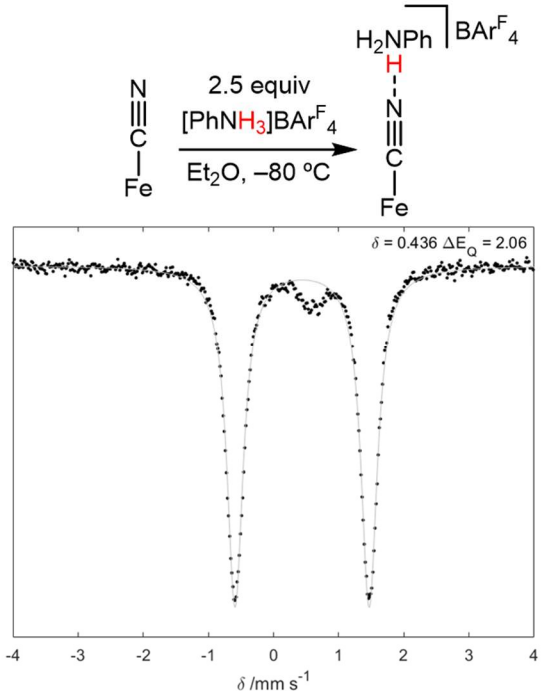

Figure B.48. Freeze-quenched Mössbauer of reaction of [FeCN] with $[PhNH_3]BAr^F{}_4$.

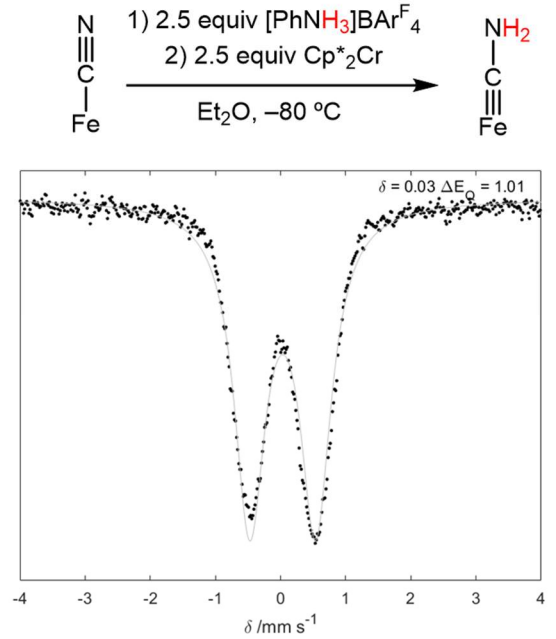

Figure B.49. Freeze-quenched Mössbauer of reaction of [FeCN] with $[PhNH_3]BAr^F{}_4$ and $Cp^*{}_2Cr$.

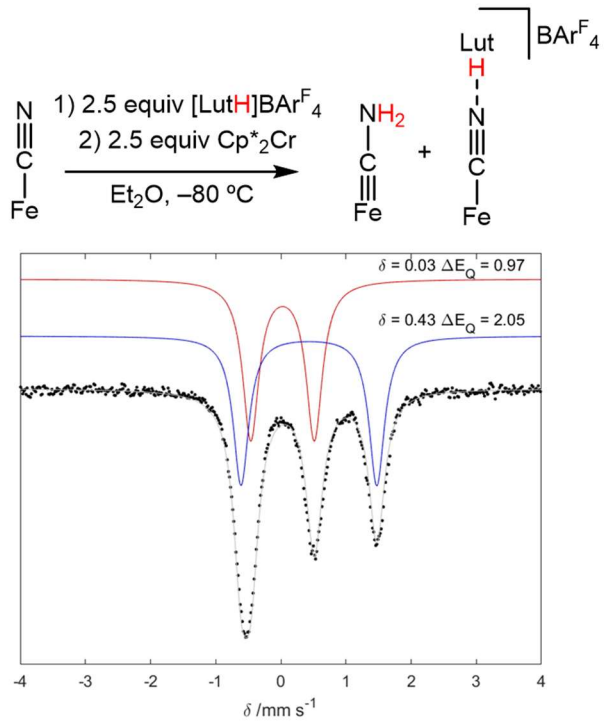

Figure B.50. Freeze-quenched Mössbauer of reaction of [FeCN] with $[LutH]BAr^F{}_4$ and $Cp^*{}_2Cr$.

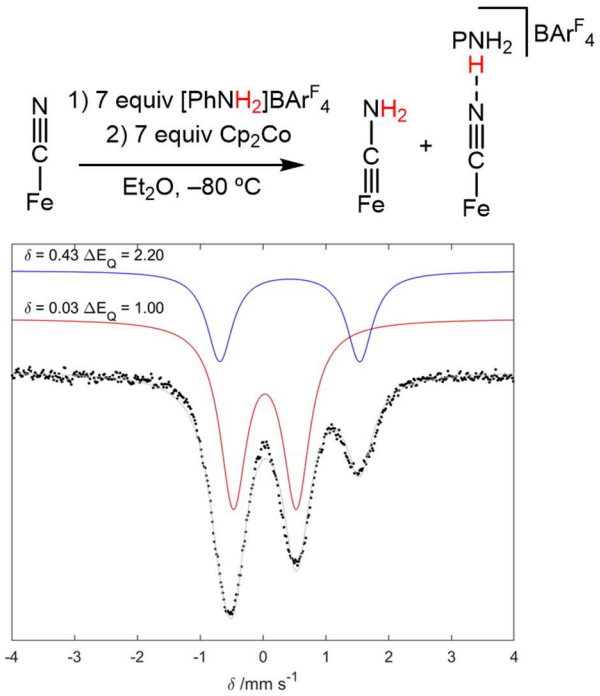

Figure B.51. Freeze-quenched Mössbauer of reaction of [FeCN] with $[PhNH_2]BAr^F{}_4$ and $Cp^*{}_2Cr$.

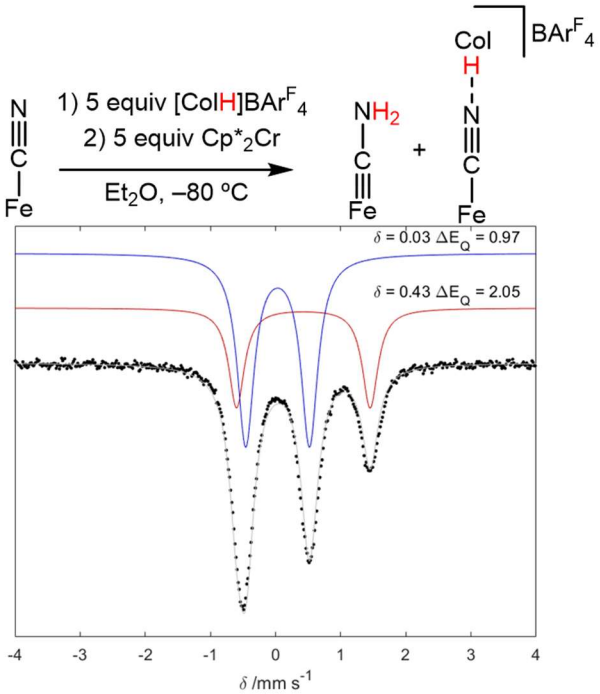

Figure B.52. Freeze-quenched Mössbauer of reaction of [FeCN] with $[ColH]BAr^F{}_4$ and $Cp^*{}_2Cr$.

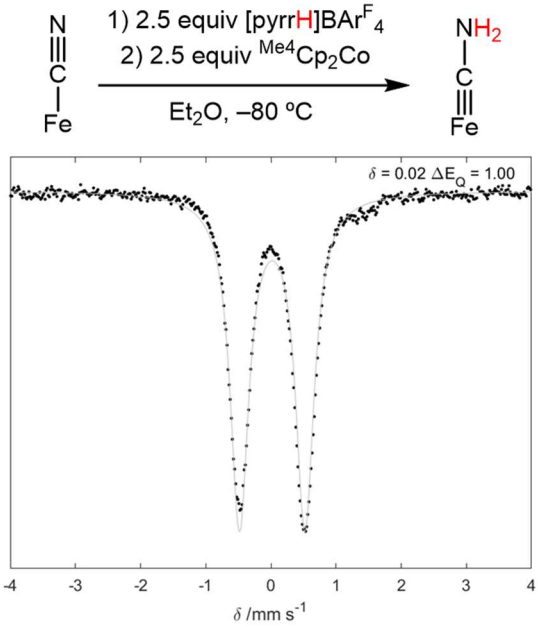

Figure B.53. Freeze-quenched Mössbauer of reaction of [FeCN] with [pyrrH]BAr$^F_4$ and $^{Me4}Cp_2Co$.

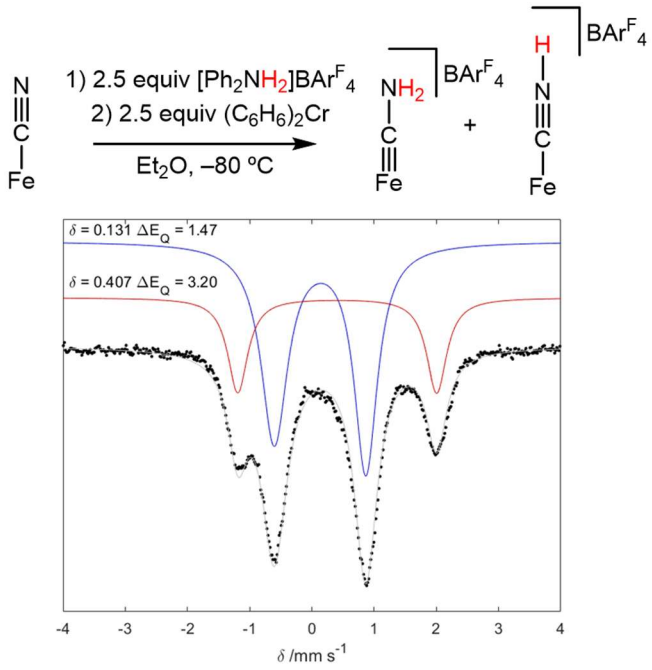

Figure B.54. Freeze-quenched Mössbauer of reaction of [FeCN] with [Ph$_2$NH$_2$]BAr$^F_4$ and Cp_2Co.

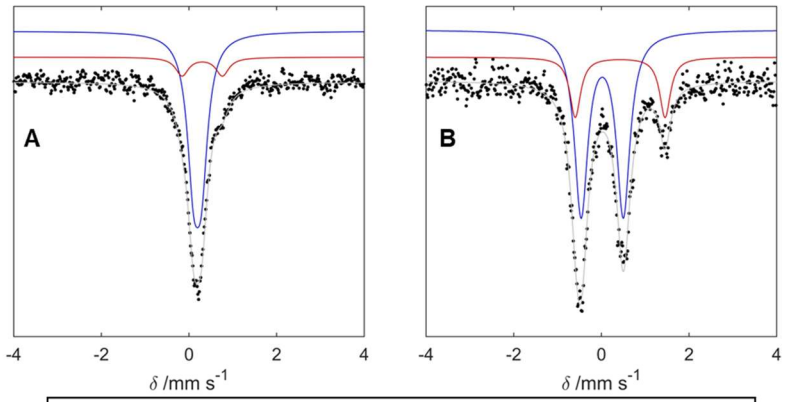

^{57}Fe spectra A			
δ(mm s^{-1})	ΔE_Q (mm s^{-1})	Γ (mm s^{-1})	Rel. area
0.20±0.01	0.18±0.05	0.35±0.05	86% (Blue)
0.30±0.01	0.92±0.05	0.36±0.03	14% (Red)

^{57}Fe spectra B			
δ(mm s^{-1})	ΔE_Q (mm s^{-1})	Γ (mm s^{-1})	Rel. area
0.02±0.01	0.96±0.01	0.37±0.01	80% (Blue)
0.43±0.01	2.09±0.01	0.30±0.01	20% (Red)

Figure B.55. Mössbauer spectrum of reaction of P_3^{Si}FeCN with sequentially KC_8 (excess), spectra A and 2 equiv $[H(OEt_2)_2]BAr^F{}_4$.

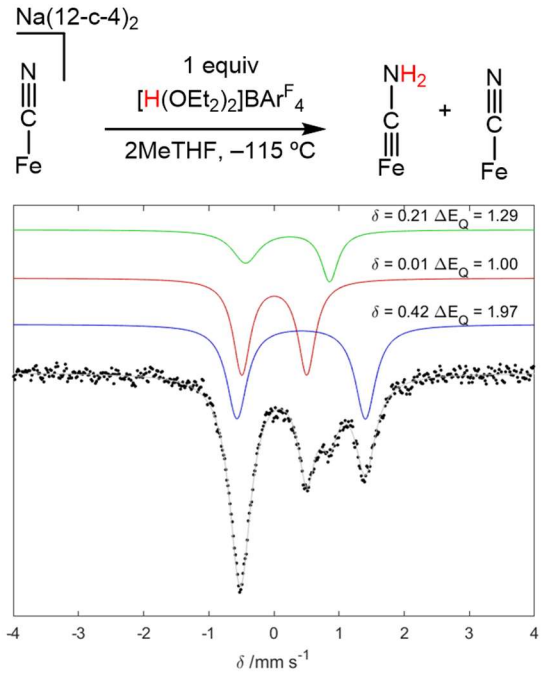

Figure B.56. Freeze-quenched Mössbauer of reaction of [FeCN][Na(12-c-4)$_2$] with $[H(OEt_2)_2]BAr^F{}_4$.

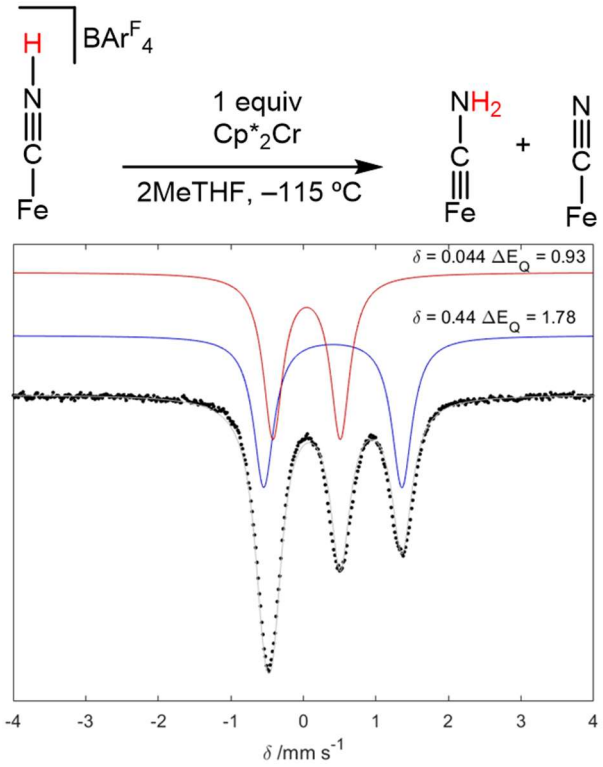

Figure B.57. Freeze-quenched Mössbauer of reaction of [FeCNH]BAr$^F_4$ with Cp*$_2$Cr.

B.6 IR spectroscopy

B.6.1 Solution state IR measurement of [FeCN···HNH$_2$Ph]BAr$^F_4$

B.6.1.1 General procedure

Inside the dry box a 5 mM solution of [FeCN] in 2-MeTHF 1 mL, was loaded into an IR-cell with KBr-windows and cooled to −78°C in the cold-well. After equilibration (15 minutes), the cell was rapidly removed from the cold-well and placed in an IR holder, allowing the beam to transport to the cell. After collection, the same procedure was followed, but 2.5 equiv [PhNH$_3$]BAr$^F_4$ (12.5 mM) was added.

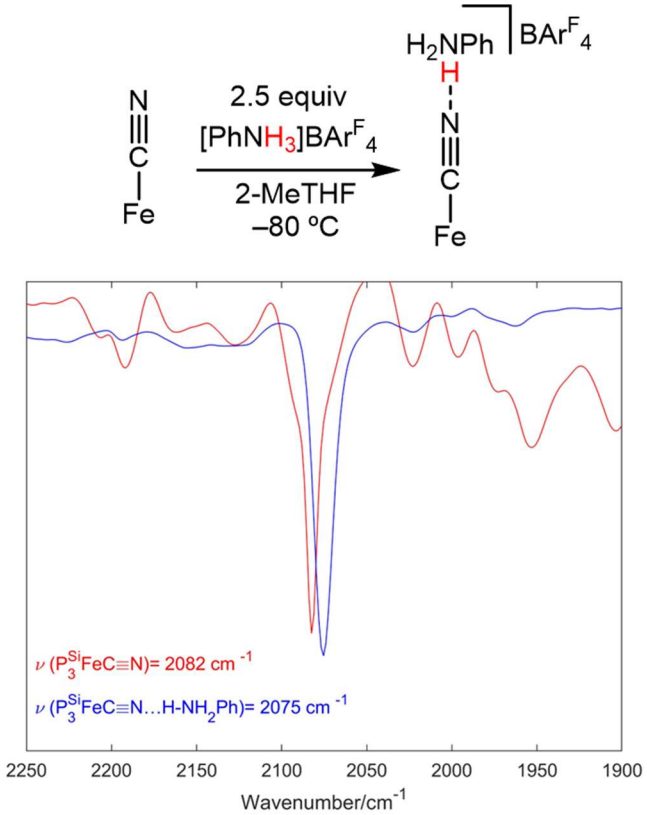

Figure B.58. IR comparison of [FeCN] with and without 2.5 equiv $[PhNH_2]OTf$ added. The weak shift of ν_{CN} suggests weak activation of [FeCN] consistent with an H-bond.

B.6.2 Solid state IR measurement of [FeCN···HTBD]

B.6.2.1 General procedure

Inside the dry box a, 10 mM solution of $[FeCN][Na(12\text{-}c\text{-}4)_2]$ (5 mg, 4.7 μmol) in 0.5 mL Et_2O was cooled to −78°C. $[TBDH]BAr^F_4$ (4.7 mg, 1 equiv) was added, and the reaction was allowed to stir for 5 minutes. 10 mL benzene was added slowly, such that it froze rapidly, upon addition. Subsequently, the solvent was removed in vacuo with care taken such that the benzene remained frozen, forming a lyophilized powder. This solid was then analyzed by IR, showing a slightly activated ν_{CN} = 1978 cm^{-1} compared to 2014 cm^{-1} in the $[FeCN][Na(12\text{-}c\text{-}4)_2]$ starting material. This stretch was confirmed to be from CN^- ligand by using the $[FeC^{15}N][Na(12\text{-}c\text{-}4)_2]$; the resulting ν_{C15N} = 1944 cm^{-1} is consistent with isotopic labeling (1947 cm^{-1} assuming harmonic oscillator model).

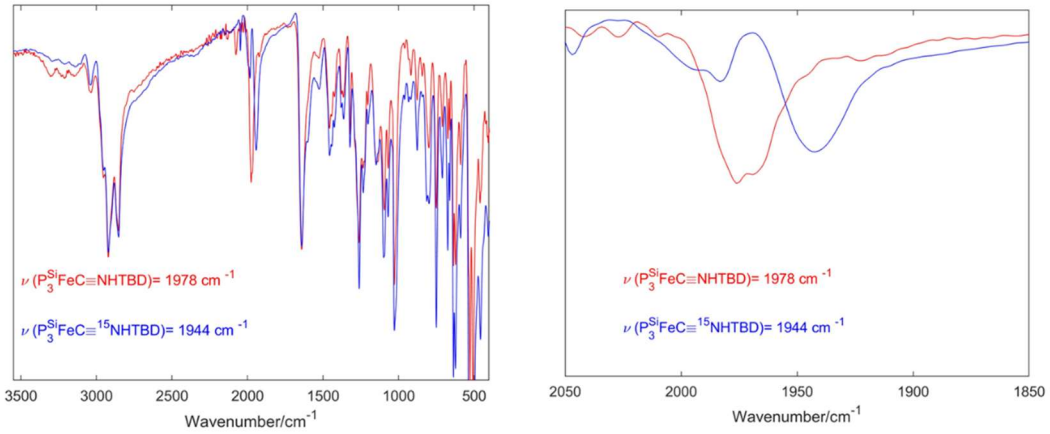

Figure B.59. Solid state IR of [FeCN···HTBD] and [FeC^{15}N···HTBD].

B.7 EPR spectroscopy

B.7.1 Generation of cw-EPR samples

The reaction of [FeCN] with weak acid ([TMGH]BAr$^{F}_{4}$ or [TBDH]BAr$^{F}_{4}$) and Cp*$_2$Co was monitored by cw-EPR. A 0.5 mL solution of [FeCN] (4 mM) in 2-MeTHF was cooled to −78°C, and acid (5 equiv) and reductant (5 equiv) were added as solids. The solution was allowed to stir for 5 minutes, then rapidly transferred to a X-band EPR tube, frozen at 77 K, and then analyzed.

Samples of [FeCN][Na(12-c-4)$_2$] + [TBD]OTf and [FeCN] with Cp*$_2$Co were prepared analogously, but only acid or reductant was added.

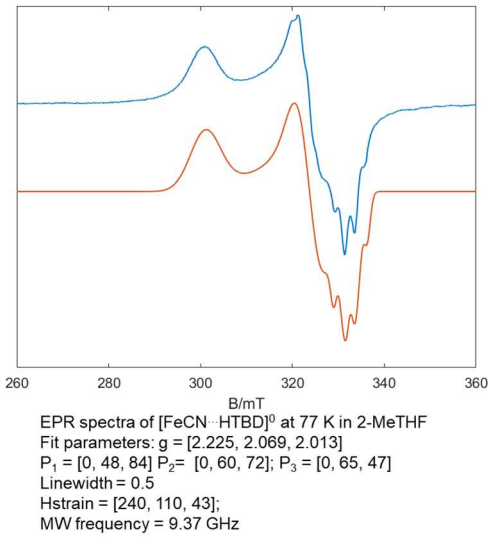

Figure B.60. X-band EPR spectra of independently synthesized $[Fe^{I}CN\cdots HTBD]^{0}$ (blue trace), collected at 2 mM concentration in 2-MeTHF at 77 K with fit (orange trace).

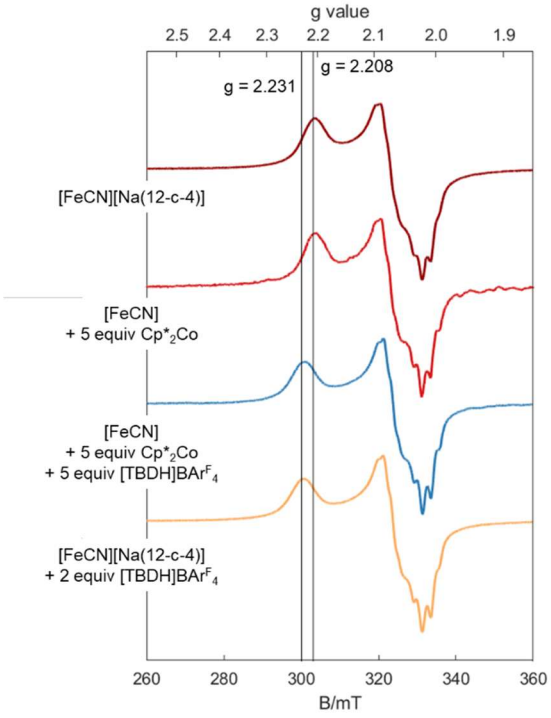

Figure B.61. X-band EPR spectra of compounds and reactions listed, collected at 2 mM concentration in 2-MeTHF at 77 K. Lines at g = 2.31 and 2.208 used to highlight shift in $g_{\parallel}$ between H-bonded and non H-bonded $[Fe^{I}CN]^{-}$ species.

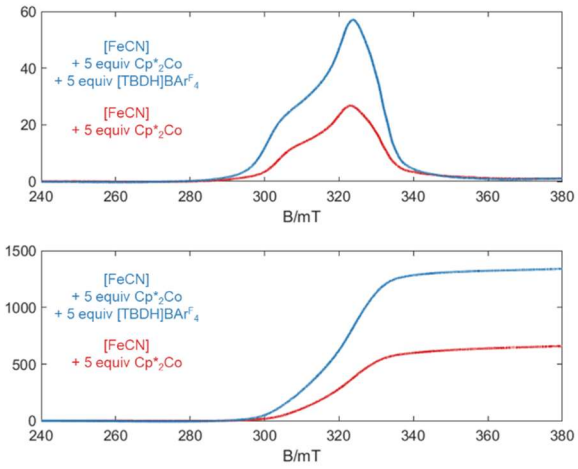

Figure B.62. Integral (top) and double integral (bottom) of X-band EPR spectra of compounds and reactions listed, collected at 2 mM concentration in 2-MeTHF at 77 K. Double integral shows that reaction with [TBDH]BAr^F_4 accounts for ~ double the intensity of the reaction without acid.

B.8 Electrochemical methods

B.8.1 General procedure

Electrochemical measurements were conducted with a glassy carbon working electrode, a platinum wire counter electrode, and an Ag/AgOTf reference electrode isolated by a CoralPor™ frit (obtained from BASi) and referenced externally to $Fc^{+/0}$. Unless specified, NaK-dried THF was used as a solvent, with 0.2 M [TBA][PF_6] electrolyte. Measurements conducted with a CH Instruments 600B electrochemical analyzer.

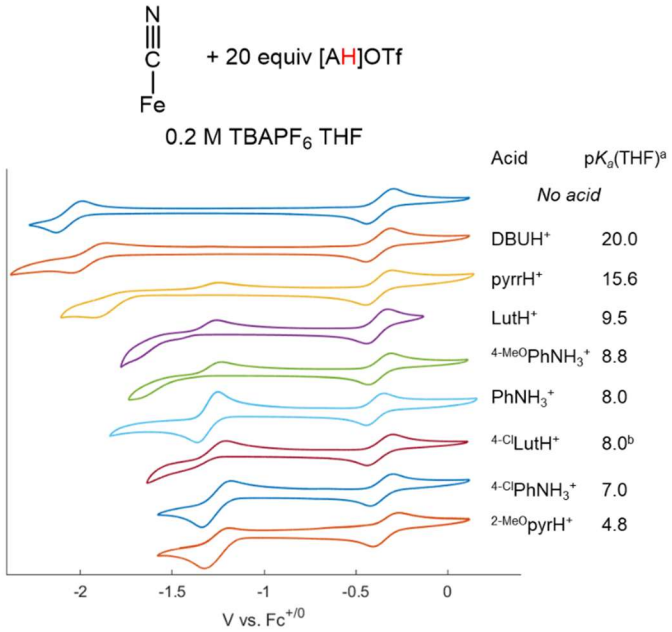

Figure B.63. Cyclic voltammetry of [FeCN] (1 mM, dashed lines) in 0.2 M [TBA]PF_6, in THF with added acid (20 mM [acid]OTf) at 100 mV s^{-1} scan rate. [a]pK_a from ref [10]; [b]pK_a measured in section B.9.

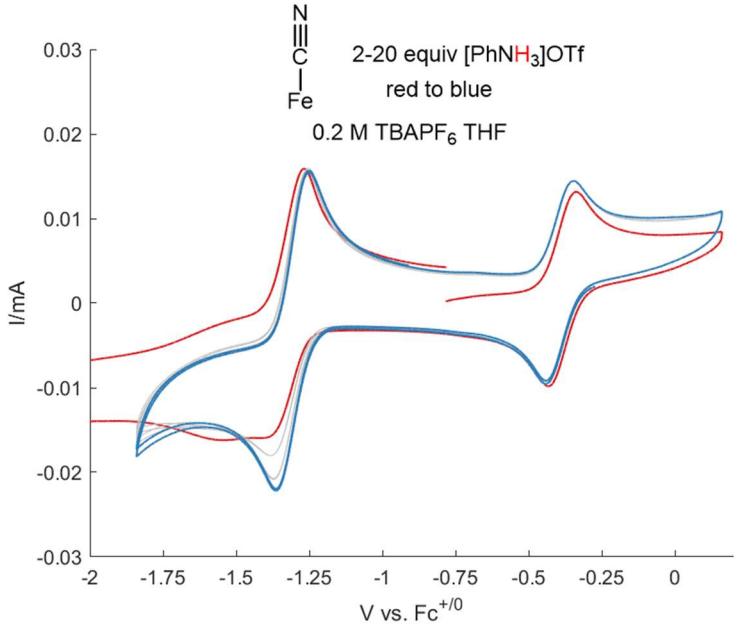

Figure B.64. Cyclic voltammetry of [FeCN] (1 mM, dashed lines) in 0.2 M [TBA]PF_6, in THF with added [$PhNH_3$]OTf (2 to 20 mM [acid]OTf).

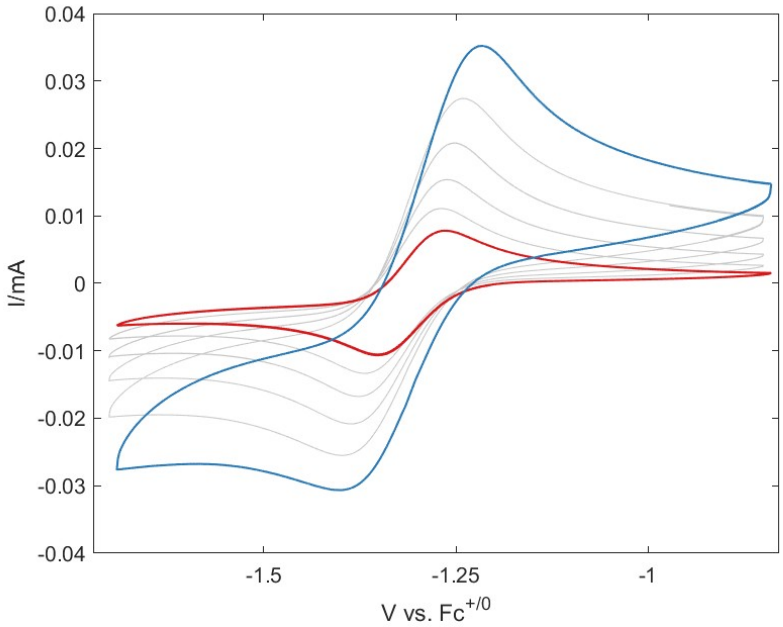

Figure B.65. Cyclic voltammetry of [FeCN] (1 mM, dashed lines) in 0.2 M [TBA]PF_6, in THF with added 20 mM [$PhNH_3$]OTf. Scan rate is varied from 25 mV s^{-1} to 800 mV s^{-1}.

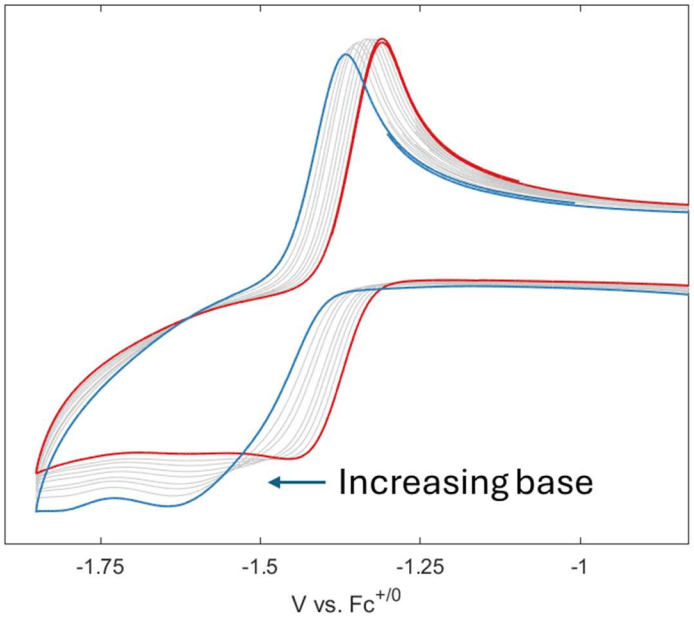

Figure B.66. Cyclic voltammetry of [FeCN] (1 mM, dashed lines) in 0.2 M [TBA]PF_6, in THF with added 20 mM [$PhNH_3$]OTf and varying amounts of [$PhNH_2$] (8 mM to 50 mM). Scan rate is 100 mV s^{-1}.

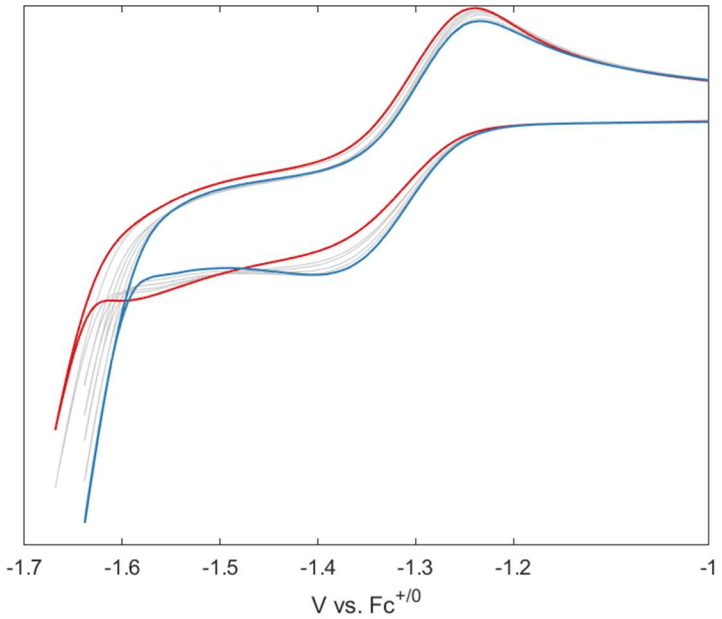

Figure B.67. Cyclic voltammetry of [FeCN] (1 mM, dashed lines) in 0.2 M [TBA]PF_6, in THF with added [$^{4\text{-Cl-2,6-Me}}$pyrH]OTf (10 to 60 mM; red to blue). Scan rate is 100 mV s^{-1}.

B.8.2 Additional comment on cyclic voltammograms of [FeCN] with acids

The differences observed between chemical (Figure 3.5) and electrochemical reductions (Figure B.63) are worth commenting on beyond the limited discussion in the main text. Monitoring chemical reduction of [FeCN] for a wide range of pK_a (7.0-15), the formation of the thermodynamically favored products is observed to occur rapidly, and in the case of Lut, equilibration is demonstrated. Monitoring the electrochemical reduction of [FeCN], we observe only strong acids (pK_a ~8) display reversible behavior. We attribute this to the weaker H-bonds formed under electrochemical conditions and a faster timescale of measurement that might disfavor sluggish reactions. In addition, for the oxidative half-wave, there is no shift of redox peaks with acid pK_a, suggesting that the oxidation of [$FeCNH_2$] is no longer redox-coupled, so only acids that for reduction of [FeCN] to [$FeCNH_2$] close to E([$FeCNH_2$]$^{+/0}$) might display a reversible $2H^+/2e^-$ wave.

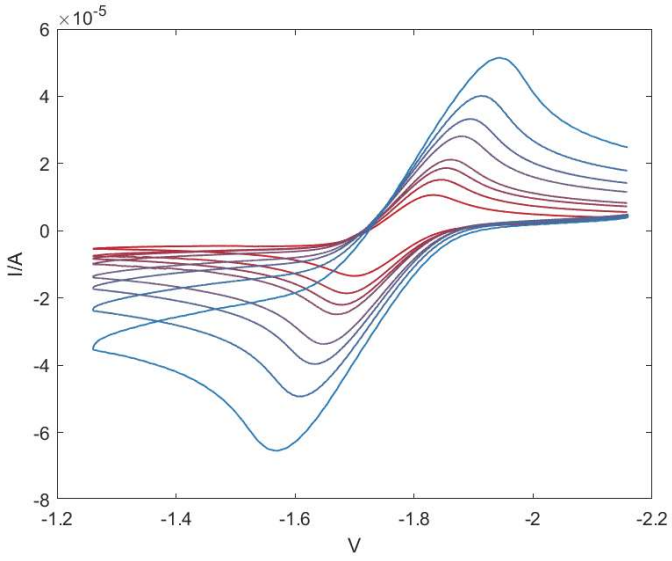

Figure B.68. Cyclic voltammetry of starting $^{Me4}Cp_2Co$ (1 mM, dashed lines) in 0.2 M [TBA]PF_6, in THF with varying scan rate from 25 (red trace) to 1000 mv s^{-1} (blue trace). Measured reduction potential measured as $E°$=−1.76 V vs $Fc^{+/0}$.

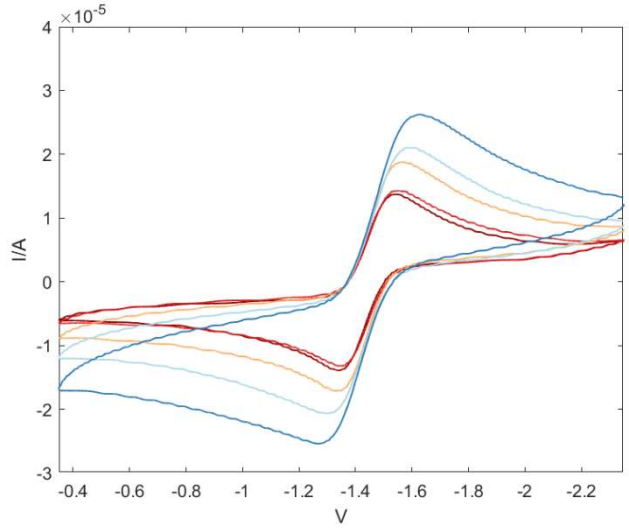

Figure B.69. Cyclic voltammetry of starting $^{Et}Cp_2Co$ (1 mM, dashed lines) in 0.2 M [TBA]PF_6, in THF with varying scan rate from 25 (red trace) to 1000 mv s^{-1} (blue trace). Measured reduction potential measured as $E°$=−1.45 V vs $Fc^{+/0}$.

B.9 Measurement of pK_a by NMR

B.9.1 General procedure

The acidity of $^{4\text{-Cl-2,6-Me}}$pyr had not been measured in THF. Given its central use in our discussion of the electrochemical reduction of [FeCN], we wanted to measure the acidity in THF against $PhNH_2$ to provide a tight and internally consistent comparison.

Using a method similar to what our group has previously used,[11] we started with an NMR tube with a known concentration of [$^{4\text{-Cl-2,6-Me}}$pyrH]OTf. Varying amounts of a $PhNH_2$ stock solution were added, and the shifts of ^{1}H NMR peaks were recorded. By comparing the position (as indicated in Figure B.70) to the acid (BH^+) and base (B) of the two components, we estimated the relative ratio of [acid]/[base] for both species.

$$[\mathrm{BH^+}] = \frac{(\delta_{obs} - \delta_{\mathrm{B}})}{(\delta_{\mathrm{BH+}} - \delta_{\mathrm{B}})} * [\mathrm{B}]_{tot} \quad \text{(eqn B.10)}$$

$$[\mathrm{B}] = [\mathrm{B}]_{tot} - [\mathrm{BH^+}] \quad \text{(eqn B.11)}$$

These values were used to estimate $K_{eq,\,exp}$ the equilibrium constant for each spectrum.

$$K_{eq} = \frac{[\mathrm{PhNH_3{}^+}][^{4-\mathrm{Cl-\ ,6-M}}\ \mathrm{Pyr}]}{[\mathrm{PhNH_2}][^{4-\mathrm{Cl-\ ,6-Me}}\mathrm{PyrH^+}]} \quad \text{eqn (B.12)}$$

The average of these values was used to determine K_{eq} = 0.90±0.03 M^{-1}, which via the pK_a of $PhNH_2$ (pK_a 8.0),[10] allows us to determine the pK_a of $^{4\text{-Cl-2,6-Me}}$pyr.

$$p\mathrm{K_a}(^{4-\mathrm{Cl-\ ,6-Me}}\mathrm{PyrH^+}) = p\mathrm{K_a}(\mathrm{PhNH_3{}^+}) - log_{10}(K_{eq}) \quad \text{eqn(B.13)}$$

$$= 8.0 - log_{10}(0.9) = 8.0$$

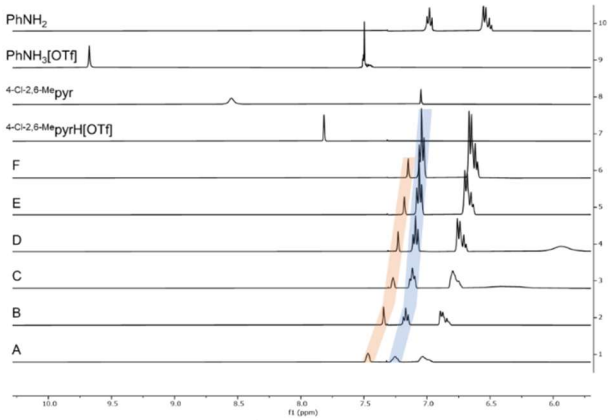

Figure B.70. Titration of [$PhNH_2$] in [$^{4\text{-Cl-2,6-Me}}$pyrH]OTf in THF as monitored by ^{1}H NMR. Peaks used to calculate acid/base ratio and positions of peaks in authentic acids and base are indicated as shown. Amount of [$PhNH_2$] added increases from A to F.

Note: All spectra were measured in h_8-THF with solvent suppression applied and with spectra shimmed on the ^{1}H peaks through the lock-channel.

Table B.4. Table with peak positions recorded based on Figure B.71 with subsequent amounts of titration components calculated along with $K_{eq,exp}$ and K_{eq} with associated error bars.

Entry	$PhNH_2$ added (equiv)	Vol. (mL)	^{1}H NMR pos. $^{4\text{-Cl-2,6-Me-}}$pyr (ppm)	Conc. $[^{4\text{-Cl-2,6-Me-}}$pyrH$]^+$ (mM)	Conc. $[^{4\text{-Cl-2,6-Me-}}$pyr] (mM)	^{1}H NMR pos. $PhNH_2$ (ppm)	Conc. $[PhNH_3]^+$ (mM)	Conc. $[PhNH_2]$ (mM)	$K_{eq,\ exp}$ (M^{-1})
Acid		0.6	7.82			7.50			
Base			7.05			6.98			
A	0.9	0.61	7.46	5.2	4.6	7.25	4.8	4.4	0.94
B	1.8	0.62	7.35	3.8	5.9	7.17	6.3	11.1	0.90
C	2.7	0.63	7.27	2.7	6.8	7.12	6.9	19.0	0.91
D	3.6	0.64	7.23	2.2	7.2	7.09	7.1	26.6	0.87
E	5.5	0.66	7.18	1.5	7.6	7.06	7.6	42.3	0.88
F	7.6	0.68	7.15	1.1	7.7	7.04	7.6	59.1	0.86

$K_{eq,\ exp}$ (M^{-1})	0.90
Error (M^{-1})	0.03

B.10 Computational studies and implementation of ECW model

B.10.1 General overview of computational details

For our computational studies we employed the TPSS functional[12] and a def2-TZVP basis set on transition metals and a def2-SVP basis set on all other atoms,[13] which we have previously demonstrated accurately replicate BDFEs on similar platforms.[14] The ORCA open source software package was used.[15] The numerical frequencies of the minimized structures were calculated to ensure that these structures represented local minima and not saddle points. The energies of relevant structures are displayed in Table B.6.

B.10.2 ECW model

The ECW model was used to classify the strength and type of Lewis basicity displayed by $P_3{}^BFeNN$, $P_3{}^BFeNNH$ and $P_3{}^BFeNNH_2$. Using the calculated gas phase enthalpies of the $P_3{}^BFeNN(H)_x\cdots LA$ (x = 0,1 or 2) adducts and the known C_A and E_A parameters of five Lewis acids (HNCS, PhOH, PhSH, BF_3 and BMe_3, see table B.6). A minimal solution was then found to these five simultaneous equations. An additional binding energy (ΔH_{disp}) of ~8 kcal mol^{-1}, a weak dispersive interaction, was also found as the Lewis acidity trended towards 0, this was accounted for as an additional parameter in the five simultaneously solved equations.

$$-\Delta H = C_A C_B + E_A E_B - \Delta H_{disp} \quad \text{eqn(B.14)}$$

The C_B and E_B parameters also allow us to compare $P_3{}^BFeNN(H)_x$ to other known Lewis bases, this is shown in Figure B.71.

With these determined values the Lewis adduct strength, we can also predict the $BDFE_{N\text{-}H}$ of stabilized diazenido and hydrazido complexes using eqn B.15

$$\mathrm{BDFE_{X-H\cdots LA}} = \mathrm{BDFE_{X-H}} + (\Delta H_{\mathrm{X-H}} - \Delta H_X) \quad \text{eqn(B.15)}$$

Table B.6. E_A and C_A parameters of Lewis acids used to determine E_B, C_B and ΔH_{disp} for $P_3{}^BFeNN$, P_3FeNNH and $P_3{}^BFeNNH_2$.

Lewis acid	E_A $(kcal\ mol^{-1})^{1/2}$	C_b $(kcal\ mol^{-1})^{1/2}$	W $(kcal\ mol^{-1})$
BF_3	6.1	2.87	0
BMe_3	2.9	3.6	0
PhOH	2.27	1.07	0
PhSH	0.58	0.37	0
HNCS	2.85	0.7	0

Table B.7. Computed E_B, C_B and ΔH_{disp} parameters for $P_3{}^BFeNN$, P_3FeNNH and $P_3{}^BFeNNH_2$.

Lewis base	E_A $(kcal\ mol^{-1})^{1/2}$	C_b $(kcal\ mol^{-1})^{1/2}$	ΔH_{disp} $(kcal\ mol^{-1})$
$P_3{}^BFeNN$	0.9±0.3	0.0±0.35	9.8
$P_3{}^BFeNNH$	2.8±0.4	0.4±0.7	8.7
$P_3{}^BFeNNH_2$	2.1±0.5	0.0±0.8	7.6

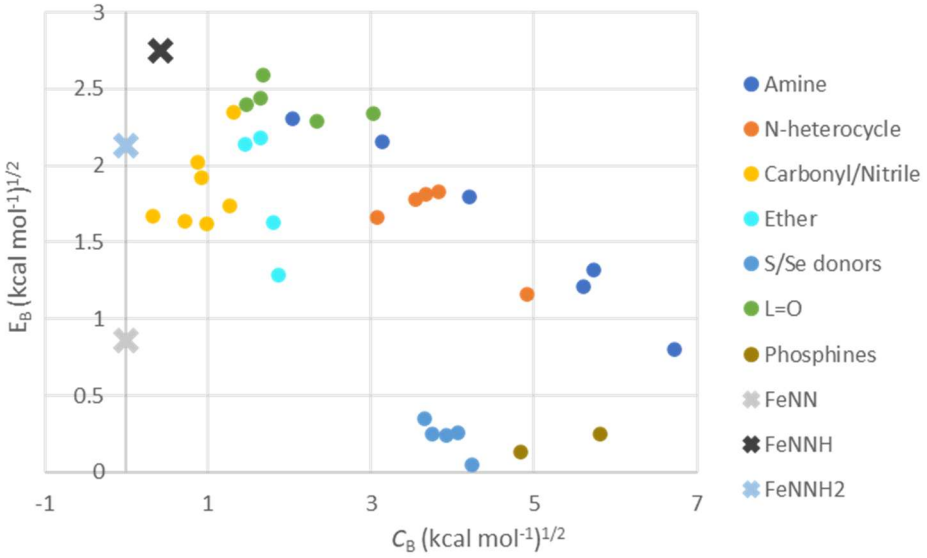

Figure B.71. Comparison of E_B and C_B parameters for $P_3{}^BFeNN$, P_3FeNNH and $P_3{}^BFeNNH_2$ with other Lewis bases.

Table B.8. Estimated $BDFE_{N-H}$ for Lewis acid stabilized adduct of $P_3{}^BFeNN$, P_3FeNNH and $P_3{}^BFeNNH_2$.

Lewis acid	BDFE(FeNNH) (kcal mol^{-1})	BDFE($FeNNH_2$) (kcal mol^{-1})
None	26.9	38.2
CH_2Cl_2	26.3	36.7
$HCCl_3$	27.2	36.2
^tBuOH	27.5	36.3
C_4H_4NH	27.6	36.1
$C_8H_{17}OH$	27.7	36.2
HNCO	27.7	36.0
HNCS	28.2	35.5
$(CH_3)_3SnCl$	28.2	35.5
CF_3CH_2OH	28.5	35.6
SO_2	28.8	36.0
$^{4\text{-Me}}PhOH$	28.5	35.6
PhOH	28.6	35.6
$^{4\text{-CF3}}PhOH$	29.0	35.4
cobalt(II) protoporhyrin IX dimethyl ester IX	29.1	35.4
I_2	29.6	35.7
$(CF_3)_2CHOH$	29.4	35.1
ZnTPP	29.5	35.1
ICl	30.0	34.9
$Cd[N(Si(CH_3)_2]_2$	30.1	35.0
$1/2[Pd(\pi\text{-ally})Cl]_2$	30.3	35.1
$(CF_3)_3COH$	30.4	34.8
$Zn[N(Si(CH_3)_3]_2$	31.1	34.6
$1/2[Rh(COD)_2Cl]_2$	31.4	34.6
$Cu(HFacac)_2$	31.7	34.7
IBr	32.2	34.6
$Ga(C_2H_5)_3$	31.2	33.4
$InMe_3$	32.3	33.2
BMe_3	33.5	33.8
$1/2[MeCo(Hdmg)_2]_2$	34.0	33
BF_3	33.4	32.9
$1/2[Rh(COD)_2Cl]_2$	35.0	32.9
$AlMe_3$	35.9	31.4
$SbCl_5$	46.1	29.4

B.11 X-ray crystallographic data

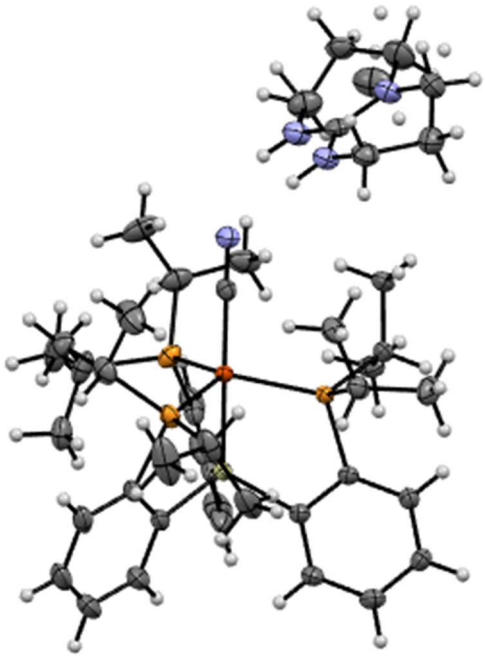

Figure B.72. ORTEP plot of [FeCN][HTBD] with H-atoms and disorder (in $TBDH^+$) shown.

Table B.9. Comparison of XRD parameters for [FeCN][HTBD] to [FeCN] species[1,2] and [TBDH]BPh_4.[16]

	[FeCN][HTBD]	[FeCN][$Na(12\text{-}c\text{-}4)_2$]	[FeCNMe]	[TBDH]BPh_4
C−N (Å)	1.172(3)	1.170(2)	1.186(2)	-
Fe−C (Å)	1.914(2)	1.949(2)	1.821(2)	-
Fe−P (Å)	2.2670(7)	2.252(1)	2.287(1)	-
Fe−P (Å)	2.2378(7)	2.231(1)	2.2729(8)	-
Fe−P (Å)	2.2353(6)	2.2242(4)	2.2560(7)	-
Mean (Fe-P) (Å)	2.2467	2.262067	2.271967	-
Fe−Si (Å)	2.2209(7)	2.242(1)	2.2732(8)	-
N_c-C (Å)	1.341(3)	-	-	1.328
N_a-C_d (Å)	1.328(3)	-	-	1.33
N_b-C_d (Å)	1.327(3)	-	-	1.33
$N_{a,TBD}$-N_{CN} (Å)	2.943(3)	-	-	-
$N_{b,TBD}$-N_{CN} (Å)	2.864(3)	-	-	-
<P-Fe-P °	131.04(2)	128.08(3)	122.87(2)	-
<P-Fe-P °	114.92(3)	114.11(3)	117.82(2)	-
<P-Fe-P °	108.58(2)	111.70(3)	112.49(2)	-
Σ<P-Fe-P	354.54	353.89	353.18	-
<Fe-C-N °	177.8(2)	177.4(2)	177.6(1)	-

Table B.10. Data relevant to crystal structure of [P_3^{Si}FeCN][HTBD].

Table 1 Crystal data and structure refinement for P_3^{Si}FeCN[HTBD]	
Identification code	
Empirical formula	$C_{42}H_{68}N_4SiP_3Fe$
Formula weight	805.85
Temperature/K	100.0
Crystal system	monoclinic
Space group	$P2_1/c$
a/Å	11.5710(4)
b/Å	18.3047(6)
c/Å	21.3059(7)
α/°	90
β/°	103.861(2)
γ/°	90
Volume/Å³	4381.3(3)
Z	4
ρ_{calc}g/cm³	1.222
μ/mm⁻¹	4.302
F(000)	1732.0
Crystal size/mm³	? × ? × ?
Radiation	CuKα (λ = 1.54178)
2Θ range for data collection/°	6.448 to 158.584
Index ranges	-14 ≤ h ≤ 14, -22 ≤ k ≤ 20, -26 ≤ l ≤ 26
Reflections collected	108896
Independent reflections	9339 [R_{int} = 0.0640, R_{sigma} = 0.0268]
Data/restraints/parameters	9339/0/501
Goodness-of-fit on F²	1.134
Final R indexes [I>=2σ (I)]	R_1 = 0.0418, wR_2 = 0.1316
Final R indexes [all data]	R_1 = 0.0493, wR_2 = 0.1402
Largest diff. peak/hole / e Å⁻³	0.46/-0.58

B.12 References for Appendix B

1. Rittle, J.; Peters, J. C. *Angew. Chem. Int. Ed.* **2016**. 55, 12262–12265.
2. Rittle, J.; Peters, J. C. *J. Am. Chem. Soc.* **2017**. 139, 3161–3170.
3. Del Castillo, T. J.; Thompson, N. B.; Peters, J. C. *J. Am. Chem. Soc.* **2016**. 138, 5341–5350.
4. Köhler, F. H.; Doll, K. *Z. Für Naturforschung B* **1982**. 37, 144–150.
5. Chalkley, M. J.; Del Castillo, T. J.; Matson, B. D.; Peters, J. C. *J. Am. Chem. Soc.* **2018**. 140, 6122–6129.
6. Fajardo, J.; Peters, J. C. *J. Am. Chem. Soc.* **2017**. 139, 16105–16108.

7. Fulmer, G. R.; Miller, A. J. M.; Sherden, N. H.; Gottlieb, H. E.; Nudelman, A.; Stoltz, B. M.; Bercaw, J. E.; Goldberg, K. I. *Organometallics* **2010**. 29, 2176–2179.
8. Stoll, S.; Schweiger, A. *J. Magn. Reson.* **2006**. 178, 42–55.
9. Perkampus, H.-H. *UV-VIS Spectroscopy and Its Applications*; Springer Science & Business Media, 2013.
10. Garrido, G.; Rosés, M.; Ràfols, C.; Bosch, E. *J. Solut. Chem.* **2008**, 37, 689–700. .
11. Chalkley, M. J.; Garrido-Barros, P.; Peters, J. C. *Science* **2020**. 369, 850–854.
12. Tao, J.; Perdew, J. P.; Staroverov, V. N.; Scuseria, G. E. *Phys. Rev. Lett.* **2003**, 91, 146401–146404.
13. Weigend, F. *Phys. Chem. Chem. Phys.* **2006**, 8, 1057–1065.
14. Matson, B. D.; Peters, J. C. *ACS Catal.* **2018**, 8, 1448–1455.
15. Neese, F.; Wennmohs, F.; Becker, U.; Riplinger, C. *J. Chem. Phys.* **2020**, 152, 224108.
16. Khalaf, M. S.; Oakley, S. H.; Coles, M. P.; Hitchcock, P. B. *CrystEngComm* **2008**. 10, 1653–1661.

Appendix C

Supplementary Information for Chapter 4

C.1 Materials and Methods

C.1.1 General Considerations

All manipulations were carried out using standard Schlenk or glovebox techniques under an N_2 atmosphere. Solvents were deoxygenated and dried by thoroughly sparging with N_2, followed by passage through an activated alumina column in a solvent purification system by SG Water, USA LLC. Nonhalogenated solvents were tested with sodium benzophenone ketyl in tetrahydrofuran (THF) to confirm the absence of oxygen and water. Deuterated solvents were purchased from Cambridge Isotope Laboratories, Inc., degassed, and dried over activated 3-Å molecular sieves prior to use.

C.1.2 Reagents

HEH_2,[1] $PNPMoBr_3$,[2] [ColH]OTf,[2] $[P_3^BFe]BAr^F_4$ (P_3^B = tris[2-(diisopropylphosphino)phenyl]borane),[3] BTH_2,[4] $NaBAr^F_4$,[5] ^{15}N-Col,[6] $phenH_2$,[7] $phenazH_2$,[8] $[TBA][^{15}NO_3]$[9] were prepared according to literature procedures. Triflic acid, ethyl acetoacetate, and 37% aqueous formaldehyde were purchased from Sigma Aldrich and used without further purification. $Ir(ppy)_3$, $Ir(ppy)_2(dtbbpy)[PF_6]$, $[Ir(dF(CF_3)ppy)_2(dtbbpy)]PF_6$, $[Ir(p\text{-}F(Me)ppy)_2(dtbbpy)]PF_6$ were purchased from Strem and used without further purification. $[TBA]NO_3$ was purchased from Alfa Aesar, and was dissolved in THF, filtered over activated alumina to dry to purify prior to use. $^{15}N_2$ was obtained from Cambridge Isotope Laboratories, Inc. (Lot number: I-25854/XZ732957). $^{15}NH_4Cl$ (99% ^{15}N, 98% purity) and $Na^{15}NO_3$ (98% ^{15}N, 98% purity) were purchased from Cambridge Isotope Laboratories, Inc. and used without further purification. Collidine was purchased from Sigma Aldrich and was distilled prior to use. 9,10-dihydroacridine (98%) was purchased from Combi Blocks and used without further purification. 1-benzyl-1,4-dihydronicotinamide was purchased from TCI and used without further purification. Acetylene (99.6% purity) was purchased from Matheson Gas. Tetrahydrofuran (THF) used in the experiments herein was stirred over Na/K ($\geq$ 12 hours) and filtered over activated alumina or vacuum-transferred before use unless otherwise stated.

Photoinduced reactions were performed using Kessil® 34 W 150 Blue lamps.

C.1.3 Physical Methods

NMR: Nuclear Magnetic Resonance (NMR) measurements were recorded with a Varian 400 MHz spectrometer. ^{1}H NMR chemical shifts are reported in ppm relative to tetramethylsilane, using ^{1}H resonances from residual solvent as internal standards.[10]

UV-Vis: Ultraviolet-visible (UV-vis) absorption spectroscopy measurements were collected with a Cary 50 UV-vis spectrophotometer using a 1 cm path length quartz cuvette. All samples had a blank sample background subtraction applied.

EPR Spectroscopy: All X-band continuous-wave electron paramagnetic resonance (CW-EPR) spectra were obtained on a Bruker EMX spectrometer using a quartz liquid nitrogen immersion dewar on solutions prepared as frozen glasses in 2-MeTHF.

Steady-state fluorimetry: Steady-state fluorimetry was performed in the Beckman Institute Laser Resource Center (BILRC; California Institute of Technology). Samples for luminescence measurements were prepared in dry THF and transferred to a 1-cm pathlength fused quartz cuvette sealed with a high-vacuum Teflon valve (Kontes). Steady-state emission spectra were collected on a Jobin S4 Yvon Spec Fluorolog-3-11 with a Hamamatsu R928P photomultiplier tube detector with photon counting.

C.1.4. Synthetic details

^{15}N-labelled 2,6-Dimethyl-3,5-dicarboethoxy-l,4-dihydropyridine (^{15}N-HEH$_2$).

Adapted from ref 1. Aqueous formaldehyde (37%, 78 μL) and ethyl acetoacetate (280 μL, 2.19 mmol) were placed in a 10 mL round-bottom flask equipped with a stir bar and fitted with a reflux condenser. $^{15}NH_4Cl$ (305 mg, 5.7 mmol) in 1 mL H_2O was added to a 1 mL aqueous solution of NaOH (228.3 mg, 5.7 mmol). The resulting solution of $^{15}NH_4OH$ was added to the flask through the neck of the condenser. The condenser neck was rinsed into the flask with 0.5 mL ethanol. The reaction mixture was heated at reflux for 1.5 hrs and then chilled in an ice bath. The resulting precipitate was collected by filtration and washed with cold ethanol (~3 mL) and Et_2O to yield the title compound as a pale yellow powder (60 mg, 22% yield). ^{1}H NMR (400 MHz, DMSO-d_6) δ 8.28 (d, $^{1}J_{H,N}$ =

94.6 Hz, 1H), 4.05 (q, J = 7.1 Hz, 4H), 3.11 (s, 2H), 2.11 (d, J = 2.9 Hz, 6H), 1.19 (t, J = 7.1 Hz, 6H) ppm.

^{15}N-labelled 2,4,6-Dimethylpyridinium (^{15}N-[ColH]OTf).

An identical procedure to what has previously been reported with unlabeled Col was employed.[2] ^{1}H NMR (400 MHz, DMSO-d_6) δ 14.87 (broad s, 1H), 7.57 (d, $^3J_{H,N}$ = 2.8 Hz, 2H), 2.62 (d, $^3J_{H,N}$ = 2.9 Hz, 6H), 2.49 (s, 3H) ppm.

[4,4′-Bis(1,1-dimethylethyl)-2,2′-bipyridine-N1,N1′]bis[2-(2-pyridinyl-N)phenyl-C]iridium(III) Tetrakis(3,5-bis(trifluoromethyl)phenyl)borate ([Ir]BAr$^F_4$).

Ir(ppy)$_2$(dtbbpy)[PF$_6$] (100 mg, 0.11 mmol) and Na[BAr$^F_4$] (92.2 mg, 0.10 mmol, 0.95 eq) were stirred in 5 mL Et$_2$O at room temperature for 1 hour. The solution was filtered through celite, layered with pentane, and stored at -40°C overnight to yield the title compound as yellow crystals (161 mg, 90% yield). ^{1}H NMR (400 MHz, MeCN-d_3) δ 8.48 (s, 2H), 8.06 (d, 2H, J = 8.2 Hz), 7.93-7.76 (m, 6H), 7.74-7.64 (m, 10H), 7.58 (d, J = 5.8 Hz, 2H), 7.50 (dd, J = 5.9, 1.9 Hz, 2H), 7.03 (t, J = 6.8 Hz, 2H), 6.91 (t, J = 6.8 Hz, 2H), 6.28 (d, J = 6.3 Hz, 2H), 1.40 (s, 18H) ppm.

C.2 NH$_3$ generation experiments

C.2.1 Standard NH$_3$ Generation Reaction Procedure

All solvents are stirred with Na/K for ≥2 hours and filtered prior to use. In a nitrogen-filled glovebox, the precatalysts ([MoBr$_3$] and/or [Ir]BAr$^F_4$) (2.3 μmol) are weighed in individual vials.* The precatalysts are then transferred quantitatively into a Schlenk tube using THF. The THF is then evaporated to provide a thin film of precatalyst at the bottom of the Schlenk tube. The tube is then charged with a stir bar and the acid and Hantzsch ester (HEH_2) are added as solids. The tube is cooled to 77 K in a cold well. The base ([Col]) is dissolved in 1 mL solvent. To the cold tube is added the 1 mL solution of base and solvent to produce a concentration of precatalyst of 2.3 mM. The temperature of the system is allowed to equilibrate for 5 minutes, and then the tube is sealed with a Teflon screw-valve. This tube is passed out of the box into a liquid N_2 bath and transported to a fume hood. For experiments run at -78 °C, the tube is then transferred to a dry ice/isopropanol bath, where it

thaws and is allowed to stir under blue LED irradiation at -78 °C for a minimum of three hours before warming. For experiments run at 23 °C, the tube is instead transferred to a water bath where it thaws and is allowed to stir for 12 hours. To ensure reproducibility, all experiments were conducted in 200 mL Schlenk tubes (50 mm OD) using 10 mm egg-shaped stir bars, and stirring was conducted at ~600 rpm. Both the water bath and the dry ice/isopropanol bath were contained in highly reflective dewars. The Blue LED was placed above the bath as close to the stirring reaction.

* In cases where less than 2.3 μmol of precatalyst were used, stock solutions were used to avoid having to weigh very small amounts.

C.2.2 NH_3 Generation Reaction Procedure under Partial H_2 Atmosphere

Catalytic runs done under a mixture of H_2 and N_2 were conducted similarly to those under N_2 atmosphere, with a few differences described below. The loadings were the same as in Table 4.1, Entry 10.

Catalysis is performed in the same Schlenk tubes as under N_2, which are charged with precatalyst, HEH_2, [ColH]OTf, and a stir bar in a nitrogen-filled glovebox as described above. After addition of the solids, the tube is wrapped in aluminum foil and the base (Col) is added in 1 mL of Na/K dried THF at room temperature. Half of the headspace volume is then removed using a calibrated bulb and then backfilled with H_2 which has been passed through a liquid nitrogen trap. The aluminum foil is removed, and the reaction is allowed to stir under Blue LED irradiation for 12 hours. Variation from the standard procedure (addition of THF/Col at room temperature and allowing to stir without irradiation for 30 min before exposing to blue LED) were found to not perturb the yield of NH_3.

C.2.3 NH_3 detection by optical methods

Reaction mixtures are cooled to 77 K and allowed to freeze. The reaction vessel is then opened to atmosphere and to the frozen solution an excess of a solution of HCl (3 mL of a 2.0 M solution in Et_2O, 6 mmol) is added over 1-2 minutes. This solution is allowed to freeze, then the headspace of the tube is evacuated, and the tube is sealed. The tube is then allowed to warm to RT and stirred at RT for at least 10 minutes. Solvent is removed *in vacuo*,

and the solids are extracted with 1 M HCl(aq) and filtered to give a total solution volume of 10 mL. A 5 mL aliquot is taken and washed repeatedly with n-butanol to remove Hantzsch pyridine (HE) and collidinium. After n-butanol washing additional 1 M HCl(aq) is added to give a final total volume of 5 mL. From these 5 mL solutions, a 100 µL aliquot is analyzed for the presence of NH_3 (present as $[NH_4][Cl]$) by the indophenol method. Quantification was performed with UV-vis spectroscopy by analyzing the absorbance at 635 nm.[11] When specified, a further aliquot of this solution was analyzed for the presence of N_2H_4 (present as $[N_2H_5][Cl]$) by a standard colorimetric method.[12] Quantification was performed with UV-vis spectroscopy by analyzing the absorbance at 458 nm.

C.2.4 NH_3 detection by ^1H NMR

Reaction mixtures are cooled to 77 K and allowed to freeze. The reaction vessel is then opened to atmosphere and to the frozen solution an excess (with respect to acid) NaO^tBu solution in MeOH (0.25 mM) is added over 1-2 minutes. This solution is allowed to freeze, then the headspace of the tube is evacuated, and the tube is sealed. The tube is then allowed to warm to RT and stirred at RT for at least 10 minutes. An additional Schlenk tube is charged with HCl (3 mL of a 2.0 M solution in Et_2O, 6 mmol) to serve as a collection flask. The volatiles of the reaction mixture are vacuum transferred at RT into this collection flask. After completion of the vacuum transfer, the collection flask is sealed and warmed to RT. Solvent is removed in vacuo, and the remaining residue is dissolved in 0.7 mL of DMSO-d_6 containing 20 mM 1,3,5-trimethoxybenzene as an internal standard. Integration of the ^1H NMR peak observed for NH_4^+ is then integrated against the two peaks of trimethoxybenzene to quantify the ammonium present. This ^1H NMR detection method was also used to differentiate $[^{14}NH_4][Cl]$ and $[^{15}NH_4][Cl]$ produced in the control reactions conducted with $^{15}N_2$, ^{15}N-Col/[ColH]OTf, or ^{15}N-HEH_2.

C.2.5 NH_3 detection results

C.2.5.1 Catalytic results in main text (Table 4.1)

Table C.1: Catalytic yields for photodriven transfer hydrogenation of N_2 to NH_3.

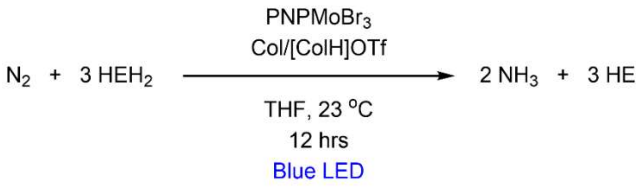

Run	Conditions	[Mo] load (µmol)	acid (µmol)	base (µmol)	Ir (µmol)	HEH_2 equiv /Mo	NH_3 equiv /Mo	N_2H_4 equiv/ Mo	NH_3 yield/ HEH_2 (%)
Table 4.1, entry 1: Standard conditions									
A1	THF, 23 °C	2.3	124.2	124.2	0	54	9.5	-	
B1	THF, 23 °C	2.3	124.2	124.2	0	54	8.3	-	
C1	THF, 23 °C	2.3	124.2	124.2	0	54	10.8	-	
	THF, 23 °C	2.3	124.2	124.2	0	54	9.5±1		26.5±3
Table 4.1, entry 2: 0.575 mM [$MoBr_3$]									
D1	THF, 23 °C	0.575	124.2	124.2	0	216	22.6	-	
E1	THF, 23 °C	0.575	124.2	124.2	0	216	20.9	-	
	THF, 23 °C	0.575	124.2	124.2	0	216	21.8±0.8		15.1±06
Table 4.1, entry 3: No Mo									
F1	THF, 23 °C	0	124.2	124.2	0	54	<0.1	<0.1	
G1	THF, 23 °C	0	124.2	124.2	0	54	<0.1	<0.1	
	THF, 23 °C	2.3	124.2	124.2	0	54	<0.1	<0.1	<0.3
Table 4.1, entry 4: No light									
H1	THF, 23 °C no light	2.3	124.2	124.2	0	54	<0.1	<0.1	
I1	THF, 23 °C no light	2.3	124.2	124.2	0	54	<0.1	<0.1	
	THF, 23 °C no light	2.3	124.2	124.2	0	54	<0.1	<0.1	<0.3
Table 4.1, entry 5: No buffer									
J1	THF, 23 °C	2.3	**0**	**0**	0	54	0.74	-	
K1	THF, 23 °C	2.3	**0**	**0**	0	54	1.11	-	
	THF, 23 °C	2.3	**0**	**0**	0	54	0.9±0.2		2.6±0.5
Table 4.1, entry 6: 5 equiv Col/[ColH]OTf									
L1	THF, 23 °C	2.3	11.5	11.5	0	54	2.7	<0.1	
M1	THF, 23 °C	2.3	11.5	11.5	0	54	3.2	<0.1	
N1	THF, 23 °C	2.3	11.5	11.5	0	54	2.8	-	
	THF, 23 °C	2.3	11.5	11.5	0	54	2.9±0.2	<0.1	8.1±0.6
Table 4.1, entry 7: benzene instead of THF									
O1	C_6H_6, 23 °C	2.3	124.2	124.2	0	54	4.8	-	
P1	C_6H_6, 23 °C	2.3	124.2	124.2	0	54	4.6	-	
	C_6H_6, 23 °C	2.3	124.2	124.2	0	54	4.7±0.1		13±0.3

Run	Conditions	[Mo] load (μmol	acid (μmol)	base (μmol)	Ir (μmol)	HEH_2 equiv /Mo	NH_3 equiv /Mo	N_2H_4 equiv/ Mo	NH_3 yield/ HEH_2 (%)
Table 4.1, entry 8: 216 equiv Col/[ColH]OTf									
Q1	THF, 23 °C	2.3	496.8	496.8	0	54	19.5	-	
R1	THF, 23 °C	2.3	496.8	496.8	0	54	21.1	-	
	THF, 23 °C	2.3	496.8	496.8	0	54	20.3±0.8		56±2
Table 4.1, entry 9: with 10 equiv TBABr									
S1	THF, 23 °C	2.3	124.2	124.2	0	54	9	-	
T1	THF, 23 °C	2.3	124.2	124.2	0	54	8.6	-	
	THF, 23 °C	2.3	124.2	124.2	0	54	8.8±0.3		23.6±0.8
Table 4.1, entry 10: Added [Ir]BAr^F_4									
U1	THF, 23 °C	2.3	124.2	124.2	2.3	54	29.8	-	
V1	THF, 23 °C	2.3	124.2	124.2	2.3	54	20.6	-	
W1	THF, 23 °C	2.3	124.2	124.2	2.3	54	20.5	-	
X1	THF, 23 °C	2.3	124.2	124.2	2.3	54	25.4	-	
	THF, 23 °C	2.3	124.2	124.2	2.3	54	24±4		67±10
Table 4.1, entry 11: Added [Ir]BAr^F_4, 5 equiv Col/[ColH]OTf									
Y1	THF, 23 °C	2.3	11.5	11.5	2.3	54	16.02	<0.1	
Z1	THF, 23 °C	2.3	11.5	11.5	2.3	54	16.6	<0.1	
AA1	THF, 23 °C	2.3	11.5	11.5	2.3	54	14.7		
	THF, 23 °C	2.3	11.5	11.5	2.3	54	15.8±0.8	<0.1	44±2
Table 4.1, entry 12: Added [Ir]BAr^F_4, t = ½ h									
AB1	THF, 23 °C t = ½ h	2.3	124.2	124.2	2.3	54	19.5	-	
AC1	THF, 23 °C t = ½ h	2.3	124.2	124.2	2.3	54	17.7	-	
	THF, 23 °C t = 1/2 h	2.3	124.2	124.2	2.3	54	18.6±0.9		52±3
~75 % completion compared to entry 10									
Table 4.1, entry 13: t = 2 h									
AD1	THF, 23 °C t = 2 h	2.3	124.2	124.2	0	54	4.9	-	
AE1	THF, 23 °C t = 2 h	2.3	124.2	124.2	0	54	7.9	-	
AF1	THF, 23 °C t = 2 h	2.3	124.2	124.2	0	54	10	-	
	THF, 23 °C t = 2 h	2.3	124.2	124.2	0	54	7.6±2		21±6
~80 % completion compared to entry 1									
Table 4.1, entry 14: Added [Ir]BAr^F_4, 5 equiv Col/[ColH]OTf, 0.575 mM [$MoBr_3$]									
AG1	THF, 23 °C	0.575	11.5	11.5	2.3	216	26.83	-	
AH1	THF, 23 °C	0.575	11.5	11.5	2.3	216	25.96	-	
	THF, 23 °C	0.575	11.5	11.5	2.3	216	26±0.4		18.4±0.4
Table 4.1, entry 15: Added [Ir]BAr^F_4, 5 equiv Col/[ColH]OTf, no light									
AI1	THF, 23 °C no light	2.3	11.5	11.5	2.3	54	<0.1	<0.1	
AJ1	THF, 23 °C no light	2.3	11.5	11.5	2.3	54	<0.1	<0.1	
	THF, 23 °C no light	2.3	11.5	11.5	2.3	54	<0.1	<0.1	<0.3

Run	Conditions	[Mo] load (μmol	acid (μmol)	base (μmol)	Ir (μmol)	HEH_2 equiv /Mo	NH_3 equiv /Mo	N_2H_4 equiv /Mo	NH_3 yield/ HEH_2 (%)
Table 4.1, entry 16: Added [Ir]BAr^F_4, 5 equiv Col/[ColH]OTf, no [$MoBr_3$]									
AK1	THF, 23 °C	**0**	11.5	11.5	2.3	54	<0.1	<0.1	
AL1	THF, 23 °C	**0**	11.5	11.5	2.3	54	<0.1	<0.1	
	THF, 23 °C	**0**	11.5	11.5	2.3	54	<0.1	<0.1	<0.3
Table 4.1, entry 17: Added [Ir]BAr^F_4, 5 equiv Col/[ColH]OTf, no HEH_2									
AM1	THF, 23 °C	2.3	11.5	11.5	2.3	**0**	<0.1	<0.1	
AN1	THF, 23 °C	2.3	11.5	11.5	2.3	**0**	<0.1	<0.1	
	THF, 23 °C	2.3	11.5	11.5	2.3	**0**	<0.1	<0.1	<0.3
Table 4.1, entry 18: Added [Ir]BAr^F_4, subH_2 = 9,10-dihydroacridine									
AO1	THF, 23 °C	2.3	124.2	124.2	2.3	54[a]	6.7	-	
AP1	THF, 23 °C	2.3	124.2	124.2	2.3	54[a]	6.1	-	
	THF, 23 °C	2.3	124.2	124.2	2.3	54[a]	6.4±0.3		17.7±0.8
[a]9,10-dihydroacridine used instead of HEH_2									
Table 4.1, entry 19: Added [Ir]BAr^F_4, subH_2 = 5,6-dihydrophenanthridine									
AQ1	THF, 23 °C	2.3	124.2	124.2	2.3	54[b]	4.5	-	
AR1	THF, 23 °C	2.3	124.2	124.2	2.3	54[b]	5.1	-	
	THF, 23 °C	2.3	124.2	124.2	2.3	54[b]	4.6±0.8		13±2
[b]5,6-dihydrophenanthridine used instead of HEH_2									
Table 4.1, entry 20: Added [Ir]BAr^F_4, subH_2 = 1-benzyl-1,4-dihydronicotinamide									
AS1	THF, 23 °C	2.3	124.2	124.2	2.3	54[c]	1.31	-	
AT1	THF, 23 °C	2.3	124.2	124.2	2.3	54[c]	1.12	-	
	THF, 23 °C	2.3	124.2	124.2	2.3	54[c]	1.2±0.1		3.3±0.3
[c]1-benzyl-1,4-dihydronicotinamide used instead of HEH_2									
Table 4.1, entry 21: Added [Ir]BAr^F_4, 0.5 atm H_2, 0.5 atm N_2									
AU1	THF, 23 °C $P_{N2} = P_{H2}$ = 0.5 atm	2.3	124.2	124.2	2.3	54	16.1	-	
AV1	THF, 23 °C $P_{N2} = P_{H2}$ = 0.5 atm	2.3	124.2	124.2	2.3	54	11.0	-	
	THF, 23 °C $P_{N2} = P_{H2}$ = 0.5 atm	2.3	124.2	124.2	2.3	54	14±4		36±9
Table 4.1, entry 22: Added [Ir(dF(CF_3)ppy)$_2$(dtbbpy)]PF_6 , t = 2 h									
AW1	THF, 23 °C t = 2 h	2.3	124.2	124.2	2.3	54	1.8	-	
AX1	THF, 23 °C t = 2 h	2.3	124.2	124.2	2.3	54	2.6	-	
	THF, 23 °C t = 2 h	2.3	124.2	124.2	2.3	54	2.2±0.6		6±1
Table 4.1, entry 23: Added [Ir]PF_6, t = 2 h									
AY1	THF, 23 °C t = 2 h	2.3	124.2	124.2	2.3	54	18.4	-	
AZ1	THF, 23 °C t = 2 h	2.3	124.2	124.2	2.3	54	23.5	-	
	THF, 23 °C t = 2 h	2.3	124.2	124.2	2.3	54	21±4		58±10
Table 4.1, entry 24: Added [Ir(*p*-F(Me)ppy)$_2$(dtbbpy)]PF_6 , t = 2 h									

Run	Conditions	[Mo] load (μmol	acid (μmol)	base (μmol)	Ir (μmol)	HEH_2 equiv /Mo	NH_3 equiv /Mo	N_2H_4 equiv/Mo	NH_3 yield/ HEH_2 (%)
BA1	THF, 23 °C t = 2 h	2.3	124.2	124.2	2.3	54	21.5	-	
BB1	THF, 23 °C t = 2 h	2.3	124.2	124.2	2.3	54	23.1	-	
	THF, 23 °C t = 2 h	2.3	124.2	124.2	2.3	54	22±1		62±3

Table 4.1, entry 25: Added $Ir(ppy)_3$, t = 2 h

BC1	THF, 23 °C t = 2 h	2.3	124.2	124.2	2.3	54	7.8	-	
BD1	THF, 23 °C t = 2 h	2.3	124.2	124.2	2.3	54	5.8	-	
	THF, 23 °C t = 2 h	2.3	124.2	124.2	2.3	54	7±1		19±4

Table 4.1, entry 26: Added [Ir]BAr^F_4, no Col/[ColH]OTf

BE1	THF, 23 °C t = 2 h	2.3	124.2	124.2	2.3	54	7.03	-	
BF1	THF, 23 °C t = 2 h	2.3	124.2	124.2	2.3	54	7.83	-	
	THF, 23 °C t = 2 h	2.3	124.2	124.2	2.3	54	7.4±0.4		20.7±1

C.2.5.2 Additional catalytic experiments

Table C.2: Canvassing H_2 carriers

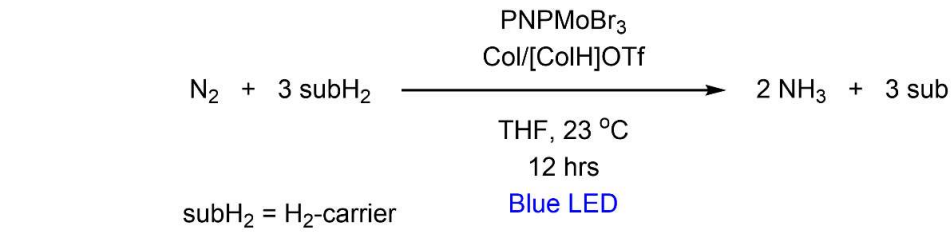

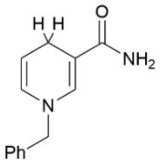

BNAH
(1-benzyl-1,4-dihydronicotinamide)

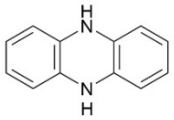

$phenazH_2$
(5,10-dihydrophenazine)

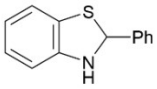

BTH_2
(2-phenylbenzothiazolin)

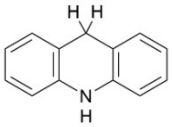

$acrH_2$
(9,10-dihydroacridine)

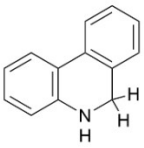

$phenH_2$
(5,6-dihydrophenanthridine)

Run	subH₂	[MoBr₃] load (µmol)	acid (µmol)	base (µmol)	Ir (µmol)	subH₂ equiv /Mo	NH₃ equiv /Mo	N₂H₄ equiv/Mo	NH₃ yield/ subH₂ (%)
A2	BNAH	2.3	124.2	124.2	**0**	54	0.55	-	
B2	BNAH	2.3	124.2	124.2	**0**	54	0.30	-	
	BNAH	2.3	124.2	124.2	**0**	54	0.4±0.1		1.2±0.3
C2	$PhenazH_2$	2.3	124.2	124.2	**2.3**	54	<0.1	-	
D2	$PhenazH_2$	2.3	124.2	124.2	**2.3**	54	<0.1	-	
	$PhenazH_2$	2.3	124.2	124.2	**2.3**	54	<0.1		<0.1
E2	BTH_2	2.3	124.2	124.2	**2.3**	54	<0.1	-	
F2	BTH_2	2.3	124.2	124.2	**2.3**	54	<0.1	-	
	BTH_2	2.3	124.2	124.2	**2.3**	54	<0.1		<0.1
G2	$AcrH_2$	2.3	124.2	124.2	**0**	54	0.09	-	
H2	$AcrH_2$	2.3	124.2	124.2	**0**	54	0.24	-	
	$AcrH_2$	2.3	124.2	124.2	**0**	54	0.16±0.08		0.5±0.2
I2	$PhenH_2$	2.3	124.2	124.2	**0**	54	0.216	-	
J2	$PhenH_2$	2.3	124.2	124.2	**0**	54	0.205	-	
	$PhenH_2$	2.3	124.2	124.2	**0**	54	0.211±0.008		0.66±0.02

Table C.3. Additional time course experiments.

Run	Conditions	Mo loading (μmol)	acid (μmol)	base (μmol)	Ir (μmol)	HEH_2 equiv /Mo	NH_3 equiv /Mo	N_2H_4 equiv/Mo	NH_3 yield/ HEH_2 (%)
A3	THF, 23 °C t = 2 h	2.3	124.2	124.2	2.3	54	24.5	-	
B3	THF, 23 °C t = 2 h	2.3	124.2	124.2	2.3	54	25.5	-	
	THF, 23 °C t = 2 hours	2.3	124.2	124.2	2.3	54	25±0.5		69.4±1.5
Approximately 100% completion compared to Table 4.1, entry 10									
C3	THF, rt, 10 min	2.3	124.2	124.2	2.3	54	8.2	-	22.8
Approximately 30% completion compared to Table 4.1, entry 10									

Table C.4 Catalysis using [ColH]OTf or Col instead of buffered solution

Run	Conditions	Mo loading (μmol)	acid (μmol)	base (μmol)	Ir (μmol)	HEH_2 equiv /Mo	NH_3 equiv /Mo	N_2H_4 equiv/Mo	NH_3 yield/ HEH_2 (%)
A4	THF, 23°C	2.3	496.8	**0**	**0**	54	5.8	-	
B4	THF, 23°C	2.3	496.8	**0**	**0**	54	5.5	-	
	THF, 23°C	2.3	496.8	**0**	**0**	54	5.65±.15		15.7±0.4
C4	THF, 23°C	2.3	**0**	496.8	**0**	54	1.2	-	
D4	THF, 23°C	2.3	**0**	496.8	**0**	54	2.0	-	
	THF, 23°C	2.3	**0**	496.8	**0**	54	1.6±0.4		4.7±1.1

Table C.5. Solvent screen

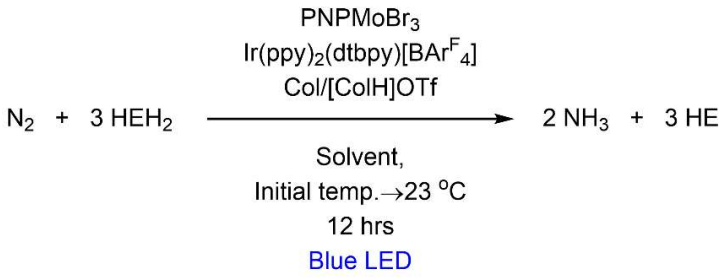

Run	Conditions	Mo loading (μmol)	acid (μmol)	base (μmol)	Ir (μmol)	HEH_2 equiv /Mo	NH_3 equiv /Mo	N_2H_4 equiv/Mo	NH_3 yield/ HEH_2 (%)
A5	THF, -78 →23°C	2.3	11.5	11.5	2.3	54	15.47	-	
B5	THF, -78 →23°C	2.3	11.5	11.5	2.3	54	16.06	-	
	THF, -78 →23°C	2.3	11.5	11.5	2.3	54	15.7±0.3		44.8±0.8
C5	Tol, 23°C	2.3	11.5	11.5	2.3	54	7	-	
D5	Tol, 23°C	2.3	11.5	11.5	2.3	54	7.3	-	
	Tol 23°C	2.3	11.5	11.5	2.3	54	7.15±0.15		19.8±0.8
E5	Tol, -78 →23°C	2.3	11.5	11.5	2.3	54	13.01	-	
F5	Tol, -78 →23°C	2.3	11.5	11.5	2.3	54	14.24	-	
	Tol, -78 →23°C	2.3	11.5	11.5	2.3	54	13.6±0.6		38±2
G5	Et_2O, -78 →23°C	2.3	11.5	11.5	2.3	54	4.08	-	
H5	Et_2O, -78 → 23°C	2.3	11.5	11.5	2.3	54	3.97	-	
	Et_2O, -78 → 23°C	2.3	11.5	11.5	2.3	54	4.0±0.1		11.2±0.2
I5	THF, -78 →23°C	2.3	11.5	11.5	2.3[a]	54	7.4	-	
J5	THF, -78 →23°C	2.3	11.5	11.5	2.3[a]	54	11.7	-	
	THF, -78 →23°C	2.3	11.5	11.5	2.3[a]	54	9.6±2		27±7
K5	MeCy, 23°C	2.3	124.2	124.2	0	54	<0.1	-	
L5	MeCy, 23°C	2.3	124.2	124.2	0	54	<0.1	-	
	MeCy, 23°C						<0.1		<0.3

[a]$Ir(ppy)_3$ used as photosensitizer
Tol = toluene; MeCy = methylcyclohexane

Solubility of reagents:
Collidine: Soluble in THF, Et_2O, Toluene, C_6H_6, MeCy
Collidinium triflate: Soluble in THF, insoluble in Et_2O, Toluene and C_6H_6, MeCy

[$MoBr_3$]: Soluble in THF, Toluene and C_6H_6. Sparingly soluble in Et_2O, MeCy
HEH_2: Partially soluble in THF, Et_2O, Toluene and C_6H_6. Most soluble in THF, MeCy
[Ir]BAr^F_4: Soluble in THF, Et_2O, partially soluble in C_6H_6 and Toluene

Table C.6 Attempted catalysis with [P_3^BFe]BAr^F_4

Run	Conditions	Fe loading (µmol)	acid (µmol)	base (µmol)	Ir (µmol)	HEH_2 equiv /Fe	NH_3 equiv /Fe	N_2H_4 equiv/Fe	NH_3 yield/ HEH_2 (%)
A6	THF, 23°C	2.3	124.2	124.2	2.3	54	<0.1	<0.1	
B6	THF, 23°C	2.3	124.2	124.2	2.3	54	<0.1	<0.1	
	THF, 23°C	2.3	124.2	124.2	2.3	54	<0.1	<0.1	<0.1
C6	THF, 23°C	2.3	124.2	124.2	0	54	<0.1	<0.1	
D6	THF, 23°C	2.3	124.2	124.2	0	54	<0.1	<0.1	
	THF, 23°C	2.3	124.2	124.2	0	54	<0.1	<0.1	<0.1

C.2.6 NH_3 detection results from ^{15}N-HEH_2, ^{15}N-Col/^{15}N-[ColH]OTf and $^{15}N_2$ experiments

C.2.6.1 $^{15}N_2$ experiments

Catalytic runs done under a $^{15}N_2$ atmosphere were conducted similarly to those under a $^{14}N_2$ atmosphere, with a few differences described below. The loadings were the same as in Table 4.1, Entry 1.

Catalysis is performed in the same catalytic tubes as natural abundance experiments, which are charged with precatalyst, HEH_2, [ColH]OTf, and a stir bar in a nitrogen-filled glovebox, as described above. After addition of the solids, the tube is then cooled to 77 K in a cold well. The base (Col) is added by micropipette to the frozen tube by opening the Kontes. The Kontes was closed, and the tube was kept frozen, then passed out of the glovebox into a liquid N_2 bath. The headspace of the tube is evacuated while still submerged in liquid N_2.

Na/K dried THF is filtered, and 1 mL is placed into a separate Schlenk tube. The solvent undergoes freeze-pump thaw cycles (3 cycles) and is then vacuum transferred into the catalysis tube. This tube is allowed to warm up briefly and charged with $^{15}N_2$ via a vacuum bridge. The tube is refrozen at 77 K and then transferred to a water bath, where it thaws and is allowed to stir under Blue LED irradiation for 12 hours.

C.6.2 ^{15}N-HEH$_2$, ^{15}N-Col/^{15}N-[ColH]OTf experiments

Catalytic runs were set-up as described in **C.2.1** but using either ^{15}N-HEH$_2$ as H$_2$-carrier or ^{15}N-Col/[ColH]OTf as buffer using the same conditions as Table 4.1, Entry 1.

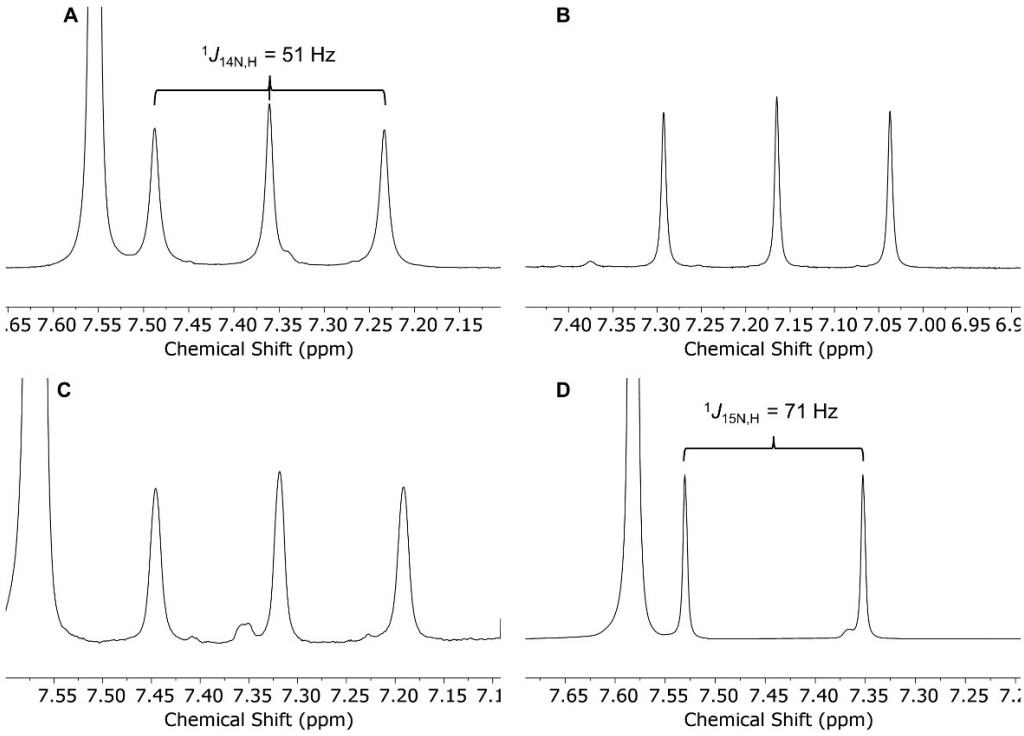

Figure C.1. ^{1}H NMR (DMSO-d_6, 400 MHz) of: A) ^{14}NH$_4$Cl obtained from reaction of natural abundance reactants under ^{14}N$_2$ (Ir-free conditions in Table 4.1, entry 1); B) ^{14}NH$_4$Cl obtained from reaction of ^{15}N-labeled HEH$_2$ (otherwise natural abundance reactants) under ^{14}N$_2$ (Ir-free conditions in Table 4.1, entry 1); C) ^{14}NH$_4$Cl obtained from reaction of ^{15}N-labeled Col/[ColH]OTf (otherwise natural abundance reactants) under ^{14}N$_2$ (Ir-free conditions in Table 4.1, entry 1); D) ^{15}NH$_4$Cl obtained from reaction under ^{15}N$_2$ (otherwise natural abundance reactants, Ir-free conditions in Table 4.1, entry 1).

C.2.7 Analysis of non-NH$_3$ catalysis products

After a complete catalytic run, instead of quenching the reaction (with acid or base) the solvent from the reaction mixture was removed *in vacuo*. The resulting film was taken up in minimal DMSO-d_6 and analyzed by NMR.

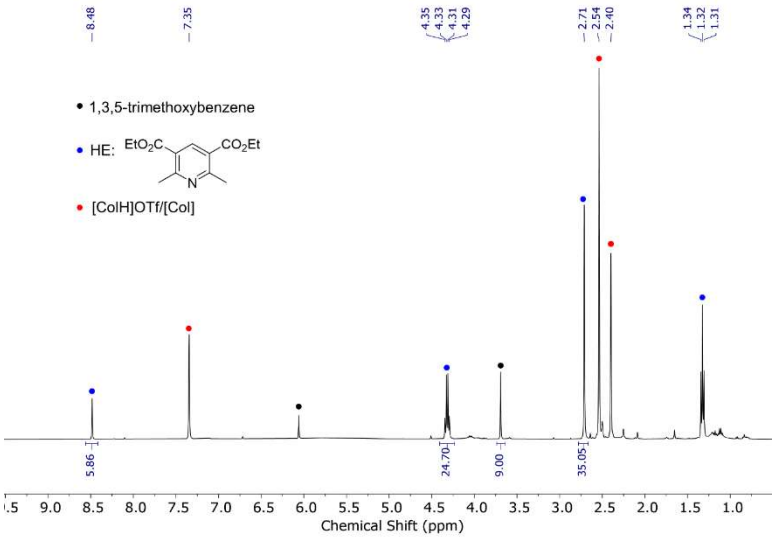

Figure C.2. ^{1}H NMR (DMSO-d_6, 400 MHz) of the nonvolatile products of the Mo-catalyzed reaction of HEH_2, [ColH]OTf, [Col], and N_2 under blue LED irradiation (Table 4,1, entry 1).

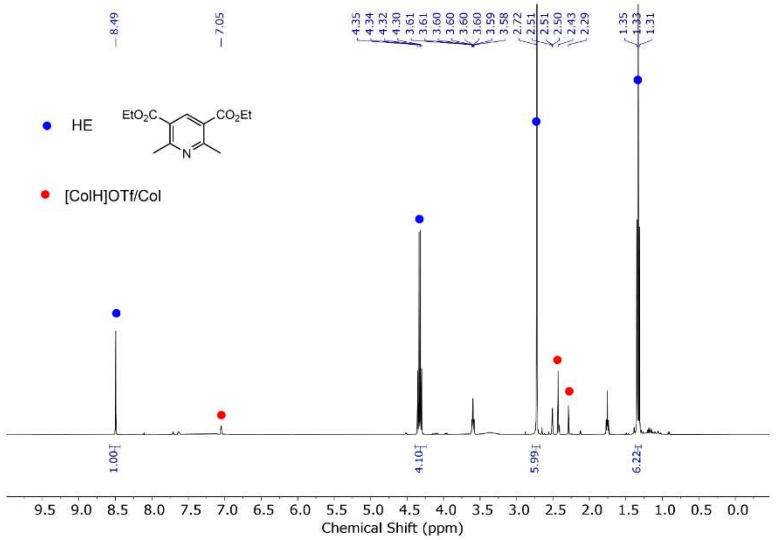

Figure C.3. ^{1}H NMR (DMSO-d_6, 400 MHz) of the nonvolatile products of the Col/[ColH]OTf-, Ir- and Mo-catalyzed reaction of HEH_2 and N_2 under blue LED irradiation (Table 4.1, entry 11, catalytic buffer).

C.2.8 ^{1}H NMR time course experiments

Procedure: A J.Young NMR tube was loaded with [$MoBr_3$], HEH_2, [ColH]OTf, Col, and N_2 and irradiated under blue LED. Conditions (concentration, temperature) were the

same as in Table 4.1, entry 1, but using THF-d_8 as solvent. Slightly slower reaction times are attributed to less efficient illumination and lack of stirring in the NMR tube compared to Schlenk flasks.

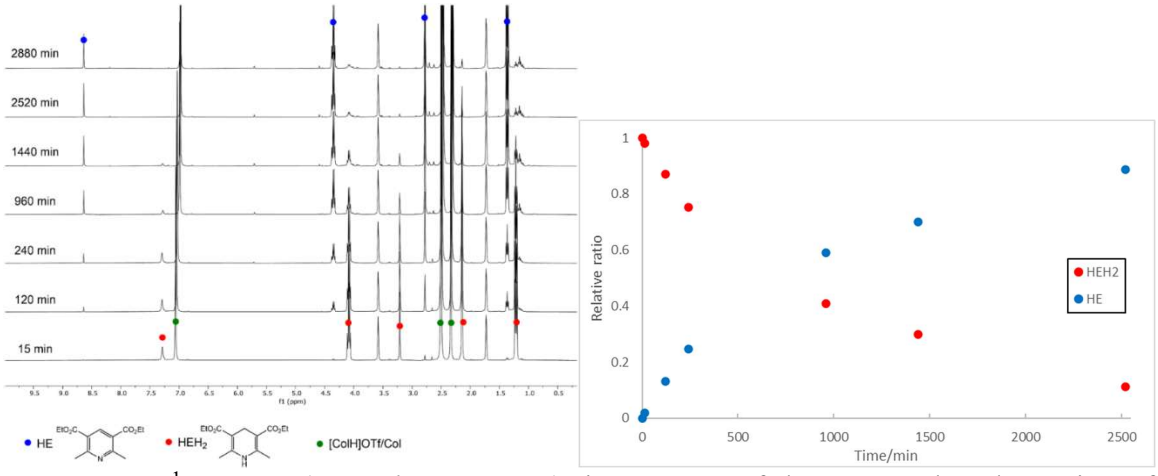

Figure C.4. ^{1}H NMR (THF-d_8, 400 MHz) time course of the Mo-catalyzed reaction of HEH_2, [ColH]OTf, Col, and N_2 under blue LED irradiation in a J. Young tube (Table 4.1 entry 1) (left). Relative ratio of HE and HEH_2 plotted over time (right).

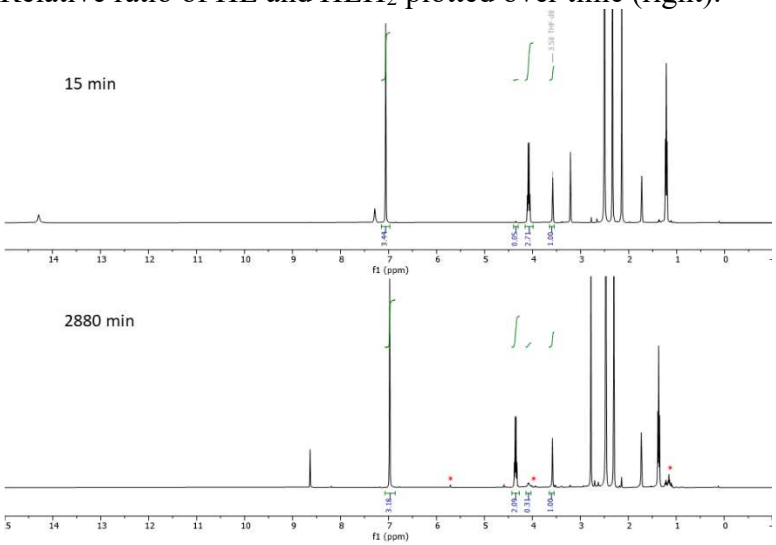

Figure C.5. ^{1}H NMR (THF-d_8, 400 MHz) of 15 minutes and 48 hour time points of the reaction of the Mo-catalyzed reaction of HEH_2, [ColH]OTf, Col, and N_2 under blue LED irradiation in a J.Young tube (Figure C.4). Integrals of HEH_2 and HE quartet peak at ~ 4.0 ppm are compared to constant THF solvent residual peaks to estimate total recovery of HEH_2 and HE. Approx. 90% is recovered. Similarly, integrals of Col/[ColH]OTf aromatic peak at ~ 7.0 ppm are compared to constant THF solvent residual peaks to estimate total recovery of Col/[ColH]OTf. Approx. 90% is recovered. *indicates minor organic impurity that grows in, see Figure C.6.

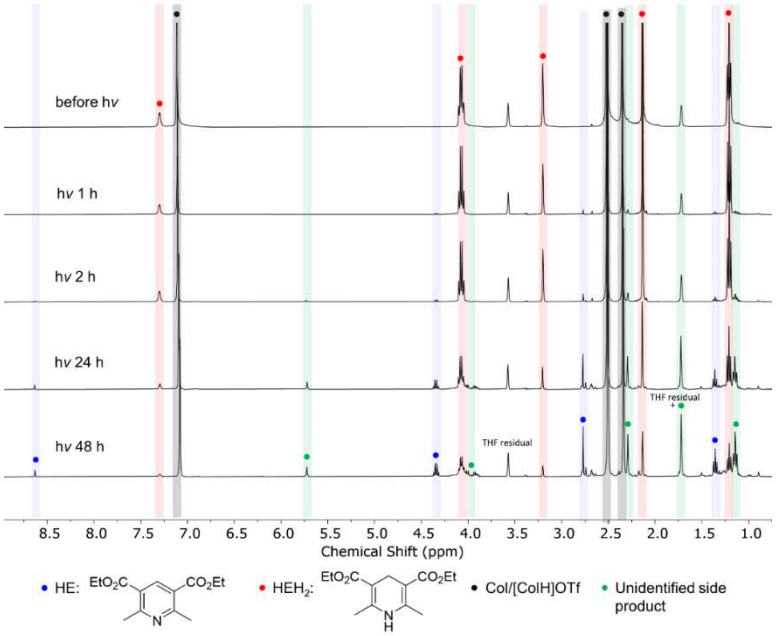

Figure C.6. ^{1}H NMR (THF-d_8, 400 MHz) before irradiation and at indicated timepoints following blue LED irradiation of the reaction of HEH_2 with 1 equiv Col and 1 equiv [ColH]OTf in a J. Young tube. Integration relative to the THF residual peak at 3.58 ppm indicates that after 48 hours, 79% of HEH_2 and 10% of the total initial buffer loading are consumed, while HE is produced in 16% conversion along with the same major organic side product peaks observed in N_2R with [$MoBr_3$] (Figure C.4 and C.5).

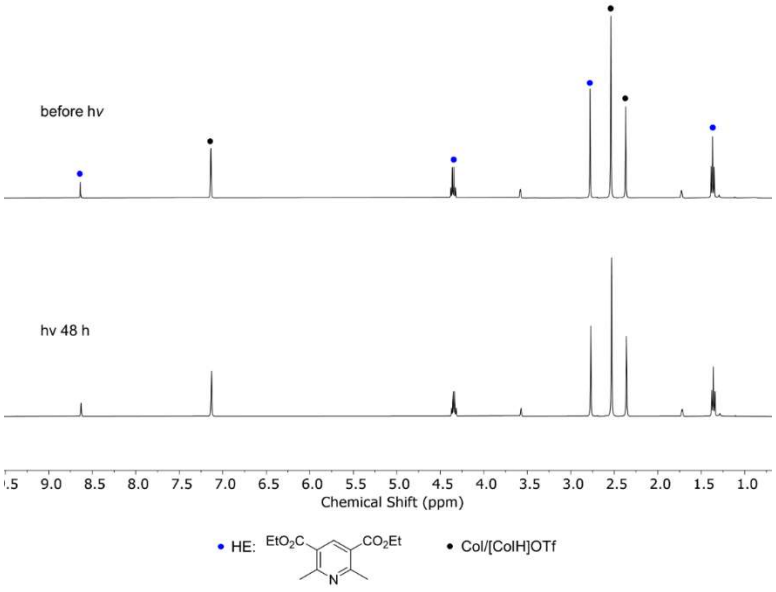

Figure C.7. ^{1}H NMR (THF-d_8, 400 MHz) before irradiation and at indicated timepoints following blue LED irradiation of HE with 1 equiv Col and 1 equiv [ColH]OTf in a J. Young tube. No reaction is observed.

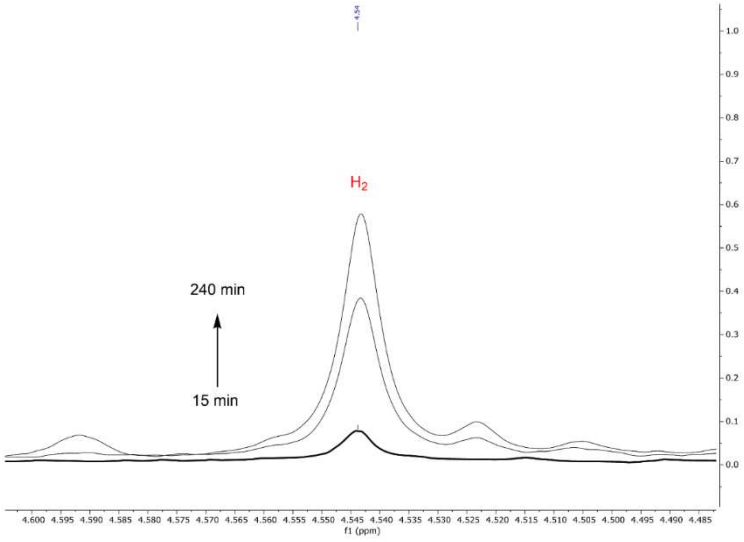

Figure C.8. ^{1}H NMR (THF-d_8, 400 MHz) of 15 minutes to 240 min of the Mo-catalyzed reaction of HEH_2, [ColH]OTf, Col, and N_2 under blue LED irradiation in a J.Young tube (Figure C.4). The H_2 peak (4.54 ppm)[10] grows in over time.

C.3 Steady-State Fluorescence Measurements

C.3.1 Procedure for Fluorimetry Studies

1 cm quartz glass cuvettes were loaded with 0.5 mM HEH_2 solutions in dry THF, with varying concentrations of quencher (either Col or [ColH]OTf) in a nitrogen glovebox. Stock solutions were used to assure consistency. Solutions were excited at 390 nm wavelength to avoid interference of the excitation wavelength and steady-state fluorescence spectra. Experiments were conducted at 23 °C.

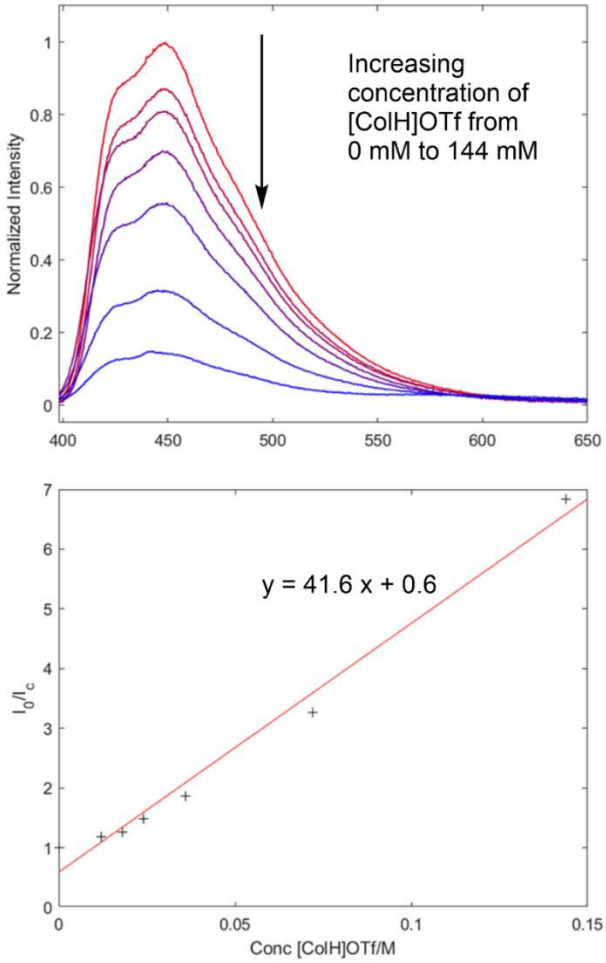

Figure C.9. Steady-state fluorescence of HEH_2 (0.5 mM) with varying amounts of [ColH]OTf (18 mM to 144 mM) (Top). Stern-Vollmer quenching plot of I_0/I_C against concentration of [ColH]OTf (bottom). Slope is 42±2.4 M^{-1}; R^2 =0.98.

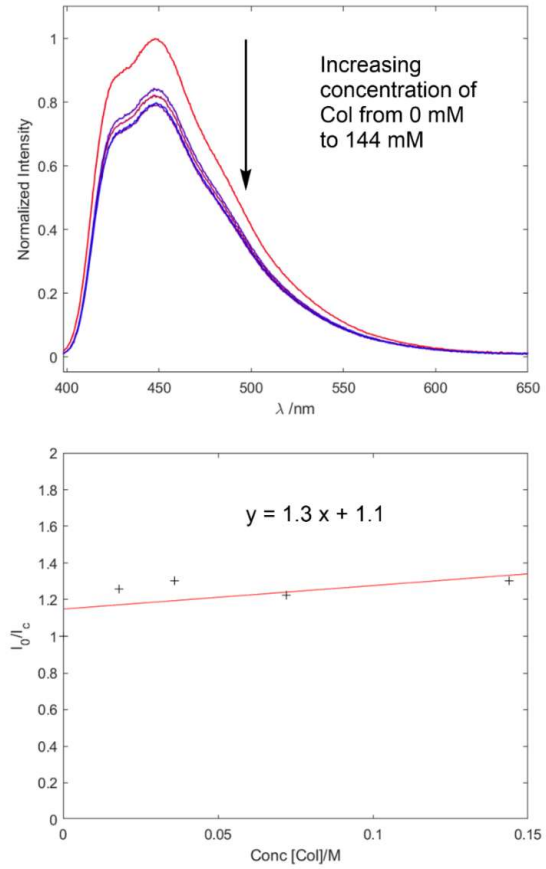

Figure C.10. Steady-state fluorescence of HEH_2 (0.5 mM) with varying amounts of Col (18 mM to 144 mM) (Top). Stern-Vollmer quenching plot of I_0/I_C against concentration of Col (bottom). Slope is 1.3±0.9 M^{-1}.

C.3.2 Calculation of Stern-Volmer quenching constants

Using the previously measured excited state-lifetime measured (τ_0) for HEH_2 we can calculate the Stern-Vollmer quenching lifetime using the equation:

$$I_0/I_c = 1 + k_q \cdot \tau_0 [Q] \text{ (eqn C.1)}$$

$$k_q = \text{slope}/\tau_0 \text{ (eqn C.2)}$$

While τ_0 has not been measured in THF at 25 °C, the measurements in DMSO at 25 °C (0.419 ns) provide a useful estimate.[17] Accordingly, the quenching constants are:

$$k_{colH} = 1.0 \pm 0.1 \cdot 10^{11}\ M^{-1}\ s^{-1}$$

$$k_{col} = 3 \pm 2 \cdot 10^{9}\ M^{-1}\ s^{-1}$$

While these values have considerable errors, particularly the Col quenching, these nonetheless provide useful order of magnitude estimates. The large rate constant for k_{colH+} suggests the presence of static quenching pathways.

C.4 UV-visible measurements

C.4.1 Procedure for UV-vis measurements.

1 cm quartz glass cuvettes were loaded with 0.1 mM HEH_2 solutions in dry THF inside the glovebox. The cuvette was taken out of the glovebox, and spectra were collected. Concentrated (50 mM) solutions of Col or [ColH]OTf were titrated into the cuvettes. The Col or [ColH]OTf solutions had 0.1 mM HEH_2 added to maintain the HEH_2 concentration throughout the experiments. Titrations were done under a sparging N_2 atmosphere to maintain an O_2 free environment. Experiments were conducted at 23 °C.

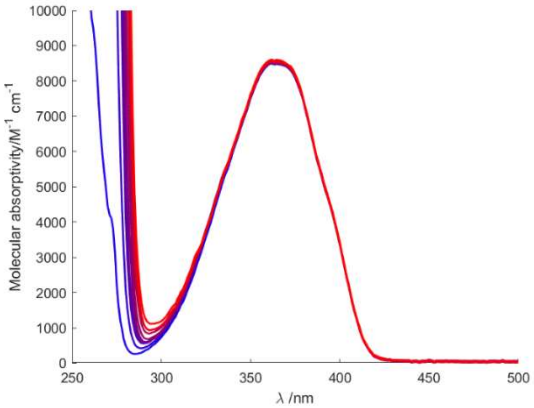

Figure C.11. UV-vis of HEH_2 (0.1 mM) with 0 mM (blue) to 14 mM (red) Col concentration.

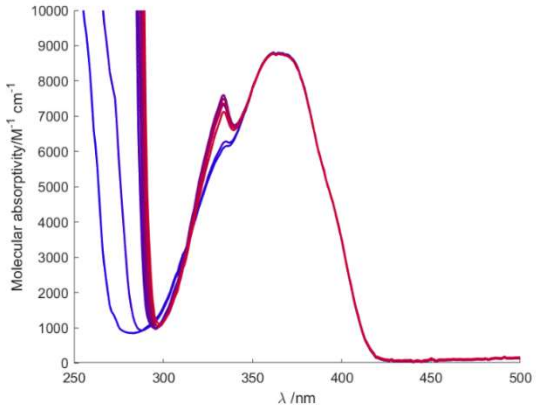

Figure C.12. UV-vis of HEH_2 (0.1 mM) with 0 mM (blue) to 11 mM (red) [ColH]OTf concentration.

C.5 Reduction of [TBA]NO_3

Proposed balanced equation:

$$[TBA]NO_3 + 4\,HEH_2 + [ColH]OTf \longrightarrow NH_3 + 4\,HE + 3\,H_2O + Col + [TBA]OTf$$

Scheme C.1. Balanced equation for the catalytic reduction of [TBA]NO_3 to generate NH_3.

C.5.1 Standard [TBA]NO_3 Reduction Generation Reaction Procedure

Catalytic experiments for the reduction of [TBA]NO_3 were conducted in a manner similar to the reduction of N_2 (section **S1.1**). All solvents are stirred with Na/K for ≥2 hours and filtered prior to use. In a nitrogen-filled glovebox, the precatalysts ([$MoBr_3$] and [Ir]$BAr^F{}_4$) (2.3 μmol) are weighed in individual vials.* The precatalysts are then transferred quantitatively into a Schlenk tube using THF. The THF is then evaporated to provide a thin film of precatalyst at the bottom of the Schlenk tube. The tube is then charged with a stir bar, and the [TBA]NO3, acid, and Hantzsch ester (HEH 2) are added as solids. The tube is cooled to 77 K in a cold well, and the base ([Col]) is added. The tubes were passed out of the glovebox without warming and thoroughly degassed. 1 mL of degassed (three freeze-pump thaw cycles) THF solvent was vacuum transferred into the catalytic tube. The tube was allowed to warm briefly and was backfilled with argon. The tube is instead transferred to a

water bath, where it thaws and is allowed to stir for 12 hours. To ensure reproducibility, all experiments were conducted in 200 mL Schlenk tubes (50 mm OD) using 10 mm egg-shaped stir bars, and stirring was conducted at ~600 rpm. The water bath was contained in highly reflective dewars. The Blue LED was placed above the bath as close to the stirring reaction as possible.

C.5.2 NH_3 detection

NH_3 was detected by ^1H NMR, as detailed in C.2.4 NH_3 detection by ^1H NMR.

C.5.3 Catalytic reduction of [TBA]$^{15}NO_3$

Catalytic runs were set-up as described in **S5.1** but using [TBA]$^{15}NO_3$.

C.5.4 Catalytic reduction of [TBA]NO_3

Table C.7. Catalytic yields for photodriven transfer hydrogenation of [TBA]NO_3 to NH_3

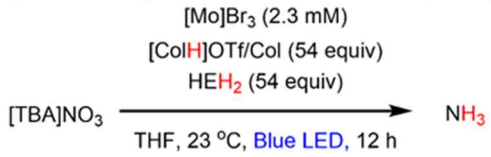

Run	Conditions	[$MoBr_3$] load (μmol)	acid (μmol)	base (μmol)	Ir (μmol)	HEH_2 /Mo	[TBA] NO_3 equiv/Mo	NH_3 equiv /Mo	NH_3 yield/ HEH_2 (%)
Table 4.1, entry 27: Standard conditions for reduction of [TBA]NO_3									
A7	THF, 23 °C	2.3	124.2	124.2	**0**	54	18	8.5	
B7	THF, 23 °C	2.3	124.2	124.2	**0**	54	18	11.0	
	THF, 23 °C	2.3	124.2	124.2	0	54	18	9.8±1.2	73±9
Table 4.1, entry 28: with [$MoBr_3$] , with [Ir]$BAr^F{}_4$									
C7	THF, 23 °C	2.3	124.2	124.2	**2.3**	54	18	9.9	
D7	THF, 23 °C	2.3	124.2	124.2	**2.3**	54	18	10.9	
	THF, 23 °C	2.3	124.2	124.2	**2.3**	54	18	10.4±0.5	77±4
Table 4.1, entry 29: No [$MoBr_3$]									
E7	THF, 23 °C	2.3	124.2	124.2	**2.3**	54	18	2	
F7	THF, 23 °C	2.3	124.2	124.2	**2.3**	54	18	1.4	
	THF, 23 °C	2.3	124.2	124.2	**2.3**	54	18	1.7±0.3	13±2
Table 4.1, entry 30: No [$MoBr_3$] , with [Ir]$BAr^F{}_4$									
F7	THF, 23 °C	2.3	124.2	124.2	**2.3**	54	18	3.0	
G7	THF, 23 °C	2.3	124.2	124.2	**2.3**	54	18	5.4	
	THF, 23 °C	2.3	124.2	124.2	**2.3**	54	18	4.2±1.2	31±9

Table 4.1, entry 31: no light, with [$MoBr_3$] , with [Ir]BAr^F_4

H7	THF, 23 °C No light	2.3	124.2	124.2	**2.3**	54	18	0.1	
I7	THF, 23 °C No light	2.3	124.2	124.2	**2.3**	54	18	0.1	
	THF, 23 °C No light	2.3	124.2	124.2	**2.3**	54	18	0.1±0.05	0.7±0.3

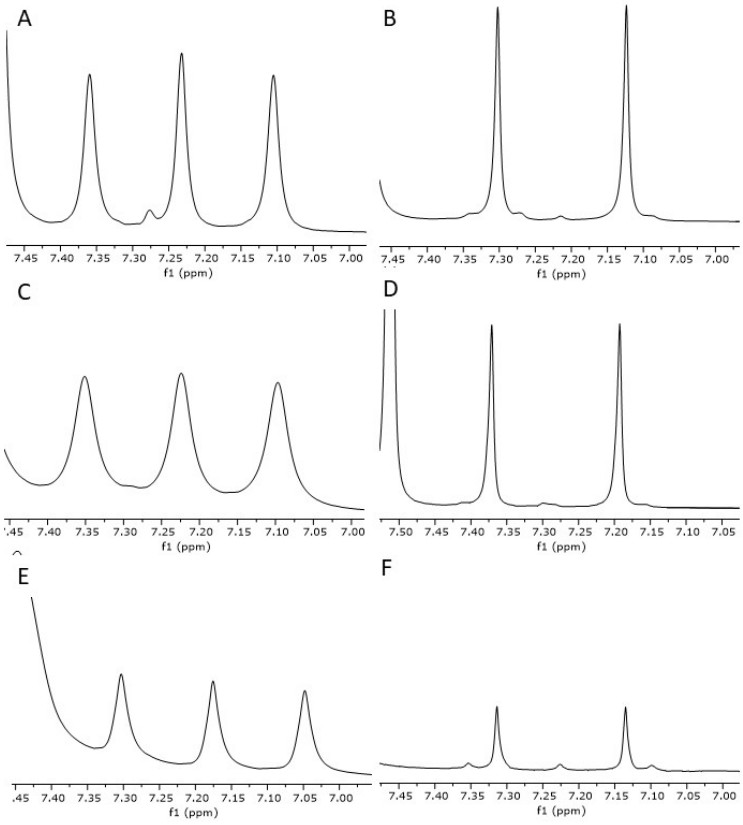

Figure C.13. ^{1}H NMR (DMSO-d_6, 400 MHz) of: A) $^{14}NH_4Cl$ obtained from reaction of natural abundance [TBA]NO_3 with HEH_2, buffer, and [$MoBr_3$] under blue light irradiation (Table C.7 entry A7); B) $^{15}NH_4Cl$ obtained from reaction of [TBA]$^{15}NO_3$ with HEH_2, buffer, and [$MoBr_3$] under blue light irradiation; C) $^{14}NH_4Cl$ obtained from reaction of natural abundance [TBA]NO_3 with HEH_2, buffer, [$MoBr_3$] and [Ir]BAr^F_4 under blue light irradiation (Table C.7, entry C7); D) $^{15}NH_4Cl$ obtained from reaction of [TBA]$^{15}NO_3$ with HEH_2, buffer, [$MoBr_3$] and [Ir]BAr^F_4 under blue light irradiation; E) $^{14}NH_4Cl$ obtained from reaction of natural abundance [TBA]NO_3 with HEH_2, buffer, and [Ir]BAr^F_4 under blue light irradiation (Table C.7, entry F7); F) $^{15}NH_4Cl$ obtained from reaction of [TBA]$^{15}NO_3$ with HEH_2, buffer, and [Ir]BAr^F_4 under blue light irradiation.

C.5.5 Comment on nitrate reduction in the absence of light or [$MoBr_3$].

It is worth commenting on the fact that [TBA]NO_3 reduction can occur both in the absence of light and [$MoBr_3$], albeit with diminished yields. This differs from N_2R where both are required and no NH_3 can be detected. Nitrate differs as a substrate from N_2 in that it is more activated and forms relatively stable intermediates during reduction (NO_2^-, NO), and the thermodynamics of reduction are more favorable. This is illustrated in Figure C.14, showing the thermodynamics between different intermediates in the reduction of N2 and NO_3^- (in aqueous solution vs NHE). Therefore, a molecular catalyst might not be required to activate the substrate prior to reduction/protonation and stabilize intermediates that form during reduction. The role of [$MoBr_3$] might, therefore, be primarily as a Lewis acid or a solubilizing agent. Ultimately, these results suggest that higher yields/efficiencies and possibly even nitrate reduction without illumination may all be possible with a more careful choice of catalyst and warrant further exploration.

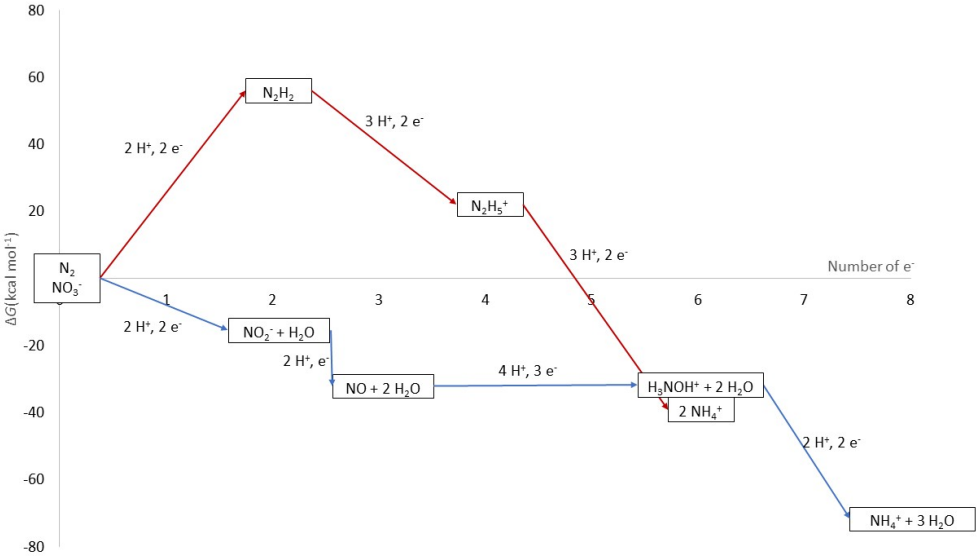

Figure C.14. Comparison of ΔG (in kcal mol^{-1}) in aqueous solution of pH 0 referenced to NHE.[13,14] While the 6 e^- reduction and 8 e^- reduction of N_2 and NO_3^-, respectively, are both downhill, only the intermediates of NO_3^- are also thermodynamically favored to form.

C.6 Reduction of acetylene

Proposed balanced equations:

$$C_2H_2 + HEH_2 \longrightarrow C_2H_4 + HE$$

$$C_2H_4 + HEH_2 \longrightarrow C_2H_6 + HE$$

Scheme C.2. Balanced equations for the catalytic reduction of acetylene to generate ethylene and ethane.

C.6.1 Standard acetylene reduction reaction procedure

Catalytic experiments for the reduction of acetylene were conducted in a manner similar to the reduction of N_2 (section **S1.1**). All solvents are stirred with Na/K for ≥2 hours and filtered prior to use. In a nitrogen-filled glovebox, the precatalysts ([$MoBr_3$] and [Ir]BAr^F_4) (2.5 μmol) are weighed in individual vials. The precatalysts are then transferred quantitatively into a Schlenk tube using THF. The THF is then evaporated to provide a thin film of precatalyst at the bottom of the Schlenk tube. The tube is then charged with a stirbar and [ColH]OTf and Hantzsch ester (HEH_2) are added to the vial as solids. The tube is wrapped in aluminum foil and Col and THF-d_8 (0.7 mL) are added. The tube is sealed, passed out of the glovebox, and degassed (three freeze-pump thaw cycles). The desired volume of acetylene gas is added using a calibrated bulb while the tube is cooled in liquid nitrogen. The headspace of the tube is then backfilled to 1 atm with argon while cooled in a dry ice/acetone bath. The tube is transferred to a water bath and is irradiated with Blue LED for the time specified. The water bath was contained in highly reflective dewars. The Blue LED was placed above the bath as close to the reaction as possible.

After 12 hours of irradiation, the volatiles of the reaction mixture are vacuum transferred into a J. Young NMR tube of known volume containing a known amount of 1,3,5-trimethoxybenzene. In the ^{1}H NMR spectrum of the resulting sample, the peaks corresponding to ethylene (5.36 ppm) and ethane (0.85 ppm) are distinguishable when present.[10] Integration to the internal standard provides the yield of dissolved gases. Henry's constant for each gas in THF[15] was used to estimate their partial pressures in the headspace.

C.6.2 Ethylene and ethane detection results

Table C.8. Catalytic yields for photodriven transfer hydrogenation of acetylene to ethylene and ethane.

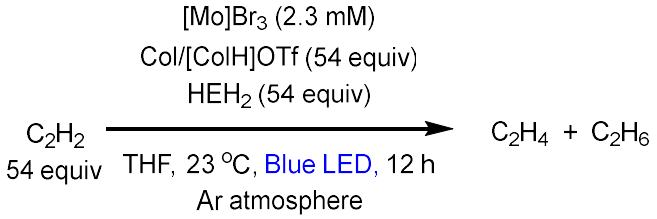

Run	Conditions	[Mo] load (μmol)	acid (μmol)	base (μmol)	Ir (μmol)	HEH_2 equiv /Mo	C_2H_4 equiv /Mo	C_2H_6 equiv/ Mo	Total yield/ HEH_2 (%)
Table 4.1, entry 32: standard conditions									
A8	THF, 23 °C	2.5	135	135	0	54	8.2	1.3	
B8	THF, 23 °C	2.5	135	135	0	54	11.4	1.7	
	THF, 23 °C	2.5	135	135	0	54	10±2	1.5±0.3	24±5
Table 4.1, entry 33: with [$MoBr_3$], with [Ir]BAr^F_4									
C8	THF, 23 °C	2.5	135	135	2.5	54	6.4	1.3	
D8	THF, 23 °C	2.5	135	135	2.5	54	4.9	0.9	
	THF, 23 °C	2.5	135	135	2.5	54	6±1	1.1±0.3	15±3
Table 4.1, entry 34: no [$MoBr_3$], no [Ir]BAr^F_4									
E8	THF, 23 °C	2.5	135	135	0	54	0.048	<0.03	
F8	THF, 23 °C	2.5	135	135	0	54	0.059	<0.03	
	THF, 23 °C	2.5	135	135	0	54	0.054± 0.008	<0.03	<0.3
Table 4.1, entry 35: no [$MoBr_3$], with [Ir]BAr^F_4									
G8	THF, 23 °C	0	135	135	2.5	54	0.8	0.02	
H8	THF, 23 °C	0	135	135	2.5	54	3.0	0.14	
	THF, 23 °C	0	135	135	2.5	54	2±2	0.08± 0.08	4±3
Table 4.1, entry 36: with [$MoBr_3$], with [Ir]BAr^F_4, no light									
I8	THF, 23 °C no light	2.5	135	135	2.5	54	<0.01	<0.01	
J8	THF, 23 °C no light	2.5	135	135	2.5	54	<0.01	<0.01	
	THF, 23 °C no light	2.5	135	135	2.5	54	<0.01	<0.01	<0.04

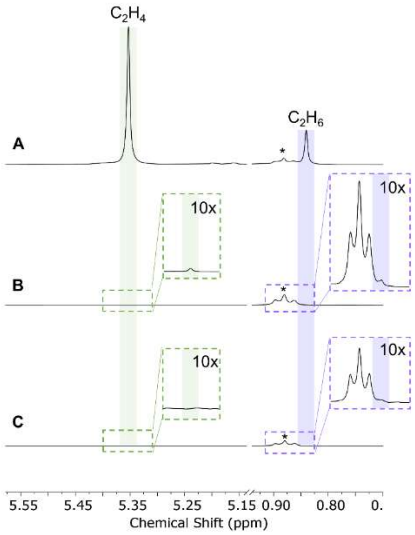

Figure C.15. ^{1}H NMR (THF-d_8, 400 MHz) of the volatiles obtained from the acetylene reduction reaction in Table C.8: A) Standard conditions (Table C.8, entry A8); B) No [$MoBr_3$] (Table C.8, entry E8); C) No irradiation (Table C.8, entry I8). *Trace pentane.

C.7. Additional mechanistic schemes

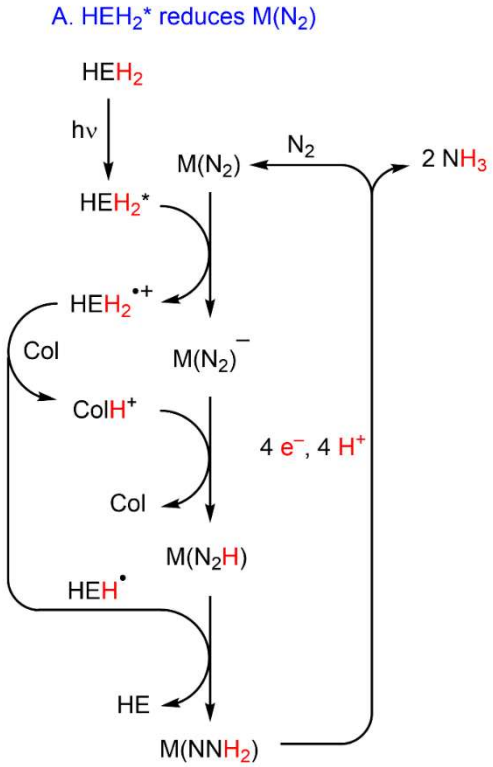

Figure C.16. Mechanistic scenario in absence of photoredox catalyst in which $[HEH_2]^*$ is quenched by a $M(N_2)$ intermediate.

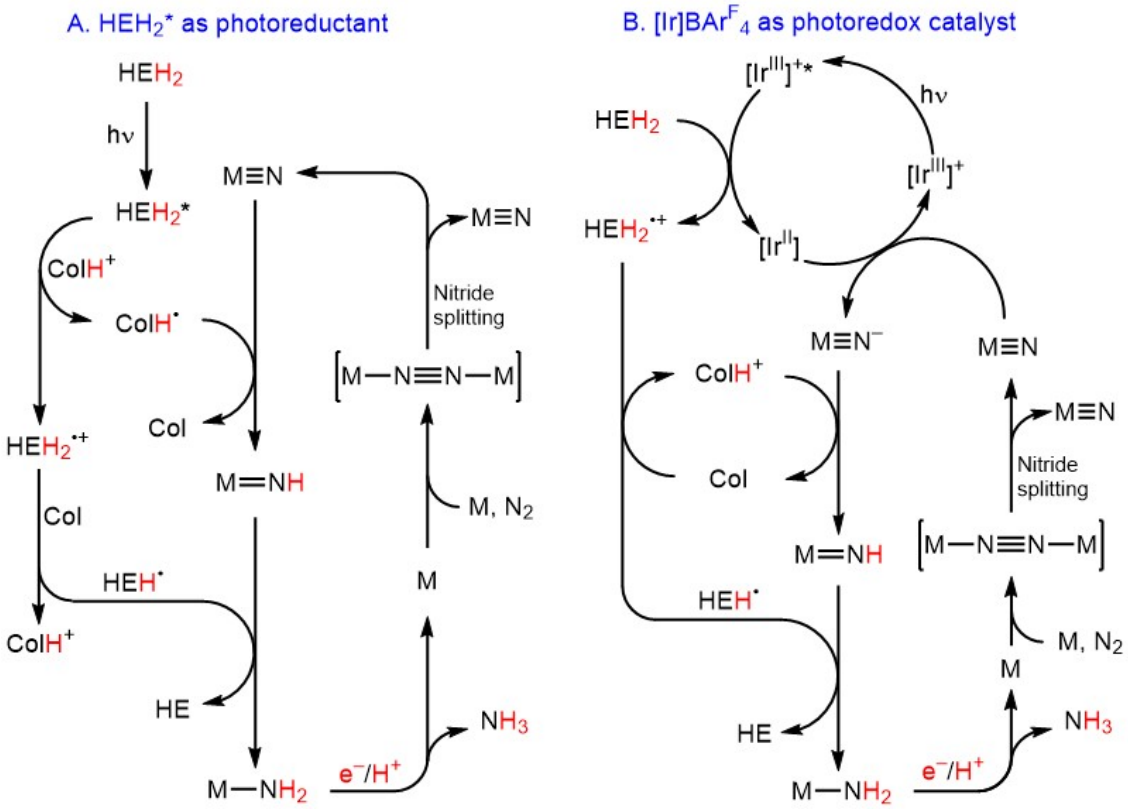

Figure C.17. Possible scenarios for photodriven transfer hydrogenation from HEH_2 to N_2 mediated by a metal catalyst and buffer system (Col/$[ColH]^+$). These schemes depict a mechanism in which N_2 cleavage occurs and the subsequent M≡N is hydrogenated. (A) Scenario in the absence of photoredox catalyst, in which $[HEH_2]$* is oxidatively quenched by $[ColH]^+$ to generate $[ColH]^•$. (B) Scenario with photoredox catalyst, in which $[Ir^{III}]^+$* is reductively quenched by HEH_2.

C.8 Derivation of thermodynamic values.

C.8.1 Summary of thermochemistry of Hantzsch ester (HEH_2) and derivatives

Table C.9 lists $BDFE_{X–H}$, pK_a, and E_{ox} values for various protonation and oxidation states of HEH_2. As has been established by Mayer and coworkers,[16] bond dissociation enthalpies (BDEs) can be converted to BDFEs based on the assumption that the entropies of R–H and R$^•$ are similar. Subtraction of $TS°(H^•)_{solv}$ (6.37 kcal mol^{-1} in MeCN) from the BDE values reported in ref. 4 yields the estimated BDFE values in Table C.9. With these values and reported potentials of oxidation, relevant pK_a values were then estimated using the thermodynamic cycles laid out below.

Table C.9. Reported and estimated thermochemical values for various protonation and oxidation states of HEH_2 relevant to this study. [a] kcal mol^{-1} in MeCN at 298 K. [b] V vs. $Fc^{+/0}$ in MeCN at 298 K. [c] Ref. 4. [d] Estimated using the E_{00} reported in ref. 17.

	BDE[a]	BDFE[a]	E_{ox}[b]	pK_a
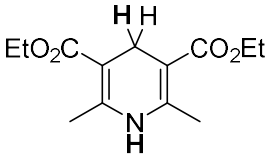 HEH_2	68.7 (C–H), 86.6 (N–H)[c]	62.3 (C–H), 80.2 (N–H)	0.48[c]	31.8 (N–H)
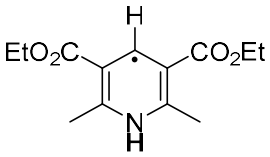 $HEH^{\bullet}$	46.9 (N–H)[c]	40.5 (N–H)		
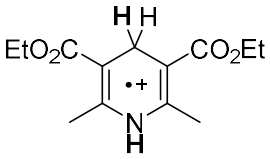 $HEH^{\bullet+}$				–1.0 (C–H)
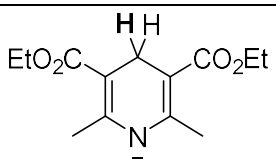 HEH^{-}			–0.695[c]	
$[HEH_2]$*		–8.5 (C–H)[d]	–2.5[d]	–20(N–H)[d]

Estimation of the N–H pK_a of HEH_2:

$HEH^{\bullet} + e^{-} \rightleftharpoons HEH^{-}$ $\quad -23.06(E_{ox}(HEH^{-})) = 16$ kcal mol^{-1}
$H^{\bullet} \rightleftharpoons H^{+} + e^{-}$ $\quad -C_G = -52.6$ kcal mol^{-1}
$\underline{HEH_2 \rightleftharpoons HEH^{\bullet} + H^{\bullet} \quad BDFE_{N-H}(HEH_2) = 80.2 \text{ kcal mol}^{-1}}$
$HEH_2 \rightleftharpoons HEH^{-} + H^{+}$ $\quad 1.37(pK_a)$
$pK_{a,N-H}(HEH_2) = \mathbf{31.8}$

Estimation of the C–H pK_a of $HEH_2^{\bullet+}$:

$HEH_2^{\bullet} + e^{-} \rightleftharpoons HEH_2$ $\quad -23.06(E_{ox}(HEH_2)) = -11.1$ kcal mol^{-1}
$H^{\bullet} \rightleftharpoons H^{+} + e^{-}$ $\quad -C_G = -52.6$ kcal mol^{-1}
$\underline{HEH_2 \rightleftharpoons HEH^{\bullet} + H^{\bullet} \quad BDFE_{C-H}(HEH_2) = 62.3 \text{ kcal mol}^{-1}}$
$HEH_2^{\bullet+} \rightleftharpoons HEH^{\bullet} + H^{+}$ $\quad 1.37(pK_a)$
$pK_{a,C-H}(HEH^{\bullet+}) = \mathbf{-1.0}$

Estimation of the excited-state N–H pK_a of [HEH_2]*:

$HEH_2^* \rightleftharpoons HEH_2$ $\quad -23.06(E_{00}) = -70.8$ kcal mol^{-1}
$\underline{HEH_2 \rightleftharpoons HEH^- + H^+ \quad 1.37(pK_{a,N-H}(HEH_2)) = 43.6 \text{ kcal mol}^{-1}}$
$HEH_2^* \rightleftharpoons HEH^- + H^+ \quad 1.37(pK_a)$
$pK_{a,N-H}(HEH_2^*) = \mathbf{-20}$

Estimation of the excited-state $BDFE_{C-H}$ of [HEH_2]*:

$HEH_2^* \rightleftharpoons HEH_2$ $\quad -23.06(E_{00}) = -70.8$ kcal mol^{-1}
$\underline{HEH_2 \rightleftharpoons HEH^- + H^+ \quad BDFE_{C-H}(HEH_2) = 62.3 \text{ kcal mol}^{-1}}$
$HEH_2^* \rightleftharpoons HEH^- + H^+ \quad BDFE_{C-H}(HEH_2^*) = \mathbf{-8.5 \text{ kcal mol}^{-1}}$

C.8.2 Derivation of effective BDFE values ($BDFE_{eff}$) relevant to this work

C.8.2.1 Derivation of $BDFE_{eff}$ for H_2-carrier

Estimation of $BDFE_{eff}$ for HEH_2:

½ $HEH_2 \rightleftharpoons$ ½ $HEH^\bullet$ + ½ $H^\bullet$ ½ $BDFE_{C-H}(HEH_2) = 31.2$ kcal mol^{-1}
$\underline{\text{½ } HEH^\bullet \rightleftharpoons \text{½ } HE + \text{½ } H^\bullet \text{ ½ } BDFE_{N-H}(HEH^\bullet) = 20.3 \text{ kcal mol}^{-1}}$
½ $HEH_2 \rightleftharpoons$ ½ HE + $H^\bullet$ $BDFE_{eff}(HEH_2) = \mathbf{51.4 \text{ kcal mol}^{-1}}$

Estimation of $BDFE_{eff}$ for $acrH_2$:

$acrH_2 \rightleftharpoons acrH_2^{\bullet+} + e^-$ $23.06(E_{ox}(acrH_2)) = 11.3$ kcal mol^{-1} (Ref 18)
$acrH_2^{\bullet+} \rightleftharpoons acrH^+ + H^\bullet$ $BDE(acrH_2^{\bullet+}) - TS°(H^\bullet)_{solv} = 43.5 - 6.37$ kcal mol^{-1} $= 37.1$ kcal mol^{-1} (Ref 51)
$\underline{e^- + H^\bullet \rightleftharpoons H^- \quad \Delta G° = 26.0 \text{ kcal mol}^{-1} \text{ (Ref 16)}}$
$acrH_2 \rightleftharpoons acrH^+ + \underline{H^-}$ $\quad \Delta G(acrH_2)_{H^-} = \mathbf{74.4 \text{ kcal mol}^{-1}}$

½ $acrH_2 \rightleftharpoons$ ½ $acrH^+$ + ½ H^- ½ $\Delta G(acrH_2)_{H^-} = 37.2$ kcal mol^{-1}
½ $acrH^+ \rightleftharpoons$ ½ acr + ½ H^+ ½ $1.37(\underline{pK_a}) = 8.7$ kcal mol^{-1} (Ref 19)
½ H^- + ½ $H^+ \rightleftharpoons$ ½ H_2 $\quad$ ½ $\Delta G° = -38$ kcal mol^{-1} (Ref 16)
$\underline{\text{½ } H_2 \rightleftharpoons H^\bullet \quad \text{½ } BDFE_{N-H}(H_2) = 52 \text{ kcal mol}^{-1}}$
½ BNAH + $\underline{\text{½}}$ $[ColH]^+ \rightleftharpoons$ ½ BNA + ½ Col + $H^\bullet$ $\quad BDFE_{eff}(acrH_2) = \mathbf{59.9 \text{ kcal mol}^{-1}}$

Estimation of $BDFE_{eff}$ for $phenH_2$:

½ $phenH_2 \rightleftharpoons$ ½ $phenH^\bullet$ + ½ $H^\bullet$ ½ $BDFE_{C-H}(phenH_2) = 33.1$ kcal mol^{-1} (Ref 4)
$\underline{\text{½ } phenH^\bullet \rightleftharpoons \text{½ phen} + \text{½ } H^\bullet \text{½ } BDFE_{N-H}(phenH^\bullet) = 19.1 \text{ kcal mol}^{-1} \text{ (Ref 4)}}$
½ $phenH_2 \rightleftharpoons$ ½ phen + $H^\bullet$ $BDFE_{eff}(phenH_2) = \mathbf{52.2 \text{ kcal mol}^{-1}}$

Estimation of $BDFE_{eff}$ for BNAH:

BNAH is a 1 H^+ /2 e^- donor. As such, to balance the equation for the 6 H^+/6 e^- reduction of N_2, we posit that [ColH]OTf must also be consumed giving a balanced reaction:
$N_2 + 3\ BNAH + 3\ [ColH]^+ \rightarrow NH_3 + 3\ [BNA]^+ + 3\ Col$
To estimate $BDFE_{eff}$, we instead combine the hydricity of BNAH and the acidity of [ColH]OTf

½ BNAH ⇌ ½ BNA + ½ H^- ½ $\Delta G(BNAH)_{H^-}$ = 29.5 kcal mol^{-1} (Ref 18)
½ $[ColH]^+$ ⇌ ½ Col + ½ H^+ ½ 1.37(pK_a) = 10.3 kcal mol^{-1} (Ref 20)
½ H^- + ½ H^+ ⇌ ½ H_2 ½ $\Delta G°$ = −38 kcal mol^{-1} (Ref 16)
½ H_2 ⇌ $H^•$ ½ $BDFE_{N–H}(H_2)$ = 52 kcal mol^{-1}
½ BNAH + ½ $[ColH]^+$ ⇌ ½ BNA + ½ Col + $H^•$ $BDFE_{eff}(BNAH/ColH^+)$ = **53.8 kcal mol^{-1}**

C.8.2.2 Derivation of $BDFE_{eff}$ for reductant (photosensitizer or *HEH_2) and acid

Estimation of $BDFE_{eff}$ for $[HEH_2]$* as reductant and $[ColH]^+$ as acid:

$HEH_2^* \rightleftharpoons HEH_2^{•+} + e^-$ 23.06(E_{ox}([*HEH_2]) = –57.7 kcal mol^{-1}
$[ColH]^+ \rightleftharpoons Col + H^+$ 1.37(pK_a) = 20.6 kcal mol^{-1}
$H^+ + e^- \rightleftharpoons H^•$ C_G = 52.6 kcal mol^{-1}
$HEH_2^* + [ColH]^+ \rightleftharpoons HEH_2^{•+} + Col + H^•$ $BDFE_{eff}$ = **15.5 kcal mol^{-1}**

Estimation of $BDFE_{eff}$ for $Ir^{II}(ppy)_2$(dtbbpy) as reductant and $[ColH]^+$ as acid:

$[Ir^{II}] \rightleftharpoons [Ir^{III}]^+ + e^-$ 23.06(E_{ox}([Ir^{II}]) = –43.8 kcal mol^{-1} (Ref 21)
$[ColH]^+ \rightleftharpoons Col + H^+$ 1.37(pK_a) = 20.6 kcal mol^{-1}
$H^+ + e^- \rightleftharpoons H^•$ C_G = 52.6 kcal mol^{-1}
$HEH_2^* + [ColH]^+ \rightleftharpoons HEH_2^{•+} + Col + H^•$ $BDFE_{eff}$ = **29.3 kcal mol^{-1}**

Estimation of $BDFE_{eff}$ for Ir^{II}(*p*-F(Me)ppy)$_2$(dtbbpy) as reductant and $[ColH]^+$ as acid:

$[Ir^{II}] \rightleftharpoons [Ir^{III}]^+ + e^-$ 23.06(E_{ox}([Ir^{II}]) = –43.4 kcal mol^{-1} (Ref 22)
$[ColH]^+ \rightleftharpoons Col + H^+$ 1.37(pK_a) = 20.6 kcal mol^{-1}
$H^+ + e^- \rightleftharpoons H^•$ C_G = 52.6 kcal mol^{-1}
$HEH_2^* + [ColH]^+ \rightleftharpoons HEH_2^{•+} + Col + H^•$ $BDFE_{eff}$ = **29.8 kcal mol^{-1}**

Estimation of $BDFE_{eff}$ for $Ir^{II}(dF(CF_3)ppy)_2$(dtbbpy) as reductant and $[ColH]^+$ as acid:

$[Ir^{II}] \rightleftharpoons [Ir^{III}]^+ + e^-$ 23.06(E_{ox}([Ir^{II}]) = –40.4 kcal mol^{-1} (Ref 23)
$[ColH]^+ \rightleftharpoons Col + H^+$ 1.37(pK_a) = 20.6 kcal mol^{-1}
$H^+ + e^- \rightleftharpoons H^•$ C_G = 52.6 kcal mol^{-1}
$HEH_2^* + [ColH]^+ \rightleftharpoons HEH_2^{•+} + Col + H^•$ $BDFE_{eff}$ = **32.8 kcal mol^{-1}**

Estimation of $BDFE_{eff}$ for $[Ir^{II}(ppy)_3]^-$ as reductant and $[ColH]^+$ as acid:

$[Ir^{II}] \rightleftharpoons [Ir^{III}]^+ + e^-$ $23.06(E_{ox}([Ir^{II}]) = -59.3$ kcal mol^{-1} (Ref 23)
$[ColH]^+ \rightleftharpoons Col + H^+$ $1.37(pK_a) = 20.6$ kcal mol^{-1}
$H^+ + e^- \rightleftharpoons H^\bullet$ $C_G = 52.6$ kcal mol^{-1}
$HEH_2^* + [ColH]^+ \rightleftharpoons HEH_2^{\bullet+} + Col + H^\bullet$ $BDFE_{eff}$ = **13.9 kcal mol^{-1}**

Estimation of $BDFE_{eff}$ for $[Ir^{III}(ppy)_3]^*$ as reductant and $[ColH]^+$ as acid:

$[Ir^{II}] \rightleftharpoons [Ir^{III}]^+ + e^-$ $23.06(E_{ox}([Ir^{III*}]) = -48.7$ kcal mol^{-1} (Ref 23)
$[ColH]^+ \rightleftharpoons Col + H^+$ $1.37(pK_a) = 20.6$ kcal mol^{-1}
$H^+ + e^- \rightleftharpoons H^\bullet$ $C_G = 52.6$ kcal mol^{-1}
$HEH_2^* + [ColH]^+ \rightleftharpoons HEH_2^{\bullet+} + Col + H^\bullet$ $BDFE_{eff}$ = **24.5 kcal mol^{-1}**

C.8.3 Estimation of overpotential for hydrogenation of N_2 with HEH_2 to NH_3

We derive the BDFE of H_2 in MeCN at 298 K explicitly here for clarity, using recently updated thermochemical values (*36*):

$H_{2(g)} \rightleftharpoons 2\ H^+ + 2\ e^-$ $2\times23.06(E°(H^+/H_2)) = 2\times23.06(-0.028\ V) = -1.29$ kcal mol^{-1} (Ref 16)
$2\ H^+ + 2\ e^- \rightleftharpoons 2H^\bullet$ $2(C_G) = 105.2$ kcal mol^{-1}
$H_{2(g)} \rightleftharpoons 2H^\bullet$ $BDFE(H_2)$ = **103.9 kcal mol^{-1}**

C.8.3.1 Determination of overpotential for dark reactions

The overpotential $\Delta\Delta G_f(NH_3)$ for a source of hydrogen atom equivalents with a given $BDFE_{eff}$ is described by eqn C.3:

$$\Delta\Delta G_f(NH_3) = 3(BDFE(H_2)/2 - BDFE_{eff}) \text{ (eqn C.3)}$$

For the dark reaction, $\frac{1}{2}\ N_2 + \frac{3}{2}\ HEH_2 \rightleftharpoons NH_3 + \frac{3}{2}\ HE$:

$$\Delta\Delta G_f(NH_3) = 3(103.9/2 - 51.4) = \textbf{1.7 kcal mol}^{-1}$$

For the dark reaction, $\frac{1}{2}\ N_2 + \frac{3}{2}\ acrH_2 \rightleftharpoons NH_3 + \frac{3}{2}\ acr$:

$$\Delta\Delta G_f(NH_3) = 3(103.9/2 - 59.9) = \textbf{-23.9 kcal mol}^{-1}$$

For the dark reaction, $\frac{1}{2}\ N_2 + \frac{3}{2}\ phenH_2 \rightleftharpoons NH_3 + \frac{3}{2}\ phen$:

$$\Delta\Delta G_f(NH_3) = 3(103.9/2 - 52.2) = \textbf{-0.8 kcal mol}^{-1}$$

For the dark reaction, $\frac{1}{2}\ N_2 + \frac{3}{2}\ (BNAH + ColH^+) \rightleftharpoons NH_3 + \frac{3}{2}\ (BNA^+ + Col)$:

$$\Delta\Delta G_f(NH_3) = 3(103.9/2 - 53.8) = \textbf{-5.5 kcal mol}^{-1}$$

With the dark reaction values value, we can also estimate the absolute driving force for hydrogenation of N_2 with $subH_2$.

$\Delta G_f(NH_3)$ in MeCN at 298 K:

$^1/_2$ N_2 + $^3/_2$ $H_{2(g)}$ ⇌ NH_3 $\Delta G_f(NH_3) = -3\times23.06(E°(N_{2(g)}/NH_3)) = -3\times23.06(0.063$ V vs. $H_2)$ (Ref 36)

$$= \mathbf{4.36\ kcal\ mol^{-1}}$$

We then estimate the following:

$^1/_2$ N_2 + $^3/_2$ HEH_2 ⇌ NH_3 + $^3/_2$ HE$\Delta G_{rxn} = \Delta G_f(NH_3) - \Delta\Delta G_f(NH_3, HEH_2) = -4.4 - 1.7$ kcal mol^{-1}

$$= \mathbf{-6.1\ kcal\ mol^{-1}}$$

$^1/_2$ N_2 + $^3/_2$ $phenH_2$ ⇌ NH_3 + $^3/_2$ phen $\Delta G_{rxn} = \Delta G_f(NH_3) - \Delta\Delta G_f(NH_3, phenH_2) = -4.4 + 0.8$ kcal mol^{-1}

$$= \mathbf{-3.6\ kcal\ mol^{-1}}$$

$^1/_2$ N_2 + $^3/_2$ $acrH_2$ ⇌ NH_3 + $^3/_2$ acr $\Delta G_{rxn} = \Delta G_f(NH_3) - \Delta\Delta G_f(NH_3, acrH_2) = -4.4 + 23.9$ kcal mol^{-1}

$$= \mathbf{19.5\ kcal\ mol^{-1}}$$

$^1/_2$ N_2 + $^3/_2$ (BNAH + $ColH^+$) ⇌ NH_3 + $^3/_2$ (BNA^+ + Col)

$\Delta G_{rxn} = \Delta G_f(NH_3) - \Delta\Delta G_f(NH_3, BNAH + ColH^+) = -4.4 + 5.5$ kcal mol^{-1}

$$= \mathbf{+1.1\ kcal\ mol^{-1}}$$

Table C.10. Summary of driving forces for dark reaction using different $subH_2$ (assuming 2 H^+/ 2 e^- reaction). Values are calculated in MeCN at 25 °C. [a] Since BNAH is a H^- donor, the stoichiometry requires addition of H^+, assumed to be supplied from [ColH]OTf

$subH_2$	$BDFE_{eff}$ (kcal mol^{-1})	$\Delta\Delta G_f(NH_3)$ (kcal mol^{-1})	ΔG_{rxn} (kcal mol^{-1})
HEH_2	51.4	1.7	−6.1
$PhenH_2$	52.2	−0.8	−3.6
$AcrH_2$	59.9	−23.9	19.5
BNAH + [ColH]OTf [a]	53.8	−5.5	1.1

C.8.3.2 Determination of overpotential for light reactions

For the Ir-free reaction, in which $[HEH_2]$* is thought to be the strongest reductant accessed and $[ColH]^+$ serves as acid:

$$\Delta\Delta G_f(NH_3) = 3(103.9/2 - 15.5) = \mathbf{109\ kcal\ mol^{-1}}$$

For the Ir-photosensitized reaction with $[Ir(ppy)_2(dtbbpy)]BAr^F{}_4$, in which $[Ir^{II}]$ is thought to be the strongest reductant accessed and $[ColH]^+$ serves as acid:

$$\Delta\Delta G_f(NH_3) = 3(103.9/2 - 29.3) = \mathbf{68.0\ kcal\ mol^{-1}}$$

For the Ir-photosensitized reaction with $[Ir(dF(CF_3)ppy)_2(dtbbpy)]PF_6$, in which $[Ir^{II}]$ is thought to be the strongest reductant accessed and $[ColH]^+$ serves as acid:

$$\Delta\Delta G_f(NH_3) = 3(103.9/2 - 32.8) = \mathbf{58.3\ kcal\ mol^{-1}}$$

For the Ir-photosensitized reaction with $[Ir(p\text{-}F(Me)ppy)_2(dtbbpy)]PF_6$, in which $[Ir^{II}]$ is thought to be the strongest reductant accessed and $[ColH]^+$ serves as acid:

$$\Delta\Delta G_f(NH_3) = 3(103.9/2 - 29.8) = \mathbf{67.3\ kcal\ mol^{-1}}$$

For the Ir-photosensitized reaction with $Ir(ppy)_3$, in which $[Ir^{II}]$ is thought to be the strongest reductant accessed and $[ColH]^+$ serves as acid:

$$\Delta\Delta G_f(NH_3) = 3(103.9/2 - 13.9) = \mathbf{115.0\ kcal\ mol^{-1}}$$

For the Ir-photosensitized reaction with $Ir(ppy)_3$, in which $[Ir^{III}]$* is thought to be the strongest reductant accessed and $[ColH]^+$ serves as acid:

$$\Delta\Delta G_f(NH_3) = 3(103.9/2 - 24.5) = \mathbf{83.2\ kcal\ mol^{-1}}$$

Table C.11: Summary of driving forces for different photosensitizers. All $BDFE_{eff}$ and $\Delta\Delta G_f(NH_3)$ measurements made pairing reductant with [ColH]OTf (pK_a 15) Values are calculated in MeCN at 25 °C.

Reductant	E_{ox} (V vs. $Fc^{+/0}$)	$BDFE_{eff}$ (kcal mol^{-1})	$\Delta\Delta G_f(NH_3)$ (kcal mol^{-1})
HEH_2*	−2.5	15.5	109
$[Ir^{II}]$ ($Ir^{II}(ppy)_2dtbbpy$)	−1.90	29.3	68.0
$Ir^{II}(dF(CF_3)ppy)_2(dtbbpy)$	−1.75	32.8	58.3
Ir^{II}(*p*-F(Me)ppy)$_2$(dtbbpy)	−1.88	29.8	67.3
$Ir^{II}(ppy)_3^-$	−2.57	13.9	115.0
$Ir^{III}(ppy)_3$*	−2.11	24.5	83.2

C.9 NMR spectra

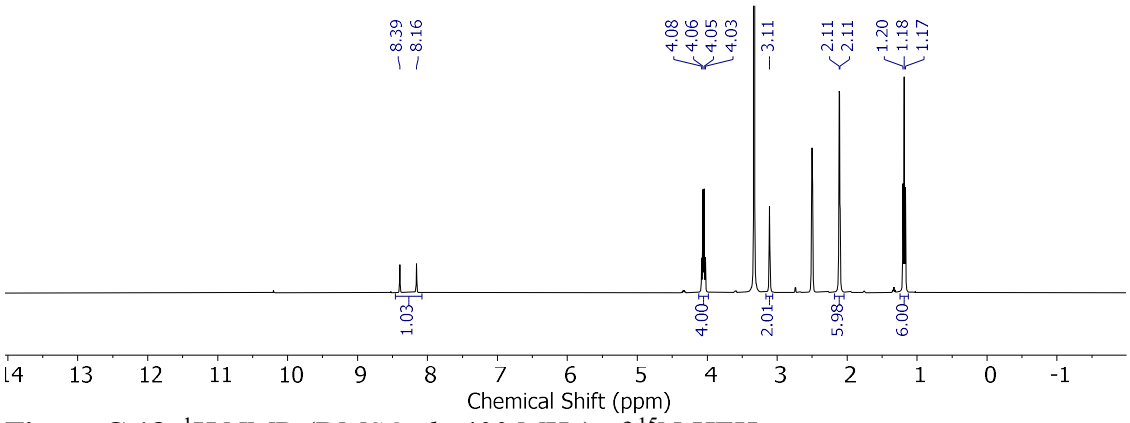

Figure C.18. ^{1}H NMR (DMSO-d_6, 400 MHz) of ^{15}N-HEH$_2$.

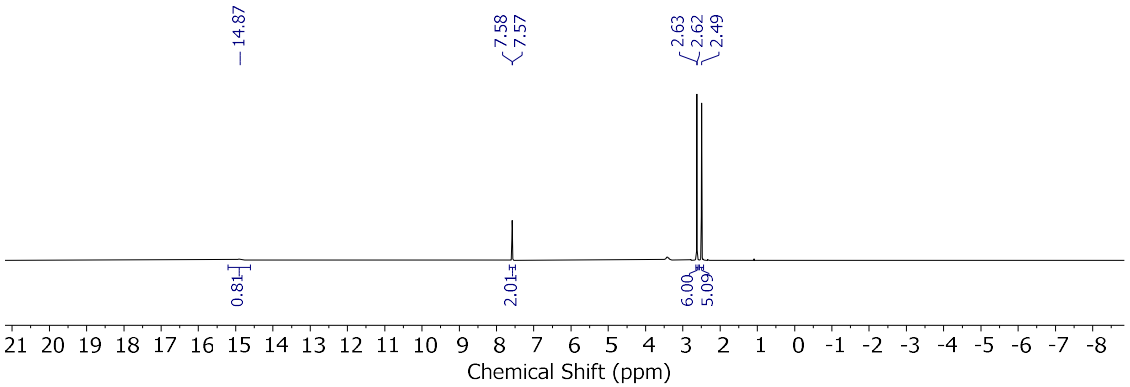

Figure C.19. ^{1}H NMR (DMSO-d_6, 400 MHz) of ^{15}N-labelled [ColH]OTf.

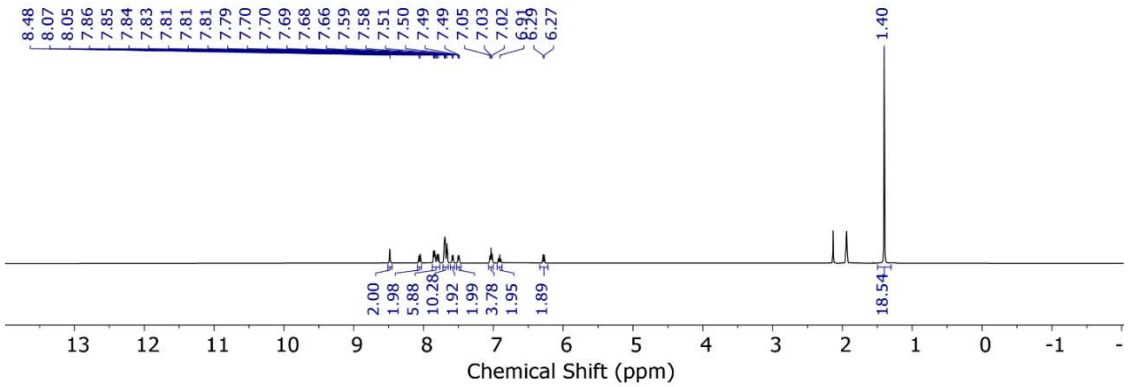

Figure C.20 ^{1}H NMR (MeCN-d_3, 400 MHz) of [Ir]BAr$^{F}_4$.

C.10 References for Appendix

1. Norcross, B. E.; Clement, G.; Weinstein, M.; *J. Chem. Educ.* **1969**. 46, 694.
2. Arashiba, K.; Eizawa, A.; Tanaka, H.; Nakajima, K.; Yoshizawa, K.; Nishibayashi, Y. *Bull. Chem. Soc. Jpn*. **2017**. 90, 1111–1118.
3. Anderson, J. S.; Moret, M. E.; Peters, J. C. *J. Am. Chem. Soc*. **2013**. 135, 534–537.
4. Shen, G.-B.; Fu, Y.-H.; Zhu, X.-Q. *J. Org. Chem*. **2020**. 85, 12535–12543.
5. Del Castillo, T. J.; Thompson, N. B.; Peters, J. C. *J. Am. Chem. Soc.* **2016**. 138, 5341–5350.
6. N. S. Golubev, S. N. Smirnov, P. Schah-Mohammedi, I. G. Shenderovich, G. S. Denisov, V. A. Gindin, H. H. Limbach, *Russ. J. Gen. Chem.* **1997**. 67, 1082–1087.
7. Matesic, L.; Locke, J. M.; Vine, K. L.; Ranson, M.; Bremner, J. B.; Skropeta D. *Tetrahedron* **2012**. 68, 6810–6819.
8. Brišar, R.; Unglaube, F.; Hollmann, D.; Jiao, H.; Mejía, E. *J. Org. Chem.* **2018**. 83, 13481–13490.
9. Elrod, L. T.; Kim, E. *Inorg. Chem*. **2018**. 57, 2594–2602.
10. Fulmer, G. R.; Miller, A. J. M.; Sherden, N. H.; Gottlieb, H. E.; Nudelman, A.; Stoltz, B. M.; Bercaw, J. E.; Goldberg, K. I. *Organometallics*. **2010**. 29, 2176–2179.
11. Weatherburn, M. W. *Anal. Chem.* **1967**. 39, 971–974.
12. Watt, G. W.; Chrisp, J. D. *Anal. Chem.* **1952**. 24, 2006–2008.
13. Xu, S.; Ashley, D. C.; Kwon, H.-Y.; Ware, G. R.; Chen, C.-H.; Losovyj, Y.; Gao, X.; Jakubikova, E.; Smith, J. M. *Chem. Sci*. **2018**. 9, 4950–4958.
14. Lindley, B. M.; Appel, A. M.; Krogh-Jespersen, K.; Mayer, J. M.; Miller, A. J. M. *ACS Energy Lett*. **2016**. 1, 698–704.
15. Gibanel, F.; López, M. C.; Royo, F. M.; Santafé, J.; Urieta, J. S. *J. Solution Chem*. **1993**. 22, 211–217.

16. Agarwal, R. G.; Coste, S. C.; Groff, B. D.; Heuer, A. M.; Noh, H.; Parada, G. A.; Wise, C. F.; Nichols, E. M.; Warren, J. J. ; Mayer, J. M. *Chem. Rev*. **2022**. 122, 1–49.
17. Jung, J.; Kim, J.; Park, G.; You, Y.; Cho, E. J. *Adv. Synth. Catal*. **2016**. 358, 74–80.
18. Ilic, S.; Pandey Kadel, U.; Basdogan, Y.; Keith, J. A.; Glusac, K. D. *J. Am. Chem. Soc*. **2018**. 140, 4569–4579.
19. Ilic, S.; Pandey Kadel, U.; Basdogan, Y.; Keith, J. A.; Glusac, K. D. *J. Am. Chem. Soc*. **2018**. 140, 4569–4579.
20. Tshepelevitsh, S.; Kütt, A.; Lõkov, M.; Kaljurand, I.; Saame, J.; Heering, A.; Plieger, P. G.; Vianello, R.; Leito, I. *Eur. J. Org. Chem*. **2019**. 2019, 6735–6748.
21. Slinker, J. D.; Gorodetsky, A. A.; Lowry, M. S.; Wang, J.; Parker, S.; Rohl, R.; Bernhard, S.; Malliaras, G. G. *J. Am. Chem. Soc*. **2004**. 126, 2763–2767.
22. Capacci, A. G.; Malinowski, J. T.; McAlpine, N. J.; Kuhne, J.; MacMillan, D. W. C. *Nat. Chem.* **2017**. 9, 1073–1077.
23. Koike, T.; Akita, M. *Inorg. Chem. Front*. **2014**. 1, 562–576.

A p p e n d i x D

Supplementary Information for Chapter 5

D.1 General considerations

All manipulations were carried out using standard Schlenk or glovebox techniques under an N_2 atmosphere. Solvents were deoxygenated and dried by thoroughly sparging with N_2, followed by passage through an activated alumina column in a solvent purification system by SG Water, USA LLC. Nonhalogenated solvents were tested with sodium benzophenone ketyl in tetrahydrofuran (THF) to confirm the absence of oxygen and water. Deuterated solvents were purchased from Cambridge Isotope Laboratories, Inc., degassed, and dried over activated 3-Å molecular sieves prior to use.

D.1.1 Materials

HEH_2,[1] $[MoBr_3]$,[2] $[PCPMoCl_3]$,[3] [ColH]OTf,[4] [TBA][$^{15}NO_3$],[4] $^{15\text{-}N}HEH_2$,[4] $^{15\text{-}N}$[ColH]OTf,[4] $^{15\text{-}N}$Col,[5] d_2-HEH_2,[6] d_1-HEH_2 (N-H proton is deuterated),[7] d_3-HEH_2,[8] [ImidH]OTf,[9] were synthesized using literature procedures. d_2-$^{15\text{-}N}HEH_2$ was synthesized as $^{15\text{-}N}HEH_2$ or d_2-HEH_2 but using both [$^{15}NH_4$]Cl and d_2-paraformaldehyde._tolNO_2, ^{Me2N}PhCHO, ^{MeO}PhCHO, [TBA][NO_3], ^{n}PrNO_2, benzyl acetone, Me_3NO, imidazole, and dimethylterphatalate were purchased from Sigma and used without further purification. Col was purchased from Ambeed and distilled prior to use. ^{15N}Col was also distilled following synthesis. [$^{15}NH_4$]Cl, d_2-paraformaldehyde, D_2O and d_1-EtOD were purchased from Cambridge Isotope Laboratories, Inc.

D.1.2 Spectroscopy

Nuclear Magnetic Resonance spectroscopy: Nuclear Magnetic Resonance (NMR) measurements were recorded with a Varian 400 MHz spectrometer. ^{1}H NMR chemical shifts are reported in ppm relative to tetramethylsilane, using ^{1}H resonances from residual solvent as internal standards.[10]

Ultraviolet-visible spectroscopy: Ultraviolet-visible (UV-vis) absorption spectroscopy measurements were collected with a Cary 50 UV-vis spectrophotometer using a 1 cm path length quartz cuvette. All samples had a solvent background subtraction applied.

Continuous-wave Electron Paramagnetic Resonance spectroscopy: All X-band continuous-wave electron paramagnetic resonance (CW-EPR) spectra were obtained on a

Bruker EMX spectrometer using a quartz liquid nitrogen immersion dewar on samples prepared as frozen THF solutions unless otherwise noted.

Infrared spectroscopy: Solution state infrared (IR) spectra were obtained using a Bruker Alpha Platinum ATR spectrometer with OPUS software in a glovebox under an N_2 atmosphere. All IR data were collected as solution state spectra in a KBr-cell in THF and, unless stated, have had THF background spectra subtracted.

Steady-state Fluorimetry: Steady-state fluorimetry was performed in the Beckman Institute Laser Resource Center (California Institute of Technology). Samples for luminescence measurements were prepared in dry THF and transferred to a 1-cm path length–fused quartz cuvette sealed with a high-vacuum Teflon valve (Kontes). Steady-state emission spectra were collected on the Jobin S4 Yvon Spec Fluorolog-3-11 with a Hamamatsu R928P photomultiplier tube detector with photon counting.

Transient absorbance spectroscopy: Transient Absorption Samples in stirred air-tight cuvettes were excited with 355-nm or 450-nm pulses from a Q-switched Nd:YAG laser (Spectra-Physics Quanta-Ray PRO-Series) or a tunable Nd:YAG-pumped optical parametric oscillator (Opotek Radiant QX8130U), both operating at a 10 Hz repetition rate. Probe light from a current-pulsed (1 ms) 75-W Xe arc lamp was directed with all-reflective optics collinearly with the laser excitation through the cuvette and wavelength selected using a double monochromator (ISA DH10). Wavelength-selected probe light was detected by a photomultiplier tube (PMT, Hamamatsu R955) wired for 5 gain stages. The PMT output was amplified (Femto DHPCA-100), offset in a wideband differential amplifier, and digitized at speeds up to 1 GS/s with a transient digitizer (GageScope). For luminescence decay measurements, the probe light was blocked, and sample fluorescence was detected by the PMT. Data collection was controlled by a PC with software written in LabView (National Instruments). Signals were averaged for several hundred laser shots to optimize signal-to-noise levels.

Time-resolved Fluorescence: Laser excitation was provided by regeneratively amplified (Continuum) pulses from a diode pumped passively mode-locked Nd:YAG laser (Spectra Physics Vanguard 2000). The output from the regenerative amplifier was tripled

(355 nm, ~10 ps) and directed onto the sample held in a stirred 1-cm air-tight fluorescence cuvette. Fluorescence was collected at 90° using reflective optics and focused onto the entrance slit of a 0.275 m spectrograph (Acton SpectraPro 275). A fiber bundle at the spectrograph image plane collected the fluorescence and directed it to the entrance slit of a picosecond streak camera (Hamamatsu C5680). The streak camera was operated in photon counting mode using High-Performance Digital Temporal Analyzer software (Hamamatsu). The instrument time resolution is ~20 ps.

D.2 NH_3 generation experiments

D.2.1 Standard NH_3 Generation Reaction Procedure

In a nitrogen-filled glovebox, the precatalyst ([$MoBr_3$]) (2.3 μmol) is weighed into individual vials. The precatalyst is then transferred quantitatively into a Schlenk tube using THF. The THF is then evaporated to provide a thin film of precatalyst at the bottom of the Schlenk tube. The tube is then charged with a stir bar, and dihydropyridine (124 μmol) is added as solids. The acid and base (124 μmol of each) are dissolved in 1 mL solvent and added to the tube to produce a concentration of precatalyst of 2.3 mM. This tube is sealed, passed out of the box, and transported to a fume hood, where the tube is transferred to a water bath, where it is allowed to stir for 12 hours while irradiated by a Kessil™ as indicated. To ensure reproducibility, all experiments were conducted in 50 mL Schlenk tubes (20 mm OD) using 10 mm egg-shaped stir bars and stirring at ~600 rpm. The water bath was contained in highly reflective dewars. The LED was placed above the bath as close to the stirring reaction without touching the tube or the dewar.

Following completion, the reaction mixtures are cooled to 77 K and allowed to freeze. The reaction vessel is then opened to the atmosphere, and the frozen solution is slowly added to excess of a solution of HCl (3 mL of a 2.0 M solution in Et_2O, 6 mmol) over 1-2 minutes. This solution is allowed to freeze, then the headspace of the tube is evacuated, and the tube is sealed. The tube is then allowed to warm to RT and stirred at RT for at least 10 minutes. Solvent is removed *in vacuo*, and the solids are extracted with 1 M $HCl_{(aq)}$ and filtered to give a total solution volume of 10 mL. A 5 mL aliquot is taken and washed

repeatedly with n-butanol to remove Hantzsch pyridine (HE) and collidinium. After n-butanol washing additional 1 M HCl(aq) is added to give a final total volume of 5 mL. From these 5 mL solutions, a 100 µL aliquot is analyzed for the presence of NH_3 (present as $[NH_4][Cl]$) by the indophenol method. Quantification was performed with UV-vis spectroscopy by analyzing the absorbance at 635 nm.[11]

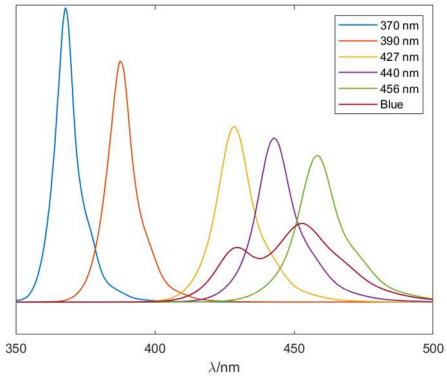

Figure D.1. Lamp relative emission spectra of Kessil™ H160 and H150 lamps used in this study. Emission spectra are measured as photoncount and normalized to wattage. All spectra were measured at multiple intensities to avoid detector saturation.

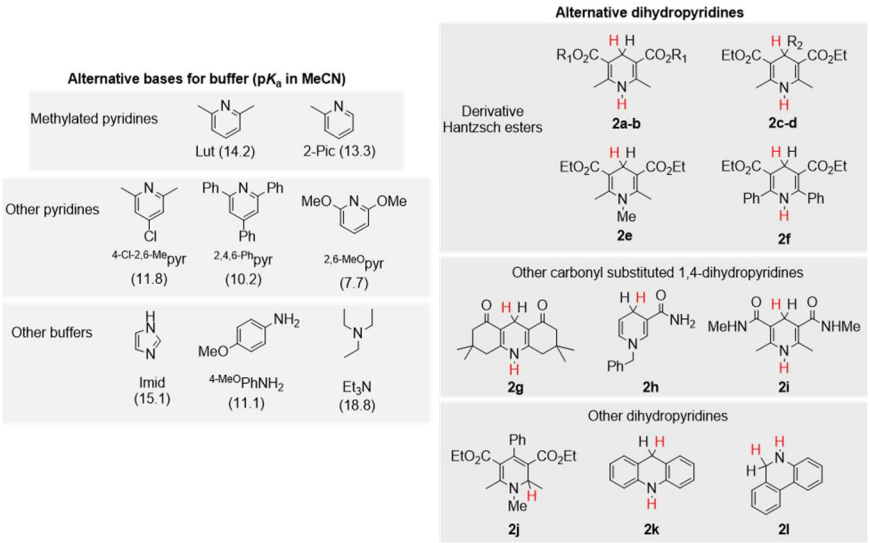

Figure D.2. Structures of buffers and dihydropyridines canvassed for N_2R in Table D.7. Hantzsch ester derivatives are labeled as follows: 2a: R_1 = Me; 2b: R_1 = ^{t}Bu; 2c: R_2 = Ph; 2d: R_2 = $^{4\text{-CN}}$Ph.

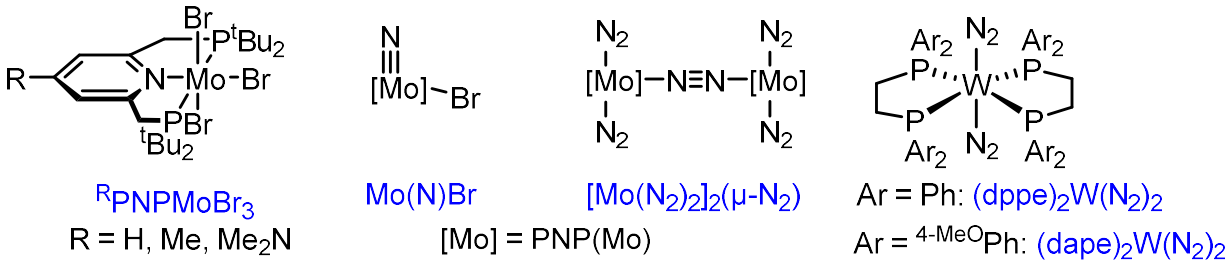

Figure D.3. Additional transition metal catalysts tested for photodriven N_2R.

Table D.1. Catalytic yields for reduction of N_2 to yield NH_3 varying the irradiation wavelength.

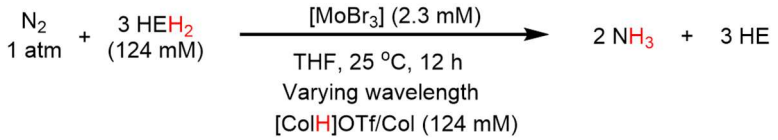

Entry	Lamp	NH_3 (equiv/ Mo)	NH_3 yield/ HEH_2 (%)
1	H150 Blue[a], 34 W	9.5 ± 1	26.5 ± 3
2	H150 Blue, 68 W	13 ± 2	36 ± 5
3	H160 456 nm	<0.1	<0.3
4	H160 440 nm	1.5 ± 0.5	4 ± 1
5	H160 440 nm, 80 W, 24 hrs	4.6 ± 0.2	12.6 ± 0.05
6	H160 427 nm	6.6 ± 0.9	18 ± 2.5
7	H160 427 nm, 80 W	20.4 ± 0.6	57 ± 2
8	H160 427 nm, 80 W, 0.575 mM Mo	28 ± 3	19 ± 2
9	H160 390 nm	15.9 ± 1.4	44 ± 4
10	H160 390 nm, 80 W	17.6 ± 0.4	49 ± 1
11	H160 370 nm	2.7 ± 0.7	7.5 ± 2

[a] Yields taken from ref 4.

Table D.2. Yields for wavelength dependence for organic products (HE and HEH_2) from N_2R.

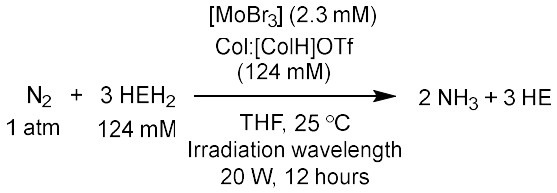

Entry	Lamp	Other Variations	HE yield (%)	HEH_2 yield
1	H160 456 nm		12%	86%
2	H160 440 nm	12 hours, 20 W	69%	19%
3	H160 440 nm	24 hours, 80 W	85%	<1%
4	H150 Blue LED		85%	<1%
5	H160 390 nm		68%	<1%
6	H160 370 nm		59%	<1%
7	H150 Blue LED	Lut-buffer	55%	<1%

Table D.3. Catalytic yields for reduction of N_2 to yield NH_3 varying the irradiation wavelength $PCPMoCl_3$ as precatalyst.

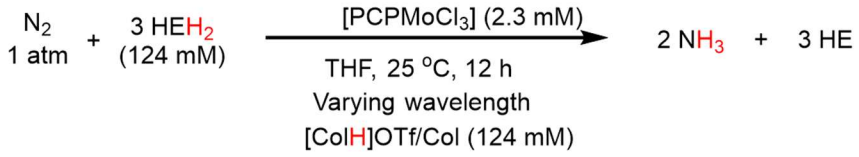

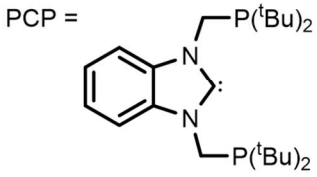

Entry	Lamp	NH_3 (equiv/ Mo)	NH_3 yield/ HEH_2 (%)
1	H160 456 nm	<0.1	<0.3
2	H160 440 nm	1.2	3
3	H160 427 nm	4.3	12

Table D.4. Catalytic yields for reduction of N_2 to yield NH_3 varying the irradiation wavelength in the absence of buffer.

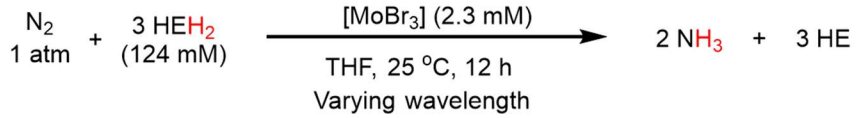

Entry	Lamp	NH_3 (equiv/ Mo)	NH_3 yield/ HEH_2 (%)
1	H150 Blue LED[a]	0.9 ± 0.2	2.6 ± 0.5
2	H160 440 nm,	<0.1	<0.3
3	H160 427 nm	<0.1	<0.3
4	H160 390 nm	0.4 ± 0.3	1.1 ± 0.8
5	H160 370 nm	<0.1	<0.3

[a] Yields taken from ref 4.

Table D.5. Catalytic yields for reduction of N_2 to yield NH_3 varying the buffer loading using either the Blue LED lamps or the H160 390 nm lamp.

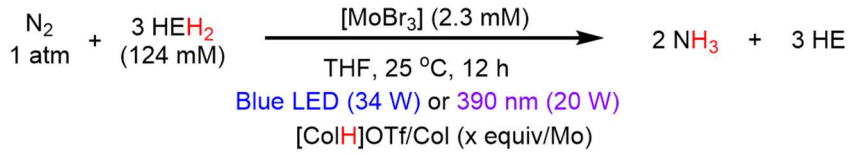

Entry	Lamp and buffer loading	NH_3 (equiv/ Mo)	NH_3 yield/ HEH_2 (%)
1	H160 390 nm, no buffer	0.4 ± 0.3	1.1 ± 0.8
2	H160 390 nm, 5 equiv buffer	6.9 ± 0.3	19 ± 1
3	H160 390 nm, 54 equiv buffer	15.9 ± 1.4	44 ± 4
4	H160 390 nm, 108 equiv buffer	9.2 ± 0.9	26 ± 2.5
5	H160 390 nm, 216 equiv buffer	8.3 ± 0.4	23 ± 1
6	H150 Blue LED, no buffer[a]	0.9 ± 0.2	2.6 ± 0.5
7	H150 Blue LED, 5 equiv buffer[a]	2.9 ± 0.2	8.0 ± 0.6
8	H150 Blue LED, 54 equiv buffer[a]	9.5 ± 1	26.5 ± 3
9	H150 Blue LED, 108 equiv buffer	16 ± 2	44 ± 6
10	H150 Blue LED, 216 equiv buffer[a]	20.3 ± 1.1	56 ± 3

[a] Yields taken from ref 4.

Table D.6. Individual runs for catalytic yields for reduction of N_2 to yield NH_3 when varying the irradiation wavelength (Figure 5.3 and Table D.1).

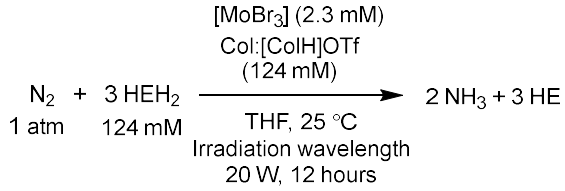

Entry	Lamp	Other Variations	NH_3 (equiv/ Mo)	Yield per HEH_2 (%)
A1	H150 Blue LED	68 W	10.7	30
B1	H150 Blue LED	68 W	13.8	38
C1	H150 Blue LED	68 W	14.9	41
Table D.1, entry 3	**H150 Blue LED**		**13 ± 2**	**36 ± 5**
D1	H160 456 nm		<0.1	<0.3
E1	H160 456 nm		<0.1	<0.3
F1	H160 456 nm		<0.1	<0.3
Table D.1, entry 3	**H160 456 nm**		**<0.1**	**<0.3**
G1	H160 440 nm		2.0	6
H1	H160 440 nm		0.8	2
I1	H160 440 nm		1.8	5
Table D.1, entry 4	**H160 440 nm**		**1.5±0.5**	**4±1**
J1	H160 440 nm	24 hours, 80 W	4.4	**12.2**
K1	H160 440 nm	24 hours, 80 W	**4.9**	**13.6**
Table D.1, entry 5	**H160 440 nm**	**24 hours, 80 W**	**4.6±0.2**	**12.6±0.05**
L1	H160 427 nm		7.5	21
M1	H160 427 nm		5.7	16
Table D.1, entry 6	**H160 427 nm**		**6.6±0.9**	**18±2.5**
N1	H160 427 nm	80 W	20.7	57
O1	H160 427 nm	80 W	18.6	52
P1	H160 427 nm	80 W	21.5	60
Q1	H160 427 nm	80 W	20.6	57
Table D.1, entry 7	**H160 427 nm**	**80 W**	**20.4±0.6**	**57±2**
R1	H160 427 nm	80 W, 0.575 mM Mo	30.8	21.4
S1	H160 427 nm	80 W, 0.575 mM Mo	24.7	17.1
Table D.1, entry 8	**H160 427 nm**	**80 W, 0.575 mM Mo**	**28±3**	**19±2**
T1	390 nm		18.1	50.2
U1	390 nm		15.1	41.9
V1	390 nm		14.2	39.4
W1	390 nm		16.1	44.7
Table D.1, entry 9	**H160 390 nm**		**15.9±1.4**	**44±4**
X1	390 nm	80 W	17.2	47.8
Y1	390 nm	80 W	18.0	50
Table D.1, entry 10	**H160 390 nm**	**80 W**	**17.6±0.4**	**49±1**
Z1	370 nm		3.4	9.4
AA1	370 nm		2.1	5.8
Table D.11, entry 11	**H160 370 nm**		**2.7±0.7**	**7.5±2**

Table D.7. NH_3 yields when varying dihydropyridine and buffer structure. For the benefit of the reader, the discussion is presented in this caption.

In brief, replacing Col-buffer (pK_a 15.0; table D.7, entry 1)[12] with other methylated pyridines showed attenuated efficacy for N_2R; 2,6-dimethylpyridine (Lut, pK_a 14.2; entry 2) buffer yielded 7.1±0.8 and 2-methylpyridine (2-pic, pK_a 13.3; entry 3) yielded 1.7±0.05 equiv NH_3, per Mo. Other buffers, such as more acidic pyridines (entry 4) or structurally distinct alternatives (imidazole, aniline, alkylamine; entry 5) with a similar pK_a to Col, each led to less than 0.4 equiv NH_3 per Mo.

Likewise, canvassing alternative dihydropyridines, we found that HEH_2 was most competent for photodriven N_2R (Table D.7, entries 1 and 6-9). Interestingly, the dihydropyridines we canvassed can be categorized into three groups (Figure D.2, bottom): Hantzsch ester derivates 1,4-dihydropyridines that maintain the ester groups at the 3,5 position and methyl groups at the 2,6 positions (2a-f, entries 6 and 7); 1,4-dihydropyridines with at least one carbonyl group (2g-2i, entry 8); other dihydropyridines (2j-2l, entry 9). Generally, the dihydropyridine that maintains the 3,5-diester functionality produces the most NH_3, suggesting that this motif may be crucial in the parent conditions (HEH_2/Col-buffer).

Varying buffer and dihydropyridine

Entry	Variation from standard conditions	Yield NH_3/Mo
1	None	13 ± 1.7
	Varying buffer (instead of Col-buffer)	
2	Lut as buffer	7.1 ± 0.8
3	2-pic as buffer	1.7 ± 0.1
4	$^{2\text{-MeO}}$pyr, $^{4\text{-Cl-2,6-Me}}$pyr or $^{2,4,6\text{-Ph}}$pyr as buffer	0 − 0.3
5	Imid, $^{4\text{-MeO}}$pyr or Et_3N as buffer	<0.2
	Varying dihydropyridine (instead of HEH_2)	
6	**2a** as dihydropyridine	3.2 ± 0.4
7	**2b-2f** as dihydropyridine	0.4 − 1.9
8	**2g-2i** as dihydropyridine	0.2 − 0.5
9	**2j-k** as dihydropyridine	<0.2

Table D.8. Individual runs for catalytic yields for reduction of N_2 to yield NH_3 when varying the buffer (Table D.7).

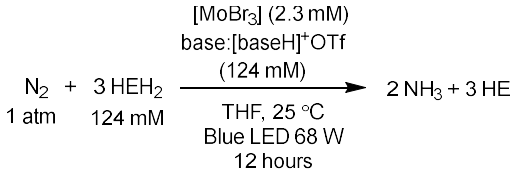

Entry	Base	Notes	NH_3 (equiv/ Mo)	Yield per HEH_2 (%)
A2	Col		10.7	30
B2	Col		13.8	38
C2	Col		14.9	41
Table D.7, entry 1	**Col**		**13 ± 2**	**36 ± 5**
D2	2,6-lutidine		6.4	18
E2	2,6-lutidine		8.0	22
Table D.7, entry 2	**2,6-lutidine**		**7.15±0.8**	**20 ± 2**
F2	2-picoline		1.65	4.6
G2	2-picoline		1.72	4.7
Table D.7, entry 3	**2-picoline**		**1.7±0.05**	**4.7±0.1**
H2	2,6-Me-4-Cl-pyr		0.2	0.6
I2	2,6-Me-4-Cl-pyr		0.4	1.1
Table D.7, entry 4	**2,6-Me-4-Cl-pyr**		**0.3±0.1**	0.8**±0.3**
J2	2,4,6-Ph-pyr		0.1	0.3
K2	2,4,6-Ph-pyr		0.1	0.3
Table D.7, entry 4	**2,4,6-Ph-pyr**		**0.1±0.05**	0.3**±0.15**
L2	2,6-MeO-Pyr		<0.1	<0.3
M2	2,6-MeO-Pyr		<0.1	<0.3
Table D.7, entry 4	**2,6-MeO-Pyr**		**<0.1**	**<0.3**
N2	Et_3N		0.2	0.6
O2	Et_3N		0.1	0.3
Table D.7, entry 4	**Et_3N**		**0.17±0.04**	**0.5±0.11**
P2	Imidazole		<0.1	**<0.3**
Q2	Imidazole		<0.1	**<0.3**
Table D.7, entry 5	**Imidazole**		<0.1	**<0.3**
R2	$^{4\text{-MeO}}PHNH_2$		<0.1	**<0.3**
S2	$^{4\text{-MeO}}PHNH_2$		<0.1	**<0.3**
Table D.7, entry 5	**$^{4\text{-MeO}}PHNH_2$**		<0.1	**<0.3**

Table D.9. Individual runs for catalytic yields for reduction of N_2 to yield NH_3 when varying the dihydropyridine (Table D.7).

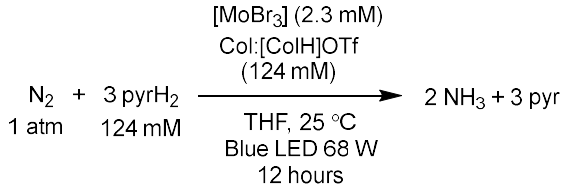

Entry	Dihydropyridine	Notes	NH_3 (equiv/ Mo)	Yield per HEH_2 (%)
A3	HEH_2		10.7	30
B3	HEH_2		13.8	38
C3	HEH_2		14.9	41
Table D.7, entry 1	**HEH_2**		**13 ± 2**	**36 ± 5**
D3	$^{MeO}HEH_2$ (2a)		3.6	10
E3	$^{MeO}HEH_2$ (2a)		2.9	8
Table D.7, entry 6	**$^{MeO}HEH_2$ (2a)**		**3.3 ± 0.4**	**9.0 ± 1.0**
F3	$^{tBuO}HEH_2$ (2b)		0.5	1.4
G3	$^{tBuO}HEH_2$ (2b)		1.1	3.1
Table D.7, entry 7	**$^{tBuO}HEH_2$ (2b)**		**0.7 ± 0.3**	**2±1**
H3	$^{4\text{-}Ph}HEH_2$ (2c)		0.7	1.9
I3	$^{4\text{-}Ph}HEH_2$ (2c)		0.8	2.2
Table D.7, entry 7	**$^{4\text{-}Ph}HEH_2$ (2c)**		**0.75±0.05**	**2.1±0.1**
J3	$^{4\text{-}PhCN}HEH_2$ (2d)		1.85	5.2
K3	$^{4\text{-}PhCN}HEH_2$ (2d)		1.65	4.6
Table D.7, entry 7	**$^{4\text{-}PhCN}HEH_2$ (2d)**		**1.75±0.15**	**4.9±0.4**
L3	$^{N\text{-}Me}HEH_2$ (2e)		1.0	2.8
M3	$^{N\text{-}Me}HEH_2$ (2e)		1.6	4.4
Table D.7, entry 7	**$^{N\text{-}Me}HEH_2$ (2e)**		**1.3 ± 0.3**	**3.6 ± 0.8**
N3	**2f**		2.7	7.5
O3	**2f**		1.1	3
Table D.7, entry 7	**2f**		**1.9±0.8**	**5±2**
P3	**2g**		0.3	0.8
Q3	**2g**		0.3	0.8
R3	**2g**		0.2	0.6
Table D.7, entry 8	**2g**		**0.25±0.04**	0.7**±0.1**

Cont. table D.9				
S3	BNAH (2h)		0.5	1.4
T3	BNAH (2h)		0.3	0.8
U3	BNAH (2h)		0.6	1.7
V3	BNAH (2h)		0.3	0.8
Table D.7, entry 8	**BNAH (2h)**		**0.44±0.13**	**1.2±0.4**
W3	$^{MeNH}HEH_2$ (**2i**)		0.49	1.4
X3	$^{MeNH}HEH_2$ (**2i**)		0.45	1.25

Table D.10. Individual runs for catalytic yields for reduction of N_2 to yield NH_3 when varying the precatalyst.

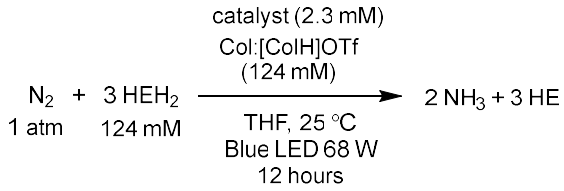

Entry	Catalyst	Notes	NH_3 (equiv/ Mo)	Yield per HEH_2 (%)
A4	[$MoBr_3$]		10.7	30
B4	[$MoBr_3$]		13.8	38
C4	[$MoBr_3$]		14.9	41
	[$MoBr_3$]		**13 ± 2**	**36 ± 5**
D4	[MoNBr]		12.1	34
E4	[MoNBr]		11.4	32
	[MoNBr]		**11.8±0.4**	**33 ± 1**
F4	$^{Me}PNPMoBr_3$		**7**	19
G4	$^{Me}PNPMoBr_3$		8.8	24
	$^{Me}PNPMoBr_3$		**7.9±1.3**	**22 ± 4**
H4	**$^{Me2N}PNPMoBr_3$**		**6.3**	**17.5**
I4	[$Mo(N_2)_2]_2(\mu\text{-}N_2)$		2.8	7.8
J4	[$Mo(N_2)_2]_2(\mu\text{-}N_2)$		3.2	8.9
	[$Mo(N_2)_2]_2(\mu\text{-}N_2)$		**3.0±0.2**	**8.3±0.6**
K4	$(dape)_2W(N_2)_2$		2.7	7.5
L4	$(dape)_2W(N_2)_2$		1.8	5
	$(dape)_2W(N_2)_2$		**2.25±0.5**	**6.2±1.4**
M4	$(dape)_2W(N_2)_2$	No HEH_2	<0.1	<0.3
N4	$(dape)_2W(N_2)_2$	No HEH_2	<0.1	<0.3
	$(dape)_2W(N_2)_2$	**No HEH_2**	**<0.1**	**<0.3**
O4	$(dppe)_2W(N_2)_2$		0.10	0.3
P4	$(dppe)_2W(N_2)_2$		0.25	0.7
	$(dppe)_2W(N_2)_2$		**0.17±0.07**	**0.5±0.2**

Table D.11. Individual runs for catalytic yields for reduction of N_2 to yield NH_3 when varying the counteranion.

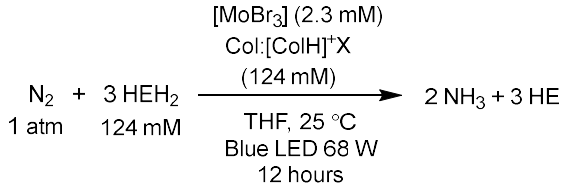

Entry	Counteranion (X)	Notes	NH_3 (equiv/ Mo)	Yield per HEH_2 (%)
A5	$[OTf]^-$		10.7	30
B5	$[OTf]^-$		13.8	38
C5	$[OTf]^-$		14.9	41
	$[OTf]^-$		**13 ± 2**	**36 ± 5**
D5	$[BAr^F{}_4]^-$		5.8	16.1
E5	$[BAr^F{}_4]^-$		4.5	12.5
	$[BAr^F{}_4]^-$		**5.15 ± 0.6**	**14.3±1.7**
F5	$[OTs]^-$		**4.0**	11.1
G5	$[OTs]^-$		2.7	7.5
	$[OTs]^-$		**3.4± 0.6**	**9.4±1.7**
H5	I^-		<0.1	<0.3
I5	I^-		<0.1	<0.3
	I^-		**<0.1**	**<0.3**

D.3. Photoreductions of organic substrates

D.3.1 General procedure

To an oven-dried Schlenk tube HEH_2 (15.6 mg, 62 μmol) and substrate (124 μmol for 1 e^- reduction 62 μmol for 2 e^- reduction, 31 μmol for 4 e^- reduction, 20.6 μmol for 6 e^- reduction and 15.5 μmol for 8 e^- reduction) were added to a Schlenk tube inside the drybox. Dry THF (0.5 mL) with or without 124 mM dissolved buffer was added to the tube, the tube was sealed with a Konte's valve and brought out of the glovebox. The tube was placed in a water bath and irradiated (20 W, H160 427 LED Kessil lamp) for the noted amount of time.

For most substrates, upon completion of the reaction, the solvent was removed *in vacuo*, and a known and weighed amount of 1,3,5-trimethoxybenzene (~3 mg) was added to the tube. Subsequently, the contents of the tube were taken out and analyzed by ^1H NMR, integrating against the TMB standard to calculate the yield of the reaction.

For basic, volatile products (NH_3, propyl amine, trimethylamine), upon completed reaction the tube was frozen to 77 K, and 1 mL NaO^tBu (0.25 M) in MeOH was added via syringe. Upon equilibration, the tube was evacuated, and the contents were vacuum transferred to a receiving flask with 3 mL 2 M HCl in Et_2O. After the transfer, the receiving flask was thawed, and the solvent was removed *in vacuo*. The resulting film was taken up in d_6-DMSO with 10 mM TMB added and analyzed by ^1H NMR to calculate the yield of the reaction.

For some substrates ($tolNO_2$, [TBA][NO_3], and $^{4\text{-Me2N}}PhCHO$), reactivity with additional buffers was analyzed; these results are given in Tables D.12-D.17.

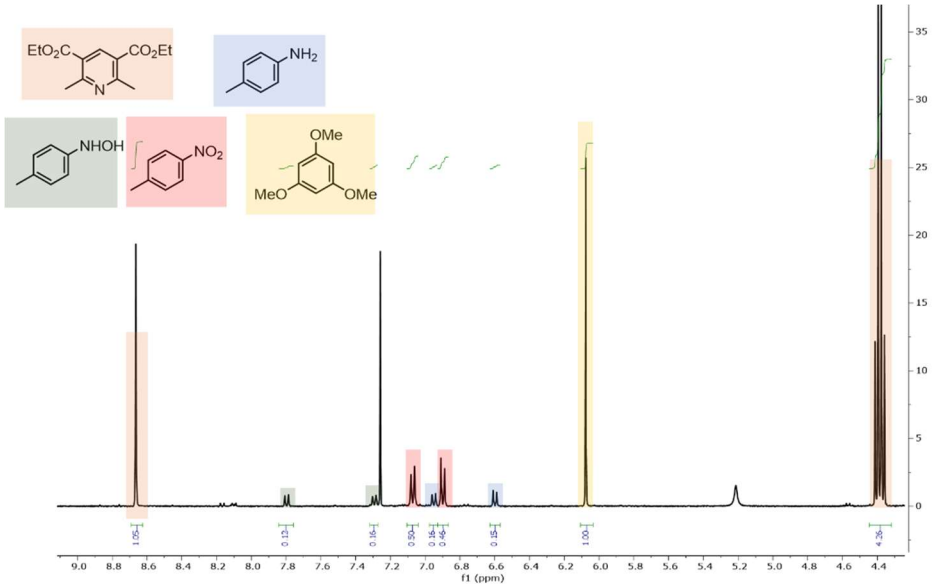

Figure D.4. ^1H NMR ($CDCl_3$ 7.26 ppm) of a typical crude reaction mixture reacting $tolNO_2$ with HEH_2 in the absence of Col-buffer. Identifiable products include: $tolNH_2$ (δ 6.92, d, 2H, J = 8 Hz, δ 6.57, d, 2H, J = 8 Hz, 2H, δ 2.19, s, 3H), tolNHOH (δ 7.07, d, 2H, J = 8 Hz, δ 6.90, d, 2H, J = 8 Hz, 2H, δ 2.28, s, 3H), $tolNO_2$ (starting material) (δ 7.79, d, 2H, J = 8 Hz, δ 7.29, d, 2H, J = 8 Hz, 2H, δ 2.41, s, 3H), along with HE and TMB as indicated.

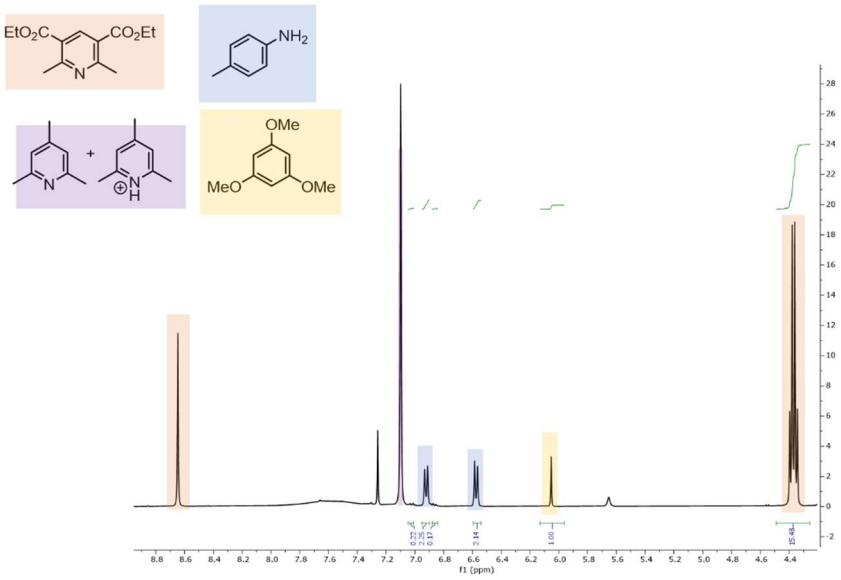

Figure D.5. ^{1}H NMR ($CDCl_3$ 7.26 ppm) of a typical crude reaction mixture reacting $tolNO_2$ with HEH_2 and Col-buffer. Identifiable products include: $tolNH_2$ (δ 6.92, d, 2H, J = 8 Hz, δ 6.57, d, 2H, J = 8 Hz, 2H, δ 2.19, s, 3H), tolNHOH (δ 7.07, d, 2H, J = 8 Hz, δ 6.90, d, 2H, J = 8 Hz, 2H, δ 2.28, s, 3H), $tolNO_2$ (starting material) (δ 7.79, d, 2H, J = 8 Hz, δ 7.29, d, 2H, J = 8 Hz, 2H, δ 2.41, s, 3H), along with HE, Col-buffer and TMB as indicated.

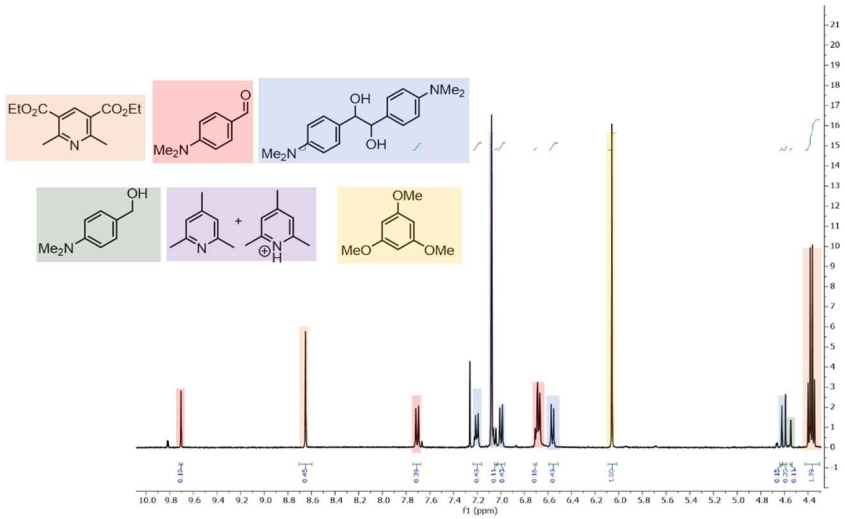

Figure D.6. ^{1}H NMR ($CDCl_3$ 7.26 ppm) of a typical crude reaction mixture reacting ^{4Me2N}PhCHO with HEH_2 and Col-buffer. Identifiable products include: pinacol product *meso* (δ 7.20, d, 4H, J = 8 Hz; δ 6.69 d, 4H, J = 8 Hz; δ 4.63, s, 2H; δ 2.91, s, 12H) and *dl* (δ 7.00, d, 4H, J = 8 Hz; δ 6.57 d, 4H, J = 8 Hz; δ 4.59, s, 2H; δ 2.91, s, 12H), alcohol (δ 7.14, d, 2H, J = 8 Hz; δ 6.69, d, 2H, J = 8 Hz, 2H; δ 4.50, s, 2H; δ 2.28, s, 6H), benzaldehyde (starting material) (δ 9.70, s, 1H; δ 7.71, d, 2H, J = 8 Hz; δ 6.67, d, 2H, J = 8 Hz; 6H, δ 3.10, s, 6H), along with HE, Col-buffer and TMB as indicated.

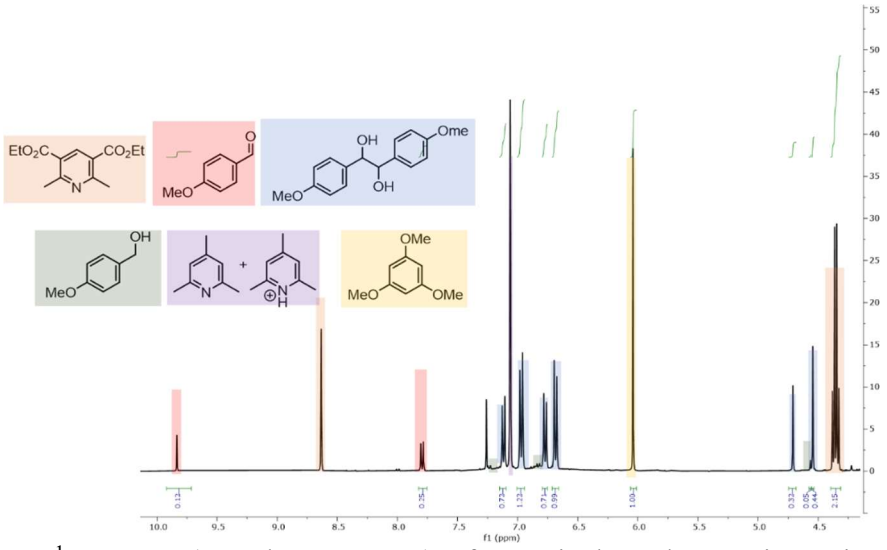

Figure D.7. ^{1}H NMR ($CDCl_3$ 7.26 ppm) of a typical crude reaction mixture reacting ^{4MeO}PhCHO with HEH_2 and Col-buffer. Identifiable products include: pinacol product *meso* (δ 7.12, d, 4H, *J* = 8 Hz; δ 6.77 d, 4H, *J* = 8 Hz; δ 4.74, s, 2H; δ 3.72, s, 6H) and *dl* (δ 6.96, d, 4H, *J* = 8 Hz; δ 6.68 d, 4H, *J* = 8 Hz; δ 4.52, s, 2H; δ 3.72, s, 6H), alcohol (δ 7.23, d, 2H, *J* = 8 Hz; δ 6.82, d, 2H, *J* = 8 Hz, 2H; δ 4.53, s, 2H; δ 3.75, s, 3H), benzaldehyde (starting material) (δ 9.80, s, 1H; δ 7.74, d, 2H, *J* = 8 Hz; δ 6.96, d, 2H, *J* = 8 Hz; 6H, δ 3.86, s, 3H), along with HE, Col-buffer and TMB as indicated.

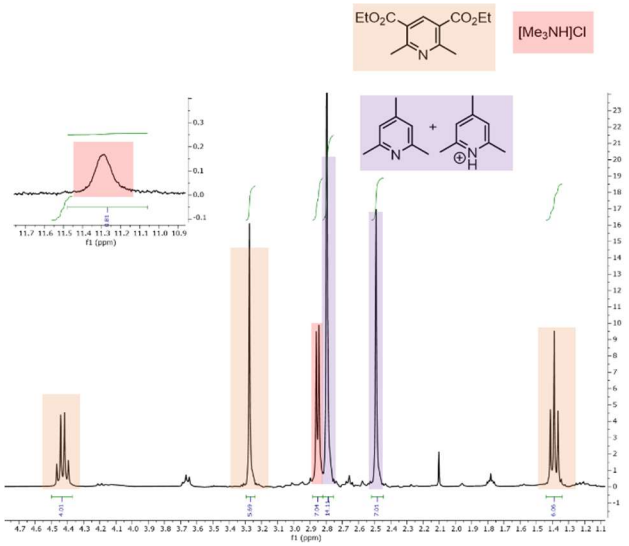

Figure D.8. ^{1}H NMR ($CDCl_3$ 7.26 ppm) of a typical crude reaction mixture reacting Me_3NO with HEH_2 and Col-buffer Typical spectra generated to quantify of products from photoreduction of $tolNO_2$. Identifiable products include: $[Me_3NH]Cl$ (δ 11.28, br, 1H, δ 2.85, d, 9H, *J* = 8 Hz, 2H) along with HE, Col-buffer as indicated.

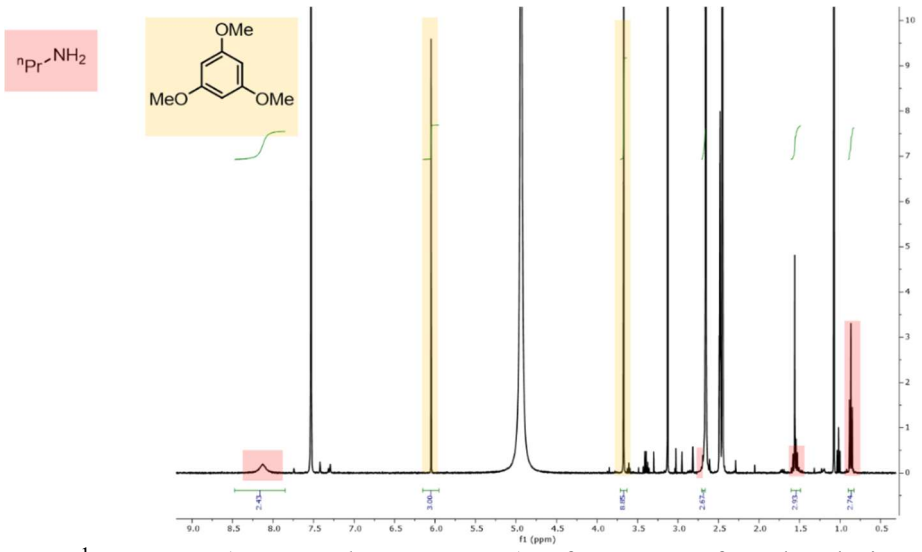

Figure D.9. ^{1}H NMR (DMSO-d_6, 400 MHz) of vac transferred solution following reduction of ^{n}PrNO$_2$ by HEH$_2$ and Col-buffer.

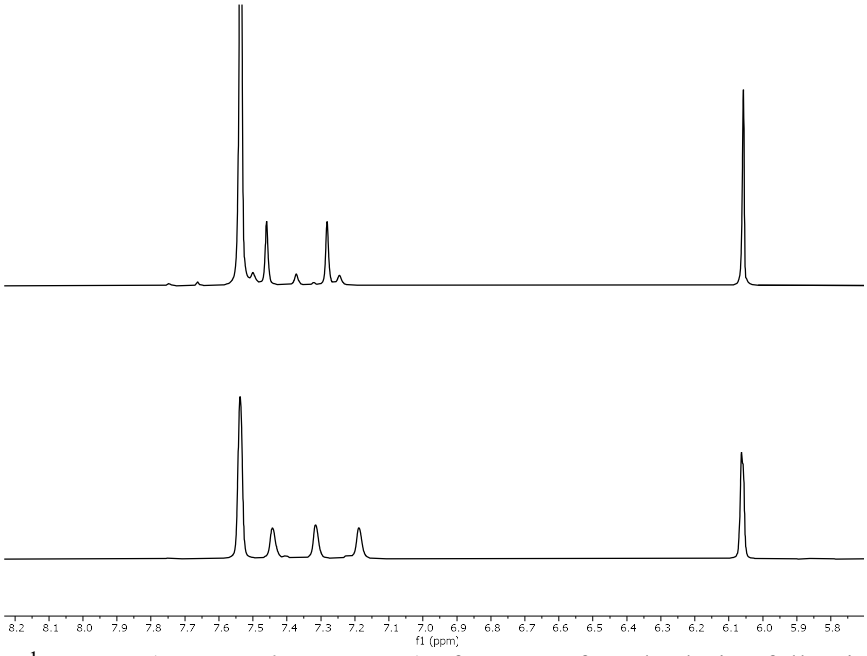

Figure D.10. ^{1}H NMR (DMSO-d_6, 400 MHz) of vac transferred solution following reduction of [TBA][NO$_3$] by HEH$_2$ and Col-buffer/ (Top) ^{15}NH$_4$Cl obtained from reaction of natural abundance [TBA]^{15}NO$_3$ with HEH$_2$ and buffer, under blue light irradiation; (bottom) NH$_4$Cl obtained from reaction of [TBA]NO$_3$ with HEH$_2$ and buffer, under blue light irradiation.

Table D.12. Summary of product yields for $tolNO_2$ reductions.

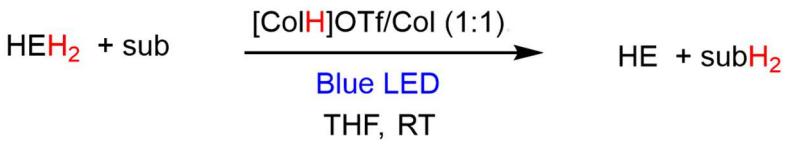

Entry	Variation from standard conditions	Product yield (% per HEH_2)	
	sub = $tolNO_2$	tolNHOH	$tolNH_2$
1	[ColH]OTf/Col buffer	19 ± 14%	77 ± 14%
2	no buffer	31.5 ± 2.5%	13 ± 1%
3	[LutH]OTf/Lut buffer	57±17 %	23±2%
4	[ImidH]OTf/Imid buffer	52 ± 2%	14.9 ± 0.1%
5	Only [ColH]OTf	5%	73%
6	Only Col	56%	22%
7	[$^{2\text{-Me}}$pyrH]OTf/$^{2\text{-Me}}$pyr buffer	40 %	31%
8	[Et_3NH]OTf/Et_3N buffer	11%	26%
9	[$^{4\text{-MeO}}PhNH_3$]OTf/$^{4\text{-MeO}}PhNH_2$ buffer	17%	30%
10	[$^{4\text{-Cl}}$LutH]OTf/$^{4\text{-Cl}}$Lut buffer	50%	0

Table D.13. Yields for individual experiments for $tolNO_2$ reductions.

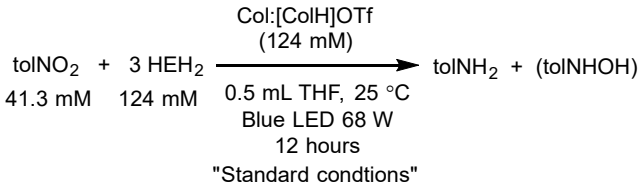

Entry	Variation from standard conditions	Yield $tolNH_2$ (μmol)	Yield $tolNH_2$ per HEH_2 (%)	Yield tolNHOH (μmol)	Yield tolNHOH per HEH_2 (%)	Total yield per HEH_2 (%)
A6	None	19	92	1.5	5	97
B6	None	13	63	7.0	33	96
	None	**16±3**	**77±15**	**4.3±2.7**	**19±14**	**96.5±0.5**
C6	No buffer	2.8	14	9.0	29	43
D6	No buffer	2.4	12	10.6	34	46
	No buffer	**2.6±0.2**	**13±1**	**9.8±0.8**	**31.5±2.5**	**44.5±1.5**
E6	Imid-buffer	3.1	15	15.6	50	65
F6	Imid-buffer	3.0	14.7	16.6	54	69
	Imid-buffer	**3±0.0.05**	**14.8±0.2**	**16.1±0.5**	**52±2**	**67±2**
G6	Lut-buffer	2.1	15	23	74	89
H6	Lut-buffer	5.6	27	12.7	40	67
	Lut-buffer					
I6	Only [ColH]OTf	**15**	**73**	**1.5**	**5**	**78**
J6	Only Col	**4.6**	**22**	**17.2**	**56**	**78**
K6	$^{2\text{-Me}}$pyr-buffer	**6.4**	**31**	**12.5**	**40**	**71**
L6	Et_3N-buffer	**5.4**	**26**	**3.5**	**11**	**37**
M6	$^{4\text{-MeO}}PhNH_2$-buffer	**6.2**	**30**	**5.3**	**17**	**47**
N6	$^{4\text{-Cl-2,6-Me}}$pyr-buffer	**<0.1**	**<0.3**	**15.6**	**50**	**50**

Table D.14. Yields for individual experiments for [TBA][NO_3] reductions.

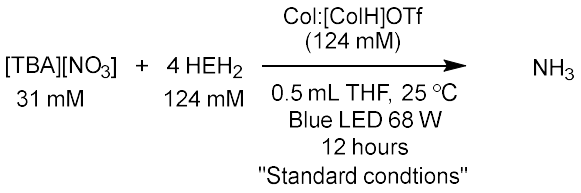

Entry	Variation from standard conditions	Yield NH_3 (μmol)	Yield NH_3 per HEH_2 (%)
A7	None	5.8	37.5
B7	1 mL THF, (unchanged conc)	10.0	32.2
	Col-buffer		**35±3**
C7	No buffer 1 mL THF, (unchanged conc)	0.4	1.4
D7	No buffer 1 mL THF, (unchanged conc)	0.4	1.4
	No buffer		1.4**±0.1**
E7	Imid-buffer	0.11	1.0
F7	Imid-buffer	0.15	1.3
	Imid-buffer		1.2**±0.1**

Table D.15. Yields for individual experiments for 1-nitropropane reductions.

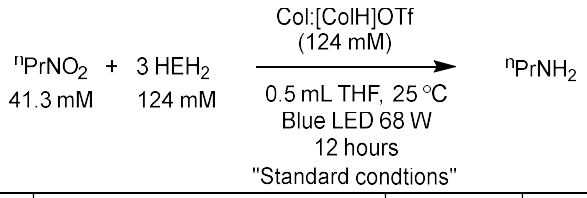

Entry	Variation from standard conditions	Yield $^{n}PrNH_2$ (μmol)	Yield $^{n}PrNH_2$ per HEH_2 (%)
A8	None	5.2	25
B9	None	7.4	36
	Col-buffer	**6.3±1.1**	**30±5**
C9	No buffer	<0.2	<1
D9	No buffer	<0.2	<1
	No buffer	**<0.2**	**<1**

Table D.16. Yields for individual experiments for trimethylamine N-oxide reductions.

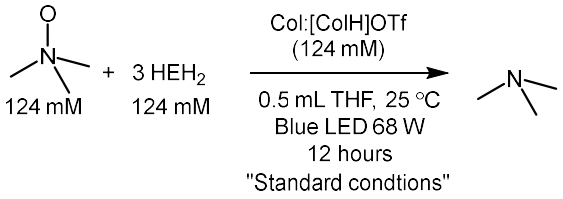

Entry	Variation from standard conditions	Yield Me_3N (µmol)	Yield Me_3N per HEH_2 (%)
A10	None	59.5	96
B10	None	53.2	86
	Col-buffer	**56±3**	**91±5**
C10	No buffer	21.1	34
D10	No buffer	14.2	23
	No buffer	**18±3**	**29±5**

Table D.17. Yields for individual experiments for aldehyde reductions.

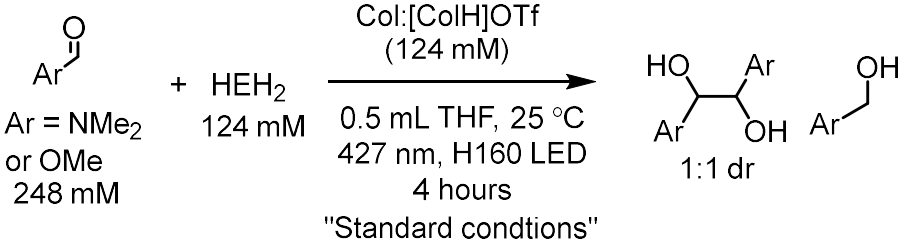

Entry	Variation from standard conditions	Yield pinacol (µmol)	Yield pinacol per HEH_2 (%)	Yield alcohol (µmol)	Yield alcohol per HEH_2 (%)	Total yield per HEH_2 (%)
A11	Ar = NMe_2	31.5	50.8	2.3	3.7	54.7
B11	Ar = NMe_2	30.5	49.2	<1	<2	49.2
C11	Ar = NMe_2	33.5	54.0	<1	<2	54.0
	Ar = NMe_2	**31.8±1.1**	**51.3±1.7**	**<1.5**	**<2.5**	**53±2**
D11	Ar = NMe_2, no buffer	<1.5	<2.5	3.3	5.4	5.4
E11	Ar = NMe_2, no buffer	<1.5	<2.5	3.5	5.6	5.6
	Ar = NMe_2, no buffer	**<1.5**	**<2.5**	**3.4±0.1**	**5.5±0.1**	**5.5±0.1**
F11	Ar = NMe_2, Imid-buffer	**10.6**	**17.1**	**<0.5**	**<1**	**17.1**
G11	Ar = NMe_2, only [ColH]OTf	**11.5**	**18.5**	**11.6**	**18.7**	**37.2**
H11	Ar = NMe_2, only Col	**10**	**16.1**	**<0.5**	**<0.1**	**16.1**
I11	Ar = OMe	54.5	87.9	2.4	3.8	91.7
J11	Ar = OMe	55.3	89.2	1.2	1.9	91.1
		54.9±0.4	**88.6±0.7**	**1.8±0.6**	**2.9±0.9**	**91.4±0.4**
K11	Ar = OMe, No buffer	16.4	26.4	2.4	3.8	30.2
L11	Ar = OMe, No buffer	17.6	28.3	2.2	3.5	31.8
	Ar = OMe, No buffer	**17.0±0.4**	**27.4±0.9**	**2.3±0.1**	**3.6±0.2**	**31.0±0.8**

D.3.2 Light on/off study of tolNO$_2$ reduction

A J. Young-NMR tube was loaded with 124 mM HEH$_2$, 124 mM Col-buffer, and 41.3 mM tolNO$_2$ in 0.7 mL d_8-THF. A spectrum (time =0) was collected, with care being taken to avoid additional irradiation of the NMR tube. Subsequently, the tube was irradiated for 10 minutes, and ^{1}H NMR was collected. The tube was then kept in the dark, and the NMR was recollected. This procedure was continued as indicated in **Figure D.11.**

It was observed that tolNO$_2$ was nearly completely consumed before tolNH$_2$ formation began. Formation of both tolNH$_2$ and tolNHOH was associated with consumption of HEH$_2$. However, upon extended irradiation, tolNHOH does decompose slightly to give more tolNH$_2$, but this is a minor contribution to the total tolNH$_2$ formation.

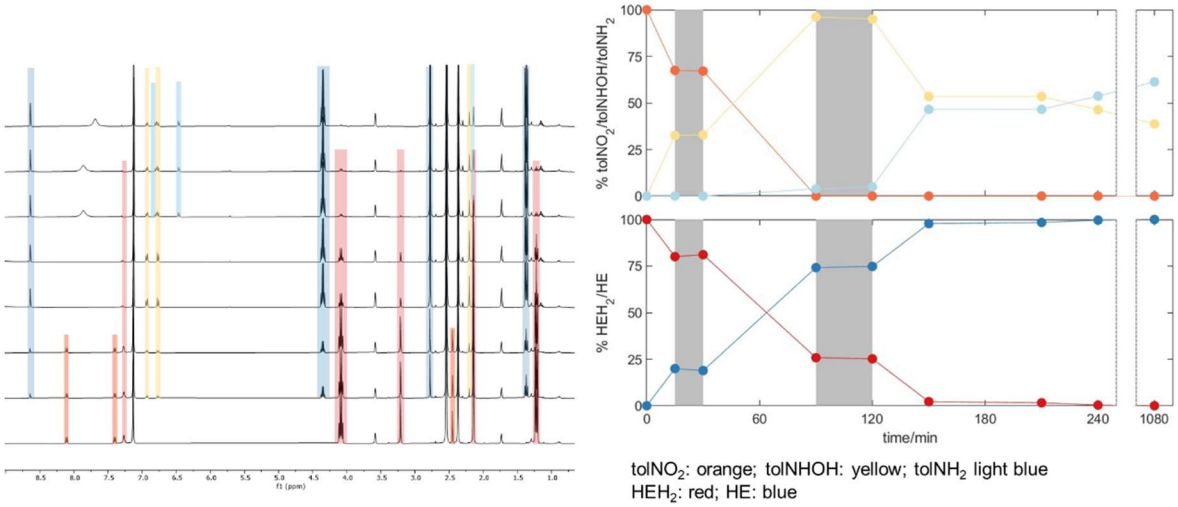

Figure D.11. Light on/off study for tolNO$_2$ reduction. Left panel shows spectra collected from t = 0 (bottom) to 1080 min (top). tolNO$_2$ and HEH$_2$ species are tracked with irradiation off indicated by greyed-out panels in the right panel.

D.3.3 Chemical quantum yield measurements

The organic reaction quantum yield reactions were setup as the uncatalyzed chemical reactions (D.4.1), the H160 427 nm light lamps were used with 10 W irradiation and 15-minute reaction time. The rate (in μmol min^{-1}) was compared to the rate of photon flux measured in this setup.

D.3.3.1 Actinometry measurement

Relative quantum yield was determined through the potassium ferrioxalate chemical actinometry method to determine the light intensity for the setup used for quantum yield experiments (10 W, 427 nm Blue LED). $K_3Fe(C_2O_4)_3$ was prepared and used in solution by making a 10 mM Fe_2SO_4 and 60 mM $K_2C_2O_4$ stock solution in 4% H_2SO_4 (aq). 3 mL of this solution was irradiated at 390 nm for 5 seconds in the same setup as employed for all reactions. Care was taken to minimize light exposure between irradiation cycles.[13]

$$2Fe^{3+} + C_2O_4^{2-} \xrightarrow{h\nu} 2Fe^{2+} + 2CO_2$$

A 0.2% by weight solution of 1,10-phenanthroline in water and a 0.6 M NaOAc buffer in 1% H_2SO_4 (aq) were prepared separately. A 100 µL aliquot of the irradiated solution was placed into a 10 mL volumetric flask along with 200 µL of the phenanthroline solution and 50 µL of buffer, and the solution was diluted with water. The complexation of Fe^{2+} with 1,10-phenanthroline resulted in a bright red solution that had a characteristic absorption at 510 nm. For the control, these steps were repeated with a 100 µL aliquot of non-irradiated solution.

Because complete conversion was not reached after 10 s, but rather sometime between 5 and 60 s, the runs at 10 s were chosen for analysis. These gave an average absorbance of 0.366 ± 0.02 at 510 nm vs. dark.

$$I\ (\text{mol} \cdot \text{min}^{-1}) = \frac{AV_2V_3}{\varepsilon b \phi_\lambda t V_1} \quad (\text{eqn } A5.1)$$

where

A = absorbance at 510 nm

V_2 = volume of actinometer irradiated (0.5 mL)

V_3 = final volume of quantified sample (10 mL)

ε = extinction coefficient of ferrous 1,10-phenanthroline at 510 nm (~1.11×10^4 $M^{-1} \cdot cm^{-1}$)

b = path length of cuvette (1 cm)

ϕ_λ = quantum yield of ferrous production at 427 nm (~1.11)

t = irradiation time (10 s)

V_1 = volume of aliquot of an irradiated sample taken (100 µL).

Giving a light intensity in mol of photons per unit time. Using the gathered absorbance data, a light intensity of $9 \pm 0.5 \times$ µmol · min^{-1} was obtained, and this photon flux was used to calculate all relative quantum yields.

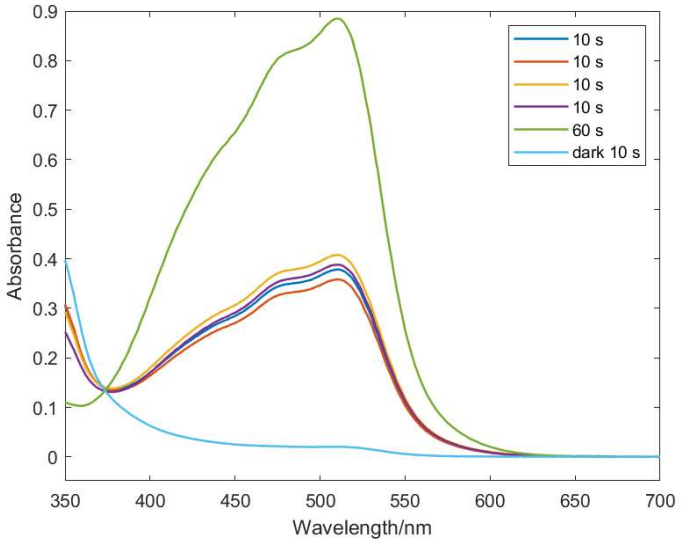

Figure D.12. UV-vis spectra of solutions used for light intensity quantification at different irradiation times.

D.3.2 Individual experiments for chemical quantum yield results

Table D.18. Yields for individual experiments for tolNO$_2$ reductions for quantum yield measurements (Figure 5.8).

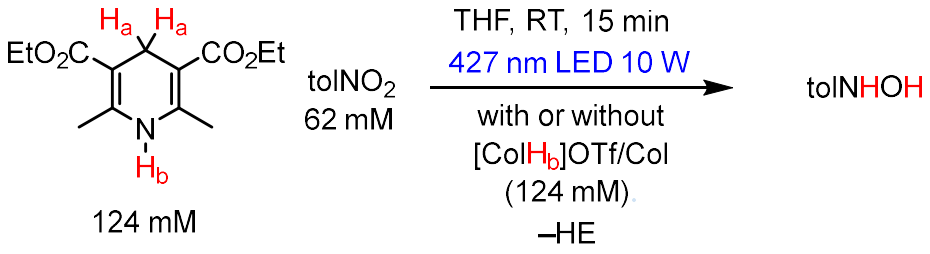

Entry	Variation from standard conditions	Yield tolNHOH (μmol)	Rate (μmol min^{-1})	Quantum yield (x100)	Notes
A12	None	3.5			
B12	None	4.1			
C12	None	3.7			
D12	None	4.0			
	None	**3.8±0.16**	**0.25±0.011**	**0.028±0.0015**	
E12	No buffer	0.6			
F12	No buffer	0.9			
	No buffer	**0.75±0.21**	**0.05±0.014**	**0.006±0.002**	
G12	Only [ColH]OTf	2.9			
H12	Only [ColH]OTf	2.2			
	Only [ColH]OTf	**2.5±0.5**	**0.17±0.03**	**0.019±0.004**	
I12	Only Col	2.25			
J12	Only Col	1.7			
	Only Col	**2.0±0.4**	**0.13±0.03**	**0.015±0.003**	
K12	H_a = D	3.9			
L12	H_a = D	3.8			
M12	H_a = D	3.7			
N12	H_a = D	4.0			
	H_a = D	**3.85±0.07**	**0.26±0.005**	**2.88±0.06**	**KIE = 0.99±0.06**
O12	H_b = D	5.2			
P12	H_b = D	4.2			
Q12	H_b = D	4.2			
R12	H_b = D	4.6			
	H_b = D	**4.6±0.3**	**0.30±0.02**	**3.4±0.2**	**KIE = 0.84±0.09**
S12	*N*-MeHEH$_2$ (2c), Col-buffer	0.93			
T12	*N*-MeHEH$_2$ (2c), Col-buffer	1.00			
	***N*-MeHEH$_2$ (2c), Col-buffer**	**0.97±0.03**		**0.007±0.00025**	
U12	*N*-MeHEH$_2$ (2c), No buffer	0.16			
V12	*N*-MeHEH$_2$ (2c), No buffer	0.29			
	***N*-MeHEH$_2$ (2c), No buffer**	**0.22±0.06**		**0.0016±0.0004**	

Table D.19. Yields for individual experiments for aldehyde reductions for quantum yield measurements.

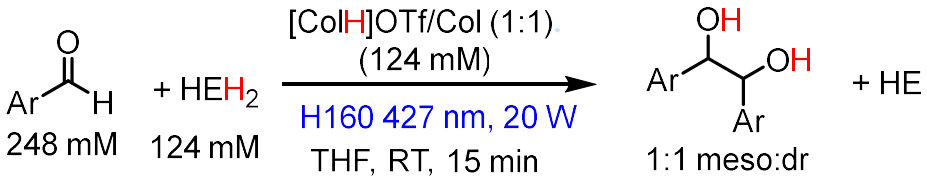

Entry	Variation from standard conditions	Yield tolNHOH (μmol)	Rate (μmol min^{-1})	Quantum yield (x100)
A13	R = NMe_2	11.8		
B13	R = NMe_2	13.7		
	R = NMe_2	**12.75±0.9**	**0.85±0.06**	**0.094±0.008**
C13	R = NMe_2, No buffer	<0.5		
D13	R = NMe_2, No buffer	<0.5		
	R = NMe_2, No buffer	**<0.5**	**<0.03**	**<0.003**
E13	R = OMe	13.2		
F13	R = OMe	13.4		
	R = OMe	**13.3±0.1**	**0.887±0.007**	**0.0986±0.0008**
G13	R = OMe, No buffer	2.8		
H13	R = OMe, No buffer	3.4		
	R = OMe, No buffer	**3.1±0.3**	**0.21±0.02**	**0.023±0.002**

D.4: UV-vis spectroscopy

D.4.1 General procedure

All solutions for UV-vis measurements were prepared inside a glovebox using dried solvent unless otherwise specified. For static spectra (Figures D.13, D.14, D.16 and D.17) an oven-dried cuvette was used and sealed with a Teflon valve.

For titration experiments (Figure D.15), an oven-dried cuvette was loaded in the glove box and sealed with a septum. The titrant was added via syringe against a counterflow of N_2 to maintain an O_2-free atmosphere throughout the experiment.

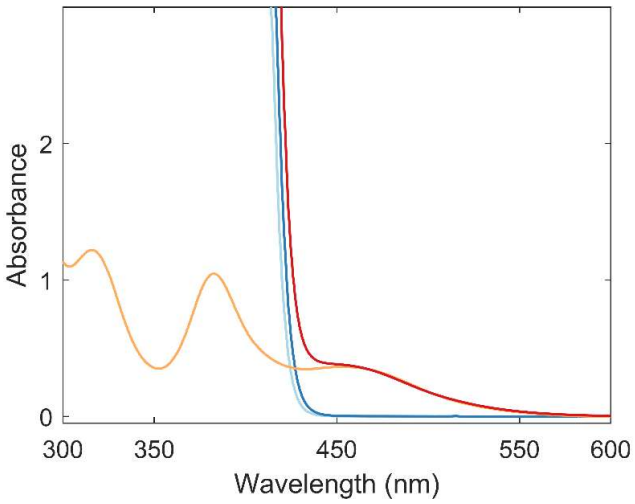

Figure D.13. UV-vis spectra of reaction components in 1 mm cuvette in THF at 25 °C. Traces are [$MoBr_3$], 2.3 mM (yellow); HEH_2 124 mM (light blue); HEH_2 + Col-buffer 124 mM (dark blue), and all reaction components (red trace).

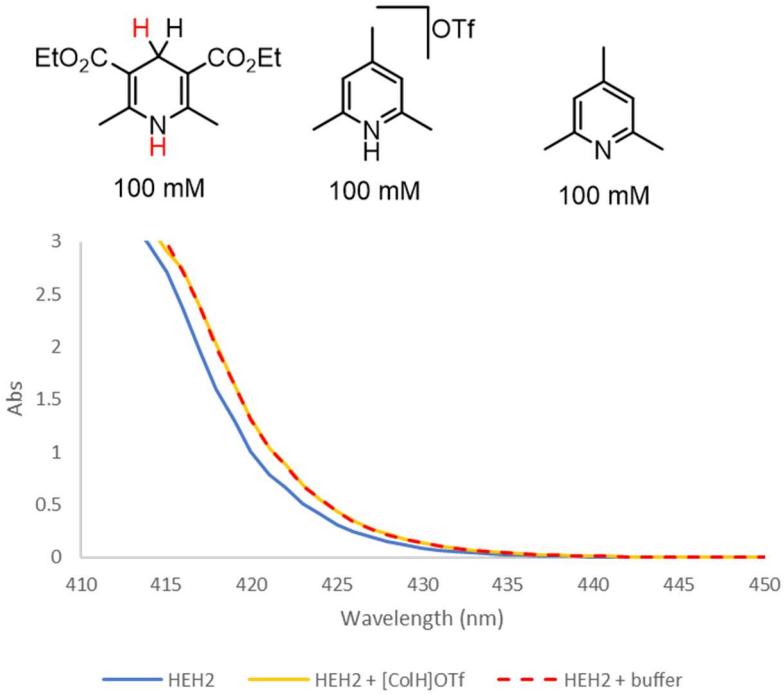

Figure D.14. UV-vis spectra of HEH_2 (100 mM; light blue); HEH_2 + [ColH]OTf (100 mM each; yellow), and HEH_2 + [ColH]OTf + Col (100 mM each; red dashed) collected in a 1 cm cuvette in THF at 25°C.

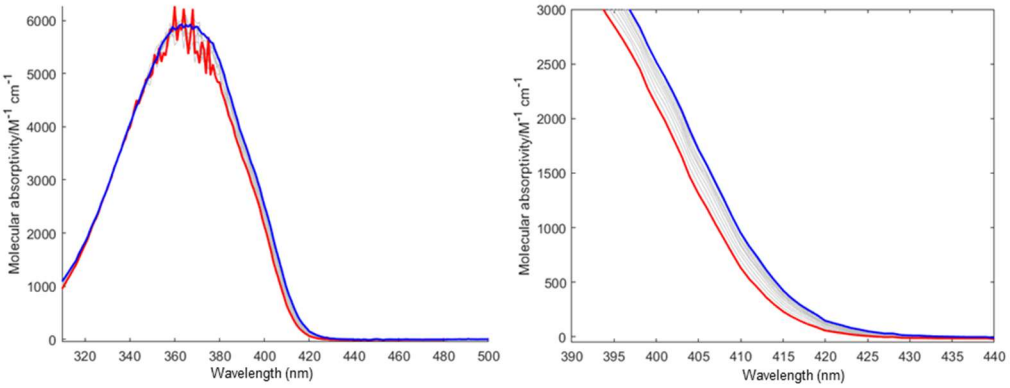

Figure D.15. UV-vis spectra of HEH_2 (0.1 mM) with [ColH]OTf titrated from 0 (red) to 160 mM (blue). Collected in a 1 cm cuvette in THF at 25°C.

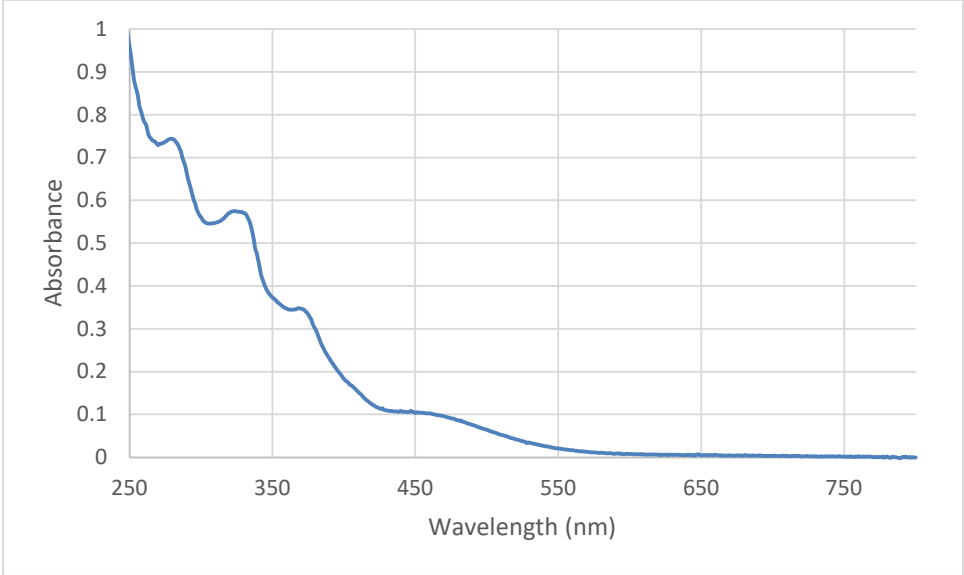

Figure D.16. UV-vis spectra of $PCPMoCl_3$ (0.1 mM) in a 1 cm cuvette in THF at 25°C.

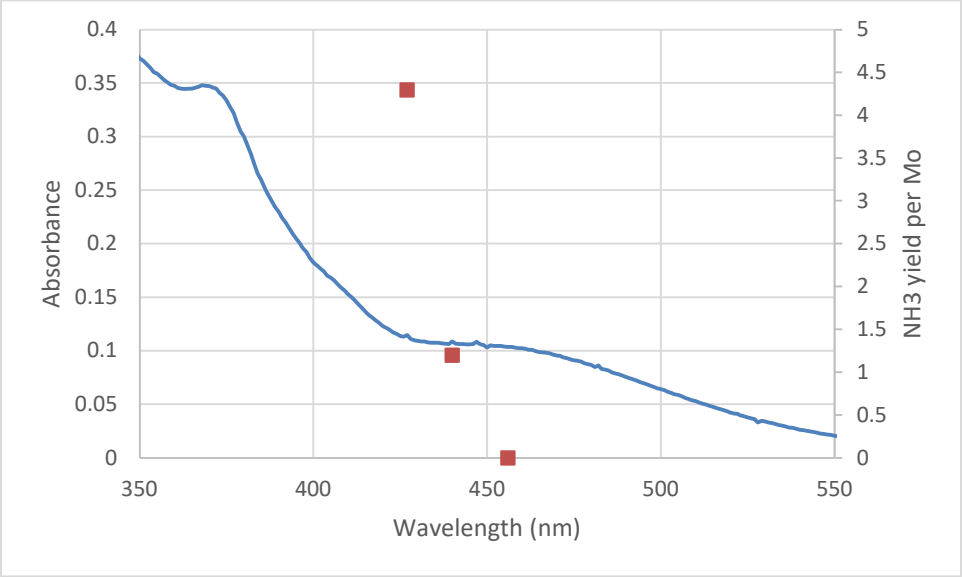

Figure D.17. UV-vis spectra of $PCPMoCl_3$ (0.1 mM) in a 1 cm cuvette in THF at 25°C with NH_3 yields from photodriven N_2R overlayed (from table D.3).

D.5 Fluorescence experiments

D.5.1General procedure

Steady-state fluorimetry was performed in the Beckman Institute Laser Resource Center (California Institute of Technology). Samples for luminescence measurements were prepared in dry THF and transferred to a 1-cm path length–fused quartz cuvette sealed with a high-vacuum Teflon valve (Kontes). Steady-state emission spectra were collected on the Jobin S4 Yvon Spec Fluorolog-3-11 with a Hamamatsu R928P photomultiplier tube detector with photon counting.

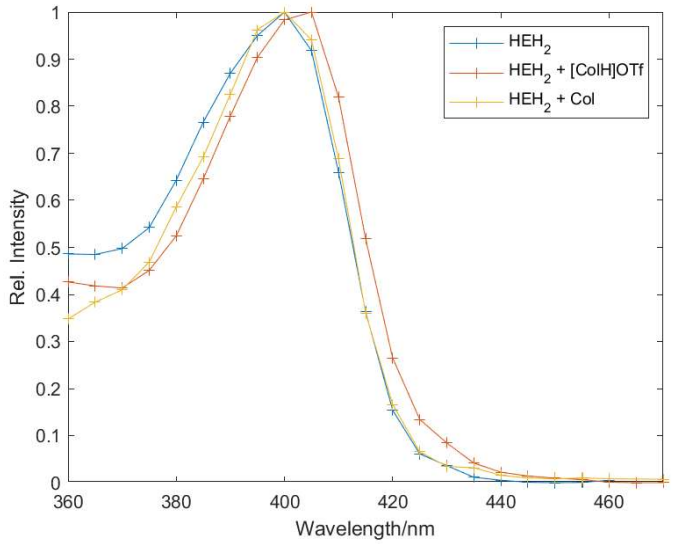

Figure D.18. Excitation spectra monitoring relative emission intensity (500 nm) of HEH_2 (0.5 mM) in the absence (blue trace) presence of [ColH]OTf (320 mM, orange trace) or Col (320 mM, yellow trace). A slight blue-shift is observed with HEH_2 and [ColH]OTf, as is also observed by UV-vis.

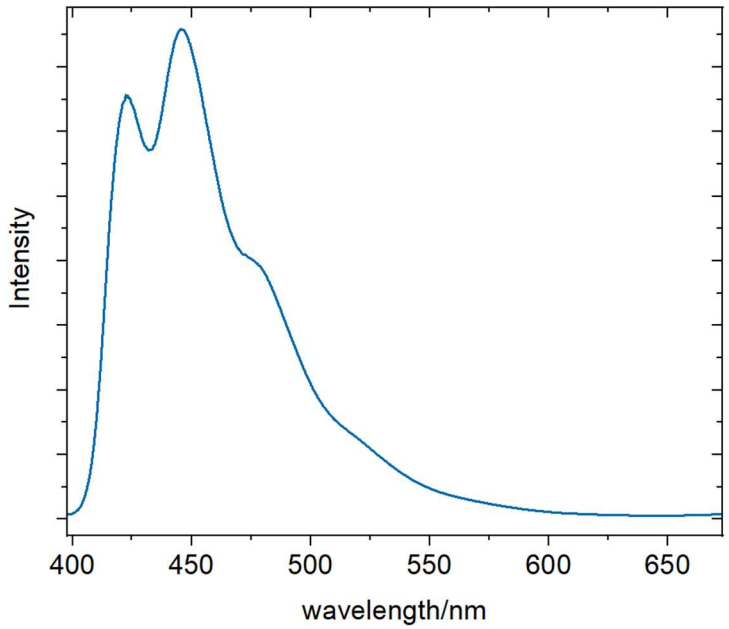

Figure D.19. Low temperature (77 K) emission spectrum of HEH_2 (1.2 mM) in THF. (Excitation wavelength: 355nm).

D.5.2 Fluorescence Quantum yield measurements

Fluorescence quantum yield of HEH_2 was measured against a 9,10-diphenyl anthracene standard (taken to be 1.0 in THF at 380 nm irradiation). Solution of both samples prepared such that the absorbance <0.1, and the integrated emission spectra upon exciting at 380±5 nm. Due to the low signal-to-noise ratio of 10x (100 ms vs 10 ms), integration time was required for HEH_2. The equation:

$$\frac{QY_{\mathrm{HEH2}}}{QY_{\mathrm{anth}}} = \frac{\int \mathrm{emission}_{\mathrm{HEH2}}}{\int \mathrm{emission}_{\mathrm{anth}}} \left(\frac{\mathrm{abs}_{\mathrm{anth,380}}}{\mathrm{abs}_{\mathrm{HEH2,380}}}\right) * \left(\frac{1}{10}\right) \quad \text{(eqn D. 2)}^{14}$$

gives $QY_{HEH2} = 0.018$. The factor of 1/10 is required due to the 10x longer integration time for the HEH_2 emission spectra. See **Figure D.20**.

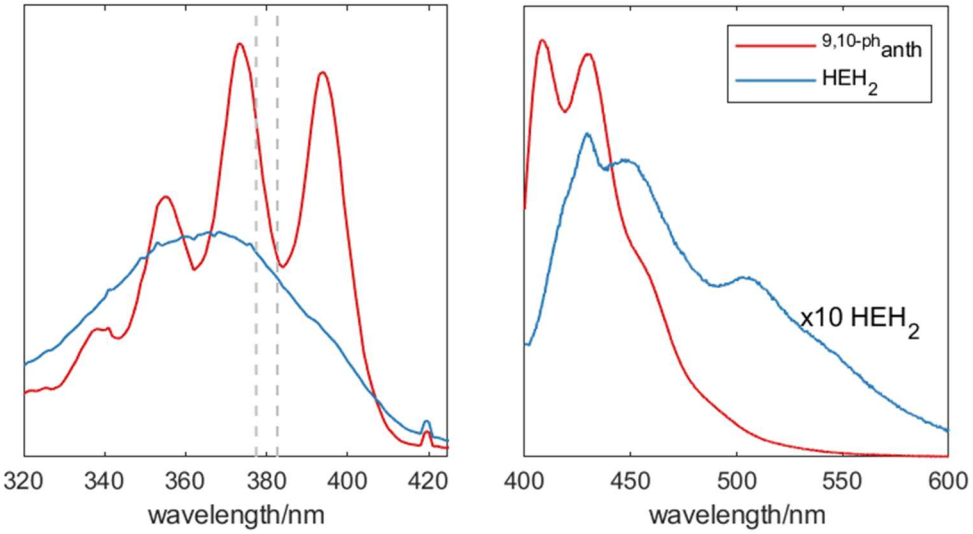

Figure D.20. Absorption spectra and emission spectra of HEH_2 and 9,10-diphenylanthracene. Note that HEH_2 is multiplied by 10x in the emission spectra, and generated using 10x integration time, resultingly the final integral is about 1/100 the intensity of 9,10-diphenylanthracene.

D.5.3 Quenching studies

D.5.3.1 Procedure for quenching studies

1 cm quartz glass cuvettes were loaded with 0.5 mM HEH_2 solutions in dry THF, with varying concentrations of quencher (either Col or [ColH]OTf) in a nitrogen glovebox. Stock solutions were used to assure consistency. Solutions were excited at 390 nm wavelength to avoid interference of the excitation wavelength and steady-state fluorescence spectra. Experiments were conducted at 23 °C.

D.5.3.2 Calculation of Stern-Volmer quenching constants

Using the previously measured excited state-lifetime measured (τ_0) for HEH_2 we can calculate the Stern-Vollmer quenching both via a diffusional constant (k_{diff}) and an equilibrium static quenching constant (K_{stat}) using the equation:

$$I_0/I_c = 1 + (k_{diff} \cdot \tau_0 + K_{stat})\,[Q] + (k_{diff} \cdot \tau_0 \cdot K_{stat})\,[Q]^2 \quad \text{(eqn D.3)}.^{14}$$

K_q and τ_0 are given by the lifetime quenching ($6.7\ 10^9\ M^{-1}\ s^{-1}$ and 200 ps, respectively; see figure D.23) to give $k_{diff} \cdot \tau_0 = 1.34\ M^{-1}$. Accordingly, an updated model (red line, figure D.21) uses $K_{stat} = 20\ M^{-1}$. This suggests slightly less static quenching compared to when solely static quenching is assumed ($22\ M^{-1}$, dashed, blue line).

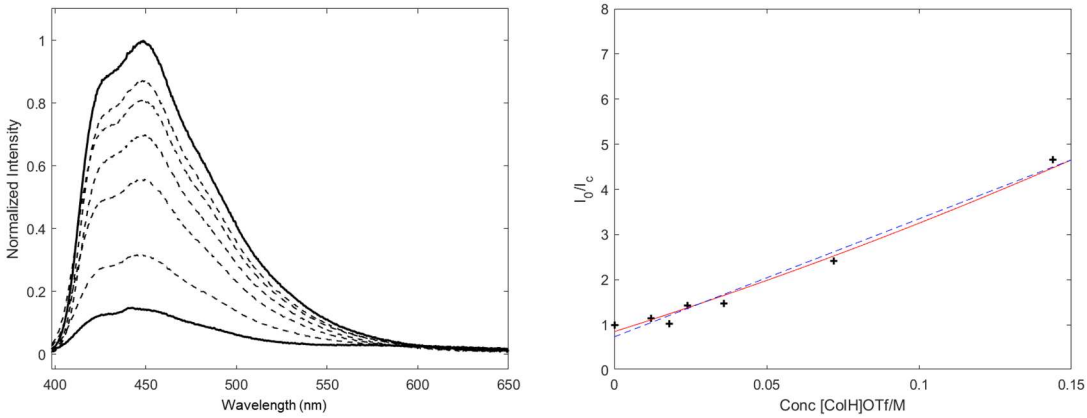

Figure D.21. Steady-state fluorescence of HEH_2 (0.5 mM) with varying amounts of [ColH]OTf (18 mM to 144 mM) (Left). Stern-Vollmer quenching plot of I_0/I_C against concentration of [ColH]OTf (right). Two models are presented, one assuming only static

quenching (blue dashed line) and one considering static and diffusional quenching as determined by luminescence lifetimes (red line).

Given the much lower value of the luminescence lifetime, adding this factor is not required based on this data, but as the luminescence spectroscopy suggests, it is present. The addition does improve the model slightly, as would be expected.

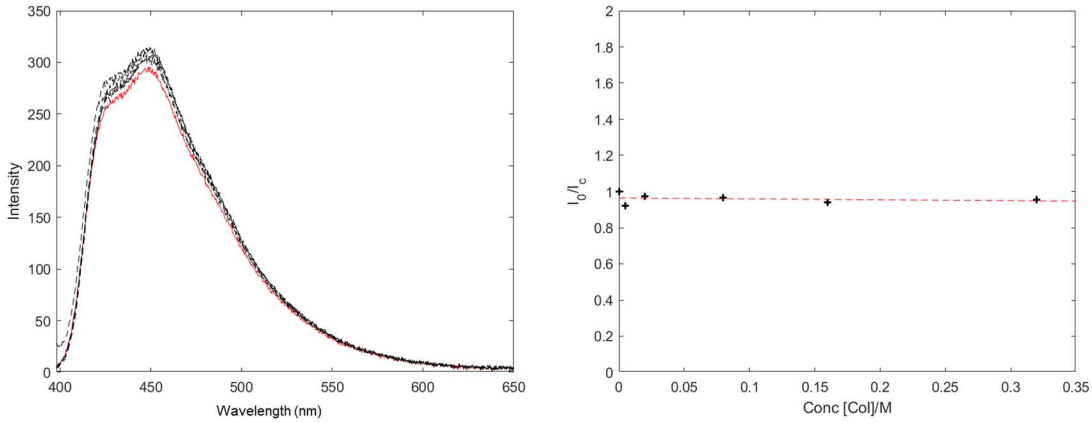

Figure D.22. Steady-state fluorescence of HEH_2 (0.5 mM) with varying amounts of Col (5 mM to 320 mM) (left). Stern-Vollmer quenching plot of I_0/I_C against concentration of Col (right). Slope is -0.05±0.1 M^{-1}, suggesting little to no quenching.

D.6 Time-resolved luminescence experiments

D.6.1 General procedure

Time-resolved luminescence measurements and transient absorption measurements were carried out in the Beckman Institute Laser Resource Center at Caltech. All measurements were performed with samples under an N_2 atmosphere at room temperature. Samples were prepared in air-tight 1 cm path-length quartz cuvettes in the dark, N_2-filled glovebox. Prior to measurement, all samples were protected from light by wrapping in aluminum foil.

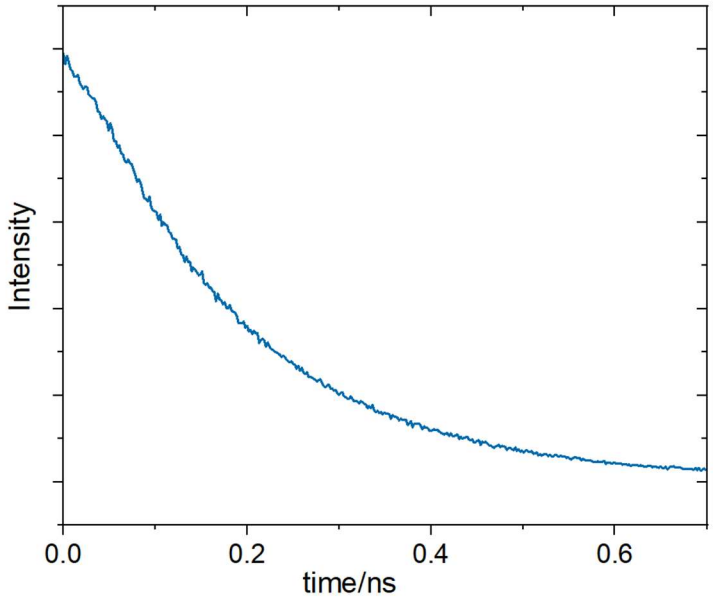

Figure D.23. Luminescence lifetime of HEH_2 (1.2mM) in THF. (Excitation wavelength: 355nm, detection wavelength: 450 nm).

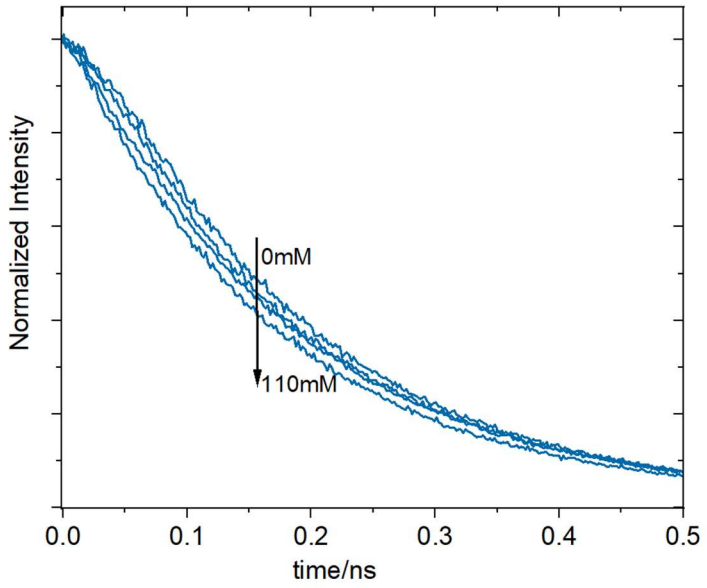

Figure D.24. Luminescence lifetime of HEH_2 (1.2mM) in THF after titration with [ColH]OTf (50mM-110mM). (Excitation wavelength: 355nm, detection wavelength: 450 nm).

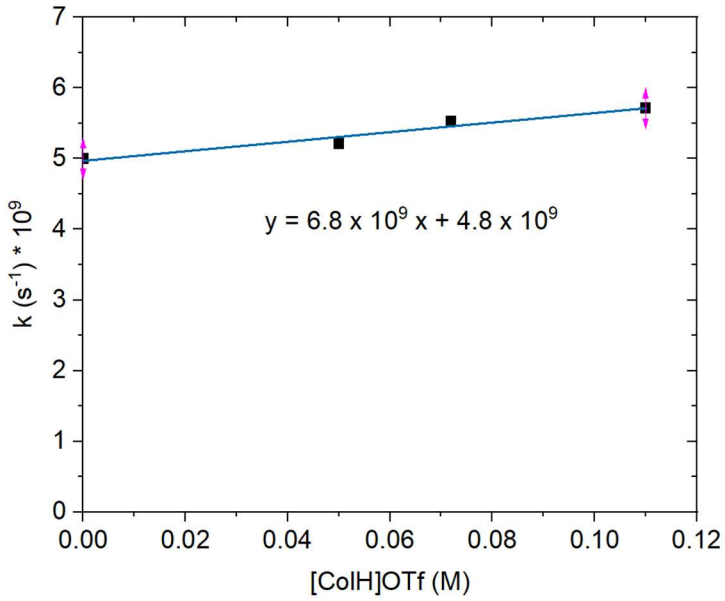

Figure D.25. Kinetic constants plot extrapolated from luminescence lifetime of HEH_2 (1.2mM) in THF after titration with [ColH]OTf (50mM-110mM).

Table D.20. Luminescence lifetime of HEH_2 (1.2mM) in THF after titration with [ColH]OTf (50mM-110mM).

	Lifetime
HEH_2	200 ps ± 10
HEH_2 + ColH (50mM)	192 ps ± 5
HEH_2 + ColH (72mM)	181 ps ± 4
HEH_2 + ColH (110 mM)	175 ps ± 9

D.6.2 Studies of [$MoBr_3$] luminescence

In addition to the study of HEH_2, we have also investigated the photophysical properties of [$MoBr_3$]. We find that excitation at 450 nm does result in the formation of a long-lived excited state. Importantly, this excited state is not quenched by HEH_2 both in the

presence and absence of buffer, supporting that HEH_2 is the photosensitizer during N_2R (Figures D.26-D.28).

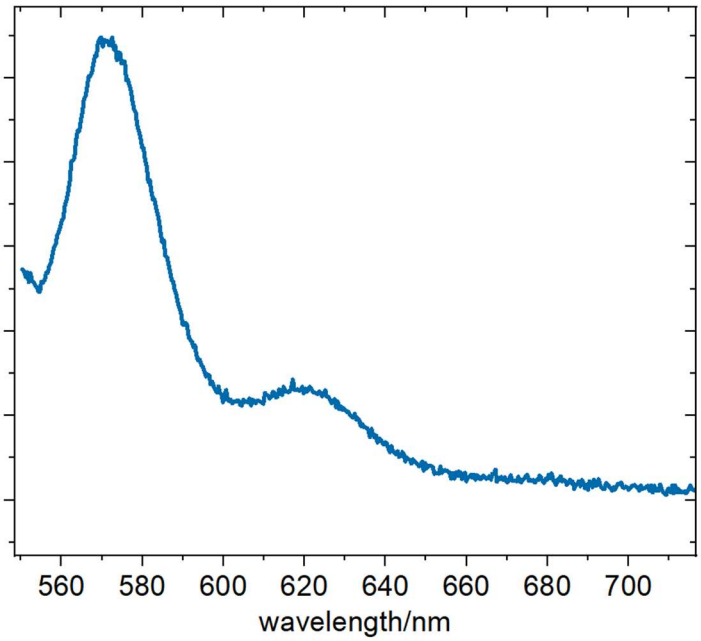

Figure D.26. Emission spectrum of [$MoBr_3$] in THF (0.1 mM; Excitation: 450nm).

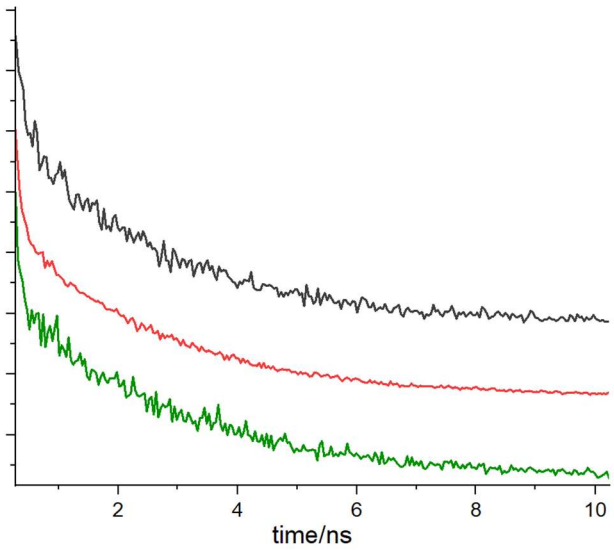

Figure D.27. Luminescence lifetime of [$MoBr_3$] (0.5 mM) in THF after titration with HEH_2 0 equiv (black), 25 equiv (red), 50 equiv (green) (Excitation: 450nm, Detection: 570 nm). Translated to more clearly show traces.

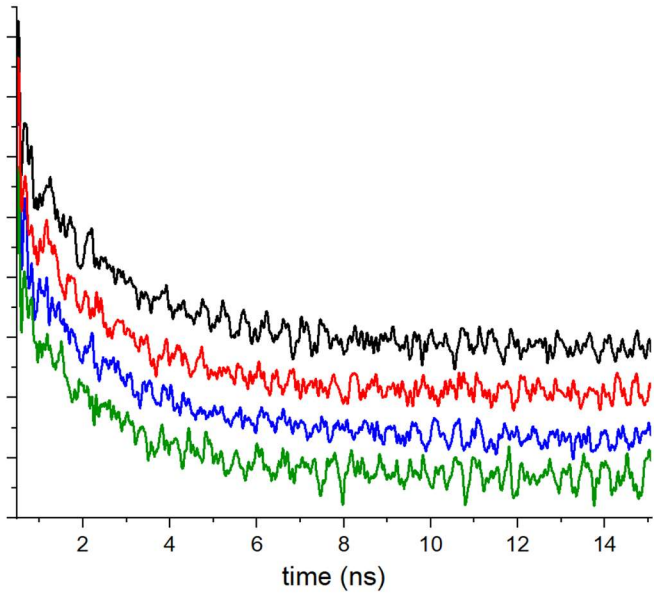

Figure D.28. Luminescence lifetime of [$MoBr_3$] (0.5 mM, black trace) in THF after addition of HEH_2 (50 equiv, red trace), HEH_2 (50 equiv), and 100 equiv of Buffer (blue trace) and HEH_2 (50 equiv) and 200 equiv of Buffer (green trace) (Excitation: 450nm, Detection: 570 nm). Translated to more clearly show traces.

D.7 Transient Absorption Studies

D.7.1 General procedure.

Transient absorption measurements were carried out in the Beckman Institute Laser Resource Center at Caltech. All measurements were performed with samples under an N_2 atmosphere at room temperature. Samples were prepared in air-tight 1 cm path-length quartz cuvettes in the dark, N_2-filled glovebox. Prior to measurement, all samples were protected from light by wrapping in aluminum foil.

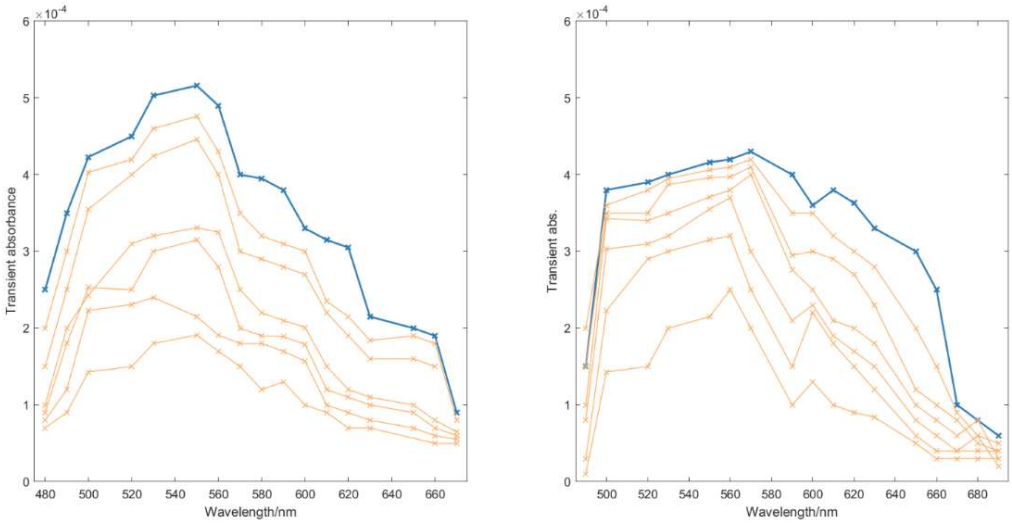

Figure D.29. TA spectrum of short-lived radical species generated from excitation (355 nm) of HEH_2 (1.2 mM) in the presence of [ColH]OTf (12 mM) and [ColH]OTf + Col (12 mM). Intensity decreases from 1.5 μs (blue trace) to 35 μs.

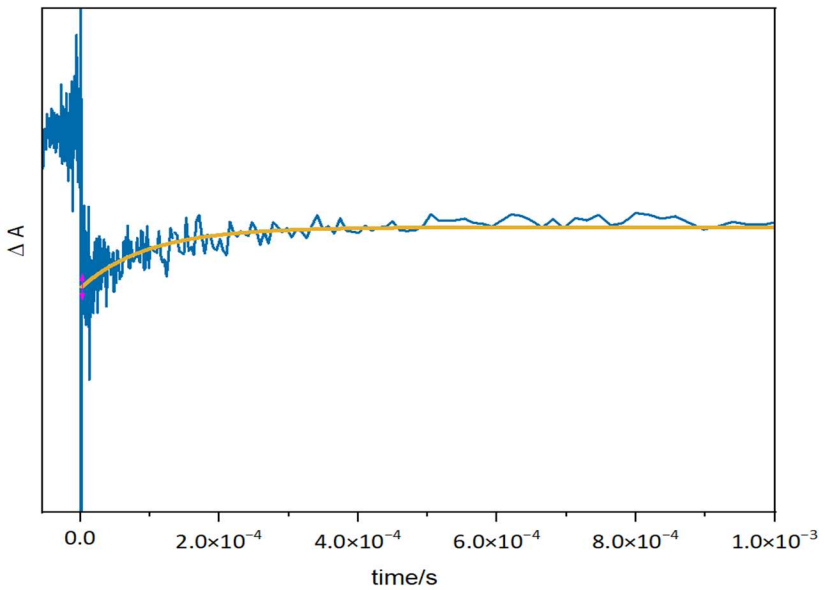

Figure D.30. Bleaching at 370 nm generated from HEH_2 (1.2 mM) in THF. (Excitation wavelength: 355nm, detection wavelength: 370 nm).

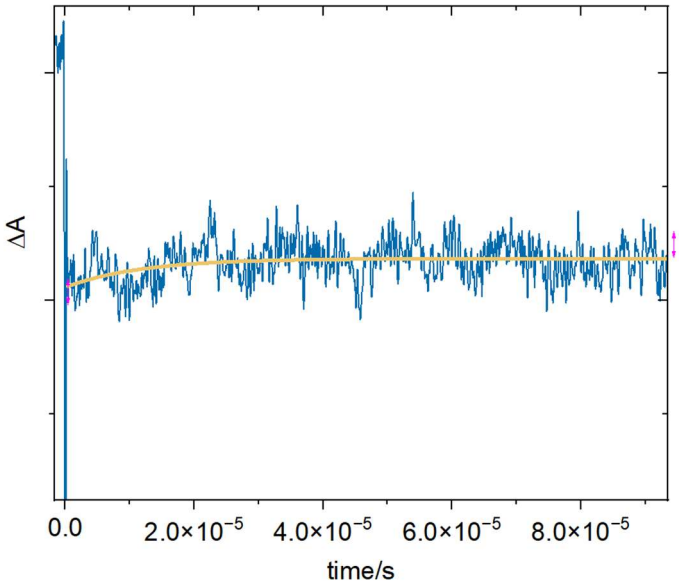

Figure D.31. Bleaching at 370 nm generated from HEH_2 (1.2 mM) in THF in the presence of [ColH]OTf (12 mM). (Excitation wavelength: 355nm, detection wavelength: 370 nm).

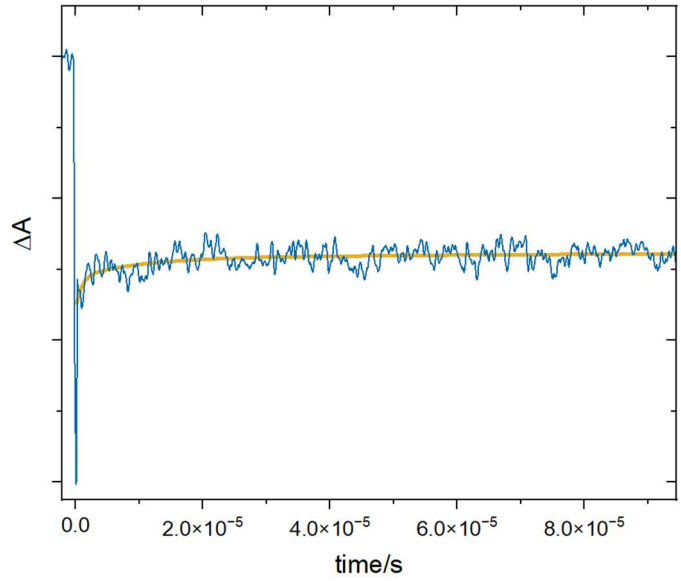

Figure D.32. Bleaching at 370 nm generated from HEH_2 (1.2 mM) in THF in the presence of [ColH]OTf (110 mM). (Excitation wavelength: 355nm, detection wavelength: 370 nm).

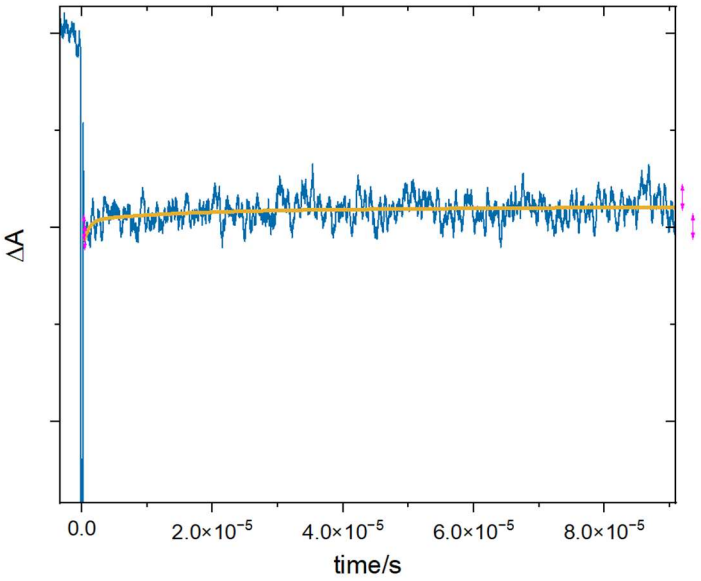

Figure D.33. Bleaching at 370 nm generated from HEH_2 (1.2 mM) in THF in the presence of [ColH]OTf (12 mM) and Col (50 mM). (Excitation wavelength: 355nm, detection wavelength: 370 nm).

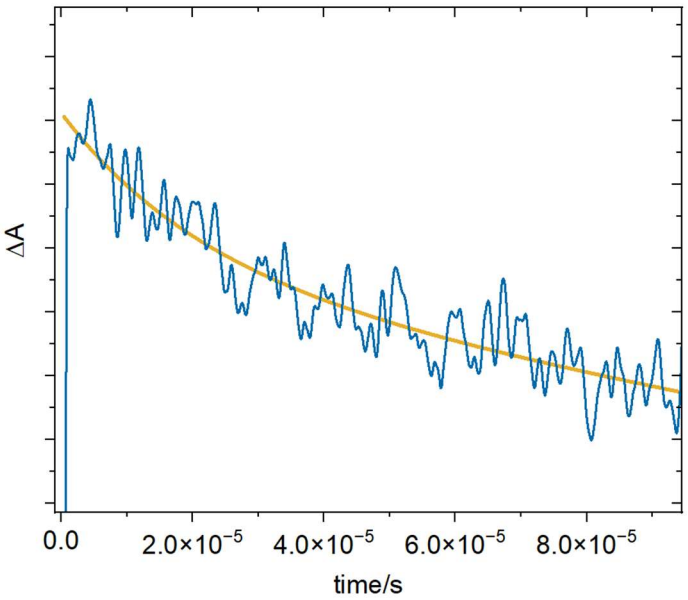

Figure D.34. Absorption at 500 nm generated from HEH_2 (1.2 mM) in THF in the presence of [ColH]OTf (12 mM). (Excitation wavelength: 355nm, detection wavelength: 500 nm).

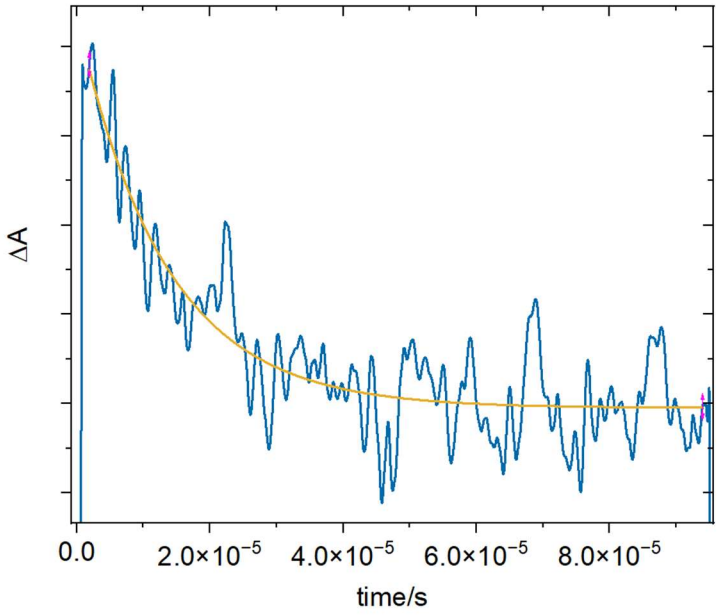

Figure D.35. Absorption at 500 nm generated from HEH_2 (1.2 mM) in THF in the presence of [ColH]OTf (12 mM) and Col (36 mM). (Excitation wavelength: 355nm, detection wavelength: 500 nm).

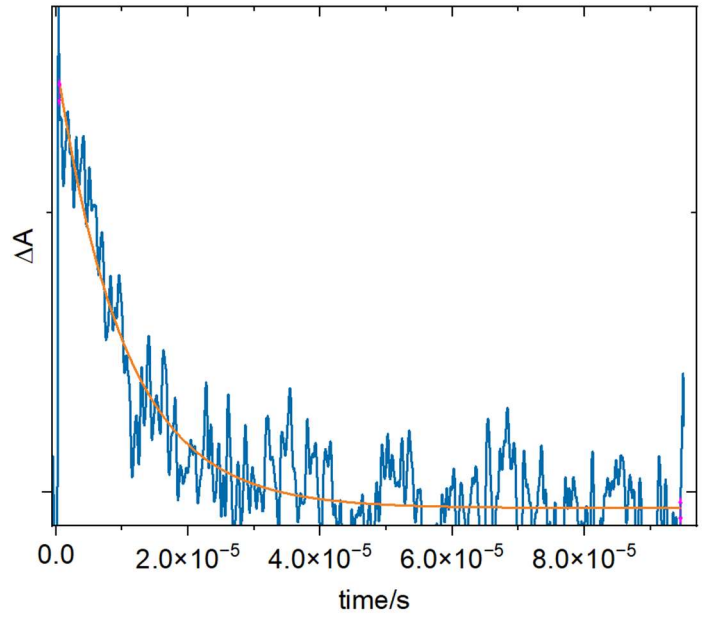

Figure D.36. Absorption at 500 nm generated from HEH_2 (1.2 mM) in THF in the presence of [ColH]OTf (12 mM) and Col (48 mM). (Excitation wavelength: 355nm, detection wavelength: 500 nm).

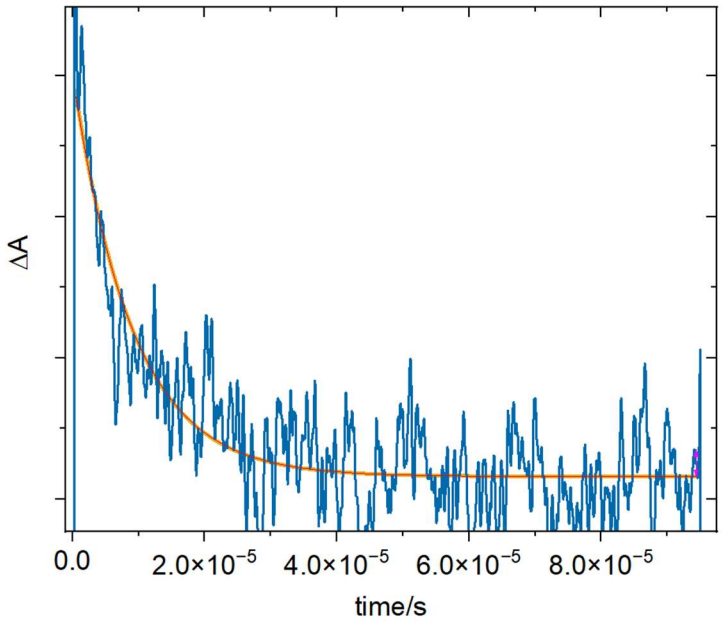

Figure D.37. Absorption at 500 nm generated from HEH_2 (1.2 mM) in THF in the presence of [ColH]OTf (12 mM) and Col (60 mM). (Excitation wavelength: 355nm, detection wavelength: 500 nm).

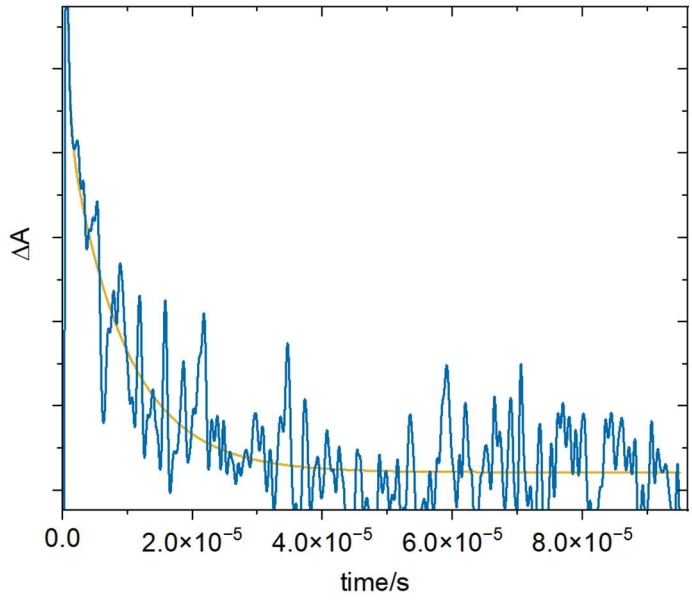

Figure D.38. Absorption at 500 nm generated from HEH_2 (1.2 mM) in THF in the presence of [ColH]OTf (12 mM) and Col (72 mM). (Excitation wavelength: 355nm, detection wavelength: 500 nm).

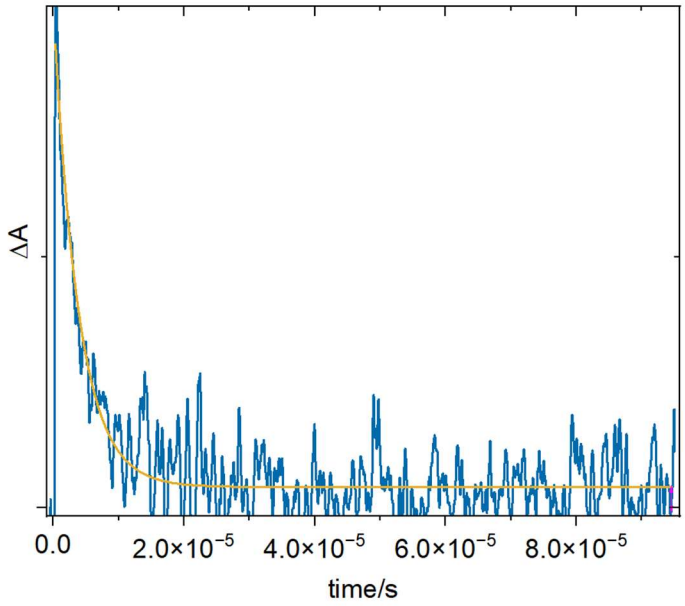

Figure D.39. Absorption at 500 nm generated from HEH_2 (1.2 mM) in THF in the presence of [ColH]OTf (12 mM) and Col (120 mM). (Excitation wavelength: 355nm, detection wavelength: 500 nm).

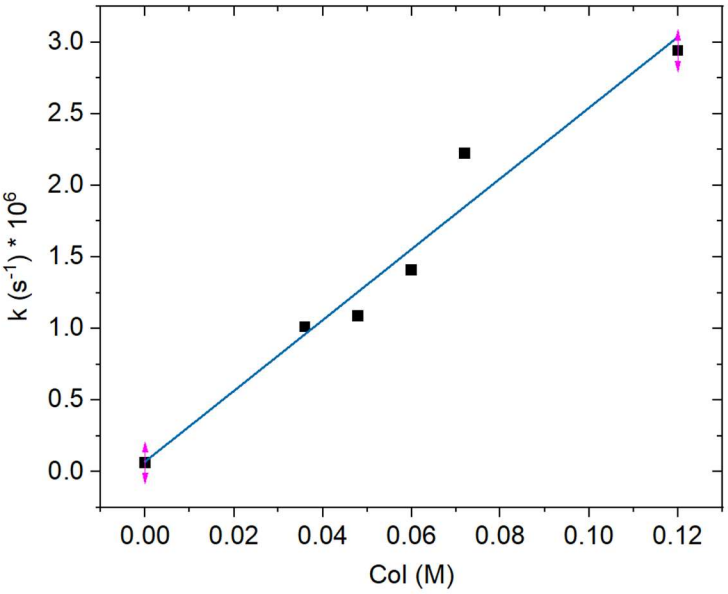

Figure D.40. Kinetic constants plot extrapolated from the lifetime of absorption signals generated after titrating HEH_2 (1.2mM) + [ColH]OTf (12 mM) with Col (36-120mM).

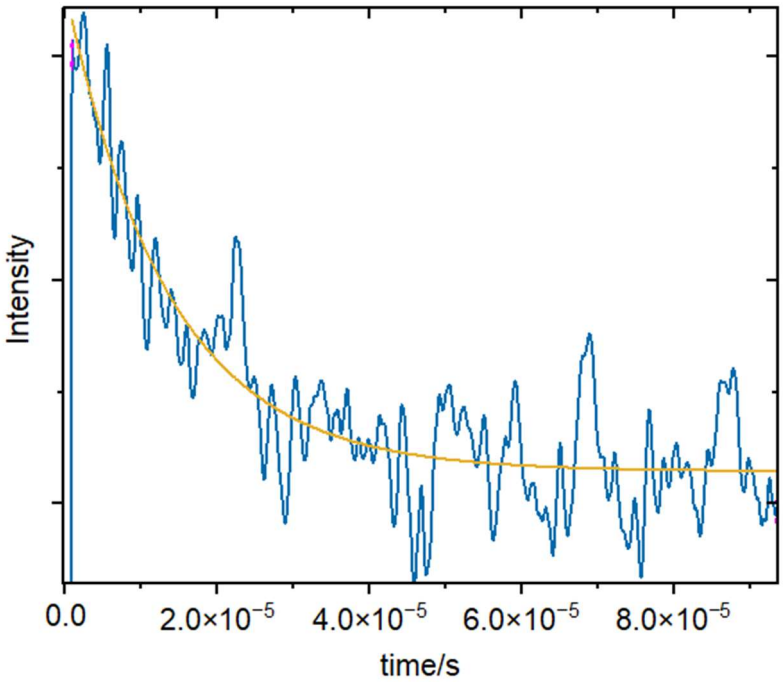

Figure D.41. Absorption at 500 nm generated from HEH_2 (1.2 mM) in THF in the presence of [ColH]OTf (60 mM). (Excitation wavelength: 355nm, detection wavelength: 500 nm).

Table D.21. Lifetime of absorption signals generated after titrating HEH_2 (1.2mM) + [ColH]OTf (12 mM) with Col (36-120mM).

	Lifetime (μs)
HEH_2 + [ColH]OTf	16 ± 5
HEH_2 + [ColH]OTf + Col (36 mM)	9 ± 2
HEH_2 + [ColH]OTf + Col (48 mM)	8 ± 1
HEH_2 + [ColH]OTf + Col (60 mM)	7.2 ± 0.5
HEH_2 + [ColH]OTf + Col (72 mM)	4.5 ± 0.5
HEH_2 + [ColH]OTf + Col (120 mM)	3.6 ± 0.5

Table D.22. Lifetime of absorption signals generated from HEH_2 (1.2mM) in the presence of [ColH]OTf (12-60 mM). The lifetime is not affected by the amount of [ColH]OTf added.

	Lifetime (μs)
HEH_2 + [ColH]OTf (12mM)	16 ± 5
HEH_2 + [ColH]OTf (36mM)	13 ± 3
HEH_2 + [ColH]OTf (48mM)	19 ± 5
HEH_2 + [ColH]OTf (60mM)	17 ± 3

D.8 EPR spectroscopy

D.8.1 General procedure for generation of freeze-quenched organic radicals

In a typical experiment, a J. Young-EPR tube was loaded with HEH_2 and Col-buffer (or other additives) in 100 mM concentration (unless otherwise noted) in THF. The tube was sealed and removed from the glovebox and irradiated in a highly reflective dewar. At the noted time (2 minutes, unless otherwise noted), the dewar was filled with liquid nitrogen to freeze the tube at 77 K. Irradiation was constant during the freezing of the tube. Subsequently, the EPR spectrum was measured in a 77 K immersion dewar using standard techniques.

For quantitative-EPR (Figure D.52), the spectra were collected at 0.002 mW power to avoid saturation of the signal. The double integral was compared to that of a 1 mM standard of TEMPO. The yield of the organic radical is in the presence of buffer ~ 10 μM. In the absence of buffer, the yield of the organic radical is lower (~5 μM).

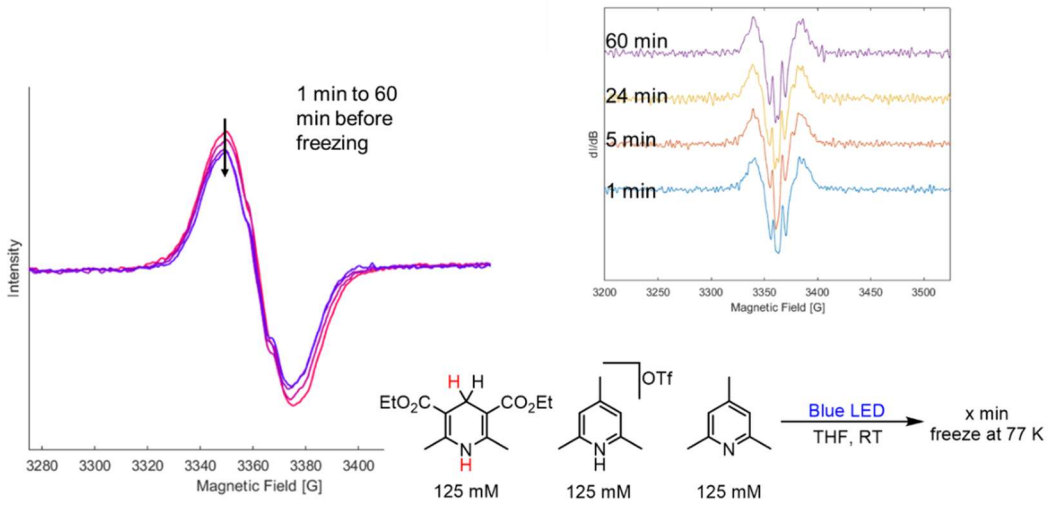

Figure D.42. CW-EPR data of HEH_2 with buffer varying reaction time before freeze-quenching. Acquisition parameters: temperature = 77 K; MW frequency = 9.38 GHz; MW power = 2 mW; modulation frequency = 100 kHz; modulation amplitude = 0.4 mT; conversion time = 20.5 ms.

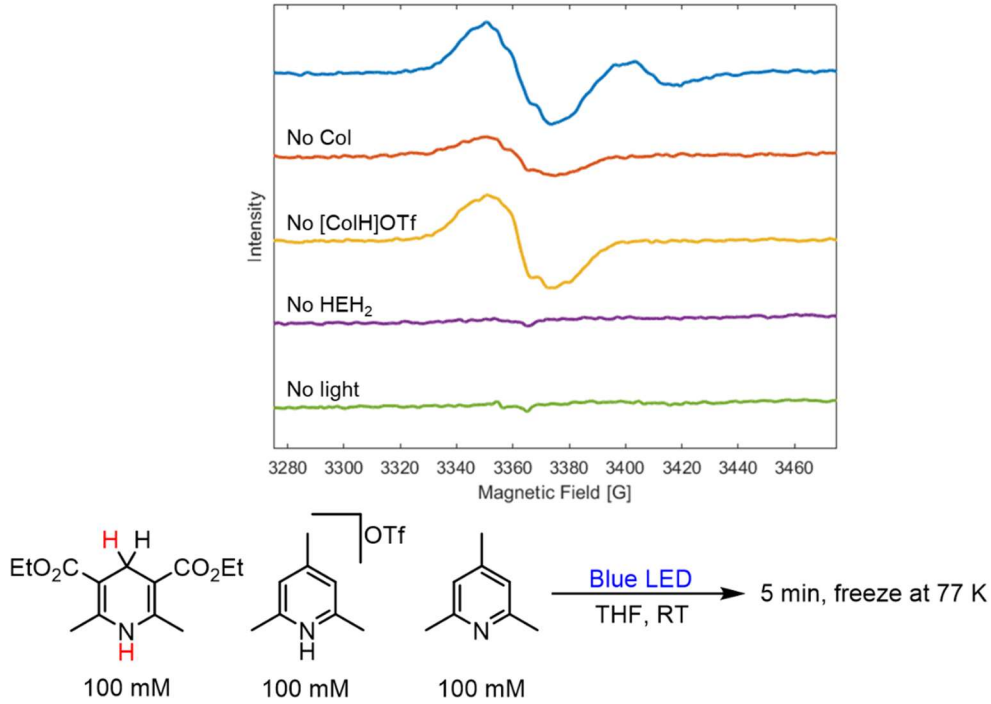

Figure D.43. CW-EPR data of HEH_2 with buffer and removing reaction components. Acquisition parameters: temperature = 77 K; MW frequency = 9.38 GHz; MW power = 2 mW; modulation frequency = 100 kHz; modulation amplitude = 0.4 mT; conversion time = 20.5 ms.

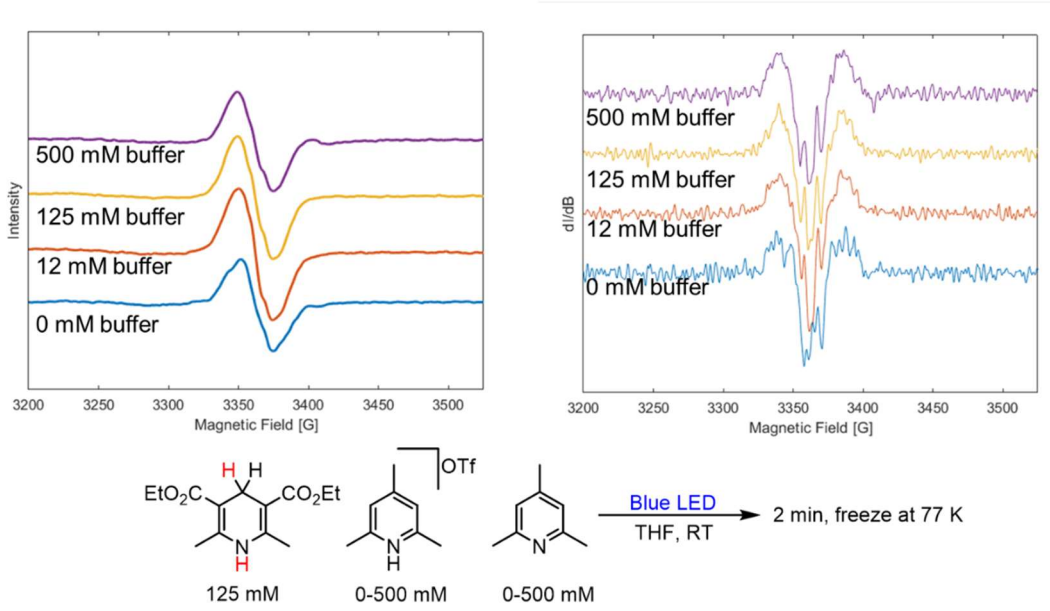

Figure D.44. CW-EPR data of HEH_2 with varying buffer loading. Acquisition parameters: temperature = 77 K; MW frequency = 9.38 GHz; MW power = 2 mW; modulation frequency = 100 kHz; modulation amplitude = 0.4 mT; conversion time = 20.5 ms.

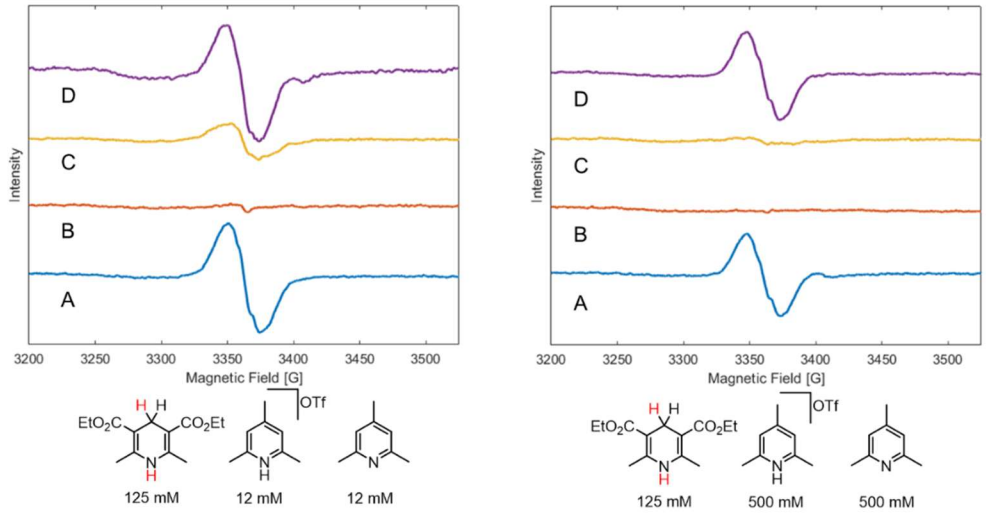

Figure D.45. CW-EPR data of HEH_2 with varying buffer loading. Spectra are labeled as follows: (A): Irradiate for 2 min, freeze at 77 K; (B): Thaw to RT, refreeze after 2 min without irradiation; (C): Irradiate while frozen; (D): Allow to thaw to RT, irradiate for 2 min, freeze at 77 K. Acquisition parameters: temperature = 77 K; MW frequency = 9.38 GHz; MW power = 2 mW; modulation frequency = 100 kHz; modulation amplitude = 0.4 mT; conversion time = 20.5 ms.

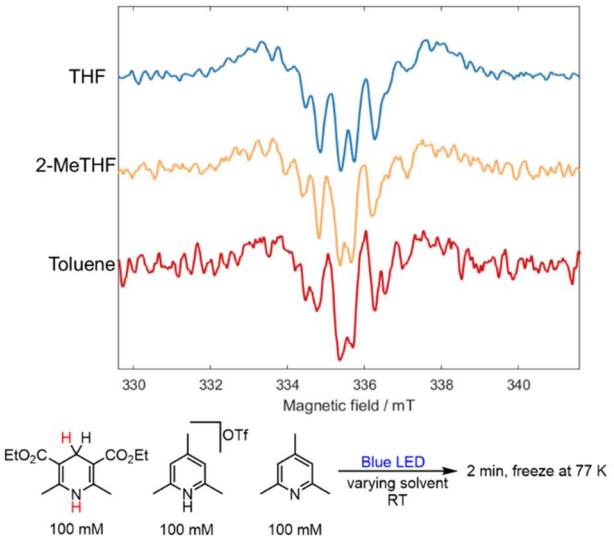

Figure D.46. CW-EPR spectra of freeze quenched reaction of HEH_2 with 100 mM Col-buffer irradiated for 2 minutes before freezing. The solvent is varied between experiments. Acquisition parameters: temperature = 77 K; MW frequency = 9.38 GHz; MW power = 2 mW; modulation frequency = 100 kHz; modulation amplitude = 0.1 mT; conversion time = 20.5 ms.

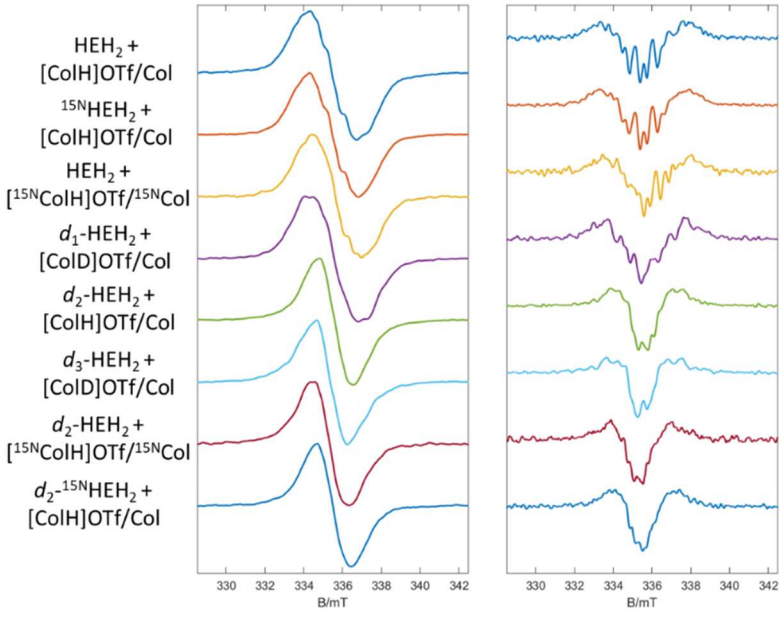

Figure D.47. CW-EPR spectra and 2nd derivative (hyperfine) spectra of reaction of HEH_2 and [ColH]OTf/Col with varying isotopologues. All reactions were conducted with 100 mM of reagents in THF, irradiating for 2 minutes before freeze-quenching. Assignment is

detailed in main text. Acquisition parameters: temperature = 77 K; MW frequency = 9.38 GHz; MW power = 2 mW; modulation frequency = 100 kHz; modulation amplitude = 0.1 mT; conversion time = 20.5 ms.

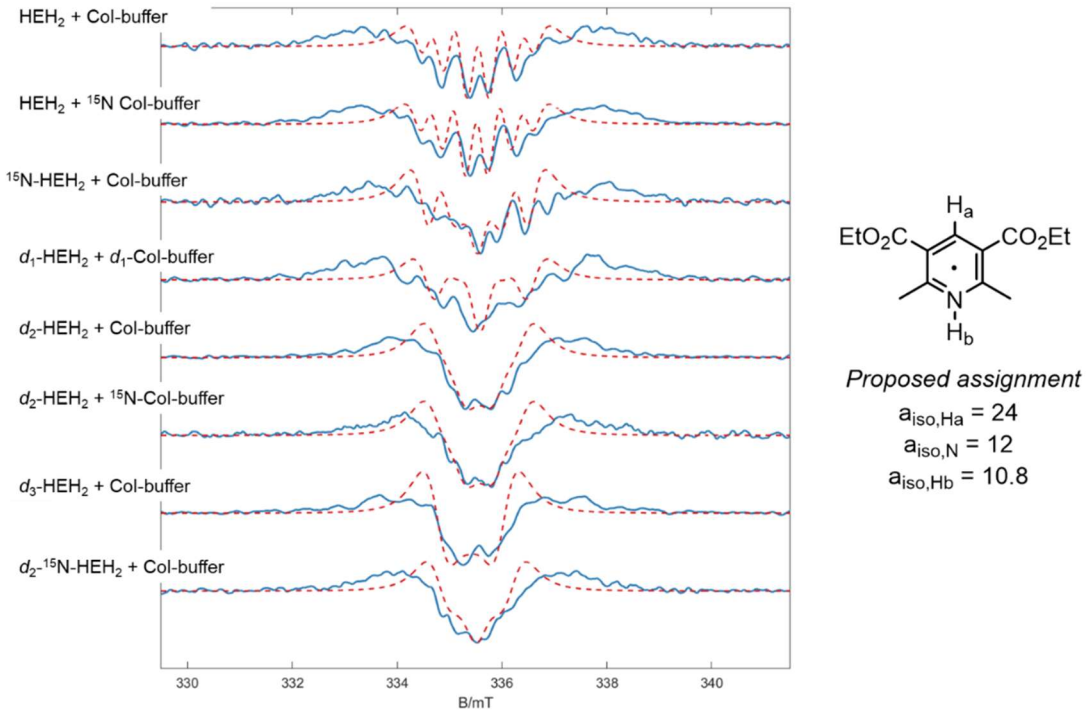

Figure D.48. 2nd derivative (hyperfine) spectra of HEH_2 with 100 mM Col-buffer, irradiated (Blue LED) and freeze-quenched after 2 minutes. Isotopologues of HEH_2 and Col-buffer are used. The lower quality fits for d_1-HEH_2/d_1-Col buffer, and d3-HEH2/d3-Col buffer is attributed to a lower degree of deuteration (compared to d_2-HEH_2) and partial exchange with trace water from HEH_2. Acquisition parameters: temperature = 77 K; MW frequency = 9.38 GHz; MW power = 2 mW; modulation frequency = 100 kHz; modulation amplitude = 0.1 mT; conversion time = 20.5 ms.

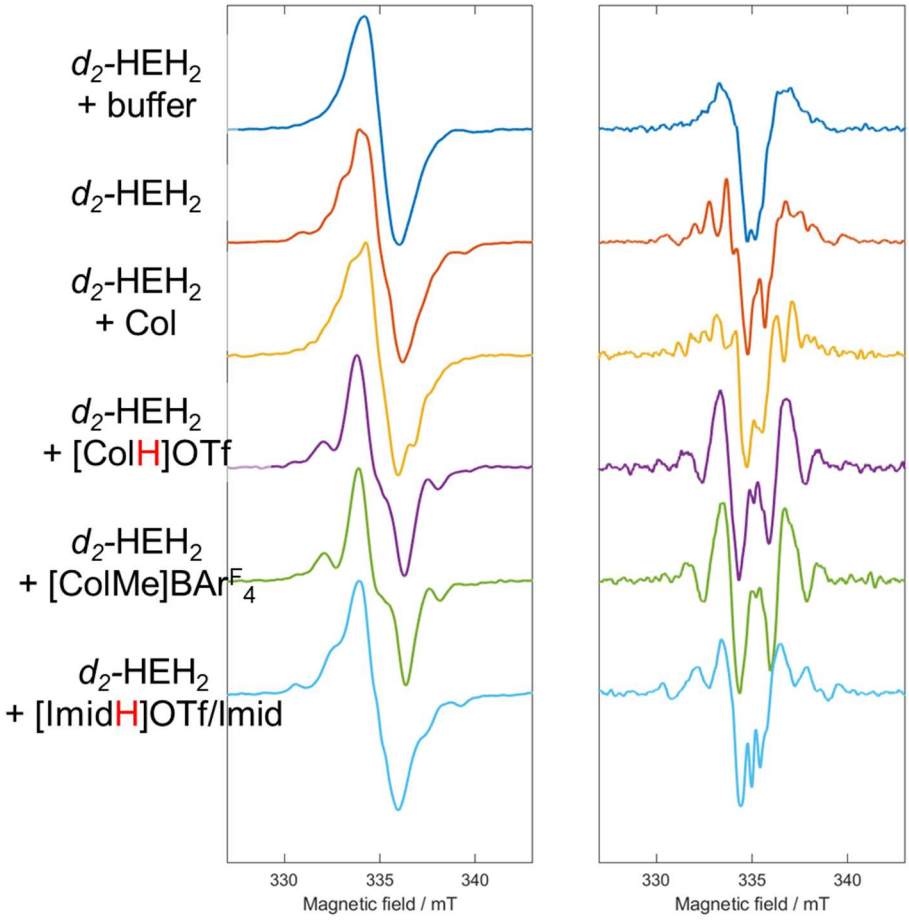

Figure D.49.. The differences between different reagent combinations are best visualized in the CW and 2nd derivate spectra of d_2-HEH$_2$ and various additives. CW-EPR spectra and 2nd derivative (hyperfine) spectra of d_2-HEH$_2$ with 100 mM buffers/additives are shown. No buffer, Col, and Imid-buffer all look similar. [ColH]OTf and [ColMe]BAr$^F_4$ also look different from HEH$_2$ and Col-buffer. We note that the difference between HEH$_2$ + Col-buffer and HEH$_2$ + [ColH]OTf is much clearer with d_2-HEH$_2$. Acquisition parameters: temperature = 77 K; MW frequency = 9.38 GHz; MW power = 2 mW; modulation frequency = 100 kHz; modulation amplitude = 0.1 mT; conversion time = 20.5 ms.

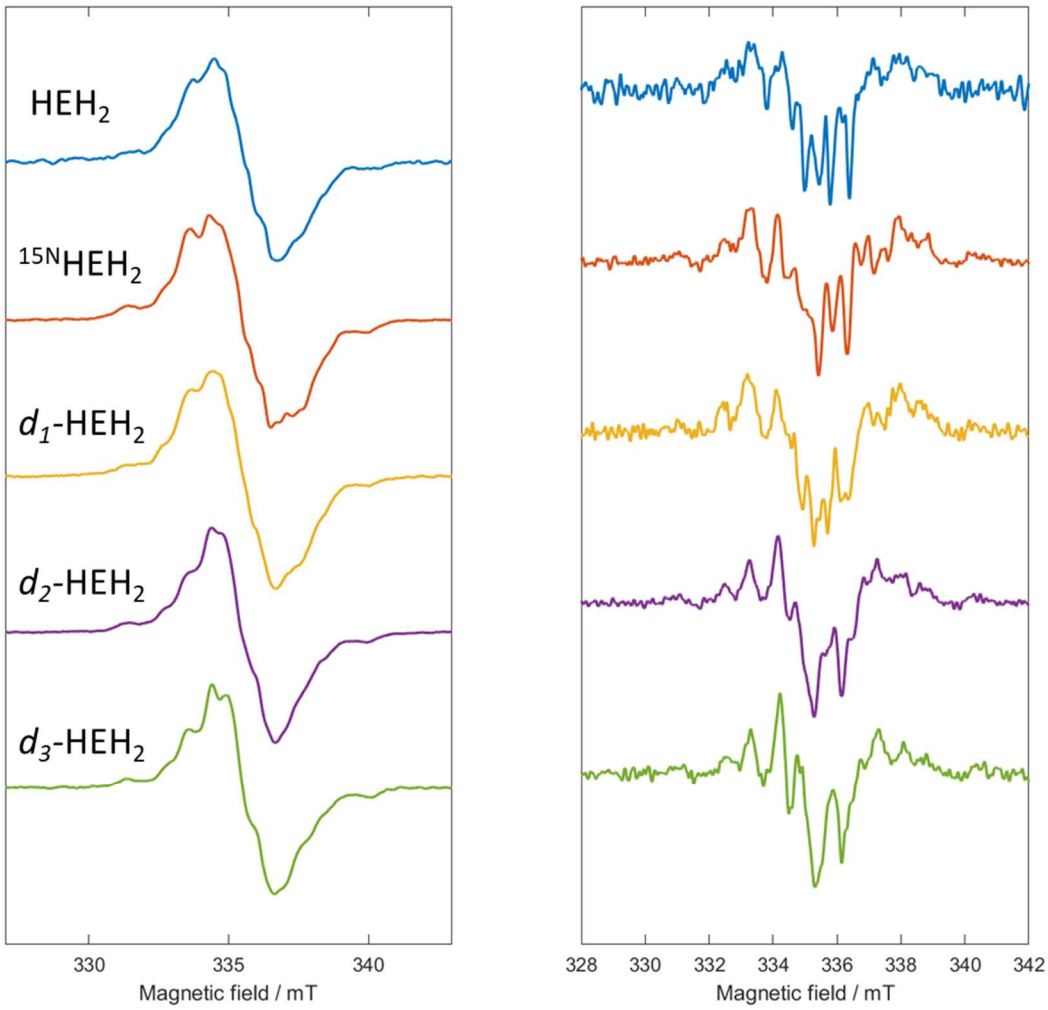

Figure D.50. CW-EPR spectra and 2nd derivative (hyperfine) spectra of HEH_2 isotopologues (100 mM) in THF, 2 minutes irradiation before freeze-quenching. Attempts to assign these spectra were challenged by the low intensity of the signal. Acquisition parameters: temperature = 77 K; MW frequency = 9.38 GHz; MW power = 2 mW; modulation frequency = 100 kHz; modulation amplitude = 0.1 mT; conversion time = 20.5 ms.

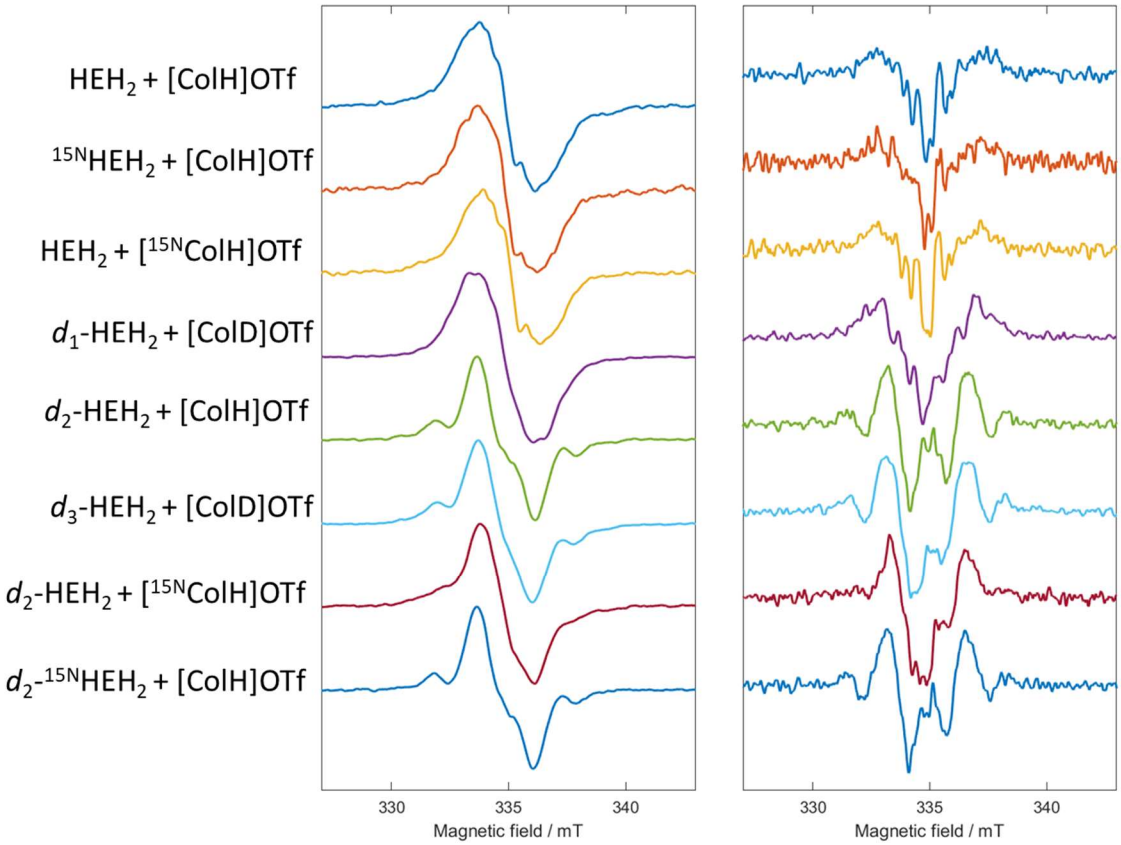

Figure D.51. CW-EPR spectra and 2nd derivative (hyperfine) spectra of reaction of HEH_2 and [ColH]OTf with varying isotopologues. All reactions were conducted with 100 mM of reagents in THF, irradiating for 2 minutes before freeze-quenching. Attempts to assign these spectra were challenged by the low intensity of the signal. Dependance on ^{15N}-Col and ^{15N}-HEH_2 labelling suggest that multiple species are associated with this signal. Acquisition parameters: temperature = 77 K; MW frequency = 9.38 GHz; MW power = 2 mW; modulation frequency = 100 kHz; modulation amplitude = 0.1 mT; conversion time = 20.5 ms.

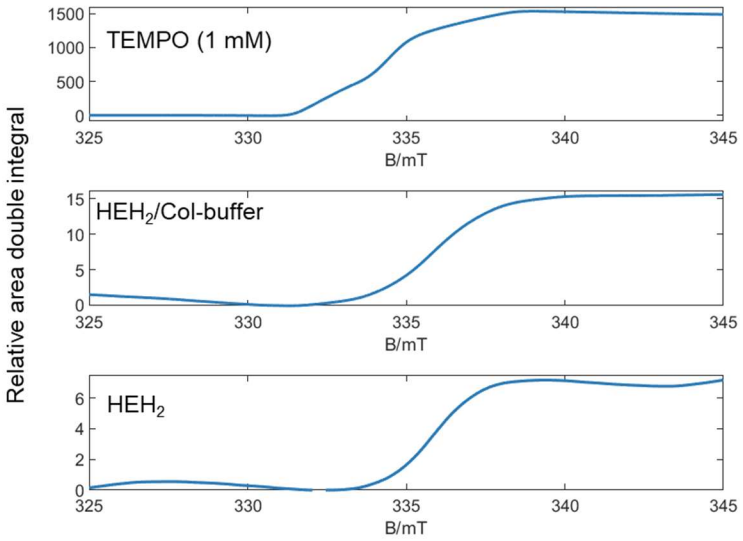

Figure D.52. Double integral of CW-EPR spectra of organic radical generated at low power (0.002 mW).

D.9 Electrochemical measurements

D.9.1 General procedure

Electrochemical measurements were conducted with a glassy carbon working electrode, a platinum wire counter electrode, and Ag/AgOTf (1mM AgOTf in 0.2 M [TBA][PF_6]) reference electrode isolated by a CoralPor™ frit (obtained from BASi) and referenced externally to $Fc^{+/0}$. Unless otherwise specified, NaK dried THF was used as solvent, with 0.2 M [TBA]PF_6 electrolyte. Measurements were conducted with a CH Instruments 600B electrochemical analyzer. For irreversible chemical events, oxidation of HEH_2 and reduction of [ColMe]$BAr^F{}_4$ were estimated using the inflection point potential to estimate $E_{1/2}$.[15]

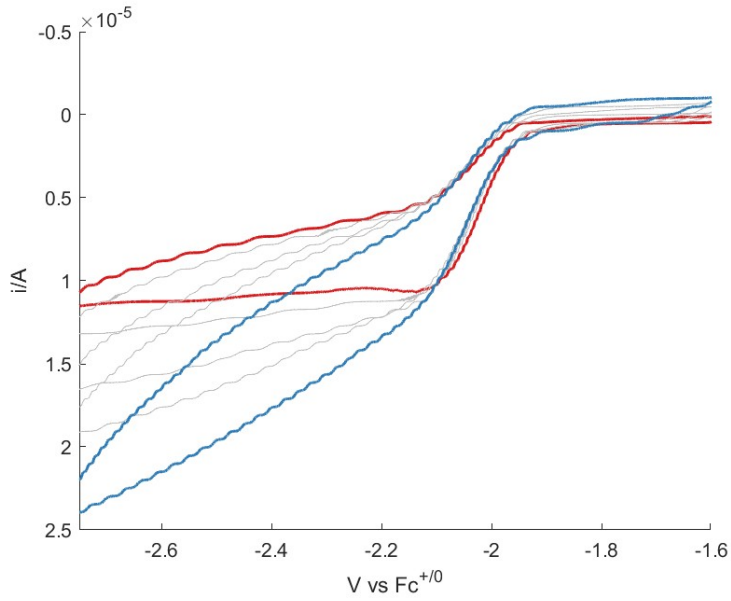

Figure D.53. Cyclic voltammograms of [ColMe]BAr^F_4 (2 mM, dashed lines) in 0.2 M [TBA]PF_6 in THF, with increasing scan rate from 25 mV s^{-1} (red trace) to 400 mV s^{-1} (blue trace).

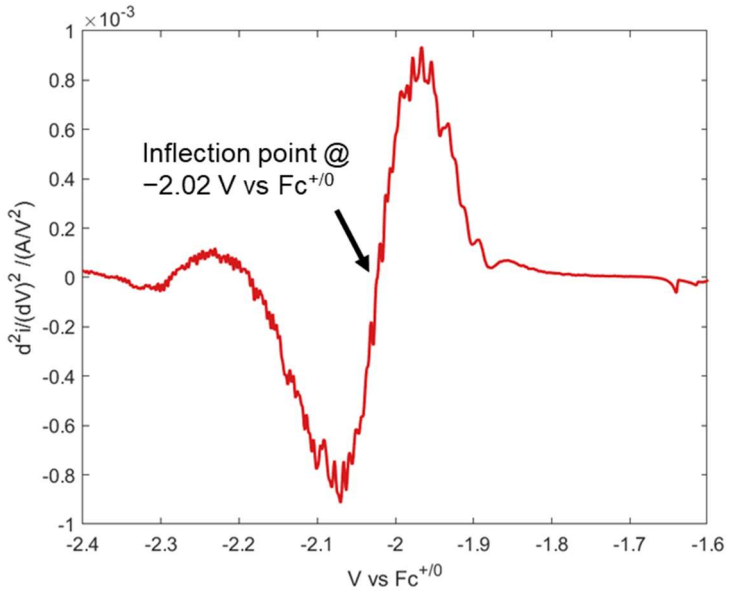

Figure D.54. 2nd derivative of linear sweep of [ColMe]BAr^F_4 (2 mM, dashed lines) in 0.2 M [TBA]PF_6 in THF, at 25 mV s^{-1} to determine inflection point (−2.02 V vs $Fc^{+/0}$).

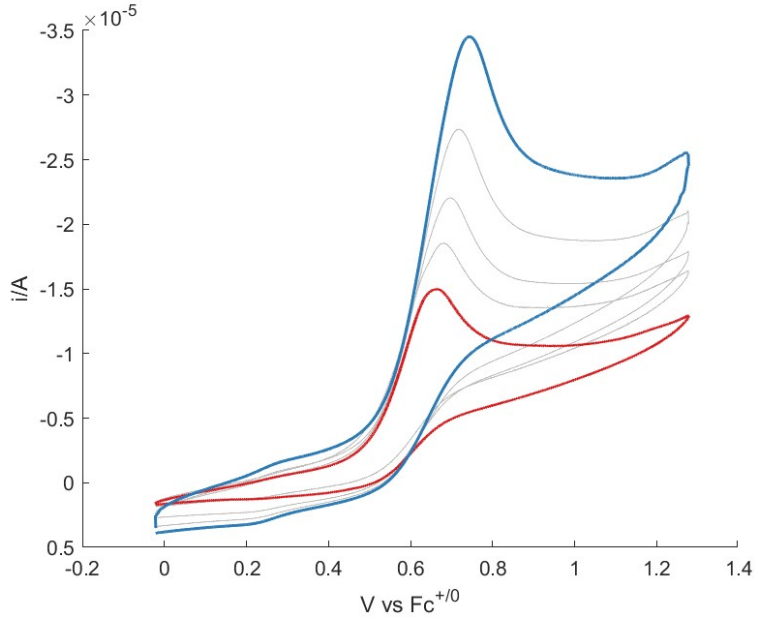

Figure D.55. Cyclic voltammograms of HEH_2 (2 mM, dashed lines) in 0.2 M $[TBA]PF_6$ in THF, with increasing scan rate from 25 mV s^{-1} (red trace) to 400 mV s^{-1} (blue trace).

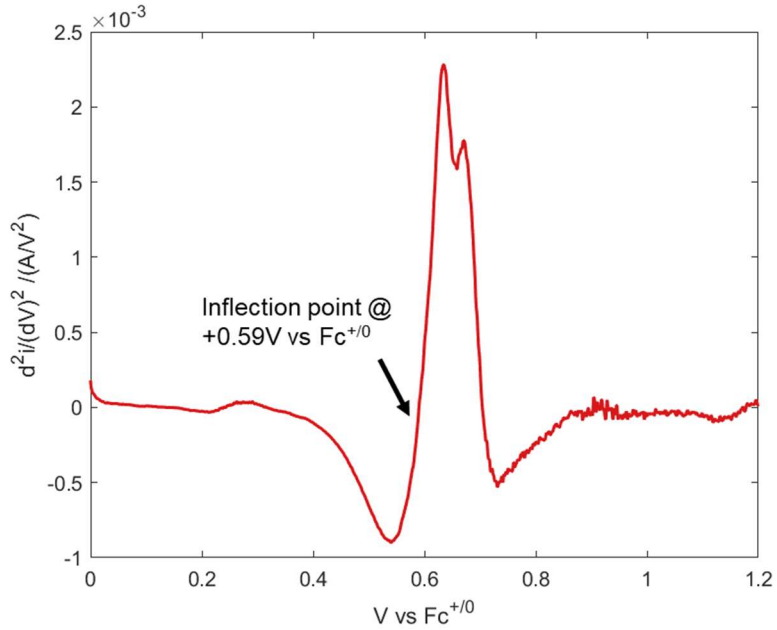

Figure D.56. 2nd derivative of linear sweep of HEH_2 (2 mM, dashed lines) in 0.2 M $[TBA]PF_6$ in THF, at 25 mV s^{-1} to determine inflection point (0.59 V vs $Fc^{+/0}$).

D.10 Infrared spectroscopy

D.10.1 General considerations

All IR data were collected as solution state spectra in a KBr-cell in THF. All data, unless stated, have had THF background spectra subtracted. This results in the regions 636-1500 and 2657-3050 cm^{-1} being completely blocked out due to the intensity of the much more intense THF peaks. Nonetheless, key IR transitions, specifically carbonyl and C=C double bonds, land largely outside this region, providing valuable probes for interactions between HEH_2 and [ColH]OTf.

In some cases, specifically, when acids are used, issues with subtractions result in artifacts in the region 2050-2550 cm-1 (Figures D.59, D.63, and D.64). These artifacts align exactly with THF overtones in the background spectra. We also note a much greater intensity of HEH_2 N−H over $ColH^+$ N−H (see Figures D.65-D.66). This limited the possibility of observing H-bonding between $[ColH]^+$ and HEH_2 as these signals are covered by the HEH_2 N−H stretch.

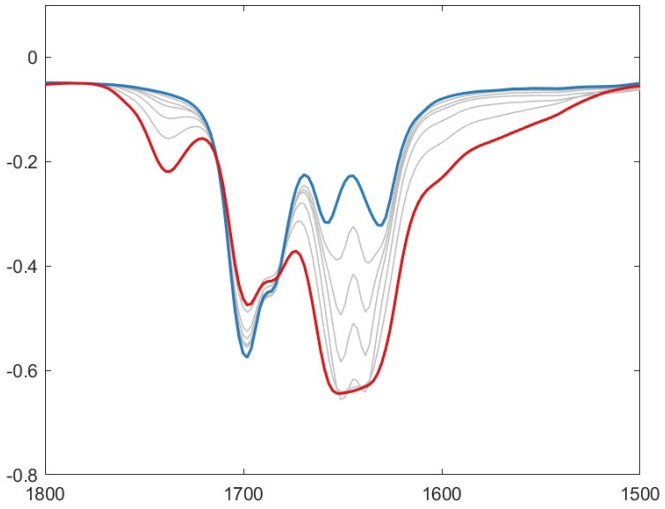

Figure D.57. Infrared spectra of 10 mM solution of HEH_2. [ColH]OTf was titrated in from 0 to 80 mM acid. Upon titration of acid the HEH_2 carbonyl stretch at 1695 cm^{-1} decreases, while a new peak at 1730 cm^{-1} grows in.

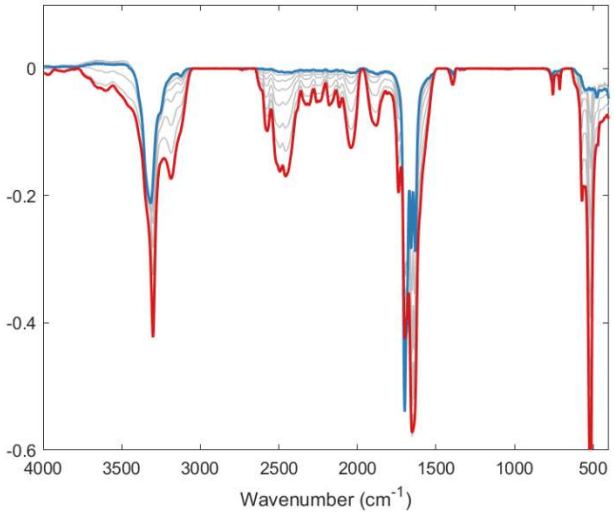

Figure D.58. Infrared spectra of 10 mM solution of HEH_2 (Blue). [ColH]OTf was titrated in from 0 to 80 mM acid (red trace 80 mM). Upon titration of acid the HEH_2 carbonyl stretch at 1695 cm^{-1} decreases, while a new peak at 1730 cm^{-1} grows in. In addition, peaks assignable to [ColH]+ grow in, including C-C π-stretches at 1650, 1638 cm-1, and N−H stretch at 3300 cm^{-1}.

Peaks from 1900-2650 align exactly with THF overtones that have their linewidths (but not peak position) affected by the titration of [ColH]OTf. This results in a poor THF subtraction in this region. See Figure D.63 for details).

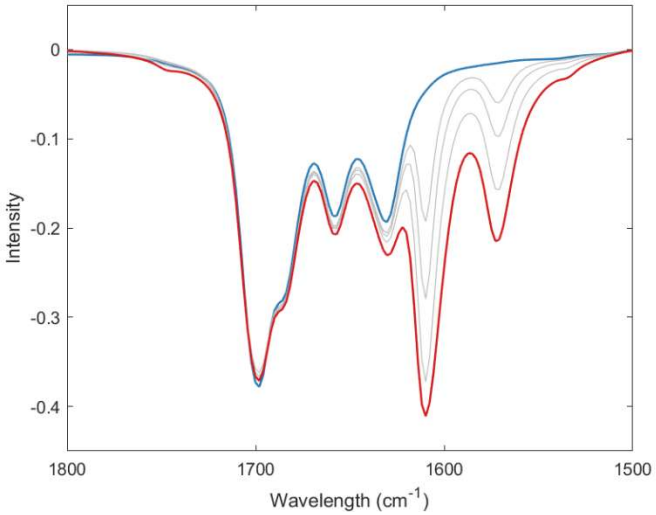

Figure D.59. Infrared spectra of 10 mM solution of HEH_2 (blue). Col was titrated in from 0 to 80 mM base (red trace 80 mM). The peak intensity of the HEH_2 carbonyl stretches at 1700, 1685 cm^{-1} remain unchanged.

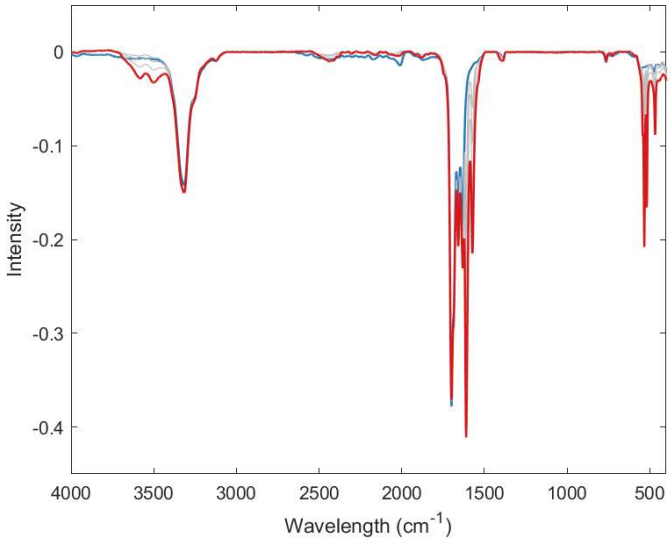

Figure D.60. Infrared spectra of 10 mM solution of HEH_2 (blue). Col was titrated in from 0 to 80 mM base (red trace 80 mM).

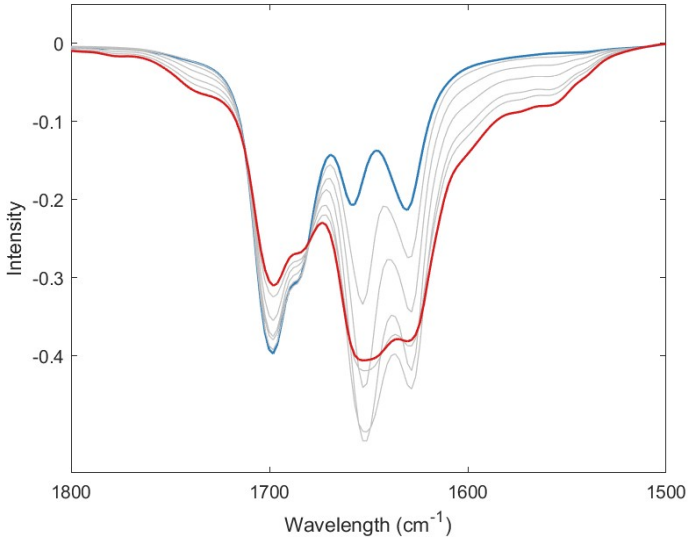

Figure D.61. Infrared spectra of 10 mM solution of HEH_2. [LutH]OTf was titrated. Upon titration of acid, the HEH2 carbonyl stretch at 1695 cm-1 decreases, while a new peak at 1730 cm-1 grows, similar to what is observed with [ColH]OTf. Despite being slightly more acidic than $[ColH]^+$, the magnitude of the decrease of the HEH_2 carbonyl stretches are similar between $[LutH]^+$ and $[ColH]^+$.

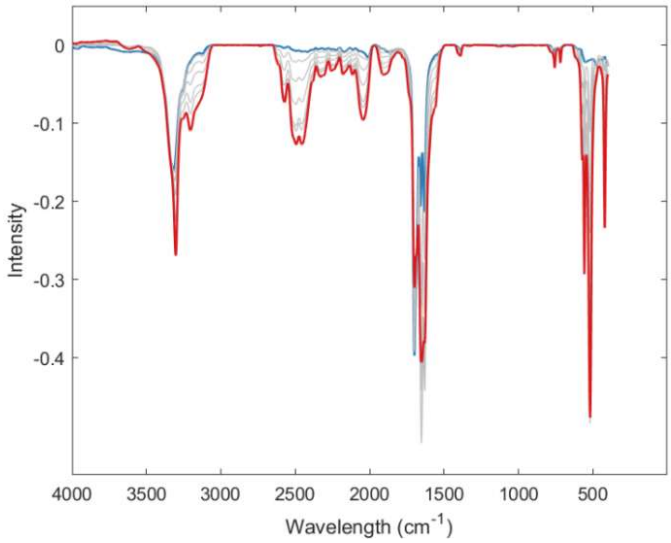

Figure D.62. Infrared spectra of 10 mM solution of HEH_2 (Blue). [LutH]OTf was titrated in from 0 to 80 mM acid (red trace 80 mM). Upon titration of acid the HEH_2 carbonyl stretch at 1695 cm^{-1} decreases, while a new peak at 1730 cm^{-1} grows in. In addition, peaks assignable to [LutH]+ grow in, including C-C π-stretches at 1650, 1638 cm-1, and N−H stretch at 3300 cm^{-1}.

Peaks from 1900-2650 align exactly with THF overtones that have their intensity and linewidths but not peak position affected. This results in a poor THF subtraction in this region. This effect appears to be the same as for $[ColH]^+$.

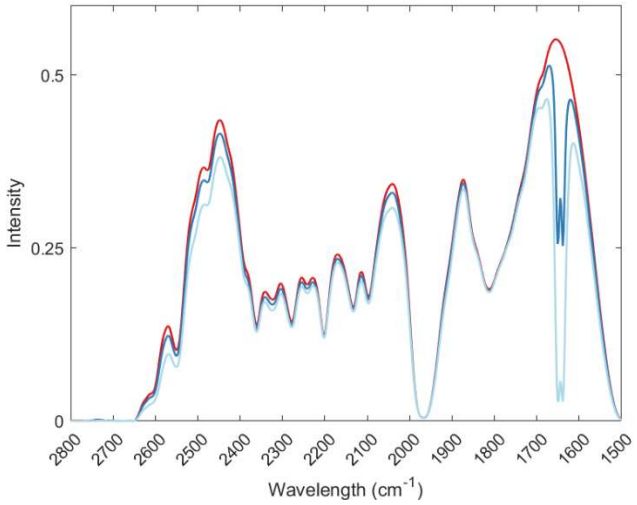

Figure D.63. Unsubtracted transmission infrared spectra of THF (red trace), 10 mM solution of [ColH]OTf in THF (Blue), and 40 mM [ColH]OTf (light blue). We wish to draw attention to the poor alignment between certain THF transmission overtones, specifically the peaks at 2550, 2480, 2330, and 2220 cm^{-1} and transmission minima at 2450, 2100, and 2050 cm^{-1}. While the origin of this poor alignment is unclear, we note that there

are not shifts in the position of these peaks, consistent with these new peaks not corresponding to [ColH]OTf vibrational modes.

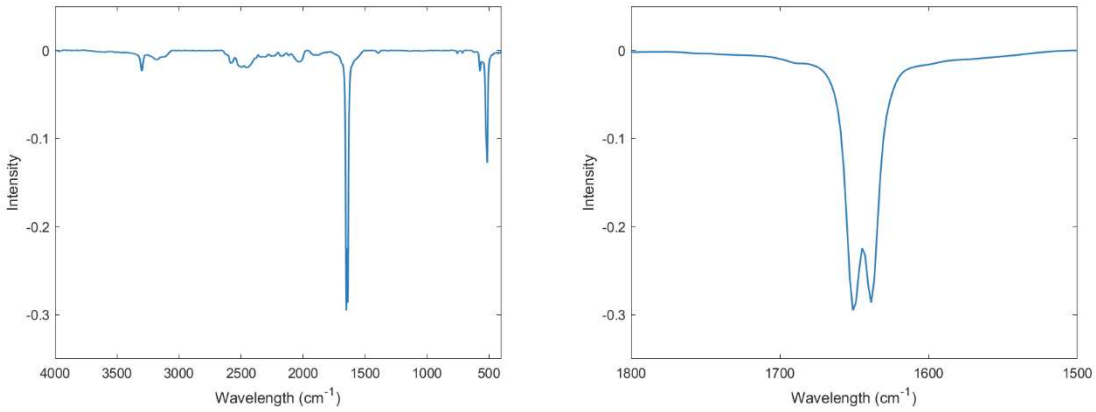

Figure D.64. [ColH]OTf (10 mM) in THF, both wide and zoomed in on the double bond region, with C-C π-stretches at 1650, 1638 cm-1, and N−H stretch at 3300 cm-1, and C−H stretches at 3180 and 3116 cm^{-1} observed.

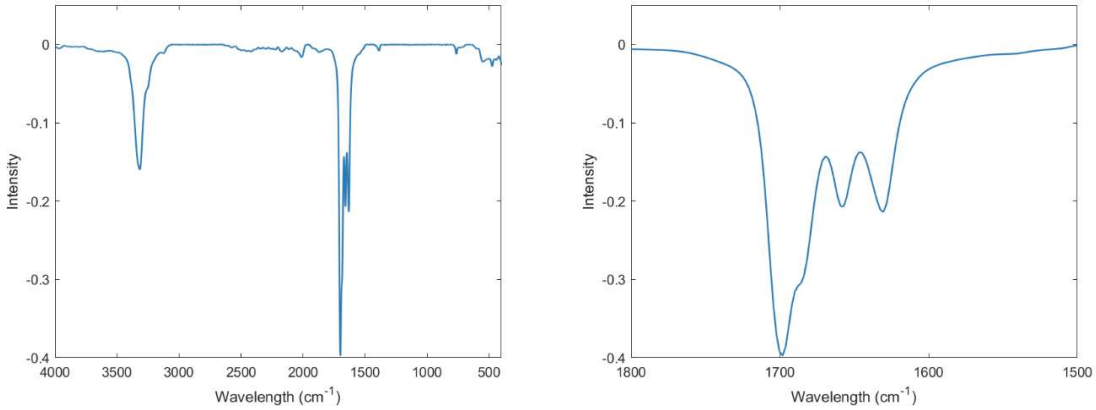

Figure D.65. HEH_2 (10 mM) in THF, both wide and zoomed in on double bond region, including C-C π-stretches at 1660, 1630 cm^{-1}, C=O bonds 1685, 1700 cm^{-1} and N−H stretch at 3310 cm^{-1} observed.

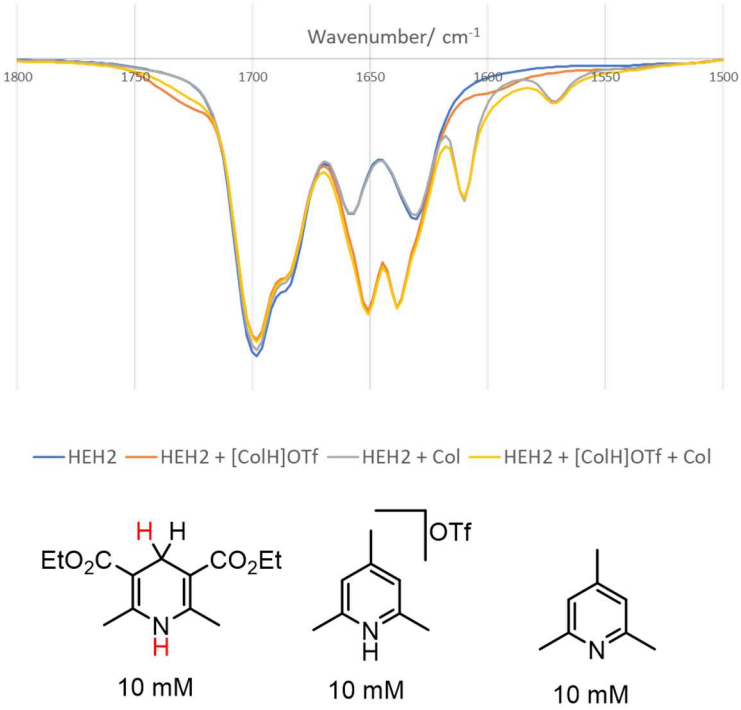

Figure D.66. Infrared spectra of 10 mM solution of HEH_2 (blue trace), 10 mM solution of HEH_2 + [ColH]OTf (10 mM each, orange trace), HEH_2 + Col (10 mM each, grey trace), and HEH_2 + [ColH]OTf/Col (10 mM each, yellow trace). Shoulder at 1730 cm^{-1} appears upon the addition of acid or in the buffer mixture.

D.11 Measurement of HEH_2 excited state pK_a

D.11.1 General considerations

The excited state pK_a of HEH_2 was calculated in MeCN to allow a good comparison with the existing pK_a of $[ColH]^+$ in organic solvent.[12] The resulting values were confirmed to hold in THF by steady-state fluorimetry (Figure D.70).

The excited state pK_a in MeCN was measured using the Förster equation:

$$pK_a^* = pK_a + E_{00,EH2-} - E_{00,HEH2} \quad \text{(eqn D.4)}[14]$$

using these values as derived from Figures D.71-D.72. We calculate pK_a* (HEH_2) 23.8±0.6. This is notable ΔpK_a 8 from that of Col, the buffer during N_2R. Accordingly, the excited state deprotonation of HEH_2 should not play a role during catalysis.

UV-vis and fluorescence experiments were conducted as previously detailed.

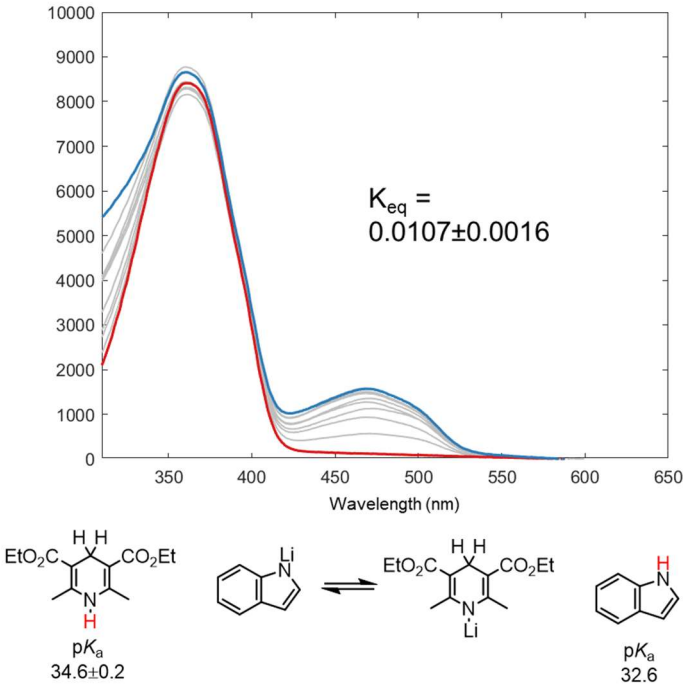

Figure D.67. Measure of pK_a of HEH_2 in MeCN via titration of sodium indolate (pK_a 32.6 in MeCN)[12], used to derive pK_a of HEH_2 at 34.6.

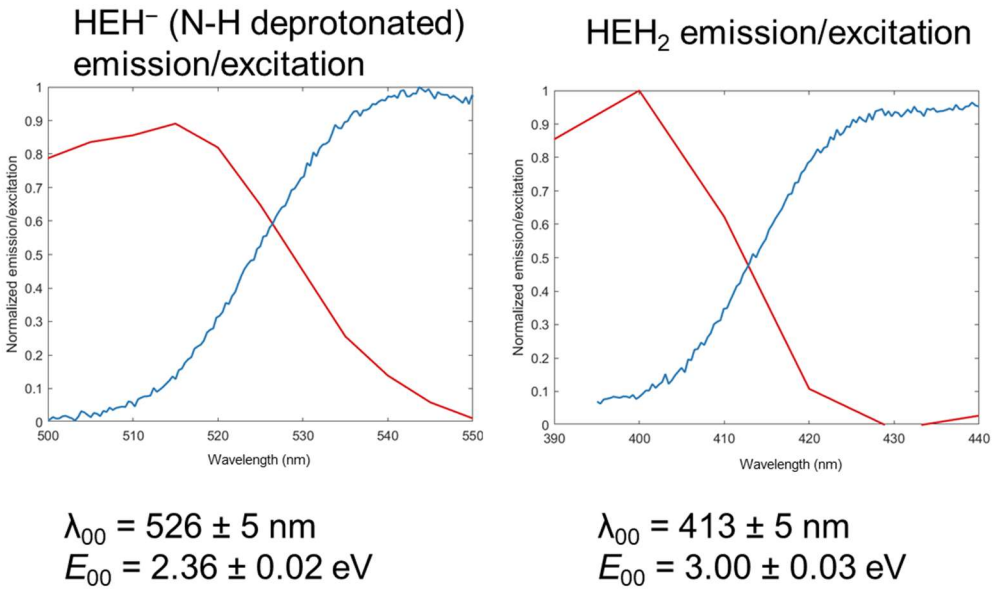

Figure D.68. Measure of E_{00} of Na[HEH_C] (0.5 mM) and HEH_2 (0.5 mM) in MeCN.

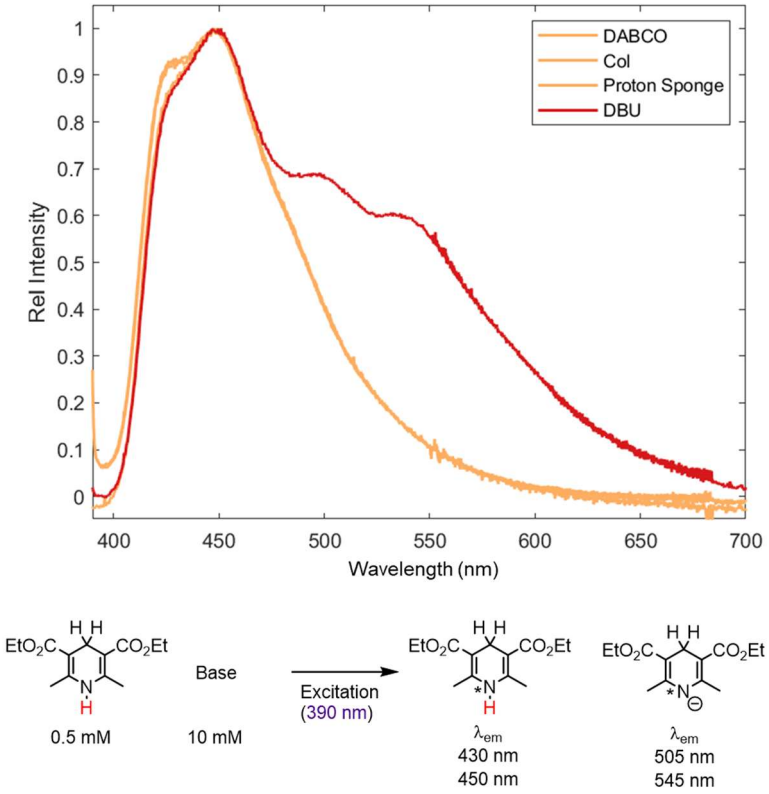

Figure D.69. Measure of pK_a of HEH_2 in THF via the addition of increasingly strong bases. Only when DBU is added is excited state deprotonation of HEH_2 observed. Weaker bases (Col, DABCO, proton sponge) do not deprotonate $^*HEH_2$.

D.12 Summary of thermochemistry of Hantzsch ester (HEH_2) and derivatives and [ColH]$^\bullet$

D.12.1 General considerations

Table D.22 lists $BDFE_{X–H}$, pK_a, and E_{ox} values for various protonation and oxidation states of HEH_2. As has been established by Mayer and coworkers,[16] bond dissociation enthalpies (BDEs) can be converted to BDFEs based on the assumption that the entropies of R–H and R$^\bullet$ are similar. Subtraction of $TS°(H^\bullet)_{solv}$ (6.37 kcal mol^{-1} in MeCN) from the BDE values reported in ref. 17 yields the estimated BDFE values in Table D.22.

$$\mathrm{BDFE}_{\mathrm{estimated}} = 23.06\,E + 1.37\,\mathrm{p}K_a + C_{\mathrm{G}} \quad (\text{eqn } A5.5)$$

Given the proposed role of ColH$^{\bullet}$ radicals, it is useful to experimentally estimate the $BDFE_{N-H}$ using the Bordwell equation.[18] This can be compared to relevant BDFEs of HEH_2 and its semi-oxidized intermediates for which bond strengths have previously been thermochemically derived.[17] The pK_a of $[ColH]^+$ has been measured in MeCN and THF as 15.0 and 10.4, respectively.[12,19] As it is difficult to accurately measure $E(ColH^{+/0})$[20] due to the earlier onset of proton reduction, we rely on $E(ColMe^{+/0})$ as a substitute, measuring $E(ColMe^{+/0})$ as −1.90 V and −2.02 V vs $Fc^{+/0}$ in MeCN[21] and THF. Using eqn D.5 and C_G of 52.6 and 59.9 kcal mol^{-1} in MeCN and THF, we calculate $BDFE_{estimated}$ as 29 kcal mol^{-1} (MeCN) and 28 kcal mol^{-1} (THF), respectively.

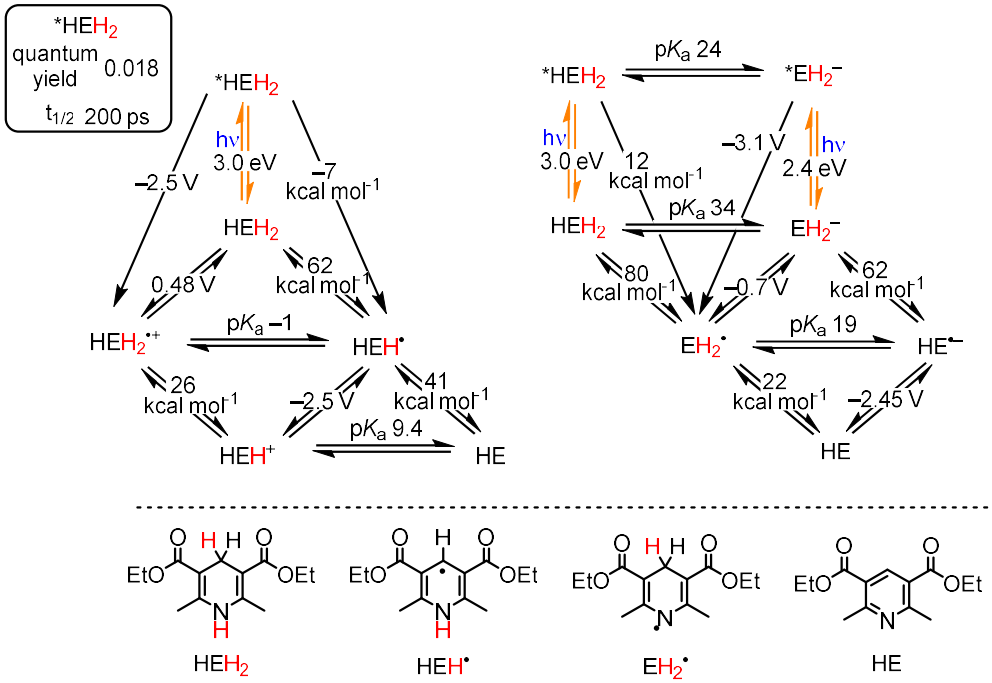

Figure D.70. Overview of measured thermochemistry (in MeCN) of HEH_2 based on either initial C−H or N−H bond oxidation, with excitation (3.0 eV) added to show changes in driving force from excited state.

Table D.22. Reported and estimated thermochemical values for various protonation and oxidation states of HEH_2 relevant to this study. [a] kcal mol^{-1} in MeCN at 298 K. [b] V vs. $Fc^{+/0}$ in MeCN at 298 K. [c] Ref. 18.
[d] Measured in this report, in THF vs $Fc^{+/0}$, see Figures D.54-D.55. [e]Measured in this (in MeCN) report see Section S10. [f]E_{00} measured in this report see Figure D.69, using Rehm-Weller approximation.[22] [g] Ref. 12 [h] Ref. 19 [i]Estimated from $[ColMe]^{+/0}$, measured previously by Pragst and coworkers, Ref 21. [j]Estimated from $[ColMe]^{+/0}$, measured in this report see Figures D.52-D.53.

	BDE[a]	BDFE[a]	E_{ox}[b]	pK_a
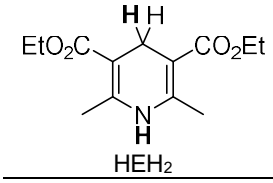 HEH_2	68.7 (C–H), 86.6 (N–H)[c]	62.3 (C–H), 80.2 (N–H)	0.48[c] 0.59[d]	31.8 (N–H) 34.6 (N–H)[e]
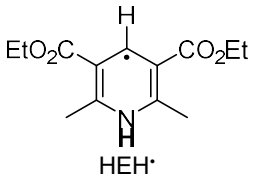 $HEH^{\bullet}$	46.9 (N–H)[c]	40.5 (N–H)		
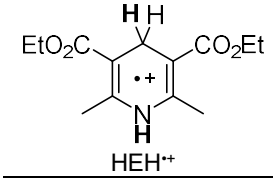 $HEH^{\bullet+}$				–1.0 (C–H)
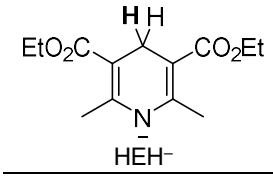 HEH^{-}			–0.695[c]	
$[HEH_2]^*$		–8.5 (C–H)	–2.5[f] –2.4[f]	23.8 (N–H)
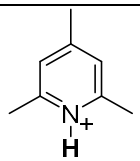				15.0 (N–H)[g] 10.4 (N–H)[h]
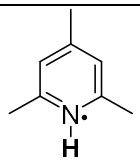		29.4 (N–H) 27.6 (N–H)	−1.90[i] −2.02[j]	

D.13 Additional mechanistic schemes

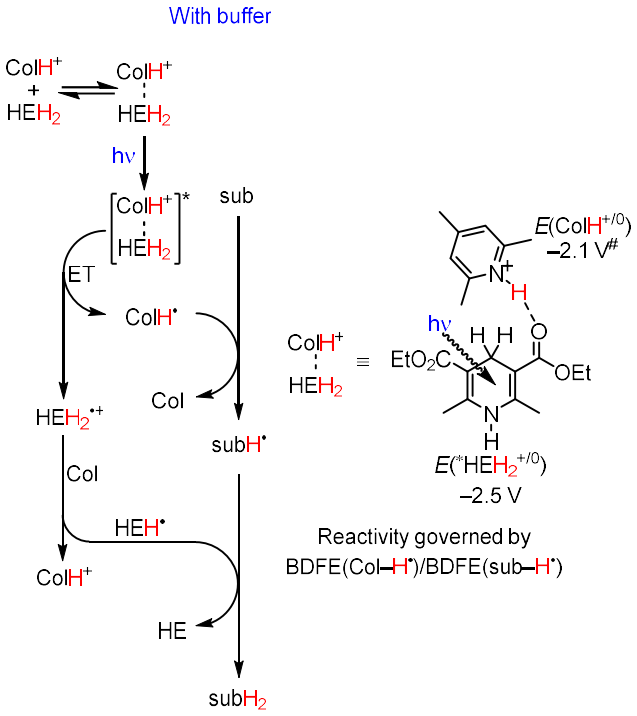

Figure D.71. Proposed mechanism for 2 H^+/2 e^- reduction of sub to $subH_2$ by HEH_2 mediated by Col-buffer.

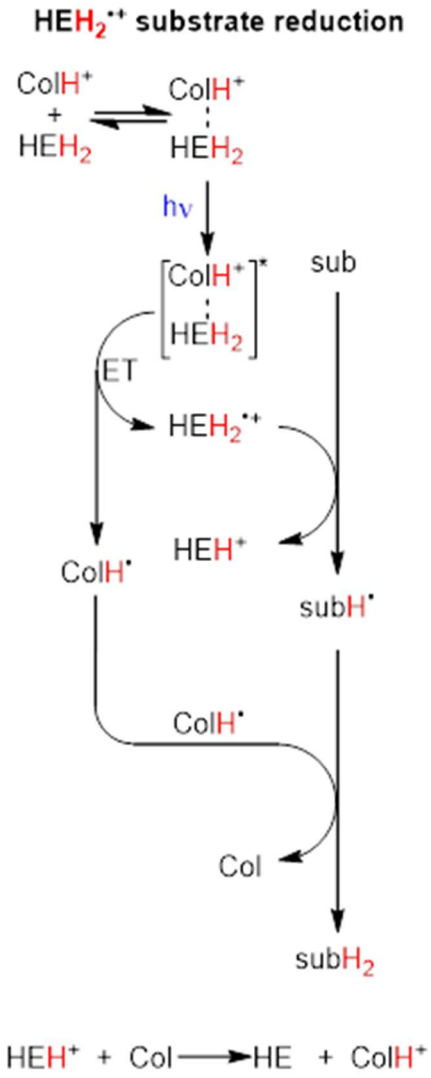

Figure D.72. Schemes depicting mechanism for 2 H^+/2 e^- reduction of sub to $subH_2$ by HEH_2 mediated by Col-buffer if direct reduction of substrate by $HEH_2^{\bullet+}$ occurs (right).

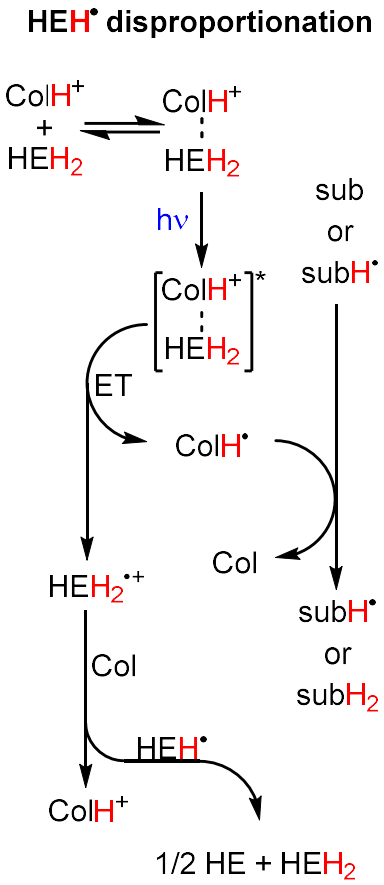

Figure D.73. Schemes depicting mechanism for 2 H^+/2 e^- reduction of sub to $subH_2$ by HEH_2 mediated by Col-buffer, if $HEH^•$ disproportionated to form 0.5 equiv HE and 0.5 equiv.

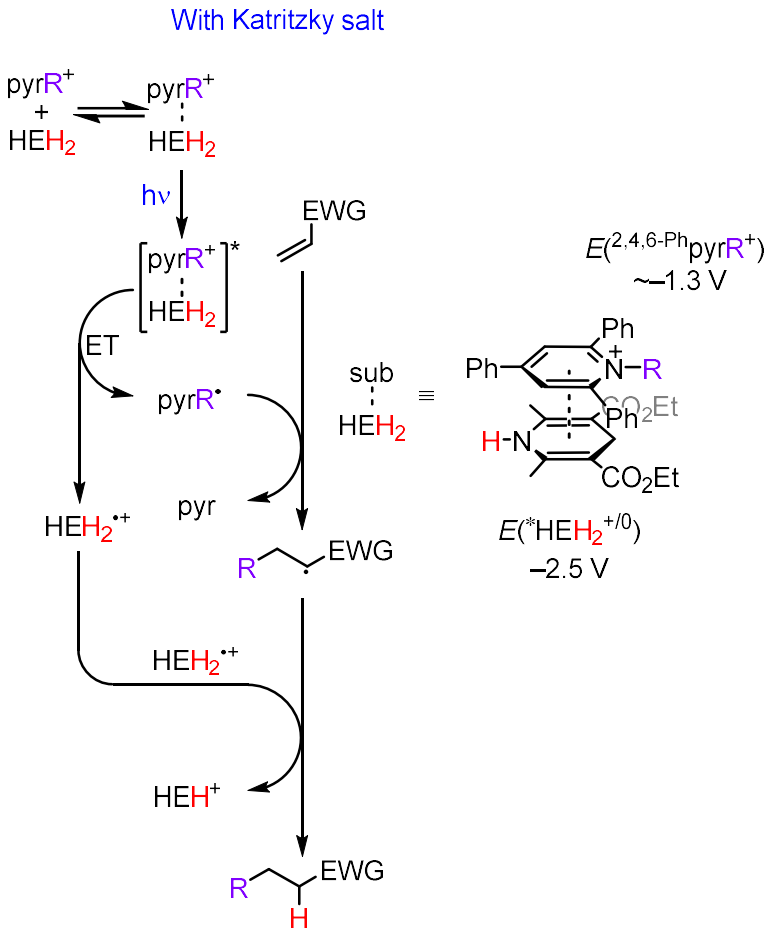

Figure D.74. Typically invoked mechanism for R• addition to sub (e.g., alkene as depicted here) by HEH_2 and Katritizky salt ($[^{2,4,6\text{-Ph}}pyrR]^+$).

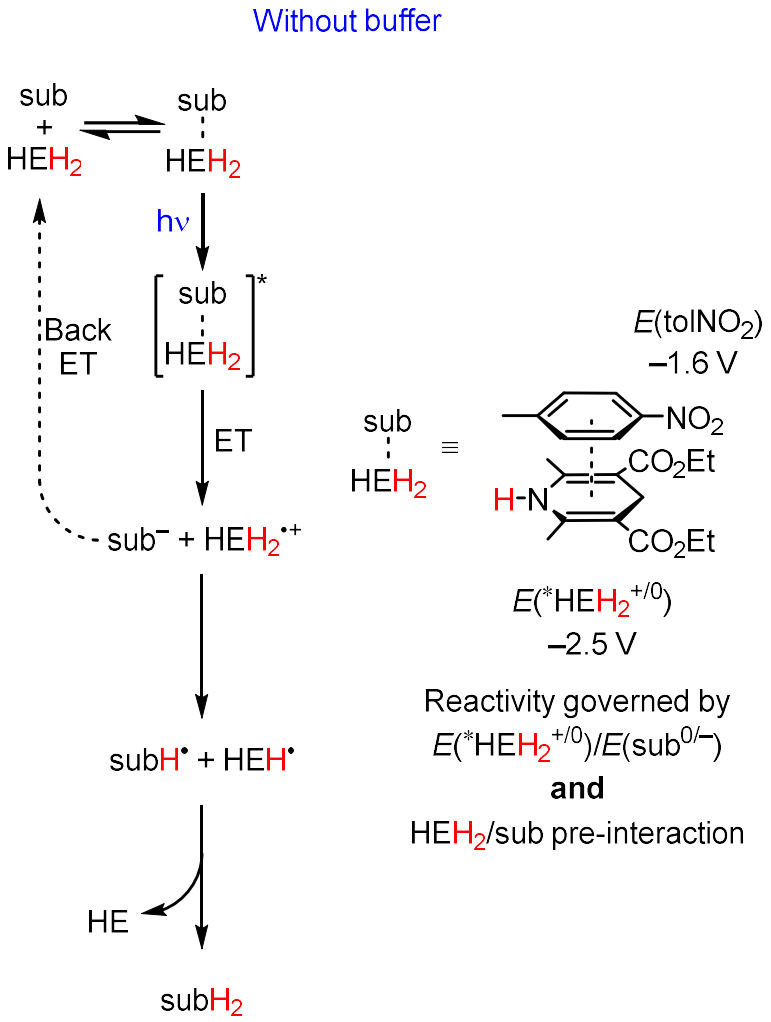

Figure D.75. Proposed mechanism for 2 H^+/2 e^- reduction of sub to $subH_2$ by HEH_2 in the absence of Col-buffer.

D.14 Computational methods

D.14.1 General overview of computational methods

As stated in the main text for our computational studies, we employed the TPSS functional[23] and a def2-TZVP basis set on transition metals and a def2-SVP basis set on all other atoms.[24] This set of functionals was chosen upon a small screen of relevant measured BDFEs. A CPCM solvent model (either MeCN or THF) was used. The ORCA 5 open-source software package was used.[25,26]

The numerical frequencies of the minimized structures were calculated to ensure that these structures represented local minima and not saddle points.

TD-DFT analysis was conducted on optimized structures using TPSSh[23,27] and a def2-TZVP basis set. This updated methodology was found to predict the $^1HEH_2$ π-π* transition more accurately and was used for all other TD-DFT calculations.

D.14.2 Treatment of H•

The treatment of $S(H^\bullet)$ and $\Delta G(H^\bullet)_{solvation}$ can be a source of systematic error in DFT calculations, therefore it is useful to detail how this value has been derived. By calculating a set of known C−H and N−H BDFEs and comparing the computed BDFE ($BDFE_{calc}$) to the measured (Table D.22), we found that the experimental values were most closely reproduced using the following formula:

$$\mathrm{BDFE}_{corrected} = \mathrm{BDFE}_{calculated} + 2.6 \ \ (\mathrm{eqn}\ D.6).$$

All calculated BDFE values cited in the main text are $BDFE_{corrected}$.

It is also worth noting that as this procedure is done on every calculated BDFE, errors in the treatment of $S(H^\bullet)$ and $\Delta G(H^\bullet)_{solvation}$ will be canceled when comparing two different BDFEs.

D.14.3 Computational evaluation of weak interactions between HEH_2 and $[ColH]^+$

When considering the relative energy of interactions between HEH_2 and [ColH]OTf the possibility for multiple conformers of HEH_2 must be accounted for. We find three major conformers can be formed, defined by the rotation of the ester bond. We define them as HEH_2 (A), the lowest energy conformer with the ester carbonyl bonds both pointing towards the 2,6-methyl groups, HEH_2 (B), intermediate energy, with one ester carbonyl group pointing towards the 2-methyl group and one carbonyl parallel with the C_4−H bonds, and HEH_2 (C) with both carbonyls parallel with the C_4−H bond (Figure D.67).

Crucially, we find that the H-bonding is only slightly disfavored to the HEH_2 (B) form, specifically with the $[ColH]^+$ coordinating to the carbonyl parallel with the C_4−H bonds. The relative energy of all three isomers and H-bonding or π-stacking interactions are summarized in Figure D.79.

D.14.4 Calculation of equilibrium isotope effects

Equilibrium isotope effects were calculated using the !PRINTTHERMOCHEM function in ORCA 5, recalculating the entropic and internal energy contributions from an optimized structure but swapping the relevant H-atoms for D-atoms.

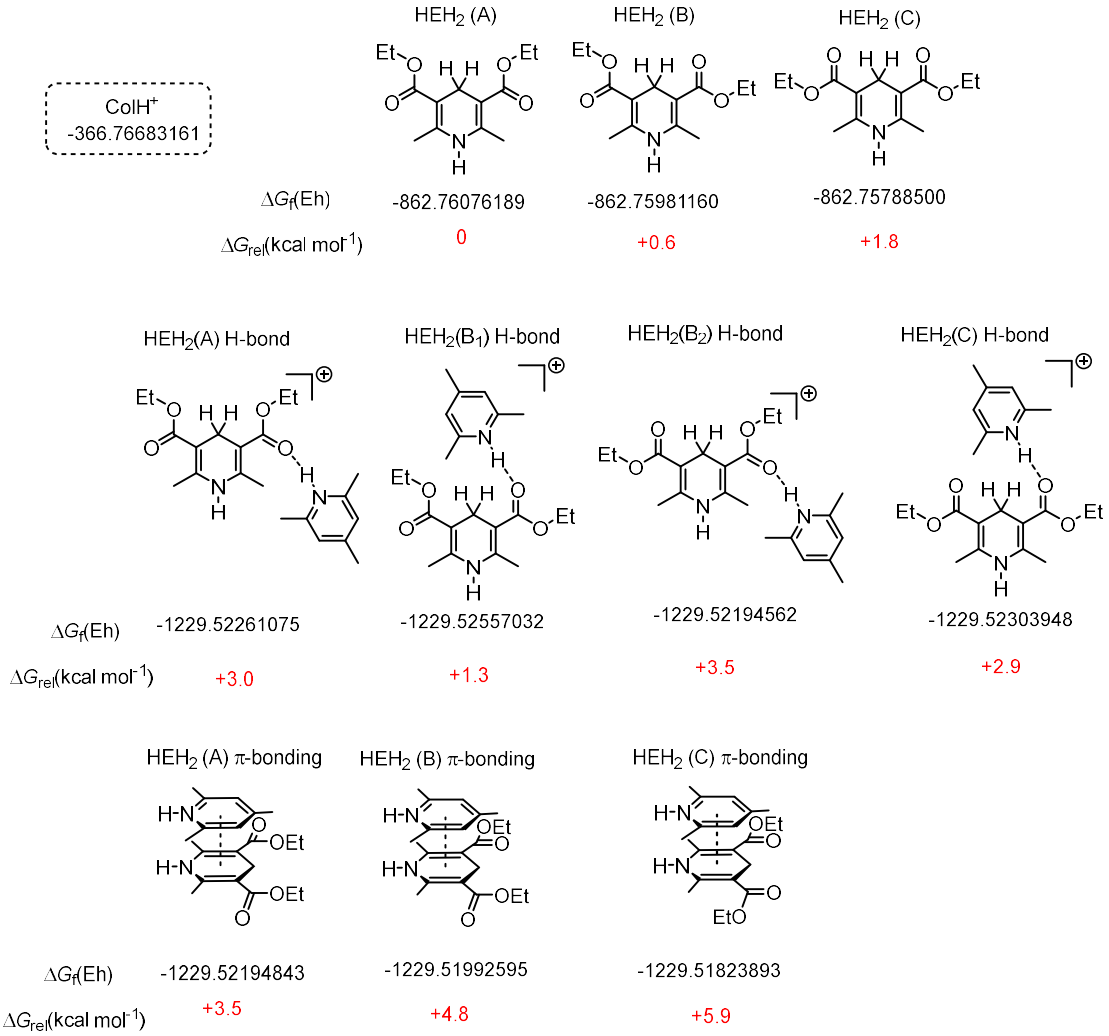

Figure D.76. Evaluation of conformers of HEH_2/$[ColH]^+$ coordination.

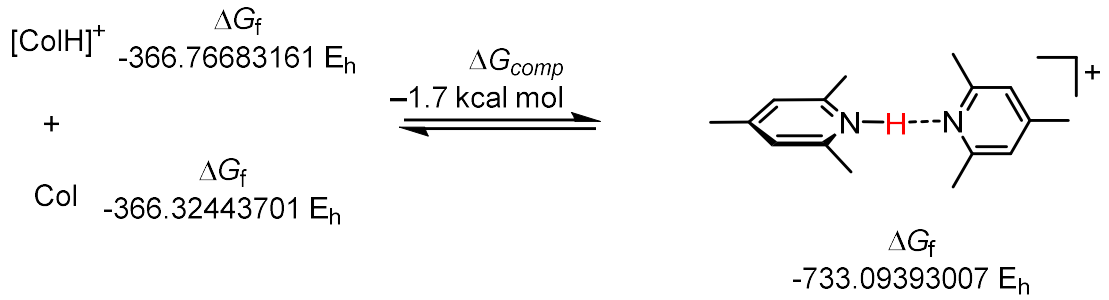

Figure D.77. Evaluation of Col-buffer homodimer, predicted to be favored in solution.

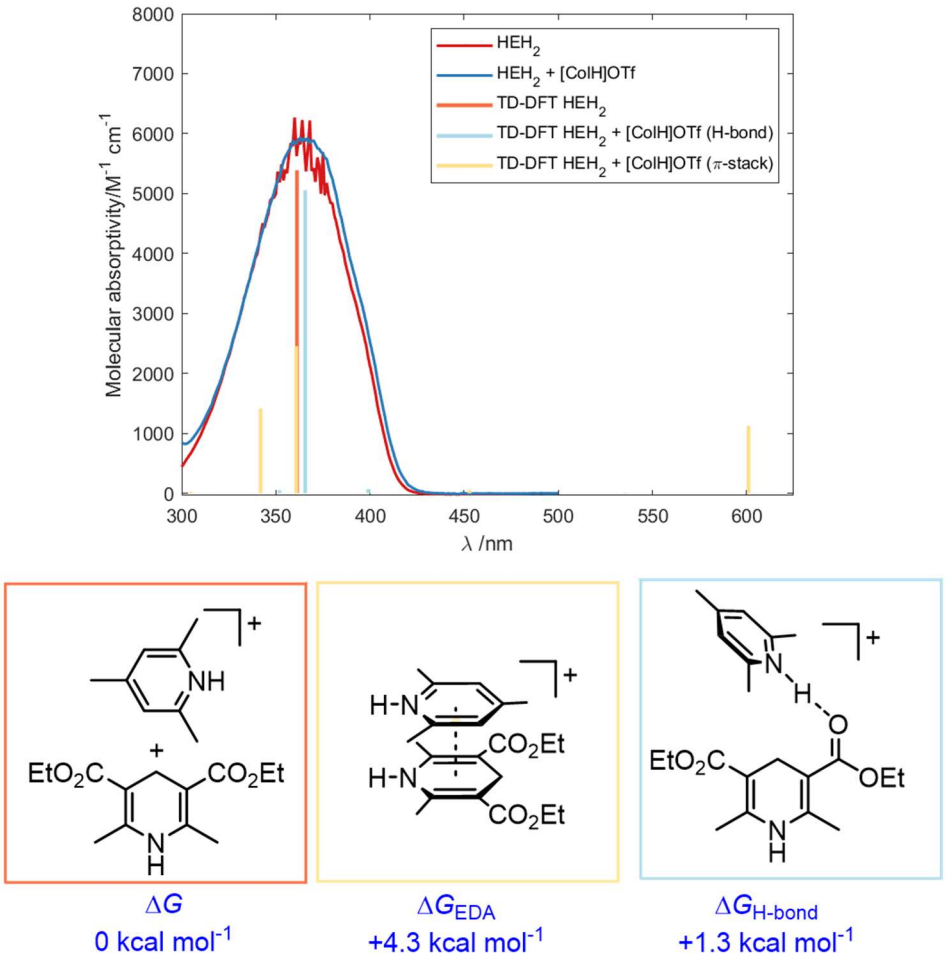

Figure D.78. Comparison of predicted absorption spectroscopy transitions of HEH_2 depending on interaction with $[ColH]^+$ (H-bond or EDA complex).

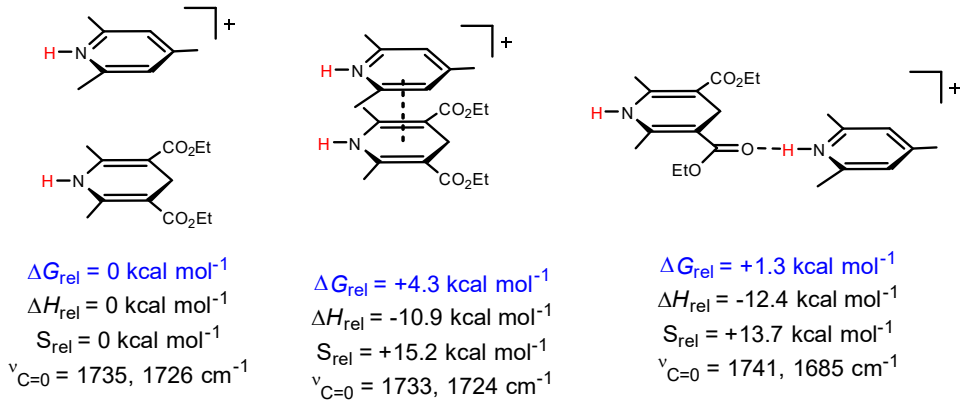

Figure D.79. Predicted vibrational modes for interactions between HEH_2 and Col-buffer.

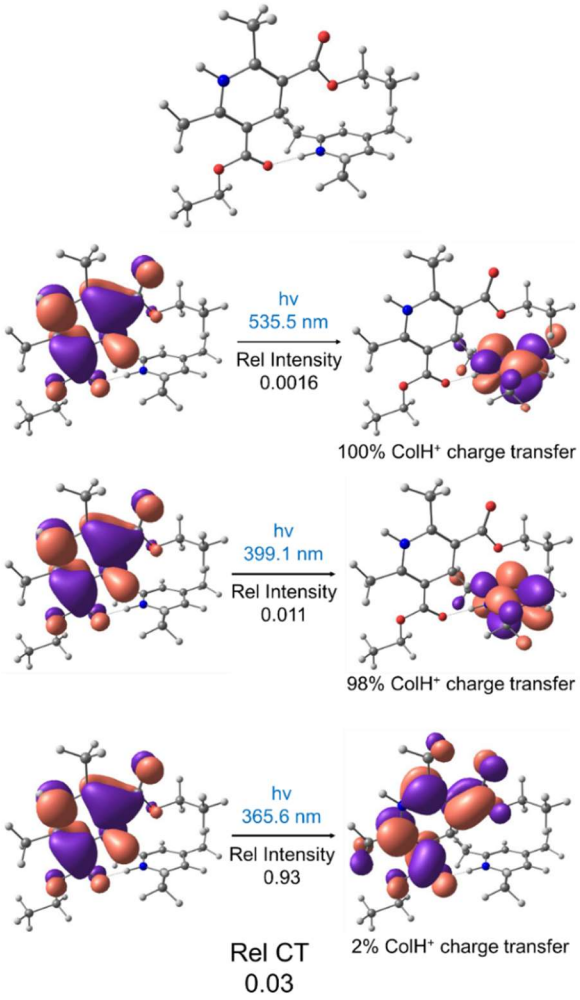

Figure D.80. Optical transitions within relevant to $[ColH]^+$ reduction with wavelength and charge transfer associated with transition to give Rel. Charge Transfer, for HEH_2, $[ColH]^+$ H-bonding interaction.

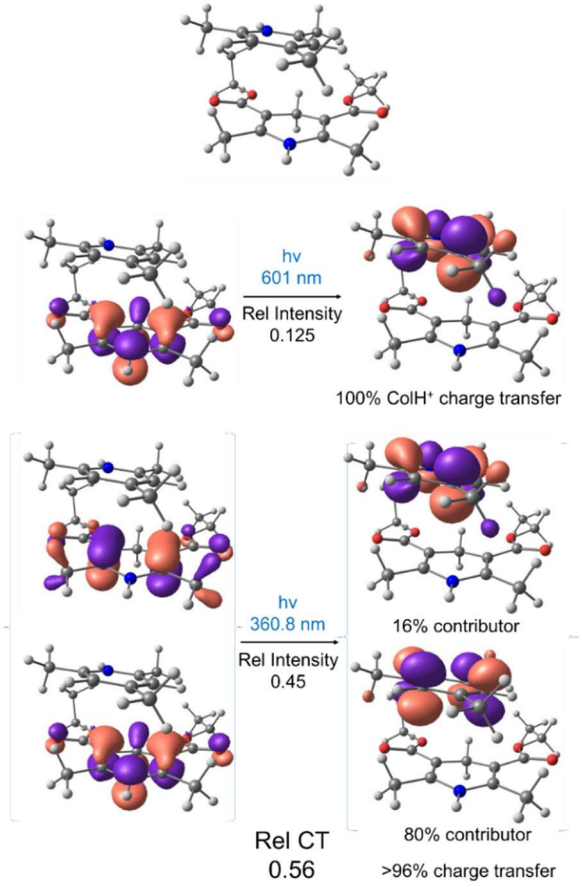

Figure D.81. Optical transitions within relevant to $[ColH]^+$ reduction with wavelength and charge transfer associated with transition to give Rel. Charge Transfer, for HEH_2, $[ColH]^+$ EDA-interaction.

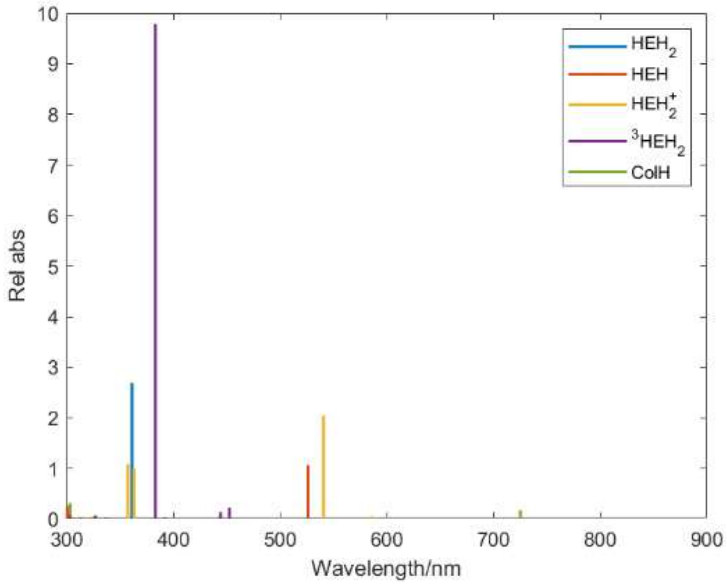

Figure D.82. Predicted TD-DFT transitions for possible species detected by Transient Absorbance spectroscopy.

We note that [ColH]$^{\bullet}$ is predicted to be far less absorbing than [HEH_2]$^{\bullet+}$. [HEH]$^{\bullet}$ is less absorbing than [HEH_2]$^{\bullet+}$, and partially overlaps with this more intense signal. Radical cations being more intense and slightly red-shifted of the corresponding, deprotonated radicals have been observed previously.[28,29,30] These predicted absorbances rationalize why these radicals cannot be picked out in the TA data.

Table D.23. ΔG_f of species relevant to H$^{\bullet}$ calibration. All species were calculated with a CPCM solvent model in MeCN.

Compound	Spin state	ΔG_f (E_h)
HEH_2	0	-861.814
EH_2	1/2	-861.185
HEH	1/2	-861.199
HE	0	-860.64
HEH^+	0	-861.08
HEH_2^+	1/2	-861.627
ColH	1/2	-366.874
Col	0	-366.325
H	1/2	-0.5102

Table D.24. Calculated BDFE for C−H and N−H bond strengths used for calibration. The error is minimized upon adding a factor of +2.6 kcal mol^{-1}; this factor is introduced to all subsequent BDFE calculations. All values measured in MeCN and a CPCM solvent model was likewise used in the calculations.

There is a large discrepancy between the DFT-calculated versus the estimated (from measured data and the Bordwell equation) $BDFE_{N–H}$ of $HEH^{\bullet}$. A contributing factor to this discrepancy might be the reversible formation of an $HEH^{\bullet}$ dimer, leading to a higher measured apparent $BDFE_{N–H}$ than expected for the idealized reaction $HEH^{\bullet} \rightarrow HE + H^{\bullet}$.

	ΔG_{comp} (E_h)	ΔG_{comp} (kcal mol^{-1})	ΔG_{corr} (kcal mol^{-1})	ΔG_{exp} (kcal mol^{-1})	Error, computed (kcal mol^{-1})	Error, calculated (kcal mol^{-1})
$HEH_2 \rightarrow HEH + H$	0.104	65.3	67.9	62.3	3.0	5.6
$HEH_2 \rightarrow EH_2 + H$	0.119	74.4	77.0	80.2	-5.8	-3.2
$1/2HEH_2 \rightarrow 1/2HE + H$	0.077	48.2	50.8	51.4	-3.2	-0.6
$HEH_2^+ \rightarrow HEH^+ + H$	0.037	23.2	25.8	25.63	-2.4	0.2
$ColH \rightarrow Col + H$	0.039	24.3	26.9	29	-4.7	-2.1
					Error calc. (kcal mol^{-1}), ±4.0	Error corr. (kcal mol^{-1}), ±3.1

Table D.25. Thermochemistry of substrate semihydrogenation. (top) ΔG_f of species relevant to calculated substrate BDFEs (main text Figure 5.9). All species were calculated with a CPCM solvent model in THF. (bottom) Calculated BDFE for O−H bonds in substrates used in main text Figure 5.9.

Substrate	Spin state	ΔG_f (E_h)
H	1/2	-0.510
Me_3NO	0	-249.694
Me_3NOH	1/2	-250.289
$PhNO_2$	0	-436.950
$PhNO_2H$	1/2	-437.523
$nPrNO_2$	0	-323.774
$nPrNO_2H$	1/2	-324.340
$nPrN(H)O_2$	1/2	-324.281
NO_3^-	0	-280.626
HNO_3^-	1/2	-281.186
HNO_3	0	-281.071
$NO(OH)_2$	1/2	-281.629
$^{4\text{-Me2N}}PhCHO$	0	-479.691
$^{4\text{-Me2N}}PhCH(OH)$	1/2	-480.241
$^{4\text{-MeO}}PhCHO$	0	-460.268
$^{4\text{-MeO}}PhCH(OH)$	1/2	-460.822
$^{4\text{-MeO2C}}PhCOOMe$	0	-688.270
$^{4\text{-MeO2C}}PhC(OH)Ome$	1/2	-688.812
Benzylacetone	0	-463.639
benzylacetoneH	1/2	-464.180

	ΔG (E_h), calc.	ΔG (kcal mol^{-1}), calc.	ΔG (*k*cal mol^{-1}), corr.
$Me_3NOH \rightarrow Me_3NO + H$	0.085	53.4	56.0
$PhNO_2H \rightarrow PhNO_2 + H$	0.062	39.2	41.8
$nPrNO_2H \rightarrow nPrNO_2 + H$	0.056	35.2	37.8
$HNO_3^- \rightarrow NO_3^- + H$	0.050	31.2	33.8
$NO(OH)_2 \rightarrow HNO_3 + H$	0.048	29.9	32.5
$^{4\text{-MeO}}PhCH(OH) \rightarrow {}^{4\text{-MeO}}PhCHO + H$	0.044	27.6	30.2
$^{4\text{-Me2N}}PhCH(OH) \rightarrow {}^{4\text{-Me2N}}PhCHO + H$	0.040	24.9	27.5
$^{4\text{-MeO2C}}PhC(OH)OMe \rightarrow {}^{4\text{-MeO2C}}PhCOOMe + H$	0.031	19.7	22.3
benzylacetoneH → benzylacetone + H	0.031	19.6	22.2

Table D.26. Thermochemistry ofpossible HAT donors formed. (top) ΔG_f of species relevant to calculated ColH/HEH_2 based BDFEs. All species were calculated with a CPCM solvent model in THF. (bottom) calculated ColH/HEH_2 based BDFE for N/C−H bonds.

Substrate	Spin state	ΔG_f (E_h)
H	1/2	-0.5102
HEH_2	0	-862.761
EH_2	1/2	-862.132
HEH	1/2	-862.145
HE	0	-861.587
HEH^+	0	-862.017
HEH_2^+	1/2	-862.565
ColH	1/2	-366.873
Col	0	-366.324
$ColH^+$	0	-366.767
$^3HEH_2$	1	-862.69

	ΔG (E_h), calc.	ΔG (kcal mol^{-1}), calc.	ΔG (*k*cal mol^{-1}), corr.
$HEH_2 \rightarrow HEH + H$	0.106	66.5	69.1
$HEH_2 \rightarrow EH_2 + H$	0.119	74.7	77.3
$HEH \rightarrow HE + H$	0.047	29.4	32.0
$EH_2 \rightarrow HE + H$	0.034	21.3	23.9
$HEH_2^+ \rightarrow HEH^+ + H$	0.038	23.6	26.2
$^3HEH_2 \rightarrow HEH + H$	0.035	22.2	24.8
$ColH \rightarrow Col + H$	0.038	24.1	26.7

Table D.27. Calculated entropy and internal energy for minimized structures of HEH_2, $ColH^+$ and Col with varying isotopologues.

	Entropy and internal energy (298 K), E_h	$\Delta\Delta G_{H\text{-}D}$ (kcal mol^{-1})
$ColH^+$	0.1473	-
$ColD^+$	0.1437	-
$\Delta G(ColH^+) - \Delta G(ColD^+)$	-	2.3
HEH_2	0.2566	
d_1-HEH_2	0.2531	
d_2-HEH_2	0.2499	
$\Delta G(HEH_2) - \Delta G(d_1\text{-}HEH_2)$	-	2.2
$\Delta G(HEH_2) - \Delta G(d2\text{-}HEH_2)$	-	4.2
$HEH_2\cdots HCol^+$ (H-bond)	0.4278	-
d_1-$HEH_2\cdots DCol^+$ (H-bond)	0.4208	-
d_2-$HEH_2\cdots HCol^+$ (H-bond)	0.4211	-
$\Delta G(HEH_2\cdots HCol^+$ (H-bond)) − $\Delta G(d_1\text{-}HEH_2\cdots DCol^+$ (H-bond))	-	4.4
$\Delta G(HEH_2\cdots HCol^+$ (H-bond)) − $\Delta G(d_2\text{-}HEH_2\cdots HCol^+$ (H-bond))	-	4.2
$HEH_2\cdots HCol^+$ (π-stack)	0.4290	-
d_1-$HEH_2\cdots DCol^+$ (π-stack)	0.4219	-
d_2-$HEH_2\cdots HCol^+$ (π-stack)	0.4223	-
$\Delta G(HEH_2\cdots HCol^+$ (π-stack)) − $\Delta G(d_1\text{-}HEH_2\cdots DCol^+$ (π-stack))	-	4.5
$\Delta G(HEH_2\cdots HCol^+$ (π-stack)) − $\Delta G(d_2\text{-}HEH_2\cdots HCol^+$ (π-stack))	-	4.2
$ColH\cdots Col^+$	0.3011	-
$ColD\cdots Col^+$	0.2979	-
$\Delta G(ColH^+\cdots Col)$ − ΔG(ColD+…Col)	-	2.0

Table D.28. Calculated equilibrium isotope effects (based on table D.27) for pre-complexation.

Reaction	Difference in entropy and internal energy (298 K), E_h	$\Delta\Delta G_{H\text{-}D}$ (kcal mol^{-1})	KIE
ColH$^+$ + HEH_2 -> HEH_2···HCol$^+$ (H-bond)	0.0239	15.0	-
ColD$^+$ + d_1-HEH_2 -> d_1-HEH_2···DCol$^+$ (H-bond)	0.0240	15.1	-
ColH$^+$ + $d2$-HEH_2 -> d_2-HEH_2···HCol$^+$ (H-bond)	0.0238	15.0	-
$\Delta\Delta G$(H-D for N-D)	-0.0001	-0.1	1.16
$\Delta\Delta G$(H-D for C-D)	0	0	0.96
ColH$^+$ + HEH_2 -> HEH_2···HCol$^+$ (π-stack)	0.0251	15.8	
ColD$^+$ + d_1-HEH_2 -> d_1-HEH_2···DCol$^+$ (π-stack)	0.0251	15.8	
ColH$^+$ + $d2$-HEH_2 -> d_2-HEH_2···HCol$^+$ (π-stack)	0.0251	15.7	
$\Delta G(HEH_2) - \Delta G(d_1\text{-}HEH_2)$	0	0	1.00
$\Delta G(HEH_2) - \Delta G(d2\text{-}HEH_2)$	0	0	0.96
ColH$^+$···Col + HEH_2 -> HEH_2···HCol$^+$ + Col (H-bond)	-0.1299	-81.5	
ColD$^+$···Col + d_1-HEH_2 -> d_1-HEH_2···DCol$^+$ + Col (H-bond)	-0.1302	-81.7	
ColH$^+$···Col + $d2$-HEH_2 -> d_2-HEH_2···HCol$^+$ + Col (H-bond)	-0.1300	-81.6	
ΔG(HEH_2···HCol$^+$ (H-bond)) − ΔG(d_1-HEH_2···DCol$^+$ (H-bond))	0.0003	0.1	0.80
ΔG(HEH_2···HCol$^+$ (H-bond)) − ΔG(d_2-HEH_2···HCol$^+$ (H-bond))	0.0001	0.0	0.96
ColH$^+$···Col + HEH_2 -> HEH_2···HCol$^+$ + Col (π-stack)	-0.0846	-53.1	
ColD$^+$···Col + d_1-HEH_2 -> d_1-HEH_2···DCol$^+$ + Col (π-stack)	-0.0846	-53.1	
ColH$^+$···Col + $d2$-HEH_2 -> d_2-HEH_2···HCol$^+$ + Col (π-stack)	-0.0846	-53.1	
ΔG(HEH_2···HCol$^+$ (H-bond)) − ΔG(d_1-HEH_2···DCol$^+$ (π-stack))	-	0.0	0.97
ΔG(HEH_2···HCol$^+$ (H-bond)) − ΔG(d_2-HEH_2···HCol$^+$ (π-stack))	-	0.0	0.96

D.15 References for Appendix D

1. Norcross, B. E.; Clement, G.; Weinstein, M. *J. Chem. Educ.* **1969**. 46, 694.
2. Arashiba, K.; Eizawa, A.; Tanaka, H.; Nakajima, K.; Yoshizawa, K.; Nishibayashi, Y. *Bull. Chem. Soc. Jpn.* **2017**. 90, 1111-1118.
3. Ashida, Y.; Arashiba, K.; Nakajima, K.; Nishibayashi, Y. *Nature* **2019**. 568, 536–540.
4. Johansen, C. M.; Boyd, E. A.; Peters, J. C. *Sci. Adv.* **2022**. 8, eade3510.
5. Golubev, N. S.; Smirnov, S. N.; Schah-Mohammedi, P.; Shenderovich, I. G.; Denisov, G. S.; Gindin, V. A.; Limbach, H. H. *Russ. J. Gen. Chem.* **1997**. 67, 1082–1087.
6. Ren, C.; Ji, G.; Li, X.; Zhang, J. *Chem. – Eur. J.* **2022**. 28, e202201442.
7. Zhang, D.; Wu, L.-Z.; Zhou, L.; Han, X.; Yang, Q.-Z.; Zhang, L.-P.; Tung, C.-H. *J. Am. Chem. Soc.* **2004**. 126, 3440–3441.
8. Li, H.; Liu, Y.; Chiba, S. *Chem. Commun.* **2021**. 57, 6264–6267.
9. Tricoli, V.; Orsini, G.; Anselmi, M. *Phys. Chem. Chem. Phys.* **2012**. 14, 10979–10986.
10. Fulmer, G. R.; Miller A. J. M.;, Sherden, N. H.; Gottlieb, H. E.; Nudelman, A.; Stoltz, B. M.; Bercaw, J. E.; Goldberg, K. I. *Organometallics* **2010**. 29, 2176–2179.
11. Weatherburn, M. W. *Anal. Chem.* **1967**. 39, 971–974.
12. Tshepelevitsh, S.; A. Kütt, M. Lõkov, I. Kaljurand, J. Saame, A. Heering, P. G. Plieger, R. Vianello, I. Leito, *Eur. J. Org. Chem.* **2019**. 2019, 6735–6748.
13. Hatchard, C. G.; Parker, C. A.; Bowen, E. J. *Proc. R. Soc. Lond. Ser. Math. Phys. Sci.* **1997**. 235, 518–536.
14. Lakowicz, J. R., *Principles of Fluorescence Spectroscopy*. **2006** Springer.
15. Espinoza, E. M.; Clark, J. A.; Soliman, J.; Derr, J. B.; Morales, M.; Vullev, V. I. *J. Electrochem. Soc.* **2019**. 166, H3175.

16. Agarwal, R. G.; Coste, S. C.; Groff, B. D.; Heuer, A. M.; Noh, H.; Parada, G. A.; Wise, C. F.; Nichols, E. M.; Warren, J. J.; Mayer, J. M. *Chem. Rev.* **2022**. 122, 1–49.
17. Shen, G.-B.; Fu, Y.-H.; Zhu, X.-Q. *J. Org. Chem.* **2020**. 85, 12535–12543.
18. Bordwell, F. G.; Cheng, J. P.; Harrelson, J. A. *J. Am. Chem. Soc.* **1988**. 110, 1229–1231.
19. Garrido, G.; Rosés, M.; Ràfols, C.; Bosch, E. *J. Solut. Chem.* **2008**. 37, 689–700.
20. Munisamy, T.; Schrock, R. R. *Dalton Trans.* **2011**. 41, 130–137.
21. Pragst, F.; Šantrůček, M. *J. Für Prakt. Chem.* **1987**. 329, 67–80.
22. Rehm, D.; Weller, A. *Isr. J. Chem.* **1970**. 8, 259–271.
23. Tao, J.; Perdew, J. P.; Staroverov, V. N.; Scuseria, G. E. *Phys. Rev. Lett.* **2003**. 91, 146401–146404.
24. Weigend, F. *Phys. Chem. Chem. Phys.* **2006**. 8, 1057–1065.
25. Neese, F.; Wennmohs, F.; Becker, U.; Riplinger, C. *J. Chem. Phys.* **2020**. 152, 224108.
26. Neese, F. *WIREs Comput. Mol. Sci.* **2022**. 12, e1606.
27. Staroverov, V. N.; Scuseria, G. E.; Tao, J.; Perdew, J. P. *J. Chem. Phys.* **2003**. 119, 12129–12137.
28. Czochralska, B.; Lindqvist, L. *Chem. Phys. Lett.* **1983**. 101, 297–299.
29. Anne, A.; Hapiot, P.; Moiroux, J.; Neta, P.; Saveant, J. M. *J. Am. Chem. Soc.* **1992**. 114, 4694–4701.
30. Zielonka, J.; Marcinek, A.; Adamus, J.; Gębicki, J *J. Phys. Chem. A* **2003**. 107, 9860–9864.

Appendix E

Supplementary Information for Chapter 6

E.1.1 Materials and Methods

All manipulations were carried out using standard Schlenk or glovebox techniques under an N_2 atmosphere. Solvents were deoxygenated and dried by thoroughly sparging with N_2, followed by passage through an activated alumina column in a solvent purification system by SG Water, USA LLC. Nonhalogenated solvents were tested with sodium benzophenone ketyl in tetrahydrofuran (THF) to confirm the absence of oxygen and water. Deuterated solvents were purchased from Cambridge Isotope Laboratories, Inc.

Phenyl acrylate was purchased from Ambeed, degassed, and used without further purification. Cyclohexanedione monoethylene ketal (**1**) was purchased from TCI and used without further purification. All bases (DBU, Et_3N, pyridine, 2,6-lutidine) were purchased from Sigma Aldrich and distilled prior to use. $Sm(OTf)_3$, $Gd(OTf)_3$, and MgI_2 were purchased from Sigma–Aldrich. $Ir(ppy)_2(dtbbpy)[PF_6]$ was purchased from Strem and used without further purification. 3DPA2FBN (2,4,6-tris(diphenylamino)-3,5-difluorobenzonitrile) was purchased from Ambeed and used without further purification. 9,10-dihydroacridine was purchased from Combi-blocks and purified by sublimation prior to use. Hexamethylphosphoramide, ethylene glycol, and 2-(2-(2-methoxyethoxy)ethoxy)ethan-1-ol were purchased from Sigma Aldrich and degassed. Tetraheptylammonium iodide was purchased from TCI and dried at 100°C under dynamic vacuum for 16 hours. Tetrabutylammonium bromide was acquired from Strem and then dried by heating to 85°C for 48 hours under dynamic vacuum using P_2O_5 as a desiccant. 1-Butyl-1-methylpiperidinium (BMPipTFSI) was purchased from TCI chemicals and used without further purification.

$SmI_2(THF)_2$,[1] $phenH_2$,[2] BINAPO,[3] aminodiol (L*),[4] and [LutH]TFSI[5] were synthesized following literature procedures. HEH_2[6] synthesized following literature procedure and then dried by heating to 80 °C for 24 hours under dynamic vacuum using P_2O_5 as a desiccant.

The 2-MeTHF used was dried extensively prior to use in ketyl-olefin coupling experiments. Inhibitor-free solvent was refluxed over CaH_2 for 24 hours (under N_2 atmosphere) and distilled into a Strauss flask. This flask was brought into the glovebox,

where NaK was added, and the solvent was stirred for 24 hours. The solvent was then vacuum transferred into a fresh Strauss flask and stored over activated sieves.

E.1.2 Physical Methods

NMR: Nuclear Magnetic Resonance (NMR) measurements were recorded with a Varian 400 MHz spectrometer. ^{1}H NMR chemical shifts are reported in ppm relative to tetramethylsilane, using ^{1}H resonances from residual solvent as internal standards.

UV-Vis: Ultraviolet-visible (UV-vis) absorption spectroscopy measurements were collected with a Cary 50 UV-vis spectrophotometer using a 1 cm path-length quartz cuvette. All samples had a blank sample background subtraction applied. Temperature regulation for UV-Vis measurements was carried out with a Unisoku cryostat.

Electrochemistry: All electrochemical experiments were conducted using a CH instruments 600B electrochemical analyzer. A nonaqueous $Ag^{+/0}$ reference electrode (BASi) consisting of a silver wire immersed in 5 mM AgOTf in DME containing 0.2 M $^{n}Bu_4NPF_6$ separated from the working solution by a CoralPor® frit was used for all experiments. All reported potentials are referenced to the ferrocenium/ferrocene ($Fc^{+/0}$) couple used as an external standard. All CVs were carried out in an N_2-filled glovebox in a 20 mL scintillation vial fitted with a septum cap containing punched-out holes for insertion of electrodes. A glassy carbon disk (3 mm diameter) was used as the working electrode for all CVs. It was freshly polished with 1, 0.3, and 0.05 μm alumina powder water slurries, rinsed with water and acetone, and dried before use. A platinum wire was used as the auxiliary electrode for CVs. CVs are plotted using IUPAC convention. Unless otherwise noted, IR compensation was applied, accounting for 85% of the total resistance.

E.2. Catalytic ketone-olefin coupling reactions

E.2.1.1 Standard procedure in the absence of Ir-photocatalyst

In the glovebox, HEH_2 (40.4 mg, 160 μmol) was added as a solid to a Schlenk flask. 2-MeTHF (0.5 mL) was added to the flask. A freshly prepared stock solution of $SmI_2(THF)_2$ in 2-MeTHF (2.2 mg per mL, 4 mM) was added to the flask (1 mL added). A stock solution of the remaining organics: ketone (12.6 mg per mL; 80 mM), phenyl acrylate (22 μL per mL; 160 mM), and (when used) base, was prepared, and 0.5 mL was added to the reaction flask.

The color of SmI_2 (purple) rapidly changes to yellow upon the addition of the organic reagents. The reaction flask is sealed and brought out of the glovebox, where it is irradiated by two H160 PR Kessil™ 440 nm Blue LED lamps for 90 minutes in a water bath in a reflective dewar. The reaction was continuously stirred (1200 rpm). The temperature of the water bath was monitored and did not exceed 25 °C during the reaction.

Following completion of the reaction, the flask was opened to air, and 2 mL Et_2O was added. The contents of the flask was filtered through a silica plug into a vial containing a known amount of 1,3,5-trimethoxybenzene (TMB; ~7 mg). The reaction flask was washed with additional Et_2O (2x1 mL), and the washes were passed through the silica plug into the vial. The solvent was removed *in vacuo* and the products were taken up in $CDCl_3$ and analyzed by ^1H NMR integrating against the TMB standard.

Lactone product (**2**; 1,4,9-trioxadispiro[4.2.48.25]tetradecan-10-one) is detected by ^1H NMR with features matching literature spectra (Figure E.4).

Note: This reaction is very sensitive to solvent drying, and the CaH2/NaK method laid out in the general considerations is required. Similarly, the HEH2 must be dried as described. The reaction is sensitive to both water and air, as shown in Table E.2.

E.2.1.2 Standard procedure with an Ir-photocatalyst

In the glovebox, $Ir(ppy)_2(dtbbpy)[PF_6]$ (0.36 mg, 0.4 μmol) was dissolved in THF and added to a Schlenk flask, and the solvent was removed *in vacuo*, depositing a thin film. Following this HEH_2, $SmI_2(THF)_2$ and organics were added as described in **S2.1.1**

E.2.2 Yields for ketone-olefin coupling reactions

Table E.1. Yields of individual catalytic experiments.

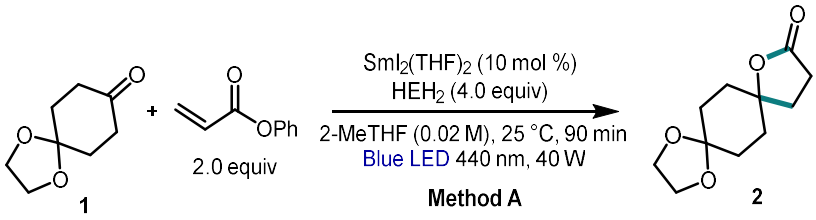

Entry	Variation from standard conditions	Yield lactone	Ketone recovery
A1	None	81%	14%
A2	None	74%	13%
A3	None	75%	15%
A4	None	73%	14%
Entry 1, Table 6.1A	None	76±3%	14±1%
A5	No light	5%	89%
A6	No light	4%	93%
Entry 2, Table 6.1A	No light	4±1%	91±2%
A7	No Sm	<1%	102%
A8	No Sm	<1%	100%
Entry 3, Table 6.1A	No Sm	<1%	101±1%
A9	$SmOTf_3$ (10 mol%) MgI_2 (50 mol%) instead of SmI_2	59%	41%
A10	$SmOTf_3$ (10 mol%) MgI_2 (50 mol%) instead of SmI_2	60%	42%
Entry 4, Table 6.1A	$SmOTf_3$ (10 mol%) MgI_2 (50 mol%) instead of SmI_2,	60±1%	41±1%
A11	$GdOTf_3$ (10 mol%) MgI_2 (50 mol%) instead of SmI_2,	<1%	101%
A12	$GdOTf_3$ (10 mol%) MgI_2 (50 mol%) instead of SmI_2,	<1%	95%
Entry 5, Table 6.1A	$GdOTf_3$ (10 mol%) MgI_2 (50 mol%) instead of SmI_2	<1%	98±3%
A13	2 equiv pyr	72%	8
A14	2 equiv pyr	72%	10
Entry 6, Table 6.1A	2 equiv pyr	72±1%	9±1%
A15	2 equiv Et_3N	6%	79%
A16	2 equiv Et_3N	5%	72%
Entry 8, Table 6.1A	2 equiv Et_3N	5±1%	75±4%
A17	$phenH_2$ instead of HEH_2	<1%	37%
A18	$phenH_2$ instead of HEH_2	<1%	39%
Entry 9, Table 6.1A	$phenH_2$ instead of HEH_2	<1%	38±1%
A19	15 min reaction time	29%	63%
A20	15 min reaction time	29%	65%
Entry 10, Table 6.1A	15 min reaction time	29±1%	64±1%
A21	Ethyl acrylate instead of phenyl acrylate	36%	46%
A22	Ethyl acrylate instead of phenyl acrylate	25%	52%
Entry 11, Table 6.1A	Ethyl acrylate instead of phenyl acrylate	31±5%	49±3%

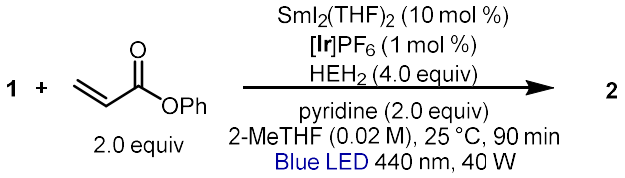

entry 10

Entry	Variation	Yield lactone	Ketone recovery
B1	None	87%	7%
B2	None	89%	6%
B3	None	89%	5%
B4	None	89%	4%
Entry 1, Table 6.1B	None	88.6±0.8%	5.7±1.1%
B5	No light	4%	94%
B6	No light	4%	92%
Entry 2, Table 6.1B	No light	4±1%	93±1%
B7	No Sm	<1%	89%
B8	No Sm	<1%	82%
Entry 3, Table 6.1B	No Sm	0%	86±3%
B9	$SmOTf_3$ (10 mol%) MgI_2 (50 mol%) instead of SmI_2	85%	14%
B10	$SmOTf_3$ (10 mol%) MgI_2 (50 mol%) instead of SmI_2	84%	13%
Entry 4, Table 6.1B	$SmOTf_3$ (10 mol%) MgI_2 (50 mol%) instead of SmI_2	85±1%	14±1%
B11	$GdOTf_3$ (10 mol%) MgI_2 (50 mol%) instead of SmI_2	6%	92%
B12	$GdOTf_3$ (10 mol%) MgI_2 (50 mol%) instead of SmI_2	6%	85%
Entry 5, Table 6.1B	$GdOTf_3$ (10 mol%) MgI_2 (50 mol%) instead of SmI_2	6±1%	88±4%
B13	No base	84%	8%
B14	No base	80%	8%
Entry 7, Table 6.1B	No base	82±2%	8±1%
B15	Et_3N instead of pyridine	13%	69%
B16	Et_3N instead of pyridine	17%	73%
Entry 8, Table 6.1B	Et_3N instead of pyridine	15±2%	71±2%
B17	$phenH_2$ instead of HEH_2	78%	0
B18	$phenH_2$ instead of HEH_2	76%	2
Entry 9, Table 6.1B	$phenH_2$ instead of HEH_2	77±1%	1±1%
B19	15 min reaction time	57%	43%
B20	15 min reaction time	66%	32%
Entry 10, Table 6.1B	15 min reaction time	61±4%	38±6%
B19	Ethyl acrylate instead of phenyl acrylate	59%	11%
B20	Ethyl acrylate instead of phenyl acrylate	56%	12%
Entry 11, Table 6.1B	Ethyl acrylate instead of phenyl acrylate	58±2%	12±1%

E.2.2.1 Quantification of additional organic products under standard conditions

While the work-up and detection method should account for ~100% of the ketone starting material, the limited solubility of HEH_2 in Et_2O and $CDCl_3$ and the low boiling point of phenyl acrylate result in some additional errors in these product yields. Figure E.1 presents approximate yields as integrated against a TMB standard for a reaction where care was taken to evaporate minimal phenyl acrylate.

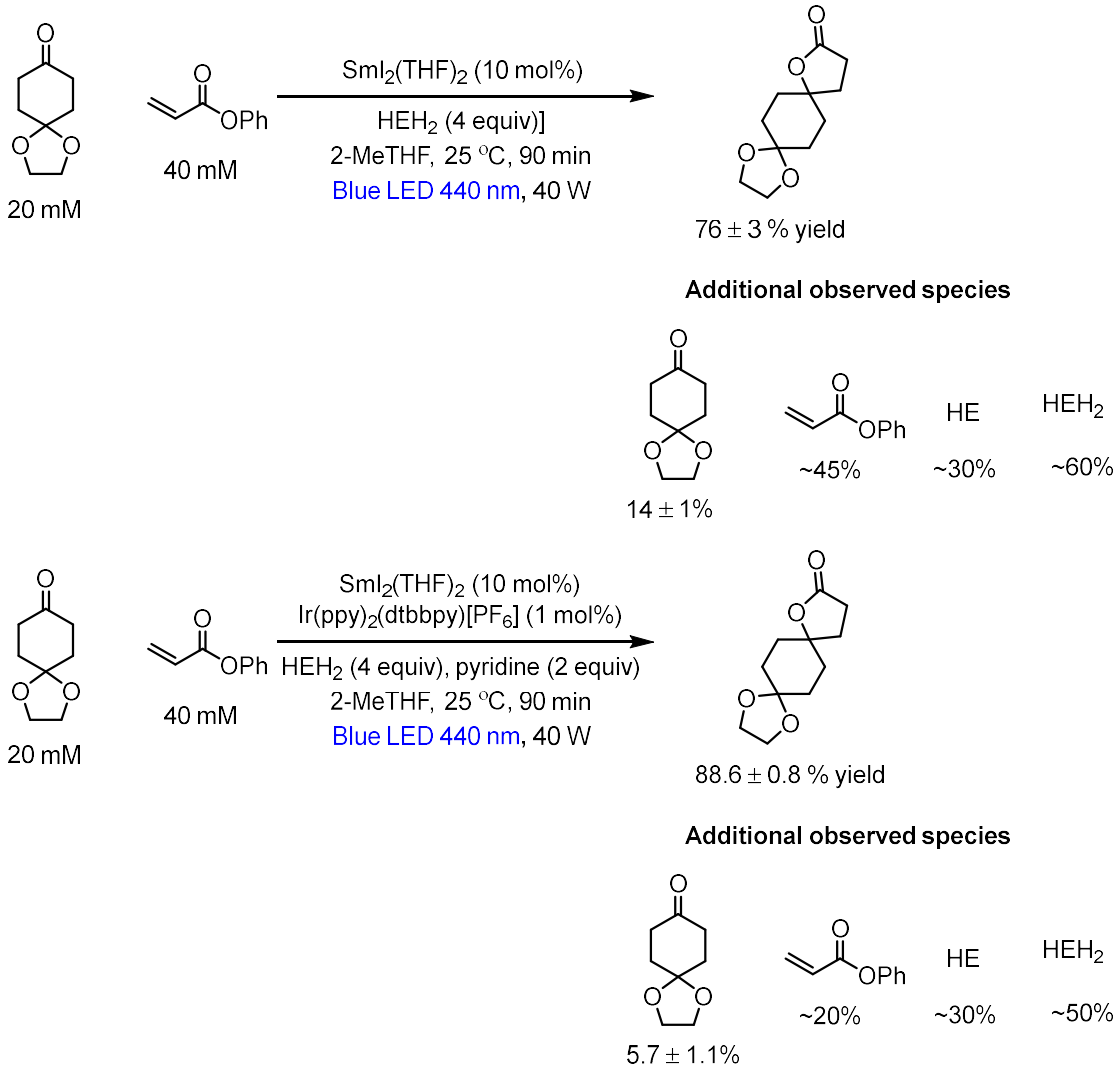

Figure E.1. Approximate yields of additional products under conditions without and with Iridium.

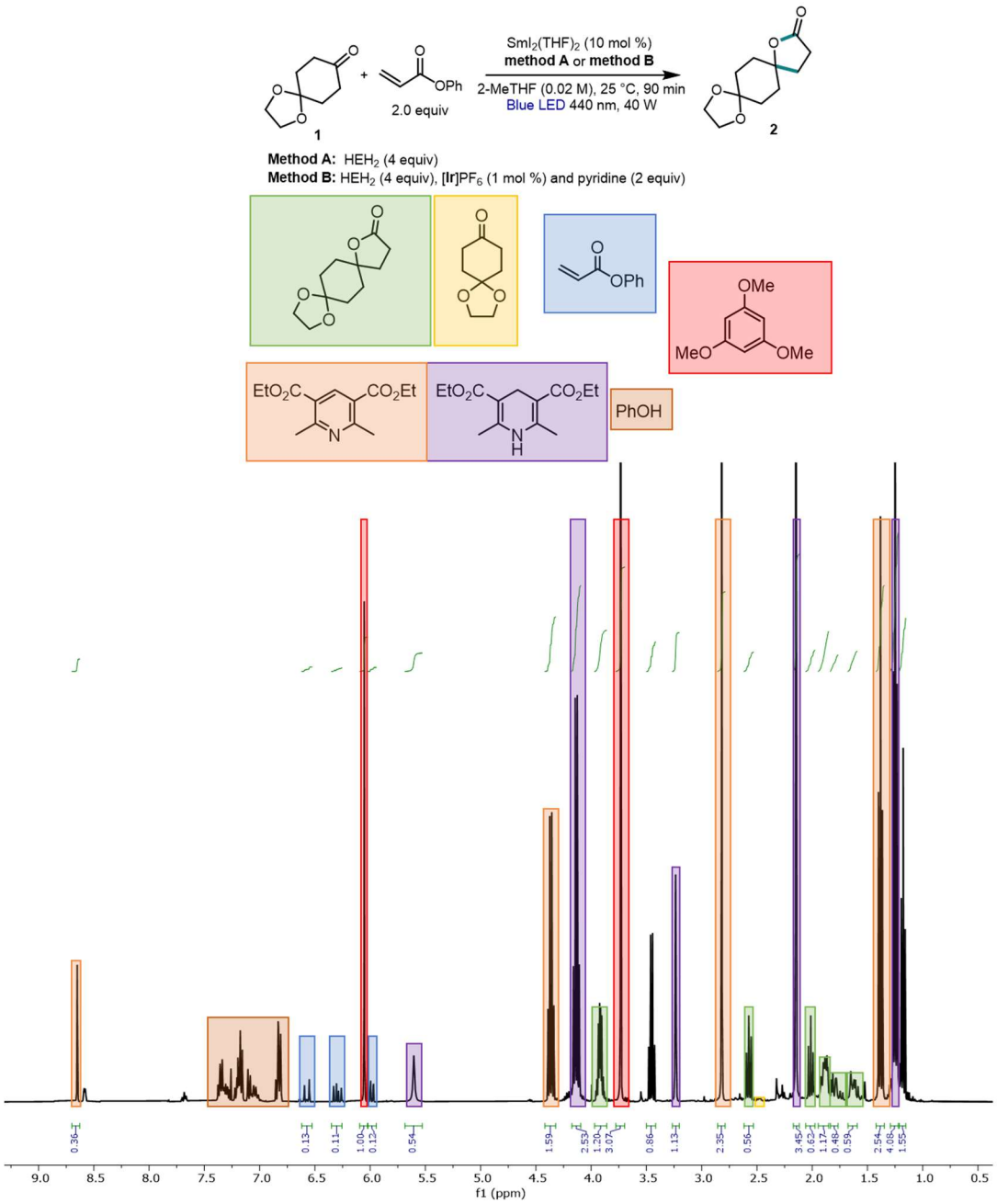

Figure E.2. ^{1}H NMR ($CDCl_3$ 7.26 ppm) of a typical crude reaction mixture reacting 1 with phenyl acrylate to produce 2 with key products/starting materials highlighted as indicated.

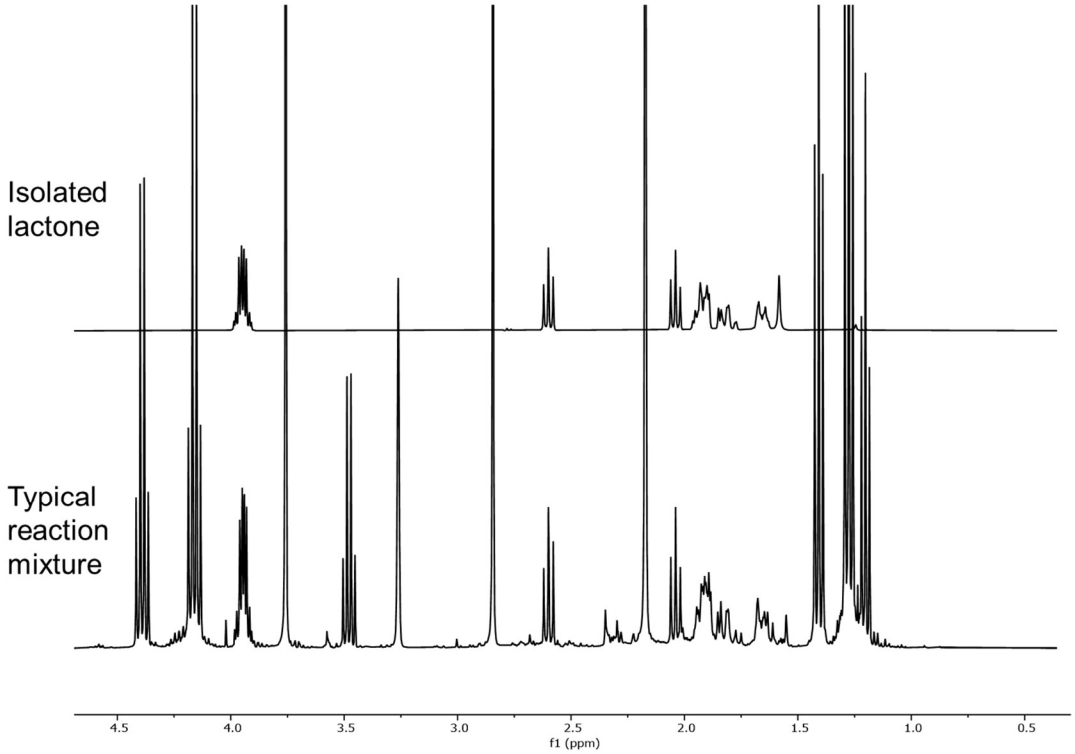

Figure E.3. Comparison of ^{1}H NMR of typical reaction spectra with authentic lactone product. ^{1}H NMR (400 MHz, $CDCl_3$): δ 4.00 – 3.90 (m, 4H), 2.60 (t, J = 8.5 Hz, 2H), 2.04 (t, J = 8.5 Hz, 2H), 1.97 – 1.88 (m, 4H), 1.82 (ddd, J = 17.5, 10.9, 4.0 Hz, 2H), 1.70 – 1.62 (m, 2H).

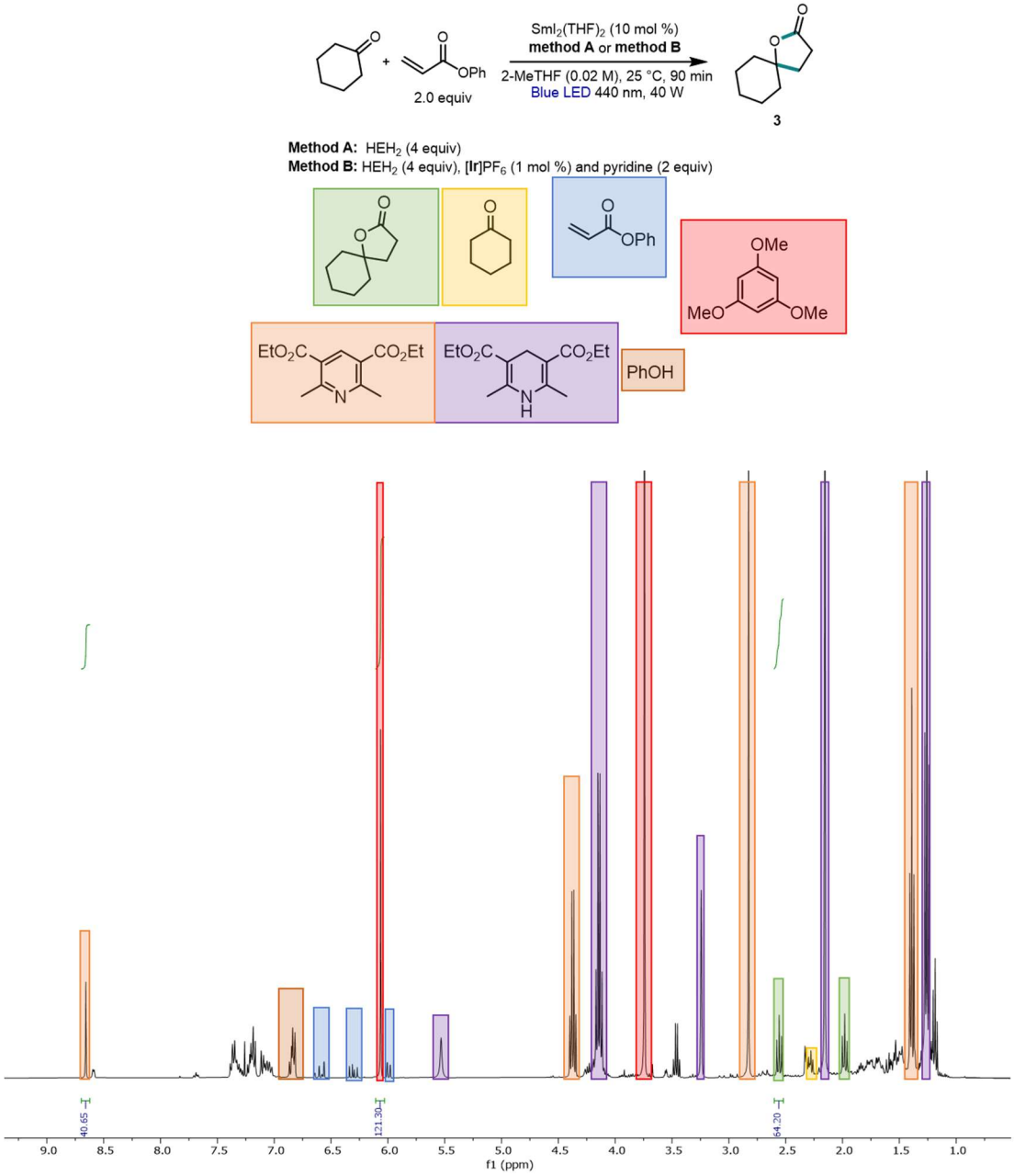

Figure E.4. ^{1}H NMR ($CDCl_3$ 7.26 ppm) of a typical crude reaction mixture reacting cyclohexanone with phenyl acrylate to produce 3 with key products/starting materials highlighted as indicated. The lactone product 3 matched previous reports.[5]

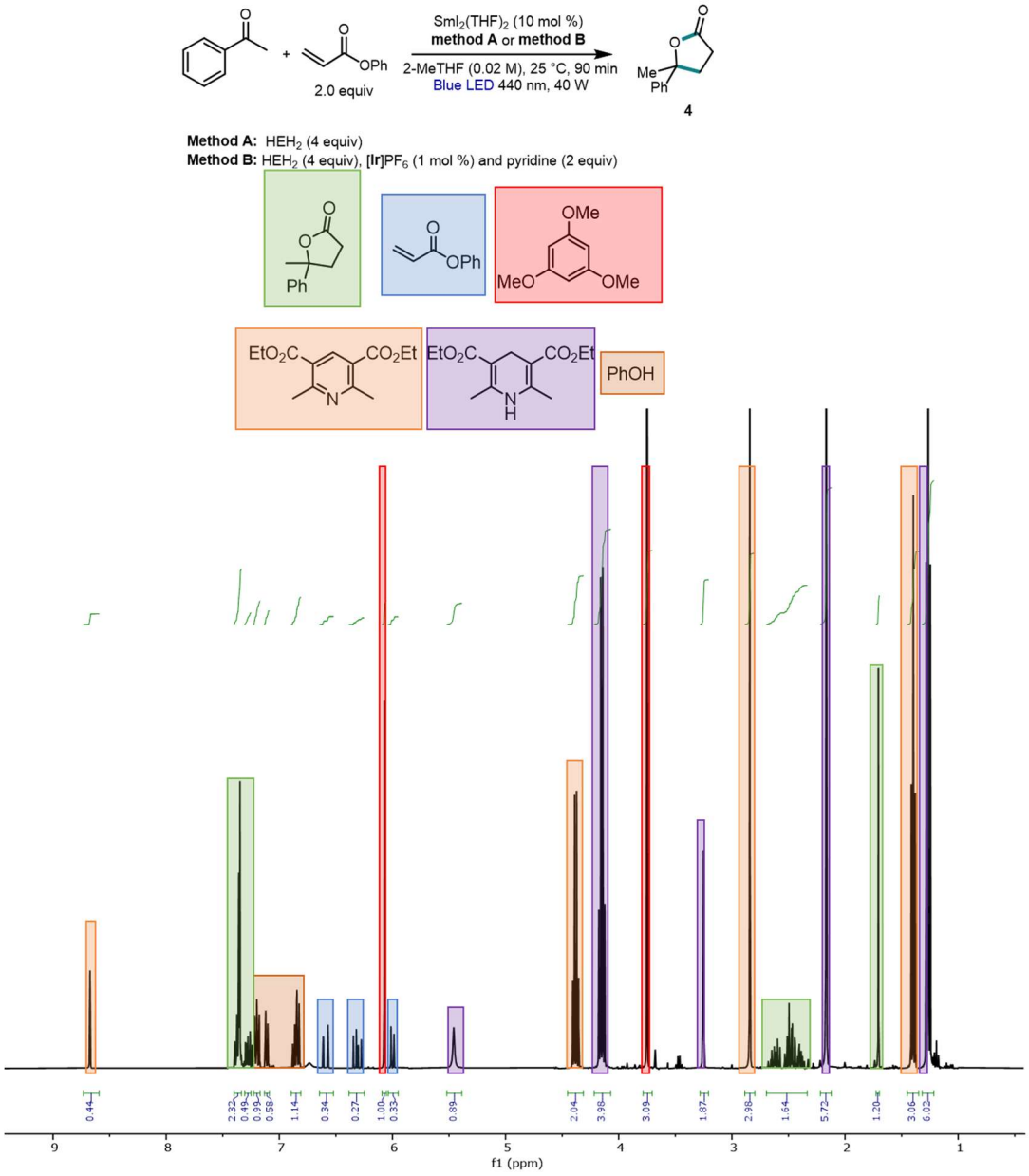

Figure E.5. ^{1}H NMR ($CDCl_3$ 7.26 ppm) of a typical crude reaction mixture reacting acetophenone with phenyl acrylate to produce 4 with key products/starting materials highlighted as indicated. The lactone product 4 matched previous reports.[5]

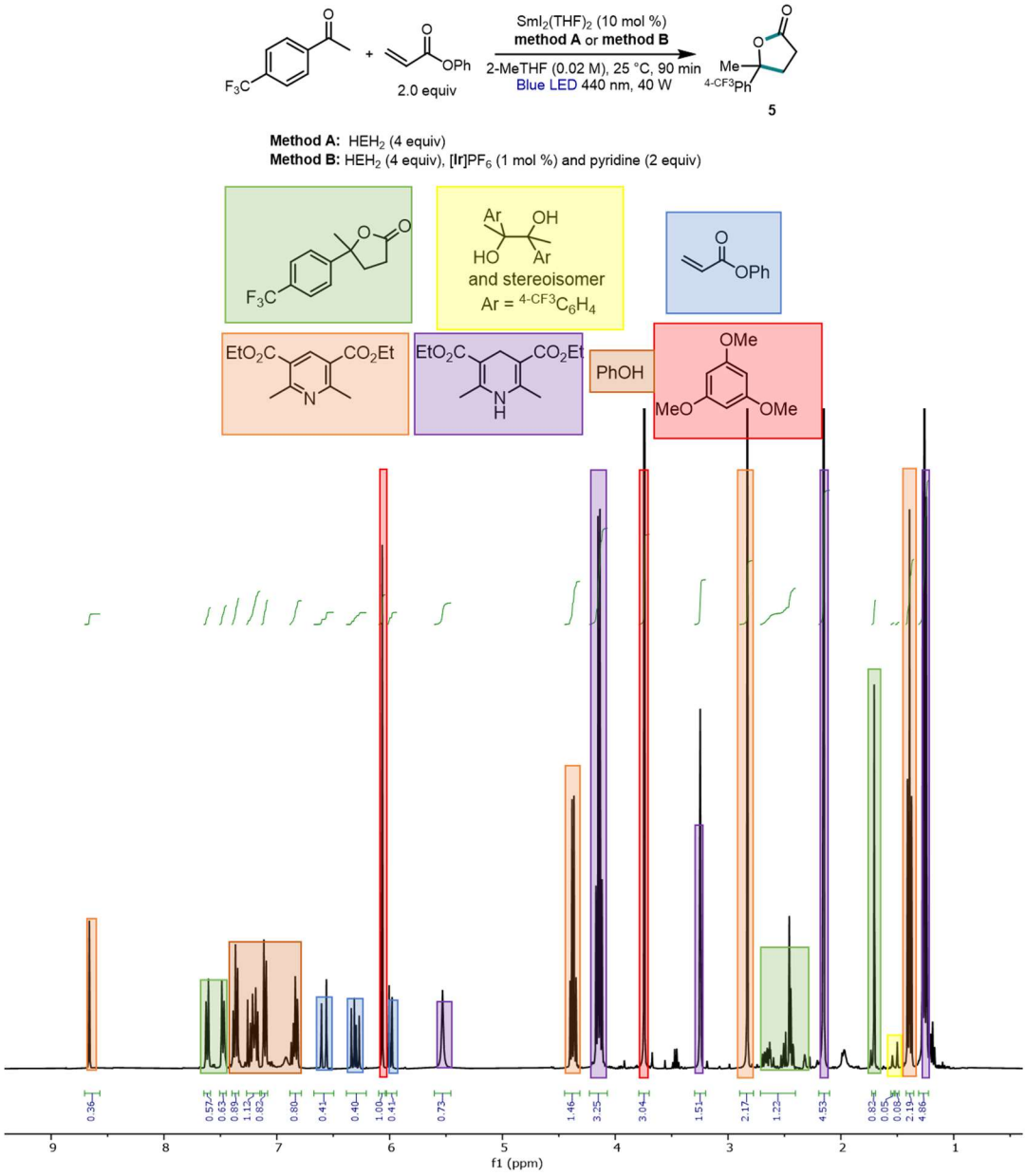

Figure E.6. ^{1}H NMR ($CDCl_3$ 7.26 ppm) of a typical crude reaction mixture reacting 4-trifluoromethyl acetophenone with phenyl acrylate to produce 5 with key products/starting materials highlighted as indicated. The lactone product 5 matched previous reports.[5]

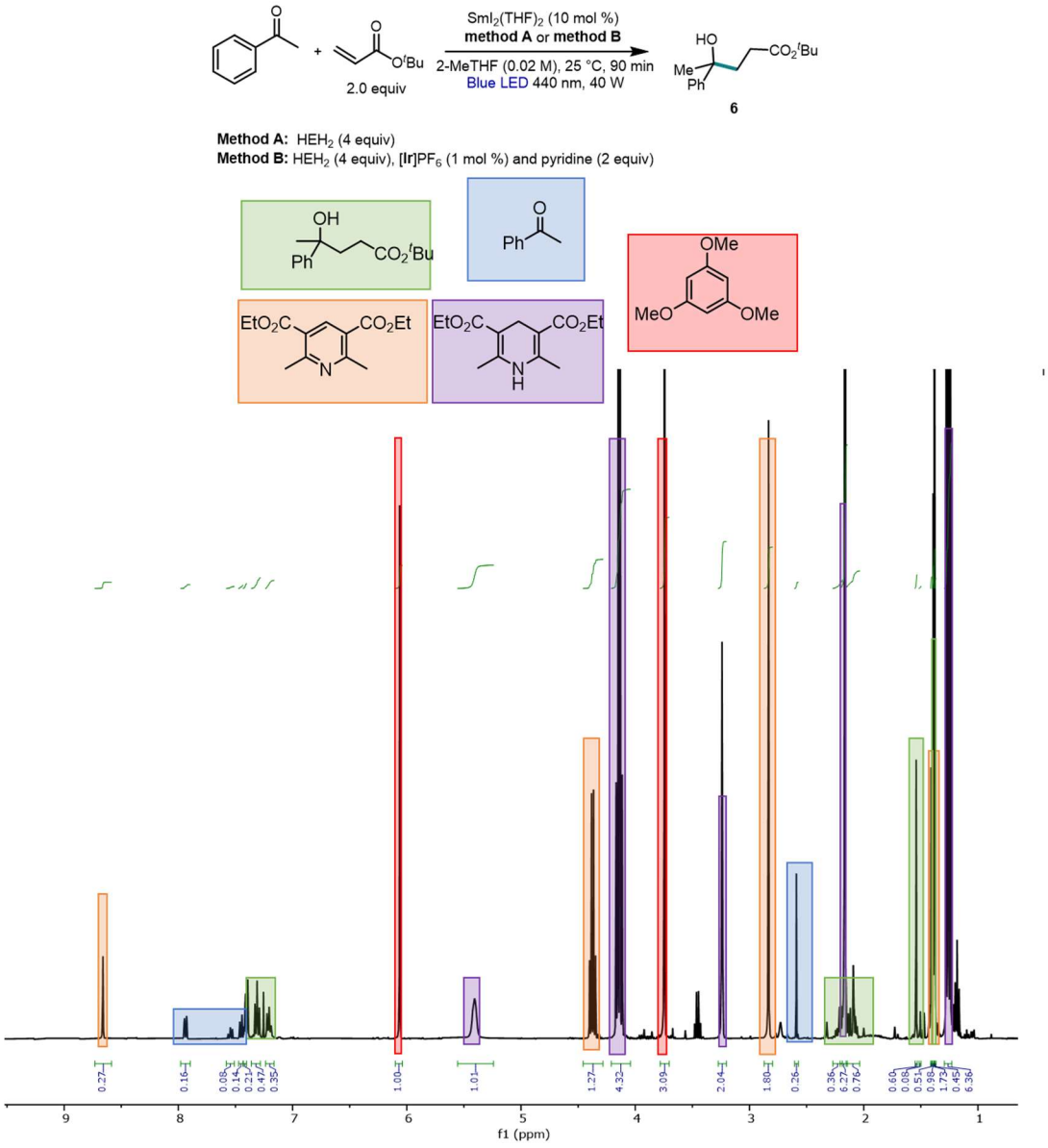

Figure E.7. ^{1}H NMR ($CDCl_3$ 7.26 ppm) of a typical crude reaction mixture reacting acetophenone with *tert*-butyl acrylate to produce 6 with key products/starting materials highlighted as indicated.

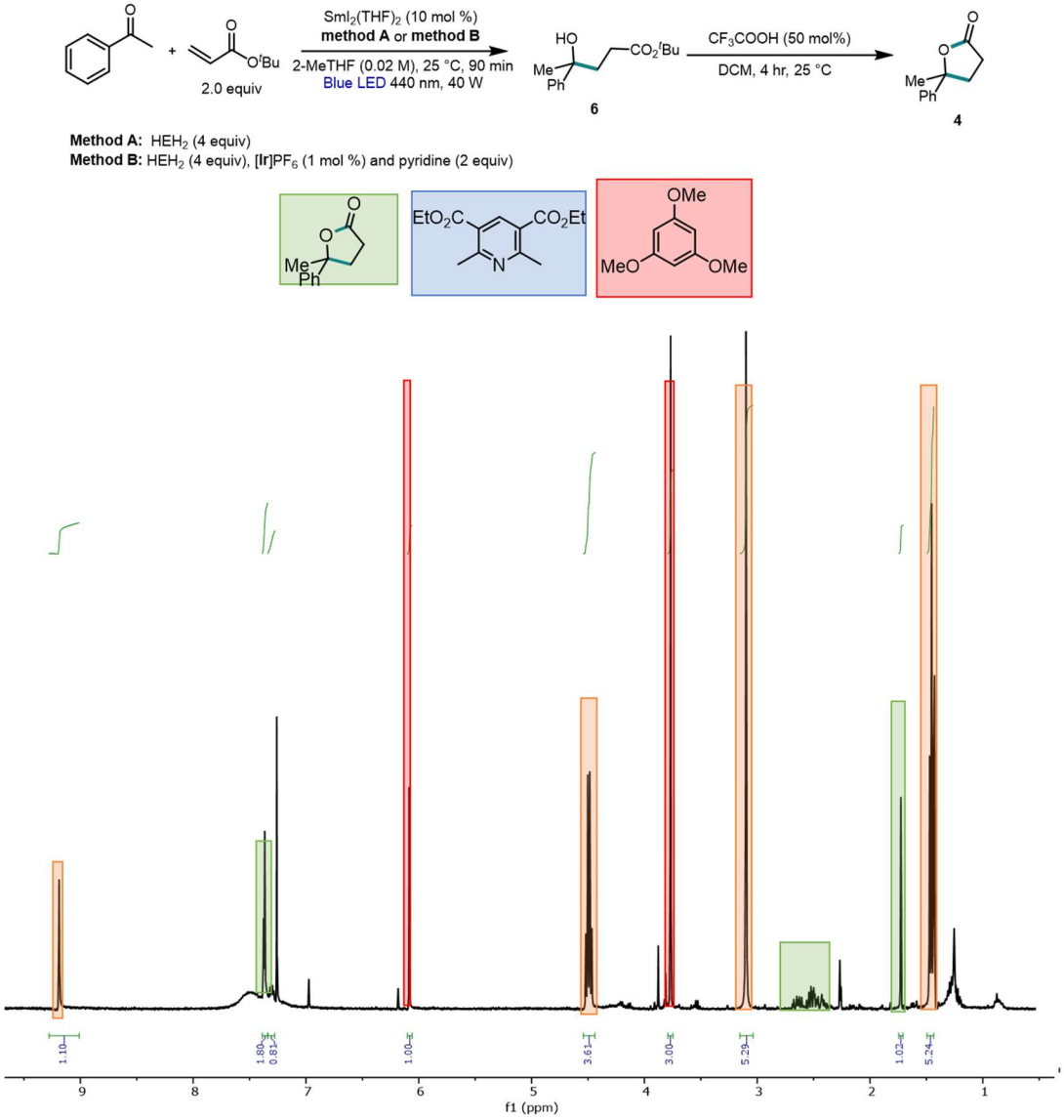

Figure E.8. ^{1}H NMR ($CDCl_3$ 7.26 ppm) of a typical crude reaction mixture reacting acetophenone with *tert*-butyl acrylate to produce 4 with key products/starting materials highlighted as indicated. The lactone product 4 matched previous reports.[5]

E.2.3 Additional catalysis tables

Table E.2. Additional catalytic experiments of ketone-acrylate coupling.

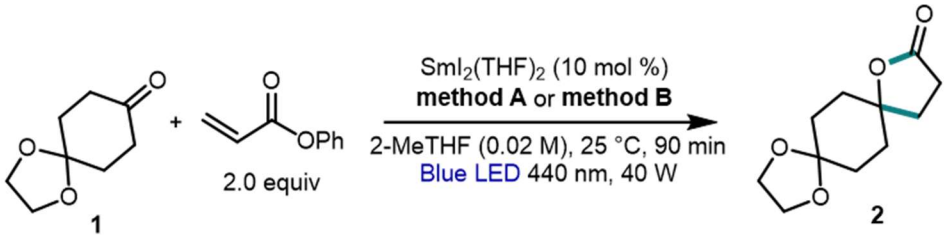

Method A: HEH_2 (4 equiv)
Method B: HEH_2 (4 equiv), **[Ir]**PF_6 (1 mol %) and pyridine (2 equiv)

Entry	Deviation	Yield (%) Method A	Yield (%) Method B
1	None	76	89
2	5.0 mol% Sm	58	79
3	2.5 mol% Sm	–	41
4	2 mL air added	4	32
5	1 equiv H_2O added	28	8
6	2 equiv Lutidine added (A)/instead of pyridine (B)	70	82
7	THF solvent	47	22
8	DBU instead of pyridine (B)	–	9
9	0 °C, 3 h	–	77
10	1 mmol scale, 0.05 M, 2 equiv HEH_2	–	89
11	1 mmol scale, 0.1 M, 2 equiv HEH_2, 6 h	–	61

Entry	12[a]	13[a]	14[b,c]
Product	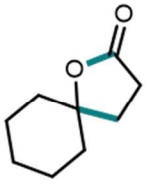	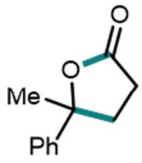	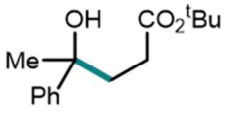
	3	4	6
method A:	30%	73%	36%
method B:	64%	83%	32%

[a]Ethyl acrylate instead of phenyl acrylate.
[b]*tert*-butyl acrylate instead of phenyl acrylate.
[c]1 equiv *tert*-butanol added.

Table E.3. Yields for pinacol coupled products in selected aryl ketone cross-coupling reactions.

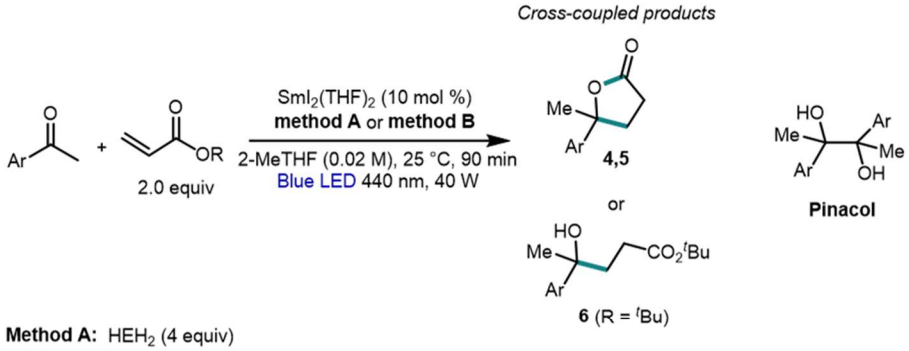

Method A: HEH_2 (4 equiv)
Method B: HEH_2 (4 equiv), **[Ir]**PF_6 (1 mol %) and pyridine (2 equiv)

Entry (Entry in Table 6.1)	Coupling partners and deviations	Product	Yield (%) Cross-coupling product Method A	Yield (%) pinacol product Method A (meso:dr)	Yield (%) Cross-coupling product Method B	Yield (%) pinacol product Method B (meso:dr)
1 (entry 13)	Ar = Ph, R = Ph	**4**	>95	–	90	8 (1:1)
2 (entry 14)	Ar = $^{4\text{-CF3}}$Ph, R = Ph	**5**	77	16 (0.6:1)	49	50 (0.8:1)
3 (entry 15)	Ar = Ph, R = ^{t}Bu	**6**	43	4 (0.4:1)	29	45 (0.7:1)
4	Ar = $^{4\text{-CF3}}$Ph, R = Ph; No Sm	–	–	15 (1:1)	–	100 (1:1)

Table E.4. Additional screening interrogating the effect of quencher (HEH_2, MeacrH, $phenH_2$, or Et_3N) on catalysis. All results with error bars represent the average and standard deviation of a minimum of two experiments.

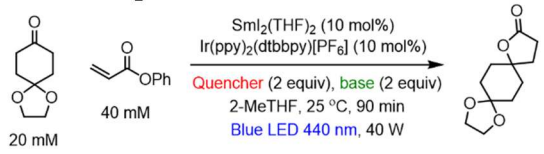

Entry	Quencher, base	Yield (%)	Recovered SM (%)
1	HEH_2, pyridine	64	~40
2	MeacrH, pyridine	52	0
3	HEH_2, lutidine	68	30
4	MeacrH, lutidine	45	~60
5	$phenH_2$, lutidine	71±2	17±2
6	Et_3N, Et_3N (1 mol% Ir)	8±1	70±2

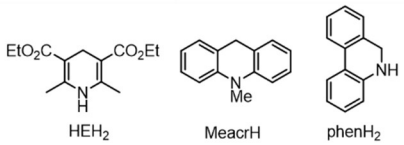

Table E.5. Additional screening interrogating the effects of additives (MgI_2 or [PyrH]TFSI) on catalysis.

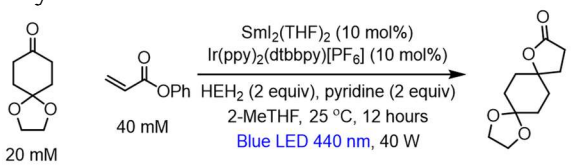

Entry	Variation	Yield (%)	Recovered SM (%)
1	None	64	~40
2	[PyrH]TFSI (2 equiv)	0	83
3	MgI_2 (1 equiv)	52	24
4	MgI_2 (1 equiv)/[PyrH]TFSI (2 equiv)	52	78
5	MeAcrH not HEH_2	52	0
6	MeAcrH instead of HEH_2; [PyrH]TFSI (2 equiv)	18	64
7	MeAcrH instead of HEH_2; MgI_2 (1 equiv)	25	39
8	MeAcrH instead of HEH_2; MgI_2 (1 equiv)/[PyrH]TFSI (2 equiv)	18	55

Table E.6. Additional screening interrogating the effect of HEH_2 loading on catalysis. All results with error bars represent the average and standard deviation of a minimum of two experiments.

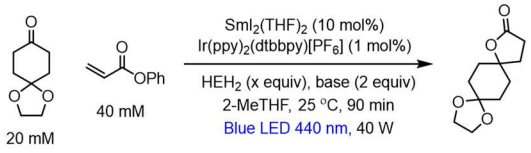

Entry	X equiv HEH_2, base	Yield (%)	Recovered SM (%)
1	2 equiv HEH_2, pyridine	70±3	4±1
2	4 equiv HEH_2, pyridine	89±1	6±1
3	1.2 equiv HEH_2, lutidine	46±6	48±6
4	2 equiv HEH_2, lutidine	68±3	22±2
5	4 equiv HEH_2, lutidine	82±1	12±1

E.3 UV-vis experiments

E.3.1 UV-vis detection of Sm interaction with dihydropyridines

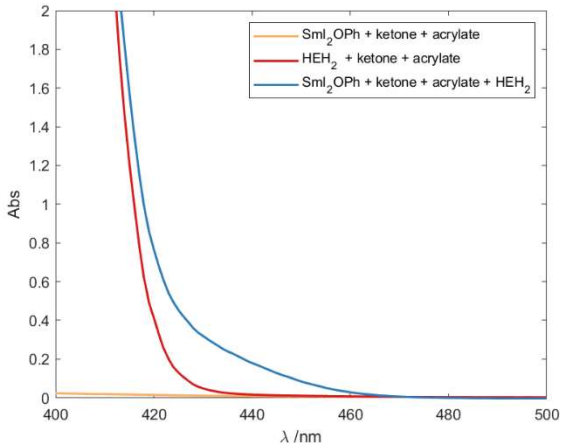

Figure E.9. Comparison of UV-vis traces (in a 1 mm path-length cuvette) of SmI_2 (2 mM) + ketone (20 mM) + acrylate (40 mM) (yellow trace, *in situ* forms colorless $Sm^{III}I_2(OPh)$); HEH_2 (80 mM) + ketone (20 mM) + acrylate (40 mM) (red trace); and SmI_2 (2 mM) + HEH_2 (80 mM) + ketone (20 mM) + acrylate (40 mM) (blue trace). All spectra collected in 2-MeTHF. Observed red-shift of the HEH_2 absorption in the presence of Sm^{III} is consistent with an interaction between species.

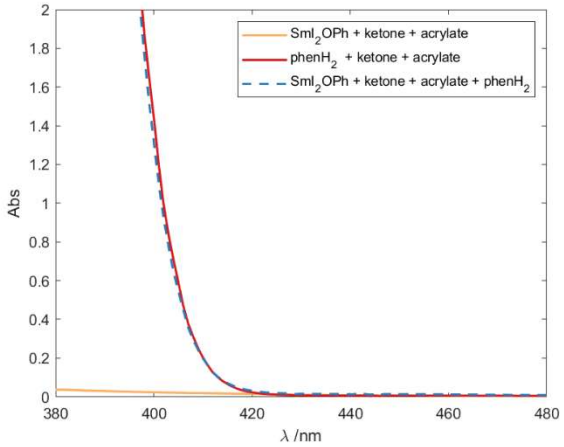

Figure E.10. Comparison of UV-vis traces (in a 1 mm path-length cuvette) of SmI_2 (2 mM) + ketone (20 mM) + acrylate (40 mM) (yellow trace, *in situ* forms colorless $Sm^{III}I_2(OPh)$); $phenH_2$ (80 mM) + ketone (20 mM) + acrylate (40 mM) (red trace); and SmI_2 (2 mM) + $phenH_2$ (80 mM) + ketone (20 mM) + acrylate (40 mM) (blue dashed trace).

All spectra collected in 2-MeTHF. Overlay suggests little to no interaction between Sm^{III} and $phenH_2$.

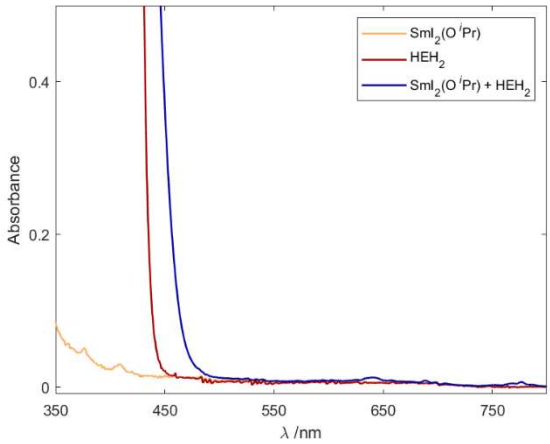

Figure E.11. Comparison of UV-vis traces (in a 1 cm path-length cuvette) of $Sm(O^iPr)_3$ (2 mM), ^{n}Hep$_4$NI (6 mM), and HTFSI (3 mM) (yellow trace, *in situ* forms colorless $Sm^{III}I_2(O^iPr)$); HEH_2 (60 mM) (red trace); and $Sm(O^iPr)_3$ (2 mM), ^{n}Hep$_4$NI (6 mM), HTFSI (3 mM), and HEH_2 (60 mM) (blue trace). All spectra collected in THF. The observed red-shift suggests interaction between Sm^{III} and HEH_2.

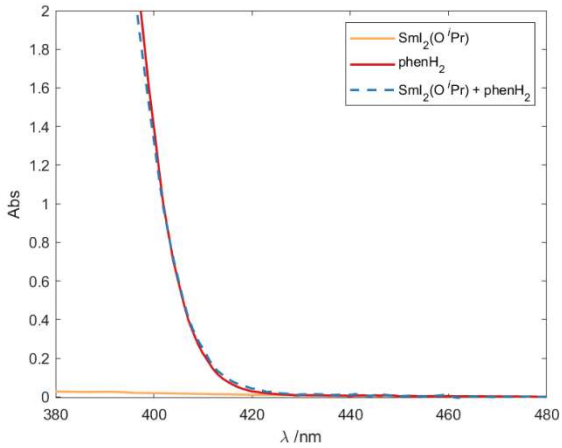

Figure E.12. Comparison of UV-vis traces (in a 1 mm path-length cuvette) of $Sm(O^iPr)_3$ (2 mM), ^{n}Hep$_4$NI (6 mM), [LutH]TFSI (3 mM) (yellow trace, *in situ* forms colorless $Sm^{III}I_2(O^iPr)$); $phenH_2$ (60 mM) (red trace); and $Sm(O^iPr)_3$ (2 mM), ^{n}Hep$_4$NI (6 mM), [LutH]TFSI (3 mM), and $phenH_2$ (60 mM) (dashed blue trace). All spectra collected in THF. Overlay suggests little to no interaction between Sm^{III} and $phenH_2$.

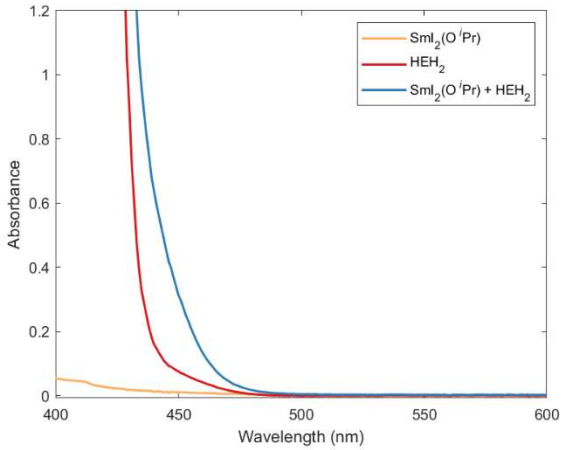

Figure E.13. Comparison of UV-vis traces (in a 1 cm path-length cuvette) of $Sm(O^iPr)_3$ (2 mM), ^{n}Hep$_4$NI (6 mM), [LutH]TFSI (3 mM) (yellow trace, *in situ* forms colorless $Sm^{III}I_2(O^iPr)$); HEH_2 (60 mM) (red trace); and $Sm(O^iPr)_3$ (2 mM), ^{n}Hep$_4$NI (6 mM), [LutH]TFSI (3 mM), and HEH_2 (60 mM) (blue trace). All spectra collected in THF. The observed red-shift suggests interaction between Sm^{III} and HEH_2.

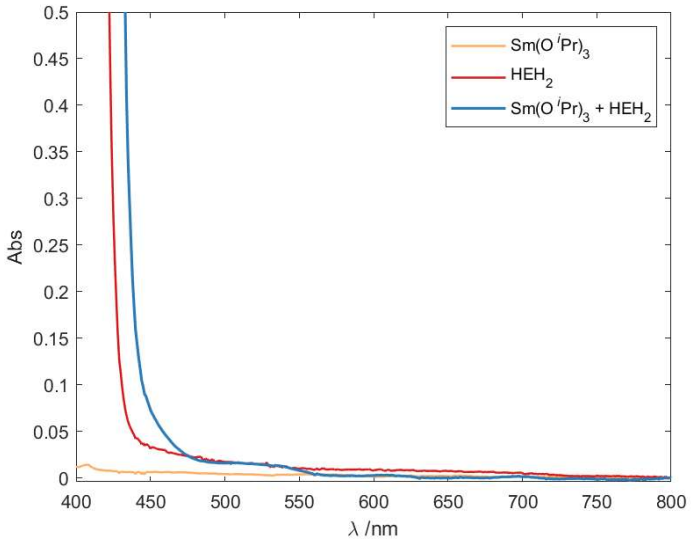

Figure E.14. Comparison of UV-vis traces (in a 1 cm path-length cuvette) of $Sm(O^iPr)_3$ (2 mM), ^{n}Hep$_4$NI (6 mM), (yellow trace, *in situ* is still colorless $Sm^{III}(O^iPr)_3$); HEH_2 (60 mM) (red trace); and $Sm(O^iPr)_3$ (2 mM), ^{n}Hep$_4$NI (6 mM), and HEH_2 (60 mM) (blue trace). All spectra collected in THF. The observed red-shift suggests interaction between Sm^{III} and HEH_2.

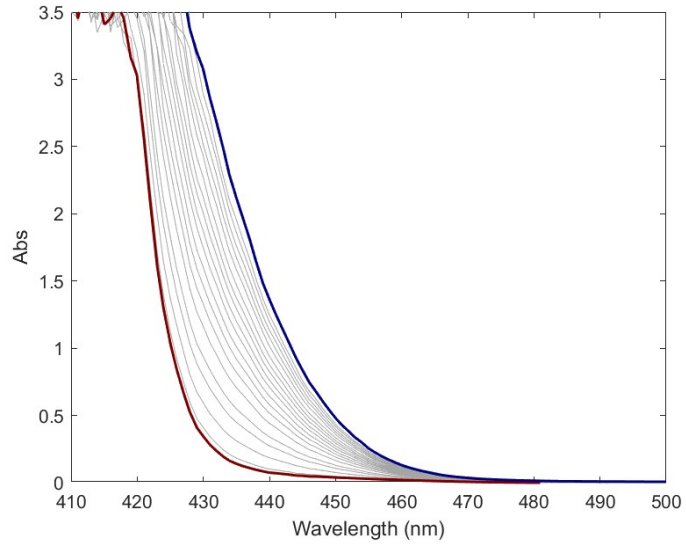

Figure E.15. Titration of $Sm(OTf)_3$ (0 to 5 mM, from red to blue trace) into a solution of HEH_2 (100 mM) in THF. Substantial red-shift observed upon titration of $Sm(OTf)_3$.

E.3.2 Sm^{II} photogeneration experiments

E.3.2.1 General procedure for Sm^{II} photogeneration experiments

A fresh 5 mM stock solution of SmI_2 in THF is prepared immediately before use. SmI_3 is prepared by titrating this 5 mM THF solution of SmI_2 with I_2 until the characteristic blue color of SmI_2 disappears.

An aliquot of the resulting SmI_3 solution (1 mL, 0.005 mmol) is added to a vial (1 mL) containing reductant (0.15 mmol, 30 equiv), and an additional 1 mL of THF, and this solution is transferred to a 1 cm path-length cuvette. 100 uL of a stock solution of photocatalyst is added to the cuvette, followed by base (0.15 mmol, 30 equiv), an additional 0.5 mL THF, and any alternative ligands (e.g., $^{n}Bu_4NBr$, BINAPO) as indicated.

E.3.2.2 General procedure for $Sm^{II}(HMPA)_4$ photogeneration experiments

For the $Sm^{II}(HMPA)^{2+}$ generation, 4 equiv HMPA was added to the isnitial SmI_2 solution prior to oxidation by I_2. The rest of the procedure was identical following E.3.2.1.

E.3.2.3 Summary of Sm^{II} photogeneration experiments

The Sm^{II} photogeneration experiments (S3.2.4) are summarized in Table E.7.

Table E.7. Summary of conditions and yields for photodriven Sm^{III} reductions. Approximate yield of Sm^{II} is determined based on the spectrum of the preparation of additive + SmI_2.

Sm^{III} + additives	**Photocat.**	**Conditions (THF and 25 °C unless otherwise specified)**	**Sm^{II} formation**
SmI_3 (2 mM)	-	HEH_2 (60 mM), Lut (60 mM), H150-Blue LED	~30%
SmI_3 (2 mM)	-	HEH_2 (60 mM), H160-440 nm LED	0%
$Sm(O^iPr)_3$ (2 mM), $^nHep_4NI$ (6 mM), HTFSI (3 mM)	-	HEH_2 (60 mM), H160-440 nm LED 40 W	~15%
$Sm(O^iPr)_3$ (2 mM), $^nHep_4NI$ (6 mM)	-	HEH_2 (60 mM), H160-440 nm LED 40 W	0%
SmI_3 (2 mM)	[Ir]PF_6 (0.2 mM)	HEH_2 (60 mM), Lut (60 mM), H160-440 nm LED 40 W	80%
SmI_3 (2 mM)	[Ir]PF_6 (0.2 mM)	HEH_2 (60 mM), H160-440 nm LED 40 W	10%
$Sm(O^iPr)_3$ (2 mM), $^nHep_4NI$ (6 mM), [LutH]TFSI (3 mM)	[Ir]PF_6 (0.2 mM)	HEH_2 (60 mM), Lut (60 mM), H160-440 nm LED 40 W	30%
SmI_3 (2 mM), $HO(CH_2)_2OH$ (2 mM)	[Ir]PF_6 (1 mM)	HEH_2 (60 mM), pyridine (60 mM), THF, 0 °C, H160-440 nm LED 40 W	15%
SmI_3 (2 mM), $MeO((CH_2)_2O)_3H$ (2 mM)	[Ir]PF_6 (1 mM)	HEH_2 (60 mM), pyridine (60 mM), THF, 0 °C,	5%
SmI_3 (2 mM), L* (2.2 mM)	[Ir]PF_6 (0.2 mM)	HEH_2 (60 mM), H160-440 nm LED 40 W	10%
SmI_3 (2 mM), $^nBu_4NBr$ (20 mM)	-	HEH_2 (60 mM), Lut (60 mM), H160-440 nm LED 40 W	0%
SmI_3 (2 mM), HMPA (8 mM)	-	HEH_2 (60 mM), Lut (60 mM), H160-440 nm LED 40 W	0%
SmI_3 (2 mM), $^nBu_4NBr$ (20 mM)	[Ir]PF_6 (0.2 mM)	Et_3N (60 mM), H160-440 nm LED 40 W	0%
SmI_3 (2 mM), HMPA (8 mM)	[Ir]PF_6 (0.2 mM)	Et_3N (60 mM), H160-440 nm LED 40 W	0%
SmI_3 (2 mM), BINAPO (2.2 mM)	[Ir]PF_6 (0.2 mM)	Et_3N (60 mM), H160-440 nm LED 40 W	0%
SmI_3 (2 mM)	3DPA2FBN (0.05 mM)	$acrH_2$ (60 mM) Et_3N (60 mM), H150-Blue LED 34 W	20%
SmI_3 (2 mM), $^nBu_4NBr$ (20 mM)	3DPA2FBN (0.05 mM)	$acrH_2$ (60 mM) Et_3N (60 mM), H160-440 nm LED 40 W	40%
SmI_3 (2 mM), HMPA (8 mM)	3DPA2FBN (0.05 mM)	$acrH_2$ (60 mM) Et_3N (60 mM), H150-Blue LED 34 W	10%
SmI_3 (2 mM), BINAPO (2.2 mM)	3DPA2FBN (0.05 mM)	$acrH_2$ (60 mM) Et_3N (60 mM), H160-440 nm LED 40 W	10%

S3.2.4 Sm^{II} photogeneration experiments

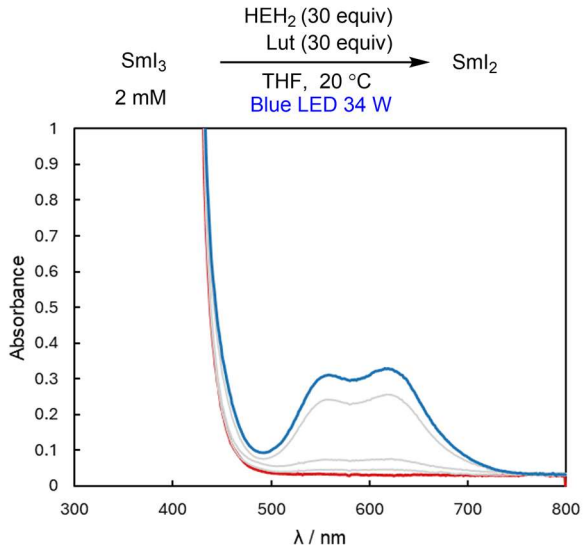

Figure E.16. Photogeneration of SmI_2 from a THF solution of SmI_3 (2 mM), HEH_2 (60 mM), and Lut (60 mM) on irradiation with H150-Blue LED; t = 0 (red trace); t =120 min (blue trace). Maximum intensity suggests about 30% conversion to SmI_2.

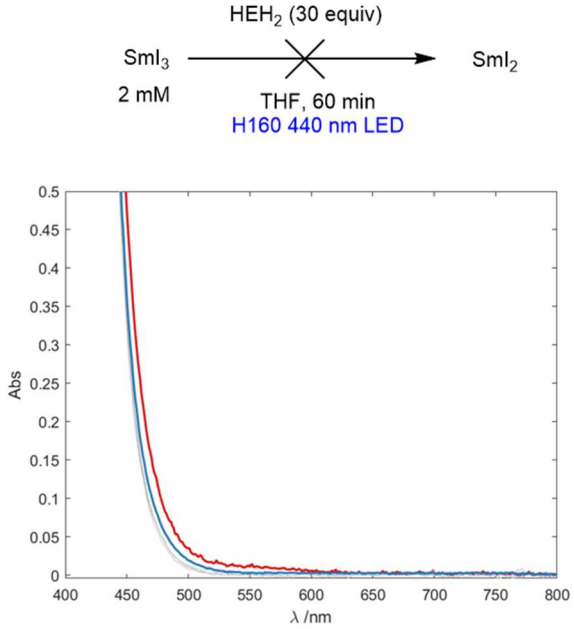

Figure E.17. Attempted photogeneration of SmI_2 from a THF solution of SmI_3 (2 mM) and HEH_2 (60 mM) on irradiation with H160-440 nm; t = 0 (red trace); t =60 min (blue trace). No SmI_2 is observed even on extended irradiation.

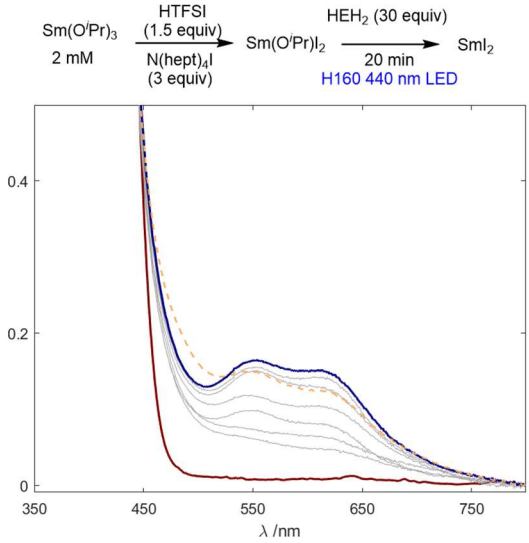

Figure E.18. Photogeneration of SmI_2 from a THF solution of $Sm(O^iPr)_3$ (2 mM), $^nHep_4NI$ (6 mM), HTFSI (3 mM), and HEH_2 (60 mM) on irradiation with H160 440 nm; t = 0 (red trace); t =20 min (lowest intensity grey trace), 80 minutes (blue trace), 180 minutes (yellow dashed trace) irradiation. Maximum intensity suggests about 15% conversion to SmI_2.

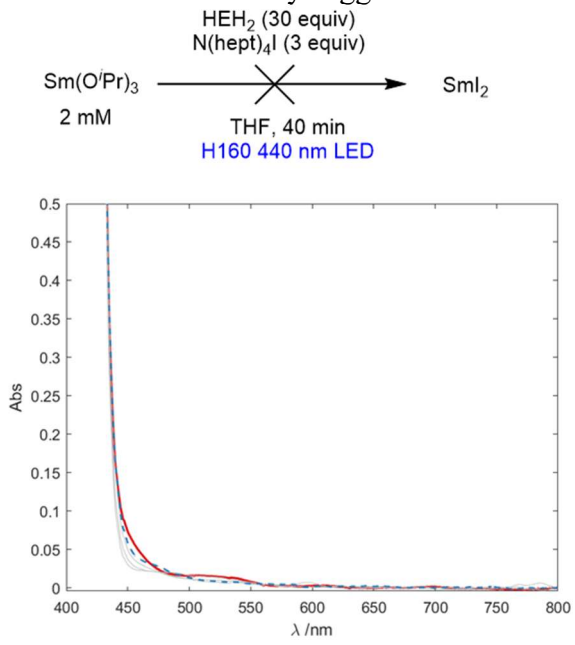

Figure E.19. Attempted photogeneration of SmI_2 from a THF solution of $Sm(O^iPr)_3$ (2 mM), $^nHep_4NI$ (6 mM), and HEH_2 (60 mM) on irradiation with H160-440 nm LED; t = 0 (red trace); t =40 min (blue dashed trace). No SmI_2 is observed even on extended irradiation.

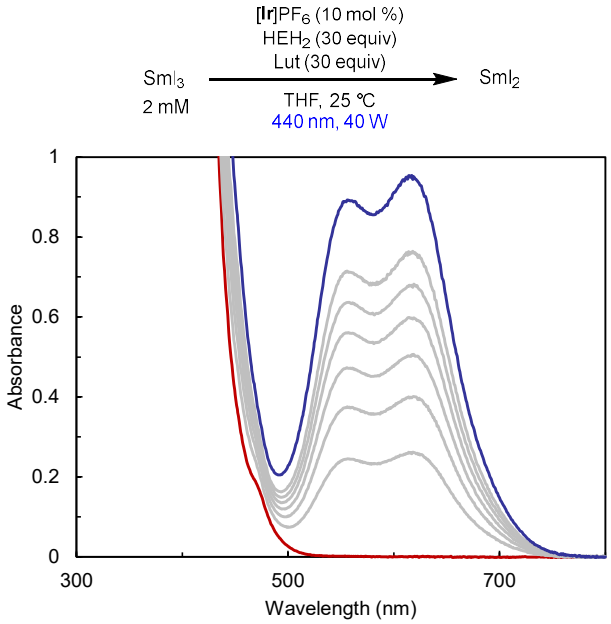

Figure E.20. Photogeneration of SmI_2 from a THF solution of SmI_3 (2 mM), HEH_2 (60 mM), and Lut (60 mM) with [Ir]PF_6 (0.2 mM) as photosensitizer on irradiation with H160-440 nm LED over t = 0 (red trace) to t = 2 min (blue trace). Maximum intensity suggests about 80% conversion to SmI_2.

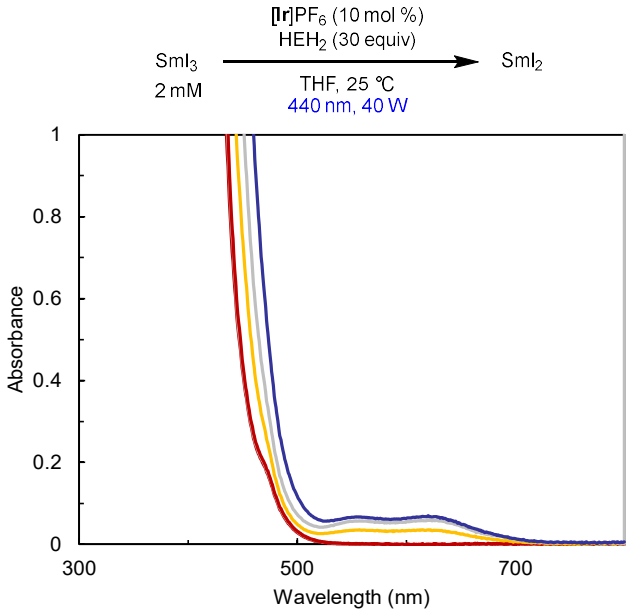

Figure E.21. Photogeneration of SmI_2 from a THF solution of SmI_3 (2 mM) and HEH_2 (60 mM) with [Ir]PF_6 (0.2 mM) as a photosensitizer in the absence of base on irradiation with H160-440 nm LED over t = 2 min (red trace), t = 6 min (yellow trace), to t = 16 min (dark blue trace). Maximum intensity suggests <10% conversion to SmI_2 over prolonged

irradiation; the absence of observed SmI_2 at 2 min (compared to 80% SmI_2 generation at the same time point in the presence of Lut) suggests that Lut accelerates SmI_2 photogeneration under these conditions.

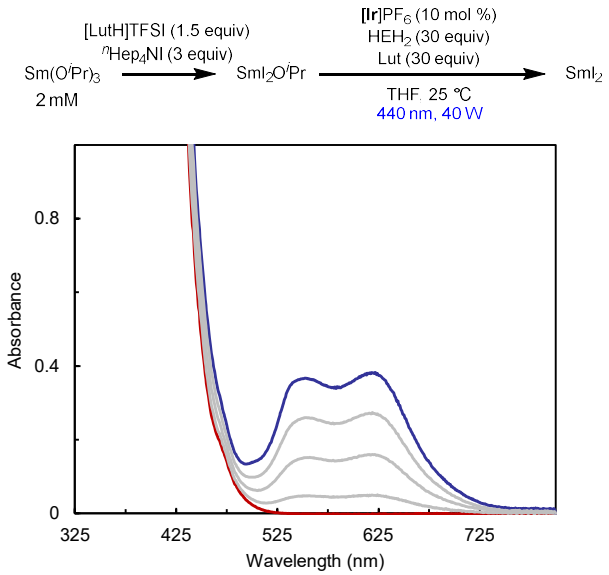

Figure E.22. Photogeneration of SmI_2 from a THF solution of $Sm(O^iPr)_3$ (2 mM), [LutH]TFSI (3 mM), $^nHep_4NI$ (6 mM), HEH_2 (60 mM), and Lut (60 mM) with $[Ir]PF_6$ (0.2 mM) as photosensitizer on irradiation with H160-440 nm LED over t = 0 (red trace) to t = 2 min (blue trace). Maximum intensity suggests ~30% conversion to SmI_2.

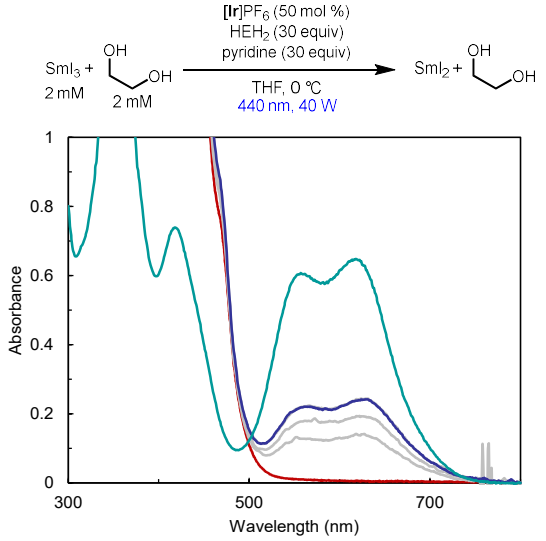

Figure E.23. Photogeneration of SmI_2 in the presence of ethylene glycol (2mM) from a THF solution of SmI_3 (2 mM), HEH_2 (60 mM), and pyridine (60 mM) with [Ir]PF_6 (1 mM) as photosensitizer on irradiation with H160-440 nm LED over t = 0 (red trace) to t = 2 min (dark blue trace). The Sm^{II} species that is generated has absorption maxima consistent with those of SmI_2 (1 mM) in the presence of ethylene glycol (1 mM) in THF (teal trace). Maximum intensity suggests ~15% steady state population of Sm^{II} under irradiation.

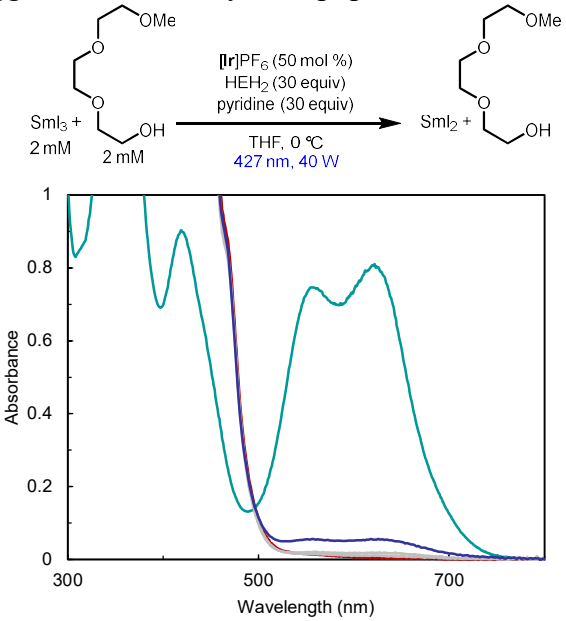

Figure E.24. Photogeneration of SmI_2 in the presence of $MeO((CH_2)_2O)_3H$ (2mM) from a THF solution of SmI_3 (2 mM), HEH_2 (60 mM), and pyridine (60 mM) with [Ir]PF_6 (1 mM) as photosensitizer on irradiation with H160-427 nm LED over t = 0 (red trace) to t = 30 min (dark blue trace). The Sm^{II} species that is generated has absorption maxima consistent

with those of SmI_2 (1 mM) in the presence of $MeO((CH_2)_2O)_3H$ (1 mM) in THF (teal trace). Maximum intensity suggests ~5% steady state population of Sm^{II} under irradiation.

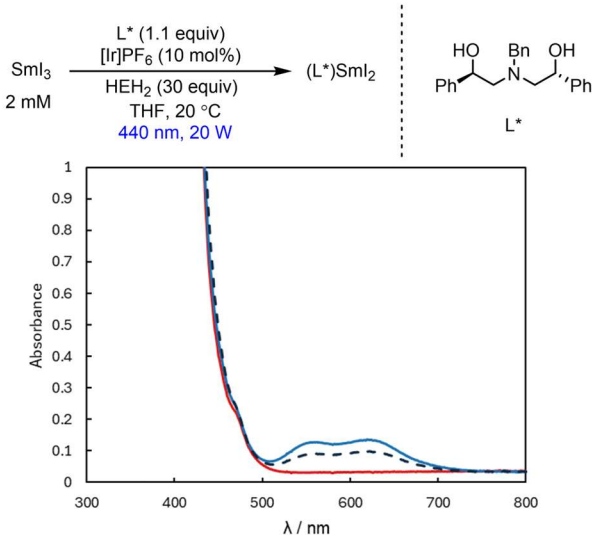

Figure E.25. Photogeneration and decay of SmI_2 from THF solution of SmI_3 (2 mM), L*(2.2 mM), $[Ir]PF_6$ (0.2 mM), HEH_2 (60 mM) on irradiation with H160-440 nm LED; t = 0 (red); t = 1 min (blue trace); t = 60 min (dashed). Maximum intensity suggests about 10% conversion to Sm^{II}. Note: the visible features of SmI_2 are unchanged in the presence of up to 2 equiv of L*, thus we are unable to assign the exact speciation of Sm(II) formed.

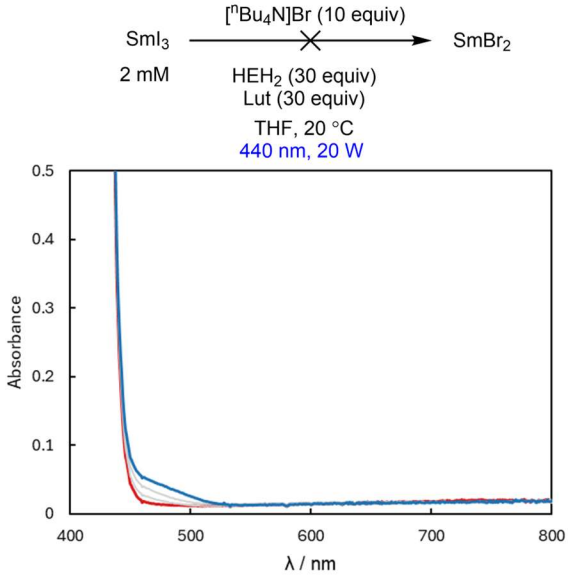

Figure E.26. Attempted photogeneration of $SmBr_2$ from a THF solution of SmI_3 (2 mM), $^{n}Bu_4NBr$ (20 mM), HEH_2 (60 mM), and Lut (60 mM) on irradiation with H160-440 nm LED; t = 0 (red trace); t = 60 min (blue trace). No $SmBr_2$ is observed.

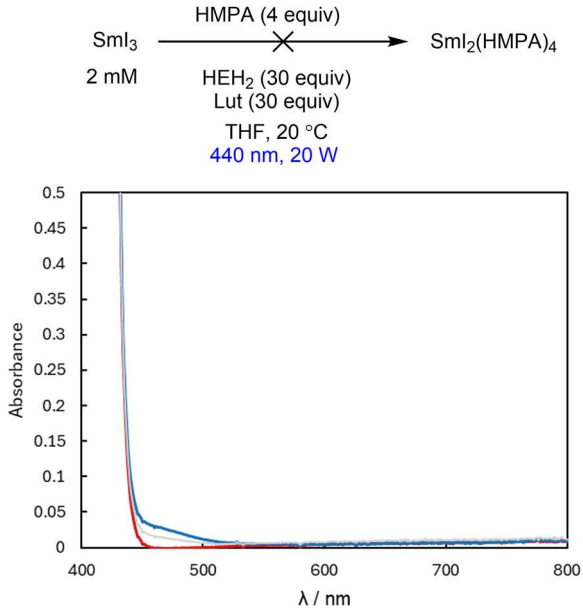

Figure E.27. Attempted photogeneration of $Sm(HMPA)_4^{2+}$ from a THF solution of SmI_3 (2 mM), HMPA (8 mM), HEH_2 (60 mM), and Lut (60 mM) on irradiation with H160-440 nm LED; t = 0 (red trace); t = 60 min (blue trace). No $Sm(HMPA)_4^{2+}$ is observed.

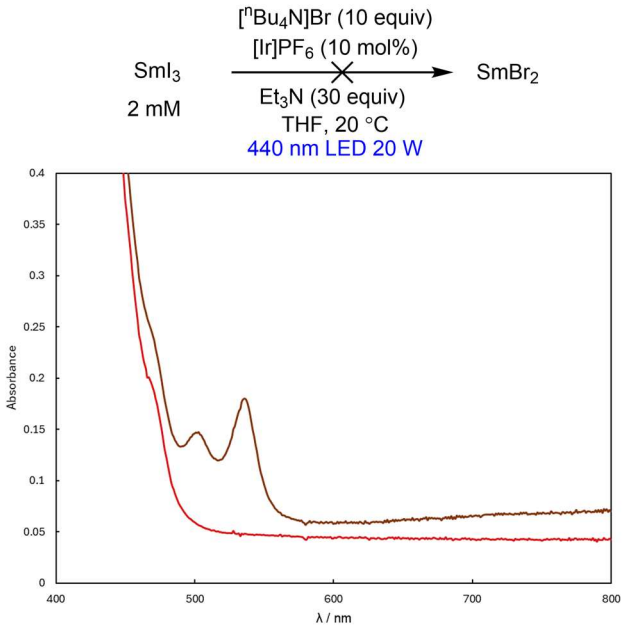

Figure E.28. Attempted photogeneration of $SmBr_2$ from a THF solution of SmI_3 (2 mM), $^{n}Bu_4NBr$ (20 mM), $[Ir(ppy)_2(dtbbpy)]PF_6$ (0.2 mM), and Et_3N (60 mM) on irradiation with H160-440 nm LED; t = 0 (red trace); t = 20 min (brown trace) shows formation of $[Ir^{II}(ppy)_2(dtbbpy)]$.[7] No $SmBr_2$ is observed.

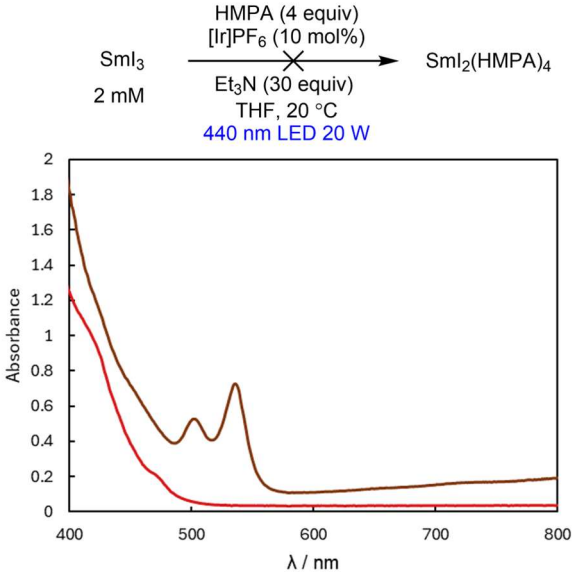

Figure E.29. Attempted photogeneration of $Sm(HMPA)_4^{2+}$ from a THF solution of SmI_3 (2 mM), HMPA (8 mM), $[Ir(ppy)_2(dtbbpy)]PF_6$ (0.2 mM), and Et_3N (60 mM) on irradiation

with H160-440 nm LED; t = 0 (red trace); t = 20 min (brown trace) shows formation of $[Ir^{II}(ppy)_2(dtbbpy)]$.[7] No $Sm(HMPA)_4^{2+}$ is observed.

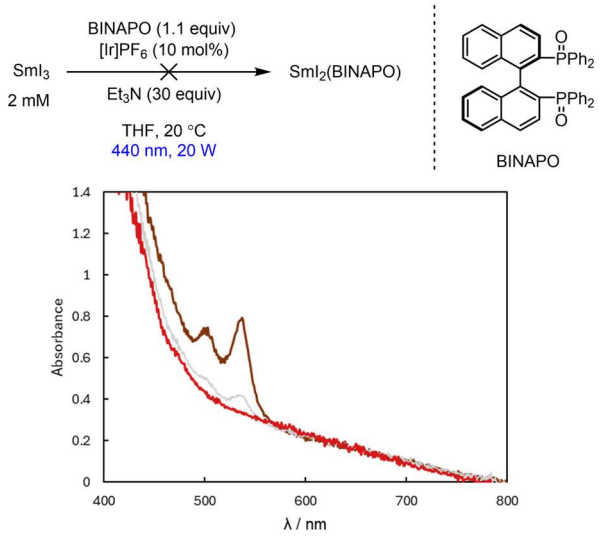

Figure E.30. Attempted photogeneration of $Sm(BINAPO)I_2$ from a THF solution of SmI_3 (2 mM), BINAPO (2.2 mM), $[Ir(ppy)_2(dtbbpy)]PF_6$ (0.2 mM), and Et_3N (60 mM) on irradiation with H160-440 nm LED; t = 0 (red trace); t = 20 min (brown trace) shows formation of $[Ir^{II}(ppy)_2(dtbbpy)]$.[7] No $Sm(BINAPO)I_2$ is observed.
Note: white solids precipitate from the solution, leading to poor transmission.

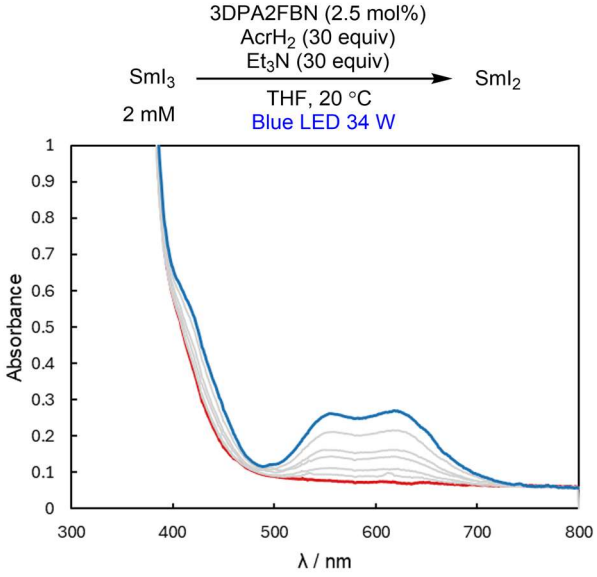

Figure E.31. Photogeneration of SmI_2 from a THF solution of SmI_3 (2 mM), 3DPA2FBN (0.05 mM), $AcrH_2$ (60 mM), and Et_3N (60 mM) on irradiation with H150-Blue LED; t = 0

(red trace); t =95 min (blue trace). Maximum intensity suggests about 20% conversion to SmI_2.

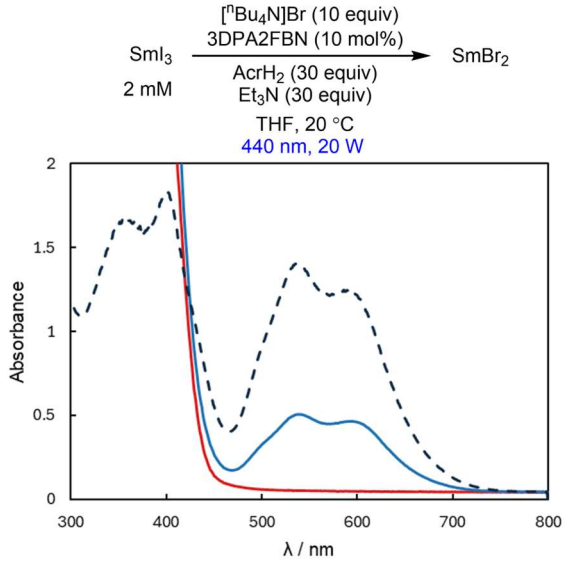

Figure E.32. Photogeneration of $SmBr_2$ from THF solution of SmI_3 (2 mM), $^nBu_4NBr$ (20 mM), 3DPA2FBN (0.2 mM), $AcrH_2$ (60 mM), and Et_3N (60 mM) on irradiation with H160-440 nm LED; t = 0 (red trace); t =1 min (blue trace); reference spectrum of 2 mM $SmBr_2$ (dashed trace). Maximum intensity (λ_{max} 588 nm and 540 nm) suggests about 40% conversion to $SmBr_2$.

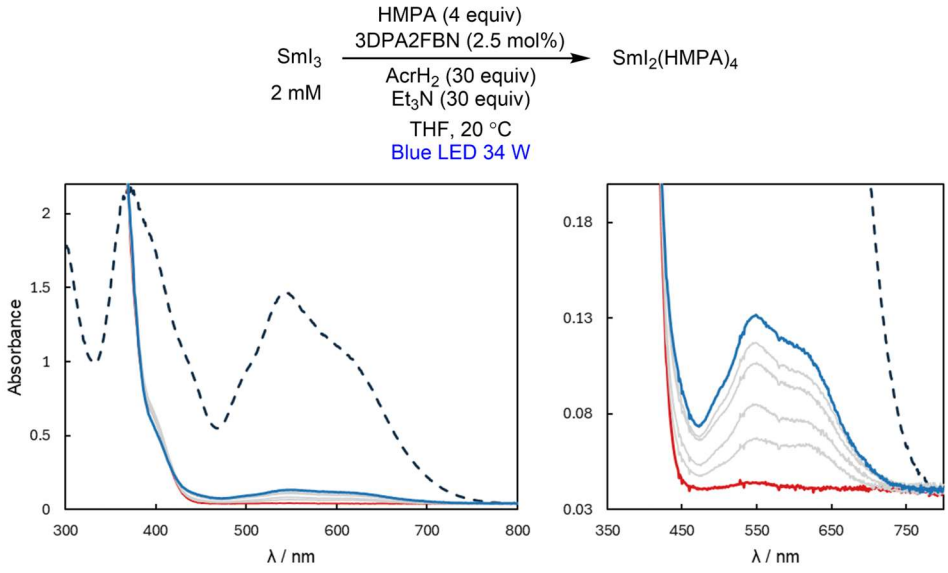

Figure E.33. Photogeneration of $SmI_2(HMPA)_4$ from THF solution of SmI_3 (2 mM), HMPA (8 mM), 3DPA2FBN (0.05 mM), $AcrH_2$ (60 mM), and Et_3N (60 mM) on irradiation

with H150-Blue LED; t = 0 (red); t = 60 min (blue). Rightmost plot shows magnified region of relevant Sm(II) absorbance. Maximum intensity (λ_{max} 540 nm) suggests about 10% conversion to $Sm(HMPA)_4I_2$.

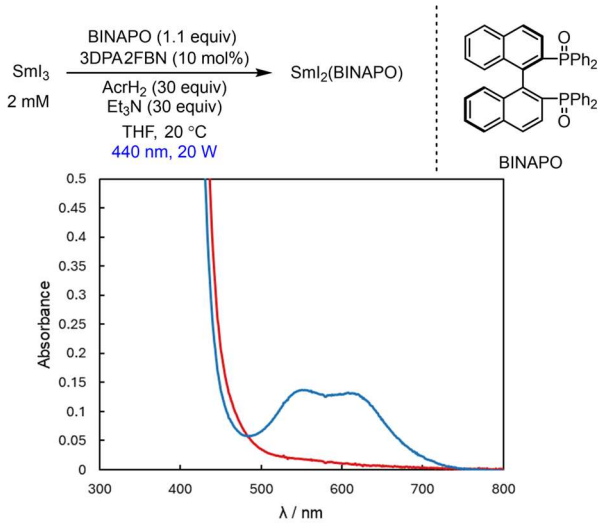

Figure E.34. Photogeneration of $Sm(BINAPO)I_2$ from THF solution of SmI_3 (2 mM), BINAPO (2.3 mM), 3DPA2FBN (0.2 mM), $AcrH_2$ (60 mM), and Et_3N (60 mM) on irradiation with H160-440 nm LED; t = 0 (red); t = 2 min (blue). Maximum intensity (λ_{max} = 550 nm and 608 nm) suggests about 10% conversion to $Sm(BINAPO)I_2$.

E.4 Electrochemical measurements

Comment on $Sm^{III/II}$ reduction potentials: The solution-phase speciation of SmX_n is ill-defined and highly dependent on the concentration of both Sm and potential ligands. As a result, rigorous definition of $Sm^{III/II}$ redox potentials for discrete species is nontrivial. Cyclic voltammetry of SmI_3 in THF is illustrative of this issue. As shown in Figure E.35, the observed $E_{1/2}$ of the reversible $Sm^{III/II}$ couple of $SmI_3(THF)_n$ (using a tetraalkylammonium triflimide salt as a relatively innocent supporting electrolyte) shifts negative by 59 mV per decade increase in ^{n}Hep$_4$NI concentration. This behavior is consistent with reversible dissociation of I^- upon reduction, with the position of the wave described by the Nernst eqn E.1:

$$E_{1/2} = E° - \frac{RT}{F} \ln([I^-]) \text{ (eqn E.1).}$$

The standard potential $E°(SmI_3/SmI_2 + I^-)$, which can be extrapolated from the intercept of a plot of $E_{1/2}$ vs $-\log[I^-]$ as −1.58 V vs $Fc^{+/0}$, is therefore only equivalent to the $E_{1/2}$ observed by CV if $[I^-] = 1$ M.

Despite this challenge, knowledge of the electrochemical properties of Sm species in the presence of various additives is useful in guiding selection of appropriate photoreductants and photoredox catalysts for Sm^{III} reduction. For the purpose of this study, we have collected CV data under a unified set of conditions, using concentrations of Sm and additives relevant to the UV-Vis studies of Sm^{II} generation. It should be emphasized, however, that the observed reduction potentials in these specific cocktails must not be treated as diagnostic standard reduction potentials for discrete $Sm^{II}L_n$ species.

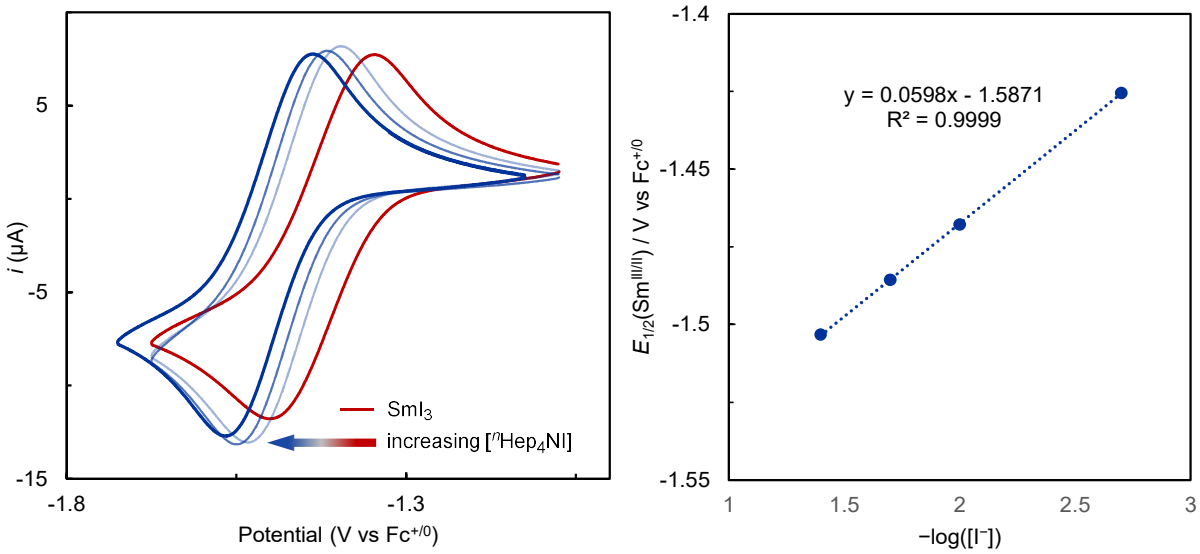

Figure E.35. Left: CVs of SmI_3 (2 mM) in the presence of 0-40 mM ^{n}Hep$_4$NI (red-dark blue traces) in THF containing 0.1 M BMPipTFSI at 25 mV s^{-1}. Right: plot of $E_{1/2}$ values from each CV vs $-\log([I^-])$.

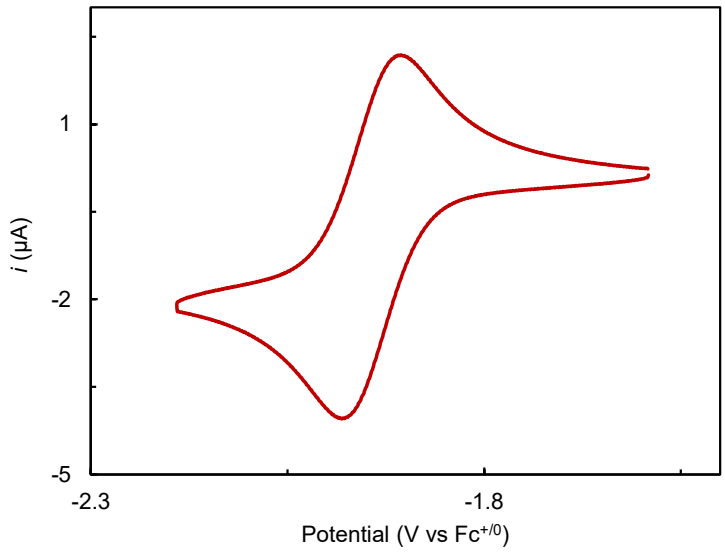

Figure E.36. CV of [Ir]PF_6 (0.5 mM) in THF containing 0.1 M BMPipTFSI at 25 mV s^{-1}.

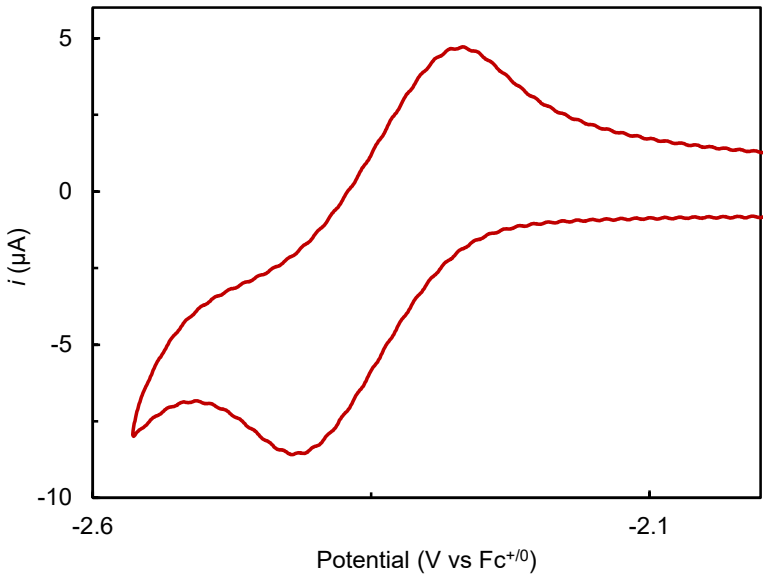

Figure E.37. CV of 3DPA2FBN (1 mM) in THF containing 0.1 M BMPipTFSI at 100 mV s^{-1}.

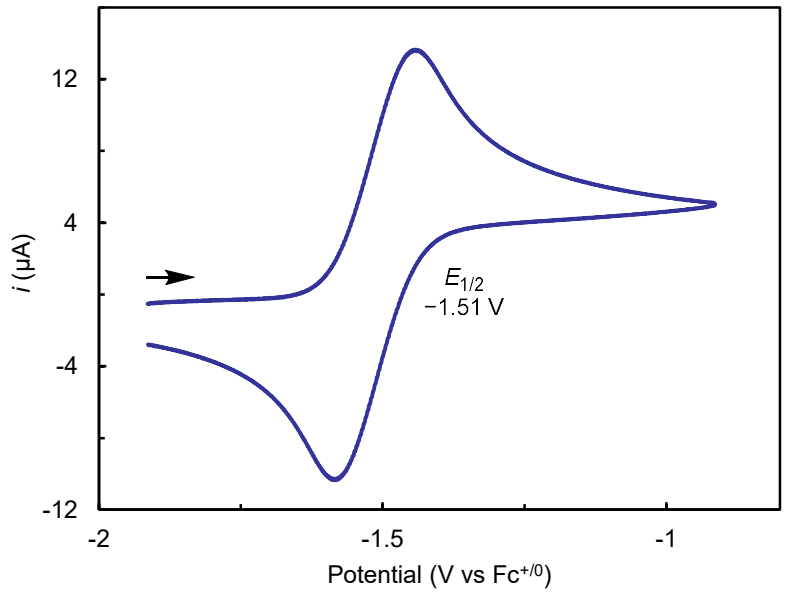

Figure E.38. CV of SmI_2 (2 mM) and $^{n}Hep_4NI$ (10 mM) in THF containing 0.1 M BMPipTFSI at 25 mV s^{-1}.

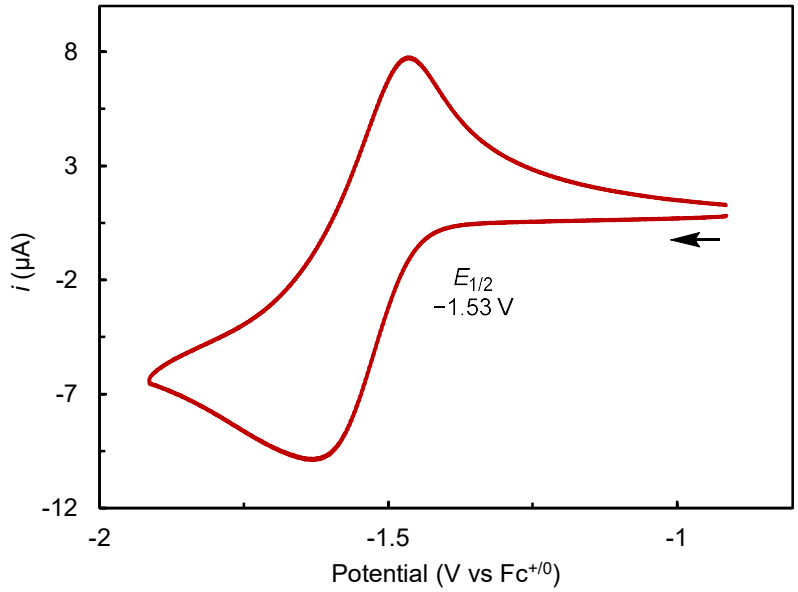

Figure E.39. CV of SmI_3 (2 mM), $^{n}Hep_4NI$ (10 mM), and ethylene glycol (2 mM) in THF containing 0.1 M BMPipTFSI at 25 mV s^{-1}.

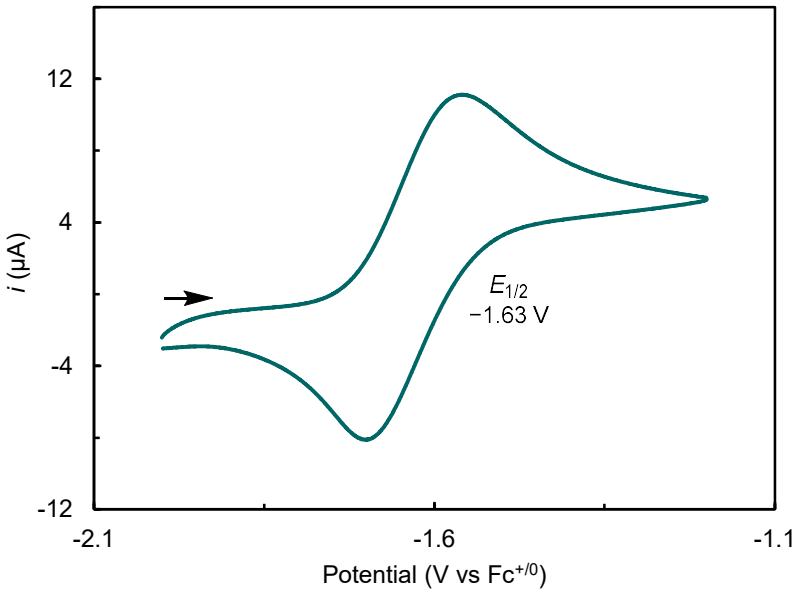

Figure E.40. CV of SmI_2 (2 mM), $^{n}Hep_4NI$ (10 mM), and $MeO((CH_2)_2O)_3H$ (2 mM) in THF containing 0.1 M BMPipTFSI at 25 mV s^{-1}.

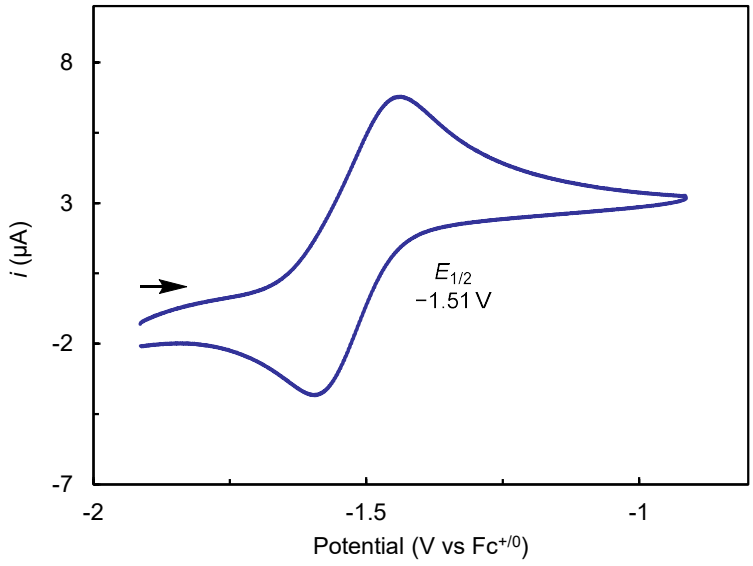

Figure E.41. CV of SmI_2 (2 mM), $^{n}Hep_4NI$ (10 mM), and 3-aza-3-benzyl-1(R),5,(R)-dihydroxy-1,5-diphenylpentane (2 mM) in THF containing 0.1 M BMPipTFSI at 25 mV s^{-1}.

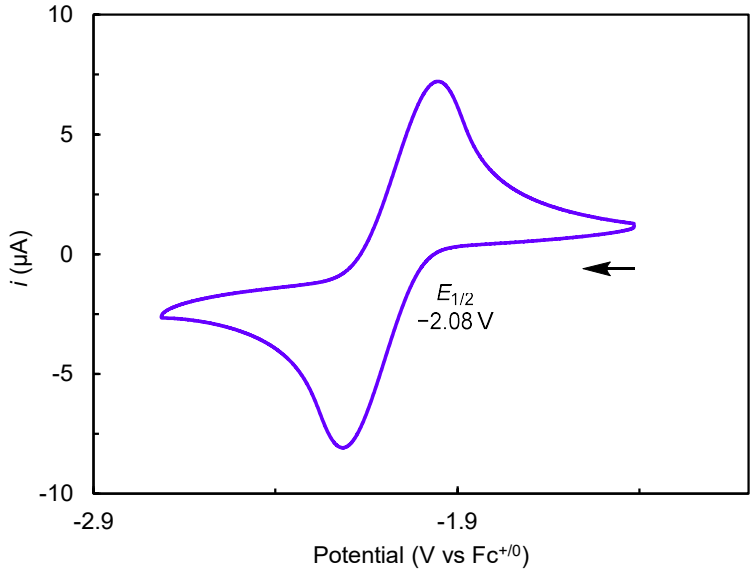

Figure E.42. CV of SmI_3 (2 mM) and $^{n}Bu_4NBr$ (20 mM) in THF containing 0.1 M BMPipTFSI at 25 mV s^{-1}.

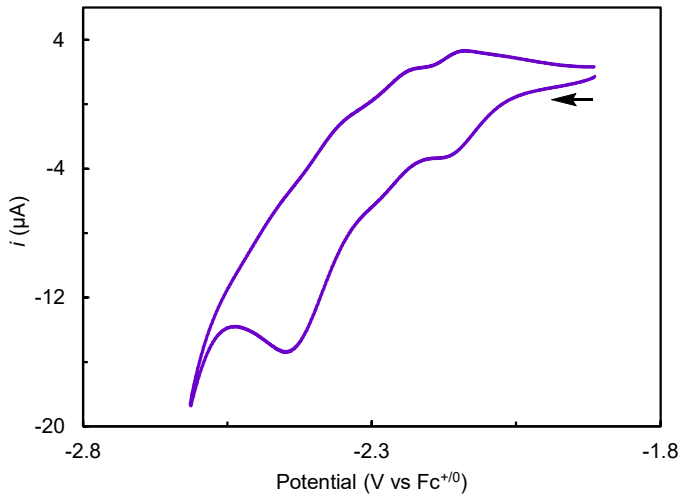

Figure E.43. CV of SmI_2 (2 mM), $^{n}Hep_4NI$ (10 mM), and BINAPO (2 mM) in THF containing 0.1 M BMPipTFSI at 25 mV s^{-1}. The speciation of this mixture is clearly complex. However, the observation that the more reducing photocatalyst 3DPA2FBN is

required to generate Sm^{II} species in the presence of BINAPO is consistent with the observation of $Sm^{III/II}$ redox waves negative of −2 V.

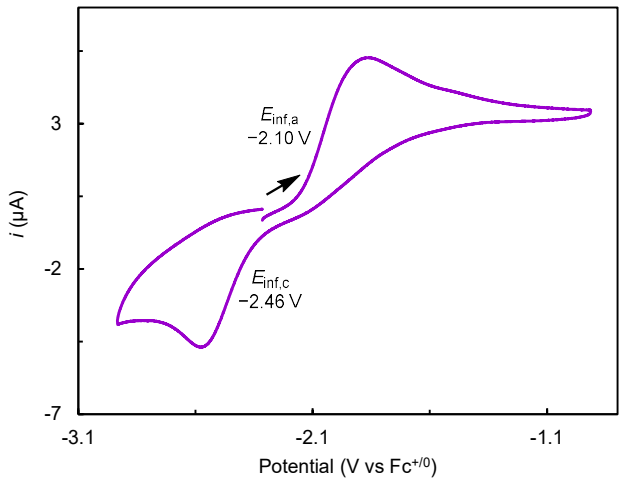

Figure E.44. CV of SmI_2 (2 mM) and HMPA (8 mM) in THF containing 0.1 M BMPipTFSI at 25 mV s^{-1}.

E.5 Additional mechanistic schemes

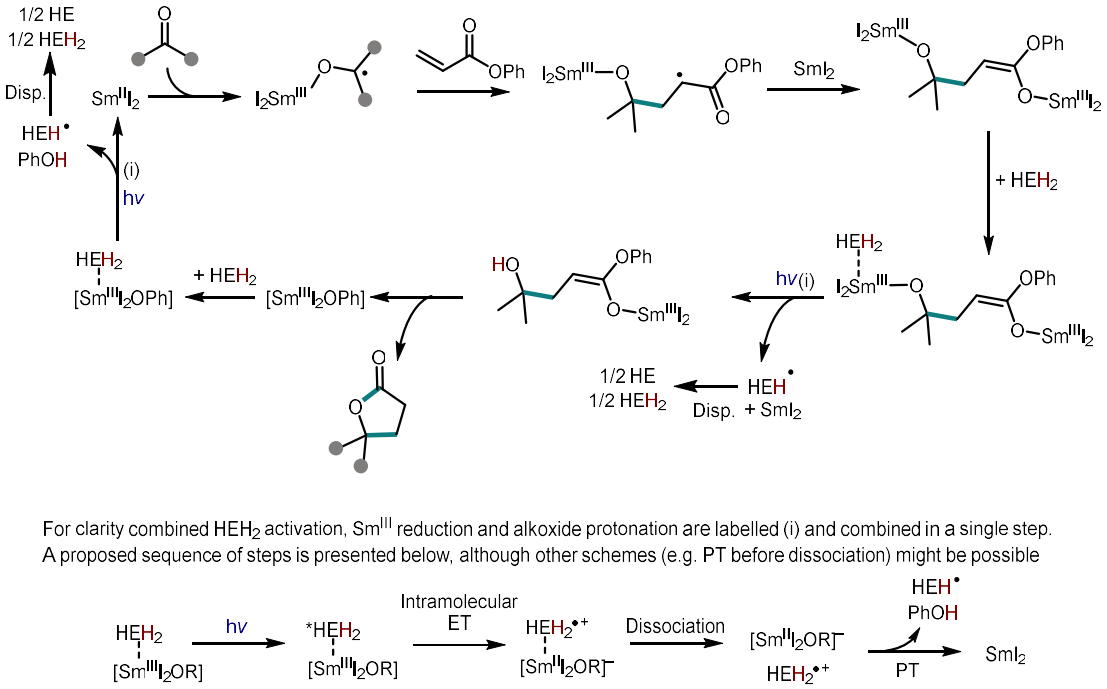

Figure E.45. An alternative scheme for catalytic ketone-acrylate coupling reaction where HEH• does not terminate radical and two equivalents of SmI_2 are required per reduction.

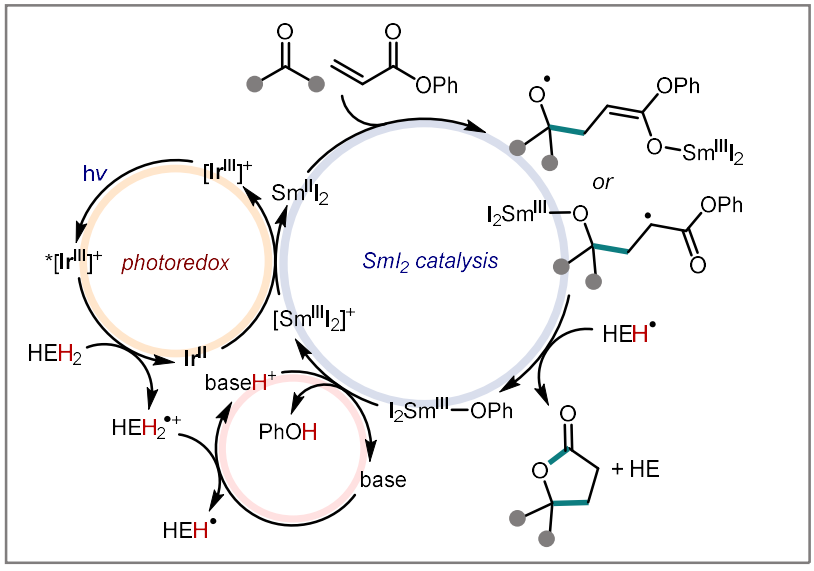

Figure E.46. A scheme for catalytic ketone-acrylate coupling reaction with $[Ir]^+$. Sm^{III}-OPh is regenerated as depicted in Figure 6.3B in chapter 6.

E.6 References for Appendix E

1. Watson, P. L.; Tulip, T. H.; Williams, I. *Organometallics* **1990**. 9, 1999–2009.
2. Matesic, L.; Locke, J. M.; Vine, K. L.; Ranson, M.; Bremner, J. B.; Skropeta, D. *Tetrahedron* **2012**. 68, 6810–6819.
3. Seki, T.; McEleney, K.; Crudden, C. M. *Chem. Commun.* **2012**. 48, 6369–6371.
4. Evans, D. A.; Nelson, S. G.; Gagne, M. R.; Muci, A. R. *J. Am. Chem. Soc.* **1993**. 115, 9800–9801.
5. Boyd, E. A.; Shin, C.; Charboneau, D. J.; Peters, J. C.; Reisman, S. E. *Science* **2024**. 385, 837-843.
6. Norcross, B. E.; Clement, G.; Weinstein, M. *J. Chem. Educ.* **1969**. 46, 694.
7. Baek, Y.; Reinhold, A.; Tian, L.; Jeffrey, P. D.; Scholes, G. D.; Knowles, R. R. *J. Am. Chem. Soc.* **2023**. 145, 12499–12508.